



GEM<sup>4</sup> 2006 Summer School:  
Cell and Molecular Mechanics in BioMedicine

## Laboratory Sessions August 9-11, 2006

Massachusetts Institute of Technology  
Cambridge, MA

<http://www.openwetware.org/wiki/GEM4labs>

# Lab 1: Tissue biomechanics and mechanobiology

**Location:** NE47-365H

**PI:** Alan Grodzinsky

**Lab Instructors:** Eliot Frank, Diana Chai

## Summary

- Mechanical testing of cartilage under static and dynamic compression and shear. We will demonstrate the use of plugs of bovine tissue run through a series of tests in the apparatus.
- Demonstrations of incubator-housed bioreactors for application of dynamic compression and shear to cartilage specimens, and the various cell- and molecular-biological outcome measures that are used to assess mechanotransduction mechanisms in cells in their native dense extracellular matrix environment.

## Recommended Reading

J. Kisiday, A. Kerin and A. Grodzinsky, "Mechanical Testing of Cell-Material Constructs," from *Methods in Molecular Biology*, ed. A. P. Hollander and P. V. Hatton, Humana Press, 2004.

C. Wheeler, *et al.*, "Cartilage mechanobiology: the response of chondrocytes to mechanical force," *Cur. Opin. Orthop.* **16**.

<http://www.openwetware.org/wiki/GEM4labs>



## Mechanical Testing of Cell-Material Constructs

*A Review*

John Kisiday, Alex Kerin, and Alan Grodzinsky

### 1. Introduction

The exponential growth in basic research and clinical trials involving tissue-engineered materials has generated a corresponding need for the evaluation of the material properties and functional performance of these constructs during development and/or after implantation. Applications focusing on musculoskeletal tissues, in particular, require detailed assessment of the biomechanical properties of neo-tissue constructs *in vitro* and *in vivo* (1). Based on the known properties of normal tissues, investigators have identified a range of biological, biochemical, and biophysical end-point parameters that must be quantified to determine the potential for success of a particular tissue-engineering methodology. Such end-point assessment is critical to our understanding of the basic scientific approaches underlying tissue engineering. In addition, biomechanical assessment is crucial for the implementation of regulatory processes that are coupled to clinical practice.

When creating musculoskeletal tissue constructs, it is important to determine whether the constructs are capable of withstanding the forces associated with locomotion *in vivo*, and whether construct properties compare to the corresponding native tissue (1,2). In some instances, it is required that the construct should be bioabsorbable, and measurement of material properties may help to quantify the mechanisms and kinetics of biodegradability. For tissue-engineering approaches in which cells must re-synthesize a functional extracellular matrix (ECM) within a scaffold, the mechanical properties of the construct will indicate whether the native structure is being replicated (3). The ability to quantify the intrinsic mechanical properties of tissue constructs is

also necessary to compare alternative techniques used to synthesize specific tissues and to compare approaches used by different research groups. Finally, the ability to monitor the mechanical properties of implanted constructs *in situ* can help to evaluate the degree of successful repair of injured or diseased tissues and organs (4).

### **1.1. Native Tissue Properties Motivate Construct Evaluation**

Musculoskeletal tissues are composed of cells surrounded by a porous, hydrated ECM (including a mineralized phase in the case of hard tissues). Biomechanical characterization of such tissues must reflect a variety of material properties, including the equilibrium behavior of the ECM and the time-dependent viscoelastic and poroelastic behavior of the tissue following deformation. For example, articular cartilage is often modeled as a poroelastic or biphasic material (5,6) with a porous solid phase and mobile interstitial fluid containing ionic (7) and other solutes. The mechanical properties are dependent on the behavior of the solid phase—which may be modeled as intrinsically elastic or viscoelastic (8)—as well as fluid–solid interactions that may accompany tissue deformation, limited by matrix porosity and electrical charge effects (6,7). These fluid–solid interactions give the tissue increased stiffness to loads that occur at higher rates (higher frequencies) (9), a property that is critical to functional behavior *in vivo*. Therefore, investigators who study the biomechanical behavior of tissue-engineered cartilage constructs look to these cartilage-like properties as hallmarks of the potential for success upon implantation (10–12).

### **1.2. Characterization of Constructs In Vitro**

Cell-seeded constructs for tendon, ligament, meniscus, cartilage, and bone are being studied with the use of a variety of cell sources (e.g., primary cells, cell lines, stem cells) cultured in natural and synthetic scaffold materials (13–15). Motivated by the tissue type and desired properties, methodologies have been developed to quantify construct properties in compression (confined and unconfined), tension, and shear. Although destructive non-sterile measurement techniques can be used to advantage, several incubator-housed testing instruments have recently been developed. Such devices enable the investigator to measure the time-dependent evolution of living construct material properties over a period of days, weeks, or even months in culture. These instruments can also be used for mechanical stimulation of cell-seeded constructs as a means of improving the functional mechanical properties of the end product.

### **1.3. Characterization of Repair Tissue In Situ**

The use of tissue engineered constructs for musculoskeletal applications *in vivo* has necessitated the development of methods for quantifying the func-

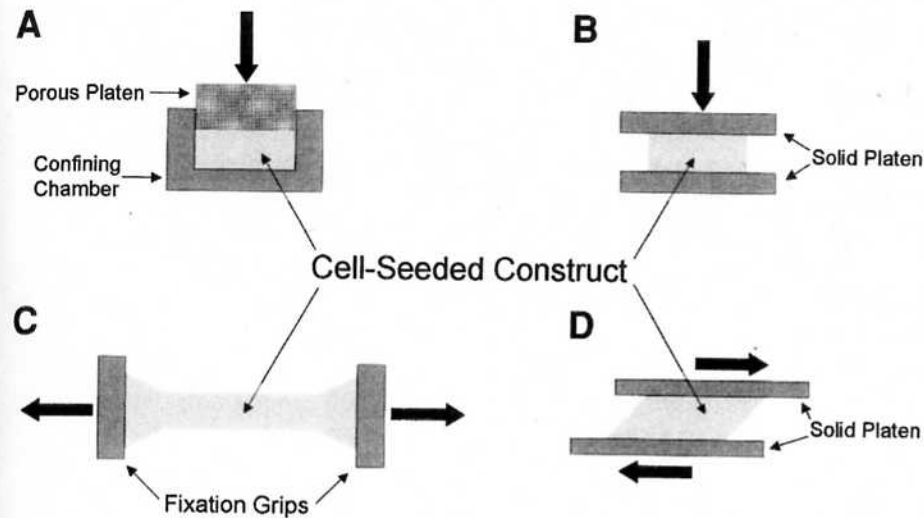


Fig. 1. Four testing configurations for measurement of intrinsic material properties of tissue-engineered constructs and cellular deformation in vitro: (A) Uniaxial confined compression. (B) Uniaxial unconfined compression. (C) Tension. (D) Shear.

tional biomechanical properties of the resulting implants as repair or unwanted degeneration ensues. After implantation into animals, it is often desirable to compare the properties of the repair tissue to those of adjacent normal tissue. Histological examination can provide valuable, qualitative information regarding the biochemical composition of the implant and tissue integration into the host. Non-destructive imaging modalities such as magnetic resonance imaging (MRI) can also provide compositional data during stages of construct development in vivo. However, it is extremely useful to have direct quantitative measurements of the biomechanical properties of the repair tissue that cannot yet be obtained by other modalities. Several new devices are now under various stages of development for direct *in situ* measurement of material properties, as summarized here.

## 2. Overview of In Vitro Biomechanical Evaluation

Upon implantation, tissue engineered constructs may be subjected to a complex physical environment. The objective of biomechanical testing in vitro is not to directly mimic *in situ* loading. Instead, mechanical tests utilizing compression, tension, or shear loading (Fig. 1) may be conducted (2) to establish the baseline intrinsic material properties of the construct (e.g., Table 1 for cartilage). These values may be compared to those of native tissues to estimate whether the construct is suitable for implantation. The material properties of

**Table 1**  
**Mechanical Properties of Acellular and Chondrocyte-Seeded Constructs**

Scaffold	Test mode	Time in culture	Modulus
Collagen-GAG Sponge (22)	Unconfined compression (equilibrium)	Acellular Type I Collagen Acellular Type II Collagen	145–730 Pa 730 Pa
Chondrocyte-seeded Agarose (3)	Confined compression (equilibrium)	0 d 70 d	20 kPa 150 kPa
Chondrocyte-seeded PGA (20,21,30)	Confined compression (equilibrium)	6 wk 7 mo	52 kPa 930 kPa
	Dynamic shear (frequency - 1 Hz)	7 d 56 d	0.8 kPa 15 kPa
PVA hydrogel (25)	Unconfined compression, (transient strain rate - 1000%/min)	Acellular	1 MPa @ 10% strain 18 MPa @ 60% strain
	Shear (transient strain rate - 75%/min)		100 MPa @ 10% strain 450 MPa @ 60% strain
Scaffold-free monolayer (28)	Tension (transient strain rate - 12%/min)	8 wk	1.3 MPa

Values are summarized for examples of compressive, tensile, and shear testing in both equilibrium and dynamic modes.

various constructs may also be compared to evaluate the relative advantages of a particular scaffold material (*see Note 1*).

### **2.1. Equilibrium Biomechanical Properties**

The equilibrium stress-strain behavior of constructs is determined by measuring the stress (load normalized to construct cross-sectional area) in response to an applied strain (change in tissue dimension normalized to the original dimension), or vice versa. Equilibrium properties may be evaluated by applying very slow ramps of load or displacement (e.g., at a low strain rate). Alternatively, a series of small increments in load (*or displacement*) may be applied, and the final steady-state displacement (*load*) attained after creep (*stress relaxation*) is used to compute the equilibrium stress-strain behavior. This stress-strain plot is used to calculate the equilibrium modulus. The simplicity of this testing protocol allows for measurements to be made using a simple-load cell and displacement system.

Constructs may exhibit an elastic region in which scaffold geometry is completely restored upon unloading. Native biological tissues are likely to be inhomogeneous and anisotropic, and may exhibit highly nonlinear stress-strain behavior. The initial deformation of tendons, for example, results in nonlinear increases in stress, the so-called “toe” region. The equilibrium stress-strain behavior beyond this toe region may be approximately linear, and is of interest in defining an equilibrium elastic modulus of the tissue—the slope of the linear stress/strain plot (*16*). Similar behavior may be expected from cell-seeded constructs, although construct properties may be initially more homogeneous if cells are evenly seeded throughout the scaffold, especially at early stages of matrix deposition.

### **2.2. Dynamic Biomechanical Properties**

Dynamic biomechanical measurements are important in characterizing construct response to periodic loading environments, such as that experienced by musculoskeletal tissues during locomotion. Thus, the rate or frequency of testing is motivated by physiological loading rates. The complex nature of dynamic testing requires more sophisticated instruments capable of feedback control of applied displacement or load. Sinusoidal, saw-tooth, pulse-like, or other waveforms are often used. Because of the poroelastic and viscoelastic properties of cell-seeded constructs, dynamic properties will depend on specimen geometry and testing conditions. In particular, dynamic properties are expected to depend on strain rate or frequency (*6*). Rapid deformation also creates a proportional increase in hydrostatic pressure within a fluid-filled cell-seeded construct. In addition, the viscoelastic relaxation properties of the ECM are limited by rapid deformation, thereby increasing material stiffness. Test sample geometry may

also complicate the measurement of biomechanical properties. Cell-seeded constructs are often limited in size. As a result, clamping of the construct by the testing grips of the instrument can cause nonuniform strain distributions within the sample. Gardiner et al. (17) demonstrates an example of the effects of sample geometry on shear properties. Guidelines for optimal sample geometry are available from the American Society for Testing and Materials (ASTM).

### **2.3. Failure Testing**

In addition to evaluating constructs in a non-destructive manner, failure testing may be used to identify the maximum load or strain that the construct may endure. For example, the strain at which a construct undergoes permanent deformation, and will not return to the original geometry upon unloading, is known as the yield strain, and the accompanying stress, the yield stress (or strength). Constructs tested in tension or shear may be deformed to the point when macroscopic fractures occur (16), corresponding to the ultimate stress (or strength). Compressive ultimate strength testing is possible, but it is sometimes difficult to define failure, especially in softer tissues. Failure properties may be compared to the mechanical environment encountered in vivo in order to predict the structural stability of the implant.

Determining which failure parameter is the most relevant depends on the expected loading as well as the tissue surrounding the construct. For example, implantation of constructs into focal defects in articular cartilage can create an interface between native and construct materials with very different compressive stiffness. Without adequate integration at the interface, joint loading forces (18) can lead to failure at the interface, a very challenging problem for cartilage tissue engineering. Similarly, implantation of constructs for bone regeneration that occupy the entire cross-section of the bone must support total structural loading. Variation in construct strain can be predicted from applied stress. Construct failure analysis is based on the understanding of subfailure and failure properties of the material, utilizing the testing configurations outlined here.

## **3. In Vitro Biomechanical Methods**

### **3.1. Confined and Unconfined Compression**

Specimen geometry for compression testing (*see Notes 2–4*) is typically cylindrical disk or slab structures, with parallel surfaces to ensure even load distribution. Compressive testing is performed with samples held in a radially unconfined or confined geometry. In unconfined compression (**Fig. 1B**), samples are allowed to freely expand radially during uniaxial compression (*see Note 5*). Under ideal conditions, the slope of the measured equilibrium stress/

strain curve in the linear region gives the equilibrium compressive Young's modulus,  $E$ , of the construct. Specimen geometry is limited to a range of aspect ratios of sample height/width to prevent testing artifacts such as buckling.

Confined compression (**Fig. 1A**) requires specimens to be tested in a tight-fitting chamber to prevent any radial expansion. Typically, the specimen is compressed by a porous platen to allow free draining of the construct fluid at the platen-construct interface during compression (*see Notes 6,7*). Both the equilibrium-confined compression modulus,  $H$ , and the dynamic stiffness can be measured in this configuration. The dynamic stiffness includes contributions from hydrostatic pressurization within the construct associated with fluid-ECM frictional forces (*6,7*). Extensive descriptions of methodological details are available in confined (*3,19,20–23*) and unconfined (*9,24,25*) geometries.

### 3.2. Tension

Tensile properties of constructs may be determined from both equilibrium and time-varying stress-strain measurements. The equilibrium Young's modulus,  $E$ , can be calculated from the linear region of the equilibrium stress-strain curve. Samples must be appropriately fixed within testing grips to prevent artefactual failure at the sample/grip interface. If the specimen size allows, test samples may be cut in a "dogbone" geometry (**Fig. 1C**) such that a large grip area relative to the working length (*26*) minimizes stress concentrations at the grip. Other fixation strategies are available for specific sample geometries (*16,27–29*). In all cases, failure of the sample within the working length is indicative of a properly fixed sample.

Tensile test sample lengths must be significantly greater than cross-sectional dimensions (*see Note 1*) to ensure uniform strain through the working length; *see* ASTM guidelines summarized in *ref. (2)*. Large working lengths may also minimize bending effects resulting from irregular samples or improper alignment in the testing apparatus. When a working length has not been defined, evaluation of strain must be representative of the working length. Extensometers, optical scanning, or other devices may be necessary to accurately evaluate strain in the region of interest.

### 3.3. Shear

Specimen geometry for shear measurements is similar to that for compression, in which flat, parallel surfaces are necessary for accurate testing. Samples are fixed between parallel platens so that shear deformation may be performed using rotational (*30,31*) or translational (*25,31–34*) displacement (*see Note 8*) (**Fig. 1D**). Translational displacements result in shear stress equal to the force normalized to specimen surface area. For rotational displacement, stress is calculated from the applied torque, sample radius, and surface polar moment of

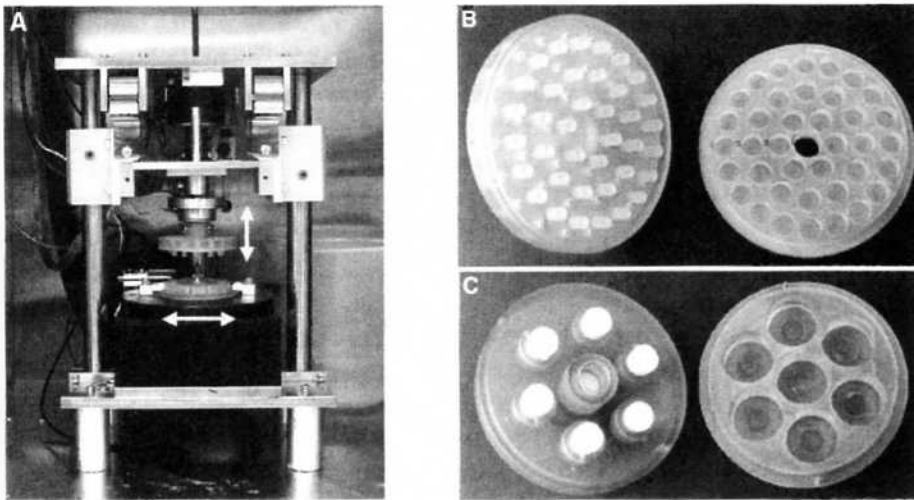


Fig. 2. (A) Example of an incubator-housed material testing instrument capable of measuring compressive, shear, and tensile properties, as well as studying the effects of applied mechanical loads on the development of tissue-engineered constructs (31). A testing chamber capable of loading 12 plugs in shear and/or compression is installed. (B) Loading chamber capable of testing or stimulating up to 38 samples in individual wells. Different well radii from the center allow three different levels of shear strain to be applied during a single loading event. (C) Chamber capable of compressive loading of up to six large cell-material constructs. A central spring ensures that the platen lifts off the samples during the unloading part of the cycle. Platens to compress the samples are porous to ensure adequate transport of feed media to center of constructs during prolonged loading.

inertia (e.g., *see ref. 32*), and shear strain is defined as the angle of deformation divided by the height of the sample. Both equilibrium and dynamic shear measurements are important for construct characterization. Under steady-state conditions, the equilibrium shear modulus  $G$  is calculated from the linear region of the stress-strain curve. The dynamic complex shear modulus,  $G^*$ , includes the so-called storage (in phase) and loss (out of phase) moduli. For ideal, infinitesimal shear deformation, there is no fluid flow within the construct, and therefore, no fluid-solid frictional interactions. Thus, the dynamic  $G^*$  reflects the frequency-dependent intrinsic viscoelastic properties of the ECM (34).

### 3.4. Biomechanics at the Cell and Nano-Molecular-Length Scales

Mechanical properties of cell-seeded tissue-engineered constructs are likely to be minimally influenced by the presence of cells. Cells typically occupy a

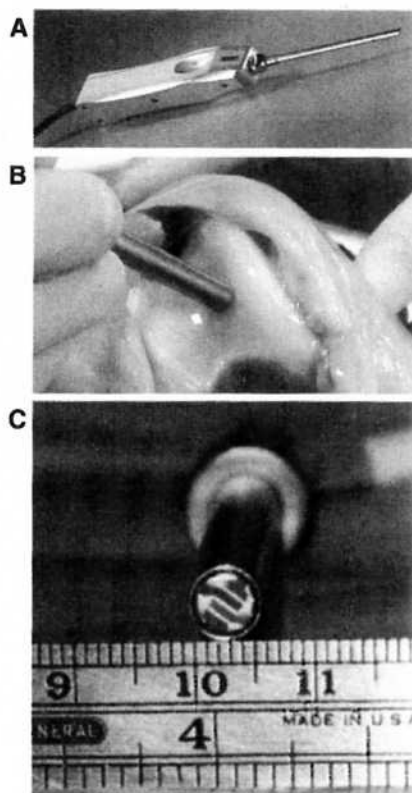


Fig. 3. (A,B) Devices capable of measuring material properties of constructs *in situ*. Artscan (Helsinki, Finland) probe capable of measuring cartilage compressive stiffness (4,49). (C) End view of sensors of surface electromechanical spectroscopy probe (51,52) capable of measuring impedance (electrical resistance) in cartilage. The impedance changes with tissue swelling and with changes in the content of charged GAGs. This probe is also capable of measuring electrical straming potentials and mechanical stress generated by a small electric currents (related to tissue content of GAG, tissue stiffness, hydraulic permeability, and other material properties).

small volume relative to overall scaffold geometry, and cell stiffness is typically low compared to that of the scaffold or newly synthesized. For example, a micropipet aspiration technique has been used to evaluate the elastic modulus of isolated chondrocytes, giving  $E \sim 0.6$  kPa (35). Atomic force microscopy (AFM) indentation analysis (36) and magnetic bead rheometry (37) have provided values of fibroblast moduli  $E \sim 3\text{--}5$  kPa and  $G \sim 20$  kPa. In comparison, the moduli of cartilage (38) and ligament and tendon (39) are at least two orders of magnitude greater than that of the individual cells because of the

presence of ECM. Scaffold material properties vary, but are likely to be greater than that of the cells for practical handling. Therefore, material properties of cell-seeded constructs are likely to be dominated by accumulated ECM, with contributions from stiffer scaffold materials. Consequently, scaffold-ECM strain will be transmitted to the seeded cells in proportion to the deformation of the localized pericellular environment. Cell deformation has been visualized in chondrocyte-seeded agarose scaffolds. With no accumulation of ECM, compressive scaffold strains of 5–15% produced axial compression and lateral extension of the cells, changing cell morphology from spherical to elliptical (40). Mechanical strain has also been observed to increase cell surface area and deform the nucleus of agarose-seeded chondrocytes (41). These experiments illustrate the potential for regulation of biosynthesis in cell-seeded constructs by mechanotransduction. Static compression (42,43), dynamic compression (43), and dynamic shear loading (44) have been found to modulate ECM biosynthesis in cartilage explant culture. Static and dynamic compression is also a potent regulator of cell metabolism in chondrocyte-seeded agarose (11,45) and alginate (46). Therefore, mechanical loading applied *in vivo* or during *in vitro* conditioning prior to implantation may be an important factor in the stimulation of an appropriate repair response using cell-seeded constructs.

### **3.5. Fatigue Testing**

The mechanical tests previously described focus on testing of constructs in a nondestructive manner. However, in many instances it is important to know how a construct will perform over repeated loading cycles as well as the maximum stress it will bear before failure. Fatigue tests are common in the study of soft tissues and tissue replacements that are loaded in tension, such as tendons (47). Fatigue during shear and compressive loading have also been addressed in detail (34,47). A nominal target stress or strain in the physiological range is typically selected, and the sample is cycled between an initial state and the target value until rupture occurs. The number of cycles to failure is the fatigue life, and is usually dependent on the stress or strain applied each cycle as well as the frequency of loading (strain rate). If enough samples are tested using a range of target values, then a graph of “load vs number of cycles to failure” can be constructed (referred to as an S-N curve). This will allow researchers to predict the fatigue life of a tissue or construct given the expected loading regimen. Tissue failure for materials such as bone or bone substitutes may be obvious. For soft tissues, a clear definition of failure must first be identified. In cartilage constructs, for example, failure could be defined as the appearance of surface fissures. Tests to failure, rather than fatigue, are characterized by a single application of load at a desired strain rate, increased until failure occurs in tension, compression, or shear.

### 3.6. In Situ Characterization of Graft-Repair Tissue

The ultimate goal of tissue engineering is the implantation of the cell-material constructs into the body. If the construct becomes well-integrated with surrounding tissue and progressively achieves functionality like the original native tissue, it can be deemed a success. Assessment of the biomechanical properties of the evolving graft, as well as other measures (e.g., histological examination) is important for documenting the ultimate success of the repair. For clinical applications, there is a critical need for the development of nondestructive, minimally invasive biomechanical measurement techniques. In the case of bone-replacement constructs, X-rays can be used to evaluate trabecular structure. However, soft-tissue structure is not so easily imaged. Although MRI technology has advanced dramatically during the past decade, biomechanical assessment is not possible with this modality, and it is necessary to use minimally invasive contact methods for such *in situ* measurements.

Several indentation probes have been developed for clinical biomechanical assessment of cartilage during routine arthroscopic examination (4,48) (Fig. 3A). These probes are designed to characterize the mechanical stiffness of cartilage repair grafts and for the diagnosis of cartilage degeneration in osteoarthritis. The use of *in situ* indentation instruments for the estimation of the tissue's Young's modulus has recently been described (49). Another probe that measures dynamic compressive and shear stiffness of cartilage has also been developed (50). The choice of such a probe and the use of an indentation modality must be made with caution, since developing tissue constructs may not be able to withstand the force of indentation testing (see Note 9).

Other probes under development focus on the electromechanical and electrical impedance properties of tissue (51,52) (Fig. 3B,C). Tissue impedance is influenced by the concentration of charged molecules within the ECM (e.g., proteoglycans) and the tissue's porosity and water content, properties that change with construct growth, repair, and degeneration. Probe application of a small electrical current into tissue constructs may also induce a mechanical stress within the ECM that is measurable by the probe. The current induces intratissue fluid flow and micromechanical motions of the developing ECM, causing a current-generated stress that also depends on ECM charge density, hydraulic permeability, and mechanical properties. Multiple electrode contacts on such probes (Fig. 3C) allow current application at several spatial wavelengths across the construct surface, thus enabling evaluation of tissue properties at various depths into the tissue.

### 3.7. Summary

Material testing is a fundamental tool for evaluating the mechanical functionality of cell-seeded constructs with respect to development of neo-tissue,

or predicting structural stability when placed in a loading environment. The methods outlined in this chapter are designed to first allow the reader to select testing parameters that best represent the ultimate functional mode of the cell-seeded construct. Then, simple testing in compression, tension, shear, indentation, or electro-mechanical means may be performed to establish tissue stiffness and other physical properties associated with normal tissue function. Evaluation of mechanical properties *in situ* extends the characterization of construct development to environments in which ultimate failure or success will be determined. In this manner, cell-seeded construct development or degradation may be closely monitored at all time-points as an indicator of neo-tissue accumulation or remodeling in the cell/scaffold system. Diagnostic testing protocols may also be modified to apply non-destructive loading as a means of conditioning cell-seeded constructs *in vitro*. Cell signaling via mechanotransduction may be utilized to increase or modify biosynthesis, controlling ECM accumulation prior to implantation.

#### 4. Notes

1. *In vitro* measurements may be performed using living tissue immersed in culture medium. Testing of previously frozen specimens requires the use of protease inhibitors to prevent degradation of the ECM during testing.
2. Micrometers or calipers may be used for dimensioning samples. However, accuracy may be compromised when samples are deformable. Feedback devices (e.g., resistance or voltage sensors) will help to identify when the measuring device is in contact with sample surfaces. The diameter of small cylindrical samples may be determined via a laser micrometer.
3. Sample thickness may also be determined using the testing apparatus. Zero strain can be defined by the position at which the testing platens produce a tare load in the specimen. Specimens must be completely immersed in appropriate medium or buffer for mechanical testing.
4. The upper platen may be fixed to the load cell if the weight of the platen affects the response of the sample to dynamic compression.
5. Unconfined compression: Test platens should be rigid and impermeable; low friction between specimen and platen will allow for appropriate radial expansion.
6. Confined compression: The upper platen must be porous, but should not deform during testing. Porous high-density or ultra-high mol-wt polyethylene (pore sizes of ~50–100  $\mu\text{m}$ ) are sufficient for most constructs.
7. Confined compression: Displacement control has an advantage over load control—stress relaxation is 4 $\times$  quicker than creep. Although load control may mimic physiologic loading conditions, displacement and load control are equivalent for deriving intrinsic material properties.
8. For shear measurements, specimens are sometimes glued to platens to prevent slipping. However, glues are often toxic to cell-seeded constructs. Therefore, platens with a rough surface will be useful. In addition, a 5–10% static offset compression may be needed to grip the specimen.

9. Indentation tests may be needed for complex, in vivo tissue geometry (e.g., cartilage on bone in the intact joint). However, when using small-diameter indentors with non-ideal construct geometries, interpretation of time-dependent indentation data to derive intrinsic material properties may be difficult. The ability to remove specimens for in vitro testing is advantageous when possible.

## References

1. Butler, D. L., Goldstein, S. A., and Guilak, F. (2000) Functional tissue engineering: the role of biomechanics. *J. Biomech. Eng.* **122(6)**, 570–575.
2. Athanasiou, K. A., Zhu, C., Lanctot, D. R., Agrawal, C. M., and Wang, X. (2000) Fundamentals of biomechanics in tissue engineering of bone. *Tissue Eng.* **6(4)**, 361–381.
3. Buschmann, M. D., Gluzband, Y. A., Grodzinsky, A. J., Kimura, J. H., and Hunziker, E. B. (1992) Chondrocytes in agarose culture synthesize a mechanically functional extracellular matrix. *J. Orthop. Res.* **10(6)**, 745–758.
4. Lyyra, T., Jurvelin, J., Pitkanen, P., Vaatainen, U., and Kiviranta, I. (1995) Indentation instrument for the measurement of cartilage stiffness under arthroscopic control. *Med. Eng. Phys.* **17**, 395–9.
5. Mak, A. F., Lai, W. M., and Mow, V. C. (1987) Biphasic indentation of articular cartilage—I. Theoretical analysis. *J. Biomech.* **20(7)**, 703–714.
6. Frank, E. H. and Grodzinsky, A. J. (1987) Cartilage electromechanics—II. A continuum model of cartilage electrokinetics and correlation with experiments. *J. Biomech.* **20(6)**, 629–639.
7. Lai, W. M., Hou, J. S., and Mow, V. C. (1991) A triphasic theory for the swelling and deformation behaviors of articular cartilage. *J. Biomech. Eng.* **113(3)**, 245–258.
8. Ehlers, W. and Markert, B. (2001) A linear viscoelastic biphasic model for soft tissues based on the theory of porous media. *J. Biomech. Eng.* **123(5)**, 418–424.
9. DiSilvestro, M. R., Zhu, Q., and Suh, J. K. (2001) Biphasic poroviscoelastic simulation of the unconfined compression of articular cartilage: II—Effect of variable strain rates. *J. Biomech. Eng.* **123(2)**, 198–200.
10. Chang, S. C., Rowley, J. A., Tobias, G., Genes, N. G., Roy, A. K., Mooney, D. J., et al. (2001) Injection molding of chondrocyte/alginate constructs in the shape of facial implants. *J. Biomed. Mater. Res.* **55(4)**, 503–511.
11. Mauck, R. L., Soltz, M. A., Wang, C. C., Wong, D. D., Chao, P. H., Valhmu, W. B., et al. (2000) Functional tissue engineering of articular cartilage through dynamic loading of chondrocyte-seeded agarose gels. *J. Biomech. Eng.* **122(3)**, 252–260.
12. Kisiday, J. D., Jin, M., Hung, H., Kurz, B., Semino, C., Zhang, S., and et al. (2002) Self-assembling peptide hydrogel fosters chondrocyte extracellular matrix production and cell division: implications for cartilage tissue repair. *PNAS* **99(15)**, 9996–10,001.
13. Glowacki, J. (2000) In vitro engineering of cartilage. *J. Rehabil. Res. Dev.* **37(2)**, 171–177.
14. Goldstein, S. A., Patil, P. V., and Moalli, M. R. (1999) Perspectives on tissue engineering of bone. *Clin Orthop* **367 Suppl** S419–S423

15. Woo, S. L., Hildebrand, K., Watanabe, N., Fenwick, J. A., Papageorgiou, C. D., and Wang, J. H. (1999) Tissue engineering of ligament and tendon healing. *Clin. Orthop.* **367 Suppl**, S312–S323.
16. Donahue, T. L., Gregersen, C., Hull, M. L., and Howell, S. M. (2001) Comparison of viscoelastic, structural, and material properties of double-looped anterior cruciate ligament grafts made from bovine digital extensor and human hamstring tendons. *J. Biomech. Eng.* **123(2)**, 162–169.
17. Gardiner, J. C. and Weiss, J. A. (2001) Simple shear testing of parallel-fibered planar soft tissues. *J. Biomech. Eng.* **123(2)**, 170–175.
18. Eckstein, F., Reiser, M., Englmeier, K. H., and Putz, R. (2001) In vivo morphometry and functional analysis of human articular cartilage with quantitative magnetic resonance imaging—from image to data, from data to theory. *Anat. Embryol.* **203(3)**, 147–173.
19. Frank, E. H. and Grodzinsky, A. J. (1987) Cartilage electromechanics—I. Electrokinetic transduction and the effects of electrolyte pH and ionic strength. *J. Biomech.* **20(6)**, 615–627.
20. Vunjak-Novakovic, G., Martin, I., Obradovic, B., Treppo, S., Grodzinsky, A. J., Langer, R., and et al. (1999) Bioreactor cultivation conditions modulate the composition and mechanical properties of tissue-engineered cartilage. *J. Orthop. Res.* **17(1)**, 130–138.
21. Freed, L. E., Langer, R., Martin, I., Pellis, N. R., and Vunjak-Novakovic, G. (1997) Tissue engineering of cartilage in space. *Proc. Natl. Acad. Sci. USA* **94(25)**, 13,885–13,890.
22. Lee, C. R., Breinan, H. A., Nehrer, S., and Spector, M. (2000) Articular cartilage chondrocytes in type I and type II collagen-GAG matrices exhibit contractile behavior in vitro. *Tissue Eng.* **6(5)**, 555–565.
23. Klisch, S. M. and Lotz, J. C. (2000) A special theory of biphasic mixtures and experimental results for human annulus fibrosus tested in confined compression. *J. Biomech. Eng.* **122(2)**, 180–188.
24. Fortin, M., Soulhat, J., Shirazi-Adl, A., Hunziker, E. B., and Buschmann, M. D. (2000) Unconfined compression of articular cartilage: nonlinear behavior and comparison with a fibril-reinforced biphasic model. *J. Biomech. Eng.* **122(2)**, 189–195.
25. Stammen, J. A., Williams, S., Ku, D. N., and Guldberg, R. E. (2001) Mechanical properties of a novel PVA hydrogel in shear and unconfined compression. *Biomaterials* **22(8)**, 799–806.
26. Catanese, J. 3rd, Featherstone, J. D., and Keaveny, T. M. (1999) Characterization of the mechanical and ultrastructural properties of heat-treated cortical bone for use as a bone substitute. *J. Biomed. Mater. Res.* **45(4)**, 327–336.
27. Cartmell, J. S. and Dunn, M.G. (2000) Effect of chemical treatments on tendon cellularity and mechanical properties. *J. Biomed. Mater. Res.* **49(1)**, 134–140.
28. Fedewa, M. M., Oegema, Jr, T. R., Schwartz, M. H., MacLeod, A., and Lewis, J. L. (1998) Chondrocytes in culture produce a mechanically functional tissue. *J. Orthop. Res.* **16(2)**, 227–236.

29. Guilak, F., Ratcliffe, A., Lane, N., Rosenwasser, M. P., Mow, V. C. (1994) Mechanical and biochemical changes in the superficial zone of articular cartilage in canine experimental osteoarthritis. *J. Orthop. Res.* **12(4)**, 474–484.
30. Stading, M. and Langer, R. (1999) Mechanical shear properties of cell-polymer cartilage constructs. *Tissue Eng.* **5(3)**, 241–250.
31. Frank, E. H., Jin, M., Loening, A. M., Levenston, M. E., and Grodzinsky, A. J. (2000) A versatile shear and compression apparatus for mechanical stimulation of tissue culture explants. *J. Biomech.* **33(11)**, 1523–1527.
32. Jin, M. and Grodzinsky, A. J. (2001) The effect of electrostatic interactions between glycosaminoglycans on the shear stiffness of cartilage: a molecular model and experiments. *Macromolecules* **34**, 8330–8339.
33. Anderson, D. R., Woo, S. L., Kwan, M. K., and Gershuni, D. H. (1991) Viscoelastic shear properties of the equine medial meniscus. *J. Orthop. Res.* **9(4)**, 550–558.
34. Simon, W. H., Mak, A. F., and Spirt, A. A. (1989) The effect of shear fatigue on bovine articular cartilage. *J. Orthop. Res.* **8(1)**, 86–93.
35. Jones, W. R., Ting-Beall, H. P., Lee, G. M., Kelley, S. S., Hochmuth, R. M., and Guilak, F. (1999) Alterations in the Young's modulus and volumetric properties of chondrocytes isolated from normal and osteoarthritic human cartilage. *J. Biomech.* **32(2)**, 119–127.
36. Rotsch, C., Jacobson, K., and Radmacher, M. (1999) Dimensional and mechanical dynamics of active and stable edges in motile fibroblasts investigated by using atomic force microscopy. *Proc. Natl. Acad. Sci. USA* **96(3)**, 921–96.
37. Bausch, A. R., Ziemann, F., Boulbitch, A. A., Jacobson, K., and Sackmann, E. (1998) Local measurements of viscoelastic parameters of adherent cell surfaces by magnetic bead microrheometry. *Biophys. J.* **75(4)**, 2038–2049
38. Eisenberg, S. R. and Grodzinsky, A. J. (1985) Swelling of articular cartilage and other connective tissues: electromechanochemical forces. *J. Orthop. Res.* **3(2)**, 148–159.
39. Danto, M. I. and Woo, S.-L. (1993) The mechanical properties of skeletally mature rabbit anterior cruciate ligament and patellar tendon over a range of strain rates. *J. Orthop. Res.* **11(1)**, 58–67.
40. Freeman, P. M., Natarajan, R. N., Kimura, J. H., and Andriacchi, T. P. (1994) Chondrocyte cells respond mechanically to compressive loads. *J. Orthop. Res.* **12(3)**, 311–320.
41. Lee, D. A., Knight, M. M., Bolton, J. F., Idowu, B. D., Kayser, M. V., and Bader, D. L. (2000) Chondrocyte deformation within compressed agarose constructs at the cellular and sub-cellular levels. *J. Biomech.* **33(1)**, 81–95.
42. Gray, M. L., Pizzanelli, A. M., Grodzinsky, A. J., and Lee, R. C. (1988) Mechanical and physiochemical determinants of the chondrocyte biosynthetic response. *J. Orthop. Res.* **6(6)**, 777–792.
43. Sah, R. L., Kim, Y. J., Doong, J. Y., Grodzinsky, A. J., Plaas, A. H., and Sandy, J. D. (1989) Biosynthetic response of cartilage explants to dynamic compression. *J. Orthop. Res.* **7(5)**, 619–636.

44. Jin, M., Frank, E. H., Quinn, T. M., Hunziker, E. B., and Grodzinsky, A. J. (2001) Tissue shear deformation stimulates proteoglycan and protein biosynthesis in bovine cartilage explants. *Arch. Biochem. Biophys.* **395**(1), 41–48.
45. Buschmann, M. D., Gluzband, Y. A., Grodzinsky, A. J., and Hunziker, E. B. (1995) Mechanical compression modulates matrix biosynthesis in chondrocyte/agarose culture. *J. Cell Sci.* **108**(Pt 4), 1497–1508.
46. Ragan, P. M., Chin, V. I., Hung, H. H., Masuda, K., Thonar, E. J., Arner, E. C., et al. (2000) Chondrocyte extracellular matrix synthesis and turnover are influenced by static compression in a new alginate disk culture system. *Arch. Biochem. Biophys.* **383**(2), 256–264.
47. Ker, R. F. (1999) The design of soft collagenous load-bearing tissues. *J. Exp. Biol.* **202** Pt 23, 3315–3124.
48. Niederauer, M. Q., Cristante, S., Niederauer, G. M., Wilkes, R. P., Singh, S. M., Messina, D. F., et al. (1998) A novel instrument for quantitatively measuring the stiffness of articular cartilage. New Orleans, LA, ORS. Transactions of the Orthopaedic Research Society.
49. Toyras, J., Lyyra-Laitinen, T., Niinimäki, M., Lindgren, R., Nieminen, M. T., Kiviranta, I., et al. (2001) Estimation of the Young's modulus of articular cartilage using an arthroscopic indentation instrument and ultrasonic measurement of tissue thickness. *J. Biomech.* **34**, 251–256.
50. Appleyard, R. C., Swain, M. V., Khanna, S., and Murrell, G. A. (2001) The accuracy and reliability of a novel handheld dynamic indentation probe for analyzing articular cartilage. *Phys. Med. Biol.* **46**, 541–550.
51. Berkenblit, S. I., Frank, E. H., Salant, E. P., and Grodzinsky, A. J. (1994) Nondestructive detection of cartilage degeneration using electromechanical surface spectroscopy. *J. Biomech. Eng.* **116**, 384–392.
52. Treppo, S., Berkenblit, S. I., Bombard, D. L., Frank, E. H., and Grodzinsky, A. J. (1999) Physical diagnostics of cartilage degeneration, in *Advances in Osteoarthritis* (Tanaka, S. and Hamanishi, C., eds.), Springer-Verlag, Tokyo, pp. 59–73.

# Lab 2: Cellular and tissue imaging with multiphoton excitation microscopy

**Location:** NE47-218

**PI:** Peter So

**Lab Instructors:** Hyuk-Sang Kwon and Daekeun Kim

## Summary

Two-photon microscopy (TPM) is a three dimensional incoherent imaging technique based on the nonlinear excitation of fluorophores. Two-photon excitation occurs only at the focal point by the simultaneous absorption of two photons each having half of the energy needed for the excitation transition, and it has four unique features. First, TPM uses high numerical aperture objective and a high peak mode-lock femto-second titanium:sapphire laser, and it is considered for various biological specimen imaging with sub micrometer resolution down to a depth of a few hundred micrometers using illumination of near infrared (NIR) wavelength light. Second, TPM causes little photodamage while imaging of living specimens. Third, TPM allows high-sensitivity imaging by eliminating the contamination of the fluorescence signal by the excitation light. Fourth, TPM can initiate a photochemical reaction within a sub-femtoliter volume inside cells and tissues. In contrast, confocal microscopy obtains three-dimensional information by eliminating out-of-focus light through the use of a pinhole, but the energy delivered by the excitation light causes extensive photodamage to living tissues. Further, the excitation wavelength used in confocal microscopes is typically in the UV and blue/green range which is scattered and absorbed strongly in tissues. This effect limits the depth of signal detection.

In this lab, we will briefly introduce the two-photon instruments (lasers, light source, etc) and we will image two sets of specimens: a slide containing cells with a fluorescent actin label from Molecular Probes, and a cartilage sample containing chondrocytes. We will image the specimen using a fluorophore or autofluorescence from the specimen: Chondrocytes in the cartilage specimen stained with cell tracker green and the SHG from cartilage collagen. We will use ImageJ to quickly look at the obtained image data in 3D.

## Recommended Reading

P. T. C. So *et al.*, "Two-photon excitation fluorescence microscopy," *Annu. Rev. Biomed. Eng.*, **2**.



# TWO-PHOTON EXCITATION FLUORESCENCE MICROSCOPY

---

Peter T. C. So<sup>1</sup>, Chen Y. Dong<sup>1</sup>, Barry R. Masters<sup>2</sup>,  
and Keith M. Berland<sup>3</sup>

<sup>1</sup>*Department of Mechanical Engineering, Massachusetts Institute of Technology,  
Cambridge, Massachusetts 02139; e-mail: ptso@mit.edu*

<sup>2</sup>*Department of Ophthalmology, University of Bern, Bern, Switzerland*

<sup>3</sup>*Department of Physics, Emory University, Atlanta, Georgia 30322*

**Key Words** multiphoton, fluorescence spectroscopy, single molecule, functional imaging, tissue imaging

■ **Abstract** Two-photon fluorescence microscopy is one of the most important recent inventions in biological imaging. This technology enables noninvasive study of biological specimens in three dimensions with submicrometer resolution. Two-photon excitation of fluorophores results from the simultaneous absorption of two photons. This excitation process has a number of unique advantages, such as reduced specimen photodamage and enhanced penetration depth. It also produces higher-contrast images and is a novel method to trigger localized photochemical reactions. Two-photon microscopy continues to find an increasing number of applications in biology and medicine.

## CONTENTS

INTRODUCTION . . . . .	400
HISTORICAL REVIEW OF TWO-PHOTON MICROSCOPY TECHNOLOGY . . .	401
BASIC PRINCIPLES OF TWO-PHOTON MICROSCOPY . . . . .	402
Physical Basis for Two-Photon Excitation . . . . .	402
Optical Properties of Two-Photon Microscopy . . . . .	403
TWO-PHOTON MICROSCOPY INSTRUMENTATION . . . . .	404
Two-Photon Laser Sources . . . . .	404
Scanning Fluorescence Microscopy Optics . . . . .	405
Fluorescence Detection System . . . . .	406
FLUORESCENT PROBES USED IN TWO-PHOTON MICROSCOPY . . . . .	406
Extrinsic and Endogenous Two-Photon Fluorophores . . . . .	406
Recent Efforts in Two-Photon Probe Development . . . . .	408
PHYSIOLOGICAL EFFECTS OF NEAR-IR MICROBEAM ILLUMINATION . . .	409
MOLECULAR-LEVEL APPLICATIONS OF TWO-PHOTON MICROSCOPY . . .	410
Single-Molecule Detection in Solution . . . . .	410
Imaging Single Molecules with Two-Photon Excitation . . . . .	411

Fluorescence Correlation Spectroscopy .....	411
Photon-Counting Histogram .....	413
CELLULAR-LEVEL APPLICATIONS OF TWO-PHOTON MICROSCOPY .....	414
Two-Photon In Vivo Cellular Imaging—Minimizing Photodamage and Bleaching .....	414
Multiphoton Imaging of Far-UV Fluorophores .....	414
Two-Photon Multiple Color Imaging .....	415
Three-Dimensional Localized Uncaging of Signaling Molecules .....	415
TISSUE LEVEL APPLICATIONS OF TWO-PHOTON MICROSCOPY .....	416
Applying Two-Photon Microscopy to Study Tissue Physiology .....	416
Applying Two-Photon Excitation for Clinical Diagnosis and Treatment .....	417
NEW DEVELOPMENTS IN TWO-PHOTON INSTRUMENTATION .....	418
Two-Photon Video Rate Microscopy .....	418
Simultaneous Two-Photon Fluorescence and Reflected-Light Confocal Microscopy .....	419
Integrating Fluorescence Spectroscopy into Two-Photon Microscopes .....	420
CONCLUSION .....	421

## INTRODUCTION

The need for better diagnostic tools has triggered a renaissance in optical-microscopy instrumentation development. Two-photon fluorescence microscopy (TPM), invented by Denk et al in 1990 (1), is a three-dimensional (3D) imaging technology based on the nonlinear excitation of fluorophores. TPM is considered a revolutionary development in biological imaging because of its four unique capabilities. First, TPM greatly reduces photodamage and allows imaging of living specimens. Second, TPM can image turbid specimens with submicrometer resolution down to a depth of a few hundred micrometers. Third, TPM allows high-sensitivity imaging by eliminating the contamination of the fluorescence signal by the excitation light. Fourth, TPM can initiate photochemical reaction within a subfemtoliter volume inside cells and tissues.

This review covers the historical development of two-photon fluorescence microscopy techniques and the underlying physical principles. The basic instrumentation design for TPM is explained. We describe the two-photon absorption properties of a number of commonly used fluorophores and the recent efforts in synthesizing two-photon optimized new probes. To effectively apply this new technique for live specimen imaging, we need to understand two-photon photodamage mechanisms. We discuss a number of biomedical uses of two-photon excitation at the molecular, cellular, and tissue levels. Finally, we survey recent instrumentation development efforts that may lead to more novel applications.

The reader is referred to several previous reviews of topics included in this chapter (2–4). The patent from the Cornell group of Webb and coworkers, which describes multiphoton excitation microscopy, is critical reading (5). An introduction to confocal microscopy and its applications is provided elsewhere (6, 7).

Confocal microscopy is reviewed in a new book of reprinted selected historical papers and patents (8).

## HISTORICAL REVIEW OF TWO-PHOTON MICROSCOPY TECHNOLOGY

The potential for highly intense light to trigger nonlinear processes has long been recognized. In particular, multiphoton excitation processes were predicted by Maria Göppert-Mayer in her doctoral dissertation on the theory of two-photon quantum transitions in atoms (9). Experimental work in nonlinear optics may have begun with the work by Franken and his group in 1961, focusing on second harmonic generation of light (10). They showed that ruby laser light, at wavelength  $\lambda$ , propagating through a quartz crystal will generate light at the second harmonic frequency with a wavelength of  $\lambda/2$ . In 1963, a few weeks after the publication of the paper by Franken et al, Kaiser & Garret published the first report on two-photon excitation (TPE) of  $\text{CaF}_2:\text{Eu}^{2+}$  fluorescence (11). They later demonstrated that TPE also can excite the fluorescence of organic dyes. Since then, many examples of TPE processes in molecular spectroscopy have been reported (12, 13). Two-photon spectroscopy has become an important tool to study the electronic structure of the molecular excited states (14, 15). Göppert-Mayer's theory was finally verified 32 years after its formulation. By analogy with the two-photon processes, three-photon excitation spectroscopy has also been described. Three-photon absorption processes were first reported by Singh & Bradley (16). Since then others have demonstrated three-photon excitation processes (17, 18). Today, the term multiphoton excitation commonly describes two and higher numbers of photon excitation processes.

After the development of nonlinear optical spectroscopy, the potential of nonlinear optical effects in microscopy was soon recognized. In a conventional light microscope, the source of the contrast is the differences in the absorption coefficients and the optical density of the specimens. For nonlinear microscopy, a specimen with a nonlinear optical cross-section will produce higher harmonic light emission under sufficiently intense illumination. The nonlinear harmonic generation is a function of the molecular structure. All materials possess third-order nonlinear susceptibility and higher-order terms; second-order nonlinear susceptibility exists in specimens that have non-centrosymmetric geometry, such as  $\text{LiNbO}_3$  crystals and some biological specimens. The principle of nonlinear scanning microscopy has been simply explained (6). Practical applications of nonlinear microscopy started with works of Freund & Kopf (18a); they determined the properties of ferroelectric domains by an analysis of the intensity and the angular distribution of the second harmonic generated within the crystals. Hellwarth & Christensen developed a second harmonic microscope to study microstructures in polycrystalline  $\text{ZnS}$  materials (19). The potential for incorporating nonlinear optical effects in scanning microscopy has been suggested by an Oxford group

(20, 21). They realized that the nonlinear processes are confined to the focal plane of the objective, because the image intensity would depend quadratically on the illumination power. However, the major impact of nonlinear optics in microscopy was not realized until the seminal work of Denk et al (1), who investigated the potential of imaging two-photon excited fluorescence in a scanning microscope with ultrafast pulsed lasers. The use of fluorescence techniques allows specific labeling of biological structures and provides a sensitive means to study biochemical processes such as calcium signaling in cells.

In addition to second- and higher-order harmonic-light generation, microscopes based on other nonlinear optical effects, such as sum frequency generation, coherent anti-Stokes Raman scattering, and parametric oscillations, have also been considered and implemented [see recent works (22–24)]. The potential of using these newer techniques for biological and medical research still requires further evaluation and is not covered in this review.

## BASIC PRINCIPLES OF TWO-PHOTON MICROSCOPY

### Physical Basis for Two-Photon Excitation

TPE of molecules is a nonlinear process involving the absorption of two photons whose combined energy is sufficient to induce a molecular transition to an excited electronic state. A comparison between one- and two-photon absorption is shown in Figure 1 (see color insert). Conventional one-photon techniques use UV or visible light to excite fluorescent molecules of interest. Excitation occurs when the absorbed photon energy matches the energy gap between the ground and excited states. The same transition can be excited by a two-photon process in which two less energetic photons are simultaneously absorbed. Quantum mechanically, a single photon excites the molecule to a virtual intermediate state, and the molecule is eventually brought to the final excited state by the absorption of the second photon.

The theory of TPE was predicted by Göppert-Mayer in 1931 (9). The basic physics of this phenomenon has also been described elsewhere (25, 26). Fluorescence excitation is an interaction between the fluorophore and an excitation electromagnetic field. This process is described by a time-dependent Schrödinger equation, in which the Hamiltonian contains an electric dipole interaction term:  $\vec{E}_\gamma \cdot \vec{r}$ , where  $\vec{E}_\gamma$  is the electric field vector of the photons and  $\vec{r}$  is the position operator. This equation can be solved by perturbation theory. The first-order solution corresponds to the one-photon excitation (OPE), and the multiphoton transitions are represented by higher order solutions. In the case of TPE, the transition probability between the molecular initial state  $|i\rangle$  and the final state  $|f\rangle$  is given by

$$P \sim \left| \sum_m \frac{\langle f | \vec{E}_\gamma \cdot \vec{r} | m \rangle \langle m | \vec{E}_\gamma \cdot \vec{r} | i \rangle}{\varepsilon_\gamma - \varepsilon_m} \right|^2 \quad (1)$$

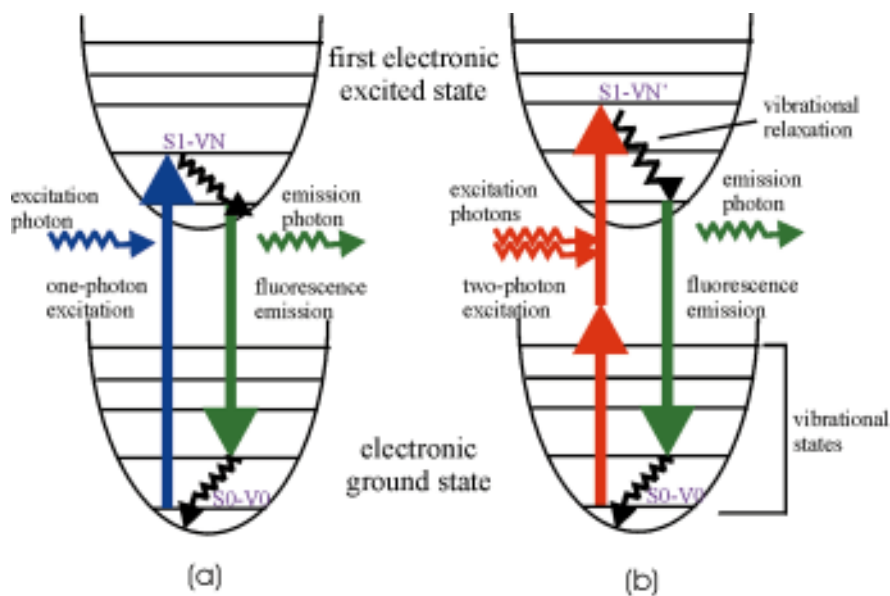


**Figure 1** Jablonski diagram for one-photon (a) and two-photon (b) excitation. Excitations occur between the ground state and the vibrational levels of the first electronic excited state. One-photon excitation occurs through the absorption of a single photon. The initial ( $S_0-V_0$ ) and final ( $S_1-V_N$ ) states have opposite parity. Two-photon excitation occurs through the absorption of two lower-energy photons via short-lived intermediate states. The initial ( $S_0-V_0$ ) and final ( $S_1-V_{N'}$ ) states have the same parity. After either excitation process, the fluorophore relaxes to the lowest energy level of the first excited electronic states via vibrational processes. The subsequent fluorescence emission processes for both relaxation modes are the same.

where  $\varepsilon_\gamma$  is the photonic energy associated with the electric field vector  $\vec{E}_\gamma$ , the summation is over all intermediate states  $m$ , and  $\varepsilon_m$  is the energy difference between the state  $m$  and the ground state. Note that the dipole operator has odd parity (i.e. absorbing one photon changes the parity of the state), and the one-photon transition moment  $\langle f | \vec{E}_\gamma \cdot \vec{r} | i \rangle$  dictates that the initial and final states have opposite parity. The two-photon moment  $\langle f | \vec{E}_\gamma \cdot \vec{r} | m \rangle \langle m | \vec{E}_\gamma \cdot \vec{r} | i \rangle$  allows transition in which the two states have the same parity (25, 26).

## Optical Properties of Two-Photon Microscopy

In TPE microscopy, a high numerical aperture objective is used to focus the excitation source to a diffraction-limited spot. The characteristic spatial profile at the focal plane for a circular lens with  $NA = \sin(\alpha)$ , focusing light of wavelength  $\lambda$ , is

$$I(u, v) = \left| 2 \int_0^1 J_0(v\rho) e^{-\frac{1}{2}u\rho^2} \rho d\rho \right|^2 \quad (2)$$

where  $J_0$  is the zeroth-order Bessel function,  $u = 4k \sin^2(\alpha/2)z$ , and  $v = k \sin(\alpha)r$  are the respective dimensionless axial and radial coordinates normalized to wave number  $k = 2\pi/\lambda$  (27, 28). Because TPE depends on the square of incident photon flux, the point spread function (PSF), which represents the geometry of the excitation volume, is  $I^2(u/2, v/2)$ . Compared with the conventional one-photon PSF,  $I(u, v)$ , the two-photon result has several major differences leading to distinct advantages for bioimaging applications.

**Three-Dimensional Localization of the Excitation Volume** A key feature of TPM is the limitation of fluorescence excitation to within a femtoliter size focal volume. Equation 1 indicates that the excitation probability is proportional to the square of laser intensity. The nonlinear feature of excitation implies that two-photon-induced absorption occurs most strongly near the focal plane, where the photon flux is highest (Figure 2; see color insert). Figure 3 (see color insert) compares the radial and axial PSF for one-photon microscopy and TPM. Note that TPE wavelength is twice that of the one-photon case. Owing to the longer wavelength used, TPM has a wider PSF when compared with the one-photon case. On the other hand, the true strength of TPM is its ability to discriminate against fluorescence originating from regions outside the focal plane. The contribution of fluorescence from each axial plane can be computed from the PSF and is shown in Figure 4 (see color insert). Assuming negligible attenuation, one can see that the total fluorescence generated is constant for each axial plane in one-photon microscopy. In contrast, the total two-photon fluorescence falls off rapidly away from the focal plane, demonstrating that most of the fluorescence generated is limited to the focal region.

This localized excitation volume results in greatly improved axial depth discrimination and improvement in image contrast, compared with conventional microscopy. This localization has other important consequences. First, reducing the region of photointeraction significantly decreases total specimen photobleaching

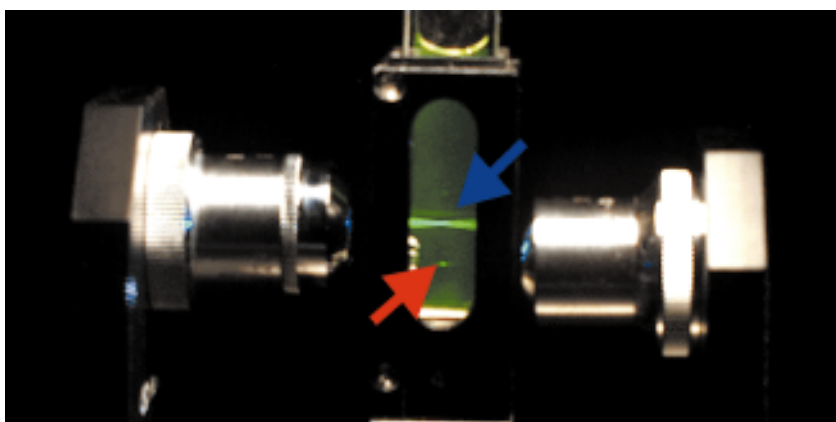


**Figure 2** A comparison of one- and two-photon excitation profiles. Fluorescein solution is excited by one-photon excitation (*blue arrow*) via a 0.1-numerical-aperture objective; fluorescence excitation is observed throughout the path of the laser beam. For two-photon excitation by using a second objective with the same numerical aperture (*red arrow*), fluorescence excitation occurs only within a 3-D localized spot.

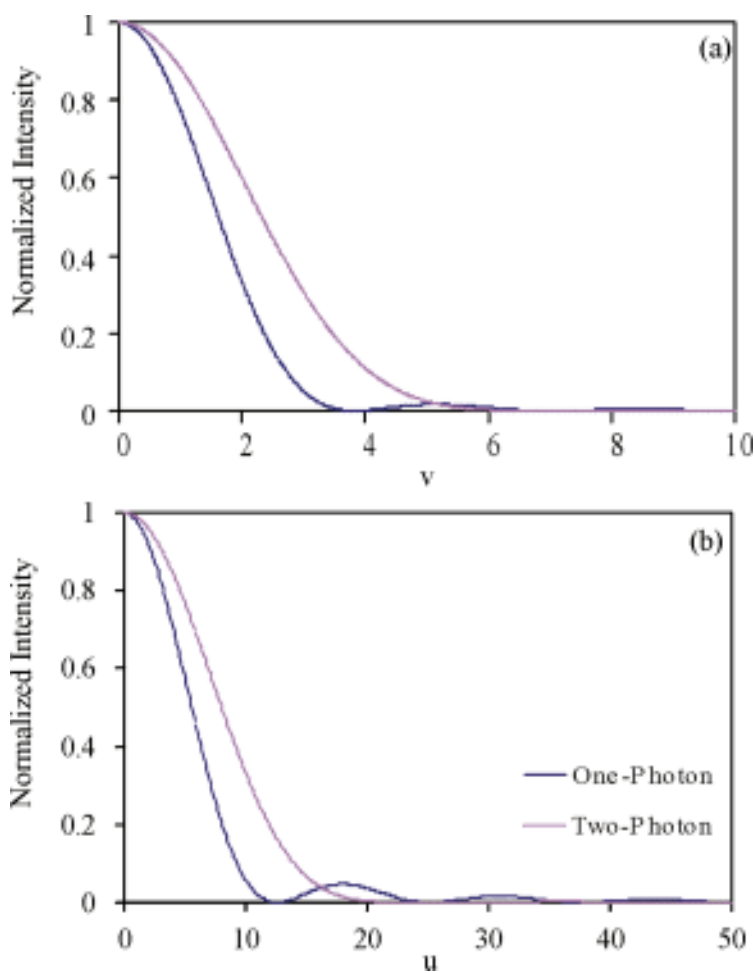


**Figure 3** A comparison of the one- and two-photon point spread functions in the (a) radial and (b) axial directions. In these figures,  $v$  and  $u$  are normalized optical coordinates along radial and axial directions as defined in the main text.

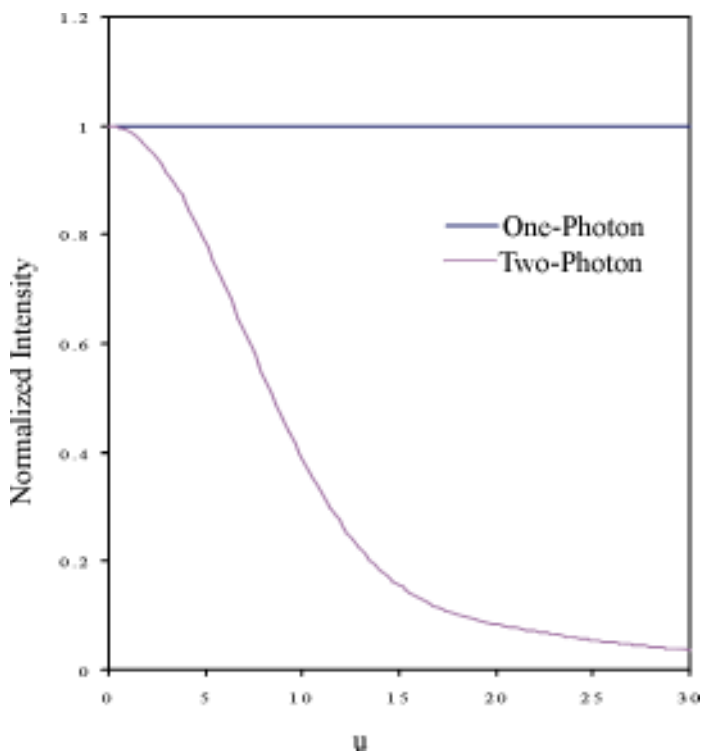


**Figure 4** Total fluorescence generated at a given  $z$ -plane is calculated. This quantity is plotted as a function of its distance from the focal plane. In the one-photon case, equal fluorescence intensity is observed in all planes and there is no depth discrimination. In the two-photon case, the integrated intensity decreases rapidly away from the focal plane.

and photodamage. Second, photoinitiated chemical reaction can be locally triggered in 3-D-resolved volumes.

***Reduced Attenuation in Biological Specimens*** Another major advantage of TPE is its ability to image thick biological specimens, owing to the reduced scattering and absorption of near IR light (relative to UV and visible wavelengths) in biological samples. In Rayleigh scattering, the scatterer is much smaller than the wavelength of light, and the scattering cross-section is inversely proportional to the fourth power of wavelength. When the equivalent wavelengths are used in OPE and TPE, a scattering event in a two-photon transition is over an order of magnitude less likely to occur than its one-photon counterpart. This results in deeper penetration of the excitation source into scattering samples. Rayleigh scattering is only an approximation of how light propagates in tissues, but the general inverse relationship between scattering and excitation wavelength remains valid. Most tissue also has reduced absorption in the near IR, thus TPE can effectively exploit the tissue “optical window” at 700–1000 nm. Tissue absorbance in this window is orders of magnitude less than the absorption in the UV or blue-green region. The deep penetration depth of TPM is a result of both reduced scattering and reduced absorption.

***High Signal-to-Background Ratio Fluorescence Detection*** In standard one-photon microscopy, the excitation wavelength is spectrally close to the fluorescence emission band. To eliminate the leak-through of the excitation light into the detection channel, the barrier filter often cuts off a part of the emission band. The result is a reduction in microscope sensitivity. For TPE, the excitation wavelength is much farther removed from the emission band, and highly efficient filters can be applied to eliminate the excitation with a minimal attenuation of the signal.

## TWO-PHOTON MICROSCOPY INSTRUMENTATION

Two-photon microscopes are commercially available; however, one can also be constructed from components (29) or by modifying an existing confocal microscope (1, 30). The basic designs of these systems are very similar, and the critical components are shown in Figure 5 (see color insert). A typical two-photon microscope features three basic components: an excitation light source, a high-throughput scanning fluorescence microscope, and a high-sensitivity detection system.

### Two-Photon Laser Sources

Because two-photon absorption is a second-order process with a small cross-section on the order of  $10^{-50}$  cm<sup>4</sup> s (defined as 1 GM in honor of Göppert-Mayer), high-photon flux needs to be delivered to the sample to generate efficient

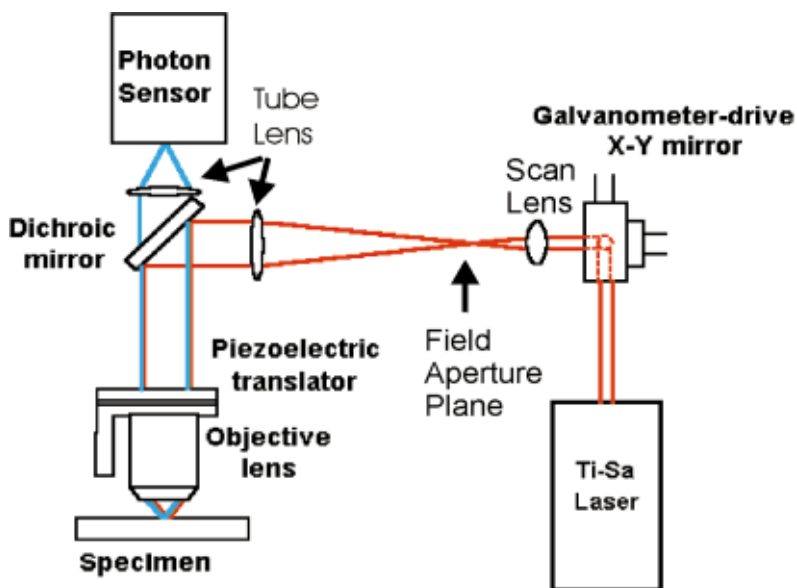


**Figure 5** Schematic of a typical two-photon microscope. The excitation light path is marked in *red* and the emission light path is marked in *blue*.

absorption. This is typically achieved using ultrashort pulsed laser excitation. It has been pointed out that  $n_a$ , the number of photons absorbed per fluorophore per pulse, is given by

$$n_a \approx \frac{p_0^2 \delta}{\tau_p f_p^2} \left( \frac{(NA)^2}{2\hbar c \lambda} \right)^2 \quad (3)$$

where  $\tau_p$  is the pulse duration,  $\delta$  is the fluorophore's two-photon absorption at wavelength  $\lambda$ ,  $p_0$  is the average laser intensity,  $f_p$  is the laser's repetition rate,  $NA$  is the numerical aperture of the focusing objective, and  $\hbar$  and  $c$  are Planck's constant and the speed of light, respectively (1). Equation 3 shows that, for the same average laser power and repetition frequency, the excitation probability is increased by increasing the NA of the focusing lens and by reducing the pulse width of the laser. Increasing NA corresponds to spatially confining the excitation power to a smaller focal volume.

Femtosecond, picosecond, and continuous-wave (cw) laser sources have been used for TPM. Currently, the most commonly used laser source for multiphoton microscopy is femtosecond titanium-sapphire (Ti-Sapphire) systems. These pulsed femtosecond systems are capable of generating a 100-fs pulse train at repetition rates of  $\sim 80$  MHz. The tuning range of Ti-Sapphire systems extends from 700 to 1000 nm. Other commonly used femtosecond sources are Cr-LiSAF and pulse-compressed Nd-YLF lasers (31). From Equation 3, it is clear that TPE can also be generated by using picosecond light sources, although at a lower excitation efficiency. Commonly available picosecond systems include mode-locked Nd-YAG ( $\sim 100$  ps), picosecond Ti-Sapphire lasers, and pulsed-dye lasers ( $\sim 1$  ps). TPE with cw lasers has also been demonstrated. Compared with a standard femtosecond light source, a cw light source requires an  $\sim 200$ -fold increase in average power to achieve the same excitation rate. This has been accomplished using cw sources such as ArKr laser and Nd-YAG laser (32). The main advantage in using cw laser sources is the significant reduction in system cost.

## Scanning Fluorescence Microscopy Optics

In a typical two-photon microscope, images are generated by raster scanning the  $x$ - $y$  mirrors of a galvanometer-driven scanner. After appropriate beam power control and pulse width compensation, the excitation light enters the microscope via a modified epiluminescence light path. The scan lens is positioned such that the  $x$ - $y$  scanner is at its eye point while the field aperture plane is at its focal point. For infinity-corrected objectives, a tube lens is positioned to recollimate the excitation light. The scan lens and the tube lens function together as a beam expander that overfills the back aperture of the objective lens. A dichroic mirror reflects the excitation light to the objective. The dichroic mirrors are short-pass filters, which maximize reflection in the IR and transmission in the blue-green region of the spectrum. Typically, high-numerical-aperture objectives are used to maximize excitation efficiency. The  $x$ - $y$  galvanometer-driven scanners provide lateral

focal-point positioning. An objective positioner translates the focal point axially and allows 3-D raster scanning.

## Fluorescence Detection System

The fluorescence emission is collected by the imaging objective and transmitted through the dichroic mirror along the emission path. An additional barrier filter is needed to further attenuate the scattered excitation light because of the high excitation intensity used. The fluorescence signal is directed to the detector system. Photodetectors that have been used in two-photon microscope systems include photomultiplier tubes (PMTs), avalanche photodiodes, and charge-coupled-device (CCD) cameras. PMTs are the most common implementation because they are robust and low cost, have large active areas, and have relatively good sensitivity.

A major advantage of TPM is that, unlike confocal microscopy, emission pinholes and descanning optics are not necessary to achieve axial depth discrimination. TPE is already localized to the focal volume, and there is no appreciable off-focal fluorescence to reject. The addition of a pinhole can enhance resolution but at a cost of signal loss (33, 34). An important consideration in designing the detection pathway is whether to implement a de-scan lens in the emission path. If the scanned region in the object plane is  $d$ , then the de-scan lens is not necessary if the detector area is larger than a characteristic area given by  $d \times M$ , where  $M$  is the overall magnification of the detection path (35). However, for nonuniform detectors, as some PMTs are, it may be desirable to implement descanning optics to prevent detection efficiency variation when the fluorescence emission is incident on different positions of the photocathode surface.

## FLUORESCENT PROBES USED IN TWO-PHOTON MICROSCOPY

It is important to examine the nonlinear absorption characteristics of fluorescent molecules. In general, most chromophores can be excited in two-photon mode at twice their one-photon absorption maximum. However, because one- and two-photon absorption processes have different quantum mechanical selection rules, a fluorophore's TPE spectrum scaled to half the wavelength is not necessarily equivalent to its OPE spectrum. Spectroscopic properties of fluorophores under nonlinear excitation need to be better quantified to optimize their use in TPM. Below, we discuss the two-photon absorption properties of some typical extrinsic and intrinsic fluorophores.

### Extrinsic and Endogenous Two-Photon Fluorophores

The spectroscopic study of rhodamine under TPE was one of the earliest efforts in this area (36). With the advent of TPM, spectral characterization of fluorophores

**TABLE 1** Two-photon cross-sections of some common fluorophores<sup>a</sup>

Fluorophores <sup>b</sup>	Excitation wavelength (nm)	$\eta_2 \delta$ ( $10^{-50}$ cm <sup>4</sup> s/photon)	$\delta$ ( $10^{-50}$ cm <sup>4</sup> s/photon)
Extrinsic fluorophores			
Rhodamine B	840		210 ( $\pm 55$ )
Fluorescein (pH 11)	782		38 ( $\pm 9.7$ )
Fura-2 (free)	700	11	
Fura-2 (with Ca <sup>2+</sup> )	700	12	
Indo-1 (free)	700	4.5 ( $\pm 1.3$ )	12 ( $\pm 4$ )
Indo-1 (high Ca)	700	1.2 ( $\pm 0.4$ )	2.1 ( $\pm 0.6$ )
Bis-MSB	691	6.0 ( $\pm 1.8$ )	6.3 ( $\pm 1.8$ )
Dansyl	700	1	
Dansyl hydrazine	700	0.72 ( $\pm 0.2$ )	
DiI <sub>C18</sub>	700	95 ( $\pm 28$ )	
Coumarin-307	776	19 ( $\pm 5.5$ )	
Cascade blue	750	2.1 ( $\pm 0.6$ )	
Lucifer yellow	860	0.95 ( $\pm 0.3$ )	
DAPI	700	0.16 ( $\pm 0.05$ )	
BODIPY	920	17 ( $\pm 4.9$ )	
Intrinsic fluorophores			
GFP wild type	~800		~6
GFP S65T	~960		~7
NADH	~700		~0.02
FMN	~700		~0.8
Phycoerythrin	1064		322 ( $\pm 110$ )

<sup>a</sup> $\eta_2$ , Fluorescence quantum efficiency under two-photon excitation (35, 42, 161).

<sup>b</sup>Abbreviations: Bis-MSB, p-bis(o-methylstyryl) benzene; DiI<sub>C18</sub>, octadecyl indocarbocyanine; DAPI, 4',6-diamidino-2-phenylindole; BODIPY, 4,4-difluoro-1,3,5,7,8-pentamethyl-4-bora-3a,4a-diazaindacene-2,6-disulfonic acid disodium salt; GFP, green fluorescent protein; NADH, reduced nicotinamide-adenine dinucleotide; FMN, flavin mononucleotide.

under nonlinear excitation took on a new urgency (37, 38). Extrinsic fluorophores are organic molecules that are designed to label biological structures and to measure biochemical functions. Recently, absorption spectra of many extrinsic fluorophores have been determined. A summary of absorption properties of these extrinsic fluorophores is presented in Table 1.

In addition to extrinsic fluorophores, biological systems often possess endogenous fluorescent molecules that can be imaged, revealing important sample characteristics without the need for labeling. Two-photon-induced fluorescence from tryptophan and tyrosine in proteins has been investigated (39–41). More recently,

the absorption cross-section of phycoerythrin has been measured and shown to be much greater than that of rhodamine 6G at the excitation wavelength of 1064 nm (42). Multiphoton-induced fluorescence of the neurotransmitter serotonin has also been demonstrated (43). The exciting development of green fluorescent protein (GFP) introduces a convenient fluorescent marker for monitoring gene expression in cells and tissues (44). Two-photon imaging parameters of the GFPs have been optimized (45,46). Nicotinamides [NAD(P)Hs] represent another intrinsic fluorophore that can be excited by using a two-photon microscope (41). NAD(P)H levels in cells are related to their metabolic rates (47), and NAD(P)H fluorescence has been used to monitor redox state in cornea (48) and skin (49). The two-photon spectroscopic characteristics of these endogenous probes are also listed in Table 1.

## Recent Efforts in Two-Photon Probe Development

One recent development in two-photon probe utilization has been in identifying drug molecules that are excitable by two-photon light sources. The ability to monitor the drug distribution in a native environment allows a better assessment of drug delivery efficiency and can be important for developing therapeutic strategies (50). However, monitoring fluorescent drugs under physiological conditions with OPE can be difficult because of short image penetration depth and high background fluorescence contribution from other naturally occurring fluorescent compounds (51). Therefore, the identification of two-photon excitable drugs has important clinical and pharmaceutical consequences. In this area, the anticancer drug topotecan has been identified as a good two-photon probe with a two-photon absorption cross-section of  $>20 \text{ GM}$  at 840-nm excitation. Under physiological conditions, two-photon-induced fluorescence from topotecan has been detected in plasma and in whole blood down to respective concentrations of  $0.05 \mu\text{M}$  and  $1 \mu\text{M}$  (51). In the foreseeable future, it is likely that further efforts in identifying two-photon-excitable pharmaceutical agents for implementation in clinical settings will be made.

Another important area is the development of extrinsic fluorophores with optimal two-photon absorption properties. The fluorophores listed in Table 1 have all been conventional one-photon excitable probes. Because OPE and TPE obey different selection rules, one should not expect these probes necessarily to have optimized properties for TPE. Recent searches for molecules with high two-photon absorption cross-sections have led to discovery of molecules with two-photon cross-sections of  $>1000 \text{ GM}$  (52). Optimizing two-photon absorption properties in fluorophores has two important consequences. The development of efficient fluorophores can reduce the excitation laser intensity required for imaging, and thus reduce specimen photodamage. Alternatively, with high two-photon cross-sections, significant excitation can be achieved with the more economical cw lasers, thus reducing the cost of two-photon systems that typically use femtosecond Ti-Sapphire lasers.

## PHYSIOLOGICAL EFFECTS OF NEAR-IR MICROBEAM ILLUMINATION

TPE reduces specimen photodamage by localizing the excitation region to within an 1-fl volume. Photodamage is also decreased by use of near-IR excitation rather than UV and visible radiation. Decreasing the photochemical-interaction volume results in a dramatic increase in biological-specimen viability. The noninvasive nature of two-photon imaging can be best appreciated in a number of embryology studies. Previous work on long-term monitoring of *Caenorhabditis elegans* and hamster embryos, using confocal microscopy, has failed because of photodamage-induced developmental arrest. However, recent TPM studies indicate that the embryos of these organisms can be imaged repeatedly over the course of hours without observable damage (53–55). It is more important that the hamster embryo was reimplanted after the imaging experiments and eventually developed into a normal, healthy, adult animal.

At the focal volume at which photochemical interactions occur, TPM can still cause considerable photodamage. Three major mechanisms of two-photon photodamage have been recognized. (a) Oxidative photodamage can be caused by two- or higher photon excitation of endogenous and exogenous fluorophores with a photodamage pathway similar to that of UV irradiation. These fluorophores act as photosensitizers in photooxidative processes (56, 57). Photoactivation of these fluorophores results in the formation of reactive oxygen species that trigger the subsequent biochemical damage cascade in cells. Current studies have found that the degree of photodamage follows a quadratic dependence on excitation power, indicating that the two-photon process is the primary damage mechanism (58–62). Experiments have also been performed to measure the effect of laser pulse width on cell viability. Results indicate that the degree of photodamage is proportional to two-photon excited fluorescence generation, and is independent of pulse width. Hence, using shorter wavelength for more efficient TPE also produces greater photodamage. An important consequence is that both femtosecond and picosecond light sources are equally effective for two-photon imaging in the absence of an IR one-photon absorber (59, 61). Flavin-containing oxidases have been identified as one of the primary endogenous targets for photodamage (62). (b) One- and two-photon absorption of the high-power IR radiation can also produce thermal damage. The thermal effect resulting from two-photon water absorption has been estimated to be on the order of 1 mK for typical excitation power and has been shown to be insignificant (3, 63). However, in the presence of a strong IR absorber such as melanin (64, 65), there can be appreciable heating caused by one-photon absorption. Thermal damages have been observed in the basal layer of human skin in the presence of high average-excitation power (66). (c) Photodamage may also be caused by mechanisms resulting from the high peak power of the femtosecond laser pulses. There are indications that dielectric breakdown occasionally occurs (58). However, further studies are required to confirm and better understand these effects.

## MOLECULAR-LEVEL APPLICATIONS OF TWO-PHOTON MICROSCOPY

In recent years, a number of technological advances in light sources, detectors, and optics have led to tremendously improved sensitivity in fluorescence methods. Single-molecule sensitivity is now routinely achieved (67–70). Although most of the single-molecule work has used OPE, two-photon methods can offer improvement in the signal-to-background ratio (SBR), owing to excitation volume localization and the wide spectral separation of the emission, excitation, and Raman bands.

It should be noted that, although ultrasensitive applications of two-photon fluorescence require careful optimization of instrumentation and experimental setups, they are not fundamentally different from two-photon fluorescence instrumentation discussed previously in this review. The following discussion of single-molecule applications of two-photon fluorescence has been divided into three parts: fluorescence burst detection of single molecules, single-molecule imaging, and fluorescence correlation spectroscopy (FCS).

### Single-Molecule Detection in Solution

The first demonstration of single-molecule detection by TPE in solution was presented by Mertz et al (71), using rhodamine B molecules in water. They observed photon bursts from single molecules diffusing through the two-photon volume, with an average SBR of  $\sim 10$ . A number of other reports have since demonstrated efficient fluorescence burst detection of single molecules by TPE in free solution (72, 73), in flow cells (74–76), and in low-temperature solids (77, 78). As anticipated, a common finding among most of these reports is the high SBR, largely caused by the very low background levels associated with TPE. A quantitative study of the two-photon background, including contributions from two-photon hyper-Rayleigh and hyper-Raman scattering of water, has shown reduced background levels for TPE vs OPE (79). Care must be taken in determining TPE illumination conditions, because too much input power can lead to continuum generation in the solvent, and thus greatly increased background levels (73).

Although the SBR has generally been favorable with TPE, the absolute count rates per molecule are not always comparable with OPE detection (71, 73, 80–82). The reduced magnitude of fluorescence yield is hypothesized to arise from long-lived, more highly excited states reached by TPE, increased photobleaching, intersystem crossing, or perhaps some other saturation or multiphoton phenomena. The mechanism is sample dependent, and there are counter examples in which the TPE fluorescence intensity is comparable with (enhanced green-fluorescence protein) or exceeds (7-amino-A-methylcoumarin) the OPE fluorescence level, at least under certain illumination conditions (73, 83). The photophysics of a given molecule of interest is thus important in determining the relative advantages of one- and two-photon fluorescence detection. Newly designed chromophores with high two-photon cross-sections may enhance the advantages of TPE in single-molecule applications (52, 84).

## Imaging Single Molecules with Two-Photon Excitation

Spatially resolved applications of ultrasensitive two-photon fluorescence have also shown promising results. Sanchez and coworkers first demonstrated two-photon imaging (far-field) of single rhodamine B molecules immobilized on glass surfaces with an SBR of 30 (80). In addition, emission spectra were acquired for individual molecules by using a cooled CCD and a spectrograph. Discrete photobleaching of individual fluorescence peaks, as well as polarized emission, served as evidence for true single-molecule detection. It is interesting that this group found that TPE leads to faster photobleaching of single rhodamine B molecules than OPE, by a factor of  $\sim 2$ . This number is expected to be sample dependent. A report by Bopp et al, also using rhodamine B, demonstrates the ability to determine molecular orientation, as well as to measure laser pulse parameters at the sample by TPE fluorescence (85). Their results also showed reduced fluorescence emission from rhodamine B for TPE vs OPE. An interesting variation of TPE imaging methods uses two-photon "wide-field" illumination ( $\sim 5\text{-}\mu\text{m}$ -diameter spot); the larger spot size is achieved by underfilling the objective lens. This approach allowed Sonnleitner et al to not only observe single molecules, but track them within the spot over time, measuring diffusion of single labeled lipid molecules (86). The authors plan to test this approach for tracking single molecules on live cell membranes.

Imaging applications of TPE have also been extended to the near-field, using uncoated fiber tips (81, 87). The study by Kirsch et al makes use of cw TPE. These applications have the exciting potential of ultraresolved imaging with high SBRs and improved  $z$ -resolution as compared with one-photon near-field imaging. To fully realize these advantages requires selection of fluorescent probes that are reasonably stable with TPE, because increased bleaching (as seen with rhodamine probes) would otherwise detract from the TPE advantages.

Finally, an apertureless variation of near-field imaging was recently introduced with the promise of extremely highly resolved imaging not limited by a minimum aperture size (88). An exciting direction in this field is the use of enhanced radiation (from electromagnetic interaction of the tip and the optical field) localized at the tip end to improve resolution and contrast. The quadratic dependence of TPE on excitation intensity makes it ideal to exploit these locally enhanced fields (89, 90). The first experimental realization of this approach demonstrated extremely high-resolution images ( $\sim 20$  nm) of photosynthetic membrane fragments and  $J$ -aggregates of pseudocyanine dye (91). Fluorescence quenching by the near-field probe is a problem for this method, which, nonetheless, has very exciting possibilities.

## Fluorescence Correlation Spectroscopy

FCS, first introduced by Magde et al (92) and Thompson (93), is proving to be a powerful method for studying a large variety of experimental systems. Applications include measurement of diffusion, chemical reactions, molecular interactions, number concentration, hydrodynamic flow, and photophysical parameters

such as triplet state lifetimes. FCS experiments are performed by recording spontaneous equilibrium fluctuations in fluorescence intensity (i.e. fluorescence bursts) from a small (<1-fl) open volume. Information about various experimental parameters is extracted through temporal analysis of these fluctuations by calculating the autocorrelation (or cross correlation) of the fluorescence signal, defined as

$$G(\tau) = \frac{\langle \delta F(t) \times \delta F(t + \tau) \rangle}{\langle F(t) \rangle^2} \quad (4)$$

Here  $F(t)$  is the time-dependent fluorescence signal,  $\delta F(t)$  is the time-dependent deviation from the average fluorescence intensity, and the angle brackets represent the time average. Because this review is focused on TPM, we here cover only two-photon FCS measurements, and the reader is referred to the above references for a more general discussion and review of the FCS literature.

TPE was first applied in FCS measurements by Berland et al. The optical sectioning of TPE was introduced as an alternative to confocal detection for FCS in 3-D systems (94). This report demonstrated the capability to measure translational diffusion coefficients of small (7- and 15-nm radius) fluorescent latex beads in solution and, for the first time using FCS, in the cytoplasm of live cells (Figure 6). The low background levels associated with TPE and reduced autofluorescence achieved by using 960-nm excitation were of critical importance for the cellular measurements. A subsequent report by these authors introduced the capability to measure molecular concentration and thus detect protein association/dissociation reactions and kinetics in solution (95). As mentioned above, FCS can also be a powerful tool in studying the photophysical characteristics of fluorescence probes,

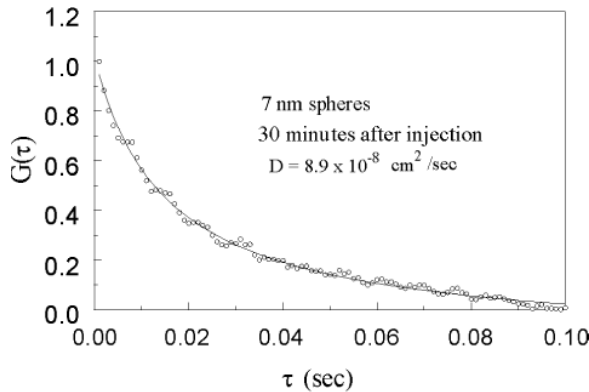


**Figure 6** Result of a fluorescence correlation spectroscopic measurement of the diffusion coefficient of 7-nm-radius latex spheres in the cytoplasm of CRL 1503 mouse embryonic fibroblast cells. The data are acquired 30 min after microinjection. The diffusion rate ( $8 \times 10^{-8} \text{ cm}^2/\text{s}$ ) is found to be  $\sim$ fivefold slower than in water ( $3 \times 10^{-7} \text{ cm}^2/\text{s}$ ). This figure is adapted from 94.

and FCS analysis provided an important tool in deciphering the fluorescence properties of the UV probe Coumarin-120 with both OPE and TPE (73). In addition to the general interest of these findings, the results from this type of analysis provide valuable information, which is useful for experimental design, particularly for two-photon imaging applications in which optimal experimental conditions are not known a priori.

The main motivation for using two-photon FCS in a given experiment, rather than one-photon confocal FCS, is to exploit the same features (discussed elsewhere in this review) that make TPE advantageous in other experiments. A very thorough comparison of OPE and TPE FCS applications can be found in a recent publication by Schwille et al (83). This excellent paper demonstrates that FCS measurements of diffusion can be performed at the single-molecule level in live cells, with similar results from both one- and two-photon FCS. Illumination and detection conditions were carefully chosen, such that the fluorescence yield was similar for both OPE and TPE. Their results resolve diffusion of rhodamines in the cytoplasm and membranes, and of Cy-3 (Amersham Pharmacia Biotech, Uppsala, Sweden)-labeled immunoglobulin E receptors in the membrane of several different cell types. The diffusion data show interesting complexity, suggesting anomalous diffusion or at least multicomponent diffusion. Whereas FCS was possible in cells using OPE, a number of TPE advantages were confirmed. First, TPE FCS measurements were possible in regions in which OPE FCS was not, such as within plant cells with highly scattering cell walls. A second major advantage was the reduced photobleaching of molecules outside the observation volume (as compared with OPE confocal). This can be exceedingly important when there are small numbers of fluorescent molecules in a cell to begin with. Third, TPE provided superior axial resolution and the ability to confine the FCS signal to a given cell region. Finally, the SBR can also be higher for TPE, depending on probes and cell types. One distinct disadvantage is that, for illumination conditions yielding comparable fluorescence intensity, TPE power levels are substantially closer to the biological damage threshold.

## Photon-Counting Histogram

The photon-counting histogram (PCH) has recently been proposed as an alternative approach to FCS for analyzing photon burst data, to accurately measure sample concentrations and detect molecular interactions (96, 97). Rather than analyzing the temporal behavior of fluorescence fluctuations, the PCH analyzes the fluctuation amplitude distributions. Chen et al have demonstrated that PCH analysis can describe fluorescence fluctuation data as a super-Poissonian distribution with great precision (97). Fluctuation data were obtained from TPE measurements of several fluorescent dyes in solution. This type of analysis is expected to be quite powerful for measuring molecular concentration and detecting and quantifying molecular interactions, as was already demonstrated for two-component systems (96).

## CELLULAR-LEVEL APPLICATIONS OF TWO-PHOTON MICROSCOPY

The ability to simultaneously monitor cellular biochemical activity and structure at the subcellular level is vital to understand many important processes. The need for functional imaging dictates the use of minimally invasive technology such as TPM. The ability of TPE to initiate photochemical reaction in a subfemtoliter volume further opens up new windows of opportunities for 3-D, localized uncaging and photobleaching experiments.

### Two-Photon In Vivo Cellular Imaging—Minimizing Photodamage and Bleaching

Although higher-resolution methods such as electron microscopy can produce images with finer details, optical microscopy is unique because it reveals dynamic processes such as signaling, intracellular transport, and cell migration. Some cellular processes have been successfully studied with white light video microscopy (98). However, many functional studies require fluorescence. Fluorescence imaging of live cells is difficult, especially when 3-D information is required. Before the invention of TPM, fluorescence confocal microscopy was the only option. The use of high-intensity UV or blue-green radiation in the confocal system results in significant photodamage and compromises the validity of the research.

This difficulty has been alleviated with the introduction of two-photon imaging. TPM enables a number of difficult studies in which sensitive specimens may be damaged under UV excitation. The study of cellular calcium signaling is one of these areas where TPE can contribute (99). The feasibility of using indicators, such as Indo I (100) and Calcium Green (29) (Molecular Probes, Eugene, OR), in two-photon microscopes for the quantification of cellular calcium level has been demonstrated. TPM has been used successfully in calcium-signaling studies such as the effect of calcium signals in keratocyte migration (101) and the mapping of the calcium channel in hair cells (102). Two-photon imaging has also been applied in systems in which the available fluorescent indicators are not very photostable. An example is the measurement of membrane fluidity in cells and vesicles with the generalized polarization probe Laurdan, which is easily photobleached (103–105).

### Multiphoton Imaging of Far-UV Fluorophores

Another interesting application of multiphoton excitation is the imaging of serotonin distribution in cells (106). Serotonin is an important neural transmitter. The far-UV (~240-nm) fluorescence excitation of serotonin makes optical microscopic studies of serotonin biology difficult. Using a conventional microscope, this spectral region is virtually inaccessible. Maiti et al (106) realized that multiphoton excitation can be used to image this class of chromophores. Serotonin was excited in the near IR by three-photon absorption, and they have demonstrated that the

distribution of serotonin in intracellular granules can be mapped. Equally important is the subsequent discovery by Shear et al (43) that serotonin may be further excited by a six-photon process in which the molecule is converted by the absorption of four photons to a two-photon-excitable by-product. Serotonin distribution can then be imaged based on the blue-green fluorescence of this by-product (43). The two basic principles described here are important. First, multiphoton excitation can be used to access new far-UV chromophores. Second, multiphoton chemical processes may be used to create new fluorophores based on endogenous cellular molecules.

## Two-Photon Multiple Color Imaging

The possibility of using TPM to simultaneously excite different color fluorophores for multiple label imaging has been explored (29, 107) (Figure 7; see color insert). Xu et al imaged rat basophilic leukemia cells simultaneously labeled with pyrene lysophosphatidylcholine, a UV-emitting plasma membrane probe; DAPI, a blue-emitting nucleic probe; Bodipy sphingomyelin, a green-emitting Golgi label; and rhodamine 123, a red-emitting mitochondria probe. This study demonstrates the simultaneous imaging of four cellular structural components and the potential for studies in which the interaction of various cellular organelles can be monitored over time in 3-D.

## Three-Dimensional Localized Uncaging of Signaling Molecules

An important property of TPM is its ability to initiate localized chemical reactions such as the uncaging of signaling molecules. Denk led the development of this novel technique by mapping the distribution of nicotin acetylcholine receptors in a muscle cell line (BC3H1) (108). The membrane potential of a chosen cell was monitored by the whole-cell patch clamp technique. Caged carbamoylcholine was placed in the medium. Upon two-photon uncaging, a 3-D localized burst of carbamoylcholine was released at the focal point of the laser light. The whole-cell current measured by the patch clamp is a function of the relative spatial distance between the carbamoylcholine burst and the proximal acetylcholine receptors. In the presence of many close-by receptors, a larger current will be observed and vice versa. By scanning the uncaging beam throughout the cell volume, the receptor distribution can be determined. Similar techniques have been subsequently applied to map glutamate receptors on hippocampal pyramidal neurons (109).

In addition to receptor mapping, localized uncaging is also valuable for the study of intracellular-signaling pathways. The ability to generate active signaling molecules localized in 3-D with submicrometer resolution allows investigators to monitor intracellular signal propagation. Localized uncaging of fluorescein has been demonstrated by Denk and coworkers (1). However, the uncaging of more important cellular messengers, such as calcium, has been difficult because of the

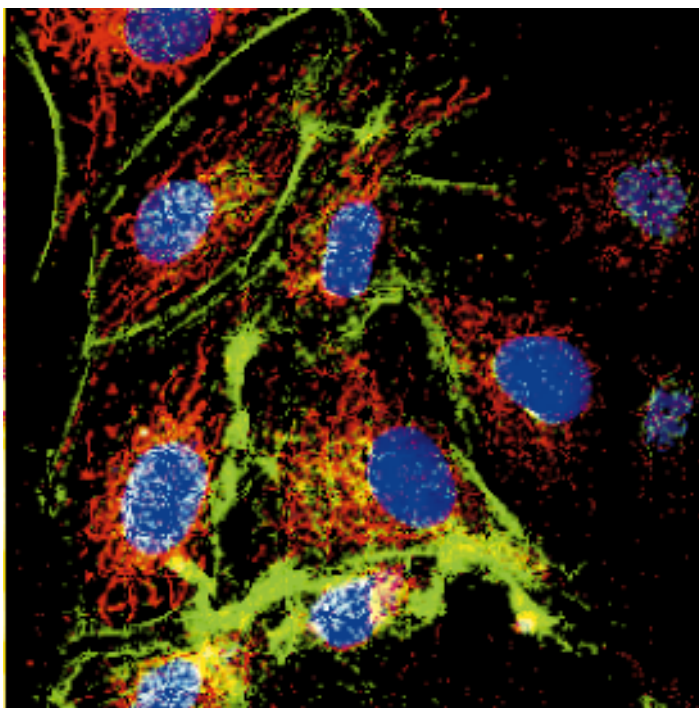


**Figure 7** Two-photon multiple color imaging of bovine pulmonary artery endothelial cells labeled with DAPI (nucleus), BODIPYO-FL phalloidin (actin), and MitoTrackero Red CMXRos (mitochondria) (Molecular Probes, Eugene, OR). All three probes were excited at 780 nm, and images were acquired by three independent detection channels.

lack of an efficient two-photon photolabile cage. This situation is improving as new cage groups targeted for two-photon applications are being developed (110). This new technology has been used in a number of pilot studies (111–116).

Two-photon photobleaching recovery is a similar technique that can be applied to measure intracellular transport, viscosity, and diffusion (117). Similar to conventional photobleaching-recovery studies, molecules labeled with fluorophores of interest can be photobleached within a 3-D localized volume. The recovery of loss fluorescence is correlated with fresh molecules diffusing back into the excitation volume and provides information on the intracellular environment.

## TISSUE LEVEL APPLICATIONS OF TWO-PHOTON MICROSCOPY

A recent comparison study has convincingly demonstrated that TPM is a superior method in the imaging of thick, highly scattering specimens (33).

### Applying Two-Photon Microscopy to Study Tissue Physiology

The potential of applying TPM to study tissue physiology has been recognized since its inception (1). Two-photon tissue imaging has been successfully applied to study the physiology of many tissue types, including the corneal structure of rabbit eyes (48, 66), the light-induced calcium signals in salamander retina (118), the human and mouse dermal and subcutaneous structures (49, 119, 120) (Figure 8; see color insert), the toxin effect on human intestinal mucosa (121), and the metabolic processes of pancreatic islets (122, 123). Today, TPM is particularly widely used in two areas—neurobiology (124) and embryology. In neurobiology studies, TPM has been applied to study the neuron structure and function in intact brain slices (125), the role of calcium signaling in dendritic spine function (126–134), neuronal plasticity and the associating cellular morphological changes (135), and hemodynamics in rat neocortex (136). In embryology studies, two-photon imaging has been used to examine calcium passage during sperm-egg fusion (137), the origin of bilateral axis in sea urchin embryos (138), cell fusion events in *C. elegans* hypodermis (53, 54), and hamster embryo development (55). It is expected that two-photon imaging will be applied to an increasing number of tissue systems as better commercial instruments become available.

It is important to examine the technological limitations of applying two-photon imaging in tissues. (a) It should be recognized that the imaging depth of different specimens could be drastically different. For example, in the cornea of the eye, a unique optically transparent organ, an autofluorescence image can be obtained from depths beyond a millimeter, whereas, inside a highly scattering specimen such as human skin, the contrast of autofluorescence images is significantly degraded at  $\sim 200\text{--}300\ \mu\text{m}$ . The maximum imaging depth depends on the scattering

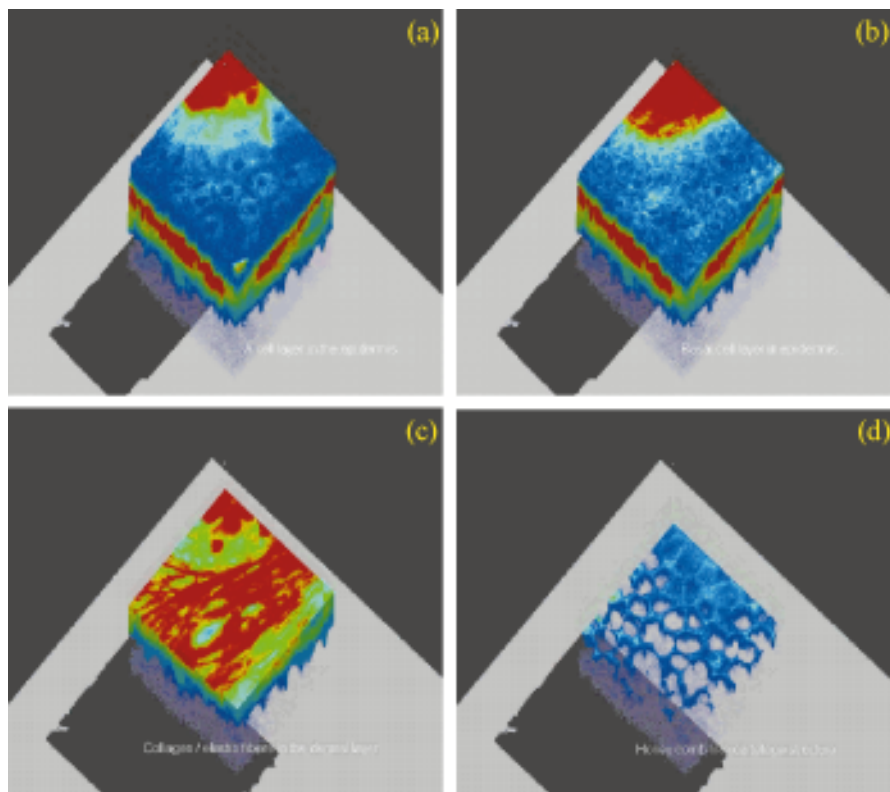


**Figure 8** Three-dimensional reconstructed two-photon images of dermal and subcutaneous structures in a mouse ear tissue specimen. The four panes show distinct structural layers: (a) epidermal keratinocytes, (b) basal cells, (c) collagen/elastic fibers, and (d) cartilage structure. This figure is adapted from (120).

and absorption coefficients of the tissue, the efficiency of the fluorophore, and the throughput of the microscope optics. (b) The two-photon PSF is well characterized in thin specimens. In a number of tissue models, two-photon PSF degradation appears to be minimal up to a depth of 100  $\mu\text{m}$  (33). However, the aberration of PSF in real tissue specimens has not been satisfactorily measured. A number of projects are now underway to better understand the physics of light propagation in turbid medium and to quantify resolution in both tissue phantoms and real tissues. (c) Fluorescence labeling of deep tissue structure is a major technical challenge. Common fluorescent probes are designed for labeling cultured cells. Diffusional delivery of these probes is not ideal in tissues. Probe distributions tend to vary greatly as a function of depth. Fluorophores could also be delivered by microinjection, but this method suffers from its invasive nature and its limited ability to label multiple cells. Tissue structure may also be imaged with endogenous fluorophores such as NAD(P)H and flavoproteins (47). Unfortunately, these fluorophores suffer from low quantum yield, and their fluorescence emissions in the blue-green spectral region are strongly attenuated by the tissue. Molecular biology methods allow the labeling of specific tissue structures with fluorescent probes such as GFP, but this method can be applied only to specimens with well-controlled genetic makeup. The lack of universal and effective methods for fluorescent labeling of living tissues is a major obstacle in two-photon tissue imaging.

## Applying Two-Photon Excitation for Clinical Diagnosis and Treatment

A promising direction for two-photon tissue imaging is clinical diagnosis and treatment. Optical biopsy is a new paradigm in clinical diagnosis. Traditional biopsy requires the removal, fixation, and imaging of tissues. The histological procedure is invasive, and tissue biochemical information is poorly preserved during these preparation steps. Optical biopsy based on TPE has been proposed in which 3-D images of tissues will be noninvasively acquired from patients. The image stack will be subsequently subjected to pathological analysis. TPM has been successfully used to image the skin structure of human volunteers down to a depth of 150  $\mu\text{m}$  (49, 139). Four distinct structural layers in the epidermis and the dermis are typically resolved (Figure 9; see color insert). The topmost layer is the stratum corneum, where the cornified cells form a protective layer. The second layer consists of epidermal keratinocytes. At the epidermal-dermal junction lies a layer of germinative basal cells. In the dermal layer, collagen/elastin fiber structures can be clearly observed. Pathological states such as atypical changes in cellular morphology or cellular hyperfoliation can often be identified. However, today, it remains unknown whether the quality of images acquired by two-photon optical biopsy is sufficient to produce pathological analysis results with accuracy comparable to that of traditional histology. If the feasibility of this technique can be demonstrated, the development of a two-photon endoscope may provide a method to biopsy other organs. Similar efforts are underway in confocal imaging (140, 141).

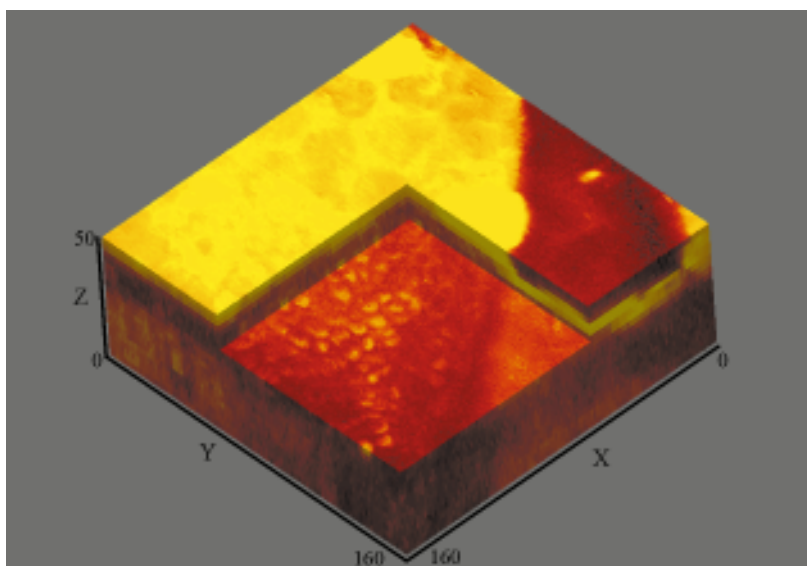


**Figure 9** Three-dimensional reconstructed two-photon images of in vivo human skin. The strata corneum and the basal layers are clearly visible. The figure is adapted from (159).

In addition to diagnosis, TPE may also find applications in clinical treatment based on photodynamic therapy. Photodynamic therapy allows the destruction of specific tissue, such as a tumor, by preferentially loading the tissue with a photosensitizer. Photosensitizer-loaded tissue is subsequently destroyed by laser illumination. Unfortunately, while the photosensitizer uptake in tumorous tissue is higher, there is often non-negligible uptake in normal tissues. Peripheral damage to healthy tissues is a common occurrence. The potential of using two-photon imaging to first localize the tumor and then of applying TPE to initiate photodynamic action at the selected site is a very attractive option. Preliminary work in this area has been reported (142–144).

## NEW DEVELOPMENTS IN TWO-PHOTON INSTRUMENTATION

Although the standard TPM, as described previously, functions very well as a general purpose instrument, a number of exciting new applications demand new instrumentation capabilities. This section describes the frontiers of two-photon instrumentation research and their biomedical potentials.

### Two-Photon Video Rate Microscopy

A major limitation of standard two-photon microscopes is their speed, which is  $\sim 0.5$  Hz, and the typical time required to obtain a high-resolution 3-D image stack is  $\sim 10$  min. This is clearly unsuitable for applications such as clinical biopsy, in which efficiency is crucial. Furthermore, this slow imaging speed is also incompatible with intravital imaging of patients or animals, in which the presence of motion artifacts is a major concern. Finally, the study of many cellular processes, such as calcium signaling or neuronal communication, requires imaging with millisecond time resolution. This problem is addressed by the development of a number of video rate two-photon microscopes.

The first video rate two-photon imaging system is based on the line-scanning approach. Image acquisition time is reduced by covering the image plane with a line instead of a point (145, 146). The line focus is typically achieved by using a cylindrical element in the excitation beam path. The resulting fluorescent line image is acquired with a spatially resolved detector such as a CCD camera. The main drawback associated with line scanning is the inevitable degradation of the image PSF, especially in the axial direction. A second approach, which has been termed “multiphoton multifocal microscopy” (147, 148), is analogous to Nipkow disk-based confocal systems (149). This elegant approach is based on a custom fabricated lenslet array, in place of the scan lens, that focuses the incident laser into multiple focal spots at the field aperture plane. The lenslet lenses are arranged in patterns similar to the traditional Nipkow disk designs. Upon the rotation of the lenslet lens, the projection of the lenslet will uniformly cover the field aperture

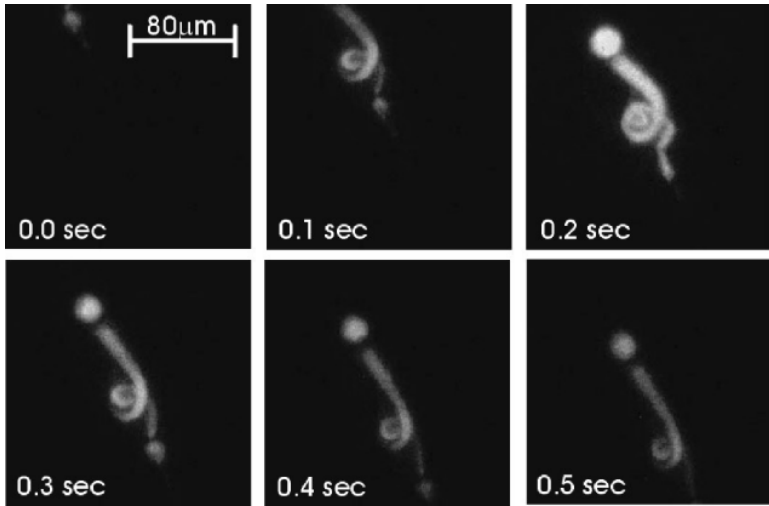


**Figure 10** Video rate two-photon image of a Calcein-AM labeled protozoa, blepharisma, as it swam across the observation area at a rate of  $\sim 100 \mu\text{m/s}$ . The figure is adapted from 151.

plane. A CCD camera is used to register the spatial distribution of the resulting fluorescent spots and integrate them into a coherent image. The ability to excite multiple sample regions simultaneously reduces total data acquisition time. This technique has less resolution degradation compared with line scanning and has the added advantage of being extremely robust. A third method has been developed based on the raster scanning of a single diffraction-limited spot by using either a high-speed resonance scanner (150) or rotating polygonal mirror (151; Figure 10). In this case, a large, single-point detector, such as a photomultiplier tube or an avalanche photodiode, can be used. The spatial information is encoded by the timing design of the raster scan pattern. By replacing the CCD imager with a single pixel detector, the image resolution may be improved by removing the dependence on the emission PSF. This is particularly important in turbid specimens in which the scattered fluorescence signal is not confined in a single pixel of the CCD imager and may degrade the image resolution.

### Simultaneous Two-Photon Fluorescence and Reflected-Light Confocal Microscopy

Imaging light scattering in biological specimens, due to changes in refractive index, can also yield important structural information not shown in fluorescent images. As such, confocal reflected light and two-photon fluorescence are complementary techniques that can allow different specimen structures to be visualized based on different contrast mechanisms. The capability of optical deep-tissue microscopy has been demonstrated by the simultaneous imaging of ex vivo human skin in

both two-photon fluorescence and reflected-light confocal modes (139). Complementary structures are clearly obtained by using either method in the basal layer (Figure 11), but TPE provides better visualization of collagen/elastin fibers in the dermis.

## Integrating Fluorescence Spectroscopy into Two-Photon Microscopes

Fluorescence spectroscopy is a powerful method to assay biological structure and functions. Spectroscopy techniques based on probe emission wavelength, lifetime, and emission polarization have been developed. Wavelength-resolved probes have been designed to measure many cell characteristics such as metabolite concentrations. Two-photon microscopes are typically designed with multiple detection channels such that emission wavelength changes can be monitored. The polarization of fluorescence emission measures the changes in the excitation and emission dipole directions of the fluorophore. One of the most common applications is the characterization of rotational diffusion rate. A polarization-resolving TPM has been designed (152) and has been applied to study rotational diffusion of single molecules in organic glasses. Fluorescence lifetime measures the residence time of the fluorophore in the excited state. Lifetime-resolved two-photon microscopes have been developed based on frequency domain (29) and time domain (153, 154) methods. Fluorescence lifetime is often highly sensitive to the

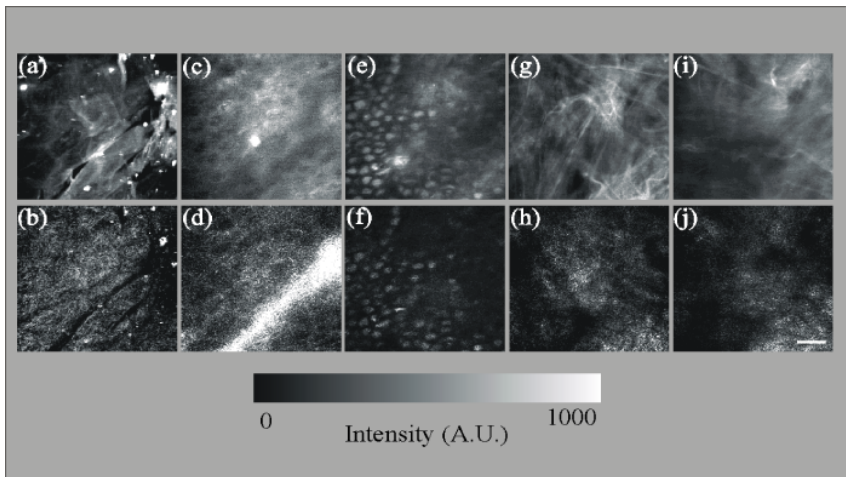


**Figure 11** A comparison of two-photon fluorescence (*top panels*) and confocal reflected light images (*bottom panels*). Three-dimensional resolved structural layers were acquired from ex vivo human skin: (*a, b*) stratum corneum; (*c, d*) epidermis; (*e, f*) basal layer; (*g, h, i, j*) dermis. This figure is adapted from 66.

fluorophore biochemical microenvironment. Lifetime-sensitive functional probes have been identified for common applications such as  $\text{Ca}^{2+}$  or pH measurements, providing a complementary approach to wavelength-resolved measurement. It is more important that there are interesting processes that can be best measured by lifetime-resolved imaging. Examples include the determination of tissue oxygenation based on lifetime changes on oxygen quenching (155, 156). Another example includes the use of lifetime resolved measurement to quantitatively monitor the proteolytic process of antigenic materials in macrophage vacuoles (157, 158) (Figure 12; see color insert).

## CONCLUSION

Within a decade after the invention of TPM, this technology has found applications in many diverse areas, ranging from the study of single molecules to tissue imaging. It is important that TPM is also starting to attract attention from the clinical and industrial communities. The development of a two-photon endoscope will be a critical step toward realizing noninvasive optical biopsy. As a complement to traditional pathology, the ability for a two-photon endoscope to rapidly and noninvasively acquire tissue-structural images may find use in areas such as surgical margin determination. TPM is also being applied by the pharmaceutical industry for high-throughput drug screening in which TPE or three-photon excitation of tryptophan or tyrosine allows label-free study of protein-drug interactions. Highly sensitive two-photon FCS and PCH may be applied for further quantitative analysis. Given the importance of studying biological systems *in vivo*, we can project that the use of TPM in academic research will continue to increase. As two-photon technology reaches maturity, it is also promising that high-impact clinical and industrial applications may be identified.

## ACKNOWLEDGMENTS

P. T. C. So acknowledges kind support from the National Science Foundation (MCB-9604382), National Institute of Health (R29GM56486-01), and American Cancer Society (RPG-98-058-01-CCE). C. Y. Dong acknowledges fellowship support from NIH 5F32CA75736-02.

**Visit the Annual Reviews home page at [www.AnualReviews.org](http://www.AnualReviews.org)**

## LITERATURE CITED

1. Denk W, Strickler JH, Webb WW. 1990. Two-photon laser scanning fluorescence microscopy. *Science* 248:73–76
2. Williams RM, Piston DW, Webb WW. 1994. Two-photon molecular excitation provides intrinsic 3-dimensional resolution for laser-based microscopy and microphotochemistry. *FASEB J.* 8:804–13
3. Denk WJ, Piston DW, Webb WW. 1995. Two-photon molecular excitation laser-

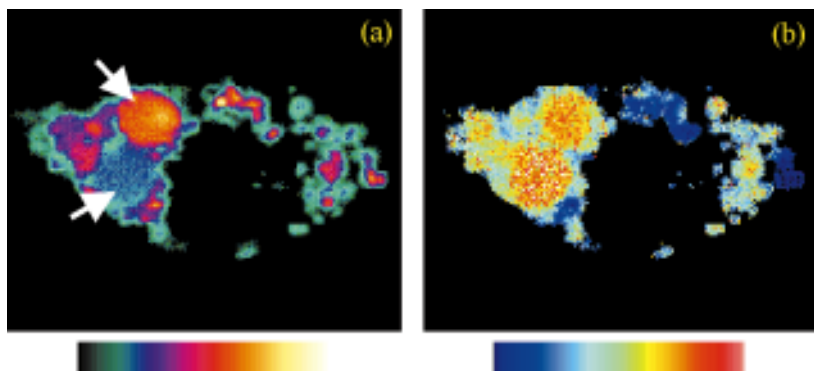


**Figure 12** Fluorescence intensity and lifetime images of mouse macrophage cells after internalizing a proteolysis probe. The probe, bovine serum albumin labeled with fluorescein at a ratio of 1:15–22 is mostly non-fluorescent and has a short lifetime in its native form owing to self-quenching. After proteolysis, the protein fragments become highly fluorescent and have a long lifetime. With only intensity information, the stages of proteolysis in different vacuoles cannot be determined because the amount of probe in each vacuole is unknown. However, lifetime measurement is independent of the probe loading concentration and can provide an accurate measure of proteolysis progress. Note that the two large vacuoles (*arrows*) at the left side of the cell have very different intensities. It would be incorrect to conclude that the vacuoles are at different stages of proteolysis. The lifetime image indicates that both vacuoles have the same lifetime. Data and images are adapted from (158, 160).

- scanning microscopy. In *Handbook of Biological Confocal Microscopy*, ed. JB Pawley, pp. 445–58. New York: Plenum
4. Hell SW. 1996. Nonlinear optical microscopy. *Bioimaging* 4:121–23
  5. Denk WJ, Strickler JP, Webb WW. 1991. *US Patent No. 5034613*
  6. Wilson T, Sheppard CJR. 1984. *Theory and Practice of Scanning Optical Microscopy*. New York: Academic. 213 pp.
  7. Pawley JB, ed. 1995. *Handbook of Confocal Microscopy*. New York: Plenum. 632 pp.
  8. Masters BR. 1996. *Selected Papers on Confocal Microscopy*. Bellingham, WA: SPIE. 702 pp.
  9. Göppert-Mayer M. 1931. Über elementarakte mit zwei quantensprungen. *Ann. Phys. (Leipzig)* 5:273–94
  10. Franken PA, Hill AE, Peters CW, Weinreich G. 1961. Generation of optical harmonics. *Phys. Rev. Lett.* 7:118–19
  11. Kaiser W, Garrett CGB. 1961. Two-photon excitation in  $\text{CaF}_2\text{:Eu}^{2+}$ . *Phys. Rev. Lett.* 7:229–31
  12. McClain WM. 1971. Excited state symmetry assignment through polarized two-photon absorption studies in fluids. *J. Chem. Phys.* 55:2789
  13. Friedrich DM, McClain WM. 1980. Two-photon molecular electronic spectroscopy. *Annu. Rev. Phys. Chem.* 31:559–77
  14. Friedrich DM. 1982. Two-photon molecular spectroscopy. *J. Chem. Educ.* 59: 472
  15. Birge RR. 1986. Two-photon spectroscopy of protein-bound fluorophores. *Acc. Chem. Res.* 19:138–46
  16. Singh S, Bradley LT. 1964. Three-photon absorption in naphthalene crystals by laser excitation. *Phys. Rev. Lett.* 12:162–64
  17. Rentzepis PM, Mitschele CJ, Saxman AC. 1970. Measurement of ultrashort laser pulses by three-photon fluorescence. *Appl. Phys. Lett.* 7:229–31
  18. Gryczynski I, Szmajkowski H, Lakowicz JR. 1995. On the possibility of calcium imaging using Indo-1 with three-photon excitation. *Photochem. Photobiol.* 62:804–8
  - 18a. Freund I, Kopf L. 1970. Long Range Order in  $\text{NH}_4\text{Cl}$ . *Phys. Rev. Lett.* 24:1017–21
  19. Hellwarth R, Christensen P. 1974. Nonlinear optical microscopic examination of structures in polycrystalline ZnSe. *Opt. Commun.* 12:318–22
  20. Sheppard CJR, Kompfner R, Gannaway J, Walsh D. 1977. *The scanning harmonic optical microscope*. Presented at IEEE/OSA Conf. Laser Eng. Appl., Washington, DC
  21. Gannaway JN, Sheppard CJR. 1978. Second harmonic imaging in the scanning optical microscope. *Opt. Quantum Electron.* 10:435–39
  22. Barad Y, Eisenberg H, Horowitz M, Silberberg Y. 1997. Nonlinear scanning laser microscopy by third harmonic generation. *Appl. Phys. Lett.* 70:922–24
  23. Squier JA, Muller M, Brakenhoff GJ, Wilson KR. 1998. Third harmonic generation microscopy. *Opt. Exp.* 3:315–24
  24. Campagnola PJ, Wei M-D, Lewis A, Loew LM. 1999. High-resolution nonlinear optical imaging of live cells by second harmonic generation. *Biophys. J.* 77:3341–49
  25. Baym G. 1974. *Lectures on Quantum Mechanics*. Menlo Park, CA: Benjamin/Cummings. 594 pp.
  26. Callis PR. 1997. The theory of two-photon induced fluorescence anisotropy. In *Nonlinear and Two-Photon-Induced Fluorescence*, ed. J Lakowicz, pp. 1–42. New York: Plenum
  27. Sheppard CJR, Gu M. 1990. Image formation in two-photon fluorescence microscope. *Optik* 86:104–6
  28. Gu M, Sheppard CJR. 1995. Comparison of three-dimensional imaging properties between two-photon and single-photon fluorescence microscopy. *J. Microsc.* 177:128–37
  29. So PTC, French T, Yu WM, Berland KM, Dong CY, Gratton E. 1995. Time-resolved fluorescence microscopy using two-photon excitation. *Bioimaging* 3:49–63

30. Diaspro A, Corosu M, Ramoino P, Robello M. 1999. Adapting a compact confocal microscope system to a two-photon excitation fluorescence imaging architecture. *Microsc. Res. Tech.* 47:196–205
31. Wokosin DL, Centonze VE, White J, Armstrong D, Robertson G, Ferguson AI. 1996. All-solid-state ultrafast lasers facilitate multiphoton excitation fluorescence imaging. *IEEE J. Sel. Top. Quantum Electron.* 2:1051–65
32. Hell SW, Booth M, Wilms S. 1998. Two-photon near- and far-field fluorescence microscopy with continuous-wave excitation. *Opt. Lett.* 23:1238–40
33. Centonze VE, White JG. 1998. Multiphoton excitation provides optical sections from deeper within scattering specimens than confocal imaging. *Biophys. J.* 75:2015–24
34. Gauderon R, Lukins RB, Sheppard CJR. 1999. Effects of a confocal pinhole in two-photon microscopy. *Microsc. Res. Tech.* 47:210–14
35. Xu C, Webb WW. 1997. Multiphoton excitation of molecular fluorophores and nonlinear laser microscopy. In *Nonlinear and Two-Photon-Induced Fluorescence*, ed. JR Lakowicz, pp. 471–540. New York: Plenum
36. Hermann JP, Ducuing J. 1972. Dispersion of the two-photon cross section in rhodamine dyes. *Opt. Commun.* 6:101–5
37. Xu C, Guild J, Webb WW, Denk W. 1995. Determination of absolute two-photon excitation cross sections by in situ second-order autocorrelation. *Opt. Lett.* 20:2372–74
38. Albota MA, Xu C, Webb WW. 1998. Two-photon fluorescence excitation cross sections of biomolecular probes from 690 to 960 nm. *Appl. Opt.* 37:7352–56
39. Lakowicz JR, Gryczynski I. 1992. Tryptophan fluorescence intensity and anisotropy decays of human serum albumin resulting from one-photon and two-photon excitation. *Biophys. Chem.* 45:1–6
40. Lakowicz JR, Kierdaszuk B, Callis P, Malak H, Gryczynski I. 1995. Fluorescence anisotropy of tyrosine using one- and two-photon excitation. *Biophys. Chem.* 56:263–71
41. Kierdaszuk B, Malak H, Gryczynski I, Callis P, Lakowicz JR. 1996. Fluorescence of reduced nicotinamides using one- and two-photon excitation. *Biophys. Chem.* 62:1–13
42. Chen ZP, Kaplan DL, Yang K, Kumar J, Marx KA, Tripathy SK. 1997. Two-photon-induced fluorescence from the phycoerythrin protein. *Appl. Opt.* 36:1655–59
43. Shear JB, Xu C, Webb WW. 1997. Multiphoton-excited visible emission by serotonin solutions. *Photochem. Photobiol.* 65:931–36
44. Chalfie M, Tu Y, Euskirchen G, Ward WW, Prasher DC. 1994. Green fluorescent protein as a marker for gene expression. *Science* 263:802–5
45. Niswender KD, Blackman SM, Rohde L, Magnuson MA, Piston DW. 1995. Quantitative imaging of green fluorescent protein in cultured cells: comparison of microscopic techniques, use in fusion proteins and detection limits. *J. Microsc.* 180:109–16
46. Potter SM, Wang CM, Garrity PA, Fraser SE. 1996. Intravital imaging of green fluorescent protein using two-photon laser-scanning microscopy. *Gene* 173:25–31
47. Masters BR, Chance B. 1999. Redox confocal imaging: intrinsic fluorescent probes of cellular metabolism. In *Fluorescent and Luminescent Probes for Biological Activity*, ed. WT Mason, pp. 361–74. London: Academic
48. Piston DW, Masters BR, Webb WW. 1995. Three-dimensionally resolved NAD(P)H cellular metabolic redox imaging of the in situ cornea with two-photon excitation laser scanning microscopy. *J. Microsc.* 178:20–27
49. Masters BR, So PTC, Gratton E. 1997. Multiphoton excitation fluorescence microscopy and spectroscopy of in vivo human skin. *Biophys. J.* 72:2405–12

50. Wang X, Krebs LJ, Al-Nuri M, Pudavar HE, Ghosal S, et al. 1999. A chemically labeled cytotoxic agent: two-photon fluorophore for optical tracking of cellular pathway in chemotherapy. *Proc. Natl. Acad. Sci. USA* 96:11081–84
51. Gryczynski I, Gryczynski Z, Lakowicz JR, Yang D, Burke TG. 1999. Fluorescence spectral properties of the anticancer drug topotecan by steady-state and frequency domain fluorimetry with one-photon and multi-photon excitation. *Photochem. Photobiol.* 69:421–28
52. Albota M, Beljonne D, Bredas J-L, Ehrlich JE, Fu J-Y, et al. 1998. Design of organic molecules with large two-photon absorption cross sections. *Science* 281:1653–56
53. Mohler WA, Simske JS, Williams-Masson EM, Hardin JD, White JG. 1998. Dynamics and ultrastructure of developmental cell fusions in the *Caenorhabditis elegans* hypodermis. *Curr. Biol.* 8:1087–90
54. Mohler WA, White JG. 1998. Stereo-4-D reconstruction and animation from living fluorescent specimens. *BioTechniques* 24:1006–12
55. Squirrell JM, Wokosin DL, White JG, Bavister BD. 1999. Long-term two-photon fluorescence imaging of mammalian embryos without compromising viability. *Nat. Biotechnol.* 17:763–67
56. Keyse SM, Tyrrell RM. 1990. Induction of the heme oxygenase gene in human skin fibroblasts by hydrogen peroxide and UVA (365 nm) radiation: evidence for the involvement of the hydroxyl radical. *Carcinogenesis* 11:787–91
57. Tyrrell RM, Keyse SM. 1990. New trends in photobiology: the interaction of UVA radiation with cultured cells. *J. Photochem. Photobiol. B* 4:349–61
58. Konig K, So PTC, Mantulin WW, Tromberg BJ, Gratton E. 1996. Two-photon excited lifetime imaging of autofluorescence in cells during UVA and NIR photostress. *J. Microsc.* 183:197–204
59. Konig K, Becker TW, Fischer P, Riemann I, Halhuber K-J. 1999. Pulse-length dependence of cellular response to intense near-infrared laser pulses in multiphoton microscopes. *Opt. Lett.* 24:113–15
60. Sako Y, Sekihata A, Yanagisawa Y, Yamamoto M, Shimada Y, et al. 1997. Comparison of two-photon excitation laser scanning microscopy with UV-confocal laser scanning microscopy in three-dimensional calcium imaging using the fluorescence indicator Indo-1. *J. Microsc.* 185:9–20
61. Koester HJ, Baur D, Uhl R, Hell SW. 1999. Ca<sup>2+</sup> fluorescence imaging with pico- and femtosecond two-photon excitation: signal and photodamage. *Biophys. J.* 77:2226–36
62. Hockberger PE, Skimina TA, Centonze VE, Lavin C, Chu S, et al. 1999. Activation of flavin-containing oxidases underlies light-induced production of H<sub>2</sub>O<sub>2</sub> in mammalian cells. *Proc. Natl. Acad. Sci. USA* 96:6255–60
63. Schonle A, Hell SW. 1998. Heating by absorption in the focus of an objective lens. *Opt. Lett.* 23:325–27
64. Jacques SL, McAuliffe DJ, Blank IH, Parrish JA. 1987. Controlled removal of human stratum corneum by pulsed laser. *J. Invest. Dermatol.* 88:88–93
65. Pustovalov VK. 1995. Initiation of explosive boiling and optical breakdown as a result of the action of laser pulses on melanosome in pigmented biotissues. *Kvantovaya Elektron.* 22:1091–94
66. Buehler C, Kim KH, Dong CY, Masters BR, So PTC. 1999. Innovations in two-photon deep tissue microscopy. *IEEE Eng. Med. Biol. Mag.* 18:23–30
67. Nie SM, Zare RN. 1997. Optical detection of single molecules. *Annu. Rev. Biophys. Biomol. Struct.* 26:567–96
68. Ambrose WP, Goodwin PM, Jett JH, Orden AV, Werner JH, Keller RA. 1999. Single molecule fluorescence spectroscopy at ambient temperature. *Chem. Rev.* 99:2929–56

69. Weiss S. 1999. Fluorescence spectroscopy of single biomolecules. *Science* 283:1676–83
70. Xie XS, Lu HP. 1999. Single-molecule enzymology. *J. Biol. Chem.* 274:15967–70
71. Mertz J, Xu C, Webb WW. 1995. Single-molecule detection by two-photon-excited fluorescence. *Opt. Lett.* 20:2532–34
72. Overway KS, Duhachek SD, Loeffelmann K, Zugel SA, Lytle FE. 1996. Blank-free two-photon excited fluorescence detection. *Appl. Spectrosc.* 50:1335–37
73. Brand L, Eggeling C, Seidel CAM. 1997. Single-molecule detection of coumarin-120. *Nucleosides Nucleotides* 16:551–56
74. Song JM, Inoue T, Kawazumi H, Ogawa T. 1998. Single molecule detection by laser two-photon excited fluorescence in a capillary flowing cell. *Anal. Sci.* 14:913–16
75. Hanninen PE, Soini JT, Soini E. 1999. Photon-burst analysis in two-photon fluorescence excitation flow cytometry. *Cytometry* 36:183–88
76. Van Orden A, Cai H, Goodwin PM, Keller RA. 1999. Efficient detection of single DNA fragments in flowing sample streams by two-photon fluorescence excitation. *Anal. Chem.* 71:2108–16
77. Plakhotnik T, Walser D, Pirota M, Renn A, Wild UP. 1996. Nonlinear spectroscopy on a single quantum system: two-photon absorption of a single molecule. *Science* 271:1703–5
78. Walser D, Plakhotnik T, Renn A, Wild UP. 1997. One- and two-photon spectroscopy on single molecules of diphenyloctatetraene. *Chem. Phys. Lett.* 270:16–22
79. Xu C, Shear JB, Webb WW. 1997. Hyper-Rayleigh and hyper-Raman scattering background of liquid water in two-photon excited fluorescence detection. *Anal. Chem.* 69:1285–87
80. Sanchez EJ, Novotny L, Holtom GR, Xie XS. 1997. Room-temperature fluorescence imaging and spectroscopy of single molecules by two-photon excitation. *J. Phys. Chem. A* 101:7019–23
81. Lewis MK, Wolanin P, Gafni A, Steel DG. 1998. Near-field scanning optical microscopy of single molecules by femtosecond two-photon excitation. *Opt. Lett.* 23:1111–13
82. Schwille P, Korlach J, Webb WW. 1999. Fluorescence correlation spectroscopy with single-molecule sensitivity on cell and model membranes. *Cytometry* 36:176–82
83. Schwille P, Haupts U, Maiti S, Webb WW. 1999. Molecular dynamics in living cells observed by fluorescence correlation spectroscopy with one- and two-photon excitation. *Biophys. J.* 77:2251–65
84. Bhawalkar JD, He GS, Park C-K, Zhao CF, Ruland G, Prasad PN. 1996. Efficient, two-photon pumped green upconverted cavity lasing in a new dye. *Opt. Commun.* 124:33–37
85. Bopp MA, Jia Y, Haran G, Morlino EA, Hochstrasser RM. 1998. Single-molecule spectroscopy with 27 fs pulses: time-resolved experiments and direct imaging of orientational distributions. *Appl. Phys. Lett.* 73:7–9
86. Sonnleitner M, Schutz GJ, Schmidt T. 1999. Imaging individual molecules by two-photon excitation. *Chem. Phys. Lett.* 300:221–26
87. Kirsch AK, Subramaniam V, Striker G, Schnetter C, Arndt-Jovin DJ, Jovin TM. 1998. Continuous wave two-photon scanning near-field optical microscopy. *Biophys. J.* 75:1513–21
88. Zenhausern F, O'Boyle MP, Wickramasinghe HK. 1994. Apertureless near-field optical microscope. *Appl. Phys. Lett.* 65:1623–25
89. Novotny L, Sanchez EJ, Xie XS. 1998. Near-field optical imaging using metal tips illuminated by higher-order Hermite-Gaussian beams. *Ultramicroscopy* 71:21–29
90. Kawata Y, Xu C, Denk W. 1999. Feasibility of molecular-resolution fluorescence near-field microscopy using multi-photon

- absorption and field enhancement near a sharp tip. *J. Appl. Phys.* 85:1294–301
91. Sanchez EJ, Novotny L, Xie XS. 1999. Near-field fluorescence microscopy based on two-photon excitation with metal tips. *Phys. Rev. Lett.* 82:4014–17
  92. Magde D, Elson E, Webb WW. 1972. Thermodynamic fluctuations in a reacting system: measurement by fluorescence correlation spectroscopy. *Phys. Rev. Lett.* 29:705–8
  93. Thompson NL. 1991. Fluorescence correlation spectroscopy. In *Topics in Fluorescence Spectroscopy*, ed. JR Lakowicz, pp. 337–78. New York: Plenum
  94. Berland KM, So PTC, Gratton E. 1995. Two-photon fluorescence correlation spectroscopy: method and application to the intracellular environment. *Biophys. J.* 68:694–701
  95. Berland KM, So PTC, Chen Y, Mantulin WW, Gratton E. 1996. Scanning two-photon fluctuation correlation spectroscopy: particle counting measurements for detection of molecular aggregation. *Biophys. J.* 71:410–20
  96. Chen Y, Muller JD, Berland KM, Gratton E. 1999. Fluorescence fluctuation spectroscopy. *Methods Companion Methods Enzymol.* 19:234–52
  97. Chen Y, Muller JD, So PTC, Gratton E. 1999. The photon counting histogram in fluorescence fluctuation spectroscopy. *Biophys. J.* 77:553–67
  98. Inoue S, Spring KR. 1997. *Video Microscopy: The Fundamentals*. New York: Plenum. 741 pp.
  99. Koutalos Y. 1999. Intracellular spreading of second messengers. *J. Physiol.* 519(3):629
  100. Szmackinski H, Gryczynski I, Lakowicz JR. 1993. Calcium-dependent fluorescence lifetimes of Indo-1 for one- and two-photon excitation of fluorescence. *Photochem. Photobiol.* 58:341–45
  101. Brust-Mascher I, Webb WW. 1998. Calcium waves induced by large voltage pulses in fish keratocytes. *Biophys. J.* 75:1669–78
  102. Denk W, Holt JR, Shepherd GM, Corey DP. 1995. Calcium imaging of single stereocilia in hair cells: localization of transduction channels at both ends of tip links. *Neuron* 15:1311–21
  103. Yu WM, So PTC, French T, Gratton E. 1996. Fluorescence generalized polarization of cell membranes: a two-photon scanning microscopy approach. *Biophys. J.* 70:626–36
  104. Parasassi T, Gratton E, Zajicek H, Levi M, Yu W. 1999. Detecting membrane lipid microdomains by two-photon fluorescence microscopy. *IEEE Eng. Med. Biol. Mag.* 18:92–99
  105. Bagatolli LA, Gratton E. 1999. Two-photon fluorescence microscopy observation of shape changes at the phase transition in phospholipid giant unilamellar vesicles. *Biophys. J.* 77:2090–101
  106. Maiti S, Shear JB, Williams RM, Zipfel WR, Webb WW. 1997. Measuring serotonin distribution in live cells with three-photon excitation. *Science* 275:530–32
  107. Xu C, Zipfel W, Shear JB, Williams RM, Webb WW. 1996. Multiphoton fluorescence excitation: new spectral windows for biological nonlinear microscopy. *Proc. Natl. Acad. Sci. USA* 93:10763–68
  108. Denk W. 1994. Two-photon scanning photochemical microscopy: mapping ligand-gated ion channel distributions. *Proc. Natl. Acad. Sci. USA* 91:6629–33
  109. Pettit DL, Wang SS, Gee KR, Augustine GJ. 1997. Chemical two-photon uncaging: a novel approach to mapping glutamate receptors. *Neuron* 19:465–71
  110. Furuta T, Wang SS, Dantzker JL, Dore TM, Bybee WJ, et al. 1999. Brominated 7-hydroxycoumarin-4-ylmethyls: photolabile protecting groups with biologically useful cross-sections for two-photon photolysis. *Proc. Natl. Acad. Sci. USA* 96:1193–200

111. Jaconi M, Pyle J, Bortolon R, Ou J, Clapham D. 1997. Calcium release and influx colocalize to the endoplasmic reticulum. *Curr. Biol.* 7:599–602
112. Lipp P, Niggli E. 1998. Fundamental calcium release events revealed by two-photon excitation photolysis of caged calcium in guinea pig cardiac myocytes. *J. Physiol.* 508:801–9
113. Brown EB, Webb WW. 1998. Two-photon activation of caged calcium with submicron, submillisecond resolution. *Methods Enzymol.* 291:356–80
114. Soeller C, Cannell MB. 1999. Two-photon microscopy: imaging in scattering samples and three-dimensionally resolved flash photolysis. *Microsc. Res. Tech.* 47:182–95
115. DelPrincipe F, Egger M, Ellis-Davies GC, Niggli E. 1999. Two-photon and UV-laser flash photolysis of the  $\text{Ca}^{2+}$  cage, dimethoxynitrophenyl-EGTA-4. *Cell Calcium* 25:85–91
116. Brown EB, Shear JB, Adams SR, Tsien RY, Webb WW. 1999. Photolysis of caged calcium in femtoliter volumes using two-photon excitation. *Biophys. J.* 76:489–99
117. Brown EB, Wu ES, Zipfel W, Webb WW. 1999. Measurement of molecular diffusion in solution by multiphoton fluorescence photobleaching recovery. *Biophys. J.* 77:2837–49
118. Denk W, Detwiler PB. 1999. Optical recording of light-evoked calcium signals in the functionally intact retina. *Proc. Natl. Acad. Sci. USA* 96:7035–40
119. Masters BR, So PTC, Gratton E. 1998. Optical biopsy of in vivo human skin: multi-photon excitation microscopy. *Lasers Med. Sci.* 13:196–203
120. So PTC, Kim H, Kochevar IE. 1998. Two-photon deep tissue ex vivo imaging of mouse dermal and subcutaneous structures. *Opt. Exp.* 3:339–50
121. Riegler M, Castagliuolo I, So PTC, Lotz M, Wang C, et al. 1999. Effects of substance P on human colonic mucosa in vitro. *Am. J. Physiol.* 276:G1473–83
122. Bennett BD, Jetton TL, Ying G, Magnuson MA, Piston DW. 1996. Quantitative subcellular imaging of glucose metabolism within intact pancreatic islets. *J. Biol. Chem.* 271:3647–51
123. Piston DW, Knobel SM, Postic C, Shelton KD, Magnuson MA. 1999. Adenovirus-mediated knockout of a conditional glucokinase gene in isolated pancreatic islets reveals an essential role for proximal metabolic coupling events in glucose-stimulated insulin secretion. *J. Biol. Chem.* 274:1000–4
124. Fetcho JR, O'Malley DM. 1997. Imaging neuronal networks in behaving animals. *Curr. Opin. Neurobiol.* 7:832–38
125. Denk W, Delaney KR, Gelperin A, Kleinfeld D, Strowbridge BW, et al. 1994. Anatomical and functional imaging of neurons using 2-photon laser scanning microscopy. *J. Neurosci. Methods* 54:151–62
126. Yuste R, Denk W. 1995. Dendritic spines as basic functional units of neuronal integration. *Nature* 375:682–84
127. Yuste R, Majewska A, Cash SS, Denk W. 1999. Mechanisms of calcium influx into hippocampal spines: heterogeneity among spines, coincidence detection by NMDA receptors, and optical quantal analysis. *J. Neurosci.* 19:1976–87
128. Denk W, Sugimori M, Llinas R. 1995. Two types of calcium response limited to single spines in cerebellar Purkinje cells. *Proc. Natl. Acad. Sci. USA* 92:8279–82
129. Svoboda K, Denk W, Kleinfeld D, Tank DW. 1997. In vivo dendritic calcium dynamics in neocortical pyramidal neurons. *Nature* 385:161–65
130. Svoboda K, Helmchen F, Denk W, Tank DW. 1999. Spread of dendritic excitation in layer 2/3 pyramidal neurons in rat barrel cortex in vivo. *Nat. Neurosci.* 2:65–73
131. Helmchen F, Svoboda K, Denk W, Tank DW. 1999. In vivo dendritic calcium

- dynamics in deep-layer cortical pyramidal neurons. *Nat. Neurosci.* 2:989–96
132. Shi SH, Hayashi Y, Petralia RS, Zaman SH, Wenthold RJ, et al. 1999. Rapid spine delivery and redistribution of AMPA receptors after synaptic NMDA receptor activation. *Science* 284:1811–16
  133. Mainen ZF, Malinow R, Svoboda K. 1999. Synaptic calcium transients in single spines indicate that NMDA receptors are not saturated. *Nature* 399:151–55
  134. Maletic-Savatic M, Malinow R, Svoboda K. 1999. Rapid dendritic morphogenesis in CA1 hippocampal dendrites induced by synaptic activity. *Science* 283:1923–27
  135. Engert F, Bonhoeffer T. 1999. Dendritic spine changes associated with hippocampal long-term synaptic plasticity. *Nature* 399:66–70
  136. Kleinfeld D, Mitra PP, Helmchen F, Denk W. 1998. Fluctuations and stimulus-induced changes in blood flow observed in individual capillaries in layers 2 through 4 of rat neocortex. *Proc. Natl. Acad. Sci. USA* 95:15741–46
  137. Jones KT, Soeller C, Cannell MB. 1998. The passage of  $Ca^{2+}$  and fluorescent markers between the sperm and egg after fusion in the mouse. *Development* 125:4627–35
  138. Summers RG, Piston DW, Harris KM, Morrill JB. 1996. The orientation of first cleavage in the sea urchin embryo, *Lytechinus variegatus*, does not specify the axes of bilateral symmetry. *Dev. Biol.* 175:177–83
  139. Kim KH, So PTC, Kochevar IE, Masters BR, Gratton E. 1998. Two-photon fluorescence and confocal reflected light imaging of thick tissue structures. *SPIE Proc.* 3260:46–57
  140. Dabbs T, Glass M. 1992. Fiber-optic confocal microscopy: FOCON. *Appl. Opt.* 31:3030–35
  141. Giniunas L, Justkaitis R, Shatalin SV. 1993. Endoscope with optical sectioning capability. *Appl. Opt.* 32:2888–90
  142. Bhawalkar JD, Kumar ND, Zhao CF, Prasad PN. 1997. Two-photon photodynamic therapy. *J. Clin. Laser Med. Surg.* 15:201–4
  143. Bodaness RS, Heller DF, Krasinski J, King DS. 1986. The two-photon laser-induced fluorescence of the tumor-localizing photosensitizer hematoporphyrin derivative: Resonance-enhanced 750 nm two-photon excitation into the near-UV Soret band. *J. Biol. Chem.* 261:12098–101
  144. Fisher WG, Partridge WP Jr, Dees C, Wachter EA. 1997. Simultaneous two-photon activation of type-I photodynamic therapy agents. *Photochem. Photobiol.* 66:141–55
  145. Guild JB, Webb WW. 1995. Line scanning microscopy with two-photon fluorescence excitation. *Biophys. J.* 68:A290
  146. Brakenhoff GJ, Squier J, Norris T, Bliton AC, Wade WH, Athey B. 1996. Real-time two-photon confocal microscopy using a femtosecond, amplified Ti:Sapphire system. *J. Microsc.* 181:253–59
  147. Bewersdorf J, Pick R, Hell SW. 1998. Multifocal multiphoton microscopy. *Opt. Lett.* 23:655–57
  148. Buist AH, Muller M, Squire J, Brakenhoff GJ. 1998. Real time two-photon absorption microscopy using multi point excitation. *J. Microsc.* 192:217–26
  149. Petran M, Hadravsky M, Egger MD, Galambos R. 1958. Tandem scanning reflected light microscope. *J. Opt. Soc. Am.* 58:661–64
  150. Fan GY, Fujisaki H, Miyawaki A, Tsay RK, Tsien RY, Ellisman MH. 1999. Video-rate scanning two-photon excitation fluorescence microscopy and ratio imaging with cameleons. *Biophys. J.* 76:2412–20
  151. Kim KH, Buehler C, So PTC. 1999. High-speed, two-photon scanning microscope. *Appl. Opt.* 38:6004–9
  152. Farrer RA, Previte MJR, Olson CE, Peyser LA, Fourkas JT, So PTC. 1999.

- Single-molecule detection with a two-photon fluorescence microscope with fast-scanning capabilities and polarization sensitivity. *Opt. Lett.* 24:1832–34
153. Straub M, Hell SW. 1998. Fluorescence lifetime three-dimensional microscopy with picosecond precision using a multifocal multiphoton microscope. *Appl. Phys. Lett.* 73:1769–71
154. Sytsma J, Vroom JM, de Grauw CJ, Geritsen HC. 1998. Time-gated fluorescence lifetime imaging and microvolume spectroscopy using two-photon excitation. *J. Microsc.* 191:39–51
155. Helmlinger G, Yuan F, Dellian M, Jain RK. 1997. Interstitial pH and pO<sub>2</sub> gradients in solid tumors in vivo: high-resolution measurements reveal a lack of correlation. *Nat. Med.* 3:177–82
156. Roh HD, Boucher Y, Kalnicki S, Buchsbaum R, Bloomer WD, Jain RK. 1991. Interstitial hypertension in carcinoma of uterine cervix in patients: possible correlation with tumor oxygenation and radiation response. *Cancer Res.* 51:6695–98
157. Weaver DJ Jr, Cherukuri A, Carrero J, Coelho-Sampaio T, Durack G, Voss EW Jr. 1996. Macrophage mediated processing of an exogenous antigenic fluorescent probe: time-dependent elucidation of the processing pathway. *Biol. Cell.* 87:95–104
158. French T, So PTC, Weaver DJ Jr, Coelho-Sampaio T, Gratton E, et al. 1997. Two-photon fluorescence lifetime imaging microscopy of macrophage-mediated antigen processing. *J. Microsc.* 185:339–53
159. Masters BR, So PTC. 1999. Multi-photon excitation microscopy and confocal microscopy imaging of in vivo human skin: a comparison. *Microsc. Microanal.* 5: 282–89
160. So PTC, Konig K, Berland K, Dong CY, French T, et al. 1998. New time-resolved techniques in two-photon microscopy. *Cell Mol. Biol.* 44:771–93
161. Xu C, Webb WW. 1996. Measurement of two-photon excitation cross sections of molecular fluorophores with data from 690 to 1050 nm. *J. Opt. Soc. Am. B* 13: 481–91



## CONTENTS

PIERRE M. GALLETTI: A Personal Reflection, <i>Robert M. Nerem</i>	1
PHYSICOCHEMICAL FOUNDATIONS AND STRUCTURAL DESIGN OF HYDROGELS IN MEDICINE AND BIOLOGY, <i>N. A. Peppas, Y. Huang, M. Torres-Lugo, J. H. Ward, J. Zhang</i>	9
BIOENGINEERING MODELS OF CELL SIGNALING, <i>Anand R. Asthagiri, Douglas A. Lauffenburger</i>	31
FUNDAMENTALS OF IMPACT BIOMECHANICS: Part I - Biomechanics of the Head, Neck, and Thorax, <i>Albert I. King</i>	55
INJURY AND REPAIR OF LIGAMENTS AND TENDONS, <i>Savio L.-Y. Woo, Richard E. Debski, Jennifer Zeminski, Steven D. Abramowitch, Serena S. Chan Saw, MS, James A. Fenwick</i>	83
ELECTROPHYSIOLOGICAL MODELING OF CARDIAC VENTRICULAR FUNCTION: From Cell to Organ, <i>R. L. Winslow, D. F. Scollan, A. Holmes, C. K. Yung, J. Zhang, M. S. Jafri</i>	119
CRYOSURGERY, <i>Boris Rubinsky</i>	157
CELL MECHANICS: Mechanical Response, Cell Adhesion, and Molecular Deformation, <i>Cheng Zhu, Gang Bao, Ning Wang</i>	189
MICROENGINEERING OF CELLULAR INTERACTIONS, <i>Albert Folch, Mehmet Toner</i>	227
QUANTITATIVE MEASUREMENT AND PREDICTION OF BIOPHYSICAL RESPONSE DURING FREEZING IN TISSUES, <i>John C. Bischof</i>	257
MICROFABRICATED MICRONEEDLES FOR GENE AND DRUG DELIVERY, <i>Devin V. McAllister, Mark G. Allen, Mark R. Prausnitz</i>	289
CURRENT METHODS IN MEDICAL IMAGE SEGMENTATION, <i>Dzung L. Pham, Chenyang Xu, Jerry L. Prince</i>	315
ANTIBODY ENGINEERING, <i>Jennifer Maynard, George Georgiou</i>	339
NEW CURRENTS IN ELECTRICAL STIMULATION OF EXCITABLE TISSUES, <i>Peter J. Bassar, Bradley J. Roth</i>	377
TWO-PHOTON EXCITATION FLUORESCENCE MICROSCOPY, <i>Peter T. C. So, Chen Y. Dong, Barry R. Masters, Keith M. Berland</i>	399
IMAGING THREE-DIMENSIONAL CARDIAC FUNCTION, <i>W. G. O'Dell, A. D. McCulloch</i>	431
THREE-DIMENSIONAL ULTRASOUND IMAGING, <i>Aaron Fenster, Donal B. Downey</i>	457
BIOPHYSICAL INJURY MECHANISMS IN ELECTRICAL SHOCK TRAUMA, <i>Raphael C. Lee, Dajun Zhang, Jurgen Hannig</i>	477
WAVELETS IN TEMPORAL AND SPATIAL PROCESSING OF BIOMEDICAL IMAGES, <i>Andrew F. Laine</i>	511

MICRODEVICES IN MEDICINE, <i>Dennis L. Polla, Arthur G. Erdman, William P. Robbins, David T. Markus, Jorge Diaz-Diaz, Raed Rizq, Yunwoo Nam, Hui Tao Brickner, Amy Wang, Peter Krulevitch</i>	551
NEUROENGINEERING MODELS OF BRAIN DISEASE, <i>Leif H. Finkel</i>	577
EXTRACORPOREAL TISSUE ENGINEERED LIVER-ASSIST DEVICES, <i>Emmanouhl S. Tzanakakis, Donavon J. Hess, Timothy D. Sielaff, Wei-Shou Hu</i>	607
MAGNETIC RESONANCE STUDIES OF BRAIN FUNCTION AND NEUROCHEMISTRY, <i>Kâmil Ugurbil, Gregor Adriany, Peter Andersen, Wei Chen, Rolf Gruetter, Xiaoping Hu, Hellmut Merkle, Dae-Shik Kim, Seong-Gi Kim, John Strupp, Xiao Hong Zhu, Seiji Ogawa</i>	633
INTERVENTIONAL AND INTRAOPERATIVE MAGNETIC RESONANCE IMAGING, <i>J. Kettenbach, D. F. Kacher, S. K. Koskinen, Stuart G. Silverman, A. Nabavi, Dave Gering, Clare M. C. Tempny, R. B. Schwartz, R. Kikinis, P. M. Black, F. A. Jolesz</i>	661
CARTILAGE TISSUE REMODELING IN RESPONSE TO MECHANICAL FORCES, <i>Alan J. Grodzinsky, Marc E. Levenston, Moonsoo Jin, Eliot H. Frank</i>	691
IN VIVO NEAR-INFRARED SPECTROSCOPY, <i>Peter Rolfe</i>	715

# Lab 3: Fast fluorescence microrheology for quantitative studies of cytoskeletal mechanotransduction

**Location:** NE47-205

**PI:** Peter So

**Lab Instructors:** Maxine Jonas, Euiheon Chung and Yang-Hyo Kim

## Summary

The fluorescence laser tracking microrheometer (FLTM) is a novel instrument that proposes to assess the local, frequency-dependent mechanical properties of living cells with nanometer spatial sensitivity over a frequency range extending from 1 Hz to 50 kHz. This tutorial will familiarize researchers with the FLTM's theoretical principles and experimental routines, and will illustrate how chemically-induced cytoskeletal disruption is accompanied by reduced cellular stiffness and viscosity (as parameterized by  $G^*(\omega)$ , the frequency dependent complex shear modulus).

## Recommended Reading

S. Yamada *et al.*, "Mechanics of living cells measured by laser tracking microrheology," *Biophys. J.*, **78**.

T. G. Mason *et al.*, "Optical measurements of frequency-dependent linear viscoelastic moduli of complex fluids," *Phys. Rev. Lett.* **74**.





# Cytoskeletal Mechanics

## Fast Fluorescence Microrheology

Maxine Jonas <sup>\*</sup><sup>#</sup>, Euiheon Chung <sup>#</sup>, Yang-Hyo Kim <sup>#</sup>, and Peter T.C. So <sup>\*</sup>

**Abstract** — The fluorescence laser tracking microrheometer (FLTM) is a novel instrument that proposes to assess the local, frequency-dependent mechanical properties of living cells with nanometer spatial sensitivity over a frequency range extending from 1 Hz to 50 kHz (1). This tutorial will familiarize researchers with the FLTM’s theoretical principles and experimental routines, and will illustrate how chemically-induced cytoskeletal disruption is accompanied by reduced cellular stiffness and viscosity (as parameterized by  $G^*(\omega)$ , the frequency-dependent complex shear modulus).

### I. MICRORHEOLOGY

**T**O gain insight in mechanotransduction and understand how the mechanical properties of cells are affected by their environmental cues, an assortment of microrheology schemes have been developed. They fall into two classes:

- active techniques (e.g. micropipette aspiration, AFM: atomic force microscopy, and magnetic manipulation), which involve mechanical force application to cells, and
- passive techniques (e.g. dynamic light scattering, and LTM: laser tracking microrheology), which examine the thermal fluctuations of probe particles (2-11).

#### A. Fluorescence laser tracking microrheometry (FLTM)

We have developed a fluorescence laser tracking microrheometer (FLTM) whose strengths are several folds.

1) The FLTM proposes to characterize the solid-like vs. liquid-like behavior of biomaterials using only microscopic amounts of sample, and without any active manipulation of the probed matter. FLTM takes advantage of the thermal energy of embedded colloids and relates their displacements to the viscoelastic properties of the surrounding medium: the more viscous and/or stiff the probe’s microenvironment, the more confined its Brownian motion (12,13).

2) The FLTM’s excellent speed (up to 50 kHz) and spatial resolution (~ 4 nm) make this apparatus well suited to the study of heterogeneous and dynamic biological systems.

3) The extended frequency range (~ 0.5 Hz to 50 kHz) assayed by the FLTM allows the appraisal not only of the macroscopic viscoelasticity of molecular networks at long time scales (on the order of seconds), but also the fast bending and twisting fluctuations of single filaments at shorter time scales, which are fundamental for fast cytoskeletal dynamics.

4) Relying on fluorescent probes (of characteristic spectral signatures) enables the targeting of cellular structures with molecular specificity.

#### B. Theory

The frequency-dependent complex shear modulus  $G^*(\omega)$  characterizes both the solid-like (through its real part  $G'(\omega)$ , the storage modulus) and the liquid-like (through its imaginary part  $G''(\omega)$ , the loss modulus) behaviors of a material. FLTM experimentally derives  $G^*(\omega)$  from a sphere’s mean squared displacement,  $MSD(\tau) = \langle \Delta r^2(\tau) \rangle = \langle (r(t+\tau) - r(t))^2 \rangle_t$  (where  $r(t)$  describes the particle’s 2-dimensional trajectory, and  $\tau$  corresponds to various lag times) by exploiting a generalized Stokes-Einstein relation (GSER)(14):

$$|G^*(\omega)| \approx \frac{2k_B T}{3\pi a \langle \Delta r^2(1/\omega) \rangle \Gamma[1 + \alpha(\omega)]} \quad (\text{Eq. 1})$$

$$G'(\omega) = |G^*(\omega)| \cos(\pi\alpha(\omega)/2) \quad (\text{Eq. 2})$$

$$G''(\omega) = |G^*(\omega)| \sin(\pi\alpha(\omega)/2), \quad (\text{Eq. 3})$$

$$\alpha(\omega) \equiv \left. \frac{\partial \ln \langle \Delta r^2(\tau) \rangle}{\partial \ln \tau} \right|_{\tau=1/\omega}$$

with  $k_B$  the Boltzmann constant,  $T$  the absolute temperature,  $a$  the radius of the probe particle, and  $\Gamma$  the gamma function.

### II. FLTM EXPERIMENTS

#### A. Instrumentation: the FLTM setup

A schematic of the FLTM is presented in Figure 1: A laser beam<sup>(1)</sup> (532 nm, Verdi Nd:YVO<sub>4</sub>, Coherent) is collimated through a custom light path and a 100X NA 1.30 oil objective<sup>(2)</sup> (Olympus) and illuminates a 100  $\mu\text{m}$  x 100  $\mu\text{m}$  area of sample positioned on the stage of an Olympus IX71 inverted microscope<sup>(3)</sup> and mounted on an  $xy$  piezoelectric nanopositioning system (Queensgate). The photons emitted by the fluorescent beads<sup>(4)</sup> (Molecular Probes) contained in the excitation volume are filtered by a dichroic mirror-barrier filter combination<sup>(5)</sup> (Chroma Technology) and detected after beam expansion by a quadrant photomultiplier tube<sup>(6)</sup> (PMT,

\* Corresponding authors: jonas\_m@mit.edu, ptso@mit.edu

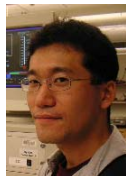
# 2006 GEM<sup>4</sup> presenters



Maxine Jonas



Euiheon Chung



Yang-Hyo Kim



Peter T.C. So



Hamamatsu). The total magnification of the system is of 2250 X, so that a 1- $\mu\text{m}$  bead is finally projected on the 18mm x 18mm quadrant PMT as a disk of diameter 2.25 mm. Position signals are inferred at the PMT level from the difference in photocurrents between opposing pairs of quadrant elements, which are further amplified into digitized voltages by a 200 kHz 16-bit simultaneous 4-channel analog-to-digital converter (ADC, Strategic Test). For instance, the  $x$ -position of the probe particle is deduced from the signal ratio  $RatioX = (\text{Ch0} + \text{Ch2})/(\text{Ch1} + \text{Ch3})$  (Fig. 1).

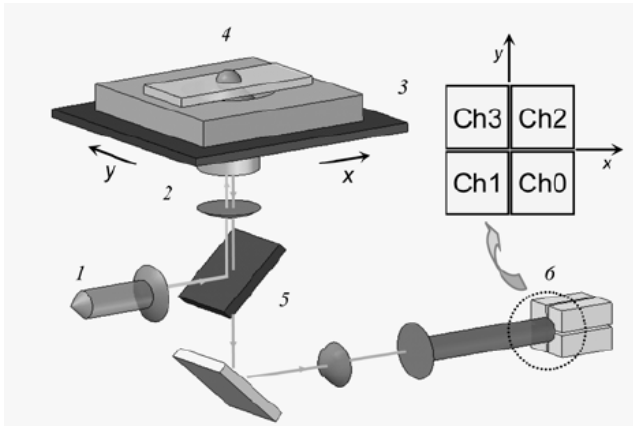


Fig. 1. Schematic diagram of the FLTM

### B. Sample preparation: cell biology

NIH 3T3 fibroblasts were grown in standard 100mm x 20mm cell culture dishes (Corning) in DMEM (Cellgro<sup>®</sup>) supplemented with 10% fetal bovine serum (Invitrogen) and 1% penicillin-streptomycin (Invitrogen). Cells were cultured at 37°C in 5% CO<sub>2</sub>. The day prior to the FLTM experiments, fibroblasts were plated on 35-mm glass-bottom cell culture dishes (MatTek) coated with collagen I (1  $\mu\text{g}/\text{cm}^2$ , Cohesion Tech). On the day of the experiments, the cell confluency had reached about 60%. 1- $\mu\text{m}$  orange fluorescent beads (Molecular Probes) coated with integrin antibodies were mixed to the growth media (at a concentration of  $5 \times 10^5$  microspheres/mL) and added to the plated cells for a period of 12 to 24 hours (for bead endocytosis). The influence of cytoskeletal components on cellular rheology was assessed by treating fibroblasts with the actin-disrupting drug cytochalasin D (10  $\mu\text{M}$ ) for 30 minutes before a final wash with culture media (Fig. 2).

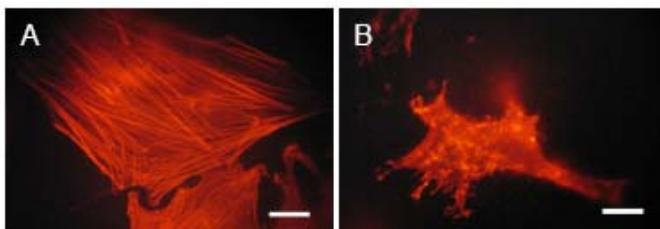


Fig. 2. Fluorescent labeling of F-actin (by Alexa Fluor<sup>®</sup> 568 phalloidin) in untreated (A) and cytochalasin-D treated (B) fibroblasts. Scale bars are 20  $\mu\text{m}$ .

### C. Data acquisition using LabVIEW (National Instruments)

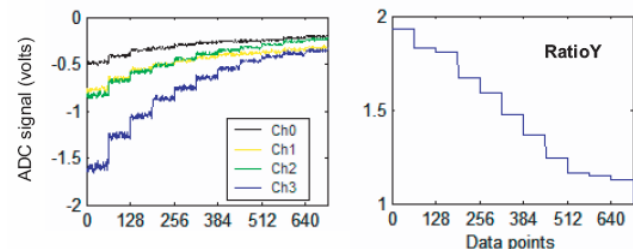
- Position a single 1- $\mu\text{m}$  bead at the center of the detector's field of view: Scan Sample Shutter Background.vi 
  - fully automated command and coordination of the Queensgate xy stage (for raster-scanning of successively smaller areas) and the ADC acquisition card,
  - very low illumination power ( $< 5 \times 10^2 \text{ W}\cdot\text{m}^{-2}$ ) to avoid photobleaching of the probe.
- Record the bead's fluorescent signal on the quadrant PMT using Record Signal With Shutter.vi
  - collection of  $2^{18} = 262,144$  data points at an ADC sampling rate of 200 kS/s.
  - high laser power ( $\sim 5 \times 10^5 \text{ W}\cdot\text{m}^{-2}$ ): open iris at fiber input.
- Calibrate the FLTM with Steps Shutter.vi
  - translation of the sample along both detection axes ( $x$ , then  $y$ ) and recording of the light distribution at each step.

### III. FLTM DATA PROCESSING (MATLAB)

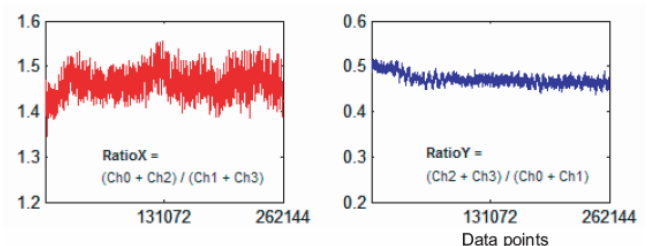


#### A. From binary file to probe trajectory

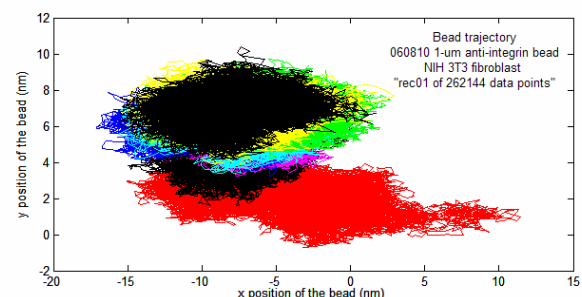
- GetSteps.m: determine what  $RatioX$  and  $RatioY$  are at each bead position of the 10-nm-spaced calibration steps.



- GetRatioXY.m: calculate the bead's fluorescent signal's  $RatioX$  and  $RatioY$  at each data point (20- $\mu\text{s}$  intervals).

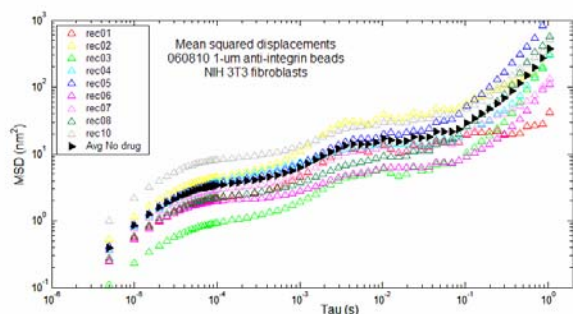


- GetTrajBead.m: for each time point, fit  $RatioX$  and  $RatioY$  to an  $(x,y)$  position doublet using the calibration curves.

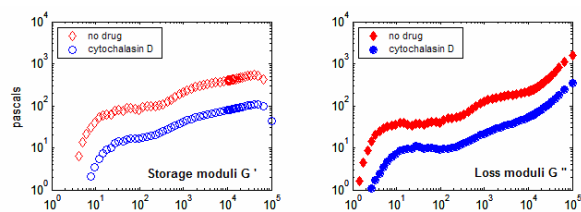


### B. From bead trajectory to cell rheology

- `GetMSD.m`: calculate and save the particle's mean squared displacement from its 2D trajectory.



- `GetGstar.m`: compute the storage and loss moduli  $G'(\omega)$  and  $G''(\omega)$  from the probes' MSDs using Eq. 1-3.



## IV. CONCLUSION

In conclusion, FLTM, benefiting from spatial and temporal sensitivities of 4 nm and 20  $\mu$ s and sampling five decades of frequency (0.5 Hz to 50 kHz), is a passive microrheology technique well-suited to investigate biological problems, as illustrated by its aptitude to quantitatively characterize (i) the effect of cytoskeleton-disrupting drugs on cellular viscoelastic profiles, (ii) the difference between intracellular and surface fluorescent probes, and (iii) the impact of bead coating proteins on rheological results (1).

## ACKNOWLEDGMENTS

This work was supported by the National Institutes of Health (NIH) P01 HL64858-01A1. The authors would like to thank Dr. Rich Lee (Brigham and Women's Hospital, Cambridge, MA) for providing fibroblasts, Thierry Savin (MIT, Cambridge, MA) and Jan Lammerding (Brigham and Women's Hospital) for constructive and helpful discussions, as well as acknowledge Helene Karcher (MIT) and Nate Tedford (MIT) for offering technical assistance and useful advice.

## NOTES

## REFERENCES

1. Jonas, M., Huang, H., Kamm, R. D., So, P. T. C. 2006. Fast Fluorescence Laser Tracking Microrheometry For Quantitative Studies of Cytoskeletal Mechanotransduction. *Biophys J*:submitted.
2. Wang, N., J. P. Butler, and D. E. Ingber. 1993. Mechanotransduction across the cell surface and through the cytoskeleton. *Science* 260:1124-1127.
3. Thoumine, O. and A. Ott. 1997. Time scale dependent viscoelastic and contractile regimes in fibroblasts probed by microplate manipulation. *J Cell Sci* 110 ( Pt 17):2109-2116.
4. Drury, J. L. and M. Dembo. 2001. Aspiration of human neutrophils: effects of shear thinning and cortical dissipation. *Biophys J* 81:3166-3177.
5. Mathur, A. B., G. A. Truskey, and W. M. Reichert. 2000. Atomic force and total internal reflection fluorescence microscopy for the study of force transmission in endothelial cells. *Biophys J* 78:1725-1735.
6. Rotsch, C. and M. Radmacher. 2000. Drug-induced changes of cytoskeletal structure and mechanics in fibroblasts: an atomic force microscopy study. *Biophys J* 78:520-535.
7. Laurent, V. M., S. Henon, E. Planus, R. Fodil, M. Balland, D. Isabey, and F. Gallet. 2002. Assessment of mechanical properties of adherent living cells by bead micromanipulation: comparison of magnetic twisting cytometry vs optical tweezers. *J Biomech Eng* 124:408-421.
8. Bausch, A. R., F. Ziemann, A. A. Boulbitch, K. Jacobson, and E. Sackmann. 1998. Local measurements of viscoelastic parameters of adherent cell surfaces by magnetic bead microrheometry. *Biophys J* 75:2038-2049.
9. Fabry, B., G. N. Maksym, J. P. Butler, M. Glogauer, D. Navajas, and J. J. Fredberg. 2001. Scaling the microrheology of living cells. *Phys Rev Lett* 87:148102.
10. Lammerding, J., P. C. Schulze, T. Takahashi, S. Kozlov, T. Sullivan, R. D. Kamm, C. L. Stewart, and R. T. Lee. 2004. Lamin A/C deficiency causes defective nuclear mechanics and mechanotransduction. *J Clin Invest* 113:370-378.
11. Yamada, S., D. Wirtz, and S. C. Kuo. 2000. Mechanics of living cells measured by laser tracking microrheology. *Biophys J* 78:1736-1747.
12. Mason, T. G. and D. A. Weitz. 1995. Optical measurements of frequency-dependent linear viscoelastic moduli of complex fluids. *Physical Review Letters* 74:1250-1253.
13. Mason T.G., G. K., van Zanten J.H., Wirtz D., Kuo S.C. 1997. Particle tracking microrheology of complex fluids. *Phys. Rev. Lett.* 79 (17):3282-3285.
14. Mason, T. G. 2000. Estimating the viscoelastic moduli of complex fluids using the generalized Stokes-Einstein equation. *Rheol Acta* 39:371-378.



# Mechanics of Living Cells Measured by Laser Tracking Microrheology

Soichiro Yamada,\* Denis Wirtz,\* and Scot C. Kuo†

\*Department of Chemical Engineering, The Johns Hopkins University, Baltimore, Maryland 21218; and †Department of Biomedical Engineering, The Johns Hopkins University, Baltimore, Maryland 21205 USA

**ABSTRACT** To establish laser-tracking microrheology (LTM) as a new technique for quantifying cytoskeletal mechanics, we measure viscoelastic moduli with wide bandwidth (5 decades) within living cells. With the first subcellular measurements of viscoelastic phase angles, LTM provides estimates of solid versus liquid behavior at different frequencies. In LTM, the viscoelastic shear moduli are inferred from the Brownian motion of particles embedded in the cytoskeletal network. Custom laser optoelectronics provide sub-nanometer and near-microsecond resolution of particle trajectories. The kidney epithelial cell line, COS7, has numerous spherical lipid-storage granules that are ideal probes for noninvasive LTM. Although most granules are percolating through perinuclear spaces, a subset of perinuclear granules is embedded in dense viscoelastic cytoplasm. Over all time scales embedded particles exhibit subdiffusive behavior and are not merely tethered by molecular motors. At low frequencies, lamellar regions ( $820 \pm 520$  dyne/cm<sup>2</sup>) are more rigid than viscoelastic perinuclear regions ( $330 \pm 250$  dyne/cm<sup>2</sup>,  $p < 0.0001$ ), but spectra converge at high frequencies. Although the actin-disrupting agent, latrunculin A, softens and liquefies lamellae, physiological levels of F-actin, alone ( $11 \pm 1.2$  dyne/cm<sup>2</sup>) are  $\sim 70$ -fold softer than lamellae. Therefore, F-actin is necessary for lamellae mechanics, but not sufficient. Furthermore, in time-lapse of apparently quiescent cells, individual lamellar granules can show  $\sim 4$ -fold changes in moduli that last  $>10$  s. Over a broad range of frequencies (0.1–30,000 rad/s), LTM provides a unique ability to noninvasively quantify dynamic, local changes in cell viscoelasticity.

## INTRODUCTION

Because a major function of cytoskeletal filaments is to support cell structure, mechanical characterization of living cells must complement characterization of reconstituted networks. Despite many plausible molecular mechanisms for controlling cytoskeletal structure, current biophysical methods lack the speed and resolution to monitor mechanics in living cells and cannot adequately test molecular models. To address these shortcomings, we have developed a new approach to cellular mechanics, laser-tracking microrheology (LTM), that quickly characterizes mechanical properties over an  $\sim 5$ -decade range of frequencies. For model polymers, LTM quantitatively provides the same viscoelastic spectra as mechanical rheometry (Mason et al., 1997b).

To measure cell mechanics, cells have been deformed by many techniques. Whole-cell deformations have used a torsional pendulum (e.g., Eichinger et al., 1996), parallel plates (e.g., Thoumine and Ott, 1997), and micropipette aspiration (see Hochmuth, 1993). Smaller mechanical probes of cells include microneedles (e.g., Felder and Elson, 1990; Nicklas, 1983), cell poker (e.g., Petersen et al., 1982) and atomic force microscopy (e.g., Radmacher et al., 1996; A-Hassan et al., 1998). Magnetic forces have been applied to particles within living cells (Bausch et al., 1999; Valberg and Albertini, 1985; Crick and Hughes, 1950), and attached to the surface of living cells (Bausch et al., 1998; Wang et al., 1993). So far, optical forces have only been applied to deforming soft subcellular structures, such as the plasma

membrane (Kuo and Sheetz, 1992; Schmidt et al., 1993). Mechanical measurements using direct deformations are slow and often invasive. Deformations can be so large as to be nonlinear and, hence, relevant to only situations mimicking the measurement protocol. Furthermore, these approaches often rely upon curve-fit models to extract values of phenomenological springs and dashpots.

Without resorting to phenomenological models, mechanical rheometers can empirically measure mechanical properties over widely varying frequencies. By using large amounts of sample material, such devices can apply very small, linear strains through oscillating surfaces. The resulting viscoelastic shear modulus,  $G^*$ , is a complex number that varies with the frequency of oscillation. Its magnitude,  $G_d (= |G^*|)$ , is the material's resistance to deformation, and its phase angle,  $\delta (= \angle(G^*))$  is an index of the material's solid-like ( $\delta = 0$ ) or liquid-like ( $\delta = \pi/2$ ) behavior. Mechanical rheometers have provided thorough characterization of reconstituted F-actin networks (e.g., Xu et al., 1998b; Janmey et al., 1994). However, mechanical data of comparable quality are not available for living cells.

LTM quantitatively provides the same viscoelastic spectra as mechanical rheometry (Mason et al., 1997b). Unlike mechanical rheometry, no external forces are applied to the material. Instead, mechanical properties are derived from the Brownian motion of individual spherical particles embedded in the viscoelastic material. Unlike percolating particles, embedded particles appear almost stationary and only move distances that are a fraction of their radii. In cytoskeletal networks, the motions of small percolating particles have been used to quantify pore size and "microviscosity" of the solution between the filaments (e.g., Hou et al., 1990; Luby-Phelps et al., 1986). For large particles embedded in

Received for publication 20 July 1999 and in final form 23 December 1999.

Scot C. Kuo, Ross Building, Rm. 724, 720 Rutland Ave., Baltimore, MD 21205. Tel.: 410-614-2528; Fax: 410-955-0549; E-mail: skuo@bme.jhu.edu.

© 2000 by the Biophysical Society

0006-3495/00/04/1736/12 \$2.00

cytoskeletal networks, particle motions reveal the elasticity of the cytoskeletal mesh itself (Xu et al., 1998a; Palmer et al., 1998, 1999).

To realize its potential beyond reconstituted networks, we use LTM to probe the mechanics of living cells. Unlike measurements using direct deformations, LTM is fast, sensitive, and quantifies liquid versus solid behavior (viscoelastic phase angle). Furthermore, to demonstrate the noninvasiveness of LTM, we chose the cell line COS7 for cellular measurements. COS7 cells have large, flat lamellae and are rich with spherical “granules” that we demonstrate are ideal for probing cytoskeletal mechanics. The mechanical properties of COS7 cytoplasm are highly heterogeneous, but elasticity generally correlates with F-actin staining. Lamellae are most rigid, but are ~70-fold more rigid than reconstituted F-actin alone. By monitoring lamellar particles, we show that their local mechanics are dynamic and that actin-disrupting agents act quickly to soften moduli. Clearly, F-actin is necessary, but not sufficient, for creating rigid lamellae in living cells.

## METHODS

### Cell culture

COS7 cells (ATCC CRL-1651) were cultured at 37°C in 5% CO<sub>2</sub> in Dulbecco’s Minimal Essential Medium without phenol red supplemented with 10% FBS, 2 mM glutamine, and 25 mM HEPES (Life Technologies Inc., Gaithersburg, MD). All measurements were performed at room temperature. Cells were grown on coverslips etched with identifying grids (Bellco Glass Inc., Vineland, NJ) so that the same cells used for laser tracking could be examined by fluorescent staining. Custom flow chambers allowed the introduction of pharmacological agents without disturbing the cell’s position on the microscope.

### Fluorescent labeling of cytoskeletal networks

For F-actin labeling, cells were fixed in 3% paraformaldehyde in Dulbecco’s phosphate-buffered saline (PBS, Life Technologies), extracted with 0.5% Triton X-100 in PBS (Sigma, St. Louis, MO), and F-actin labeled with rhodamine phalloidin (Molecular Probes, Eugene, OR). For vimentin labeling, cells were fixed in 80% methanol and stained with murine monoclonal V9 (Sigma) and rhodamine goat anti-mouse antibodies. All fluorescently labeled cells were mounted in Slowfade Light (Molecular Probes) to minimize photobleaching, and observed with a Zeiss Z-15 filter set and Plan-Neofluar 40× objective on an Axiovert 135 microscope (Carl Zeiss, Thornwood, NY). Images were acquired with a Photometrics PXL-1400 camera controlled by IPLab software (Scanalytics Inc., Fairfax, VA).

### Electron microscopy

For electron microscopy, COS7 cells were fixed in 3% glutaraldehyde in PBS. Coverslips were further fixed by 1% osmium tetroxide in 0.1 M cacodylic acid followed by 2% aqueous uranyl acetate. All electron microscopy reagents were purchased from Ted Pella, Inc. (Redding, CA). Specimens were embedded in epoxy resin after a series of dehydrations with ethanol. Hardened blocks were sectioned parallel and perpendicular to the substrate, and stained with 3% aqueous mixture of uranyl acetate and lead citrate. Electron micrographs of epoxy-embedded thin cell sections were obtained using a Zeiss EM10 electron microscope (Carl Zeiss).

## Actin preparation

Actin was extracted from rabbit skeletal muscle acetone powder as described by Spudich and Watt (1971). The resulting actin was gel filtered with Sephacryl 300 HR in buffer G (0.2 mM ATP, 0.5 mM dithiothreitol, 0.1 mM CaCl<sub>2</sub>, 1 mM NaN<sub>3</sub>, 2 mM Tris-Cl, pH 8 at 25°C). The concentration of eluted actin was determined spectrophotometrically at 290 nm (MacLean-Fletcher and Pollard, 1980). For particle tracking measurements, actin was polymerized in the presence of  $5 \times 10^{-7}$  (w/v) 1 μm-diameter carboxylated polystyrene particles (Polysciences, Warrington, PA) so that the average distance between particles was ~100 μm. Polymerization was initiated by adding one-tenth volume of 10 × KMEI (500 mM KCl, 10 mM MgCl<sub>2</sub>, 10 mM EGTA, 100 mM imidazole pH 7 at 25°C), and immediately assembled into the microscope slide chamber. To minimize wall effects, all particles used for laser tracking were at least 10 μm from the coverslip surface.

## Laser deflection particle tracking

Using a focused, low-power laser beam, we track a probe particle by monitoring its forward-scattered light with a quadrant photodiode detector (see Fig. 1). Any off-axis motion of the particle deflects energy away from the optical axis and produces imbalances between signals from photodiode quadrants. Laser powers are low (0.13 mW,  $\lambda = 670$  nm) so that optical forces are negligible. Built on an Axiovert 100TV microscope (Carl Zeiss), a custom light path for the quadrant photodiode detector was built onto the high numerical aperture (1.4 NA) condenser. Because of its limited aperture, the quadrant photodiode detector is not conjugate to the back aperture of the objective. Photocurrent differences between opposing quadrant pairs are amplified into a voltage that is subsequently digitized by a 16-bit A/D converter (ComputerBoards Inc., Middleboro, MA). Although the analog bandwidth of our photodiode circuitry is ~200 kHz, signals were filtered at 22 kHz to prevent aliasing during digitization.

## Calibration of particle displacements and sizes

Laser-tracking signals were calibrated for each probe particle by monitoring the laser signal as a function of the xy piezoelectric stage displacement

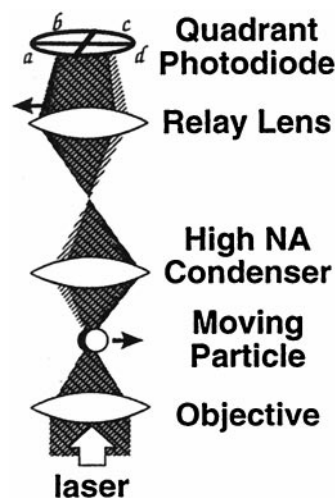


FIGURE 1 Principle of laser deflection particle tracking. A particle at the laser’s focus causes far-field scatter, and its off-axis motions cause net energy to be deflected from the optical axis. A quadrant photodetector monitors the deflected energy, and position signals are generated from the difference in photocurrents between opposing pairs of quadrant elements.

(Queensgate Instruments Ltd., East Meadow, NY). Built-in capacitance transducers directly monitor displacements of the piezoelectric stage with near-Angstrom resolution. A typical calibration curve for a 0.27- $\mu\text{m}$ -diameter polystyrene particle (Polysciences) is shown in Fig. 2. The linear range is  $\sim 300$  nm wide and all particles used for LTM stayed within this range. Used below, the slope of this linear region is the positional sensitivity of the laser-tracking signal.

To noninvasively estimate the size of lipid-storage granules, we used the fact that light scattering is very sensitive to particle size, particularly for particles smaller than the wavelength of incident light (van de Hulst, 1981). The positional sensitivity of the laser-tracking signal (see Fig. 2) can be used as a measure of light scattering. As shown in Fig. 3, the positional sensitivity of laser-tracking signals varies with the square of particle size. Because COS7 granules are highly refractile and their images are indistinguishable from polystyrene bead images (see Fig. 5, *inset*), the indices of refraction of the two types of particles must be comparable. Furthermore, light scattering has a very weak dependence on relative index of refraction (van de Hulst, 1981). Without further corrections, we use the calibration curve of Fig. 3 to estimate all granule sizes.

## PRINCIPLES

### Microrheology from particle trajectory

The Brownian motion of a particle embedded within a filamentous network is directly related to the network's mechanical properties (Xu et al., 1998a; Palmer et al., 1998, 1999; Mason et al., 1997a, b). Phenomenologically, particles exhibit larger motions when their local environments are less rigid or less viscous. As described below, both the amplitude and the time scale are important for calculating mechanical moduli. Calculated over various lag-times,  $\tau$ , we use the mean-squared-displacement (MSD)  $\langle \Delta R^2(\tau) \rangle = \text{Average}[(\vec{r}(t + \tau) - \vec{r}(t))^2]$  of the particle's trajectory,  $\vec{r}(t)$ , to quantify its amplitude of motions over different time scales.

Although the amplitude of particle motions is generally inversely related to the network's mechanical modulus, increases in both rigidity and viscosity will restrict particle motions. To distinguish viscosity from elasticity, the MSD must be measured over a large range of time scales. In purely viscous materials, MSDs of particles vary linearly with lag-times. In purely elastic materials, MSDs are constant, regardless of lag-times. For both of these ideal materials, when deformation frequency is appropriately related to lag-time, the MSD and the magnitude of viscoelastic modulus,

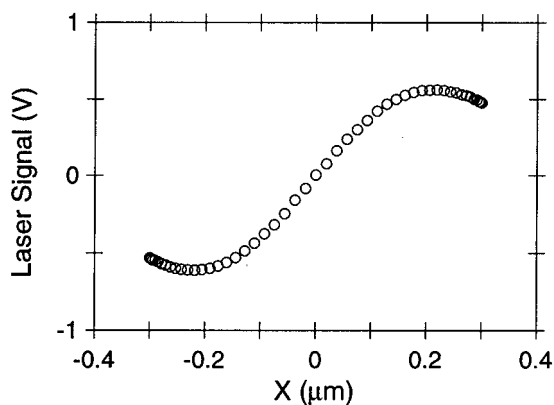


FIGURE 2 Calibrating laser deflection signals. The laser-tracking signal is calibrated by moving particles with a piezoelectric stage. Typical  $x$ -axis calibration curve (along  $y = 0$ ) for a polystyrene bead (0.27  $\mu\text{m}$ ). For estimating particle sizes, we use the positional sensitivity of the laser signal that is computed as the slope of the calibration curve at its central inflection point.

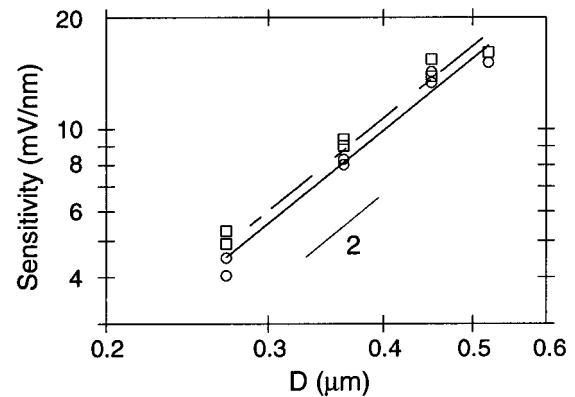


FIGURE 3 Positional sensitivity of laser signal versus the probe diameter. For polystyrene particles of various diameters, the  $x$  and  $y$  positional sensitivities (circles and squares, respectively) are shown. The positional sensitivity of the laser signal is computed as the slope of the calibration curve (see Fig. 2) at its central inflection point. All endogenous granules of COS7 fall within the region where positional sensitivity varies quadratically with particle size. For reference, a quadratic slope (power-law of two) and the power-law curve-fitting to both  $x$  and  $y$  positional sensitivities are shown.

$G_d = |G^*|$ , are inversely related by a constant factor. However, for viscoelastic materials, a more complex expression is needed to generalize the relationship.

Assuming that inertial effects are negligible, the viscoelastic shear moduli are related to MSD by (Mason and Weitz, 1995):

$$\tilde{G}(s) = s\tilde{\eta}(s) = \frac{2k_B T}{3\pi a s \langle \Delta \tilde{R}^2(s) \rangle} \quad (1)$$

where  $s$  is the complex Laplace frequency,  $k_B$  Boltzmann's constant,  $T$  the absolute temperature,  $a$  the radius of the particle, and  $\langle \Delta \tilde{R}^2(s) \rangle$  the unilateral Laplace transform of the two-dimensional MSD,  $\langle \Delta R^2(\tau) \rangle$ . For Eq. 1 to be valid there are three criteria that must be satisfied: rigid particle, spherical particle, and that the network is well-approximated as a viscoelastic continuum. Requirements for spherical and rigid particles come from generalizing Stoke's law as a complex function for the particle's resistance to motion,  $\tilde{\zeta}(s) = 6\pi a \tilde{\eta}(s)$ , within viscoelastic materials. To satisfy the continuum approximation, the particle must be much larger than the pore size of the filamentous network. As discussed later, the lipid-storage granules of COS7 within the lamellae satisfy all of these conditions.

Because numerical Laplace transforms require numerical integration and its associated pitfalls, we use the following two approximations, rather than direct evaluation of Eq. 1. From numerical simulations, both approximations require data spanning at least 2.5 decades of time and frequency for validity (data not shown), and LTM data typically span 5 decades. The complex viscoelastic moduli can be represented in polar notation as

$$\tilde{G}(i\omega) = G'(\omega) + iG''(\omega) = G_d(\omega) \exp(i\delta(\omega)),$$

where

$$G_d(\omega) = |\tilde{G}(i\omega)|$$

and

$$\delta(\omega) = \angle(\tilde{G}(i\omega)) = \arctan(G''(\omega)/G'(\omega)).$$

Using a power-law, or “wedge” (Tschoegl, 1989), approximation of  $\langle \Delta R^2(\tau) \rangle$  and its unilateral Fourier transform (Mason et al., 1997b) gives:

$$G_d(\omega) \approx \frac{2k_B T}{3\pi a \langle \Delta R^2(\tau) \rangle \Gamma\left(1 + \frac{d \ln \langle \Delta R^2(\tau) \rangle}{d \ln \tau}\right)} \Bigg|_{\tau=1/\omega} \quad (2)$$

where  $\Gamma$  is the gamma function. For ideal viscous or elastic materials, where the MSD,  $\langle \Delta R^2(\tau) \rangle$ , is either linearly related or independent of  $\tau$ , the gamma function has value of unity ( $\Gamma(2) = \Gamma(1) = 1$ ) and Eq. 2 is exact. Other phenomenological approximation methods are possible (Tschoegl, 1989), but Eq. 2 has performed very well so far (Xu et al., 1998a; Palmer et al., 1998). To extract the phase angle  $\delta(\omega)$ , we use the deceptively simple approximation derived by Booij and Thoone (1982):

$$\delta(\omega) = \frac{1}{\pi} \int_{-\infty}^{\infty} \frac{d \ln G_d(u)}{d \ln u} \ln \left| \frac{u + \omega}{u - \omega} \right| d \ln u \quad (3)$$

$$\approx \frac{\pi}{2} \left( \frac{d \ln G_d(u)}{d \ln u} \right)_{u=\omega}$$

which relates the slope of log-log plots (power law) of  $G_d$  spectra to the phase angle. With data exceeding 2 decades of frequency bandwidth, Eq. 3 is a highly accurate approximation, and its empirically determined standard deviations never exceed 5% (Booij and Thoone, 1982).

## RESULTS

### Endogenous granules as probes

In principle, LTM can be a completely noninvasive measurement of cell mechanics. When using endogenous cellular particles, no cell manipulations or deformations are needed. However, the choice of organelles as probes must proceed with rigor. The endogenous particles must be spherical and rigid to satisfy the underlying assumptions of Stokes' law (Eq. 1). Fortunately, COS7 cells are rich with highly refractile granules. Just like polystyrene beads, immobilized granules show no detectable fluctuations beyond the intrinsic noise of our instrumentation ( $<1$  nm, 30 kHz; data not shown). Transmission electron micrographs show that these granules are spherical in fixed cells (Fig. 4). These granules are probably lipid droplets, because they lack any surrounding membrane bilayer. Lipid storage granules are observed in many cell types, and appear as refractile spheres in a light microscope. When using osmium tetroxide, such lipid droplets are intensely stained in electron micrographs (Fawcett, 1981) and appear as in Fig. 4. Furthermore, these COS7 granules are intensely stained with the lipid-droplet specific fluorescent dye, Nile Red (Green-span et al., 1985), but do not immunostain with endoplasmic reticulum (ER), Golgi, or lysosomal markers (T. Schroer, personal communication). In this paper we restrict the term “endogenous granules” only to refer to these lipid droplets within COS7, and we do not refer to any other organelle.

To demonstrate the appropriateness of endogenous granules as probes, we suspended polystyrene beads and gran-

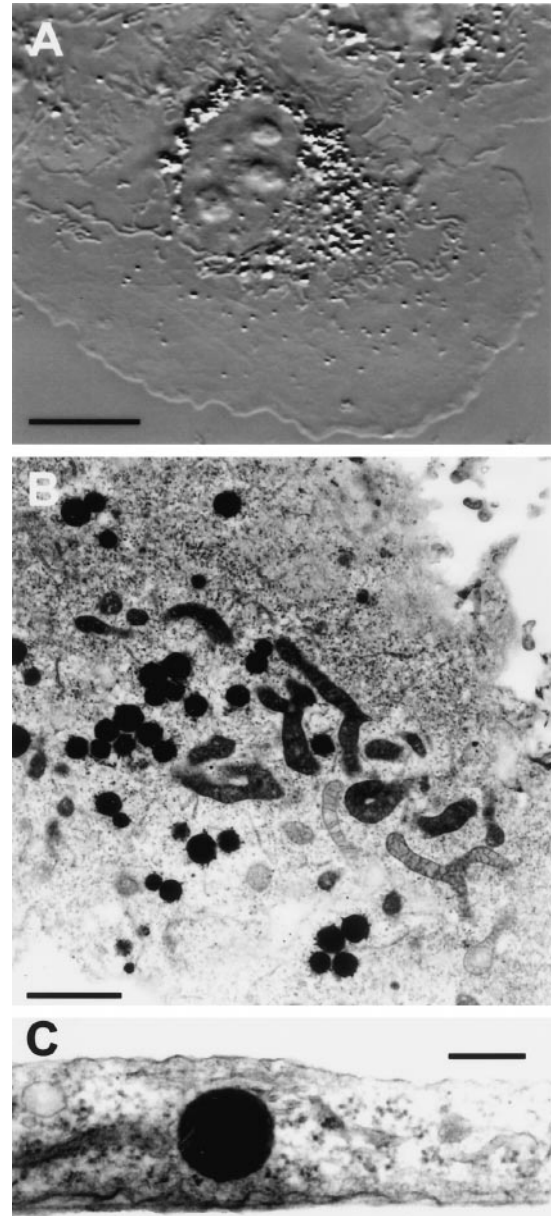


FIGURE 4 Endogenous granules of COS7. (A) Video-enhanced DIC image of COS7 cells showing many optically refractile granules distributed throughout the cytoplasm. Scale bar 10  $\mu\text{m}$ . (B) Sectioned parallel to the substrate, thin-section electron micrograph of COS7 shows granules intensely stained by uranyl acetate. Scale bar 2  $\mu\text{m}$ . (C) Sectioned orthogonally to the substrate, thin-section electron micrograph of COS7. Scale bar 0.2  $\mu\text{m}$ .

ules partially purified from COS7 into the same gelatin solution. Because granules are frequently indistinguishable from beads by DIC microscopy (see Fig. 5, *inset*), we used fluorescent beads and fluorescence microscopy to identify particles. As shown in Fig. 5, laser-tracking measurements cannot distinguish lipid-storage granules from polystyrene particles; both types of particles give identical viscoelastic spectra for gelatin. By satisfying all prerequisites, these

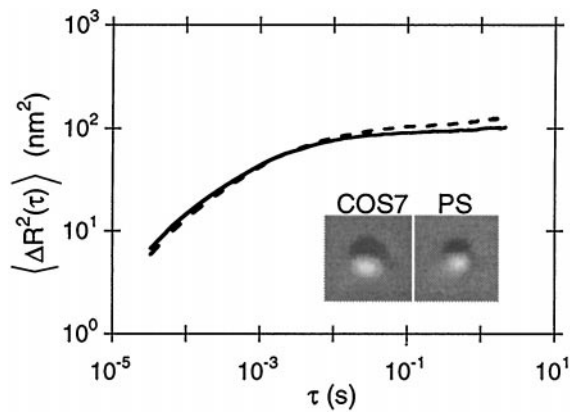


FIGURE 5 LTM of endogenous granules (COS7) and polystyrene (PS) particles co-embedded in gelatin. After lysing COS7 cells by brief sonication, granules and fluorescent polystyrene beads were mixed with molten gelatin (30 mg/ml, 37°C), assembled into slide chambers and allowed to cool to ensnare particles. MSDs were calculated from the trajectories of two adjacent particles in the gel, one a COS7 granule (*dashed line*) and the other a fluorescent microsphere (*solid line*). By laser-tracking sensitivity (see Methods), both particles appear the same size, so MSDs can be compared directly. *Inset*: DIC images of granule and polystyrene particles are indistinguishable.

granules make excellent probes for noninvasive measurements of cellular mechanics.

### Viscoelastic nature of cytoplasm

Laser tracking reveals that subcellular particles experience a viscoelastic environment. At three different time scales, Fig. 6 A shows the trajectory of a typical lipid-storage granule located in COS7 lamellae. At longer time scales, the trajectory of the granule becomes more restricted. In contrast, diffusion in a purely viscous material should produce a more sparse random walk (see Saxton, 1993). Furthermore, purely viscous diffusion predicts an MSD that is proportional to lag-time,  $\tau$ . Endogenous granules show subdiffusive behavior at all MSD lag-times (Fig. 6 B). Even at the fastest times ( $\tau < 1$  ms), the granule experiences the effects of the cytoskeletal network, which never behaves as if purely viscous. For comparison, particles merely tethered by molecular motors show purely viscous behavior on these fast time scales ( $0.1 < \tau < 23$  ms; Allersma et al., 1998). At longer time scales ( $\tau > 2$  ms), the granule's motions become progressively more constrained, but MSDs never reach a true plateau. Such plateaus would be expected for purely elastic materials. Like lamellar granules, perinuclear granules can also behave subdiffusively, but never purely elastically. Living cytoplasm is clearly a very complex viscoelastic material.

### Subcellular mechanics

Although laser-tracking alone indicates viscoelastic behavior, full LTM analysis yields quantitative spectra of cellular

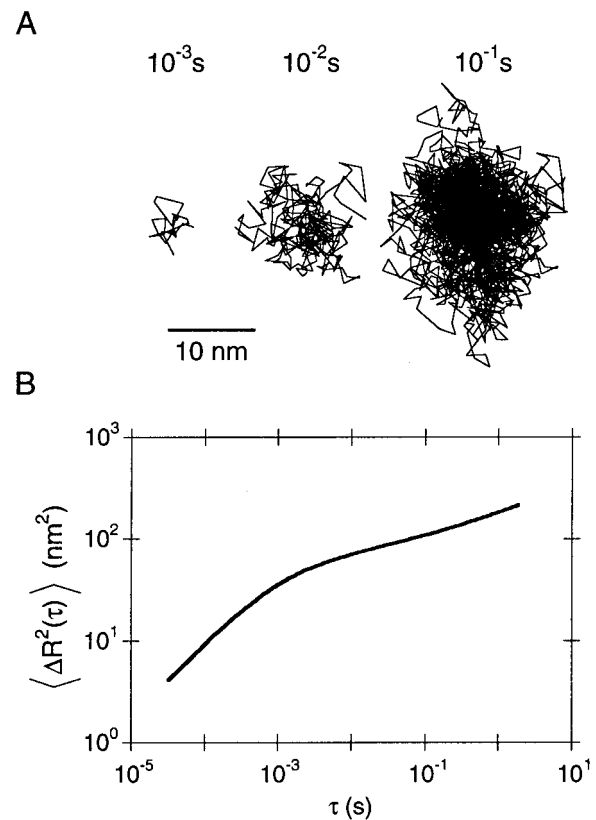


FIGURE 6 Brownian motion of an endogenous granule inside living a cell. (A) The trajectory of the endogenous granule over different time scales. (B) The mean-squared displacement of the granule's motions.

mechanics. Furthermore, with particles in appropriate locations, LTM can compare the mechanics of subcellular regions. By laser-tracking granules in lamellae and perinuclear regions of cytoplasm (14 cells, 49 different granules), LTM reveals different absolute viscoelastic moduli,  $G_d$ , and phase angle,  $\delta$ , for these two regions (Fig. 7). Spectral data for each granule were averaged from at least five separate acquisitions of data ( $>20$  s total). To make initial estimates, simple morphological rules were sufficient to identify mechanical regions in COS7: perinuclear granules were within a 20- $\mu$ m radius of the center of a nucleus (average radii of nuclei were  $9.2 \pm 1.6 \mu$ m) and lamellar particles beyond this radius. For LTM, we ignored all granules that were above or below the nucleus, showing large Brownian excursions ( $>0.2 \mu$ m), or undergoing active movements ( $>0.5 \mu$ m). Less than 5% of all granules showed active movement. Although  $>90\%$  of perinuclear granules showed Brownian excursions that were too large to track by LTM, granules adjacent to the ER and Golgi were more firmly trapped and were used for LTM. No granules within the ER/Golgi networks were used for LTM analysis. At all frequencies, lamellae regions resist particle motions (higher moduli) more than perinuclear regions (Fig. 7). While the moduli of these subcellular regions are significantly differ-

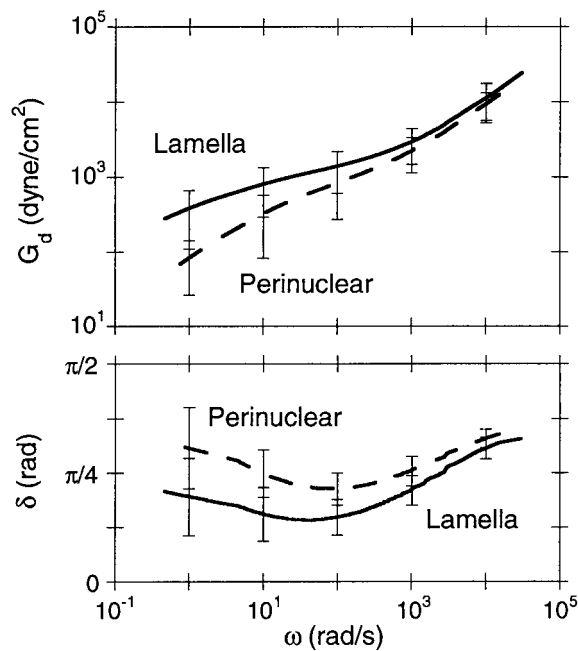


FIGURE 7 Local heterogeneity of cytoplasm. As described in Methods, viscoelastic spectra were calculated from mean-squared displacements of 49 different granules within 14 different cells. As described in the text, subcellular regions were identified by simple morphometric rules, with 11 granules perinuclear and 38 particles in the lamellae. Error bars are standard deviations.

ent at low frequencies ( $p < 0.0001$ ), they converge at higher frequencies ( $>1000$  rad/s). For both subcellular regions, the phase angles suggest viscoelastic behavior at all frequencies. Surprisingly, embedded perinuclear granules of COS7 never exhibit fully liquid-like behavior (i.e.  $\delta = \pi/2$ ), as expected for particles merely tethered by molecular motors (Allersma et al., 1998). Furthermore, they did not show any episodes of directed motion during tracking.

Fixation and fluorescent staining after LTM measurements suggest the sources of viscoelastic behavior. Microtubule immunostaining of COS7 cells was too sparse to explain viscoelastic behavior (data not shown). However, COS7 cells have a very high concentration of vimentin in their perinuclear regions (Fig. 8 B). In contrast, fluorescent phalloidin staining for F-actin is greater in lamellae than the perinuclear regions (Fig. 8 A). In general, higher phalloidin staining correlated with higher viscoelastic moduli.

Compared to LTM measurements of reconstituted materials such as F-actin (e.g., Fig. 10), cellular measurements have much higher variability in mechanics. Although much of the variability is probably due to spatial heterogeneity, a part of the variability is also due to the dynamics of cytoplasm. Fig. 9 shows the temporal variations in lamellar mechanics as individual granules were monitored over time. Data for reconstituted F-actin networks are included for comparison. For some granules, moduli can vary fourfold and changes persist for many seconds. In contrast, by high-

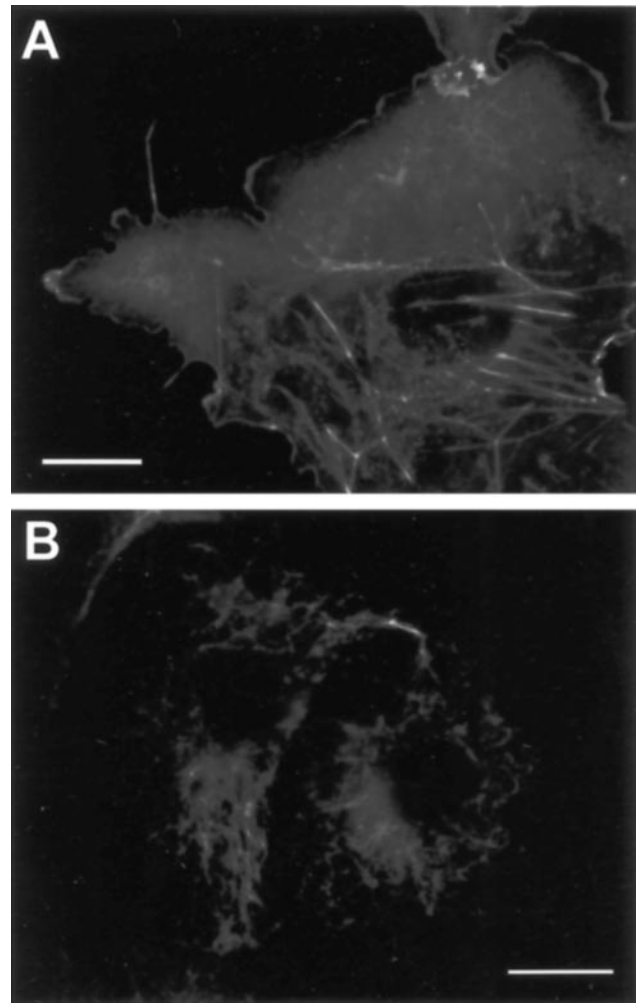


FIGURE 8 Fluorescent staining after LTM measurements. As described in Methods, cells were fixed and stained with (A) phalloidin or (B) anti-vimentin antibodies. By simple morphometric rules, F-actin was typically most concentrated in lamellae and vimentin in the perinuclear region. Scale bars are 20  $\mu\text{m}$ .

magnification video-enhanced microscopy, COS7 lamellae under these conditions appear quiescent and almost static. Little ruffling or protrusive activity is observed. Because the range of particle motions changes only twofold, these dynamics would be undetectable without the high sensitivity of laser tracking.

### Pure F-actin is softer and different from lamellae

Because F-actin staining in COS7 is richest in lamellae, we can use LTM to directly compare their viscoelastic spectra with purified actin. As shown in Fig. 10, LTM of pure F-actin networks at physiological concentrations are  $\sim 70$ -fold softer than COS7 lamellae. By mechanical rheometry and multiple light-scattering, F-actin displays a characteristic plateau in modulus at low frequencies ( $\omega < 10$  rad/s;

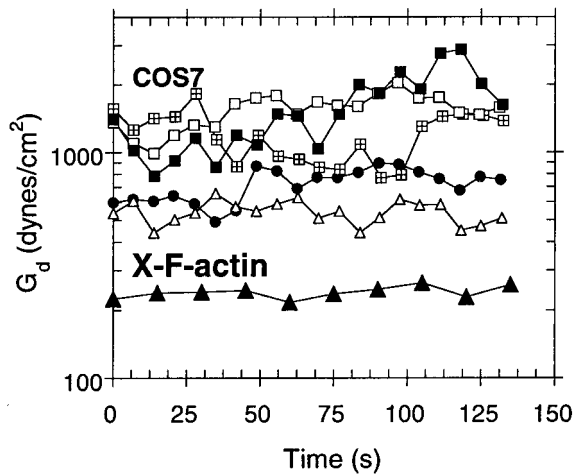


FIGURE 9 Dynamics within apparently quiescent lamellae. Individual granules in the lamellae of COS7 were monitored with LTM over time. Before each LTM acquisition re-calibration of the laser-tracking signal showed no change in instrument response. For comparison, LTM measurements of a polystyrene bead in biotinylated F-actin (12% biotinylated, 15  $\mu\text{M}$ ) cross-linked with 0.3  $\mu\text{M}$  avidin is shown (labeled *X-F-actin*). In general, LTM measurements of reconstituted polymers show much less variability than COS7 lamellae.

e.g., Janmey et al., 1994). Unlike prior attempts with laser tracking in F-actin (Schnurr et al., 1997), we have succeeded in preserving this low-frequency behavior. Our values for the plateau modulus generally agree with recently published values from other techniques (Palmer et al., 1999; Tang et al., 1999; Xu et al., 1998b).

The viscoelastic phase angle of pure F-actin indicates that it is qualitatively very different from cytoplasm. Pure F-actin exhibits biphasic behavior: solid-like at low frequencies ( $\delta < \pi/8$ ,  $\omega < 10$  rad/s) and almost liquid-like at higher frequencies ( $\omega > 500$  rad/s). Not purely viscous, this high frequency behavior shows a  $\delta \sim 3\pi/8$  relationship ( $G_d \sim \omega^{3/4}$ ) that is characteristic of semiflexible polymers (e.g., Morse, 1998). In contrast, COS7 cytoplasm show little changes in viscoelastic phase angle across frequencies ( $\delta \sim \pi/4$ ). At high frequencies, cytoplasm is both more rigid and more solid-like than F-actin alone. At low frequencies relevant for physiological function, cytoplasm is more rigid, but more liquid-like, than F-actin alone. As discussed later, such qualitative differences are likely due to the dynamics of short-lived cross-linking by actin-binding proteins.

### Latrunculin A quickly softens and liquefies quiescent lamellae

The cellular effects of actin-disrupting agents have been amply demonstrated in dynamic cells (e.g., neuronal growth cones; Forscher and Smith, 1988). However, responses from quiescent cells are typically less spectacular. With LTM, we can laser-track the granules before and after

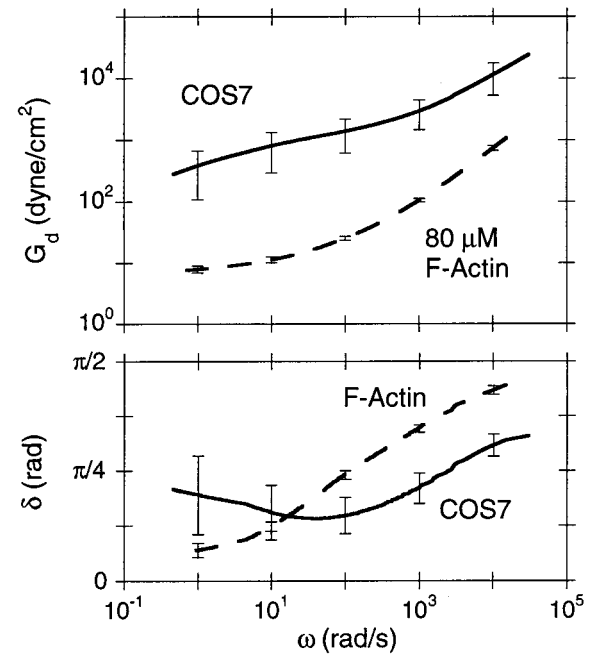


FIGURE 10 Mechanics of F-actin versus COS7 lamellae. Using LTM, viscoelastic spectra were acquired from polystyrene beads in pure F-actin at physiological concentrations (80  $\mu\text{M}$ ). Error bars are standard deviations. Compared to COS7 lamellae, there is almost a two-order magnitude difference in absolute viscoelastic moduli. From the viscoelastic phase angle, lamellae are never as liquid-like as F-actin at high frequencies ( $\omega > 200$  rad/s), but F-actin is much more solid-like at low frequencies ( $\omega < 20$  rad/s).

pharmacological treatments. As shown in Fig. 11, the environment around a lamellar granule changes dramatically after latrunculin A treatment ( $\sim 15$  min), both softening (5-fold on  $G_d$ ) and liquefying (2-fold on  $\delta$ ). Results for cytochalasin D are similar (not shown). Brief latrunculin A treatment primarily affects low-frequency behavior, consistent with filament shortening. Dominated by filament-bending modes, high-frequency behavior would be less sensitive to filament lengths (e.g., Morse, 1998). Although dramatic by LTM, such magnitude changes in cellular mechanics are difficult to resolve by other techniques.

## DISCUSSION

Laser-tracking microrheology (LTM) is a new, fast technique that can measure the full mechanical complexity of living cytoplasm. Summarized with the mean-squared-displacement function (MSD,  $\langle \Delta R^2(\tau) \rangle$ ), the primary data are the trajectories of embedded particles undergoing restricted Brownian motion. With  $\sim 5$  decade frequency bandwidth of high-resolution data, we can apply numerical methods so that the MSD yields the viscoelastic modulus and phase angle of the cytoskeletal network around the particle. As discussed later, there are approximations inherent in this

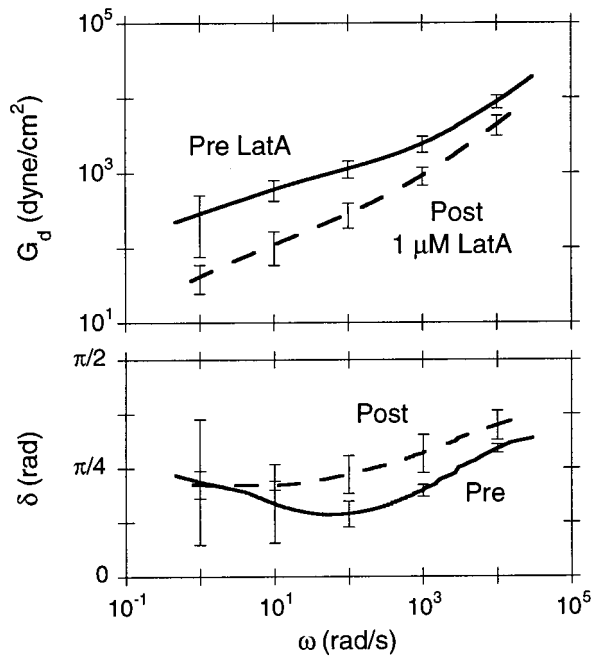


FIGURE 11 Effect of latrunculin A on COS7 lamellae. Lamellar mechanics around each endogenous granule was measured before and after 15-min exposure to 1  $\mu\text{M}$  latrunculin A. Error bars are standard deviations.

method, but endogenous granules in COS7 cells satisfy the requirements for such analysis.

The cytoplasmic viscoelasticity of COS7 cells varies with subcellular region and is dynamic. Phenomenological springs and dashpots are not useful for describing COS7 mechanics because too many parameters would be needed to curve-fit  $\sim 5$  decades of cellular data. Instead, physiologically relevant low-frequency moduli and phase angles are summarized in Table 1. In rank order, COS7 lamellae, a subset of COS7 perinuclear regions, and pure F-actin are softer and qualitatively very different. Although an F-actin gel is orders of magnitude softer than lamellae, F-actin is necessary for lamellar mechanics because actin-disrupting agents soften lamellae. Even apparently quiescent COS7

cells are dynamic. In as short as 15-s duration, lamellar granules can show changes in local moduli, some as large as fourfold in magnitude.

By offering three unique abilities in microscopic mechanics, LTM provides a new level of mechanical information to cell biology. First, LTM is the only microscopic technique capable of measuring the cytoskeleton's viscoelastic phase angle,  $\delta(\omega)$ , which is an index of the network's solid-like ( $\delta = 0$ ) or liquid-like ( $\delta = \pi/2$ ) behavior. Second, sub-millisecond resolution allows LTM to distinguish mere tethering from firm entrapment of particles within the cytoskeletal network. Third, LTM has the spatial and temporal resolution to monitor subtle mechanical changes in otherwise quiescent cells or to monitor fast physiological responses. As an added benefit, LTM provides a new tool to help bridge cell biology and biochemical reconstitution. The same technique used in cells can be used on reconstituted networks and provide high-quality spectra with parsimonious amounts ( $< 20 \mu\text{l}$ ) of protein.

### Related techniques

LTM extends the capabilities of two well-known biophysical techniques. Like LTM, fluorescence recovery after photobleaching (FRAP, e.g., Luby-Phelps et al., 1986) and video-based single-particle tracking (VSPT, e.g., Saxton and Jacobson, 1997; Sheetz et al., 1989) can measure diffusion coefficients and mobile fractions. For such measurements of "microviscosity" and permeation, the tracer particles are necessarily smaller than the pores of the mesh. Unlike FRAP and VSPT, laser tracking can also monitor the motions of seemingly stationary particles that are larger than the pores of the network. The subdiffusive motions of such particles reflect the elasticity, as well as the bulk viscosity, of the gel.

In principle, data from VSPT could be analyzed using Eq. 1 to provide viscoelastic spectra. This approach has been applied to DNA solutions (Mason et al., 1997a) and, in a more limited form, to particles bound to microtubule

TABLE 1 Mechanics of living COS7 cells

	RMS Fluctuations (nm)	<i>n</i>	$\delta$ (deg)	$G_d$ (dyne/cm <sup>2</sup> )	Relative Modulus
F-actin (80 $\mu\text{M}$ )	24.3* ( <i>d</i> = 1 $\mu\text{m}$ )	5	$23 \pm 2^\circ$	$11 \pm 1$	1
COS7					
Perinuclear (embedded subset)	15.3	11	$45 \pm 10^\circ$	$330 \pm 250$	29
Lamellae	9.9	38	$28 \pm 11^\circ$	$820 \pm 520$	72
Latrunculin A (1 $\mu\text{M}$ , 15 min)	23.6	3	$38 \pm 2^\circ$	$110 \pm 53$	10

All values of viscoelastic phase angle and absolute moduli were evaluated at 10 rad/s, and all statistics are mean  $\pm$  standard deviation. Root-mean-squared (RMS) fluctuations were calculated over 4.4 s of each acquisition. F-actin, alone, is very biphasic and behaves liquid-like at higher frequencies ( $\delta > 45^\circ$ ,  $\omega > 100$  rad/s). As described in the text, lamellae and perinuclear regions were identified by simple morphological rules.

\*Measurements of F-actin used 1  $\mu\text{m}$  beads as probes, so RMS fluctuations of 0.3  $\mu\text{m}$  beads would be at least threefold larger. As described in the text, all measurements of COS7 used endogenous granules ( $0.3 \pm 0.1 \mu\text{m}$ ) as probes.

networks (Caspi et al., 1998). With commercially available equipment, video tracking can monitor multiple particles for motions over great distances with near-nanometer resolution (Kuo et al., 1991). However, the main limitation of video tracking is its slow sampling rate (30 Hz), which can be further compounded by phosphor latency in some tube cameras. With its slow speed, minutes of video tracking are required for any numerical approximations (e.g., Eqs. 2 and 3) to be valid. Without high-frequency information, firmly enmeshed particles cannot be distinguished from merely tethered particles. When phosphor latency is present, video further distorts spectra so that information  $>3$  Hz appears overly viscous and can obscure the elasticity of polymers such as polyethylene oxide (Kuo, unpublished observations). Despite these limitations, VSPT is appealing because of its ease of implementation.

Diffusing wave spectroscopy (DWS) (Mason and Weitz, 1995) is a close relative to LTM. Rather than monitoring a single particle, DWS monitors the relative motions of a high density of particles ( $\sim 1\%$  by volume). For greatest sensitivity, the high density ensures that there is multiple light scattering from the particles. Multiply scattered laser light is collected by single-mode optical fibers, and a cross-correlator extracts the autocorrelation of intensity fluctuations. Subsequent curve-fitting yields  $\langle \Delta R^2(\tau) \rangle$  for use with Eqs. 1–3. DWS has near-picometer displacement sensitivity at MHz bandwidth, but requires reconstituted networks for seeding with high particle densities. DWS requires curve-fitting to extract  $\langle \Delta R^2(\tau) \rangle$ , whereas LTM yields  $\langle \Delta R^2(\tau) \rangle$  directly and trajectories can be individually compensated for uniform convection or drift. DWS and LTM are complementary techniques, and our data for DWS on F-actin gels are described elsewhere (Palmer et al., 1999).

Although one-dimensional, optical trapping interferometers have sufficient spatiotemporal resolution to monitor Brownian motion. The forces of optical tweezers can be calibrated by measuring the power spectrum of positional fluctuations of trapped particles (Svoboda et al., 1993). Power spectra are curve-fit with a Lorentzian functional form which is consistent with a harmonically bound Brownian particle. Recently, this power-spectrum approach has been generalized to viscoelastic materials, such as F-actin and polyacrylamide, where the functional form is not known (Gittes et al., 1997; Schnurr et al., 1997). Although much more computationally intensive, the power spectrum approach is mathematically equivalent to our MSD approach (Mason et al., 1997b).

### Approximations in LTM Analysis

Although LTM offers a wealth of data, the assumptions and approximations inherent in the approach and their implications for living cells deserve careful consideration. For any analysis of fluctuations, the most fundamental assumption is that the system is at steady state and does not have time-

varying probabilities for its underlying processes. Such an assumption is appropriate for reconstituted polymers, but living cells are dynamic and can change cytoskeletal structure in seconds. Long observation periods risk spanning different subcellular states, even in apparently quiescent cells (see Fig. 9). Fortunately, LTM can make spectral measurements in as little time as 1 s, so such risks are unlikely.

The particle's translational motion accurately reflects the forces on the particle when two minimal prerequisites are satisfied. First, particles must be more rigid than the surrounding cytoskeletal network. Fluctuations in particle shape would obscure contributions from cytoskeleton. Second, particles must be spherical. With their decreased symmetry, ellipsoidal particles complicate both laser tracking and the numerical analysis in LTM. In COS7, we show that endogenous lipid storage granules fulfill these two simple criteria. Hence, any correlation function, such as the MSD,  $\langle \Delta R^2(\tau) \rangle$ , will accurately summarize the steady-state forces on rigid, spherical granules in COS7.

To obtain viscoelastic spectra from correlation functions, we must assume that the cytoskeletal network is microscopically uniform. Such a continuum approximation is very good in lamellae where cytoskeletal pores are a small fraction of particle size. In the lamellae, granules are  $\sim 10$ -fold larger than cytoskeletal pores (24–31 nm; Provance et al., 1993; Luby-Phelps et al., 1986, 1987). However, in the perinuclear region, cytoskeletal pores are often comparable in size to granules, if not larger. In borderline situations, LTM analysis would underestimate viscoelastic moduli and overestimate phase angles. In extreme cases, particles would percolate through the pores and exhibit only liquid-like phase angles. However, the perinuclear region is not homogeneous, and exceptions to such generalizations are discussed later.

### Implications for cytoarchitecture

Although the actin-rich lamellae of vertebrate cells generally exclude organelles, the exclusion is rarely complete. For the kidney-derived cell line, COS7, spherical granules frequently exist in the lamellae (Fig. 4), despite their general concentration in the perinuclear region. These granules are lipid-storage droplets because they lack lipid bilayers, intensely stained with osmium tetroxide/uranyl acetate, and fluorescently stained with Nile Red. These granules are very rigid, as no internal fluctuations of stationary granules are detectable by our laser instrumentation. Overall, these endogenous granules make ideal probes for noninvasive application of LTM, and frequently exist within lamellae.

Because lamellae are rich in F-actin, mechanics of lamellae should be compared to F-actin. F-actin is clearly important, not only because of its enrichment in lamellae, but because of the rapidity of softening by actin-disrupting agents. However, LTM measurements of pure F-actin net-

works confirm the measurements of many investigators and techniques, ranging from mechanical rheometry (e.g., Tang et al., 1999; Xu et al., 1998b) to diffusing wave spectroscopy (e.g., Palmer et al., 1999; Gisler and Weitz, 1999). Uncross-linked F-actin networks, even at high concentrations, are orders of magnitude too soft to explain cellular mechanics. Cross-linking filaments is sufficient to increase moduli by appropriate magnitudes (e.g., Wachsstock et al., 1994). However, the lifetimes of cross-links between filaments are critical for the qualitative hardening of networks. Long-lived cross-links, such as biotin-avidin, produce “solid” F-actin networks. In contrast, short-lived cross-links not only increase moduli, but also produce higher viscoelastic phase angles, indicative of more liquid-like networks (Wachsstock et al., 1994; Palmer et al., 1998). Compared to F-actin behavior at low frequencies, such cross-linker lifetimes may explain the more liquid-like values of the phase angle observed in COS7.

LTM measurements reveal two new features of mechanics in lamellae. First, despite quiescent appearances, lamellae are dynamic, as well as heterogeneous. Second, by providing the first subcellular estimates of viscoelastic phase angles, LTM shows intermediate levels of liquid-like and solid-like behavior ( $\delta \sim \pi/4$ ) at all frequencies. Because there are no frequencies of solid or liquid behavior, simple spring-and-dashpot models are fundamentally incorrect and merely phenomenological. Even phenomenologically, a system of multiple ( $\sim 8$ ) springs and dashpots would be needed to describe cellular viscoelastic spectra across all 5 decades of frequencies.

LTM also reveals a dense viscoelastic subregion near the nucleus. Although most perinuclear granules show large Brownian motions, a subset of these granules is firmly embedded in a relatively rigid viscoelastic material. These granules are often near endoplasmic reticulum and Golgi, which are also rich in the intermediate filament, vimentin. These same regions exclude small fluorescent tracer molecules (Provance et al., 1993; Luby-Phelps et al., 1986, 1987). Because there are no obvious organelles adjacent to the embedded perinuclear granules described here, we suspect that intermediate filaments are responsible for local viscoelasticity. However, additional experiments are needed to identify the source of perinuclear viscoelasticity.

The high-frequency information from laser tracking is critical for confirming the appropriateness of LTM interpretations, particularly in the perinuclear region. Because the perinuclear region is dominated by particles displaying near-percolation behavior, apparently stationary granules may be particles tethered by molecular motors rather than embedded in a viscoelastic matrix. When particles are merely tethered to microtubules, they exhibit diffusive behavior on fast time scales ( $0.1 < \tau < 23$  ms; Allersma et al., 1998). If analyzed using Eqs. 1–3, such behavior would appear as viscoelastic phase angle values of  $\delta \sim \pi/2$  for frequencies  $\omega > 400$  rad/s. None of the embedded perinu-

clear granules or lamellar granules had any evidence of such “microviscosity.” Even though such data cannot exclude the possibility of additional filament-binding by granules, it is clear that the granules are in viscoelastic microenvironments.

Because the biological roles of various subcellular particles are different, their microenvironments are necessarily different. For example, during early phagocytosis, particles recruit actin and actin-binding proteins that should alter local mechanical properties. Depending on content, maturing phagosomes experience different fates and interact with cytoskeleton differently. In COS7, preliminary data show that late phagocytosed polystyrene beads show higher moduli ( $\sim 5$ -fold) than endogenous granules (data not shown). These differences persist despite multiple proliferative passages of bead-containing cells. Because a particle’s Brownian motion reflects its microenvironment, beads and granules must have subtly different microenvironments. Identifying the molecular differences in microenvironments requires further study. Indeed, even within the same subcellular region probed with one class of particle, our data indicate a high variability of local mechanics. With such heterogeneity of cytoplasm, the idealized concept of uniform bulk properties is not accurate, but necessary as a starting point for understanding cell structure.

### Comparison with other cellular measurements

LTM provides unique information by revealing the full viscoelastic complexity of cytoplasm. It measures the cytoplasm’s frequency-dependent modulus and phase angle over a broad range of frequencies. Although other techniques measure a smaller range of frequencies, comparisons to LTM can be restricted to corresponding frequency ranges. In addition, many of these other techniques use ligands that might activate cytoskeletal recruitment (e.g., Plopper and Ingber, 1993) or use large deformations that risk exploring nonlinear and plastic mechanical responses as well as risk spanning multiple subcellular mechanical regions. Such differences complicate comparisons between techniques, but good frequency-limited agreement occurs in methods that closely match LTM conditions (magnetic tweezers, Table 2).

Table 2 summarizes numerical estimates of cell mechanics from a number of techniques. Spanning multiple subcellular domains, most extracellular measurements deform the cortical cytoskeleton and the cytoplasm. In general, extracellular estimates are one to two orders of magnitude larger than intracellular measurements, and numerical values vary by orders of magnitude.

Intracellular measurements appear less disparate. Before LTM, only intracellular measurements using internalized magnetic particles have been reported. Inside murine macrophages, twisting a population of magnetic particles reveal a viscous cytoplasm with only a minor elastic response (Valberg and Albertini, 1985). Because most ( $\sim 80\%$ )

**TABLE 2 Selected measurements of cell mechanics**

Technique	Cell Type	Elasticity (dyne/cm <sup>2</sup> )	Viscosity (poise)	Param Model*	Citation
Extracellular or Whole Cell Measurements					
Magnetic twist	endothelial	~20	n.a.	secant	Wang et al., 1993
Micropipette	leukocyte	7.5, 238	330	3	Sung et al., 1988
Mech. rheometer	<i>D. discoideum</i>	$G' = 550$	$G'' = 250^\dagger$	direct	10 rad/s (Eichinger et al., 1996)
Cell piker	neutrophil	1180	n.a.	secant	Zahalak et al., 1990
AFM	platelet	$(1-50) \times 10^3$	n.a.	Hertz	Radmacher et al., 1996
Microplates	fibroblast	~ $10^4$	$10^3-10^5$	3	Thoumine and Ott, 1997
Spont. retraction	fibroblast	$1.7 \times 10^4$	$4 \times 10^6$	2	Ragsdale et al., 1997
Magnetic tweezers	fibroblast	~ $3 \times 10^5$	~ $2 \times 10^4$	4	Bausch et al., 1998
Intracellular Measurements					
Magnetic twist	macrophage	~150	~ $2 \times 10^4$	secant	Valberg and Albertini, 1985
Magnetic tweezers	macrophage	200-7350	2100	4	Bausch et al., 1999
<i>deduced</i>		$G' \sim 1790^\ddagger$	$G'' \sim 1182^\ddagger$	<i>deduced</i> <sup>‡</sup>	4 elem. model (10 rad/s)
LTM	epithelial	$G' = 721$	$G'' = 382^\dagger$	direct	this work (10 rad/s)

Abbreviations: n.a., not available; AFM, atomic force microscopy; LTM, laser-tracking microrheology.

\*Mechanical models for extracting values: the secant method normalizes the apparent force/displacement for the geometry of the mechanical probe. In AFM, the Hertzian model further normalizes for the changing contact area of pyramidal probes. In creep or relaxation methods, estimating viscosity typically uses mechanical spring-and-dashpot models or models that include surface tension, and the number of parameters in the model are listed in this table. In rheometry, dynamic storage ( $G'$ ) and loss ( $G''$ ) moduli are directly measured.

<sup>†</sup>Units of  $G''$  are dyne/cm<sup>2</sup>.

<sup>‡</sup>Dynamic storage and loss moduli were calculated from the 4-element mechanical model using the average of measured values (Bausch et al., 1999):  $k_0 = 1180$  dyne/cm<sup>2</sup>,  $k_1 = 2250$  dyne/cm<sup>2</sup>,  $n_0 = 2100$  poise, and  $\tau = 0.218$  s, which lead to a deduced value for  $n_1 = 169$  poise.

COS7 granules show large Brownian excursions, comparable population measurements would be similarly soft and liquid-like. Using magnetic tweezers, Bausch et al. (1999) analyzed displacements of individual ferromagnetic particles phagocytosed inside macrophages. The values for these cytoplasmic particles are almost two orders of magnitude smaller than corresponding extracellular particles (Bausch et al., 1998) and are much more variable (elastic shear moduli range 200–7350 dyne/cm<sup>2</sup>, with average  $3430 \pm 2340$  dyne/cm<sup>2</sup>). Since Bausch's model with four mechanical elements is not a unique arrangement for phenomenological characterization, numerical estimates from such a model are not directly comparable to other techniques. However, the storage and loss moduli ( $G'$  and  $G''$ , respectively) can be estimated from the model and can be compared to LTM measurements. Such a calculation is shown in Table 2. Mindful that phagocytosed particles display higher moduli than endogenous granules in COS7 (data not shown), the values from LTM are in good agreement with comparable measurements using magnetic tweezers.

LTM provides a new approach to measuring cellular mechanics and should provide a valuable complement to other cell biological techniques. For cell biology, it has three critical technical advantages: sensitivity, speed, and highly local measurements. Small changes in apparent moduli are readily discerned, and measurements can be accomplished on physiological time scales (within seconds). Because cells are highly heterogeneous, very local measurements are needed for biological relevance. Overall, LTM's ability to bridge biochemical reconstitution and cell biology should provide insights into processes that remodel cytoskeleton.

We thank K. Ganesan for developing and rebuilding the LTM apparatus, and J. McGrath for a careful reading of the manuscript. We also thank A. Palmer and J. Xu for purifying actin, K. Leong for the COS7 cell line, P. Coulombe for vimentin antibodies, and D. Murphy for fluorescence and electron microscopy access and assistance.

This work was supported in part by the Whitaker Foundation (S.C.K.), the National Science Foundation (S.C.K., D.W.), and NASA (S.C.K., D.W.).

## REFERENCES

- A-Hassan, E., W. F. Heinz, M. D. Antonik, N. P. D'Costa, S. Nageswaran, C. A. Schoenenberger, and J. H. Hoh. 1998. Relative microelastic mapping of living cells by atomic force microscopy. *Biophys. J.* 74: 1564–1578.
- Allersma, M. W., F. Gittes, M. J. deCastro, R. J. Stewart, and C. F. Schmidt. 1998. Two-dimensional tracking of ncd motility by back focal plane interferometry. *Biophys. J.* 74:1074–1085.
- Bausch, A. R., W. Moller, and E. Sackmann. 1999. Measurement of local viscoelasticity in living cells by magnetic tweezers. *Biophys. J.* 76: 573–579.
- Bausch, A. R., F. Ziemann, A. A. Boulbitch, K. Jacobson, and E. Sackmann. 1998. Local measurements of viscoelastic parameters of adherent cell surfaces by magnetic bead microrheometry. *Biophys. J.* 75: 2038–2049.
- Booij, H. C., and G. P. J. M. Thoone. 1982. Generalization of Kramers-Kronig transforms and some approximations of relations between viscoelastic quantities. *Rheol. Acta.* 21:15–24.
- Caspi, A., M. Elbaum, R. Granek, A. Lachish, and D. Zbaida. 1998. Semiflexible polymer network: a view from inside. *Phys. Rev. Lett.* 80:1106–1109.
- Crick, F. H. C., and A. F. W. Hughes. 1950. The physical properties of cytoplasm: a study by means of the magnetic particle methods. *Exp. Cell Res.* 1:37–80.
- Eichinger, L., B. Koppel, A. A. Noegel, M. Schleicher, M. Schliwa, K. Weijer, W. Witke, and P. A. Janmey. 1996. Mechanical perturbation elicits a phenotypic difference between *Dictyostelium* wild-type cells and cytoskeletal mutants. *Biophys. J.* 70:1054–1060.
- Fawcett, D. W. 1981. *The Cell*. W. B. Saunders Co., Philadelphia.

- Felder, S., and E. L. Elson. 1990. Mechanics of fibroblast locomotion: quantitative analysis of forces and motions at the leading lamellas of fibroblasts. *J. Cell Biol.* 111:2513–2526.
- Forscher, P., and S. J. Smith. 1988. Actions of cytochalasins on the organization of actin filaments and microtubules in a neuronal growth cone. *J. Cell Biol.* 107:1505–1516.
- Gisler, T., and D. Weitz. 1999. Scaling of the microrheology of semidilute F-actin solutions. *Phys. Rev. Lett.* 82:1606–1609.
- Gittes, F., B. Schnurr, P. D. Olmsted, F. C. MacKintosh, and C. F. Schmidt. 1997. Microscopic viscoelasticity: shear moduli of soft materials determined from thermal fluctuations. *Phys. Rev. Lett.* 79:3286–3289.
- Greenspan, P., E. P. Mayer, and S. D. Fowler. 1985. Nile Red: a selective fluorescent stain for intracellular lipid droplets. *J. Cell Biol.* 100:965–973.
- Hochmuth, R. M. 1993. Measuring the mechanical properties of individual human blood cells. *J. Biomech. Eng.* 115:515–519.
- Hou, L., K. Luby-Phelps, and F. Lanni. 1990. Brownian motion of inert tracer macromolecules in polymerized and spontaneously bundled mixtures of actin and filamin. *J. Cell Biol.* 110:1645–1654.
- Janmey, P. A., S. Hvidt, J. Kas, D. Lerche, A. Maggs, E. Sackmann, M. Schliwa, and T. P. Stossel. 1994. The mechanical properties of actin gels. Elastic modulus and filament motions. *J. Biol. Chem.* 269:32503–32513.
- Kuo, S. C., J. Gelles, E. Steuer, and M. P. Sheetz. 1991. A model for kinesin movement from nanometer-level measurements of kinesin and cytoplasmic dynein and force measurements. *J. Cell Sci.* (Suppl. 14):135–138.
- Kuo, S. C., and M. P. Sheetz. 1992. Optical tweezers in cell biology. *Trends Cell Biol.* 2:116–118.
- Luby-Phelps, K., P. E. Castle, D. L. Taylor, and F. Lanni. 1987. Hindered diffusion of inert tracer particles in the cytoplasm of mouse 3T3 cells. *Proc. Natl. Acad. Sci. USA.* 84:4910–4913.
- Luby-Phelps, K., D. L. Taylor, and F. Lanni. 1986. Probing the structure of cytoplasm. *J. Cell Biol.* 102:2015–2022.
- MacLean-Fletcher, S. D., and T. D. Pollard. 1980. Viscometric analysis of the gelation of *Acanthamoeba* extracts and purification of two gelation factors. *J. Cell Biol.* 85:414–428.
- Mason, T. G., A. Dhople, and D. Wirtz. 1997a. Concentrated DNA rheology and microrheology. *Mat. Res. Soc. Symp. Proc.* 463:153–158.
- Mason, T. G., K. Ganesan, J. H. Van Zanten, D. Wirtz, and S. C. Kuo. 1997b. Particle tracking microrheology of complex fluids. *Phys. Rev. Lett.* 79:3282–3285.
- Mason, T. G., and D. A. Weitz. 1995. Optical measurements of frequency-dependent linear viscoelastic moduli of complex fluids. *Phys. Rev. Lett.* 74:1250–1253.
- Morse, D. C. 1998. Viscoelasticity of concentrated isotropic solutions of semiflexible polymers. 2. Linear response. *Macromolecules.* 31:7044–7067.
- Nicklas, R. B. 1983. Measurements of the force produced by the mitotic spindle in anaphase. *J. Cell Biol.* 97:542–548.
- Palmer, A., T. G. Mason, J. Xu, S. C. Kuo, and D. Wirtz. 1999. Diffusing wave spectroscopy microrheology of actin filament networks. *Biophys. J.* 76:1063–1071.
- Palmer, A., J. Xu, and D. Wirtz. 1998. High-frequency viscoelasticity of crosslinked actin filament networks measured by diffusing wave spectroscopy. *Rheol. Acta.* 37:97–106.
- Petersen, N. O., W. B. McConnaughey, and E. L. Elson. 1982. Dependence of locally measured cellular deformability on position on the cell, temperature, and cytochalasin B. *Proc. Natl. Acad. Sci. USA.* 79:5327–5331.
- Popper, G., and D. E. Ingber. 1993. Rapid induction and isolation of focal adhesion complexes. *Biochem. Biophys. Res. Commun.* 193:571–578.
- Provance, D. W., Jr., A. McDowall, M. Marko, and K. Luby-Phelps. 1993. Cytoarchitecture of size-excluding compartments in living cells. *J. Cell Sci.* 106:565–577.
- Radmacher, M., M. Fritz, C. M. Kacher, J. P. Cleveland, and P. K. Hansma. 1996. Measuring the viscoelastic properties of human platelets with the atomic force microscope. *Biophys. J.* 70:556–567.
- Ragsdale, G. K., J. Phelps, and K. Luby-Phelps. 1997. Viscoelastic response of fibroblasts to tension transmitted through adherens junctions. *Biophys. J.* 73:2798–2808.
- Saxton, M. J. 1993. Lateral diffusion in an archipelago. Single-particle diffusion. *Biophys. J.* 64:1766–1780.
- Saxton, M. J., and K. Jacobson. 1997. Single-particle tracking: applications to membrane dynamics. *Annu. Rev. Biophys. Biomol. Struct.* 26:373–399.
- Schmidt, C. E., A. F. Horwitz, D. A. Lauffenburger, and M. P. Sheetz. 1993. Integrin-cytoskeletal interactions in migrating fibroblasts are dynamic, asymmetric, and regulated. *J. Cell Biol.* 123:977–991.
- Schnurr, B., F. Gittes, F. C. MacKintosh, and C. F. Schmidt. 1997. Determining microscopic viscoelasticity in flexible and semiflexible polymer networks from thermal fluctuations. *Macromolecules.* 30:7781–7792.
- Sheetz, M. P., S. Turney, H. Qian, and E. L. Elson. 1989. Nanometre-level analysis demonstrates that lipid flow does not drive membrane glycoprotein movements. *Nature.* 340:284–288.
- Spudich, J. A., and S. Watt. 1971. The regulation of rabbit skeletal muscle contraction. I. Biochemical studies of the interaction of the tropomyosin-troponin complex with actin and the proteolytic fragments of myosin. *J. Biol. Chem.* 246:4866–4871.
- Sung, K.-L. P., C. Dong, G. W. Schmid-Schönbein, S. Chien, and R. Skalak. 1988. Leukocyte relaxation properties. *Biophys. J.* 54:331–336.
- Svoboda, K., C. F. Schmidt, B. J. Schnapp, and S. M. Block. 1993. Direct observation of kinesin stepping by optical trapping interferometry. *Nature.* 365:721–727.
- Tang, J. X., P. A. Janmey, T. P. Stossel, and T. Ito. 1999. Thiol oxidation of actin produces dimers that enhance the elasticity of the F-actin network. *Biophys. J.* 76:2208–2215.
- Thoumine, O., and A. Ott. 1997. Time scale dependent viscoelastic and contractile regimes in fibroblasts probed by microplate manipulation. *J. Cell Sci.* 110:2109–2116.
- Tschoegl, N. W. 1989. *The Phenomenological Theory of Linear Viscoelastic Behavior: An Introduction.* Springer-Verlag, New York.
- Valberg, P. A., and D. F. Albertini. 1985. Cytoplasmic motions, rheology, and structure probed by a novel magnetic particle method. *J. Cell Biol.* 101:130–140.
- van de Hulst, H. C. 1981. *Light Scattering by Small Particles.* Dover Publications, Inc., New York.
- Wachstock, D. H., W. H. Schwarz, and T. D. Pollard. 1994. Cross-linker dynamics determine the mechanical properties of actin gels. *Biophys. J.* 66:801–809.
- Wang, N., J. P. Butler, and D. E. Ingber. 1993. Mechanotransduction across the cell surface and through the cytoskeleton. *Science.* 260:1124–1127.
- Xu, J., A. Palmer, and D. Wirtz. 1998a. Rheology and microrheology of semiflexible polymer solutions: actin filament networks. *Macromolecules.* 31:6486–6492.
- Xu, J., W. H. Schwarz, J. A. Kas, T. P. Stossel, P. A. Janmey, and T. D. Pollard. 1998b. Mechanical properties of actin filament networks depend on preparation, polymerization conditions, and storage of actin monomers. *Biophys. J.* 74:2731–2740.
- Zahalak, G. I., W. B. McConnaughey, and E. L. Elson. 1990. Determination of cellular mechanical properties by cell poking, with an application to leukocytes. *J. Biomech. Eng.* 112:283–294.

## Optical Measurements of Frequency-Dependent Linear Viscoelastic Moduli of Complex Fluids

T. G. Mason<sup>1,2</sup> and D. A. Weitz<sup>1</sup>

<sup>1</sup>*Exxon Research and Engineering Company, Route 22E, Annandale, New Jersey 08801*

<sup>2</sup>*Department of Physics, Princeton University, Princeton, New Jersey 08544*

(Received 17 August 1994)

We present a novel experimental method to measure linear viscoelastic moduli of complex fluids using dynamic light scattering. A generalized Langevin equation is used to relate the mean square displacement of a probe particle to the storage and loss moduli of the bulk complex fluid. We confirm the experimental validity of this technique by comparing the light scattering results with mechanical measurements for several complex fluids. This method probes the moduli over a greatly extended frequency range and provides significant new insight into the elastic susceptibility of complex fluids.

PACS numbers: 83.50.Fc, 82.70.-y, 83.70.Hq, 83.85.Ei

One of the most fundamental properties of any material is its elastic susceptibility, or its response to a shear excitation. For example, the primary difference between a fluid and a solid is their contrasting response to an applied shear strain; solids store mechanical energy and are elastic, whereas fluids dissipate mechanical energy and are viscous. Many materials are viscoelastic; they both store and dissipate energy, with the relative proportions depending on frequency. The elastic susceptibility is parameterized by the complex shear modulus  $G^*(\omega)$ , which determines the stress induced in a material upon application of an oscillatory shear strain at a frequency  $\omega$  [1]. The elastic component of the stress is in phase with the applied strain; the ratio of this stress to the strain is the storage modulus  $G'(\omega)$ , the real part of  $G^*(\omega)$ . The viscous component of the stress is out of phase with the strain; the ratio of this stress to the strain is the loss modulus  $G''(\omega)$ , the imaginary part of  $G^*(\omega)$ . The elastic susceptibility can also be defined in terms of the Fourier transform of the material's response to an impulsive strain [1]; because of causality,  $G'(\omega)$  and  $G''(\omega)$  are related by the Kramers-Kronig relations [2].

Complex fluids have a rich linear viscoelastic behavior. This is due to the larger length scale of the structures inherent in them; examples include colloidal dispersions and polymer or self-assembled surfactant solutions. These supramolecular structures endow complex fluids with their unique properties, and the interactions between, or within, them govern their dynamics. These dynamics typically possess several characteristic time scales which are reflected in  $G^*(\omega)$ ; moreover, both elastic and viscous components are usually significant, although their relative contributions depend on frequency. However, unlike simple fluids, these frequencies are typically low enough to be experimentally accessible. Traditionally,  $G^*(\omega)$  is determined mechanically: For example, a strain is applied and the induced stress is measured. However, because the measurements are mechanical, their frequency range is limited; no single technique can measure  $G^*(\omega)$  over an extended range.

In this Letter, we present a novel method for measuring the linear viscoelastic properties of a complex fluid over an extended range of frequencies. We show that the response of the fluid to thermal fluctuations, as probed by the average motion of small particles dispersed within the fluid, provides a close representation of the response of the bulk fluid to an imposed shear strain. The essential physics of this approach is that the bulk mechanical susceptibility of the fluid determines the response of a small particle excited by the thermal stochastic forces which lead to Brownian motion. We use dynamic light scattering to measure the mean square displacement of a probe particle,  $\langle \Delta r^2(t) \rangle$ , and relate this to  $G^*(\omega)$  by describing the motion of the particle with a generalized Langevin equation, incorporating a memory function to account for the viscoelasticity. We compare this  $G^*(\omega)$  to that measured by conventional mechanical means. Remarkably good agreement is found. We demonstrate the flexibility of this new technique by measuring the moduli of a variety of complex fluids, and illustrate its potential to determine new behavior.

We describe the motion of a small, neutrally buoyant particle dispersed in a complex fluid by means of generalized Langevin equation [2,3],

$$m\dot{v}(t) = f_R(t) - \int_0^t \zeta(t-\tau)v(\tau)d\tau, \quad (1)$$

where  $m$  is the particle mass and  $v(t)$  is the particle velocity. This equation expresses the forces on the particle;  $f_R(t)$  represents the random forces acting on the particle and includes the contribution from both direct forces between the particles and the stochastic Brownian forces; the integral term represents the viscous damping of the fluid, and incorporates a generalized time-dependent memory function  $\zeta(t)$ . Energy stored in the medium leads to profound changes in the temporal correlations of the stochastic forces acting on the particle at thermal equilibrium, and the fluctuation-dissipation theorem differs from the commonly encountered delta-function correlation of a purely viscous fluid, becoming [2]

$$\langle f_R(0)f_R(t) \rangle = k_B T \zeta(t), \quad (2)$$

where  $k_B$  is Boltzmann's constant and  $T$  is the temperature.

By taking the unilateral transform [4] of Eq. (1), and using Eq. (2), the viscoelastic memory function can be related to the velocity autocorrelation function, and, hence, to the particle's mean square displacement. We further assume that the microscopic memory function is proportional to the bulk frequency-dependent viscosity of the fluid,

$$\tilde{\eta}(s) = \frac{\zeta(s)}{6\pi a}, \quad (3)$$

where  $s$  represents the frequency in the Laplace domain. This relationship is exact in the limit of a purely viscous fluid; here we assume the same behavior for viscoelastic fluids at all frequencies, recognizing that this is only an approximation. Then,

$$\tilde{G}(s) = s\tilde{\eta}(s) = \frac{s}{6\pi a} \left[ \frac{6k_B T}{s^2 \langle \Delta \tilde{r}^2(s) \rangle} - ms \right]. \quad (4)$$

The first term in the brackets reflects the thermal fluctuation dissipation in the medium. The second term is due to inertia and is negligible except at very high frequencies. If it is neglected, Eq. (4) reflects a generalized, frequency-dependent form of the Stokes-Einstein relation. For a freely diffusing particle,  $\langle \Delta \tilde{r}^2(s) \rangle = 6D/s^2$ , and the familiar, frequency-independent viscosity is recovered,  $\eta_0 = k_B T / 6\pi a D$ , where  $D$  is the diffusion coefficient.

To compare with mechanical data, we require  $G'(\omega)$  and  $G''(\omega)$ ; however, since they obey the Kramers-Kronig relations, they are not two independent functions, and both can be determined from the single, real function  $\tilde{G}(s)$ . We could, in principle, calculate the inverse unilateral Laplace transform and then Fourier transform it. Instead, we fit  $\tilde{G}(s)$  by a functional form in the real variable  $s$ , and then obtain the complex function  $G^*(\omega)$  using analytic continuation, substituting  $i\omega$  for  $s$  in the fitted form. We then identify  $G'(\omega)$  and  $G''(\omega)$  as the real and imaginary parts; this ensures that the Kramers-Kronig relations are satisfied over the frequency range probed. This procedure establishes a general relationship between the mean square displacement of the particles and the bulk rheological properties of the complex fluid.

To test the applicability of this scheme, we apply it to several distinctly different complex fluids. The first system is a suspension of silica particles in ethylene glycol; these particles interact as hard spheres [5]. The particle radius is relatively uniform,  $a = 0.21 \mu\text{m}$ , and the volume fraction is  $\phi \approx 0.56$ . To probe the small values of the mean square displacement required, we use diffusing-wave spectroscopy (DWS), an extension of dynamic light scattering (DLS) to the multiple scattering limit [6,7]. The correlation function measured with DWS in the transmission geometry exhibits the behavior characteristic of a concentrated colloidal suspension of hard spheres near the glass transition [8]. There is an initial, rapid decay to a plateau value, followed by a final

decay at longer times. The particles are relatively small, so that DWS is slightly sensitive to collective motion; nevertheless, to a good approximation the correlation function can be inverted to obtain the mean square displacement of the particles [9]. This requires knowledge of the transport mean free path of the light,  $l^*$ , which was obtained from static transmission measurements [9]. The measured  $\langle \Delta r^2(t) \rangle$  is shown in the inset of Fig. 1. The linear increase at the shortest times reflects the initial diffusive motion of the particles; at longer times their motion is constrained by the local cage structure of their neighbors. The decay in the correlation function at the longest times, which results from the breakup of the cages, cannot be simply interpreted within DWS as a mean square displacement of individual particles, setting the upper limit of the data that can be inverted.

We numerically calculate the Laplace transform of the mean square displacement, and use Eq. (4) to determine  $\tilde{G}(s)$ . The results are shown by the open circles in Fig. 1. Because of the restricted extent of the data, the accuracy of the Laplace transform is limited at the lowest frequencies. To obtain the real and imaginary parts of the complex modulus, we fit the data by a functional form based on physical intuition about the behavior of a hard sphere colloidal glass,  $\tilde{G}(s) = g_1 - g_2 s^{-0.55} + g_3 s^{0.3} + g_4 s^{0.5} + g_5 s$ , where the  $g_i$  are positive fitting parameters. The first three terms are suggested by mode coupling theories and reflect the cage dynamics [10]; these terms account for the plateau and a low-frequency relaxation. The fourth term accounts for the predicted high-frequency elastic modulus [11,12], while the fifth term reflects the high-frequency viscosity of the suspension. The fit is indistinguishable from the data and is used to determine  $G^*(\omega)$ . Although our fit is based on intuition, any functional form that fits the data will provide equally good results.

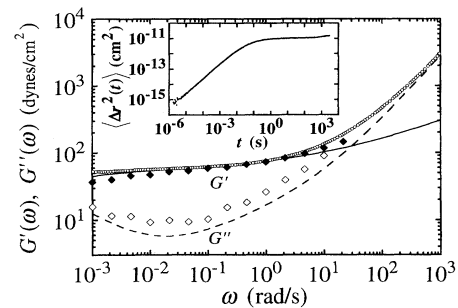


FIG. 1. Frequency-dependent linear viscoelastic moduli for a suspension of hard spheres with  $\phi = 0.56$ . Data obtained mechanically are shown by diamonds, solid for the storage modulus, and open for the loss modulus. Data obtained optically are shown by lines, solid for the storage modulus, and dashed for the loss modulus. The open circles represent  $\tilde{G}(s)$ , and are plotted on the same frequency scale. The mean square displacement, measured with DWS, is shown in the inset.

To test this scheme, we determine the moduli directly by an oscillatory mechanical measurement. We employ a controlled strain rheometer using a sample cell with a double-wall Couette geometry. The applied strains are sufficiently low to ensure linearity. In Fig. 1, we compare the measured values of  $G'(\omega)$  and  $G''(\omega)$ , shown by the diamonds, with the predictions from the light scattering, shown by the lines. Excellent agreement is found, particularly with the storage modulus, which is the larger of the two components.

As a second test, we study a polymer solution at a sufficiently high concentration that an entangled network is formed. We use polyethylene oxide with a molecular weight of  $4 \times 10^6$  dissolved in water at a concentration of 15% by weight. As probe particles, we add polystyrene latex spheres with  $a = 0.21 \mu\text{m}$  at  $\phi = 2\%$ . This  $\phi$  is sufficiently high to ensure multiple scattering from the spheres, but sufficiently low to ensure that the spheres do not contribute appreciably to the viscoelastic behavior. By contrast to the hard sphere suspension, in this case the particles act solely as probes, both for the rheological properties and for the light scattering. We compare the complex moduli obtained from light scattering with those obtained mechanically in Fig. 2; again relatively good overall agreement is obtained. The light scattering data provide a good estimate of the magnitude of the moduli and correctly predict the crossover in the behavior, with  $G''(\omega)$  dominating at low frequencies and  $G'(\omega)$  dominating at high frequencies. The discrepancy between the two methods is largest at low frequencies; this likely results from the restricted range of the light scattering data, which limits the accuracy of the Laplace transform. Nevertheless, the agreement is remarkably good.

As a third test, we study an emulsion, comprised of uniformly sized oil droplets, with  $a = 0.53 \mu\text{m}$ , stabilized with a surfactant and suspended in water [13]. The volume fraction is  $\phi = 0.62$ , resulting in elasticity arising

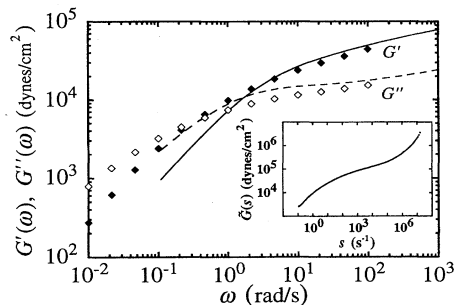


FIG. 2. Frequency-dependent linear viscoelastic moduli for a solution of  $4 \times 10^6$  molecular weight polyethylene oxide in water at a concentration of 15% by weight. Data obtained mechanically are shown by diamonds, solid for the storage modulus, and open for the loss modulus. Data obtained optically are shown by lines, solid for the storage modulus, and dashed for the loss modulus. The inset shows  $\bar{G}(s)$  over the full frequency range measured.

from the surface tension of the deformed droplets. The strong scattering of the uniformly sized droplets allows DWS to be used to probe their  $\langle \Delta r^2(t) \rangle$ . The comparison of the light scattering data with the rheological measurements is shown in Fig. 3. Again, very good agreement is obtained; the measurement of  $G'(\omega)$  agrees over the whole range of frequencies that overlap, while that of  $G''(\omega)$  agrees well at higher frequencies, but does not capture the rise at the lowest frequencies. The accuracy is again restricted by the limited frequency range of the data used for the Laplace transform; the light scattering data decay at longer time, indicating that there is an additional low frequency relaxation, which would result in an increase in  $G''(\omega)$  at low frequencies, consistent with the mechanical rheology data.

The agreement of the light scattering measurements of the elastic moduli with the mechanical ones is excellent. We emphasize, however, that these results are purely experimental; the underlying origin of this agreement is not clear. Formally, the motion of a single particle in a complex fluid can be described with a memory-function equation similar in form to Eq. (1) using projection operator techniques; the shear modulus can also be represented by a memory-function equation of the same form [14]. However, the memory function for a single particle motion represents a longitudinal density autocorrelation function; by contrast, the memory function for the shear modulus represents an autocorrelation function of nondiagonal, or transverse, elements of the stress tensor. The two memory functions are not equivalent. Heretofore, DLS has only been used to measure a longitudinal modulus [15]. Our experiments show that it can be used to measure the transverse modulus as well. It is conceivable that a single relaxation mode dominates both the longitudinal density and transverse stress correlation functions so that they exhibit the same behavior. For example, such equivalence is expected from mode coupling theory near a glass transition [16], and this may account for the data for both the hard spheres and the emulsion. Moreover, the mean

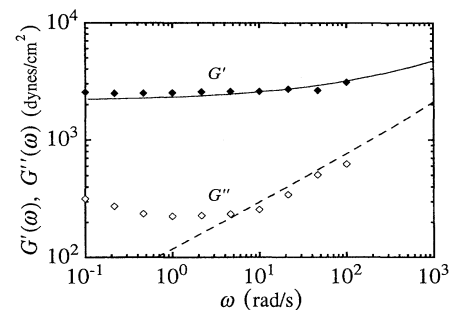


FIG. 3. Frequency-dependent linear viscoelastic moduli for a monodisperse emulsion with  $\phi = 0.62$ . Data obtained mechanically are shown by diamonds, solid for the storage modulus, and open for the loss modulus. Data obtained optically are shown by lines, solid for the storage modulus, and dashed for the loss modulus.

square displacement does couple to shear modes; this is certainly true in the limit of a simple viscous fluid, where the shear viscosity determines the particle's diffusive motion. Thus, by analogy, we expect the shear elasticity of a complex fluid to determine the mean square displacement of a probe particle. However, the motion of a probe particle, as determined by light scattering, normally reflects the behavior at wave vectors  $q$ , which are large compared to  $a^{-1}$ . By contrast, the elastic modulus of a material reflects the response in the limit of  $q \rightarrow 0$ . However, if the probe particle is large enough, its response to thermal fluctuations will presumably reflect the long wavelength limit and thus the bulk moduli of the material. Moreover, the flow pattern of a viscoelastic fluid around the particle is nonuniform, and may differ from that of a simple fluid. This will modify the coefficient in Eq. (3), and may even make it frequency dependent. Thus, the light scattering may not provide a quantitatively exact measure of the elastic moduli; nevertheless, as our results show, the overall trends are correctly captured, and the agreement is very good.

The underlying value and utility of this technique derives from the extended range of the results obtained. For example, combining DWS and traditional DLS allows the measurement of mean square displacements ranging from several angstroms to several microns; by also varying the radius of the probe particles, elastic moduli ranging from  $10^{-2}$  to  $10^7$  dyn/cm<sup>2</sup> are accessible. Similarly, the light scattering allows a much greater frequency range to be probed in a single experiment; in particular, the moduli can be measured to much higher frequencies than is possible by mechanical techniques. This range should provide new insights into the underlying physics of the elastic susceptibility of complex fluids. For example, in the inset in Fig. 2, we show the full range of  $\tilde{G}(s)$  obtained from the light scattering data for the polymer solution. It contains information about the low-frequency relaxations, where entanglements dominate, as well as the high-frequency relaxations where the glassy behavior dominates. Thus, it reflects the full relaxation spectrum of the polymer solution. Relaxation spectra are typically measured with a rheometer, and the limited frequency range is overcome using the technique of time-temperature superposition [17]. Our data suggest that light scattering can measure the complex modulus over the whole frequency range in a single experiment, without the need for changing temperature. This may be of particular potential importance in the study of polymers that crystallize, where time-temperature superposition is precluded. The light scattering data also provide convincing evidence that, for hard spheres,  $G'(\omega) \approx \omega^{0.5}$  at high frequencies, consistent with theoretical predictions which ignore lubrication effects [11,12]. This result is evident from the behavior of  $\tilde{G}(s)$  when the high-frequency term proportional to  $s$  is subtracted; the remainder clearly exhibits an  $s^{0.5}$  dependence.

Dynamic light scattering measurements have long been used to measure viscosity; they also probe the elastic moduli of gels [18]. Our results provide the framework to generalize the use of dynamic light scattering to measure the full frequency dependence of the linear viscoelastic moduli of complex fluids. They clearly illustrate the generality of this method. The complex fluids studied here represent three completely different materials: a colloidal suspension, where the probe particles themselves lead to the rheological properties of the suspension; a polymer network, where the particle merely probe the viscoelasticity of the solution; and an emulsion, where the elasticity results from the surface tension and the deformation of the probe particles. In all cases, the optical measurements of the viscoelastic moduli are in excellent agreement with mechanical measurements. We expect this technique to apply very generally to other complex fluids, although further experiments are clearly required to explore the full range of validity, and further theoretical work is clearly required to determine the underlying physics of this surprising agreement.

We thank Rudy Klein, Tom Lubensky, and Bill Graessley for helpful discussions.

- 
- [1] J.D. Ferry, *Viscoelastic Properties of Polymers* (Wiley, New York, 1980).
  - [2] P.M. Chaikin and T. Lubensky, *Principles of Condensed Matter Physics* (Cambridge University Press, Cambridge, 1994).
  - [3] W. Hess and R. Klein, *Adv. Phys.* **32**, 173 (1983).
  - [4] A.V. Oppenheim and A.S. Willsky, *Signals and Systems* (Prentice-Hall, London, 1983).
  - [5] T. Shikata and D. Pearson, *J. Rheol.* **38**, 601 (1994).
  - [6] G. Maret and P. Wolf, *Z. Phys. B* **65**, 409 (1987).
  - [7] D.J. Pine, D.A. Weitz, P.M. Chaikin, and E. Herbolzheimer, *Phys. Rev. Lett.* **60**, 1134 (1988).
  - [8] W. van Meegen and P.N. Pusey, *Phys. Rev. A* **43**, 5429 (1991).
  - [9] D.A. Weitz and D.J. Pine, in *Dynamic Light Scattering*, edited by W. Brown (Oxford University Press, Oxford, 1992).
  - [10] W. Gotze and L. Sjogren, *Phys. Rev. A* **43**, 5442 (1991).
  - [11] I.M. de Schepper, H.E. Smorenburg, and E.G.D. Cohen, *Phys. Rev. Lett.* **70**, 2178 (1993).
  - [12] R.A. Lionberger and W.B. Russel (to be published).
  - [13] J. Bibette, *J. Colloid Interface Sci.* **147**, 474 (1991).
  - [14] J.P. Boon and S. Yip, *Molecular Hydrodynamics* (McGraw Hill, New York, 1980).
  - [15] C.H. Wang and E.W. Fischer, *J. Phys. Chem.* **82**, 632 (1985).
  - [16] W. Gotze and L. Sjogren, *Rep. Prog. Phys.* **55**, 241 (1992).
  - [17] G. Martin and W.W. Graessley, *Rheol. Acta* **16**, 527 (1977).
  - [18] T. Tanaka, L.O. Hocker, and G.B. Benedek, *J. Phys. Chem.* **59**, 5151 (1973).

## Lab 4: Magnetic trap microrheology

**Location:** NE47-275

**PI:** Peter So

**Lab Instructors:** Judy Su and Heejin Choi

### Summary

Information regarding cellular rheology is needed to understand a variety of cellular processes including intracellular transport and migration. Because changes in cellular mechanical properties trigger a cascade of biological responses, an understanding of cellular rheology has implications in understanding many biomedical problems, such as the development of cardiovascular diseases (e.g. atherosclerosis) and the development of tissue engineering constructs (such as promoting cell growth over artificial surfaces). In addition, the ability to regulate cellular mechanical properties has important implications in a wide variety of fundamental processes ranging from wound healing to cellular biosensors. Magnetic tweezers belong to a class of active microrheological techniques designed to probe the rheological properties of cells. Fibronectin coated magnetic beads are dropped on the surface of the cell and allowed to internalize overnight. The tweezers are an electromagnet that generates a magnetic field which exerts a quantifiable constant force on a paramagnetic or ferromagnetic object. By varying the current through the electromagnet, the amount of force applied to the bead may be controlled. The displacement of the bead as a function of time may be modeled as a Voigt element in series with a dashpot. Based on this analysis, the viscoelastic behavior of the cell may be characterized by three mechanical parameters. In this lab you will use magnetic tweezers to measure the viscoelastic parameters of NIH3T3 fibroblast cells and compare these obtained results with values reported in the literature.

### Recommended Reading

A. R. Bausch *et al.*, "Local Measurements of Viscoelastic Parameters of Adherent Cell Surfaces by Magnetic Bead Microrheometry," *Biophys J.* **75**.

H. Huang *et al.*, "Three-Dimensional Cellular Deformation Analysis with a Two-Photon Magnetic Manipulator Workstation," *Biophys J.* **82**.



## Local Measurements of Viscoelastic Parameters of Adherent Cell Surfaces by Magnetic Bead Microrheometry

Andreas R. Bausch,\* Florian Ziemann,\* Alexei A. Boulbitch,\* Ken Jacobson,# and Erich Sackmann\*

\*Physik Department E22 (Biophysics Group), Technische Universität München, D-85748 Garching, Germany, and #Department of Cell Biology and Anatomy, University of North Carolina, Chapel Hill, North Carolina 27599-7090 USA

**ABSTRACT** A magnetic bead microrheometer has been designed which allows the generation of forces up to  $10^4$  pN on  $4.5 \mu\text{m}$  paramagnetic beads. It is applied to measure local viscoelastic properties of the surface of adhering fibroblasts. Creep response and relaxation curves evoked by tangential force pulses of 500–2500 pN (and  $\sim 1$  s duration) on the magnetic beads fixed to the integrin receptors of the cell membrane are recorded by particle tracking. Linear three-phasic creep responses consisting of an elastic deflection, a stress relaxation, and a viscous flow are established. The viscoelastic response curves are analyzed in terms of a series arrangement of a dashpot and a Voigt body, which allows characterization of the viscoelastic behavior of the adhering cell surface in terms of three parameters: an effective elastic constant, a viscosity, and a relaxation time. The displacement field generated by the local tangential forces on the cell surface is visualized by observing the induced motion of assemblies of nonmagnetic colloidal probes fixed to the membrane. It is found that the displacement field decays rapidly with the distance from the magnetic bead. A cutoff radius of  $R_c \sim 7 \mu\text{m}$  of the screened elastic field is established. Partial penetration of the shear field into the cytoplasm is established by observing the induced deflection of intracellular compartments. The cell membrane was modeled as a thin elastic plate of shear modulus  $\mu^*$  coupled to a viscoelastic layer, which is fixed to a solid support on the opposite side; the former accounts for the membrane/actin cortex, and the latter for the contribution of the cytoskeleton to the deformation of the cell envelope. It is characterized by the coupling constant  $\chi$  characterizing the elasticity of the cytoskeleton. The coupling constant  $\chi$  and the surface shear modulus  $\mu^*$  are obtained from the measured displacements of the magnetic and nonmagnetic beads. By analyzing the experimental data in terms of this model a surface shear modulus of  $\mu^* \approx 2 \cdot 10^{-3} \text{ Pa m}$  to  $4 \cdot 10^{-3} \text{ Pa m}$  is found. By assuming an approximate plate thickness of  $0.1 \mu\text{m}$  one estimates an average bulk shear modulus of  $\mu \approx (2 \div 4) \cdot 10^{-4} \text{ Pa}$ , which is in reasonable agreement with data obtained by atomic force microscopy. The viscosity of the dashpot is related to the apparent viscosity of the cytoplasm, which is obtained by assuming that the top membrane is coupled to the bottom (fixed) membrane by a viscous medium. By application of the theory of diffusion of membrane proteins in supported membranes we find a coefficient of friction of  $b_c \approx 2 \cdot 10^9 \text{ Pa s/m}$  corresponding to a cytoplasmic viscosity of  $2 \cdot 10^3 \text{ Pa s}$ .

### INTRODUCTION

Viscoelasticity plays an important role in the behavior of cells. It is a key factor in the regulation of the cell shape of resting and moving cells, and it has even been conjectured that the viscoelastic coupling between the plasma membrane and the cell nucleus plays a role in the control of genetic expression (Ingber, 1997; Forgacs, 1996). The cell viscoelasticity is determined in a complex way by the composite shell envelope composed of the lipid-protein bilayer with the associated actin cortex and by the internal cytoskeleton composed of actin microfilaments, microtubules, intermediate filaments, and their associated proteins. High-precision measurements of viscoelastic parameters of cells are thus expected to give insight into the structure of the cortical and internal cytoskeleton. Moreover, such measurements

are of great practical value in order to quantify the effect of drugs, mutations, or diseases on the cell structure. Viscoelastic measuring techniques must fulfill three conditions. First, they must allow local measurements on micrometer-to-nanometer scales to account for the inherent heterogeneous architecture of cell envelopes. Since cellular deformations may be followed by biochemically induced changes of the local viscoelastic parameters, the techniques must secondly allow repeated measurements. To compare the data, the third requirement is that the data analysis is independent of a specific cell model. These requirements are fulfilled by microrheological techniques based on optical tweezers (Choquet et al., 1997), atomic force microscopy (Radmacher et al., 1996), magnetic bead rheometry (Ziemann et al., 1994), and cell poking elastometer (Pasternak et al., 1995). An intriguing magnetic particle technique used to assay the cytoplasmic viscosity and intracellular mobilities has been developed by Valberg et al. (cf. Valberg and Feldman, 1987). It is based on the analysis of the decay of remnant magnetic fields after twisting the magnetic particles. It corresponds to our relaxation response analysis. The major differences of this technique as compared to the others is that many particles distributed within the cell are monitored. Moreover, the method yields average values of the cytoplasmic viscosities.

Received for publication 15 December 1997 and in final form 11 July 1998.

Address reprint requests to Prof. Dr. Erich Sackmann, Physikdepartment E22, Lehrstuhl für Biophysik, Technische Universität München, James-Franck-Strasse, D-85748 Garching, Germany. Tel.: +49 (089) 289-12471; Fax: +49 (089) 289-12469; E-mail: sackmann@physik.tu-muenchen.de.

This paper is dedicated to the memory of Fred Fay, an outstanding pioneer in new forms of light microscopy imaging for biology, and a good friend.

© 1998 by the Biophysical Society

0006-3495/98/10/2038/12 \$2.00

Another strategy used to measure local elastic properties was established recently. It is based on the analysis of the surface profile of adhering cells near the contact area and its alteration by viscous shear forces in terms of the elastic boundary (Simson et al., 1998).

Many cell types such as *Dictyostelium* cells, white blood cells, fibroblasts, or endothelial cells exhibit elastic moduli of the order of  $10^3$  to  $10^4$  Pa and forces in the nanonewton regime are required for the deformation of these cells (cf. Evans, 1995; Radmacher et al., 1996). For this purpose, we developed a magnetic bead microrheometer ("magnetic tweezers") allowing application of local forces of up to 10 nN on paramagnetic beads of 4.5  $\mu\text{m}$  diameter. This technique is applied to measure viscoelastic parameters of the cell envelope of fibroblasts adhering to solid substrates.

Magnetic beads (of 4.5  $\mu\text{m}$  diameter) coated with fibronectin are fixed to integrin receptors of the cell surface. Creep response and relaxation curves evoked by tangential force pulses of 500–2500 pN (and  $\sim 1$  s duration) are determined by the particle tracking technique. A linear viscoelastic response is found for forces up to 2 nN in contrast to the increase of local stiffness with stress amplitude reported by Ingber (1997).

Three-phasic creep response curves exhibiting an elastic domain, a relaxation regime, and viscous flow behavior are found. This three-phasic response is formally accounted for by a mechanical equivalent circuit consisting of a Voigt body and a dashpot in series where the Voigt element (composed of a Maxwell body and a spring in parallel arrangement) accounts for the solidlike and the dashpot for the fluidlike behavior. Based on the above analysis the viscoelastic behavior of the cell is characterized by three parameters: an elastic constant ( $k$ ), a relaxation time ( $\tau$ ), and a viscosity ( $\gamma_0$ ).

To relate these parameters to viscoelastic moduli of the cell envelope and the cytoplasm, the adhering cell lobe is modeled by a thin elastic plate which is coupled to a viscoelastic layer fixed on the side opposite to the substrate. The elasticity of the top plate (representing the plasma membrane) is characterized by a surface shear modulus  $\mu^*$ . It is related to the shear modulus  $\mu$  of the material as  $\mu^* = \mu h$ , where  $h$  is the thickness of the shell composed of the membrane and actin cortex. The elastic effect of the intermediate layer is characterized by a phenomenological coupling constant  $\chi$ , referred to as the cytoskeleton coupling constant.

According to a theory of A. Boulbitch (1998, submitted for publication; cf. Appendix for summary) the displacement field generated by a local tangential force on the top membrane exhibits a logarithmic behavior in the plane of the membrane at distances  $r$  much smaller than a screening length  $R_c$  while it decays exponentially at  $r \gg R_c$ . The screening length  $R_c$  is related to the shear modulus  $\mu^*$  and the coupling constant  $\chi$  by  $R_c = \kappa^{-1} = (\mu^*/\chi)^{1/2}$ .

Experimental evidence for such a screened elastic deformation of the cell surface is provided by accompanying displacement field mapping experiments (Schmidt et al.,

1996). The local displacement of the membrane surface evoked by the local tangential force is directly visualized by observing the induced motion of colloidal probe beads attached to the cell membrane in the neighborhood of the magnetic bead. It is demonstrated that the displacement field decays rapidly with a cutoff radius of  $R_c \approx 7 \mu\text{m}$ . By analyzing the observed decay of the displacement field with the distance from the magnetic bead in terms of the theoretical model, one obtains values of  $\chi$  and  $\mu^*$ . It is thus possible to relate the elastic constant ( $k$ ) obtained from the equivalent circuit analysis to an absolute shear modulus of the cell envelope.

For the evaluation of the viscous flow regime it is assumed that the top membrane of the adhering cell lobe is coupled to the bottom (fixed) membrane by a viscous fluid. The apparent viscosity of this fluid is obtained from the velocity of the magnetic bead by application of a theory previously elaborated to describe the diffusion of proteins embedded in a bilayer membrane coupled to a solid surface through a thin lubricating film (Evans and Sackmann, 1988). This theory predicts that the viscous flow field in the membrane is again screened by this frictional coupling (Evans and Sackmann, 1988). Thus the viscosity of the cytoplasm can also be related to the value of the viscosity of the dashpot  $\gamma_0$ . The screened penetration of the shear field into the cytoplasm was observed by the induced deflection of intracellular compartments.

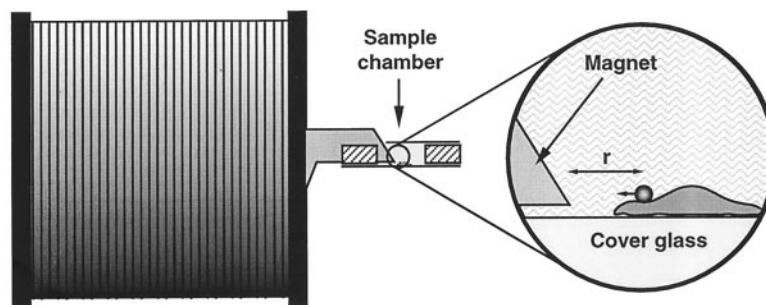
## MATERIALS AND METHODS

### The high force magnetic bead rheometer

The microrheometer resembles the experimental set-up described previously (Ziemann et al., 1994; Schmidt et al., 1996). It consists of a central measuring unit comprised of a sample holder and a magnetic coil with 1200 turns of 0.7 mm copper wire. The sample holder with dimension  $50 \times 55 \times 50 \text{ mm}^3$  is mounted on an AXIOVERT 10 microscope (Zeiss, Oberkochen, Germany). The coil current is produced by a voltage-controlled current supply built in the authors' laboratory that transforms the voltage signal of a function generator FG 9000 (ELV, Leer, Germany) in a current signal with amplitudes of up to 4 A. The microscope image is recorded by a CCD camera (C3077, Hamamatsu Photonics, Hamamatsu City, Japan) connected to a VCR (WJ-MX30, Matsushita Electric Industrial Co., Osaka, Japan). The recorded sequences are digitized using an Apple Power Macintosh 9500 (Apple Computer, Cupertino, CA) equipped with a LG3 frame grabber card (Scion Corp., Frederick, MD). The position of the particles is determined with an accuracy of  $\sim 10$  nm using a self-written single particle tracking algorithm implemented in the public domain image processing software National Institutes of Health Image (National Institutes of Health, Bethesda, MD).

The important modification of the present apparatus, compared to the previous one, is that only one magnetic coil is used in which the edge of the pole piece can be positioned as close as 10  $\mu\text{m}$  from the magnetic particle (see Fig. 1). Because of the very high field gradient in the close vicinity of the pole piece, forces could be increased by a factor of  $\sim 10^3$  compared to the earlier design (Ziemann et al., 1994). Thus, forces of up to 10 nN on a 4.5- $\mu\text{m}$  paramagnetic bead were achieved (cf. Fig. 2). By using ferromagnetic beads such forces could be achieved with bead diameters of 0.5  $\mu\text{m}$ . A second magnet cannot be used in the present device because of the strong magnetic induction generated between the pole pieces at such small distances.

FIGURE 1 Central measuring unit of the improved magnetic bead rheometer set-up. The magnet consists of a coil (1200 turns of 0.7 mm copper wire) and a soft iron core, which penetrates the sample chamber. The coil is fixed with a holder that can be placed on the microscope stage. The tip of the pole piece can be positioned close to the magnetic bead (at distances of  $r = 10\text{--}100\ \mu\text{m}$ ) to obtain maximal forces of up to 10,000 pN on a 4.5- $\mu\text{m}$  paramagnetic bead.



## Force calibration of the set-up

To calibrate the distance dependence of the force acting on the magnetic bead in the high force set-up, the bead velocity was determined near the pole piece in liquids of known viscosity at different coil currents ranging from 250 to 2500 mA. The bead velocity was computed from the measured displacement-time-graphs by numerical differentiation. Fig. 2 shows the results of a typical calibration of the force on a 4.5- $\mu\text{m}$  paramagnetic bead (DYNABEADS M-450, DYNAL, Oslo, Norway). We used dimethyl-polysiloxane with a kinematic viscosity of 12,500 cSt (DMPS-12M, Sigma Chemical Company, St. Louis, MO) as a calibrating liquid.

The velocity curves were converted into force curves using Stokes law and plotted versus the distance to the pole piece (see Fig. 2 *a*). For the highest coil currents, forces of up to 10,000 pN on a 4.5- $\mu\text{m}$  paramagnetic bead were reached. The curves shown in Fig. 2 *a* were all obtained by using the same bead. For each measurement the bead was aspirated by a micropipette and pulled back to its starting position (at a distance of 110  $\mu\text{m}$  to the pole piece). Thus, the errors resulting from different bead sizes and iron contents ( $\sim 15\text{--}20\%$ ) could be avoided.

In Fig. 2 *b* the magnetic force is plotted versus the coil current for different distances from the pole piece. This graph shows a linear dependence between force and current indicating that the paramagnetic bead is fully magnetized and therefore does not exhibit a field-dependent magnetic moment, which would be the case for paramagnetic particles in low magnetic fields.

The overall error of the method for measuring absolute forces is determined by the standard deviations of the bead size and the iron content and was estimated to 15–20%. For relative measurements (performed with the same bead), the overall error depends only on the accuracy of the determination of the bead velocity and of the coil current. This leads to a small total error for relative measurements of forces and viscoelastic constants of 1–2%.

## Sample preparation

The rheological measurements presented here were performed on National Institutes of Health 3T3 murine fibroblasts employing paramagnetic mi-

crobeads of 4.5  $\mu\text{m}$  diameter bound to the cell membrane. National Institutes of Health 3T3 cells were provided by the Max-Planck-Institut für Zellbiologie (Martinsried, Germany). The cells were cultured in an incubator at 37°C and 5% CO<sub>2</sub>. The cell culture medium consisted of DMEM with 10% v/v fetal calf serum (both from Life Technologies, Frederick, MD).

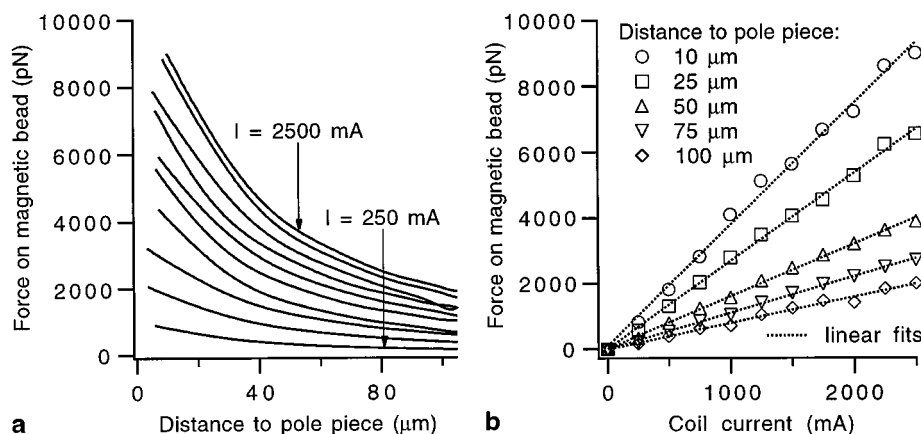
As shown in Fig. 3, the microbeads were coated with fibronectin, which provides indirect coupling to the actin cortex via integrins located in the cell membrane (Miyamoto et al., 1995; Wang et al., 1993). Fibronectin was covalently conjugated to 4.5- $\mu\text{m}$  diameter paramagnetic polystyrene beads coated with reactive tosyl groups (DYNABEADS M-450 tosylactivated, DYNAL) according to the procedure provided by the supplier. Carboxylated latex beads with a diameter of 1  $\mu\text{m}$  (POLYBEADS, Polysciences, Warrington, PA) were used as nonmagnetic colloidal probes for the visualization of the displacement field on the cell membrane (cf. Fig. 8). These beads were also coated with fibronectin to ensure the coupling to the integrins.

Immediately before sample preparation the functionalized magnetic beads were washed once in PBS (phosphate buffered saline, Sigma Chemical Co.) using a magnetic separation device (MPC-1, DYNAL) and the bead concentration was adjusted to  $\sim 10^5$  beads/ml. Cells were then detached from the substratum using a trypsin-EDTA solution (Life Technologies) and transferred onto suitable coverglasses. After an incubation time of 1–2 h to allow complete adhesion of the cells, 1.5 ml bead solution per coverglass was added. Beads were incubated with cells for 15 min and washed gently before mounting the coverglass on the sample holder of the magnetic bead rheometer.

## Evaluation of creep experiments by mechanical equivalent circuit

Creep experiments are performed by recording the deflection and relaxation of the magnetic beads (or nonmagnetic probe beads) following rectangular force pulses. The trajectories of the beads are determined by the single particle tracking technique with an accuracy of  $\pm 10$  nm. Fig. 4 shows a typical sequence of responses of a magnetic bead to a sequence of

FIGURE 2 Force calibration of a 4.5- $\mu\text{m}$  magnetic bead for the high force set-up. (*a*) Distance dependence of the force on the bead for 10 different coil currents (250–2500 mA). (*b*) Force-versus-current curves for the five distances indicated in the inset showing a linear relationship between the coil current and the force on the (fully magnetized) paramagnetic bead.



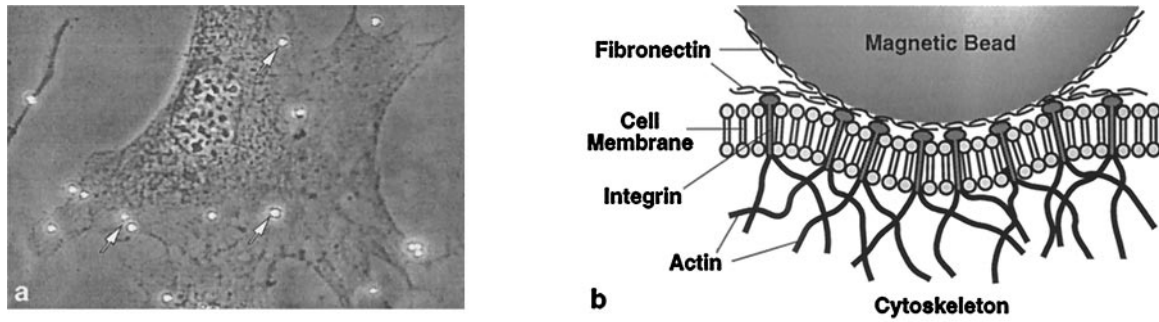


FIGURE 3 (a) Micrograph of a mouse 3T3 fibroblast with magnetic microbeads bound to the cell membrane (white arrows). (b) Schematic drawing of a fibronectin-coated bead that is coupled to the cell cytoskeleton via integrins.

rectangular force pulses of duration  $\Delta t = 2.5$  s. The responses exhibit three regimes: a fast elastic response (I), a relaxation regime (II), and a flow regime (III).

The time-dependent deflection  $x(t)$  of the body of Fig. 5 a evoked by a stepwise force  $F(t)$  can be easily expressed as superposition of the deflection of the Voigt body and of the dashpot according to Fung (1993). Therefore, the deflection of the bead (normalized by the applied force amplitude  $F$ ) is given by

$$\frac{x(t)}{F} = \frac{1}{k_0} \left( 1 - \frac{k_1}{k_0 + k_1} \cdot \exp(-t/\tau) \right) + \frac{t}{\gamma_0}, \quad (1a)$$

where the relaxation time  $\tau$  is given by

$$\tau = \frac{\gamma_1(k_0 + k_1)}{k_0 k_1}. \quad (1b)$$

The characteristic time behavior of the equivalent circuit is shown in Fig. 5 b and the similarity with the sequence of response and relaxation curves in Fig. 4 is evident. As shown in Fig. 6 the creep response curves are very well reproduced by Eq. 1a.

The four parameters characterizing the equivalent circuit can be reduced to three observables with the following physical meaning: because the amplitude of the elastic displacement (regime I) is determined by  $x = F/(k_0 + k_1)$  the sum  $k = k_0 + k_1$  is a measure of the effective spring constant of the system. As defined in Eq. 1b,  $\tau$  is the relaxation time required for the transition from the elastic to the viscous regime and  $\gamma_0$  is a measure for the effective viscous friction coefficient of the bead in the viscous flow regime.

The analysis of the viscoelastic response curves evoked by the tangential force pulses in terms of the three observables defined above is a first and straightforward step of data analysis. It is sufficient to observe local variations of the viscoelastic properties on the cell surface or to study differences between different cells (cf. Fig. 7). However, it is a much more

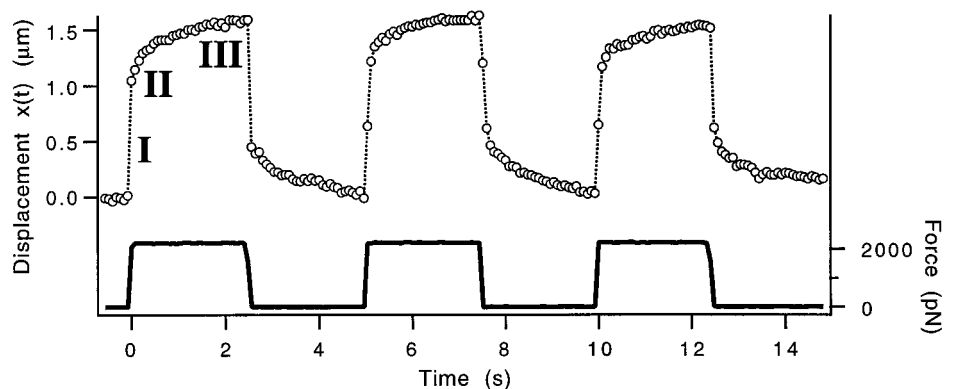
difficult task to relate these parameters to viscoelastic moduli of the cell surface or the cytoplasm. This will be attempted below by introduction of a simplified model of the adhering cell lobes.

## RESULTS AND DISCUSSION

### Evaluation of response curve in terms of equivalent circuit

We studied the creep response curves of 10 cells while analyzing several magnetic beads on each cell. Moreover, measurements were performed for three to five different traction forces for each magnetic bead. The three viscoelastic parameters  $k$ ,  $\tau$ , and  $\gamma_0$  defined above (cf. Eqs. 1) were determined by analysis of the creep-response curves as described in Fig. 5. The data are summarized in Fig. 7. To distinguish the results obtained for different cells or on different sites on the adhering lobe of one cell the individual measurements are plotted separately. Values for different cells are distinguished by different symbols. Open and closed symbols of the same shape characterize measurements of the same cell but at different sites. Measurements performed with the same particle but with different force amplitudes are marked with equal symbols. A closer inspection of the data shows that all viscoelastic parameters may differ by up to an order of magnitude from cell to cell, but that the values obtained for each individual cell differ by much less.

FIGURE 4 Typical creep response and relaxation curves observed for a 4.5- $\mu\text{m}$  bead bound to the membrane of a 3T3 fibroblast through a presumed fibronectin-integrin linkage. Force pulses of an amplitude of  $F = 2000$  pN and a duration of  $\Delta t = 2.5$  s were applied.



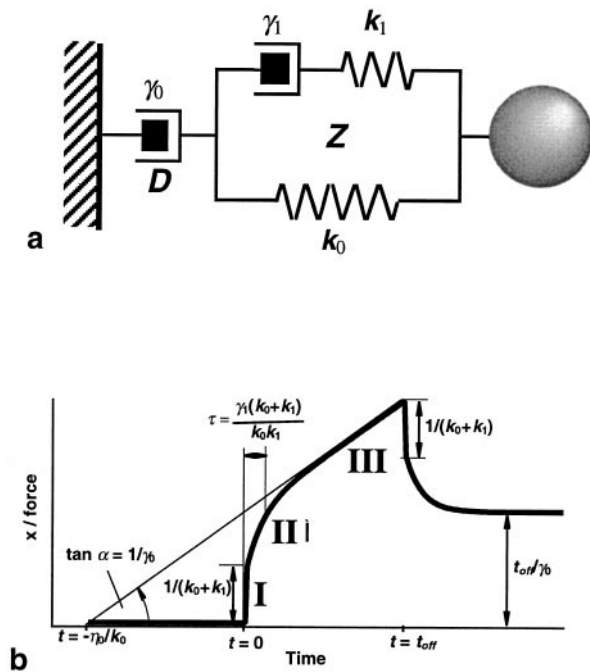


FIGURE 5 Mechanical equivalent circuit enabling formal representation of creep response and relaxation curves. (a) Mechanical model consisting of a Kelvin (or Zener) body (Z) and a dashpot (D) in series. (b) Creep response and relaxation curve of the mechanical equivalent circuit exhibiting the three experimentally observed regimes of response (I–III).

To check the linearity of the viscoelastic response, the creep response curves were recorded as a function of the applied forces ranging from 500 to 2000 pN. In Fig. 8 the time-dependence of the displacements (normalized by the applied force) obtained for different applied forces is plotted. In this example the curves coincide within experimental error with the exception of the curve for  $F = 2213$  pN. This implies that the viscoelastic behavior of the system is linear for at least forces of up to  $\sim 2000$  pN. The measurements of the viscoelastic moduli presented in Fig. 7 were performed in the linear regime using forces up to 2000 pN.

### Strain field mapping experiment

A typical experiment is shown in Fig. 9. A number of nonmagnetic colloidal latex beads (numbered 1 to 9) are deposited on the cell surface together with one magnetic bead (marked as M). Beads are bound to integrins via the fibronectin coating. The creep response and relaxation curves generated by rectangular force pulses of 3700 pN were recorded by using the particle tracking technique. The amplitudes of deflection generated by pulses of 1 s duration normalized with respect to the polar angle  $\cos \theta$  (cf. Eq. 2 below) were measured and plotted in Fig. 9 c. Although the relaxation time  $\tau$  is of the order of 0.1 s we use the amplitudes at  $t = 1$  s as a measure for the elastic displacement. Because all creep response curves exhibit essentially the same shape, this approximation procedure is justified. These measurements were also performed at a force larger

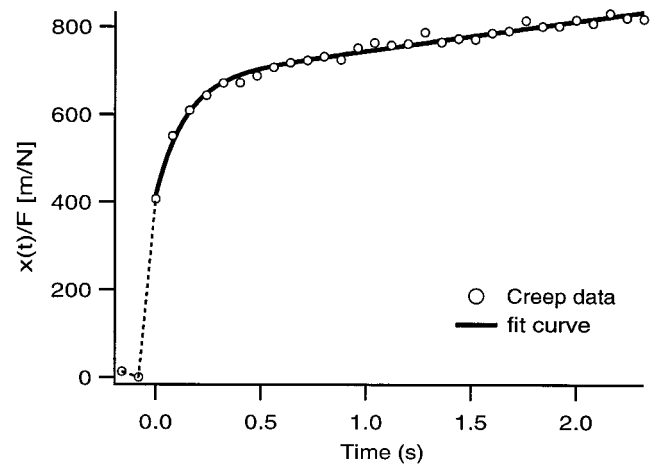


FIGURE 6 Typical fit to measured creep data for a force of  $F = 1100$  pN. The dotted line represents the instantaneous elastic response of the magnetic bead corresponding to a jump in the displacement of  $1/(k_0 + k_1)$ .

than 2000 pN to facilitate the observation of the particle deflections. However, several displacement field mapping experiments performed with lower forces yielded the same distance-dependence of the normalized deflections.

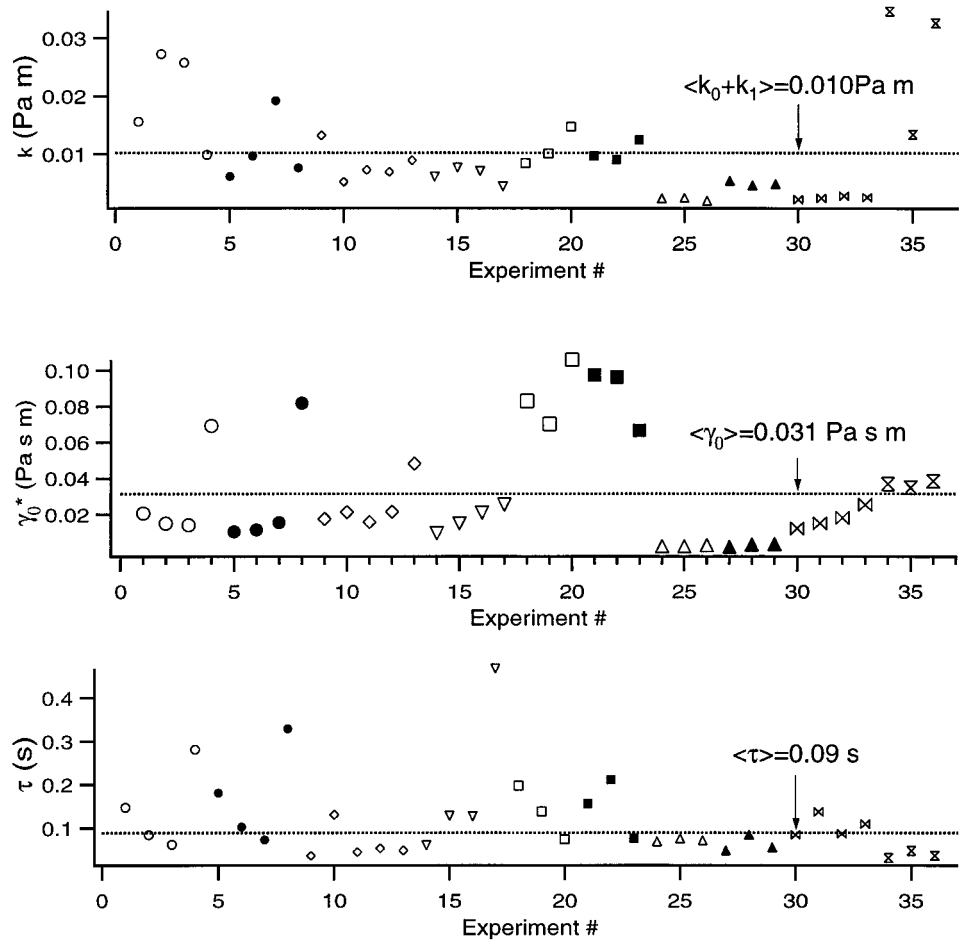
The three nonnumbered beads in Fig. 9 were also deflected, but the deflection amplitude could not be measured accurately enough since the images overlap, thus preventing the application of the particle tracking procedure. Another intriguing way to determine the displacement field is the use of intracellular particles as markers instead of latex particles. In Fig. 10 an experiment is presented demonstrating that cell vacuoles exhibit detectable induced deflection amplitudes (see bottom row in Fig. 10 b). The experiment shows that the shear displacement field penetrates partially into the cell cytoplasm; thus intracellular particles may potentially be used as probes to estimate the local penetration depth of the displacement field.

### Evaluation of the displacement field data by a simple cell model

To determine real elastic moduli (and shear viscosities) of the cell envelope from the viscoelastic parameters obtained by analyzing the creep response curves in terms of the equivalent circuit, one requires a theory of the elastic displacement of the adhering cell lobe generated by local tangential forces acting on the cell surface. Such models yield the geometric prefactor relating the elastic modulus of the cell surface to the spring constant of the equivalent circuit.

Because the microscopic structure of the cell lobe is not known, one has to introduce suitable models. One obvious possibility would be to consider the cell lobe as a thin homogeneous elastic slab, one side of which is fixed to a solid surface. However, this model would not account for the fact that the cell lobe is composed of two juxtaposed

FIGURE 7 Summary of three pertinent viscoelastic parameters of 3T3 fibroblasts: the effective elastic modulus  $k = k_0 + k_1$ , the viscosity  $\gamma_0$ , and the relaxation time  $\tau$  (defined by Eq. 1b) are obtained by analyzing the creep response curves in terms of the equivalent circuit. To distinguish the results obtained for different cells or on different sites on the adhering lobe of one cell, the individual measurements are plotted separately. Values for different cells are distinguished by different symbols. Open and closed symbols of the same shape characterize measurements of the same cell but at different sites. Measurements performed with the same particle but with different force amplitudes are marked with equal symbols.



membranes and that these are interconnected by an intracellular cytoskeleton, as follows from the distribution of intracellular compartments in the cell lobe.

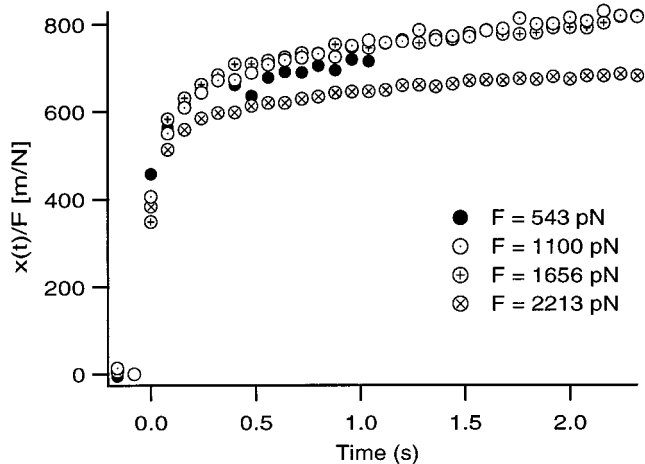
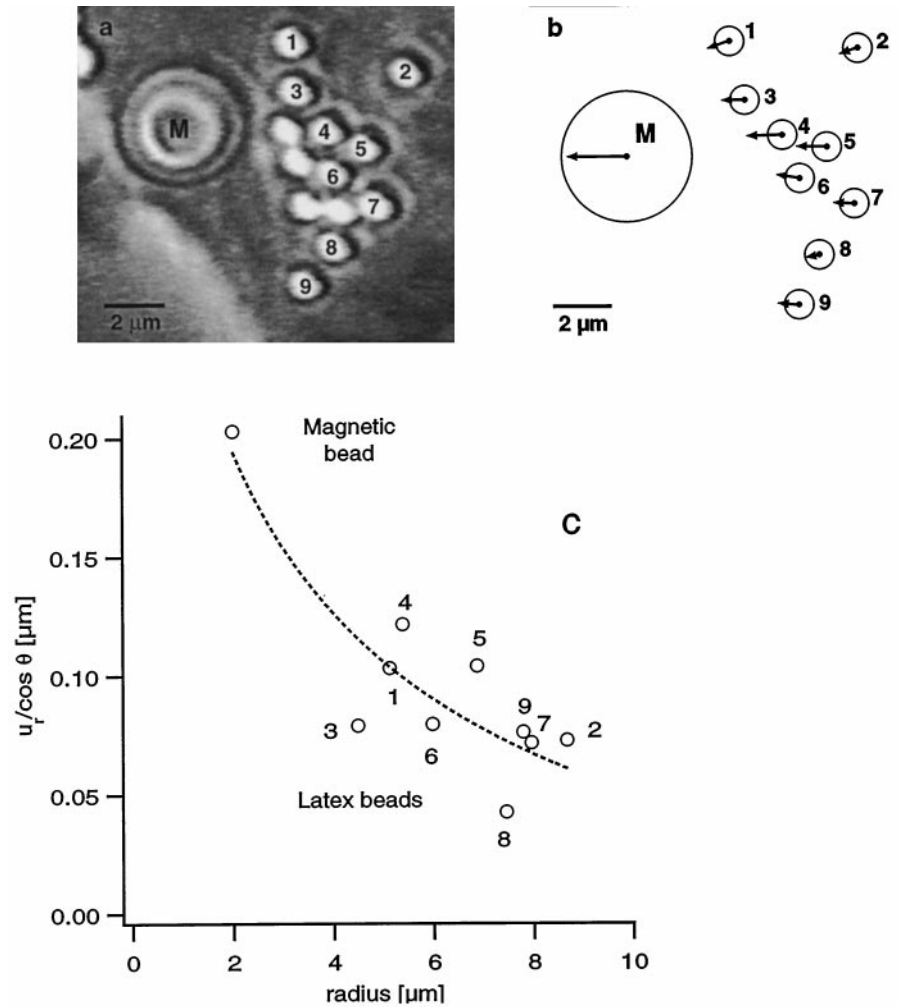


FIGURE 8 Time dependence of the deflection of the magnetic bead normalized with respect to the force for four different forces indicated, demonstrating linear viscoelasticity up to forces of at least 2000 pN. The maximum displacement is  $u(r) = 1 \mu\text{m}$  for the maximum force of 2000 pN. Most measurements were performed at 500-1000 pN. The maximal value of the strain tensor component was 5%.

In view of these considerations, we assume that the cell lobe can be considered as a partially collapsed shell composed of a lipid-protein bilayer with associated actin cortex (called the composite plasma membrane), and which is filled by a viscoelastic gel coupled to the actin cortex. Therefore the adhering cell lobe is mimicked as two juxtaposed elastic sheets of shear modulus  $\mu^*$  (representing the composite membrane), which are attached to an elastic medium (accounting for the cytoskeleton). The coupling between the actin cortex and the cytoskeleton is characterized by a phenomenological coupling constant  $\chi$ , which is a measure for the cytoskeleton membrane coupling strength per unit area (see the Appendix for details). It is further assumed that the bottom shell is fixed to the surface and it is not deformed during our measurements. This assumption is justified by the fact that the displacement field decays rapidly within the cytoplasm (cf. Fig. 9).

The problem of the elastic deformation of such a body by a tangential point force acting on the surface has been solved by A. Boulbitch (1998, submitted for publication). The essential results are summarized in the Appendix where the general expression for the displacement field is given. The main result is that the displacement field  $\mathbf{u}(r, \theta)$  caused by the local force is screened. It depends logarithmically on the radial distance from the point where the force is applied

FIGURE 9 Typical displacement field mapping experiment on the plasma membrane of a fibroblast. (a) Microscopic picture showing a region of the cell with one magnetic bead (M, radius  $2.25 \mu\text{m}$ ) and a number of nonmagnetic particles (1–9, radius  $0.5 \mu\text{m}$ ). (b) Graphic representation of the displacement field after a force pulse of 1-s duration. The bead sizes and positions are drawn to scale, while the bead deflections are enlarged by a factor of 10. The three non-numbered beads were also deflected, but the deflection amplitude could not be measured accurately enough since the images overlap, thus preventing the application of the particle tracking procedure. (c) Resulting distance dependence of the reduced radial component of bead deflection  $u_r/\cos \theta$  as defined in Eq. 2. The dotted line is an optimal fit of Eq. 2 to the  $u_r/\cos \theta$ -versus- $r$  plot giving the values of  $\chi$  and  $\mu^*$ . Closer inspection of Fig. 8 shows that the orientation of the deflection of the colloidal probes with respect to their angular position deviates from the theoretical prediction (Eqs. A5 and A6). The most likely explanation for these deviations is that the membrane is coupled to intracellular stress fibers, which is expected to lead to deviations from the isotropic displacement field. Moreover, the values of the deflections  $u_r(\mathbf{r})$  show large scattering. This could also be caused by stress fibers, but could be due to variations in the degree of coupling of the colloidal probes to the integrin receptors of the membrane or differences in coupling of the receptors to the membrane-associated cytoskeleton.



if  $r \ll R_c$  while  $\mathbf{u}(r, \theta)$  decays exponentially if  $r$  is large compared to the screening length  $R_c$ .

To test the validity of such a screened displacement field we analyzed the distance-dependence of the displacement field by the displacement-field mapping technique (cf. Fig. 9). The displacement vector  $\mathbf{u}(r, \theta)$  can be written in cylindrical coordinates (cf. Eq. A7). The radial component is given by

$$\frac{u_r(r)}{\cos \theta} = \frac{F_0}{2\pi\mu^*} \left\{ \frac{3(1-\sigma)}{4} K_0(\kappa_1 r) - \frac{K_1(\kappa r)}{\kappa r} + \left( \frac{1-\sigma}{2} \right)^{1/2} \frac{K_1(\kappa_1 r)}{\kappa r} \right\} \quad (2)$$

where  $\mathbf{r}$  is the radius-vector from the center of the magnetic bead to the nonmagnetic colloidal probes,  $r$  is its absolute value, and  $\theta$  is the angle between the force direction and  $\mathbf{r}$ . In Fig. 9 c the reduced radial displacement component  $u_r/\cos \theta$  is plotted as a function of  $r$ .

By fitting the theoretical displacement field to the observed data one can estimate  $\kappa$  and thus  $R_c$ . This has been done in four cases yielding cutoff radii in the range of a few

micrometers. The fit shown in Fig. 9 c yields a value  $\kappa \approx 0.15 \mu\text{m}^{-1}$  corresponding to a cutoff radius  $R_c \approx 7 \mu\text{m}$  and a surface shear modulus  $\mu^*$  of  $4 \cdot 10^{-3} \text{ Pa m}$ . As  $\kappa^2 = \chi/\mu^*$  the coupling constant is  $\chi = 10^7 \text{ Pa m}^{-1}$ .

The surface shear modulus  $\mu^*$  is also obtained by considering the absolute deflection of the magnetic bead in the direction of the magnetic field as a function of the force. The relationship between the deflection and the force is obtained by averaging the displacement  $\mathbf{u}(R, \theta)$  at the boundary of the bead adhesion disk over all angles  $\theta$ . At the present stage of analysis the radius is assumed to be about equal to the radius of the bead. Equation A2 yields

$$\begin{aligned} \langle u_x(R) \rangle &= \frac{1}{2\pi} \int_0^{2\pi} u(R, \theta) d\theta \\ &= \frac{F_{\text{ex}}}{4\pi\mu^*} [K_0(\kappa R) + (1-\sigma)K_0(\kappa_1 R)] \end{aligned} \quad (3)$$

Comparison of Eq. 3 with Eq. A1 shows that the spring constant  $k$  of the equivalent circuit is related to the surface

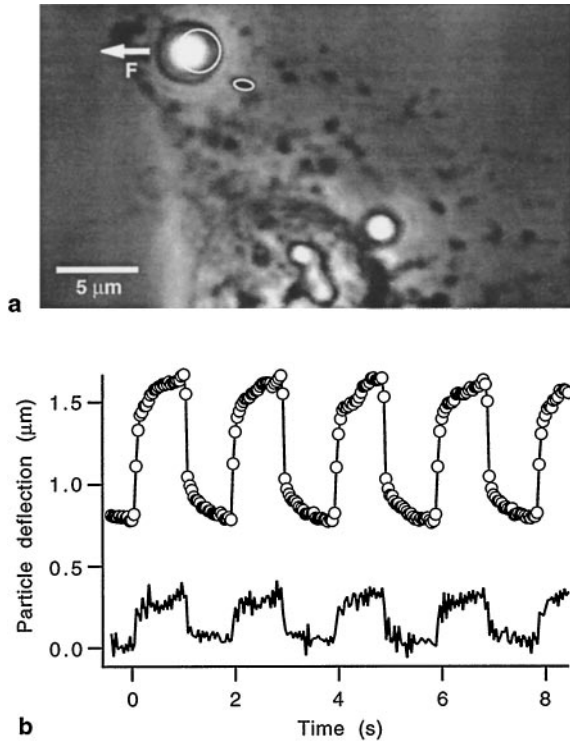


FIGURE 10 Demonstration of the penetration of the shear displacement field into the cell cytoplasm induced by displacement of the magnetic bead using cell vacuoles as markers. (a) Phase contrast image showing the magnetic bead (arrow pointing in the direction of the magnetic force) and some intracellular particles attributed to cell vacuoles in the deflected state. The initial position of the particles is marked by bright circular contours. Note that compartments further away from the magnetic bead, but at the same height as the one encircled, and those buried deeper in the cytoplasm do not move appreciably. (b) *Top trace*: sequence of creep response curves of magnetic bead following force pulses of duration  $\Delta t = 1$  s. *Bottom trace*: Viscoelastic response curves of the marked cell vacuole.

shear modulus  $\mu^*$  as

$$\mu^* = \frac{K_0(\kappa R) + (1 - \sigma)K_0(\kappa_1 R)}{4\pi} k \quad (4)$$

Values of the surface shear moduli can be related to the spring constant  $k$  presented in Fig. 7 by assuming that the plate is incompressible ( $\sigma \approx 0.5$ ) and that the screening length of the advancing lobes is about the same for all cells. With the value of  $\kappa$  obtained from the displacement field mapping experiments, the transformation factor  $\{K_0(\kappa R) + (1 - \sigma)K_0(\kappa_1 R)\}/4\pi$  in Eq. 4 becomes 0.17 for a magnetic bead of the radius  $R = 2.25 \mu\text{m}$ . The average spring constant  $k \approx 0.01 \text{ Pa m}$  (cf. Fig. 7) thus yields an average surface shear modulus  $\mu^* \approx 2 \cdot 10^{-3} \text{ Pa m}$ . Considering the large variability of the viscoelastic moduli of individual cells, this value agrees reasonably well with  $\mu^* \approx 4 \cdot 10^{-3} \text{ Pa m}$  obtained from the above analysis of the displacement field experiment.

The three-dimensional (3D) shear modulus of the cell envelope is related to  $\mu$  by  $\mu = \mu^*/h$ . The thickness  $h$  of the composite membrane is certainly smaller than the cell lobe,

which is  $1\text{--}2 \mu\text{m}$ . By assuming a value of  $h \approx 0.1 \mu\text{m}$  [as it was measured for neutrophils by Zhelev et al. (1994)] one obtains a 3D shear modulus of  $\mu \approx 2 \cdot 10^4$  to  $4 \cdot 10^4 \text{ Pa}$ .

It is important to experimentally estimate the values of the strain tensor to find out whether the linear approximation used for the calculations is valid. This can be done by calculating the measured relative displacements of the latex beads. This yields strains in the range of 2–5%, indicating that the measurements take place in the linear regime.

### Evaluation of the viscous flow in terms of effective cytoplasmic viscosity

To relate the two-dimensional (2D) viscosity  $\gamma_0$  of the equivalent circuit to the viscosity of the adhering cell lobe we assume that the magnetic bead is moving in a fluid membrane coupled to a solid surface through a viscous medium of thickness  $d_c$ . The situation is very similar to that of protein diffusion in fluid-supported membranes, which are separated from the solid surface by a lubricating film of viscosity  $\eta_c$ . This problem has been treated previously both theoretically and experimentally (Evans and Sackmann, 1988; Merkel et al., 1989). The viscous drag force on a disk embedded in the membrane and moving with velocity  $v$  is

$$F_d = 4\pi\eta_m \left[ \frac{1}{4} \epsilon^2 + \epsilon \frac{K_1(\epsilon)}{K_0(\epsilon)} \right] v \quad (5)$$

where  $K_0(\epsilon)$  and  $K_1(\epsilon)$  are modified Bessel functions. The dimensionless parameter  $\epsilon$  is defined by  $\epsilon = R(b_s/\eta_m)^{1/2}$ . Here  $\eta_m$  is the 2D viscosity of the bilayer membrane,  $R$  is the radius of the disk which in our case is equal to the contact area between the magnetic bead and the membrane, and  $b_s$  is the friction coefficient of the coupling medium, which is related to the viscosity of the viscoelastic layer of thickness  $d_c$  by  $b_s = \eta_c/d_c$ . For large values of  $\epsilon$  (in practice, for  $\epsilon > 1$ ), the second term on the right side of Eq. 5 can be neglected. The drag force in this limit does not depend on the membrane viscosity and is  $F_d = \pi R^2 d_c^{-1} \eta_c v$ . The 2D viscosity of membranes is of the order of  $\eta_m = 10^{-9} \text{ N s/m}$  (Merkel et al., 1989),  $d_c$  is  $\sim 2 \mu\text{m}$ , and  $\eta_c$  is typically of the order of  $200 \text{ Pa s}$  (Bausch et al., 1998, submitted for publication). Therefore,  $\epsilon \approx 10^2$  and the above approximation is well fulfilled in our case. Consequently, the effective viscosity  $\gamma_0$  of the equivalent circuit is related to the friction coefficient of the coupling medium (the cytoplasm) by the obvious relation:  $b_s = \gamma_0/\pi R^2$ .

The viscosity  $\gamma_0$  obtained from the slope of the viscous flow regime of the creep response curve is  $\gamma_0 = 0.03 \text{ Pa s m}$ . By assuming that the radius of the contact area of the bead on the membrane is about equal to the bead radius ( $R = 2.25 \mu\text{m}$ ) one obtains for the friction coefficient of the cytoplasm a value of  $b_s \approx 2 \cdot 10^9 \text{ Pa s/m}$ . By assuming  $d_c \approx 2 \mu\text{m}$  our estimation yields  $\eta_c \approx 4 \cdot 10^3 \text{ Pa s}$ .

## DISCUSSION

The magnetic bead rheometer designed in the present work allows generation of forces in the nanonewton range, which are strong enough to enable local measurements of viscoelastic parameters of cell envelopes (comprising the lipid/protein bilayer and the associated actin cortex). By application of the high-resolution particle tracking technique bead deflections may be measured with at least 10 nm lateral resolution and a time resolution of 0.04 s. The viscoelastic response is linear at least up to forces of 2000 pN, corresponding to maximum displacement amplitudes of 1  $\mu\text{m}$ . Most measurements, with the exception of some of the displacement field experiments, were performed at 500–1000 pN, corresponding to displacements of 250–500 nm.

The creep response curves of the cells are analyzed in terms of the equivalent circuit because this model can be most easily adapted to the observed creep response curves in a model-free manner. The relationships between the viscoelastic parameters of the equivalent circuit and the viscoelastic moduli of the cell surface are, however, model-dependent and it is therefore most convenient to analyze measurements first in terms of the equivalent circuit.

Our displacement field mapping experiments show that the elastic displacement of the cell surface generated by local tangential forces is screened at lateral distances of a few micrometers from the point of attack. Strong screening of the elastic deformation has also been established recently in the cytoplasm by similar displacement field mapping experiments (Bausch et al., 1998, submitted for publication; unpublished data of this laboratory). This screening of the elastic deformation of the membrane and the cytoskeleton is an important condition for the local measurement of viscoelastic parameters on cell surfaces. However, local measurements are important for at least two reasons. First, they allow the study of viscoelastic properties of closed shells by restricting to the analysis of local deformations. Second, cell envelopes generally exhibit heterogeneous lateral organizations, and the elastic deformation may also be anisotropic due to coupling of various cytoskeletal elements including stress fibers to the actin cortex.

The absolute values for the shear modulus and the viscosity obtained by modeling the cell lobe as two elastic sheets coupled by a viscoelastic gel are certainly rough estimates. However, the values agree rather well with data obtained by other techniques. In our study an average 3D shear modulus of  $\mu \approx 2 \cdot 10^4$  to  $4 \cdot 10^4$  Pa is obtained. This value is in acceptable agreement with the AFM measurements. Thus, AFM measurements performed on human platelets by Radmacher et al. (1996) yield bulk moduli of 1–50 kPa, while in chicken cardiocytes the elastic moduli range from 10 to 200 kPa. The latter value is measured on top of stress fibers (Hofmann et al., 1997).

Our results are in contrast to findings of Wang et al. (1993), who used a twisting rheometer to measure the viscoelastic properties of bovine capillary endothelial cells. Apparent Young's moduli of  $\sim 8$  Pa and viscosities of 5–10

Pas were obtained, about four orders of magnitude smaller than our values. The discrepancy may be due to the way the deformation is applied: we apply a real shear force, whereas in the experiments of Wang et al. (1993) a twisting force is applied. This also makes it difficult to compare the absolute values of the applied stresses. Assuming an approximate radius of the adhesion area of the bead of 1–2.25  $\mu\text{m}$ , we estimate applied stresses of  $\sim 300$ – $60 \text{ Nm}^{-2}$ , while in the measurements of Wang et al. the stresses are only  $3 \text{ Nm}^{-2}$ . In separate experiments we found that application of such small forces leads to detectable deflections only if the beads are attached to the extracellular matrix. Furthermore, the strain hardening reported by these authors could not be reproduced in our studies. As can be seen in Fig. 10, saturation effects were observed only for forces exceeding 2000 pN.

Our analysis yields an average value for the cytoplasmic viscosity of  $2 \cdot 10^3$  Pa s. Sato et al. (1984) found for the cytoplasmic viscosity of the axoplasm of squid axon a value of  $10^4$ – $10^5$  Pa s, while Valberg and Butler (1987) and Valberg and Feldman (1987) using twisting rheometry have found values ranging from 250 to 2800 Pa s inside macrophages, in good agreement with our results.

The viscosity obtained by our method should be compared with the value measured by the micropipette aspiration technique developed by Evans (1995) which was applied by Tsai et al. to human neutrophils (1994). In this case the viscosity is obtained from the speed of penetration of the cell into the pipette at a constant suction pressure. Typical values found are of the order of 100 Pa s, which are an order of magnitude smaller than our value. This may be due to the fact that our measurements are done on the rather flat advancing lobe of the fibroblast, which may exhibit a much higher viscosity than the whole cell body of blood cells.

It should be also noted that the origin of the viscous flow regime is not understood yet. In the framework of the present model it would be determined by the rate of decoupling (fracture) of the connections between the membrane-associated actin cortex and the intracellular cytoskeleton. It could, however, be determined equally well by the fracture of lateral cross-links within the actin cortex. A decision between these two possibilities cannot be made on the basis of the present experiments.

An intriguing finding of the current analysis is that the displacement field seems to be anisotropic, as is demonstrated by the large deviations of the direction of deflection of the colloidal probes from the direction of an isotropic displacement field. This may be a consequence of the coupling of the actin cortex to local stress fibers. By improving the technique of selective coupling of smaller probe beads to membrane receptors, the displacement field mapping technique could probe local elastic anisotropies of the plasma membrane and the underlying cytoskeleton.

The magnetic bead technique provides a versatile tool for cell rheometry. By deposition of several beads it allows simultaneous measurements at different sites on the cell surface (cf. Fig. 3 a). The technique can be simultaneously

applied to the cell surface and the cytoplasm. As it is essentially a nonperturbing technique creep, response curves can be recorded repeatedly. This allows detection of temporal changes of the local viscoelasticity. It may thus also be applied to evaluate local changes of the cytoskeletal structure (e.g., the formation of stress fibers) caused by local mechanical agitations or by the binding of integrins. Such local modifications of the cytoskeleton were recently reported for endothelial cells by Chicurel et al. (1998). Evidence was provided that coupling of colloidal beads to integrins leads to a local reorganization of the actin cortex, resulting in an increase of the messenger RNA concentration near the focal adhesion site 20 min after integrin binding.

The above considerations suggest that magnetic bead rheometry is a promising new technique to gain insight into such biochemically induced changes of the local constitution of the cell cytoskeleton.

**APPENDIX**

**Elastic deformations of juxtaposed coupled membranes by local tangential force**

The cell membrane, consisting of the lipid bilayer attached to the actin cortex, is represented by a thin elastic plate supported by a viscoelastic substrate. The lobe shape makes it possible to assume that its top membrane is flat. The bottom membrane is considered as rigid and fixed to the solid substrate. A basic assumption of the present model is that the actin cortex is coupled to the bulk cytoskeleton consisting of microtubules, intermediate, and actin filaments. To consider the effect of this gel on the membrane deformation we adopt the simplified mechanical model of the cell lobe displayed in Fig. 11. The bulk cytoskeleton is assumed to consist of pre-stressed and unstressed compartments. The former consist of the stress fibers, which either penetrate the whole thickness of the lobe connecting the top and the bottom membranes (cf. Fig. 11, *b* and *c*; filaments numbered 1), or connect the top membrane to a stressed region of the network, which is attached to the bottom membrane by another stress fiber (cf. Fig. 11, *b* and *c*; fibers marked by number 2). Assume that the lobe possesses  $n_{st}$  such stress fibers per unit area and that they exhibit an average tension  $T$ . Besides the pre-stressed fibers, the bulk cytoskeleton

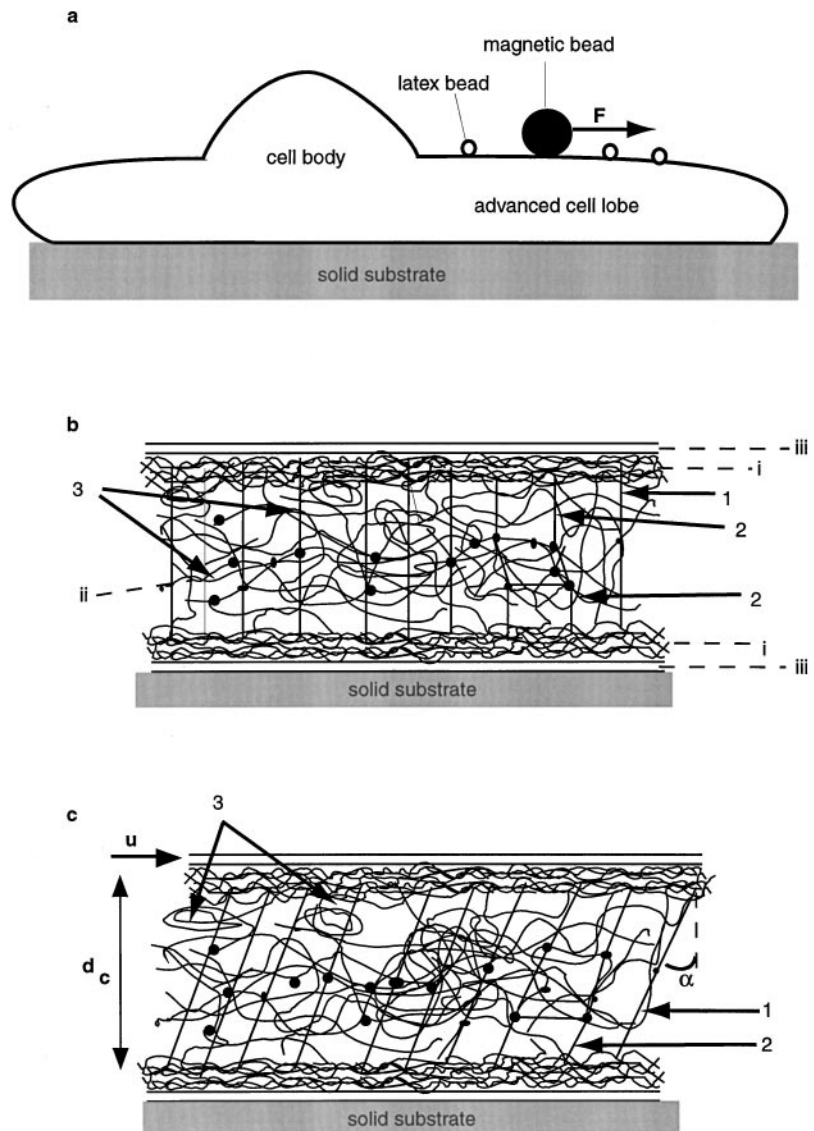


FIGURE 11 Schematic view of the mechanical model of the cell lobe. (a) General view of the mouse fibroblast. The numbers indicate (1) the solid substrate, (2) the cell body, (3) the advanced cell lobe, (4) the non-magnetic, and (5) the magnetic beads coupled to the top membrane of the lobe. (b) Schematic view of the structure of the undeformed lobe. (i) Actin cortexes of the top and the bottom membranes, (ii) bulk cytoskeleton, (iii) lipid bilayers, (iiii) solid substrate. The Arabic numbers indicate (1) the stress fibers penetrating through the whole lobe, (2) stress fibers connected with the pre-stressed parts of the bulk cytoskeleton, and (3) unstressed components of the cytoskeleton connected with the actin cortex. (c) Shear displacement of the complex membrane/actin cortex causes tilting of the stressed fibers by the angle  $\alpha \approx u/d_c$  and stretching of those unstressed parts of the cytoskeleton that are cross-linked to the actin cortex.

may contain unstressed parts of the network coupled to the actin cortex (cf. Fig. 11, *b* and *c*; fibers number 3). An in-plane displacement of the cortex  $\mathbf{u} = (u_x, u_y)$  is followed by tilting of the stress fibers in the pre-stressed parts of the cytoskeleton. It causes bending of the stiff microtubules and intermediate filaments and stretching of wrinkles and meshes of the unstressed parts of the cytoskeleton. Therefore, the unstressed parts of the cytoskeleton can be characterized by the number density  $n_{un}$  of attachments of these components to the actin cortex and by an average spring constant  $k_{un}$ . Under a lateral membrane displacement  $u$  both mechanisms give rise to a restoring force  $|\mathbf{F}_{rest}| = S(Tn_{st} \tan \alpha + k_{un}n_{un}|u|)$ , where  $S$  is the membrane area. The first term describes the contribution of the pre-stressed and the second of the unstressed cytoskeletal components. Making use of the relation  $\tan \alpha \approx u/H$  one finds

$$\mathbf{F}_{rest} = -S \left( \frac{Tn_{st}}{d_c} + k_{un}n_{un} \right) \mathbf{u} \quad (\text{A1})$$

One defines the coupling constant  $\chi$  as  $\mathbf{F}_{rest} = -S\chi\mathbf{u}$  where

$$\chi = k_{un}n_{un} + \frac{Tn_{st}}{d_c} \quad (\text{A2})$$

In a real cell the mechanism of formation of the restoring force can be more complicated. Therefore, one should consider  $\chi$  as a phenomenological parameter that has the dimension of a spring constant per unit membrane area.

The displacement field generated by a local tangential force on the top membrane has been calculated by Boulbitch (1998, submitted for publication) and the theory is summarized below.

The equation of the mechanical equilibrium of a 3D body is well-known (Landau and Lifshitz, 1959). To transform it to the case of a thin plate, an averaging procedure (over the direction perpendicular to the plane) has to be performed (Muschelishvili, 1963). This allows expression of the equation of equilibrium in terms of a membrane shear modulus  $\mu^*$  obtained by integrating the shear modulus over the membrane thickness  $h$ :  $\mu^* = \mu h$ . Taking into account the restoring force mentioned above, one obtains the following equation of the mechanical equilibrium of the composite membrane:

$$\Delta \mathbf{u} + \frac{1 + \sigma}{1 - \sigma} \text{grad div } \mathbf{u} - \kappa^2 \mathbf{u} = -\frac{\mathbf{F}}{\mu^*} \quad (\text{A3})$$

where  $\kappa^2 = \chi/\mu^*$ . Here  $\kappa^{-1}$  is a length scale. As will become evident below,  $R_c = \kappa^{-1} = (\mu^*/\chi)^{1/2}$  is a cutoff radius that accounts for the screening of the displacement field by the cytoskeleton. By considering Eq. A2 one obtains

$$R_c = \left( \frac{\mu^* d_c}{k_{un} n_{un} d_c + T n_{st}} \right)^{1/2} \quad (\text{A4})$$

In the case of a thin lobe ( $d_c \ll T/k_{un}$ ) one finds  $R_c \approx (d_c \mu^*/T n_{st})^{1/2}$ . In the opposite case  $R_c \approx (\mu^*/k_{un} n_{un})^{1/2}$ .

If the cutoff radius is much larger than the radius of the magnetic bead  $R$  ( $R_c \gg R$ ) one can assume that the force is point like  $\mathbf{F} = F_0 \delta(\mathbf{r})$  where  $F_0$  is the absolute value of the force acting on the magnetic bead along the  $x$  axis. The displacement field for the local tangential force is given by the following expressions:

$$u_x(\mathbf{r}) = \frac{F_0}{2\pi\mu^*} \left\{ \frac{1}{2} K_0(\kappa r) + \frac{1 - \sigma}{2} K_0(\kappa_1 r) - \cos 2\theta \left[ \frac{K_1(\kappa r)}{\kappa r} - \sqrt{\frac{1 - \sigma}{2}} \frac{K_1(\kappa_1 r)}{\kappa r} + \frac{1}{2} K_0(\kappa r) - \frac{1 - \sigma}{4} K_0(\kappa_1 r) \right] \right\} \quad (\text{A5})$$

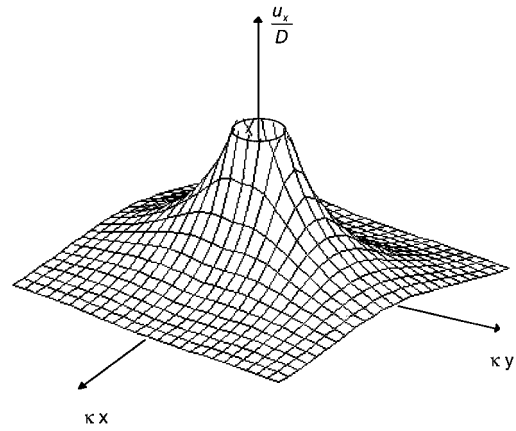


FIGURE 12 Dependence of the displacement vector component  $u_x(\mathbf{r})$  on coordinates as described by Eq. A5. The normalizing factor is  $D = 4\pi\mu^*/F_0$ .

$$u_y(\mathbf{r}) = -\frac{F_0 \sin 2\theta}{2\pi\mu^*} \left\{ \frac{K_1(\kappa r)}{\kappa r} - \sqrt{\frac{1 - \sigma}{2}} \frac{K_1(\kappa_1 r)}{\kappa r} + \frac{1}{2} K_0(\kappa r) - \frac{1 - \sigma}{4} K_0(\kappa_1 r) \right\} \quad (\text{A6})$$

where  $K_0$  and  $K_1$  are modified Bessel functions of the second kind (and order zero and one, respectively) and  $\kappa_1 = [(1 - \sigma)/2]^{1/2} \kappa$ . Note that for the limiting case  $R \rightarrow \infty$  the equations (A5–A6) describe the elastic deformation of a single thin plate, the displacement field exhibiting the well-known logarithmic behavior usual for the flat theory of elasticity (Muschelishvili, 1963). The component  $u_x$  of the displacement as a function of coordinates is shown in Fig. 12.

The displacement components can be expressed in cylindrical coordinates. Introducing the unit vector  $\mathbf{n} = (\cos \theta, \sin \theta)$  directed along the radius-vector  $\mathbf{r}$  the radial component of the displacement vector  $\mathbf{u}$ :  $u_r = (\mathbf{u} \cdot \mathbf{n})$  is given by

$$u_r(\mathbf{r}) = \frac{F_0}{2\pi\mu^*} \cos \theta \left\{ \frac{3(1 - \sigma)}{4} K_0(\kappa_1 r) - \frac{K_1(\kappa r)}{\kappa r} + \sqrt{\frac{1 - \sigma}{2}} \frac{K_1(\kappa_1 r)}{\kappa r} \right\} \quad (\text{A7})$$

which gives Eq. 2 above.

The authors thank G. Marriot (Max-Planck-Institut für Zellbiologie, Martinsried, Germany) for providing the National Institutes of Health 3T3 murine fibroblasts.

This work was supported by the Deutsche Forschungsgemeinschaft (Sa 246/22-3) and the Fonds der Chemischen Industrie.

## REFERENCES

- Chicurel, M. E., R. H. Singer, C. J. Meyer, and D. E. Ingber. 1998. Integrin binding and mechanical tension induce movement of mRNA and ribosomes to focal adhesions. *Nature*. 392:730–733.
- Choquet, D., D. P. Felsenfeld, and M. P. Sheetz. 1997. Extracellular matrix rigidity causes strengthening of integrin-cytoskeleton linkages. *Cell*. 88:39–48.

- Evans, E. 1995. Physical action in biological adhesion. In Handbook of biological Physics, Vol 1. R. Lipowsky and E. Sackmann, editors. Elsevier, Amsterdam.
- Evans, E., and E. Sackmann. 1988. Translational and rotational drag coefficients for a disk moving in a liquid membrane associated with a rigid substrate. *J. Fluid Mech.* 194:553–561.
- Forgacs, G. 1996. Biological specificity and measurable physical properties of cell surface receptors and their possible role in signal transduction through the cytoskeleton. *Biochem. Cell Biol.* 73:317–326.
- Fung, Y. C. 1993. Biomechanics: Mechanical Properties of Living Tissues. Springer Verlag, New York.
- Hofmann, U. G., C. Rotsch, W. J. Parak, and M. Radmacher. 1997. Investigating the cytoskeleton of chicken cardiocytes with the atomic force microscope. *J. Struct. Biol.* 119:84–91.
- Ingber, D. E. 1997. Tensegrity: the architectural basis of cellular mechanotransduction. *Annu. Rev. Physiol.* 59:575–599.
- Landau, L. D., and E. M. Lifshitz. 1959. Theory of Elasticity. Pergamon Press, Oxford.
- Merkel, R., E. Sackmann, and E. Evans. 1989. Molecular friction and epitactic coupling between monolayers in supported bilayers. *J. Phys. France.* 50:1535–1555.
- Miyamoto, S., S. K. Akiyama, and K. M. Yamada. 1995. Synergistic roles for receptor occupancy and aggregation in integrin transmembrane function. *Science.* 267:883–885.
- Muschelishvili, N. J. 1963. Some Basic Problems of the Mathematical Theory of Elasticity. Noordhoff Verlag, Groningen.
- Pasternak, C., S. Wong, and E. L. Elson. 1995. Mechanical function of dystrophin in muscle cells. *J. Cell Biol.* 128:355–361.
- Radmacher, M., M. Fritz, C. M. Kacher, J. P. Cleveland, and P. K. Hansma. 1996. Measuring the viscoelastic properties of human platelets with the atomic force microscope. *Biophys. J.* 70:556–567.
- Sato, M., T. Z. Wong, D. T. Brown, and R. D. Allen. 1984. Rheological properties of living cytoplasm: a. Preliminary investigation of squid axoplasm (*Loligo pealei*). *Cell Motil.* 4:7–23.
- Schmidt, F. G., F. Ziemann, and E. Sackmann. 1996. Shear field mapping in actin networks by using magnetic tweezers. *Eur. Biophys. J.* 24: 348–353.
- Simson, R., E. Wallraff, J. Faix, J. Niewöhner, G. Gerisch, and E. Sackmann. 1998. Membrane bending modulus and adhesion energy of wild-type and mutant cells of *Dictyostelium* lacking talin or cortexillins. *Biophys. J.* 74:514–522.
- Tsai, M. A., R. S. Frank, and R. E. Waugh. 1994. Passive mechanical behavior of human neutrophils: effect of cytochalasin B. *Biophys. J.* 66:2166–2172.
- Valberg, P. A., and J. P. Butler. 1987. Magnetic particle motions within living cells. Physical theory and techniques. *Biophys. J.* 52:537–550.
- Valberg, P. A., and H. A. Feldman. 1987. Magnetic particle motions within living cells. Measurement of cytoplasmic viscosity and motile assay. *Biophys. J.* 52:551–69.
- Wang, N., J. P. Butler, and D. E. Ingber. 1993. Mechanotransduction across the cell surface and through the cytoskeleton. *Science.* 260: 1124–1127.
- Zhelev, D. V., D. Needham, and R. M. Hochmuth. 1994. Role of the membrane cortex in neutrophil deformation in small pipettes. *Biophys. J.* 67:696–705.
- Ziemann, F., J. Rädler, and E. Sackmann. 1994. Local measurements of viscoelastic moduli of entangled actin networks using an oscillating magnetic bead microrheometer. *Biophys. J.* 66:2210–2216.

## Three-Dimensional Cellular Deformation Analysis with a Two-Photon Magnetic Manipulator Workstation

Hayden Huang,\* Chen Y. Dong,\* Hyuk-Sang Kwon,\* Jason D. Sutin,<sup>†</sup> Roger D. Kamm,\* and Peter T. C. So\*

\*Department of Mechanical Engineering, MIT, Cambridge, Massachusetts 02139; and <sup>†</sup>University of Illinois, Urbana-Champaign, Illinois 61801 USA

**ABSTRACT** The ability to apply quantifiable mechanical stresses at the microscopic scale is critical for studying cellular responses to mechanical forces. This necessitates the use of force transducers that can apply precisely controlled forces to cells while monitoring the responses noninvasively. This paper describes the development of a micromanipulation workstation integrating two-photon, three-dimensional imaging with a high-force, uniform-gradient magnetic manipulator. The uniform-gradient magnetic field applies nearly uniform forces to a large cell population, permitting statistical quantification of select molecular responses to mechanical stresses. The magnetic transducer design is capable of exerting over 200 pN of force on 4.5- $\mu\text{m}$ -diameter paramagnetic particles and over 800 pN on 5.0- $\mu\text{m}$  ferromagnetic particles. These forces vary within  $\pm 10\%$  over an area  $500 \times 500 \mu\text{m}^2$ . The compatibility with the use of high numerical aperture ( $\approx 1.0$ ) objectives is an integral part of the workstation design allowing submicron-resolution, three-dimensional, two-photon imaging. Three-dimensional analyses of cellular deformation under localized mechanical strain are reported. These measurements indicate that the response of cells to large focal stresses may contain three-dimensional global deformations and show the suitability of this workstation to further studying cellular response to mechanical stresses.

### INTRODUCTION

How cells respond to mechanical stresses is relevant in many physiological systems, including bone remodeling and cardiovascular disease (Burger and Klein-Nulend, 1998; Malek and Izumo, 1995). Despite this importance, little is known about the general nature of the responses by cells to a given stress. Recent studies have characterized some of the responses of cells to mechanical stimuli, including determining local viscoelastic parameters (Bausch et al., 1998), studying mechanosensitive ion channel activation (Hu and Sachs, 1997; Sackin, 1995), and gene induction (Chaour et al., 1999; Chiu et al., 1999; Khachigian et al., 1997), and considering cell geometry changes, for example, via focal adhesion shifting (Davies et al., 1994; Girard and Nerem, 1995; Kanda et al., 1993). Studies such as these indicate that the effects of mechanical forces are important in modeling cellular responses in many biomedical systems.

Typically, global stresses are applied uniformly over a large number of cells, either by fluid shear stress or by some form of membrane stretching (Brown et al., 1998). These techniques are not suitable, however, for studying individual cells or probing local cell membrane and cytoskeletal mechanics. Individual cell assays allow the determination of the statistical distribution in cell responses, in addition to the average value derived from assays using large populations. For example, a Northern blot combines the responses of several thousands to millions of cells to obtain a single

readout. Using an individual cell assay provides a clearer idea of the nature of the response, differentiating between small global changes and drastic local changes (Brown et al., 1998; Davies, 1995; Davies et al., 1999).

Some techniques are available to examine the mechanical response of single cells. Pipetting technologies are used to locally deform cells, typically blood cells, to probe the membrane stiffness, and characterize the cells as they traverse narrow channels (Mow et al., 1994). Atomic force microscopy and optical traps are used to probe cellular and subcellular forces, such as those of kinesin motors (Block et al., 1990; Kuo and Sheetz, 1993). Magnetic traps with one pole (unipolar) can generate nanoNewton levels of force on beads attached to cells and have been used to probe the properties of cell membranes (Bausch et al., 1998). These techniques have limitations, such as low force generation (optical traps), the small number of cells that can be assayed at once, and the need to place cells carefully to assay them suspended for micropipette aspiration, or positioned with submicron precision to regulate the applied force in unipolar magnetic traps.

The generation of a uniform stress field based on a magnetic trap with multiple poles was first reported in 1996 (Amblard et al., 1996). Traps based on this design can generate a force with a small variance over a relatively large area, depending on the specific trap parameters. However, two major limitations in this type of trap are that the trap cannot typically exert much force, usually on the order of 10 pN per bead, and the tight trap geometry precludes the use of short-working-distance high-numerical-aperture objectives for high-resolution microscopy imaging. This paper presents the design of a two-photon micromanipulation workstation featuring a novel magnetic trap that can exert several hundred picoNewtons of force on micromagnetic

*Submitted June 14, 2001, and accepted for publication January 14, 2002.*

Address reprint requests to Dr. Peter So, Department of Mechanical Engineering, 77 Massachusetts Avenue, Rm 3-461A, Cambridge, MA 02139. Tel.: 617-253-6552; Fax: 617-258-9346; E-mail: ptso@mit.edu.

© 2002 by the Biophysical Society

0006-3495/02/04/2211/13 \$2.00

beads. The unique design of the trap, guided by electromagnetic finite-element simulations, optimizes the field magnitude while maintaining a uniform field gradient. The geometry of the trap accommodates a high numerical aperture microscope objective so that continuous, three-dimensional fluorescence images of the sample being stressed can be acquired before, during, and after the application of the force. This combination of the magnetic manipulator and imaging technology into a cell-mechanics workstation can be used to study the mechanical properties of cells, as well as a wide range of molecular responses based on different fluorescence reporters, such as those of ion channel activation, genetic induction, or cell migration. Further, by changing the surface proteins on the micromagnetic beads attached to the cells, specific membrane proteins can be targeted to examine certain receptor functions. In this study, the design of the magnetic trap/two-photon workstation is presented. The suitability of this workstation for studying cellular deformation is demonstrated by gauging the local versus global responses of the cells, with an emphasis on the three-dimensional, long-term (minutes) deformation patterns.

## MATERIALS AND METHODS

### Magnetic trap design

The design of the magnetic trap had to satisfy the following requirements. Geometrically, the trap has to fit on the stage of a two-photon microscope, while allowing the objective to move to within the working distance of the sample. The field exerted by the trap should result in a nearly uniform field gradient in a sample region large enough to contain many tens to hundreds of cells. The magnitude and direction of the force need to be adjustable, and the trap could not heat to the extent that cells die with a few minutes of exposure. The trap was developed to satisfy these requirements while maximizing the force that would be generated on a given micromagnetic bead.

Magnetic transducers exert forces on paramagnetic or ferromagnetic objects. Ferromagnetic materials have a permanent magnetic dipole moment and will experience a force in the presence of an external magnetic field gradient:

$$F = \frac{1}{2} \mu_0 \nabla (m \times H),$$

in which  $\mu_0$  is the permeability constant,  $m$  is the magnetization of the particle which is assumed to be uniform, and  $H$  is the external magnetic field strength. Although higher forces are typically generated with ferromagnetic particles due to their higher magnetization volume, they are more difficult to manipulate because these particles aggregate once magnetized. For some applications, super-paramagnetic beads can be applied more conveniently. By definition, super-paramagnetic systems lose their magnetization once the external field is removed. The typical magnetic susceptibility of these particles is on the order of unity in SI units. The force exerted on a super-paramagnetic particle is:

$$F = \mu_0 \chi V \nabla (H \times H),$$

in which  $\chi$  is the volume susceptibility and  $V$  is the bead volume. The applied force increases with increasing field strength and increasing field

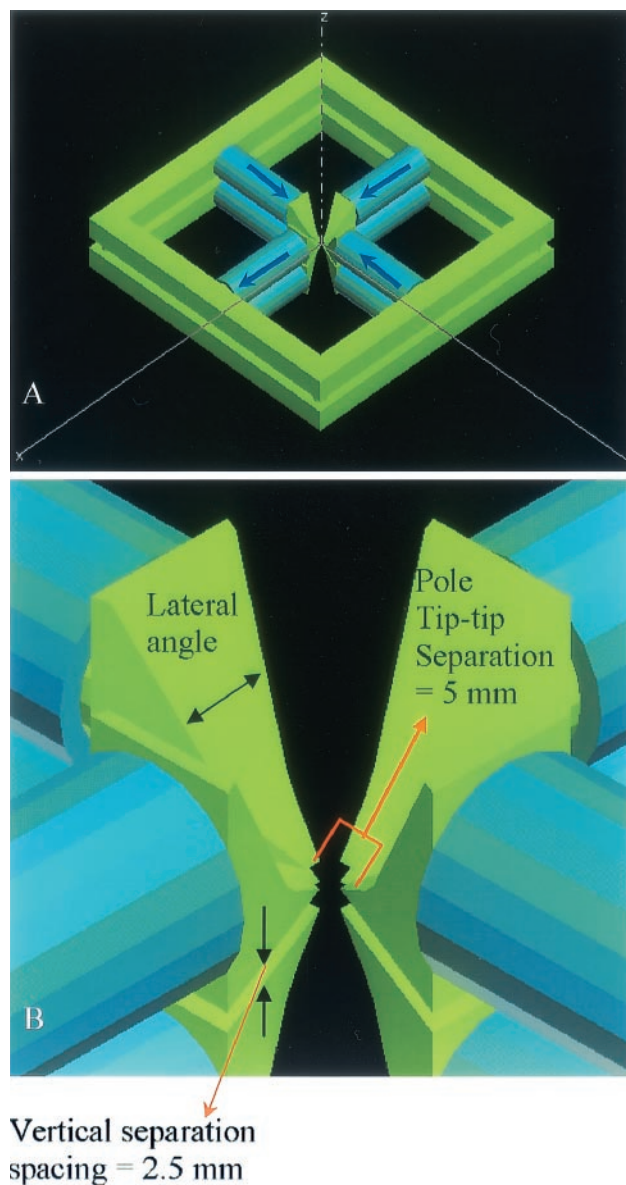


FIGURE 1 Schematic of the quadropole. (A) The backiron is the square iron connecting the four poles together. The tips converge to the center of the trap where the sample is placed. The two quadpoles are placed in a mirror image configuration with a 2.5-mm separation between them at the tips. The blue arrows indicate the direction of the magnetic flux along the poles. There are three flows into the sample region and one flow out. All currents are at the same magnitude for force generation. (B) Tip shape was primarily designed to fit a microscope objective. Other factors such as stability were also taken into account for the lateral dimensions.

gradient, up to the saturation of the transducer material in the ferromagnetic case and both the transducer and magnetic beads in the paramagnetic case.

The basic trap design for this study follows the work of Amblard et al. (1996) (Fig. 1). Enhancements to the design were guided in part by the electromagnetic simulation program Maxwell, from Ansoft (Pittsburgh, PA). This design consists of eight electromagnets (poles). Each pole is wrapped 550 times with a No. 24 gauge copper wire, turning the pole into an electromagnet. The pole material is CMI-C steel, which has a relatively high permeability and saturation. Whereas it is possible to use materials of

higher permeability and saturation (e.g., Hiperc 50), simulations indicated that for the intended current levels of a few amperes, there is no significant difference in field strength or gradient. The force levels are higher for higher saturation level materials at large currents, but at those currents the magnetic trap will quickly heat to temperatures inimical to cell function without active cooling. Active cooling was not implemented at this time, to minimize mechanical perturbations to the specimen. Further, permanent magnets were not used because they offer no easy way of precisely controlling or producing time-dependent variations in the force.

In the design presented in this study, the pole pieces are arranged in two  $x$ - $y$  planes with four pole pieces each. The four in-plane pole pieces are set along the  $x$  and  $y$  axes, with the tips pointing toward the origin, where the specimen will be placed (Fig. 1 A). This location is denoted the sample region. This set of four poles forms a magnetic quadrupole. Finite element simulation indicates that to use the field as efficiently as possible, the magnetic flux circuit must be completed. Thus, a backiron made from CMI-C rod was used to connect each set of four poles. The magnetic field in the sample region was compared for three possibilities: a magnetic trap with no backiron, with a backiron, and finally with triple-length poles and no backiron (to test the contribution of the extra material in the backiron). The mean field strength was significantly higher for the trap with a backiron arrangement (for field strength, 50%–100% higher than the triple length polar trap and >300% higher than the configuration without a backiron).

By altering the currents through these coils, the field can be changed, giving control of the force levels and directions. Instead of using four pair-wise linked poles similar to Amblard's design, the use of eight individual poles (the "octopolar" configuration) allows more flexible control over the field structure. This permits vertical force generation (force perpendicular to the microscope stage) as well as horizontal force in any planar direction. The generation of a planar field gradient and force used in these studies is achieved by directing the magnetic flux away from the center of the trap along one pair of poles and toward the center along the other three pairs.

Simulations indicated that pole tip spacing plays an important role in maximizing trap force level. The spacing between the tips of the poles for a quadrupole was chosen to be the smallest possible, given certain constraints, to minimize field deterioration. This spacing was set at a distance of 5 mm, which still accommodates water immersion objectives with long working distances (for example, the Achromat 63 $\times$ , 0.9 NA, 1.5-mm working distance or Achromat 100 $\times$ , 1.0 NA, 1.0-mm working distance, Zeiss, Thornwood, NY). The distance between the two quadrupoles was set to bring the tips 2.5 mm apart vertically. This distance was chosen partially to permit the insertion of the sample and partially based on finite-element analysis of a simplified model that indicated that a ratio of 1:2 of vertical-separation:pole-tip-separation would result in losses of field strength of ~10% to 15% (from the maximum in the plane of the tip), but that a separation of 1:1 would result in more severe losses of up to 40% to 50%. The vertical geometry of the tip was designed to fit the objective body, whereas the lateral angle was designed for stability (Fig. 1 B). Two lateral angles were tested, 50° and 90°, and the field strength did not change between these two angles when the tip-to-tip separation was kept constant. However, a 90° tip would be extremely short and thin, so the 50° tip was used in the design.

Finally, the trap was designed to be as large as possible (24 cm on a side) to maximize the field that could be generated. Although a significantly larger trap may produce a slightly higher field and generate more force, the loss of stability resulting from being larger than the microscope stage would be undesirable. Additionally, the simulations show that the trap poles are saturated in the tip and midpole regions, and thus increasing the size will lead to diminishing returns in increased force.

## Calibration and characterization of the trap

To gauge the ability of the trap to produce a horizontal linear force, a calibration was performed at various current levels. Each pole is driven by

current of the same amplitude, but the directions of the currents are different to produce the appropriate flux directions as specified in Fig. 1 A. This creates the necessary field gradient to generate a force.

Paramagnetic microspheres, 4.5- $\mu$ m diameter from Dynal (Oslo, Norway), were used to perform the calibration. A bead is placed into a chambered gasket (Coverwell, Molecular Probes, Eugene, OR) with an aqueous solution of 80% sucrose, having a viscosity of 100 centistokes. The trap was turned on, and the steady-state velocity of the bead was measured using a custom particle-tracking program. Using Stokes' formula for low Reynolds numbers flow, it is possible to calculate the corresponding force on the beads. Briefly, Stokes' formula states that

$$F = 3\pi\mu VD,$$

in which  $\mu$  is the dynamic viscosity of the fluid,  $V$  is the velocity of the bead at steady state, and  $D$  is the diameter of the bead. Reynolds number is given by

$$Re = \frac{VD}{\nu},$$

in which  $\nu$  is the kinematic viscosity. For our calibrations, the maximal velocity is 0.01 m/s with a bead diameter of 4.5  $\mu$ m and a kinematic viscosity of  $10^{-4}$  m<sup>2</sup>/s. Thus, the maximal Reynolds number for our experiment is  $4.5 \times 10^{-4} \ll 1$ , so Stokes' formula applies. Similar experiments were performed using ferromagnetic microspheres (graciously donated by Dr. Ben Fabry, Harvard University, Cambridge, MA).

To measure magnetic field uniformity, the magnetic field distribution in the trap was measured using a direct current magnetometer (Alpha Lab Inc., Salt Lake City, UT) with a miniature Hall probe. The active area of the Hall probe has dimensions of 3 mm  $\times$  2.5 mm and a thickness of 0.7 mm. Because the sample space in the trap is only ~5 mm  $\times$  5 mm  $\times$  2.5 mm, the small size of the probe is critical. The measured field distribution is the actual field distribution convoluted by the probe active area. These measurements should be a reasonable representation of the actual field distribution, because the field distribution inside the sample space of the trap varies gradually (as observed in scaled models of the current trap and in the results of the Maxwell simulation).

## Two-photon microscope

The instrumentation and design of a basic multiphoton microscope has been described in several previous publications (So et al., 1995, 1998). Briefly, the multiphoton excitation microscope design is based on a mode-locked Titanium-Sapphire laser (Mira 900, Coherent Inc., Palo Alto, CA). A Glan-Thomson polarizer is used to control the excitation power. The beam expanded laser light is directed into the microscope via a galvanometer-driven  $x$ - $y$  scanner (Cambridge Technology, Watertown, MA). Images are generated by raster scanning the  $x$ - $y$  mirrors. The excitation light enters the Zeiss Axiovert microscope (Zeiss Inc., Thornwood, NY) via a modified epilluminescence light path. The scan lens is positioned such that the  $x$ - $y$  scanner is at its eye-point, whereas the field aperture plane is at its focal point. Because the objectives are infinity corrected, a tube lens is positioned to recollimate the excitation light. The scan lens and the tube lens function together as a beam expander that over fills the back aperture of the objective lens. The dichroic reflects the excitation light to the objective. The dichroic mirrors are custom-made short pass filters (Chroma Technology Inc., Brattleboro, VT) that maximize reflection in the infrared and transmission in the blue-green region of the spectrum. Typical image sizes range from 40 to 200  $\mu$ m on a side. The objective axial position is driven by a piezo-motor interfaced to a computer. The typical image acquisition time is ~2 s for a single  $x$ - $y$  plane.

The fluorescence emission is collected by the same objective and transmitted through the dichroic mirror along the emission path. An additional barrier filter is used to further attenuate the scattered excitation light

because of the high excitation intensity. Because two-photon excitation has the advantage that the excitation and emission wavelengths are well separated (by 300–400 nm), short pass filters such as 2 mm of the BG39 Schott glass filter (CVI Laser, Livermore, CA) eliminate most of the residual scatter with a minimal attenuation of the fluorescence. A descann lens is inserted between the tube lens and the photomultiplier tube (PMT) to recollimate the excitation and to ensure that the emission light strikes the photomultiplier tube at the same position, independent of scanner motion. The fluorescence signal at each pixel is detected by a R7400-P photomultiplier tube (Hamamatsu, Bridgewater, NJ), which is a compact single photon counting module with high quantum efficiency.

## Bead protocol

Polystyrene beads, 0.5- $\mu\text{m}$  diameter, from Duke Scientific (Palo Alto, CA), were coated with human plasma fibronectin (Gibco, Rockville, MD) based on passive adsorption. All centrifugations are at  $18,000 \times g$  for 5 min at 4°C. The beads were supplied at 1% (w/v). One milliliter of the beads was pelleted by centrifugation, then washed in 1 mL of sodium phosphate buffer (pH 7.3), and pelleted again. The beads were then resuspended in 950  $\mu\text{L}$  of the sodium phosphate buffer and then transferred to a microcentrifuge tube containing 50  $\mu\text{L}$  of human plasma fibronectin (stock at 1 mg/mL) and incubated at room temperature for 3 h to overnight while being lightly agitated. The beads were then pelleted, washed once with phosphate-buffered saline, and then resuspended in 1 mL of phosphate-buffered saline for the final solution. This solution was stored at 4°C until needed, at which time it was sonicated in a bath sonicator for 10 to 30 s.

The tosylactivation protocol for fibronectin coating the magnetic beads was performed according to manufacturer's instructions. Approximately 2 to 3  $\mu\text{L}$  of the magnetic beads was used per coverslip, corresponding to approximately one million beads. Fibronectin was chosen because it forms strong bonds to cells, specifically binding the integrin units that link to the cellular cytoskeleton.

## Cell culture

Eighteen-millimeter, size 2 glass coverslips were incubated in Hanks Balanced Salt Solution (Gibco) with fibronectin at 2  $\mu\text{g}/\text{mL}$  overnight at 4°C. Human aortic smooth muscle cells were plated on fibronectin-coated coverslips at a density of 8,000 to 12,000 cells/cm<sup>2</sup>. At 1 to 3 days after plating, the cells were incubated with 1 to 5  $\mu\text{L}$  of the 0.5- $\mu\text{m}$  blue-green fluorescent diameter polystyrene beads from Duke Scientific. Cell passages between two and six were used for all experiments. After polystyrene bead loading, the cells were placed in the incubator overnight, then loaded with fibronectin coated magnetic beads for 30 min at 37°C, and placed in the magnetic trap.

For the green fluorescent protein-actin experiments, the National Institutes of Health 3T3 fibroblasts were taken from passages 5 through 10 and plated on fibronectin-coated coverslips as described for the human smooth muscle cells. Twenty-four hours after plating, the cells were transfected with a GFP-actin plasmid (kindly provided by Dr. Richard Gilbert, Massachusetts Institute of Technology, Cambridge, MA) using the lipofectin protocol according to manufacturer's instructions (Gibco). One microgram of plasmid DNA and 4  $\mu\text{L}$  of lipofectin reagent were placed in 1 mL of Opti-MEM media (Gibco) per well of a six-well plate. Cells were incubated in the transfection solution for 4 h at 37°C, and then 1 mL of Dulbecco's modified Eagle's medium with 10% fetal calf serum was added to the cells. The cells were then incubated overnight and washed the next day. Transfected cells were assayed in the following 2 or 3 days, using magnetic beads (2–3  $\mu\text{L}$ ) loaded 30 min before the experiment. One to 2  $\mu\text{L}$  of the polystyrene beads were added at the same time as the magnetic beads to the GFP-actin cells.

## Workstation usage to stress and image cells

A section of the specimen was identified that contained a cell with attached magnetic beads, and at least two polystyrene beads attached to the coverslip but not on the actual cell itself. The polystyrene beads serve as markers and are used to eliminate the residual specimen stage movement ( $\sim 100$  nm) during activation of the magnetic transducer. A three-dimensional image stack was then acquired using the two-photon microscope with a  $z$ -spacing of 0.2  $\mu\text{m}$  and a  $x$ - $y$  resolution of 512 by 512 pixels, with each pixel representing  $\sim 0.15$   $\mu\text{m}$ . This set of data is called the "before" images. The magnetic trap was then turned on, and a 1-min delay was instituted to allow the section to stabilize. The forces used in this study ranged from 50 to 120 pN. The three-dimensional stack was then recorded again, called the "after" images. Each data block took  $\sim 20$  min to complete. All images were sampled at a finer scale than diffraction limited resolutions. The image blocks were postprocessed with a blind deconvolution program (AutoDeblur, Autoquant, Watervliet, NY) to further improve image resolution.

Using the polystyrene beads as markers, any solid body displacement and rotation of the coverslip can be eliminated by matching the polystyrene beads' positions in the "before" and "after" image stacks. Then, a cross-correlation program (Insight, TSI, St. Paul, MN) was used to determine local displacements. The program takes an interrogation region, a subsection of the "before" images, 128 pixels by 128 pixels, and calculates a cross-correlation factor with respect to the "after" images. By shifting the interrogation region in the  $x$  and  $y$  directions, the cross-correlation function is obtained for all possible displacements. The  $x$  and  $y$  shifts, which maximize the cross-correlation function, corresponds to the displacement. By choosing many interrogation regions over the entire "before" picture, a map of the displacements is obtained. The images were also qualitatively analyzed for cell deformation by examining the acquired cell images.

## RESULTS

### Magnetic transducer characterization

The performance of the trap is well predicted by the finite-element model. According to the simulations, when the trap is configured to generate forces along the  $x$  direction with pole currents set at 1 A, the  $x$  component of the B field in the center of the trap is 0.17 T and has a gradient of 0.5 T/cm (Fig. 2 A). The simulation is in excellent agreement with the actual field measurement; when driving the magnet with 1A of current, the  $x$  component of the magnetic field at the center of the trap was measured to be 0.15 T at the gap center with a gradient of 0.4 T/cm. These values agree with the results of the Maxwell simulation to within 25%. The variation of the  $x$  component of the magnetic field along the  $y$  and  $z$  axes is less than 2% within 500  $\mu\text{m}$  from the trap center, and less than 10% within 1 mm of the trap center. This degree of variation is also in agreement with the Maxwell simulations. The field strengths at the four pole surfaces on the specimen plane are measured to be 0.072  $\hat{x}$  T, 0.095  $\hat{y}$  T,  $-0.095 \hat{y}$  T, and 0.25  $\hat{x}$  T. These ratios are consistent with what is expected from the basic trap design (Amblard et al., 1996). The  $y$  and  $z$  components of the magnetic field vary less than 0.025 T within 250  $\mu\text{m}$  from the trap center and less than 0.05 T within 500  $\mu\text{m}$ . This level of magnetic field and gradient corresponds to negli-

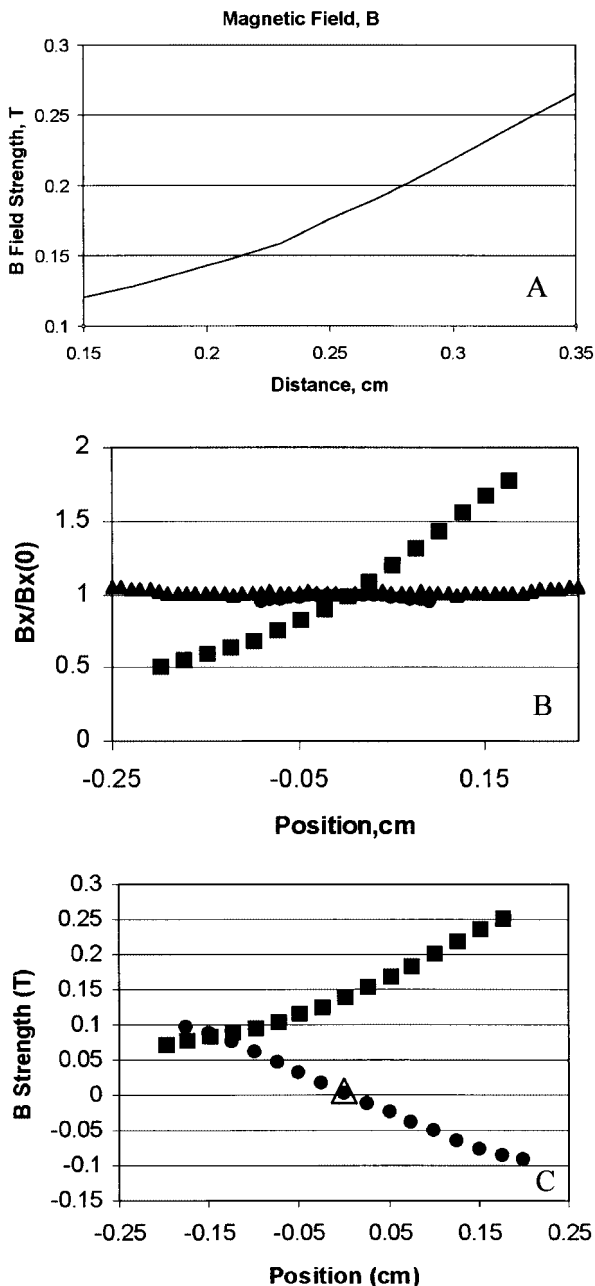


FIGURE 2 Electromagnetic simulation and Hall probe measurement results. (A) B field strength in the sample region, where 0.25 cm is the center of the trap. The field varies  $\sim 10\%$  in the center  $500 \mu\text{m}$  (0.225–0.275 cm) of the trap. The field gradient is very uniform in this region as well. (B) The  $x$  components of the magnetic field strength ( $B_x$ ) is plotted as a function of distances from the trap center along  $x$  (square),  $y$  (circle), and  $z$  (triangle) directions. The plotted field strength is normalized to the maximal value at the trap center. (C) The  $x$  components of the magnetic field strength ( $B_x$ ) is measured along  $x$  direction (square); the  $y$  components of the magnetic field strength ( $B_y$ ) is measured along  $y$  direction (circle); the  $z$  components of the magnetic field strength ( $B_z$ ) at the trap center is plotted (triangle). Due to geometric constraints of the trap,  $B_z$  can only be measured at trap center.

gible forces along the  $y$  or  $z$  directions within  $50 \mu\text{m}$  of the trap center. At a distance of  $250 \mu\text{m}$ , the force in the  $y$

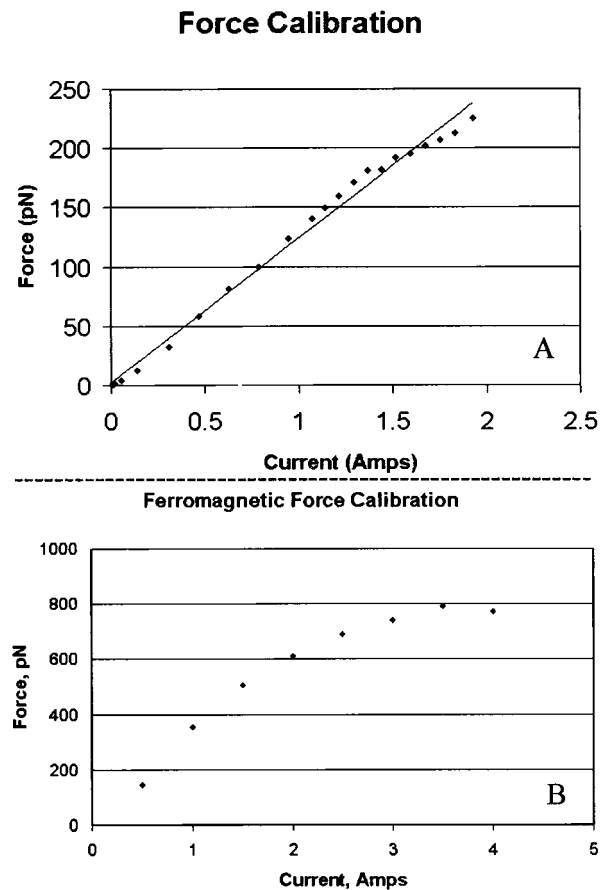


FIGURE 3 Calibration of the magnetic trap. The graphs show the calibration plots for (A) the super-paramagnetic beads and (B) for the ferromagnetic beads. The calibration in (A) also has a best fit line to illustrate the trend of the trap, and to show the effects of saturation at higher currents. These effects are clear in (B) as shown by the decrease in slope at higher currents.

direction is at most 10% of the force along  $x$  direction and increases to less than 30% at a distance of  $500 \mu\text{m}$ .

Other measurements indicate that the field gradient along the  $x$  axis is uniform and the magnitude of the field varies within  $\pm 10\%$  over a distance of  $500 \mu\text{m}$ . This is also in good agreement with the Maxwell simulation (Fig. 2 B). If a cell takes up an area of  $100 \mu\text{m}^2$ , a force that is constant to within 10% can be exerted on over 2500 cells simultaneously at full confluency. Finally, the  $y$  and  $z$  components of the magnetic field near the center of the sample section is very small in the respective  $y$  and  $z$  directions (Fig. 2 C). This indicates that there is little force in the  $y$  and  $z$  directions in the sample region.

The calibration reveals the range of forces that can be obtained using this trap. The force that can be obtained using super-paramagnetic beads is over 200 pN at 2 A driving current (Fig. 3 A). The force can be increased further using solid iron microspheres, where the force reached almost 800 pN with the application of 4 A of current (Fig.

3 *B*). The paramagnetic beads were not tested at 4 amps because saturation was evident at lower levels.

To test the suitability of the workstation to examine cells, a temperature test was performed. Under ambient conditions, the trap's temperature did not exceed 50°C at the poles and did not exceed 35°C in the sample region when the trap was operating at 100 pN for 1 h. Under forced convection conditions with a fan, the temperature at the sample region stayed at ~36° C for up to 4 h at 100 pN. Therefore, the temperature is not inimical to cell viability.

In our studies, we found that the poles developed a small but noticeable magnetization in the absence of current. Together with hysteresis effects, these changes will gradually alter trap characteristics. Although these effects are currently relatively small (on the order of a few picoNewtons), it can affect the accuracy of low force measurements. The future addition of feedback circuitry to the trap will help maintain long-term reproducibility of the force.

### Measuring cellular three-dimensional deformation under focal stresses

The workstation was used to examine the response of cells to focally applied stresses. The study of cellular mechanical responses is an active research area. However, the effect of focal stresses on the three-dimensional architecture of the cell has not been closely examined. In addition, few studies have considered the moderate-to-long-term response of cells; most studies examine only the nearly instantaneous response of the cell to applied stresses. This workstation can collect data for either time interval.

Application of 50 pN is sufficient to show deformation in the cellular structure as determined by ingested beads (Fig. 4). The cell structure shows an apparent stretching and rotation. Curiously, the stretching is almost perpendicular to the direction of the applied force. At larger forces (120 pN), the global stretching and rotation are even more evident, and the development of a large local deformation near the location of the magnetic bead becomes evident (Fig. 4). The global deformation can be quantified using a cross-correlation algorithm, which yields displacement vectors based on analysis of an interrogation region 128 by 128 pixels (Fig. 5). While the resolution of the vectors is not optimal, using this method allows the generation of a displacement map with sub-cellular resolution. The length and direction of the vectors represents the most probable displacement at a particular cellular location. The magnitudes of local cell deformation are quantified and can be used to calculate cell stretching and rotation. The vectors increase in size from the bottom of the image to the top, indicating that the displacements are increasing in magnitude. In addition, the displacement vectors exhibit a nonuniform horizontal component, indicating that the cell has rotated. We quantified the magnitude of the displacement vectors

throughout the cell in a histogram, which shows the frequency distributions of the vector's *x* and *y* components (Fig. 5, *B* and *C*). The large bias toward positive *y* displacements and the relatively balanced contributions from positive and negative *x* components is consistent with the observation that the cell is stretching and rotating. Clearly, quantitative information can be obtained from the cross-correlation vectors.

Over a period of 20 to 30 min required to acquire the data, it is possible that the cell has migrated or significantly remodeled itself even without any forces on the cell. To test this hypothesis, a "before" three-dimensional image block was acquired of another cell, and the sample holder was then gently tapped to create a global translation and rotation without actually stressing the cell, and the "after" image block was then acquired. The image-blocks were processed and shows minimal or no displacements at all (Fig. 6). A histogram of displacement vector of this cell is also presented (Fig. 6, *D* and *E*). Although this data was taken at one-half the resolution of the previous data set, cross-correlation analysis shows that the displacement vectors in the nonstressed cell image are at approximately a factor of three smaller than those of the stressed cell, and these vectors are located predominantly off the cell itself, possibly corresponding to diffusing debris in the specimen. A second test was performed where a cell with no magnetic beads attached to it was placed in the magnetic trap, a "before" data block acquired, and the trap activated to produce 120 pN of force. The "after" data block was then acquired and compared with the before. No significant changes in cell shape or location was present (data not shown). These results suggest that without an applied force, the cell does not migrate or remodel to the same extent as under a mechanical stress. The magnetic field, vibrations from operating the trap, and the temperature effects from the trap do not result in a significant change in cell morphology. When the trap was turned off, the cell remained viable for further studies, as seen in Fig. 4, where Fig. 4 *C* was acquired after the trap was turned off from Fig. 4 *B*. However, no specific long-term data were gathered on the possible recovery of the cell for this study.

Because the images form a complete three-dimensional block of data, the deformation can be visualized from a different perspective. Images reconstructed in the vertical planes show that the deformation is not limited to the surface (Fig. 7). The largest deformations are somewhat limited to the upper one-half of the cell, but they pervade the cell to the nucleus.

The magnetic trap and two-photon setup was also used to examine GFP-actin movement in 3T3 fibroblasts as well (Fig. 8). These data represent more direct evidence of intracellular deformation. The response of the cells to a focal force involves the cytoskeleton and that the nuclear shape also changes, despite being far from the magnetic bead.

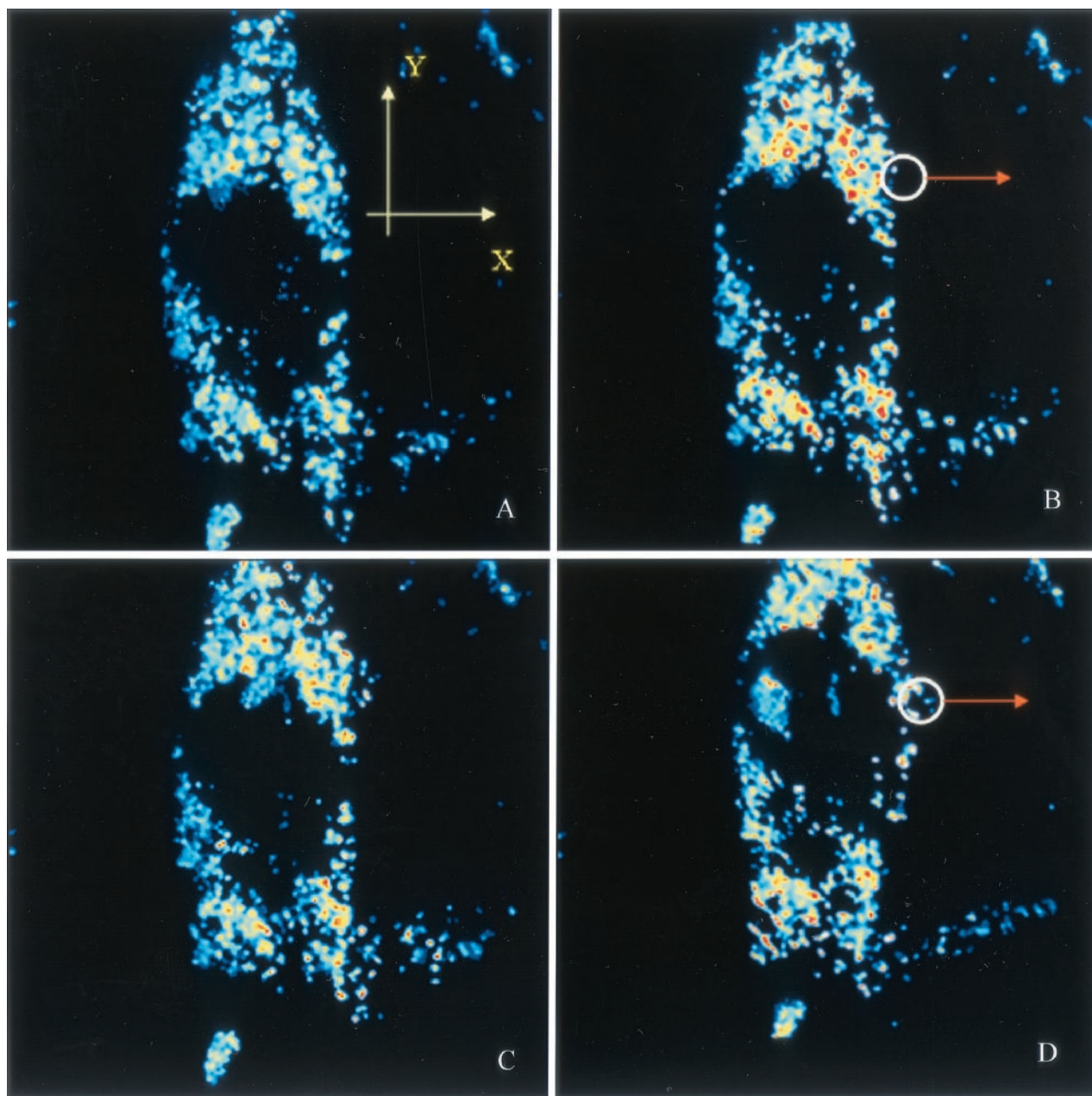


FIGURE 4 Deformation of a smooth muscle cell. The two-photon images show (A) a cell in its resting state, and (B) under 50-pN force (low force) from a single magnetic bead attached at the location shown by the small white circle in the direction depicted by the orange arrow. The cell under force is slightly rotated in the clockwise direction and is also slightly longer in a direction perpendicular to the applied force. The entire image size is  $500 \times 500$  pixels. Each pixel corresponds to  $0.15 \mu\text{m}$ . The two-photon images of the same cell as in A and B, shown in C a resting state, and D under 120 pN of force (high force) from the same magnetic bead (in the same direction). The deformation is more apparent in this case, as is a local pinching near the location of the attached bead. The cell also noticeably thins in the direction of the applied force, excepting the area near the pinching.

## DISCUSSION

A magnetic micromanipulator capable of producing uniform forces on the order of a few hundred picoNewtons over an area of  $500 \times 500 \mu\text{m}^2$  was designed. This micromanipulator is integrated with a high-resolution two-photon microscope so that three-dimensional images of deforma-

tion fields in biological specimens could be taken and analyzed. This two-photon micromanipulation workstation provides a robust way to study structural, biochemical, and genetic changes in biological systems with three-dimensional resolution.

The magnetic trap allows precise control of the magnitudes, directions, and frequencies of forces produced. The

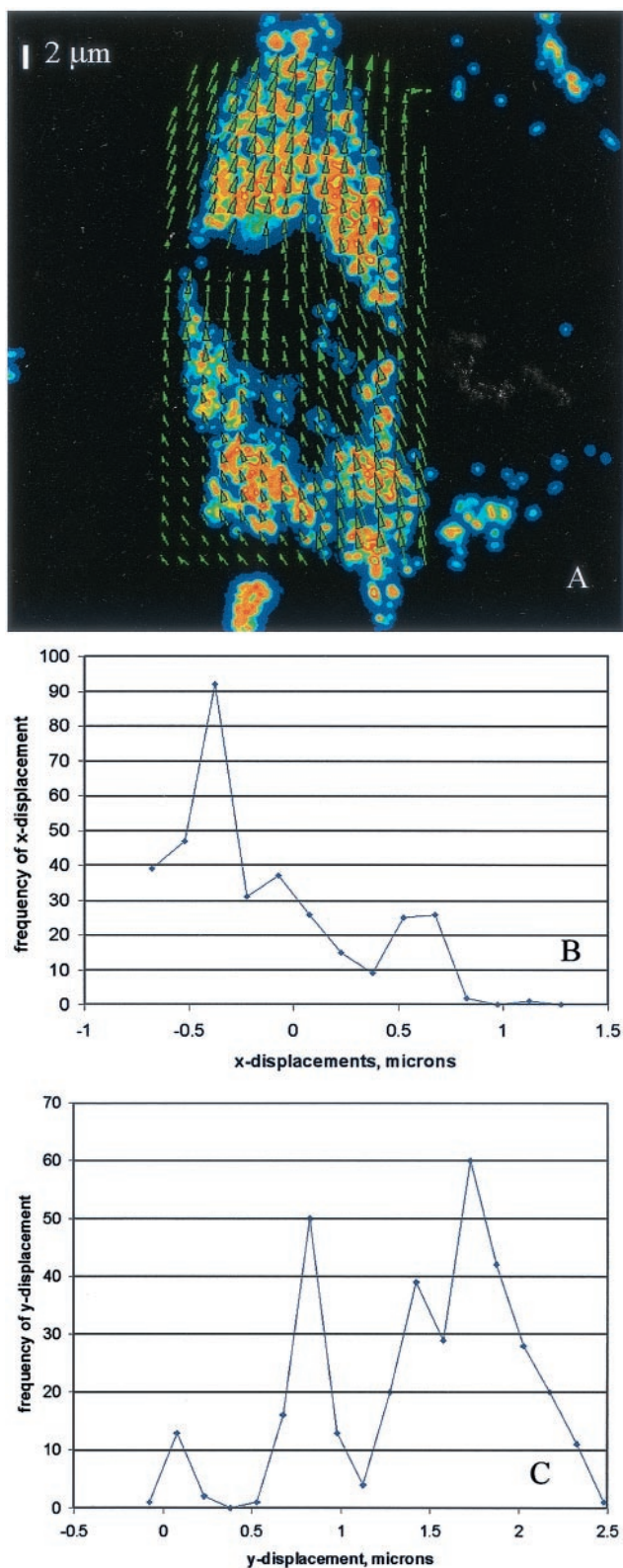


FIGURE 5 Cross-correlation analysis of the low force deformation. (A) The 50 pN “before” and “after” data were processed by a cross-correlation program with interrogation regions 128 by 128 pixels. The vectors lengthen in the  $y$  direction, indicating that the cell is elongating, and also show a  $x$  component that changes from negative to positive as  $y$  increases. This

force magnitude generated is over an order of magnitude larger than previous designs that can produce a uniform field over a large area. While a single pole magnetic manipulator such as the one designed by Bausch et al. (1998) can produce forces up to tens of nanoNewtons, the distance between the pole and the magnetic particle has to be regulated to within a few microns to obtain an accurate knowledge of the applied forces. Single pole manipulators are more appropriate for problems where the induced movement of the particle is small, for example, in the case of cell membrane studies. However, uniform field devices can provide more accurate force controls in studies where the magnetic particle may be induced to move distances of over several microns, such as in the global, stress-induced, cellular motion observed in this study, and in force spectroscopy studies of biopolymers that are significantly longer than its persistent length.

Unlike the single pole devices where only local forces can be generated, this transducer can produce uniform forces over an extended area. This feature is vital for studying many problems in cell mechanics, where the responses of many cells must be averaged to obtain statistically relevant results. Some examples include the study of calcium flux of mechano-activated channels and mechanically activated gene induction. The statistical nature of these processes requires the study of a large number of cells. This transducer generates a nearly uniform magnetic field over a  $500 \times 500 \mu\text{m}^2$  area allowing the simultaneous manipulation of over a thousand cells. The individual responses of all the cells can then be assayed microscopically. This way, both the average response and the statistical distribution information of the cell population can be obtained.

However, the generation of a uniform field over a large area has some disadvantages. One concern is that many cellular mechanical responses depend on the history of forces exerted on the cells. For example, local stiffening of integrin-cytoskeleton linkages and cytoskeletal rearrangement under external forcing have been observed (Choquet et al., 1997; Glogauer et al., 1997). After studying the responses of a given cell under magnetic manipulation, it is possible that the neighboring cells will respond differently. This effect is less of a concern for single pole traps, because the stress field decreases rapidly away from the pole tip.

An important future development involves improving mechanical stability of this trap. When the trap is toggled on/off, there is a noticeable movement in the sample section

means that the cell is also rotating or twisting in response to the applied stress. The bar indicates the length of a  $2\text{-}\mu\text{m}$  displacement vector in the  $y$  direction. These 350 vectors are decomposed into frequencies of the (B)  $x$  displacements and (C)  $y$  displacements. Thus, the histograms provide a simple way of determining which direction the cell is displacing predominantly (the positive  $y$  direction in this case) and by how much (10–15 pixels, or  $\sim 2 \mu\text{m}$ ).

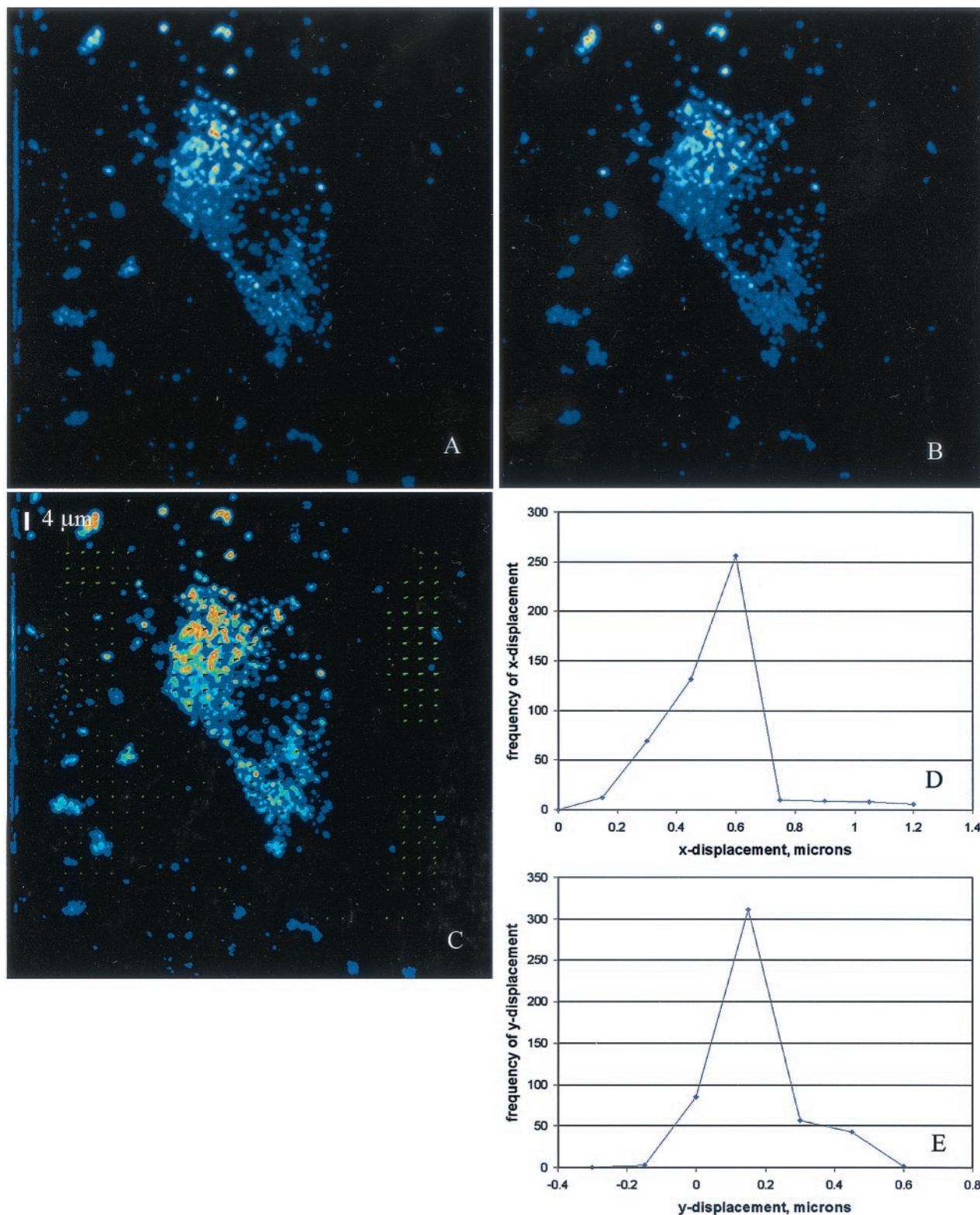
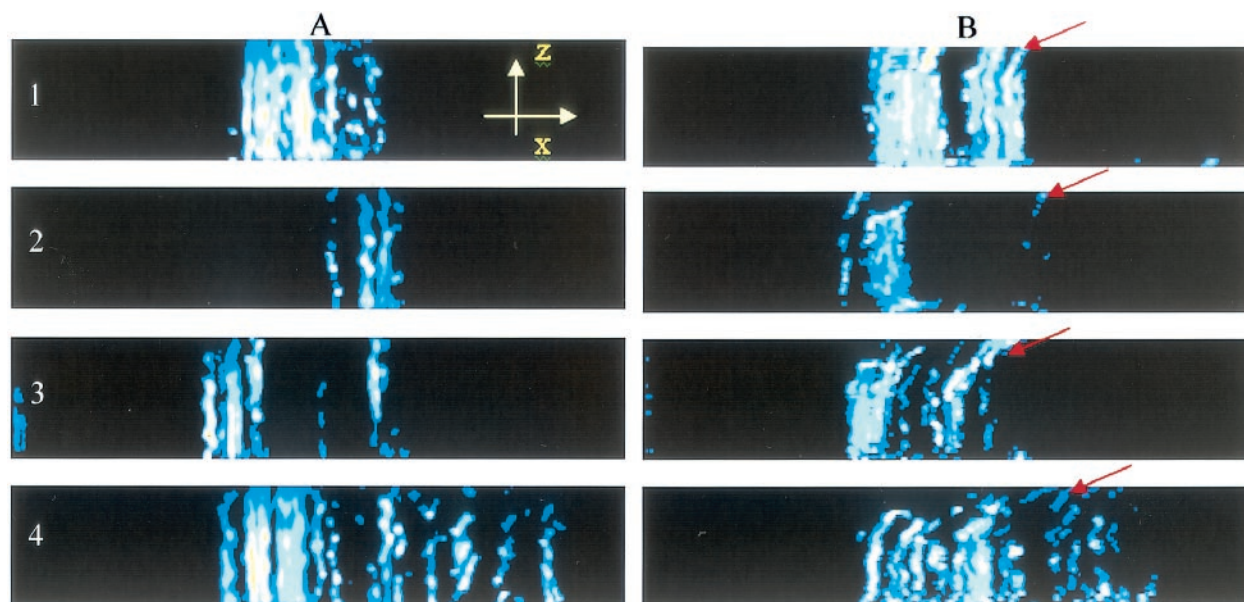


FIGURE 6 Control specimen with no applied force. The two-photon images show (A) the before and (B) after images of the same cell, with a manual perturbation of the sample holder. The two-photon image (C) shows the same cross-correlation analysis as done for Fig. 5. The vectors are shown at twice their normal size. There are no displacements in the actual cell, and only trace displacements in the vicinity of the cell, validating the cross-correlation algorithm, and the programming used to correct for rigid body displacements and rotations. The bar indicates the length of a 4 μm displacement vector in the y direction. These vectors are decomposed into frequencies of the (D) x displacements and (E) y displacements similar to those of Fig. 5. Note the much smaller magnitudes of y displacements.



**FIGURE 7** Vertical slice of a cell before and after stress is applied. These reconstructed two-photon images are taken from the same data set as used for Fig. 4 (120 pN). The vertical direction is the  $z$  axis, representing the axis parallel to gravitation. The top of the cells appears flat because the images were truncated. These images show slices at (1) 50, (2) 150, (3) 250, and (4) 350 pixels from the top of the image in Fig. 4, *C* and *D*. The cell deformation (indicated by *red arrows*) is clearly in the direction of the applied stress, and while this deformation is mostly limited at the top one-half of the cell, it also clearly penetrates the cell to the nucleus.

as viewed through the microscope (on the order of a hundred nanometers). This stability problem may be addressed in the future by the introduction of support struts, or by local

encasements of the trap joints in plastic or epoxy. If the trap is intended for repeated uses, fatigue may result and can cause the trap force to change with time. For this study, the

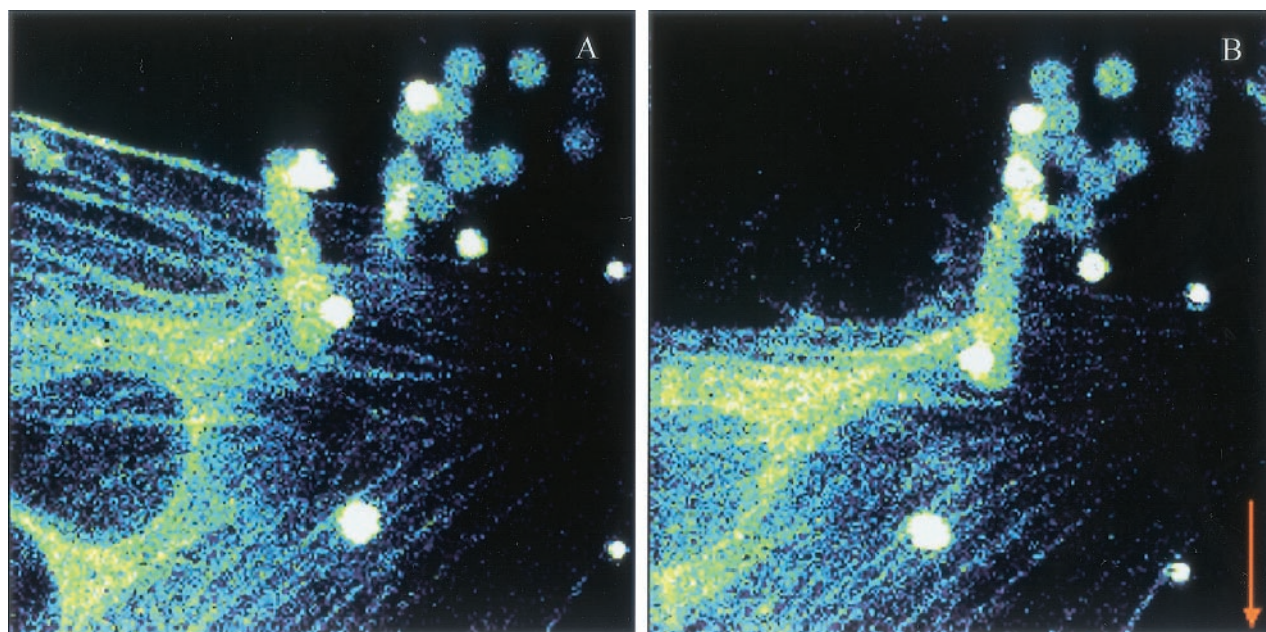


**FIGURE 8** Deformation as visualized by GFP-actin transfected 3T3 cells. The two-photon images show the (*A*) before and (*B*) after images of NIH 3T3 cells transfected with GFP actin. The stress fibers are clearly visible, and the upper fibers collapse to a thick bundle upon application of 150 pN per bead. The direction of the force is indicated by the orange arrow, and there is almost 1 nN total force on the cell. The beads are also visible as dimly fluorescent spheres in the upper right hand corner of the images. The nucleus also changes shape from an oval to a more eccentric ellipse upon the application of the force.

solid body displacement has been corrected by attaching latex particle to the coverslip as reference points.

We believe that this workstation is a very useful device for furthering the understanding of cell mechanics. Predicting the cellular responses to mechanical stimulus requires the development of theoretical models that quantify the cellular mechanical and structural modifications in response to external forces. Two of the leading theories include the tensegrity model and the open-cell foam model (Ingber, 1993, 1997; Satcher et al., 1997; Satcher and Dewey, 1996; Stamenovic and Coughlin, 1999; Stamenovic and Coughlin, 2000). These continuum models can be used to predict cellular bulk modulus. Equally importantly, these models summarize a number of the qualitative observations of how cells responses to mechanical stimulus such as the stress dependent increase in cytoskeletal stiffness (Wang et al., 1993; Wang and Ingber, 1994). In terms of experimental verification, innovative techniques such as twisting magnetic cytometry (Wang et al., 1993), micropipette aspiration (Hochmuth 2000), microplate manipulation (Thoumine et al., 1999), and atomic force microscopy (Mathur et al., 2000; Rotsch and Radmacher, 2000) allow the cellular bulk modulus to be measured and provide comparison to existing theories. While these continuum models provide reasonable quantification of bulk cell properties, the effects of mechanical stimulus on intracellular structural rearrangement is less well understood. Stress-induced modification in intracellular structures and organelle conformation has been implicated in the activation of pressure sensitive channels (Davies et al., 1997; Glogauer et al., 1997; Pommerenke et al., 1996; Wu et al., 1999), modulation of gene activation (Lundberg et al., 1995; Lyall et al., 1994; Reusch et al., 1996; Songu-Mize et al., 1996; Wagner et al., 1997; Wilson et al., 1993), and regulation of protein posttranslation modifications (Hering, 1999; Liu et al., 1999; Mourgeon et al., 1999; Noubhani et al., 1996; Parsons et al., 1999). Significant challenges remain in extending existing theories to describe intracellular structural changes on the microscopic level taking into account additional factors, such as mechanical heterogeneities in intracellular components, cell-surface adhesion forces, and cell-cell interactions. Experimentally, the quantification of cellular structural rearrangement requires imaging methods capable of mapping intracellular strain field in three-dimensional on the subcellular level. Techniques, such as two-dimensional single particle tracking (Bausch et al., 1998, 1999) and laser tracking microrheology (Yamada et al., 2000), glass needle cell pocker (Petersen et al., 1982), and atomic force microscopy (Mathur et al., 2000; Rotsch and Radmacher, 2000) allow cellular mechanical properties to be determined locally at selected locations. Extending these studies to map intracellular strain fields in three-dimensional represents an important next step. Based on three-dimensional image deconvolution, intracellular strain fields have been mapped in the presence of fluid flow (Helmke et al., 2000). The development of the two-photon

magnetic manipulator workstation represents a powerful alternative method to map the three-dimensional intracellular strain field in almost real time, while providing a method to exert directed local deformation fields with precise control.

As an evaluation of the capability of this system to quantify the distribution of intracellular deformation, human aortic smooth muscle cells with endocytosed polystyrene beads were studied with and without forces applied on them. Unlike previous studies where cellular deformation resulting from local stress is measured at a few selected points, this study allows the deformation vectors to be mapped throughout most of the cell volume except at regions where the endocytosed particles are excluded, such as the nucleus. The ability to measure deformation vectors throughout the majority of the cell volume allows us to visualize the cellular responses to mechanical stimuli in three dimensions. Even when the applied stress is planar and is generated at a single focal location, we found that cellular deformation occurs in all three dimensions. Different projections of the three-dimensional reconstruction of the data indicate that the deformations are not restricted to the surface—they extend through the cytoplasm to the nucleus. Similar results were observed in flow induced cytoskeletal deformation in endothelial cells (Helmke et al., 2001). Preliminary data support the notion that the nucleus itself changes shape when a stress is applied on the cell, which is consistent with a step-strain analysis done by Ingber et al. (Bojanowski et al., 1998; Maniotis et al., 1997). However, this data suggests that the nuclear deformation could be induced by global continuum cellular changes as well as fibrous interconnections between the cell membrane and nucleus. These results demonstrate the need for analyzing the entire architecture of the cell, and not just a two-dimensional projection, if a complete cell model is to be attained.

More in-depth examination of the displacement field provides other interesting observations. There are displacements of intracellular structure along the stress direction in the local vicinity (within a 10- $\mu\text{m}$  range) around the magnetic bead. The magnitude of this displacement is less than 1  $\mu\text{m}$  for force magnitudes less than 200 pN. A number of cells, approximately one-half of the cells examined, are observed to further lengthen globally in a direction almost perpendicular to the direction of applied force on a time scale of minutes (e.g., Fig. 5). The magnitudes of these global motions are relatively large and are on the order of 1 to 10  $\mu\text{m}$  for force magnitudes less than 200 pN. It is interesting to compare our results with previous studies (Bausch et al., 1998) using similar methods and force magnitudes under dynamic loading with a bandwidth on the order of seconds. These studies observed similar localized displacements approximately along the stress direction with magnitude comparable with the local displacement observed in our study. In our static loading study, it is clear

that global displacements becomes the dominant response mechanism on a time scale of minutes. These global motions are likely to be caused by physical processes that are different from those that generate the smaller, more instantaneous local displacements. One may postulate that these global displacements may involve active processes such as cellular cytoskeleton remodeling or focal adhesion shifting (Mathur et al., 2000). Clearly, further studies with more cells and cell types will help yield a deeper understanding of the cell responses. Such studies might include statistical analysis to quantify the bulk modulus variances over a population of cells. Statistical analysis will be needed to take account of variables such as bead location, cell orientation, and cell-cell contact.

Although the visualization of endocytosed particles has been commonly used to study cell mechanics, the correlation between the distributions of these ingested polystyrene beads and the cytoskeletal components is not well characterized. The active and passive processes involved in cellular deformation under applied stress can be better understood by directly visualizing major cellular structures responsible for the maintenance and modification of cell shapes, such as actin stress fibers, microtubules, and focal adhesion complexes. As a first step, this workstation was used to probe the responses of GFP-actin expressing fibroblasts to mechanical stresses. The actin stress fibers clearly showed a dramatic remodeling in response to the applied forces. Again, nuclear deformation was evident in these cells, indicating that the nuclear deformation induced by extracellular stress is a general feature of many cell types as observed in smooth muscle cells and fibroblasts in this report and in endothelial cells in previous studies (Bojanowski et al., 1998; Maniotis et al., 1997). This study with GFP-actin clearly indicates that the global deformation observed involves significant reconfiguration of the cytoskeleton structure. The collapse of a significant portion of the cell under stress (Fig. 8) suggests that the surface connections of a number of focal adhesion sites were severed. With the incorporation of video rate two-photon imaging capability into this workstation, it may be possible to directly track both short- and long-term stress-induced changes in actin filaments, as well as microtubules or other cellular structural components.

The two-photon magnetic-trap workstation is suitable for studying a variety of force-response behavior in biology. An immediate extension of the current work is study the effect of mechanical stresses on endothelial cells. Because the force is generally applied in a direction parallel to the substrate to which the cell is attached, the simulation of shear stress is easily achieved. Thus, it is possible to study the classical responses of endothelial cells to controlled shear stresses, such as looking at intracellular calcium concentration changes, focal adhesion shifting, and cytoskeletal rearrangement at the same time as the stress is being applied, rather than at discrete time points (Davies et al.,

1997). Another possible application of this technique is the use of this device to study three-dimensional rheological properties of biopeptide gels that are finding uses in areas such as tissue engineering.

It is possible that the generated magnetic field itself can cause biological effects when cells are being studied. Magnetic field responses of biological systems have not been well-characterized, so detailed studies with a workstation such as the one presented needs to include controls to eliminate the effects of the field. However, it is clear this workstation provides the capabilities to systematically study the cellular mechanical response to establish a more comprehensive model of cell mechanics and behavior, and that this workstation is well suited for such an application. This workstation demonstrated that it can generate large, uniform forces over a large area as designed and when used in conjunction with two-photon microscopy was capable of generating detectable deformation in living cells.

This work was supported under the Whitaker Foundation and the MIT Center for Bioengineering grant number 2897700. Thanks to Dr. Richard Gilbert for sharing the GFP-actin plasmids used in this study and to Dr. Ben Fabry for sharing the ferro-magnetic beads used in this project.

## REFERENCES

- Amblard, F., B. Yurke, A. Pargellis, and S. Leibler. 1996. A magnetic manipulator for studying local rheology and micromechanical properties of biological systems. *Biophys. J.* 67:818–827.
- Bausch, A. R., W. Moller, and E. Sackmann. 1999. Measurement of local viscoelasticity and forces in living cells by magnetic tweezers. *Biophys. J.* 76:573–579.
- Bausch, A. R., F. Ziemann, A. A. Boulbitch, K. Jacobson, and E. Sackmann. 1998. Local measurements of viscoelastic parameters of adherent cell surfaces by magnetic bead microrheometry. *Biophys. J.* 75: 2038–2049.
- Block, S. M., L. S. Goldstein, and B. J. Schnapp. 1990. Bead movement by single kinesin molecules studied with optical tweezers. *Nature.* 348: 348–352.
- Bojanowski, K., A. J. Maniotis, S. Plisov, A. K. Larsen, and D. E. Ingber. 1998. DNA topoisomerase II can drive changes in higher order chromosome architecture without enzymatically modifying DNA. *J. Cell Biochem.* 69:127–142.
- Brown, T. D., M. Bottlang, D. R. Pedersen, and A. J. Banes. 1998. Loading paradigms—intentional and unintentional—for cell culture mechanostimulus. *Am. J. Med. Sci.* 316:162–168.
- Burger, E. H., and J. Klein-Nulend. 1998. Microgravity and bone cell mechanosensitivity. *Bone.* 22:127S–130S.
- Chaqour, B., P. S. Howard, and E. J. Macarak. 1999. Identification of stretch-responsive genes in pulmonary artery smooth muscle cells by a two arbitrary primer-based mRNA differential display approach. *Mol. Cell Biochem.* 197:87–96.
- Chiu, J. J., B. S. Wung, H. J. Hsieh, L. W. Lo, and D. L. Wang. 1999. Nitric oxide regulates shear stress-induced early growth response-1: expression via the extracellular signal-regulated kinase pathway in endothelial cells. *Circ. Res.* 85:238–246.
- Choquet, D., D. P. Felsenfeld, and M. P. Sheetz. 1997. Extracellular matrix rigidity causes strengthening of integrin-cytoskeleton linkages. *Cell.* 88:39–48.
- Davies, P. F. 1995. Flow-mediated endothelial mechanotransduction. *Physiol. Rev.* 75:519–560.

- Davies, P. F., K. A. Barbee, M. V. Volin, A. Robotewskyj, J. Chen, L. Joseph, M. L. Griem, M. N. Wernick, E. Jacobs, D. C. Polacek, et al., 1997. Spatial relationships in early signaling events of flow-mediated endothelial mechanotransduction. *Annu. Rev. Physiol.* 59:527–549.
- Davies, P. F., D. C. Polacek, J. S. Handen, B. P. Helmke, and N. DePaola. 1999. A spatial approach to transcriptional profiling: mechanotransduction and the focal origin of atherosclerosis. *Trends Biotechnol.* 17: 347–351.
- Davies, P. F., A. Robotewskyj, and M. L. Griem. 1994. Quantitative studies of endothelial cell adhesion: directional remodeling of focal adhesion sites in response to flow forces. *J. Clin. Invest.* 93:2031–2038.
- Girard, P. R., and R. M. Nerem. 1995. Shear stress modulates endothelial cell morphology and F-actin organization through the regulation of focal adhesion-associated proteins. *J. Cell Physiol.* 163:179–193.
- Glogauer, M., P. Arora, G. Yao, I. Sokholov, J. Ferrier, and C. A. McCulloch. 1997. Calcium ions and tyrosine phosphorylation interact coordinately with actin to regulate cytoprotective responses to stretching. *J. Cell Sci.* 110:11–21.
- Helmke, B. P., R. D. Goldman, and P. F. Davies. 2000. Rapid displacement of vimentin intermediate filaments in living endothelial cells exposed to flow. *Circ. Res.* 86:745–752.
- Helmke, B. P., D. B. Thakker, R. D. Goldman, and P. F. Davies. 2001. Spatiotemporal analysis of flow-induced intermediate filament displacement in living endothelial cells. *Biophys. J.* 80:184–194.
- Hering, T. M. 1999. Regulation of chondrocyte gene expression. *Front Biosci.* 4:D743–D761.
- Hochmuth, R. M. 2000. Micropipette aspiration of living cells. *J. Biomech.* 33:15–22.
- Hu, H., and F. Sachs. 1997. Stretch-activated ion channels in the heart. *J. Mol. Cell Cardiol.* 29:1511–1523.
- Ingber, D. E. 1993. Cellular tensegrity: defining new rules of biological design that govern the cytoskeleton. *J. Cell Sci.* 104:613–627.
- Ingber, D. E. 1997. Tensegrity: the architectural basis of cellular mechanotransduction. *Annu. Rev. Physiol.* 59:575–599.
- Kanda, K., T. Matsuda, and T. Oka. 1993. Mechanical stress induced cellular orientation and phenotypic modulation of 3-D cultured smooth muscle cells. *Asaio J.* 39:M686–M690.
- Khachigian, L. M., K. R. Anderson, N. J. Halnon, M. A., Jr. Gimbrone, N. Resnick, and T. Collins. 1997. Egr-1 is activated in endothelial cells exposed to fluid shear stress and interacts with a novel shear-stress-response element in the PDGF A-chain promoter. *Arterioscler. Thromb. Vasc. Biol.* 17:2280–2286.
- Kuo, S. C., and M. P. Sheetz. 1993. Force of single kinesin molecules measured with optical tweezers. *Science.* 260:232–234.
- Liu, M., A. K. Tanswell, and M. Post. 1999. Mechanical force-induced signal transduction in lung cells. *Am. J. Physiol.* 277:L667–L683.
- Lundberg, M. S., D. N. Sadhu, V. E. Grumman, W. M. Chilian, and K. S. Ramos. 1995. Actin isoform and alpha 1B-adrenoceptor gene expression in aortic and coronary smooth muscle is influenced by cyclical stretch. *In Vitro Cell Dev. Biol. Anim.* 31:595–600.
- Lyll, F., M. R. Deehan, I. A. Greer, F. Boswell, W. C. Brown, and G. T. McInnes. 1994. Mechanical stretch increases proto-oncogene expression and phosphoinositide turnover in vascular smooth muscle cells. *J. Hypertens.* 12:1139–1145.
- Malek, A. M., and S. Izumo. 1995. Control of endothelial cell gene expression by flow. *J. Biomech.* 28:1515–1528.
- Maniotis, A. J., C. S. Chen, and D. E. Ingber. 1997. Demonstration of mechanical connections between integrins, cytoskeletal filaments, and nucleoplasm that stabilize nuclear structure. *Proc. Natl. Acad. Sci. U. S. A.* 94:849–854.
- Mathur, A. B., G. A. Truskey, and W. M. Reichert. 2000. Atomic force and total internal reflection fluorescence microscopy for the study of force transmission in endothelial cells. *Biophys. J.* 78:1725–1735.
- Mourgeon, E., J. Xu, A. K. Tanswell, M. Liu, and M. Post. 1999. Mechanical strain-induced posttranscriptional regulation of fibronectin production in fetal lung cells. *Am. J. Physiol.* 277:L142–L149.
- Mow, V. C. G. F., R. Tran-Son-Tay, and R. M. Hochmuth. 1994. *Cell Mechanics and Cellular Engineering*. Springer Verlag, New York.
- Noubhani, A. M., S. Sakr, M. H. Denis, S. Delrot. 1996. Transcriptional and post-translational control of the plant plasma membrane H(+)-ATPase by mechanical treatments. *Biochim. Biophys. Acta.* 1281:213–219.
- Parsons, M., E. Kessler, G. J. Laurent, R. A. Brown, and J. E. Bishop. 1999. Mechanical load enhances procollagen processing in dermal fibroblasts by regulating levels of procollagen C-proteinase. *Exp. Cell Res.* 252:319–331.
- Petersen, N. O., W. B. McConnaughey, and E. L. Elson. 1982. Dependence of locally measured cellular deformability on position on the cell, temperature, and cytochalasin B. *Proc. Natl. Acad. Sci. U. S. A.* 79: 5327–5331.
- Pommerenke, H., E. Schreiber, F. Durr, B. Nebe, C. Hahnel, W. Moller, and J. Rychly. 1996. Stimulation of integrin receptors using a magnetic drag force device induces an intracellular free calcium response. *Eur. J. Cell Biol.* 70:157–164.
- Reusch, P., H. Wagdy, R. Reusch, E. Wilson, and H. E. Ives. 1996. Mechanical strain increases smooth muscle and decreases nonmuscle myosin expression in rat vascular smooth muscle cells. *Circ. Res.* 79:1046–1053.
- Rotsch, C., and M. Radmacher. 2000. Drug-induced changes of cytoskeletal structure and mechanics in fibroblasts: an atomic force microscopy study. *Biophys. J.* 78:520–535.
- Sackin, H. 1995. Stretch-activated ion channels. *Kidney Int.* 48: 1134–1147.
- Satcher, R., C. F. Dewey Jr., and J. H. Hartwig. 1997. Mechanical remodeling of the endothelial surface and actin cytoskeleton induced by fluid flow. *Microcirculation.* 4:439–453.
- Satcher Jr., R. L., and C. F. Dewey Jr. 1996. Theoretical estimates of mechanical properties of the endothelial cell cytoskeleton. *Biophys. J.* 71:109–118.
- So, P. T. C., T. French, W. M. Yu, K. M. Berland, C. Y. Dong, and E. Gratton. 1995. Time-resolved fluorescence microscopy using two-photon excitation. *Bioimaging.* 3:49–63.
- So, P. T., K. Konig, K. Berland, C. Y. Dong, T. French, C. Buhler, T. Ragan, and E. Gratton. 1998. New time-resolved techniques in two-photon microscopy. *Cell. Mol. Biol. (Noisy-le-grand).* 44:771–793.
- Songu-Mize, E., X. Liu, J. E. Stones, and L. J. Hymel. 1996. Regulation of Na<sup>+</sup>,K<sup>+</sup>-ATPase alpha-subunit expression by mechanical strain in aortic smooth muscle cells. *Hypertension.* 27:827–832.
- Stamenovic, D., and M. F. Coughlin. 1999. The role of prestress and architecture of the cytoskeleton and deformability of cytoskeletal filaments in mechanics of adherent cells: a quantitative analysis. *J. Theor. Biol.* 201:63–74.
- Stamenovic, D., and M. F. Coughlin. 2000. A quantitative model of cellular elasticity based on tensegrity. *J. Biomech. Eng.* 122:39–43.
- Thoumine, O., A. Ott, O. Cardoso, and J. J. Meister. 1999. Microplates: a new tool for manipulation and mechanical perturbation of individual cells. *J. Biochem. Biophys. Methods.* 39:47–62.
- Wagner, C. T., W. Durante, N. Christodoulides, J. D. Hellums, and A. I. Schafer. 1997. Hemodynamic forces induce the expression of heme oxygenase in cultured vascular smooth muscle cells. *J. Clin. Invest.* 100:589–596.
- Wang, N., J. P. Butler, and D. E. Ingber. 1993. Mechanotransduction across the cell surface and through the cytoskeleton [see comments]. *Science.* 260:1124–1127.
- Wang, N., and D. E. Ingber. 1994. Control of cytoskeletal mechanics by extracellular matrix, cell shape, and mechanical tension. *Biophys. J.* 66:2181–2189.
- Wilson, E., Q. Mai, K. Sudhir, R. H. Weiss, and H. E. Ives. 1993. Mechanical strain induces growth of vascular smooth muscle cells via autocrine action of PDGF. *J. Cell Biol.* 123:741–747.
- Wu, Z., K. Wong, M. Glogauer, R. P. Ellen, and C. A. McCulloch. 1999. Regulation of stretch-activated intracellular calcium transients by actin filaments. *Biochem. Biophys. Res. Commun.* 261:419–425.
- Yamada, S., D. Wirtz, and S. C. Kuo. 2000. Mechanics of living cells measured by laser tracking microrheology. *Biophys. J.* 78:1736–1747.

# Lab 5: Optical trapping and single molecule fluorescence

**Location:** NE47-014

**PI:** Matt Lang

**Lab Instructor:** Jorge Ferrer

## Summary

Optical tweezers are an excellent experimental tool to study the biophysics of single molecule systems including the mechanics of molecular motors (kinesin, myosin, RNA polymerase), mechanical conformations/transitions of molecules (dsDNA, RNA hairpins, filamentous proteins) and interactions of receptor-ligand systems (antigen-antibody). In the most common assays, the mechanical state of the system is monitored by tracking the position of a handle (usually a dielectric microsphere with diameter of 0.5-2 $\mu$ m) tethered to the molecule of interest (protein, DNA, etc), with nanometer and piconewton resolution. The handle also serves as probe to apply force to the system to study the energetics of mechanical changes. Single molecule fluorescence allows the direct observation of the mechanical/conformational changes of the system as it is subjected to perturbations, such as force. The combination of these two techniques allows researchers to study the biophysical properties of single molecules. In this lab you will learn the basics of operating a high-end optical tweezers to record mechanical transitions of single molecules. The instrument is also equipped with a novel single molecule fluorescence technique to allow simultaneous, coincident optical trapping and single molecule fluorescence. In our demonstration we will measure the force required to unzip a double-stranded DNA molecule, with a resolution of  $\sim$ 5nm and  $\sim$ 0.1pN, while using single molecule fluorescence to confirm the location of the break. Alignment and calibration procedures will also be presented.

## Recommended Reading

R. R. Brau *et al.*, "Interlaced Optical Force-Fluorescence Measurements for Single Molecule Biophysics," *Biophys. J.* **91** (2006).

M. J. Lang *et al.*, "Simultaneous, Coincident Optical Trapping and Single-Molecule Fluorescence," *Nat. Methods* **1** (2004).





## Optical Trapping and Single Molecule Fluorescence Lab Demonstration Dual Confirmation of double-strand DNA Unzipping

### *Lab contact information:*

Supervisor: Matthew J. Lang ([mjlang@mit.edu](mailto:mjlang@mit.edu))

Student contact: Jorge M. Ferrer ([ferrerj@mit.edu](mailto:ferrerj@mit.edu))

Lab phone: 1-617-253-3735

Office area: NE47-285 (500 Technology Square, 2<sup>nd</sup> floor)

Lab location: NE47-014 (500 Technology Square, basement)

Website: <http://web.mit.edu/langlab>

**Summary:** Optical tweezers are an excellent experimental tool to study the biophysics of single molecule systems including the mechanics of molecular motors (kinesin, myosin, RNA polymerase), mechanical conformations/transitions of molecules (dsDNA, RNA hairpins, filamentous proteins) and interactions of receptor-ligand systems (antigen-antibody). In the most common assays, the mechanical state of the system is monitored by tracking the position of a handle (usually a dielectric microsphere with diameter of 0.5-2 $\mu$ m) tethered to the molecule of interest (protein, DNA, etc), with nanometer and picoNewton resolution. The handle also serves as probe to apply force to the system to study the energetics of mechanical changes. Single molecule fluorescence allows the direct observation of the mechanical/conformational changes of the system as it is subjected to perturbations, such as force. The combination of these two techniques allows researches to study the biophysical properties of single molecules. In this lab you will learn the basics of operating a high-end optical tweezers to record mechanical transitions of single molecules. The instrument is also equipped with a novel single molecule fluorescence technique to allow simultaneous, coincident optical trapping and single molecule fluorescence. In our demonstration we will measure the force required to unzip a double-stranded DNA molecule, with a resolution of  $\sim$ 5nm and  $\sim$ 0.1pN, while using single molecule fluorescence to confirm the location of the break. Alignment and calibration procedures will also be presented.

### **Recommended Reading**

R.R. Brau *et al*, "Interlaced Optical Force-Fluorescence Measurements for Single Molecule Biophysics," *Biophys. J.* **91** (2006).

M.J. Lang *et al*, "Simultaneous, coincident optical trapping and single-molecule fluorescence," *Nature Methods* **1** (2004).

(optional) Optical Trapping Review : K.C. Neuman & S.M. Block, "Optical trapping," *Rev. Sci. Instrum.* **75** (2003).



### **Equipment you will see in the Lang Lab:**

- Modified Nikon TE2000 microscope (100X, 1.40NA oil immersion objective)
  - Piezo-electric stage (1-nm resolution, 100x100x20  $\mu\text{m}$  range)
  - Manual stage
  - Position detection branch with photodiode
- Main optics box (right of microscope): enclosed breadboard housing the trapping (1064nm), detection (975nm) and fluorescence excitation (488nm and 532nm) lasers, and optics to align the beams. A pair of acousto-optic deflectors (AODs) provides 2-D control of the trapping laser location in the specimen plane and a single AOD provides modulation of the fluorescence excitation laser.
- Dark box (left of microscope): contains a CCD for bright field imaging, an intensified CCD for single molecule imaging and a pair of silicon avalanche photodiodes (SAPDs) for single molecule detection and fluorescence resonance energy transfer (FRET) detection.
- All of the above mounted on top of an optical table.

### **Experimental procedure for single molecule fluorescence using total internal reflection fluorescence (TIRF) microscopy:**

- Set up slide in scope, adjust bright field illumination and position detection branch (attached to condenser).
- Locate single dye on surface using intensified CCD.
- Move the molecule to the fluorescence collection region (pinhole) using piezo-stage.
- Collect fluorescence emission with SAPDs (counts per unit of time) until dye photobleaches (discrete reduction in fluorescence signal).

### **Combined OT and SMF to detect dsDNA unzipping:**

- Find a tethered bead, find the tether point and reposition it to the fluorescence collection region.
- Trap the bead and simultaneously record bead displacement from the center of the trap and fluorescence emission.
- An unzipping event will show both a sudden change in bead position and a discrete decrease in fluorescence emission (dye no longer in collection region).
- Calibrate the bead for both position and obtain trap stiffness using variance method (see review by Neuman & Block for details).

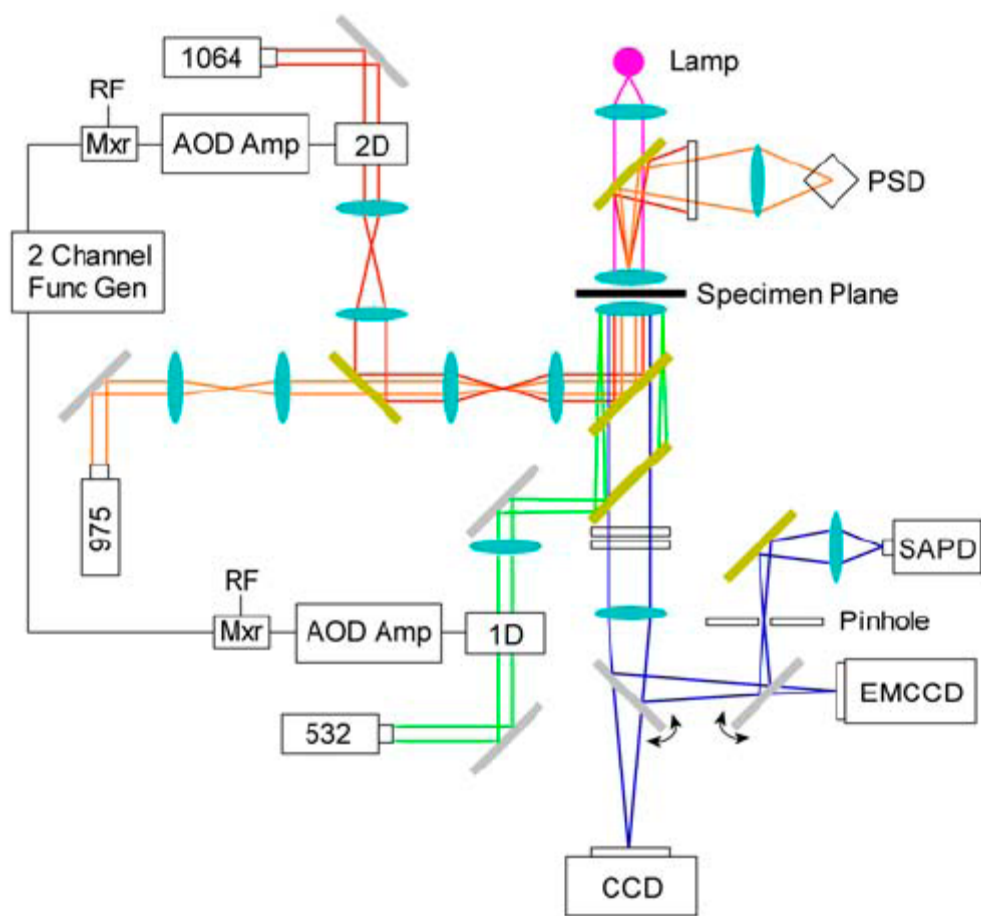


FIGURE 1. Optical layout of the instrument. All lenses, including the objective and condenser, are displayed as light-blue ovals. Filters, mirrors, and dichroics are represented as white, silver, and gold-filled rectangles, respectively. Trapping (red) and detection (orange) lasers, 1064 and 975 nm, respectively, are guided into the objective and focused on the specimen plane to form an optical trap. The position of the trapped particle is monitored by spectrally isolating and imaging the detection laser on a PSD. Total internal fluorescence excitation, supplied by a 532-nm laser (green), is focused near the back pupil of the objective. Bright-field illumination is provided by a mercury arc lamp (magenta), and images (blue) are collected by a CCD camera. Fluorescence images (blue) are collected by an electron multiplying CCD (EMCCD), and single molecule fluorescence counts are spatially filtered through a pinhole and acquired by an SAPD. The trapping and excitation lasers are modulated by AODs controlled with an electronic mixer (Mxr) that combines a preamplified radio frequency AOD drive signal with a square wave generated in a function generator.

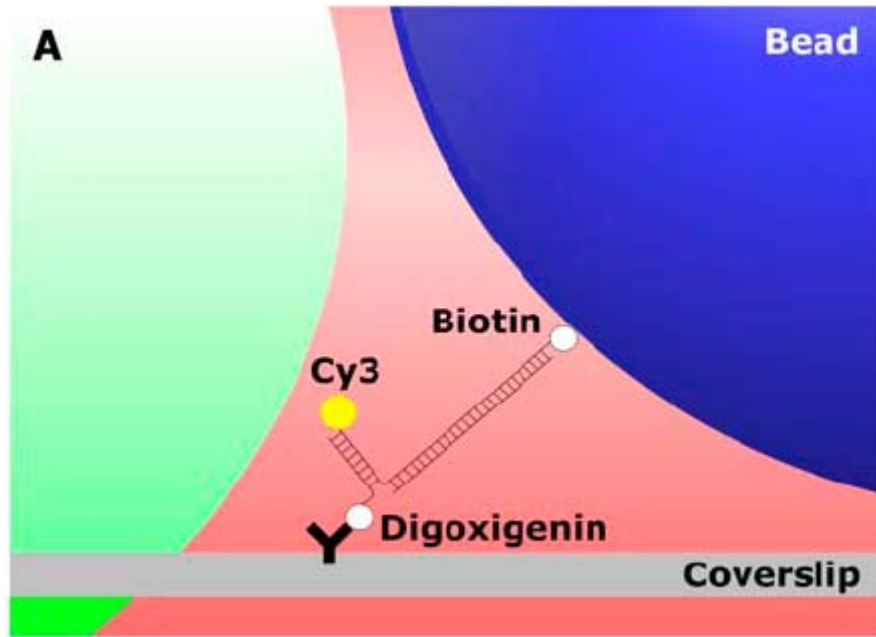


FIGURE 2. Unzipping geometry for a 15-bp dsDNA system. It is attached on one end to a trapped bead via a biotin–streptavidin interaction and immobilized on the other end by means of a digoxigenin–antibody linkage. The 15-bp region of interest is labeled with a Cy3 fluorophore to confirm the location and timing of the unzipping mechanical event.

# Interlaced Optical Force-Fluorescence Measurements for Single Molecule Biophysics

Ricardo R. Brau,\* Peter B. Tarsa,\* Jorge M. Ferrer,\* Peter Lee,\* and Matthew J. Lang\*†

\*Biological Engineering Division, and †Department of Mechanical Engineering, Massachusetts Institute of Technology, Cambridge, Massachusetts

**ABSTRACT** Combining optical tweezers with single molecule fluorescence offers a powerful technique to study the biophysical properties of single proteins and molecules. However, such integration into a combined, coincident arrangement has been severely limited by the dramatic reduction in fluorescence longevity of common dyes under simultaneous exposure to trapping and fluorescence excitation beams. We present a novel approach to overcome this problem by alternately modulating the optical trap and excitation beams to prevent simultaneous exposure of the fluorescent dye. We demonstrate the dramatic reduction of trap-induced photobleaching effects on the common single molecule fluorescence dye Cy3, which is highly susceptible to this destructive pathway. The extension in characteristic fluorophore longevity, a 20-fold improvement when compared to simultaneous exposure to both beams, prolongs the fluorescence emission to several tens of seconds in a combined, coincident arrangement. Furthermore, we show that this scheme, interlaced optical force-fluorescence, does not compromise the trap stiffness or single molecule fluorescence sensitivity at sufficiently high modulation frequencies. Such improvement permits the simultaneous measurement of the mechanical state of a system with optical tweezers and the localization of molecular changes with single molecule fluorescence, as demonstrated by mechanically unzipping a 15-basepair DNA segment labeled with Cy3.

## INTRODUCTION

Significant advances in single molecule techniques and their application to biological systems have provided new insight into the mechanistic behavior of single proteins and other biological molecules (1–3). Two such techniques, single molecule fluorescence spectroscopy and optical tweezers force spectroscopy, permit the direct observation of energetic heterogeneities and conformational differences within populations that may be otherwise lost in the inherent averaging of bulk measurements. Optical tweezers force spectroscopy yields quantitative information about the mechanical forces involved in interactions at the single molecule level (4), and single molecule fluorescence reports on binding interactions and provides insight into the structural and conformational states of proteins (5). Although these two experimental approaches independently provide different perspectives from which to approach biological problems, their combination results in a powerful tool for the analysis of molecular motors, protein–protein and protein–DNA interactions, biomolecular conformational changes, and mechanotransduction pathways (6–10). In this report, we describe a novel technique that dramatically improves both the practicality and versatility of such an arrangement by eliminating a dominant photobleaching pathway that results from the exposure of excited-state fluorophores to the high photon

flux of optical tweezers (11). This technique, in which the trapping and fluorescence excitation beams are alternately modulated, allows for the seamless integration of optical trapping and single molecule fluorescence without compromising trap stiffness or fluorescence sensitivity.

Optical tweezers force spectroscopy has been widely adopted for exploration of the effects of mechanical forces on single molecule systems (4). The high force and position sensitivity that facilitates such measurements, typically on the order of piconewtons and nanometers, respectively, is achieved by trapping and manipulating a dielectric particle within a tightly focused laser beam. In most instances, the trapped particle is tethered in close proximity to a biological specimen and can be used to noninvasively measure the mechanics of single molecules and their binding interactions (12–16). In addition, optical tweezers have found particular applicability for studying the mechanical properties of molecular motors, such as kinesin, myosin, RNA polymerase, and others (17–20).

Although optical tweezers force experiments are critical to understanding the molecular underpinnings of a variety of biological processes, the combination of this technique with single molecule fluorescence spectroscopy further extends its versatility. By incorporating direct reporting through a fluorescent label, single molecule fluorescence provides an added observable dimension that allows the examination of the localized effects of applied forces on the system of interest (7,9). However, despite technological advances that have made single molecule fluorescence more accessible (21), a practical approach for its integration with optical tweezers has remained elusive due to the destructive

---

*Submitted February 3, 2006, and accepted for publication April 5, 2006.*

Ricardo R. Brau, Peter B. Tarsa, and Jorge M. Ferrer contributed equally to this work.

Address reprint requests to Matthew J. Lang, Biological Engineering Division, Massachusetts Institute of Technology, Cambridge, MA 02139. Tel.: 617-452-2631; E-mail: mjlang@mit.edu.

© 2006 by the Biophysical Society

0006-3495/06/08/1069/09 \$2.00

doi: 10.1529/biophysj.106.082602

photobleaching effects that are caused by the trapping beam (8,11).

Several approaches pioneered the development of instruments that simultaneously combine these two techniques. For example, dual-beam optical trap configurations have been employed to separately study the motility of Cy3-labeled RNA polymerase along double-stranded DNA (dsDNA) and the mechanochemical interactions between myosin and actin filaments (22,23). These assay geometry arrangements require either filamentous proteins or dsDNA to be suspended between the two independent optical traps, limiting its adoption for experimental systems demanding coincident trapping and fluorescence. Such a design was later demonstrated using an efficient optical trap configuration in combination with objective-side fluorescence illumination, high-performance optical filters, and a judicious choice of a fluorescent marker that is not heavily susceptible to trap-induced photobleaching (8,24). This apparatus, which used fluorescence to confirm the mechanical unzipping and shearing of tetramethyl rhodamine (TMR)-labeled dsDNA, incorporates a fluorescence excitation laser and single molecule fluorescence detection equipment that can be easily interfaced with optical tweezers instrumentation. Unfortunately, neither method directly addresses the recently quantified phenomenon of trap-induced photobleaching, a process to which TMR exhibits very little susceptibility. However, it is not a popular single molecule dye because of its relatively low quantum yield and extinction coefficient and because its conjugation to proteins can lead to a considerable loss of fluorescence (25). Even if these limitations could be generally overcome at the single molecule level, complicated experimental schemes involving multiple fluorophores will necessarily employ dyes other than TMR.

Current approaches are impractical with popular single molecule dyes, such as Cy3, because their fluorescence longevity is severely reduced by over an order of magnitude when employed in a combined, coincident arrangement (11). In this report, we present a temporally based solution that extends the longevity of such fluorophores in the presence of a high-intensity optical trap by alternately modulating the trapping and fluorescence excitation beams. This technique, which we term interlaced optical force-fluorescence (IOFF), requires only minor modification of conventional optical tweezers arrangements and does not compromise trap integrity. We further demonstrate the effectiveness of this approach using Cy3, a commonly employed single molecule dye that is highly susceptible to trap-dependent photobleaching (11), to show dramatic improvement in single molecule fluorophore longevity in the presence of a trapping laser. Cy3 is an exceptionally bright dye, and, to our knowledge, this is the first instance in which Cy3 has been used in a combined, coincident optical tweezers and single molecule fluorescence arrangement. Furthermore, we effectively combine the two techniques for the mechanical unzipping of a Cy3-labeled 15-bp dsDNA. This model

system confirms the nominal effects of laser modulation on trap stiffness and represents a significant step in extending the versatility of IOFF. Such a technique may be applicable to a range of fluorophores and molecular geometries and opens the possibility for the exploration of more advanced systems, such as real-time binding kinetics or energy transfer mechanisms.

## MATERIALS AND METHODS

### Instrument design

The combined optical tweezers and single molecule fluorescence instrument (Fig. 1) is based on a heavily modified inverted microscope (Nikon, Melville, NY) and is similar to previously proven arrangements (24,26). This device combines separate lasers for optical trapping (1064 nm; Coherent, Santa Clara, CA), position detection (975 nm; Corning Lasertron, Bedford, MA), and fluorescence excitation (532 nm; World Star Tech, Toronto, ON) through a base that has improved mechanical stability, incorporated Nomarski optics, and a piezoelectric stage (Physik Instrumente, Auburn, MA). In addition, the arrangement includes a pair of computer-controlled acousto-optic deflectors (AODs; IntraAction, Bellwood, IL),

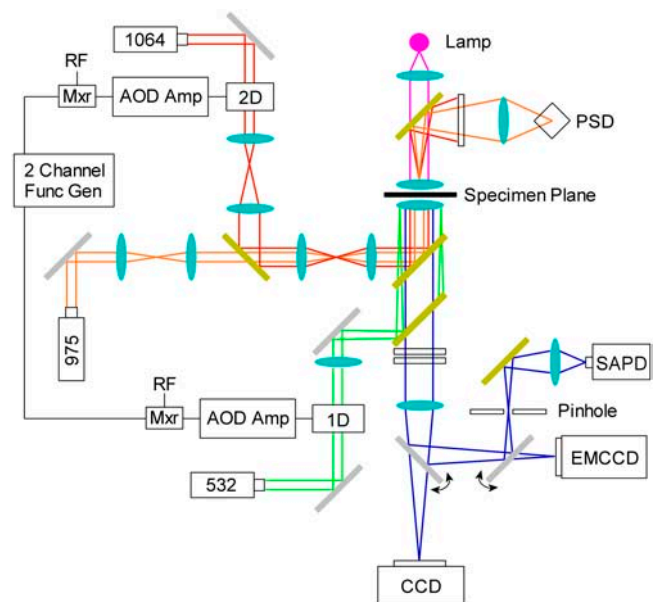


FIGURE 1 Optical layout of the instrument. All lenses, including the objective and condenser, are displayed as light-blue ovals. Filters, mirrors, and dichroics are represented as white, silver, and gold-filled rectangles, respectively. Trapping (red) and detection (orange) lasers, 1064 and 975 nm, respectively, are guided into the objective and focused on the specimen plane to form an optical trap. The position of the trapped particle is monitored by spectrally isolating and imaging the detection laser on a PSD. Total internal fluorescence excitation, supplied by a 532-nm laser (green), is focused near the back pupil of the objective. Bright-field illumination is provided by a mercury arc lamp (magenta), and images (blue) are collected by a CCD camera. Fluorescence images (blue) are collected by an electron multiplying CCD (EMCCD), and single molecule fluorescence counts are spatially filtered through a pinhole and acquired by an SAPD. The trapping and excitation lasers are modulated by AODs controlled with an electronic mixer (Mxr) that combines a preamplified radio frequency AOD drive signal with a square wave generated in a function generator.

which permit precise steering of the trapping beam in two dimensions, and remote-controlled flipper mirrors and shutters, which facilitate rapid switching between bright-field imaging (CCD camera; DAGE-MTI, Michigan City, IN) and high-sensitivity fluorescence detectors.

Both the trapping and detection lasers are guided into the microscope objective (100 $\times$ , 1.40 numerical aperture, oil infrared; Nikon, Melville, NY) via a dichroic mirror (Chroma Technology, Rockingham, VT) that reflects only near-infrared light. The diameter of the trapping laser beam is adjusted with a telescope to slightly overfill the objective pupil to ensure high-efficiency trapping. After passing through the microscope condenser lens, the detection beam is spectrally isolated (Andover, Salem, NH) from the trapping beam and imaged on a position-sensitive device (PSD; Pacific Silicon, Westlake Village, CA) for back focal plane detection (27,28). This optical tweezers arrangement was calibrated using previously described procedures (4,26) and was found to be capable of trapping 500-nm-radius polystyrene beads with a stiffness of  $\sim 0.1$  pN/nm per 100 mW of unmodulated trapping laser power.

In addition to these force capabilities, the microscope is outfitted for objective-side total internal reflection fluorescence excitation and single-molecule emission detection. The excitation laser, which is controlled by an independent AOD (IntraAction), is guided through a customized optomechanical system that replaces the microscope's fluorescence turret. This modification, which allows for focusing and off-axis translation of the excitation laser along the back focal plane of the objective, is set directly below the trap-steering dichroic mirror. It consists of a filter cube (532-nm dichroic and 540-nm long-pass filter; Chroma Technology) and a KG5 filter (Schott Glass, Elmsford, NY) to reflect the excitation light into the sample, transmit fluorescence emission, and efficiently block scattered or reflected light from the excitation, trapping, and detection lasers. Transmitted fluorescence signals are imaged with either an EMCCD intensified camera (Andor Technology, South Windsor, CT) or a photon-counting silicon avalanche photodiode (SAPD; PerkinElmer, Wellesley, MA), which collects through a pinhole (ThorLabs, Newton, NJ) conjugate with the specimen plane for the spatial signal isolation from background and bead scattering signals and a 628-nm dichroic mirror (Chroma Technology) for similar spectral separation.

To quickly modulate the intensities of both the trapping and excitation lasers, electronic mixers (Mini-Circuits, Brooklyn, NY) multiply both preamplification AOD radio frequency signals with a square wave signal from a two-channel function generator (Tektronix, Richardson, TX). This technique is similar to a recently demonstrated fluorescence sorting method (29) and to other trap modulation schemes (27,30). In essence, it temporally turns the trapping and excitation lasers on or off, allowing for their in-phase (IP) or out-of-phase (OP) synchronization. For all the experiments described in this report, the fluorescence excitation and trapping lasers were further modulated with a duty cycle of 30% and 50% and set to an average postmodulated power of 250  $\mu$ W and 100 mW, respectively. In the OP condition, the pulses of the trapping and excitation lasers are aligned such that there is a 2- $\mu$ s dark period in between pulses, as verified by a single photodiode (ThorLabs). The duration of the fluorescence excitation and trapping laser pulses are 10 and 6  $\mu$ sec, respectively. For the IP condition, the phase of the trapping laser was shifted by 180 $^\circ$ , placing the fluorescence excitation pulse squarely in the middle of the trapping laser pulse (see Fig. 3, *insets*). Custom software (LabView; National Instruments, Austin, TX) acquired all signals through a 16-bit A/D board (National Instruments) and automated all instrument components.

## Single molecule fluorescence

Flow cells were prepared as previously described (31). To prepare single molecule samples, flow cells were filled with 20  $\mu$ M antidigoxigenin polyclonal antibody (Roche Applied Science, Indianapolis, IN), incubated for 30 min, and washed with 200  $\mu$ L of Tris buffer (20 mM Tris, pH 7.5, 6 mM NaCl, 1.7 mM MgCl<sub>2</sub>, and 10% glycerol). They were then filled with 40  $\mu$ L of 25 pM fluorescent DNA complexes (Operon Biotechnologies,

Huntsville, AL) (oligo 1, 5'-Cy3-CCACTCTAGG-Dig-3'; oligo 2, 5'-CCTAGAGTGG-Biotin-3'), which were annealed in TE buffer (pH 8.0; Integrated DNA Technologies, Coralville, IA) and designed to be similar to those used in other single molecule fluorescence studies (32). After a 15-min incubation, unbound complexes were washed with 200  $\mu$ L of fluorescence buffer (Tris buffer, 120 nM catalase (Calbiochem, San Diego, CA), 25 mM  $\beta$ -D(+) glucose (Calbiochem), 1.8  $\mu$ M glucose oxidase (Calbiochem), 1%  $\beta$ -mercapto-ethanol (VWR, West Chester, PA), degassed for 30 min in a dessicator). All incubations took place in a humidity chamber at room temperature.

Single, immobilized Cy3-labeled molecules were visualized on the EMCCD camera for  $\sim 1$  s, and isolated fluorophores were chosen and, using the piezo stage, repositioned for pinhole imaging on the SAPD. Fluorescence was collected until a discrete single bleaching step was observed to return count levels to background. After photobleaching, the signal was monitored for at least 30 s to ensure that the fluorophore did not undergo an intermediate dark state electronic transition as observed in some samples. Even though a similar blinking behavior has been previously described (33), we were careful to exclude them from the analysis because they would introduce unacceptable ambiguity in experiments employing combined, coincident optical tweezers and single molecule fluorescence. All signals were acquired at 20 Hz and were analyzed using MATLAB (The MathWorks, Natick, MA).

## dsDNA unzipping assay preparation

The dsDNA unzipping assay was prepared as described previously with minor modifications (24). These include using Cy3 as a fluorescence reporter and replacing the final wash step with 200  $\mu$ L of fluorescence buffer containing 0.15 mg/mL bovine serum albumin. Once identified, tethers were precisely located to the pinhole collection zone using the position sensing system in the instrument device. This assay provides a convenient system in which to use Cy3 in a combined, coincident optical tweezers and single molecule fluorescence arrangement.

## RESULTS

### Optimal modulation frequency

When trapped with a modulated laser, the thermally driven motion of a bead is determined by the properties of the focused trapping beam and the bead itself. It is also affected by the frequency and duty cycle at which the trapping laser is modulated, suggesting that the principal effect of modulation is to alter the stiffness of a trap at a given power. These effects have been previously explored for the stable trapping of multiple particles with a single time-shared trap (27) or with holographic optical tweezers (34). Here, we further explore these effects on the force-exerting capabilities of the trap to determine optimal modulation conditions.

Thermal effects become apparent when the position of a trapped bead is monitored as a function of time for different modulation frequencies (Fig. 2 A). At low frequencies, the trapped bead is allowed to diffuse through a large volume of space, whereas at higher frequencies, the trap constrains its motion to a reduced space. To quantify the effect of modulation on the optical tweezers capabilities, the stiffness of the trap was monitored as a function of modulation frequency for different trapping powers. Trap stiffness,  $k_x$ , was measured using the equipartition theorem to relate the

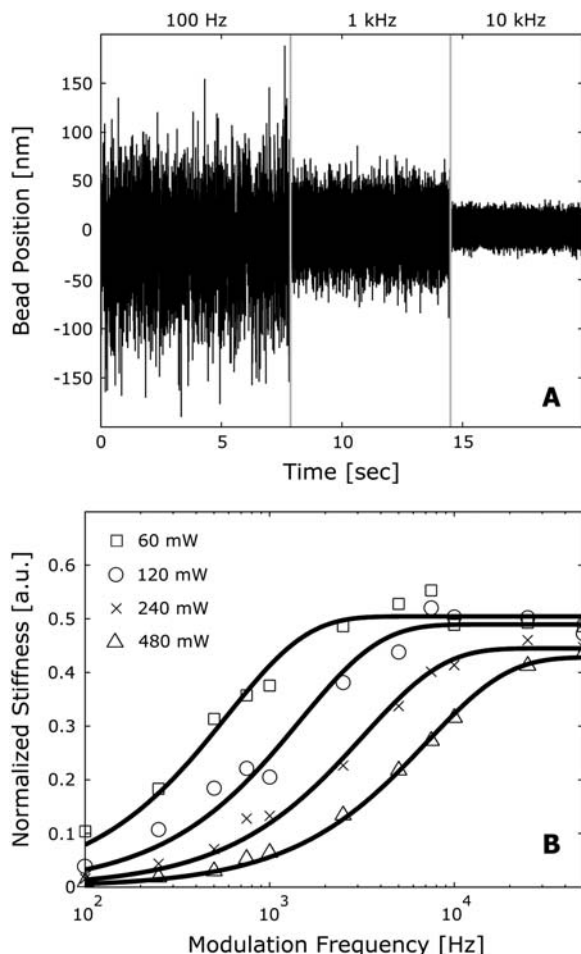


FIGURE 2 Effect of modulation on the integrity of an optical trap. (A) Position trace of a trapped bead for a 50% duty cycle with 100-Hz, 1-kHz, and 10-kHz modulation frequencies. The space explored by the bead is reduced as the modulation frequency increases. (B) Effect of modulation on the stiffness of an optical trap for 60 ( $\square$ ), 120 ( $\circ$ ), 240 ( $\times$ ), and 480 ( $\triangle$ ) mW of trapping laser power. For each power, the measured stiffness was normalized by the trap stiffness of a continuous trap. The data were fit to a simple exponential function, resulting in characteristic modulation frequencies of 0.59, 1.5, 3.2, and 7.1 kHz, respectively.

mean-squared displacement of a trapped bead,  $\langle(x^2)\rangle$ , to the thermal energy in the system,  $k_bT$ , such that  $k_x\langle(x^2)\rangle/2 = k_bT/2$ .

For a set of modulation frequencies ranging from 100 Hz to 50 kHz, the stiffness of the trap increased monotonically with frequency under constant laser trap power and modulation duty cycle. A similar behavior was also observed when the stiffness of the trap was determined with the Stokes drag and power spectrum calibration methods (results not shown). For each trapping power, the modulated stiffness values were normalized by the measured stiffness for an unmodulated trap (Fig. 2 B). The resulting trends resemble an S-curve and are well described with an exponential function of the form  $y = A(1 - \exp(-f/f_m))$ , where  $A$  is the maximum achievable stiffness,  $f$  the modulation frequency, and  $f_m$  represents a

characteristic modulation frequency for the system. As expected, all fits converge near 0.5 at high modulation frequencies ( $>10$  kHz) with a 50% duty cycle. For trapping powers of 60, 120, 240, and 480 mW, the curves are described by characteristic modulation frequencies of 0.59, 1.5, 3.2, and 7.1 kHz, respectively. These values, which have a linear dependence on average trapping power ( $R^2 > 0.99$ ), correspond to the modulation frequencies at which the trap stiffness is 63% of the maximum stiffness for a modulated trap. Therefore, for a given power, a trap must be modulated at a frequency that is higher than its characteristic frequency of modulation. For example, if it is modulated at a frequency five times greater than its  $f_m$ , the resulting trap will be characterized with a stiffness that is 99% of that of a continuous trap formed with the same average power.

In addition to the relationship between the characteristic modulation frequency and trap power, the fits produce a  $f_m$  that is  $\sim 15\%$  less than the corner frequency of an unmodulated trap at all powers studied. The corner, or roll-off frequency,  $f_c$ , describes the motion of a trapped bead and is determined by fitting the power spectral density of bead position to a Lorentzian function (4). This close dependence suggests that, for a given power, the corner frequency of an unmodulated trap can serve as a guideline to determine the minimum modulation frequency at which it resembles a continuous trap. Alternatively, modulation should occur at the highest frequency possible.

### Fluorophore longevity

Bulk fluorophore decay rates were found to be independent of modulation frequency; however, they were found to be dependent on the modulation duty cycle and average excitation laser power (results not shown). For these reasons, the fluorescence excitation laser was modulated at 50 kHz with a 30% duty cycle and set to deliver an average power of 250  $\mu$ W, whereas the trapping laser was modulated at 50 kHz with a 50% duty cycle and delivered an average power of 100 mW. These conditions permit the IP or OP synchronization of the trapping and excitation lasers while maintaining the highest possible trap stiffness, reducing the fluorophore photobleaching caused by the excitation laser, allowing good single fluorophore emission sensitivity, and keeping the trapping and excitation laser fluxes constant throughout all experiments. A third condition, in which fluorophores were exposed to the modulated excitation laser with no trapping laser (NT), was used as a control to establish the normal decay profile of the fluorophores. These schemes rely on the separation of time scales between the nanosecond relaxation time constant of excited electrons, the microsecond pulses of our modulation scheme, and the inherent millisecond averaging of the data acquisition rate.

Single Cy3 molecules, which were immobilized on glass coverslips through short DNA linkers to prevent interaction between the fluorophore and substrate, were simultaneously

exposed to modulated fluorescence excitation and optical trap lasers to quantify trap-dependent photobleaching effects. The single dyes fluoresced at a constant level before instantaneously bleaching in a single step, returning the signal to background (Fig. 3 A). For each condition, the fluorescence emission longevity of 100 Cy3 dyes was recorded, and histograms were fitted to a single exponential decay model to extract a characteristic decay constant for each condition (Figs. 3, B–D) (35,36). Cy3 fluorophores irradiated in the NT condition were found to have a decay constant of  $89.87 \pm 13.05$  s, whereas those exposed to the IP and OP arrangements had decay constants of  $1.49 \pm 0.10$  and  $32.03 \pm 5.72$  s, respectively. Clearly, the OP configuration represents a dramatic improvement in the longevity of Cy3 fluorophores over IP. In addition, this modulation condition creates enough time before photobleaching for the low loading rate measurement of mechanical events with an IOFF arrangement.

### Combined measurement

To demonstrate the suitability of our approach, we applied the OP synchronization of the trapping and fluorescence excitation lasers to the unzipping of a 15-bp region in a simple dsDNA system (Fig. 4 A). The modulation and power settings for both lasers were kept as described above. Cy3 emission was used to confirm mechanical events occurring in response to the application of external mechanical loads. In this case, upon dsDNA unzipping, the fluorescence emission was reduced to background levels simultaneously with the mechanical break, confirming that the dsDNA was unzipped (Fig. 4 C). The force required to unzip the 15-bp dsDNA region,  $\sim 10$  pN, is consistent with control experiments (Fig. 4 B) and with other similar systems (8,24,37). To our knowledge, this is the first instance in which Cy3 has been used in a combined, coincident single molecule fluorescence

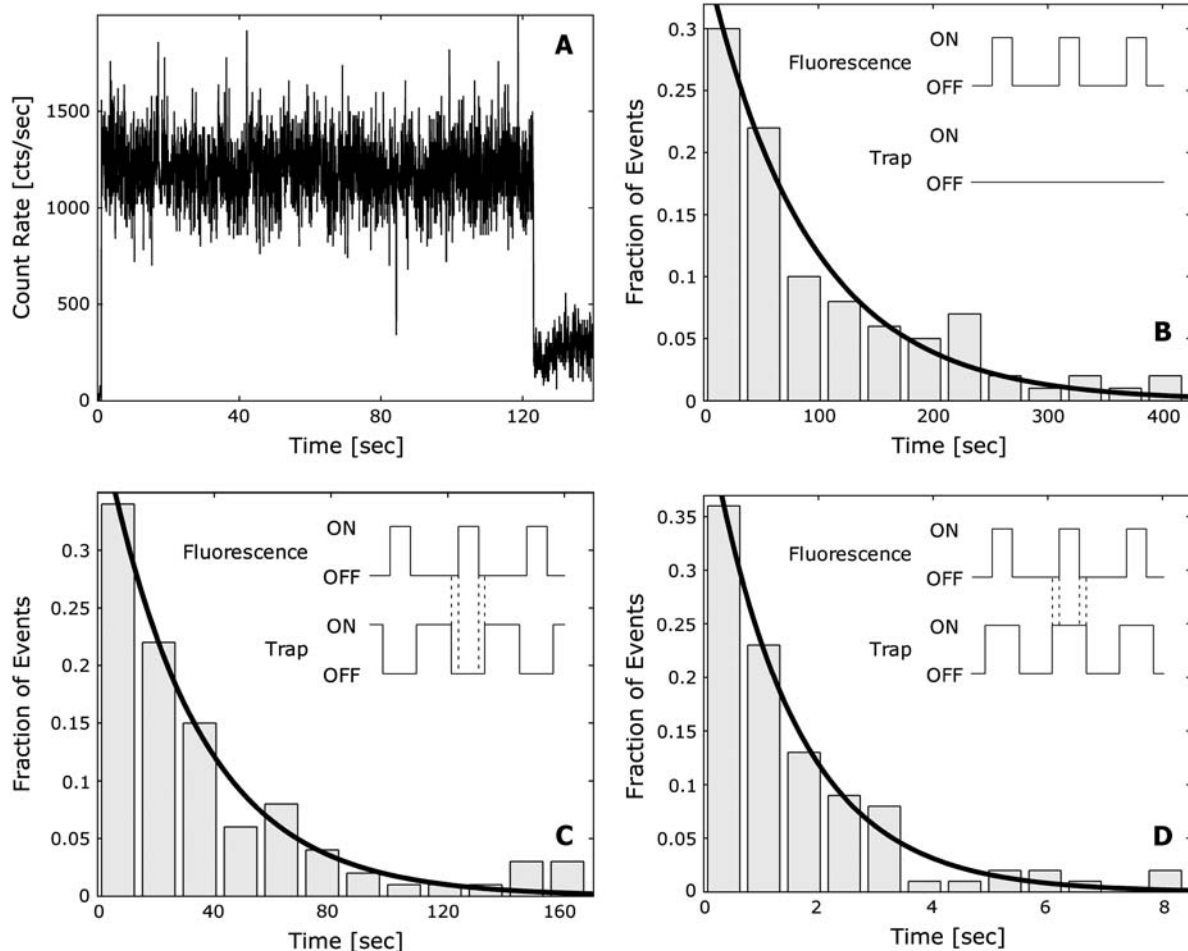
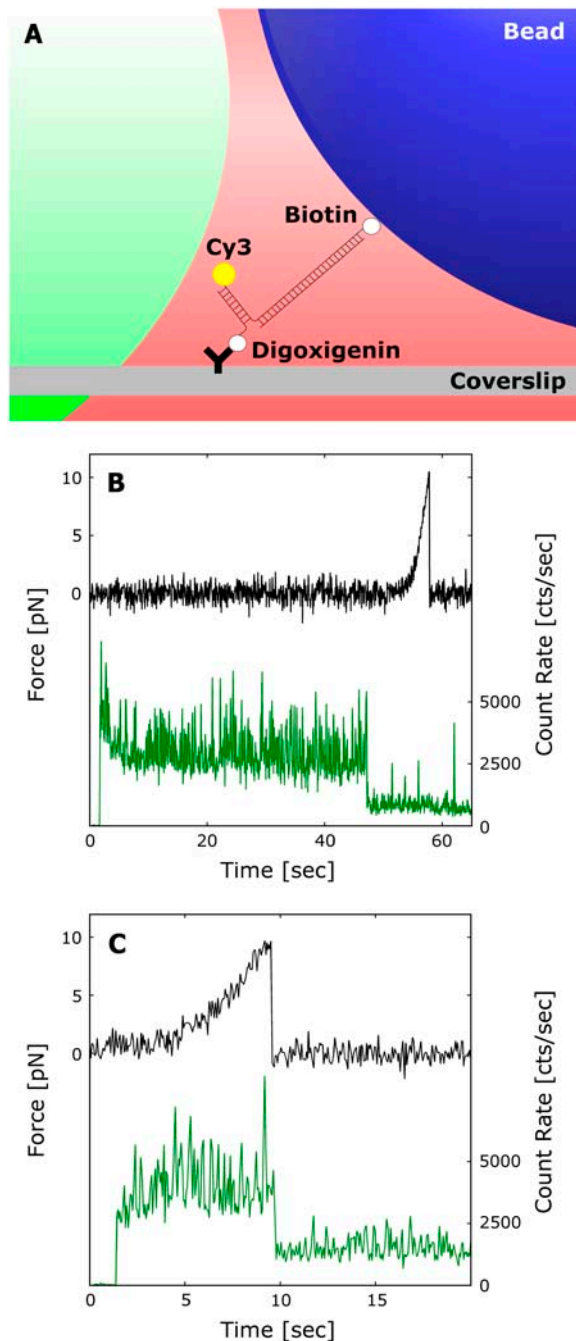


FIGURE 3 Cy3 single molecule fluorescence. (A) Example trace for a single Cy3 photobleaching event exposed to OP trapping and excitation radiation. The fluorophore emits light at a constant rate before irreversibly bleaching in a single step and returning the signal to background level. This particular Cy3 molecule had a longevity of  $\sim 120$  s. Histograms ( $n = 100$ ) of the longevities of single Cy3 fluorophores exposed to the (B) no trap (NT), (C) OP, and (D) IP modulation conditions. The data for each condition were fitted to a single exponential decay model with time constants of  $89.87 \pm 13.05$  s,  $1.49 \pm 0.10$  s, and  $32.03 \pm 5.72$  s, respectively. All fits resulted in  $R^2 > 0.95$ . Insets contain schematics of the modulation scheme employed for each condition. The hatch marks on the (C) OP and (D) IP insets mark the  $2\text{-}\mu\text{s}$  offset between the trapping and fluorescence excitation laser pulses for each condition. Both trapping and excitation lasers were modulated at 50 kHz with a duty cycle of 50% and 30%, respectively.



**FIGURE 4** Combined measurement using the interlaced modulation technique. (A) Unzipping geometry for a 15-bp dsDNA system. It is attached on one end to a trapped bead via a biotin–streptavidin interaction and immobilized on the other end by means of a digoxigenin–antibody linkage. The 15-bp region of interest is labeled with a Cy3 fluorophore to confirm the location and timing of the unzipping mechanical event. (B) This system was exposed to OP radiation and its emission monitored until irreversibly photobleaching at  $\sim 45$  s (green). Upon photobleaching, the dsDNA tether was loaded until rupture at  $\sim 10$  pN (blue). (C) Simultaneous trace of the force exerted on the dsDNA system (blue) and the photon emission rate of the Cy3 fluorophore (green). The dsDNA system was loaded at a rate of 100 nm/s until a mechanical break occurs at  $\sim 10$  pN (blue). This event is correlated with a simultaneous drop to background in the Cy3 emission rate, corroborating the location of the break. The fluorescence excitation was shuttered for 1.5 s after position acquisition started.

and optical tweezers mechanical measurement. As a control, Cy3 was irradiated with the OP arrangement until irreversibly photobleaching, which occurred at  $\sim 45$  s (Fig. 4 B). No force was exerted on the dsDNA system during this period, but after photobleaching, the tether was loaded at 100 nm/s until rupture was observed at  $\sim 10$  pN (Fig. 4 B). As expected, the fluorophore emitted at a constant level and was not disturbed by the presence of the trap. However, when compared to the traces from the system in the single molecule fluorescence longevity study, there was a small increase in background and signal noise likely due to the presence of the bead and slightly different molecular configuration.

## DISCUSSION

### Trap stiffness and modulation

A modulated trap can resemble a continuous one if it is modulated at sufficiently high frequency, dependent on the average trapping power. Our results show that a strong trap, formed with 480-mW average trapping power, should be modulated at a frequency of at least 50 kHz, whereas a weaker trap, formed with 60 mW, can be modulated with frequencies as low as 10 kHz while still maintaining trap stiffness (Fig. 2 B). This was further confirmed by fits to a simple exponential model and the resulting linear relationship between the characteristic modulation frequencies and trapping power. For a modulation frequency of 50 kHz, the trap is off for a duration of 10  $\mu$ s, giving a bead with a diffusivity of  $4.36 \times 10^{-13}$  m<sup>2</sup> s<sup>-1</sup> enough time to diffuse  $\sim 4$  nm away from the center of the trap, well within the average signal noise of a relatively weak optical trap. However, for fine measurements with position resolution on the order of 1 nm, such as those required for the resolution of molecular conformational changes and protein folding and unfolding (38,39), the optical trap must be modulated at higher frequencies to minimize diffusional noise. We further validated this technique under a Stokes drag of 10 pN to monitor the effect of modulation on the position bead when it is subject to external loads. Such measurements confirmed that for sufficiently high frequencies the effects of modulation disappear, even when the bead is driven away from the center of the trap (results not shown).

Although these results suggest that the integrity of the trap can be completely recovered at high modulation frequencies, there are practical upper limits on the frequency at which modulation can occur. Acoustic modulation is limited by both the speed of sound in the AOD medium (4.2 mm/ $\mu$ s) and the diameter of the laser ( $\sim 2.5$  mm), which in our system results in a maximum modulation frequency of  $\sim 80$  kHz. This frequency is appropriate to modulate a trap formed with up to 400 mW of trapping power and characterized with a stiffness up to 0.4 pN/nm. Higher modulation frequencies can be reached by minimizing the diameter of the laser at the AOD location, employing AOD crystal materials that

inherently provide higher sound velocities, or implementing electronic modulation techniques such as those used in telecommunications applications or for multiple color fluorescence measurements (40). Though such arrangements will further extend the versatility of this technique, our configuration is suitable for the types of experiments that are commonly approached with optical tweezers force spectroscopy.

### Trap-dependent photobleaching reduction

Trap-dependent photobleaching was observed when Cy3 fluorophores were simultaneously irradiated with the fluorescence excitation and trapping beams modulated IP. At the single molecule scale, Cy3 was irreversibly photobleached over an order of magnitude faster than when exposed to the NT condition (Fig. 3). These results are in agreement with previous observations suggesting that the absorption of 1064-nm photons by molecules already in the first excited state can lead to a pathway that accelerates photodestruction (11).

Our simple solution avoids populating these destructive states by allowing excited Cy3 molecules to return to the ground state before exposing the dye of interest to the high infrared photon flux of the trap. This technique significantly reduces destructive photobleaching effects by alternately modulating the fluorescence excitation and optical trapping lasers OP, resulting in a 20-fold longevity improvement over IP radiation (Fig. 3). Despite this improvement, which extends the characteristic longevity of single Cy3 dyes to >30 s, fluorophore longevity remains shorter than that measured in the absence of a trapping laser, suggesting that the lower energy radiation can still cause some photodestruction. Although the mechanism of this additional photobleaching pathway is unknown, it is possible that it may arise from two-photon excitation (41), the detection of which is beyond the sensitivity of our instrument for detecting single molecules. Even though there is preliminary evidence against it (11), this scenario requires further investigation. Nevertheless, by alternately modulating the two beams, the major pathway for trap-dependent photobleaching is effectively eliminated, allowing IOFF to become feasible. Furthermore, this technique can be readily extended to single molecule experiments using other common dyes, such as Alexa 488, green fluorescent protein, and fluorescent resonance energy transfer pairs.

### Modulation, optical tweezers, and single molecule fluorescence

We have successfully presented a method for efficiently combining single molecule fluorescence and optical tweezers into a single, functional instrument without sacrificing the capabilities of either technique. The effectiveness of this arrangement was demonstrated by mechanically unzipping a

15-bp dsDNA overhang model system and monitoring the event through the emission of a strategically placed Cy3 dye. This combination of force measurement and fluorescence emission provides solid evidence for the location and nature of the mechanical observations, as fluorescence signatures and force magnitudes differ for other types of breaks (24). In addition, we report an unzipping force of  $\sim 10$  pN for our 15-bp dsDNA system, which is in agreement with previously reported values for a similar system (8,24).

Though similar results have been presented with an analogous system (8,24), the benefits of our IOFF technique are necessary for combined measurements using common single molecule fluorophores. The most popular of these dyes, including Cy3, are characterized by a high quantum yield and extinction coefficient but are highly susceptible to the trap-induced photobleaching effects that are dramatically reduced by our approach. This result also improves assay development feasibility, a significant hurdle in single molecule research, for the investigation of molecular motor systems that have been independently approached with optical tweezers (42,43), single molecule fluorescence (44–46), or other methods (47,48). Such tools can now be simultaneously combined to elucidate the mechanochemical cycles governing the motion of these systems (35,49,50) and to study real-time force-induced conformational changes (51). In addition, this technique reduces the requirement of a highly efficient trap, allowing experiments involving optical tweezers to take place deep into solution, where they could be coupled with prism-side total internal reflection and other techniques. Furthermore, IOFF can be used to study protein folding and protein–protein and protein–DNA interactions and to monitor the formation of complex structures at the cellular level in response to external force (52).

We have demonstrated the significant reduction of trap-dependent photobleaching by alternately modulating fluorescence excitation and optical trapping lasers, showing a 20-fold improvement in Cy3 longevity at the single molecule level. In addition, we have successfully applied the combination of these two techniques to the fluorescence-reported unzipping of a short segment of dsDNA. This application, in which the fluorophore is held directly over the highest photon flux trapping region, suggests the broad versatility of this combined instrument. Such a seamless integration of single molecule fluorescence and optical tweezers force spectroscopy can be implemented through our temporal innovation with other common single molecule dyes in a wide range of molecular configurations for the exploration of the effects of mechanical force in biological systems.

The authors are grateful for financial support provided by the Lemelson Foundation and the Massachusetts Institute of Technology (MIT)/National Institute of General Medical Sciences Biotechnology Training Program (R.R.B.), a Minority Supplement to National Institutes of Health Grant P01HL064858 (J.M.F.), and startup funds from the School of Engineering, the Biological Engineering Division, and the Department of Mechanical Engineering at MIT (M.J.L.).

## REFERENCES

1. Ha, T. 2001. Single-molecule fluorescence methods for the study of nucleic acids. *Curr. Opin. Struct. Biol.* 11:287–292.
2. Vale, R. D., and R. A. Milligan. 2000. The way things move: Looking under the hood of molecular motor proteins. *Science*. 288:88–95.
3. Weiss, S. 1999. Fluorescence spectroscopy of single biomolecules. *Science*. 283:1676–1683.
4. Neuman, K. C., and S. M. Block. 2004. Optical trapping. *Rev. Sci. Instrum.* 75:2787–2809.
5. Kapanidis, A. N., and S. Weiss. 2002. Fluorescent probes and bio-conjugation chemistries for single-molecule fluorescence analysis of biomolecules. *J. Chem. Phys.* 117:10953–10964.
6. Wang, Y. X., E. L. Botvinick, Y. H. Zhao, M. W. Berns, S. Usami, R. Y. Tsien, and S. Chien. 2005. Visualizing the mechanical activation of Src. *Nature*. 434:1040–1045.
7. Weitzman, J. B. 2003. A marriage of techniques. *J. Biol.* 2:2.
8. Lang, M. J., P. M. Fordyce, and S. M. Block. 2003. Combined optical trapping and single-molecule fluorescence. *J. Biol.* 2:6.
9. Wallace, M. I., J. E. Molloy, and D. R. Trentham. 2003. Combined single-molecule force and fluorescence measurements for biology. *J. Biol.* 2:4.
10. Ishijima, A., and T. Yanagida. 2001. Single molecule nanobioscience. *Trends Biochem. Sci.* 26:438–444.
11. van Dijk, M. A., L. C. Kapitein, J. van Mameren, C. F. Schmidt, and E. J. G. Peterman. 2004. Combining optical trapping and single-molecule fluorescence spectroscopy: Enhanced photobleaching of fluorophores. *J. Phys. Chem. B.* 108:6479–6484.
12. Miyata, H., R. Yasuda, and K. Kinoshita. 1996. Strength and lifetime of the bond between actin and skeletal muscle alpha-actinin studied with an optical trapping technique. *Biochim. Biophys. Acta.* 1290:83–88.
13. Pant, K., R. L. Karpel, I. Rouzina, and M. C. Williams. 2005. Salt dependent binding of T4 gene 32 protein to single and double-stranded DNA: Single molecule force spectroscopy measurements. *J. Mol. Biol.* 349:317–330.
14. Koch, S. J., and M. D. Wang. 2003. Dynamic force spectroscopy of protein-DNA interactions by unzipping DNA. *Phys. Rev. Lett.* 91:028103. Erratum in *Phys. Rev. Lett.* 2003. 91:049903.
15. Greenleaf, W. J., M. T. Woodside, E. A. Abbondanzieri, and S. M. Block. 2005. Passive all-optical force clamp for high-resolution laser trapping. *Phys. Rev. Lett.* 95:208102.
16. Bustamante, C., Z. Bryant, and S. B. Smith. 2003. Ten years of tension: Single-molecule DNA mechanics. *Nature*. 421:423–427.
17. Smith, D. E., S. J. Tans, S. B. Smith, S. Grimes, D. L. Anderson, and C. Bustamante. 2001. The bacteriophage phi 29 portal motor can package DNA against a large internal force. *Nature*. 413:748–752.
18. Shaevitz, J. W., E. A. Abbondanzieri, R. Landick, and S. M. Block. 2003. Backtracking by single RNA polymerase molecules observed at near-base-pair resolution. *Nature*. 426:684–687.
19. Rief, M., R. S. Rock, A. D. Mehta, M. S. Mooseker, R. E. Cheney, and J. A. Spudich. 2000. Myosin-V stepping kinetics: A molecular model for processivity. *Proc. Natl. Acad. Sci. USA.* 97:9482–9486.
20. Asbury, C. L., A. N. Fehr, and S. M. Block. 2003. Kinesin moves by an asymmetric hand-over-hand mechanism. *Science*. 302:2130–2134.
21. Pierce, D. W., N. Hom-Booher, and R. D. Vale. 1997. Imaging individual green fluorescent proteins. *Nature*. 388:338.
22. Ishijima, A., H. Kojima, T. Funatsu, M. Tokunaga, H. Higuchi, H. Tanaka, and T. Yanagida. 1998. Simultaneous observation of individual ATPase and mechanical events by a single myosin molecule during interaction with actin. *Cell*. 92:161–171.
23. Harada, Y., T. Funatsu, K. Murakami, Y. Nonoyama, A. Ishihama, and T. Yanagida. 1999. Single-molecule imaging of RNA polymerase-DNA interactions in real time. *Biophys. J.* 76:709–715.
24. Lang, M. J., P. M. Fordyce, A. M. Engh, K. C. Neuman, and S. M. Block. 2004. Simultaneous, coincident optical trapping and single-molecule fluorescence. *Nat. Methods.* 1:133–139.
25. Panchuk-Voloshina, N., R. P. Haugland, J. Bishop-Stewart, M. K. Bhalgat, P. J. Millard, F. Mao, W. Y. Leung, and R. P. Haugland. 1999. Alexa dyes, a series of new fluorescent dyes that yield exceptionally bright, photostable conjugates. *J. Histochem. Cytochem.* 47:1179–1188.
26. Lang, M. J., C. L. Asbury, J. W. Shaevitz, and S. M. Block. 2002. An automated two-dimensional optical force clamp for single molecule studies. *Biophys. J.* 83:491–501.
27. Visscher, K., S. P. Gross, and S. M. Block. 1996. Construction of multiple-beam optical traps with nanometer-resolution position sensing. *IEEE J. Sel. Top. Quant.* 2:1066–1076.
28. Gittes, F., and C. F. Schmidt. 1998. Back-focal-plane detection of force and motion in optical traps. *Biophys. J.* 74:A183.
29. Kapanidis, A. N., N. K. Lee, T. A. Laurence, S. Doose, E. Margeat, and S. Weiss. 2004. Fluorescence-aided molecule sorting: Analysis of structure and interactions by alternating-laser excitation of single molecules. *Proc. Natl. Acad. Sci. USA.* 101:8936–8941.
30. Lee, S. H., K. Ladavac, M. Polin, and D. G. Grier. 2005. Observation of flux reversal in a symmetric optical thermal ratchet. *Phys. Rev. Lett.* 94:110601.
31. Neuman, K. C., E. A. Abbondanzieri, R. Landick, J. Gelles, and S. M. Block. 2003. Ubiquitous transcriptional pausing is independent of RNA polymerase backtracking. *Cell*. 115:437–447.
32. Ha, T., I. Rasnik, W. Cheng, H. P. Babcock, G. H. Gauss, T. M. Lohman, and S. Chu. 2002. Initiation and re-initiation of DNA unwinding by the Escherichia coli Rep helicase. *Nature*. 419:638–641.
33. Hoogenboom, J. P., E. M. van Dijk, J. Hernando, N. F. van Hulst, and M. F. Garcia-Parajo. 2005. Power-law-distributed dark states are the main pathway for photobleaching of single organic molecules. *Phys. Rev. Lett.* 95:097401.
34. Curtis, J. E., B. A. Koss, and D. G. Grier. 2002. Dynamic holographic optical tweezers. *Opt. Commun.* 207:169–175.
35. Tokunaga, M., K. Kitamura, K. Saito, A. H. Iwane, and T. Yanagida. 1997. Single molecule imaging of fluorophores and enzymatic reactions achieved by objective-type total internal reflection fluorescence microscopy. *Biochem. Biophys. Res. Commun.* 235:47–53.
36. Wennmalm, S., and R. Rigler. 1999. On death numbers and survival times of single dye molecules. *J. Phys. Chem. B.* 103:2516–2519.
37. Liphardt, J., B. Onoa, S. B. Smith, I. Tinoco, and C. Bustamante. 2001. Reversible unfolding of single RNA molecules by mechanical force. *Science*. 292:733–737.
38. Keller Mayer, M. S. Z., S. B. Smith, H. L. Granzier, and C. Bustamante. 1997. Folding-unfolding transitions in single titin molecules characterized with laser tweezers. *Science*. 276:1112–1116.
39. Rief, M., M. Gautel, F. Oesterhelt, J. M. Fernandez, and H. E. Gaub. 1997. Reversible unfolding of individual titin immunoglobulin domains by AFM. *Science*. 276:1109–1112.
40. Kapanidis, A. N., T. A. Laurence, N. K. Lee, E. Margeat, X. X. Kong, and S. Weiss. 2005. Alternating-laser excitation of single molecules. *Acc. Chem. Res.* 38:523–533.
41. So, P. T. C., C. Y. Dong, B. R. Masters, and K. M. Berland. 2000. Two-photon excitation fluorescence microscopy. *Annu. Rev. Biomed. Eng.* 2:399–429.
42. Nishiyama, M., H. Higuchi, and T. Yanagida. 2002. Chemomechanical coupling of the forward and backward steps of single kinesin molecules. *Nat. Cell Biol.* 4:790–797.
43. Veigel, C., S. Schmitz, F. Wang, and J. R. Sellers. 2005. Load-dependent kinetics of myosin-V can explain its high processivity. *Nat. Cell Biol.* 7:861–869.
44. Warsaw, D. M., G. G. Kennedy, S. S. Work, E. B. Kremntsova, S. Beck, and K. M. Trybus. 2005. Differential labeling of myosin V heads with quantum dots allows direct visualization of hand-over-hand processivity. *Biophys. J.* 88:L30–L32.
45. Yildiz, A., H. Park, D. Safer, Z. H. Yang, L. Q. Chen, P. R. Selvin, and H. L. Sweeney. 2004. Myosin VI steps via a hand-over-hand mechanism with its lever arm undergoing fluctuations when attached to actin. *J. Biol. Chem.* 279:37223–37226.

46. Gordon, M. P., T. Ha, and P. R. Selvin. 2004. Single-molecule high-resolution imaging with photobleaching. *Proc. Natl. Acad. Sci. USA*. 101:6462–6465.
47. Reck-Peterson, S. L., and R. D. Vale. 2004. Molecular dissection of the roles of nucleotide binding and hydrolysis in dynein's AAA domains in *Saccharomyces cerevisiae*. *Proc. Natl. Acad. Sci. USA*. 101:1491–1495.
48. Tolic-Norrelykke, S. F., A. M. Engh, R. Landick, and J. Gelles. 2004. Diversity in the rates of transcript elongation by single RNA polymerase molecules. *J. Biol. Chem.* 279:3292–3299.
49. Schnitzer, M. J., and S. M. Block. 1995. Statistical kinetics of processive enzymes. *Cold Spring Harb. Symp. Quant. Biol.* 60:793–802.
50. Block, S. M., C. L. Asbury, J. W. Shaevitz, and M. J. Lang. 2003. Probing the kinesin reaction cycle with a 2D optical force clamp. *Proc. Natl. Acad. Sci. USA*. 100:2351–2356.
51. Chigaev, A., T. Buranda, D. C. Dwyer, E. R. Prossnitz, and L. A. Sklar. 2003. FRET detection of cellular alpha 4-integrin conformational activation. *Biophys. J.* 85:3951–3962.
52. Galbraith, C. G., K. M. Yamada, and M. P. Sheetz. 2002. The relationship between force and focal complex development. *J. Cell Biol.* 159:695–705.

## REVIEW ARTICLE

---

### Optical trapping

Keir C. Neuman and Steven M. Block<sup>a)</sup>

*Department of Biological Sciences, and Department of Applied Physics, Stanford University, Stanford, California 94305*

(Received 15 January 2004; accepted 14 June 2004; published 2 September 2004)

Since their invention just over 20 years ago, optical traps have emerged as a powerful tool with broad-reaching applications in biology and physics. Capabilities have evolved from simple manipulation to the application of calibrated forces on—and the measurement of nanometer-level displacements of—optically trapped objects. We review progress in the development of optical trapping apparatus, including instrument design considerations, position detection schemes and calibration techniques, with an emphasis on recent advances. We conclude with a brief summary of innovative optical trapping configurations and applications.

© 2004 American Institute of Physics. [DOI: 10.1063/1.1785844]

#### I. INTRODUCTION

Arthur Ashkin pioneered the field of laser-based optical trapping in the early 1970s. In a series of seminal papers, he demonstrated that optical forces could displace and levitate micron-sized dielectric particles in both water and air,<sup>1</sup> and he developed a stable, three-dimensional trap based on counterpropagating laser beams.<sup>2</sup> This seminal work eventually led to the development of the single-beam gradient force optical trap,<sup>3</sup> or “optical tweezers,” as it has come to be known.<sup>4</sup> Ashkin and co-workers employed optical trapping in a wide-ranging series of experiments from the cooling and trapping of neutral atoms<sup>5</sup> to manipulating live bacteria and viruses.<sup>6,7</sup> Today, optical traps continue to find applications in both physics and biology. For a recent survey of the literature on optical tweezers see Ref. 8. The ability to apply piconewton-level forces to micron-sized particles while simultaneously measuring displacement with nanometer-level precision (or better) is now routinely applied to the study of molecular motors at the single-molecule level,<sup>9–19</sup> the physics of colloids and mesoscopic systems,<sup>20–29</sup> and the mechanical properties of polymers and biopolymers.<sup>18,20,30–43</sup> In parallel with the widespread use of optical trapping, theoretical and experimental work on fundamental aspects of optical trapping is being actively pursued.<sup>4,20,44–48</sup> In addition to the many excellent reviews of optical trapping<sup>9,49–53</sup> and specialized applications of optical traps, several comprehensive guides for building optical traps are now available.<sup>54–60</sup> For the purpose of this review, we will concentrate on the fundamental aspects of optical trapping with particular emphasis on recent advances.

Just as the early work on optical trapping was made possible by advances in laser technology,<sup>4</sup> much of the recent progress in optical trapping can be attributed to further technological development. The advent of commercially available, three-dimensional (3D) piezoelectric stages with ca-

pacitive sensors has afforded unprecedented control of the position of a trapped object. Incorporation of such stages into optical trapping instruments has resulted in higher spatial precision and improved calibration of both forces and displacements. In addition, stage-based force clamping techniques have been developed that can confer certain advantages over other approaches of maintaining the force, such as dynamically adjusting the position or stiffness of the optical trap. The use of high-bandwidth position detectors<sup>61</sup> improves force calibration, particularly for very stiff traps, and extends the detection bandwidth of optical trapping measurements. In parallel with these technological improvements, recent theoretical work has led to a better understanding of 3D position detection<sup>62–64</sup> and progress has been made in calculating the optical forces on spherical objects with a range of sizes.<sup>65,66</sup>

#### II. PRINCIPLES OF OPTICAL TRAPPING

An optical trap is formed by tightly focusing a laser beam with an objective lens of high numerical aperture (NA). A dielectric particle near the focus will experience a force due to the transfer of momentum from the scattering of incident photons. The resulting optical force has traditionally been decomposed into two components: (1) a scattering force, in the direction of light propagation and (2) a gradient force, in the direction of the spatial light gradient. This decomposition is merely a convenient and intuitive means of discussing the overall optical force. Following tradition, we present the optical force in terms of these two components, but we stress that both components arise from the very same underlying physics (see theoretical progress, below for a unified expression). The scattering component of the force is the more familiar of the two, which can be thought of as a photon “fire hose” pushing the bead in the direction of light propagation. Incident light impinges on the particle from one direction, but is scattered in a variety of directions, while some of the incident light may be absorbed. As a result, there

<sup>a)</sup>Electronic mail: sblock@stanford.edu

is a net momentum transfer to the particle from the incident photons. For an isotropic scatterer, the resulting forces cancel in all but the forward direction, and an effective scattering cross section can be calculated for the object. For most conventional situations, the scattering force dominates. However, if there is a steep intensity gradient (i.e., near the focus of a laser), the second component of the optical force, the gradient force, must be considered. The gradient force, as the name suggests, arises from the fact that a dipole in an inhomogeneous electric field experiences a force in the direction of the field gradient.<sup>67</sup> In an optical trap, the laser induces fluctuating dipoles in the dielectric particle, and it is the interaction of these dipoles with the inhomogeneous electric field at the focus that gives rise to the gradient trapping force. The gradient force is proportional to both the polarizability of the dielectric and the optical intensity gradient at the focus.

For stable trapping in all three dimensions, the axial gradient component of the force pulling the particle towards the focal region must exceed the scattering component of the force pushing it away from that region. This condition necessitates a very steep gradient in the light, produced by sharply focusing the trapping laser beam to a diffraction-limited spot using an objective of high NA. As a result of this balance between the gradient force and the scattering force, the axial equilibrium position of a trapped particle is located slightly beyond (i.e., down-beam from) the focal point. For small displacements ( $\sim 150$  nm), the gradient restoring force is simply proportional to the offset from the equilibrium position, i.e., the optical trap acts as Hookean spring whose characteristic stiffness is proportional to the light intensity.

In developing a theoretical treatment of optical trapping, there are two limiting cases for which the force on a sphere can be readily calculated. When the trapped sphere is much larger than the wavelength of the trapping laser, i.e., the radius ( $a$ )  $\gg \lambda$ , the conditions for Mie scattering are satisfied, and optical forces can be computed from simple ray optics (Fig. 1). Refraction of the incident light by the sphere corresponds to a change in the momentum carried by the light. By Newton's third law, an equal and opposite momentum change is imparted to the sphere. The force on the sphere, given by the rate of momentum change, is proportional to the light intensity. When the index of refraction of the particle is greater than that of the surrounding medium, the optical force arising from refraction is in the direction of the intensity gradient. Conversely, for an index lower than that of the medium, the force is in the opposite direction of the intensity gradient. The scattering component of the force arises from both the absorption and specular reflection by the trapped object. In the case of a uniform sphere, optical forces can be directly calculated in the ray-optics regime.<sup>68,69</sup> The extremal rays contribute disproportionately to the axial gradient force, whereas the central rays are primarily responsible for the scattering force. Thus, expanding a Gaussian laser beam to slightly overfill the objective entrance pupil can increase the ratio of trapping to scattering force, resulting in improved trapping efficiency.<sup>69,70</sup> In practice, the beam is typically expanded such that the  $1/e^2$  intensity points match the objective aperture, resulting in  $\sim 87\%$  of the incident power enter-

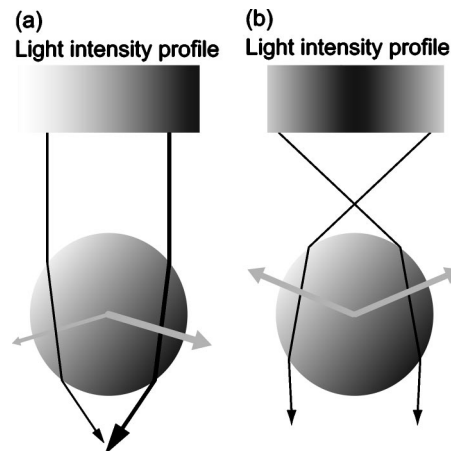


FIG. 1. Ray optics description of the gradient force. (A) A transparent bead is illuminated by a parallel beam of light with an intensity gradient increasing from left to right. Two representative rays of light of different intensities (represented by black lines of different thickness) from the beam are shown. The refraction of the rays by the bead changes the momentum of the photons, equal to the change in the direction of the input and output rays. Conservation of momentum dictates that the momentum of the bead changes by an equal but opposite amount, which results in the forces depicted by gray arrows. The net force on the bead is to the right, in the direction of the intensity gradient, and slightly down. (B) To form a stable trap, the light must be focused, producing a three-dimensional intensity gradient. In this case, the bead is illuminated by a focused beam of light with a radial intensity gradient. Two representative rays are again refracted by the bead but the change in momentum in this instance leads to a net force towards the focus. Gray arrows represent the forces. The lateral forces balance each other out and the axial force is balanced by the scattering force (not shown), which decreases away from the focus. If the bead moves in the focused beam, the imbalance of optical forces will draw it back to the equilibrium position.

ing the objective. Care should be exercised when overfilling the objective. Absorption of the excess light by the blocking aperture can cause heating and thermal expansion of the objective, resulting in comparatively large ( $\sim \mu\text{m}$ ) axial motions when the intensity is changed. Axial trapping efficiency can also be improved through the use of “donut” mode trapping beams, such as the  $\text{TEM}_{01}^*$  mode or Laguerre-Gaussian beams, which have intensity minima on the optical propagation axis.<sup>69,71–73</sup>

When the trapped sphere is much smaller than the wavelength of the trapping laser, i.e.,  $a \ll \lambda$ , the conditions for Rayleigh scattering are satisfied and optical forces can be calculated by treating the particle as a point dipole. In this approximation, the scattering and gradient force components are readily separated. The scattering force is due to absorption and reradiation of light by the dipole. For a sphere of radius  $a$ , this force is

$$F_{\text{scatt}} = \frac{I_0 \sigma n_m}{c}, \quad (1)$$

$$\sigma = \frac{128 \pi^5 a^6}{3 \lambda^4} \left( \frac{m^2 - 1}{m^2 + 2} \right)^2, \quad (2)$$

where  $I_0$  is the intensity of the incident light,  $\sigma$  is the scattering cross section of the sphere,  $n_m$  is the index of refraction of the medium,  $c$  is the speed of light in vacuum,  $m$  is the ratio of the index of refraction of the particle to the index of the medium ( $n_p/n_m$ ), and  $\lambda$  is the wavelength of the trap-

ping laser. The scattering force is in the direction of propagation of the incident light and is proportional the intensity. The time-averaged gradient force arises from the interaction of the induced dipole with the inhomogeneous field

$$F_{\text{grad}} = \frac{2\pi\alpha}{cn_m^2} \nabla I_0, \tag{3}$$

where

$$\alpha = n_m^2 a^3 \left( \frac{m^2 - 1}{m^2 + 2} \right) \tag{4}$$

is the polarizability of the sphere. The gradient force is proportional to the intensity gradient, and points up the gradient when  $m > 1$ .

When the dimensions of the trapped particle are comparable to the wavelength of the trapping laser ( $a \sim \lambda$ ), neither the ray optic nor the point-dipole approach is valid. Instead, more complete electromagnetic theories are required to supply an accurate description.<sup>74-80</sup> Unfortunately, the majority of objects that are useful or interesting to trap, in practice, tend to fall into this intermediate size range ( $0.1-10\lambda$ ). As a practical matter, it can be difficult to work with objects smaller than can be readily observed by video microscopy ( $\sim 0.1 \mu\text{m}$ ), although particles as small as  $\sim 35 \text{ nm}$  in diameter have been successfully trapped. Dielectric microspheres used alone or as handles to manipulate other objects are typically in the range of  $\sim 0.2-5 \mu\text{m}$ , which is the same size range as biological specimens that can be trapped directly, e.g., bacteria, yeast, and organelles of larger cells. Whereas some theoretical progress in calculating the force on a sphere in this intermediate size range has been made recently,<sup>65,66</sup> the more general description does not provide further insight into the physics of optical trapping. For this reason we postpone discussion of recent theoretical work until the end of the review.

### III. DESIGN CONSIDERATIONS

Implementing a basic optical trap is a relatively straightforward exercise (Fig. 2).<sup>55,58</sup> The essential elements are a trapping laser, beam expansion and steering optics, a high NA objective, a trapping chamber holder, and some means of observing the trapped specimen. Optical traps are most often built by modifying an inverted microscope so that a laser beam can be introduced into the optical path before the objective: the microscope then provides the imaging, trapping chamber manipulation, and objective focus functions. For anything beyond simply trapping and manually manipulating objects, however, additional elements become necessary. Dynamic control of trap position and stiffness can be achieved through beam steering and amplitude modulation elements incorporated in the optical path before the laser beam enters the objective. Dynamic control over position and stiffness of the optical trap has been exploited to implement position- and force-clamp systems. Position clamps, in which the position of a trapped object is held constant by varying the force, are well suited for stall force measurements of molecular motors.<sup>39,49,81-83</sup> Force clamps, in which the force on a trapped object is fixed by varying the position of the trap, are

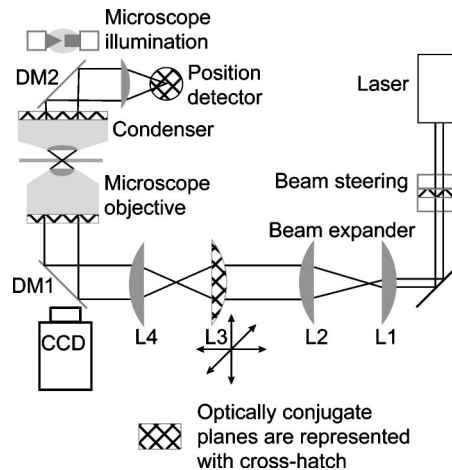


FIG. 2. Layout of a generic optical trap. The laser output beam usually requires expansion to overfill the back aperture of the objective. For a Gaussian beam, the beam waist is chosen to roughly match the objective back aperture. A simple Keplerian telescope is sufficient to expand the beam (lenses L1 and L2). A second telescope, typically in a 1:1 configuration, is used for manually steering the position of the optical trap in the specimen plane. If the telescope is built such that the second lens, L4, images the first lens, L3, onto the back aperture of the objective, then movement of L3 moves the optical trap in the specimen plane with minimal perturbation of the beam. Because lens L3 is optically conjugate (conjugate planes are indicated by a cross-hatched fill) to the back aperture of the objective, motion of L3 rotates the beam at the aperture, which results in translation in the specimen plane with minimal beam clipping. If lens L3 is not conjugate to the back aperture, then translating it leads to a combination of rotation and translation at the aperture, thereby clipping the beam. Additionally, changing the spacing between L3 and L4 changes the divergence of the light that enters the objective, and the axial location of the laser focus. Thus, L3 provides manual three-dimensional control over the trap position. The laser light is coupled into the objective by means of a dichroic mirror (DM1), which reflects the laser wavelength, while transmitting the illumination wavelength. The laser beam is brought to a focus by the objective, forming the optical trap. For back focal plane position detection, the position detector is placed in a conjugate plane of the condenser back aperture (condenser iris plane). Forward scattered light is collected by the condenser and coupled onto the position detector by a second dichroic mirror (DM2). Trapped objects are imaged with the objective onto a camera. Dynamic control over the trap position is achieved by placing beam-steering optics in a conjugate plane to the objective back aperture, analogous to the placement of the trap steering lens. For the case of beam-steering optics, the point about which the beam is rotated should be imaged onto the back aperture of the objective.

well suited for displacement measurements.<sup>49,56,81,84,85</sup> Incorporation of a piezoelectric stage affords dynamic positioning of the sample chamber relative to the trap, and greatly facilitates calibration. Furthermore, for the commonly employed geometry in which the molecule of interest is attached between the surface of the trapping cell and a trapped bead “handle,” piezoelectric stages can be used to generate a force clamp.<sup>86-88</sup> The measurement of force and displacement within the optical trap requires a position detector, and, in some configurations, a second, low power laser for detection. We consider each of these elements in detail.

#### A. Commercial systems

Commercial optical trapping systems with some limited capabilities are available. Cell Robotics<sup>89</sup> manufactures a laser-trapping module that can be added to a number of inverted microscopes. The module consists of a 1.5 W diode pumped Nd:YVO<sub>4</sub> laser ( $\lambda = 1064 \text{ nm}$ ) with electronic inten-

sity control, and all of the optics needed to both couple the laser into the microscope and manually control the position of the trap in the specimen plane. The same module is incorporated into the optical tweezers workstation, which includes a microscope, a motorized stage and objective focus, video imaging, and a computer interface. Arryx Incorporated<sup>90</sup> manufactures a complete optical trapping workstation that includes a 2 W diode pumped solid-state laser ( $\lambda=532$  nm), holographic beam shaping and steering, an inverted microscope, a motorized stage, and computer control. Holographic beam shaping provides control over the phase of the trapping laser,<sup>91,92</sup> which allows multiple, individually addressable, optical traps in addition to high order, complex trapping beams. An integrated optical trap is also available from PALM Microlaser Technologies,<sup>93</sup> either alone or incorporated with their microdissection system. The PALM system employs an infrared trapping laser and computer control of the stage, similar to the other optical trapping systems. The commercial systems tend to be expensive, but they offer turnkey convenience at the price of flexibility and control. None of the systems currently comes equipped with position detection capabilities beyond video imaging, and only one (Arpyx) provides dynamic control over the trap position, but with an unknown update rate ( $\sim 5$  Hz or less). Overall, these systems are adequate for positioning and manipulating objects but are incapable, without further modifications, of ultrasensitive position or force measurements. As commercial systems become increasingly sophisticated and versatile, they may eventually offer an “off-the-shelf” option for some optical trapping applications. In deciding between a commercial or custom-built optical trap, or among commercial systems, several factors should be considered. Basic considerations include cost, maximum trap force and stiffness, choice of laser wavelength (important for biological samples), specimen or trap positioning capability, optical imaging modes, position-detection capabilities, and sample geometry. In addition, flexibility and the possibility to upgrade or improve aspects of the system should also be considered. How easily can the optical system be modified or adapted? Can the functionality be upgraded? Perhaps the most fundamental question concerns the decision to buy or to build. Whereas building a basic optical trap is now standard practice in many labs, it requires a certain familiarity with optics and optical components (in relation to the complexity of the optical trap), as well as a significant time investment for the design, construction, and debugging phases. These factors should be weighed against the potential benefits of reduced cost, increased flexibility and greater control of home-built optical traps.

## B. Trapping laser

The basic requirement of a trapping laser is that it delivers a single mode output (typically, Gaussian TEM<sub>00</sub> mode) with excellent pointing stability and low power fluctuations. A Gaussian mode focuses to the smallest diameter beam waist and will therefore produce the most efficient, harmonic trap. Pointing instabilities lead to unwanted displacements of the optical trap position in the specimen plane, whereas power fluctuations lead to temporal variations in the optical

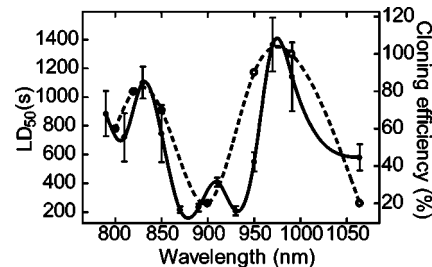


FIG. 3. The wavelength dependence of photodamage in *E. coli* compared to Chinese hamster ovary (CHO) cells. (Solid circles and solid line, left axis, half lethal dose time for *E. coli* cells (LD<sub>50</sub>); open circles and dashed line, right axis, cloning efficiency in CHO cells determined by Liang *et al.* (Ref. 96) (used with permission). Lines represent cubic spline fits to the data). The cloning efficiency in CHO cells was determined after 5 min of trapping at 88 mW in the specimen plane (error bars unavailable), selected to closely match to our experimental conditions (100 mW in the specimen plane, errors shown as  $\pm$  standard error in the mean). Optical damage is minimized at 830 and 970 nm for both *E. coli* and CHO cells, whereas it is most severe in the region between 870 and 930 nm (reprinted from Ref. 95).

trap stiffness. Pointing instability can be remedied by coupling the trapping laser to the optical trap via an optical fiber, or by imaging the effective pivot point of the laser pointing instability into the front focal plane of the objective. Both of these solutions however, trade reduced pointing stability against additional amplitude fluctuations, as the fiber coupling and the clipping by the back aperture of the microscope objective depend on beam pointing. Thus, both power and pointing fluctuations introduce unwanted noise into any trapping system. The choice of a suitable trapping laser therefore depends on several interdependent figures of merit (power, power stability, pointing stability, thermal drift, wavelength, mode quality, etc.).

Output power of the trapping laser and the throughput of the optical system will determine the maximum attainable stiffness and force. As discussed above, trapping forces depend on multiple parameters and are difficult to calculate for most conditions of practical interest. Generally speaking, maximum trapping forces on the order of 1 pN per 10 mW of power delivered to the specimen plane can be achieved with micron-scale beads.<sup>9</sup> As a specific example, trapping a 0.5  $\mu\text{m}$  polystyrene ( $n=1.57$ ) sphere in water with a TEM<sub>00</sub> 1064 nm laser that overfills a 1.2 NA objective by  $\sim 10\%$  ( $1/e^2$  intensity points matched to the aperture radius), gives a stiffness of 0.16 pN/nm per W of power in the specimen plane. In practice, laser power levels can range from a few mW to a Watt or more in the specimen plane, depending on details of the laser and setup, objective transmittance, and the desired stiffness.

Wavelength is an important consideration when biological material is trapped, particularly for *in vivo* trapping of cells or small organisms.<sup>94</sup> There is a window of relative transparency in the near infrared portion of the spectrum ( $\sim 750$ – $1200$  nm), located in the region between the absorption of proteins in the visible and the increasing absorption of water towards the infrared.<sup>9</sup> Substantial variation with wavelength of optical damage to biological specimens is observed even within the near infrared region (Fig. 3), with damage minima occurring at 970 and 830 nm<sup>95–97</sup> for bacterial cells of *Escherichia coli*. If dam-

age or “optiction”<sup>98</sup> of biological specimens is not a concern, then the choice of wavelength becomes less critical, but the potential effects of heating resulting from light absorption by the medium or the trapped particle should certainly be considered.<sup>99–101</sup> The optimal choice of trapping wavelength will also depend on the transmission of the objective used for optical trapping (discussed below), as well as the output power available at a given wavelength.

In practice, a variety of lasers has been employed for optical trapping. The factors discussed above, along with the cost, will determine the final selection of a trapping laser. The laser of choice for working with biological samples is currently the neodymium:yttrium–aluminum–garnet (Nd:YAG) laser and its close cousins, neodymium:yttrium–lithium–fluoride (Nd:YLF), and neodymium:yttrium–orthovanadate (Nd:YVO<sub>4</sub>). These lasers operate in the near infrared region of the spectrum at 1.047, 1.053, or 1.064  $\mu\text{m}$ , which helps to limit optical damage. Diode pumped versions of these lasers offer high power (up to 10 W or even more) and superior amplitude and pointing stability. An additional advantage of diode-pumped solid-state (DPSS) lasers is that the noise and heat of the laser power supply can be physically isolated from the laser itself and the immediate region of the optical trap. The output of the pump diodes can be delivered to the laser head via an optical fiber bundle, in some cases up to 10 m in length. The main drawback of such DPSS lasers is their cost, currently on the order of \$5–10 K per W of output power. Diode lasers afford a lower-cost alternative in a compact package and are available at several wavelengths in the near infrared, but these devices are typically limited to less than  $\sim 250$  mW in a single-transverse mode, the mode required for efficient trapping. Diode lasers also suffer significantly from mode instabilities and noncircular beams, which necessitates precise temperature control instrumentation and additional corrective optics. By far the most expensive laser option is a tunable cw titanium:sapphire (Ti:sapphire) laser pumped by a DPSS laser, a system that delivers high power ( $\sim 1$  W) over a large portion of the near infrared spectrum ( $\sim 750$ – $950$  nm), but at a current cost in excess of \$100 K. The large tuning range is useful for parametric studies of optical trapping, to optimize the trapping wavelength, or to investigate the wavelength-dependence of optical damage.<sup>95</sup> A Ti:sapphire laser is also employed for optical trapping *in vivo*<sup>94</sup> since it is the only laser currently available that can deliver over  $\sim 250$  mW at the most benign wavelengths (830 and 970 nm).<sup>95</sup>

In optical trapping applications where no biological materials will be trapped, any laser source that meets the basic criteria of adequate power in the specimen plane, sufficient pointing and amplitude stability, and a Gaussian intensity profile, may be suitable. Optical traps have been built based on argon ion,<sup>3</sup> helium-neon,<sup>102</sup> and diode laser sources,<sup>103,104</sup> to name a few. The DPSS lasers employed in our lab for biological work supply  $\sim 4$  W of power at 1064 nm with power fluctuations below 1%–2% and a long-term pointing stability of  $\pm 50$   $\mu\text{rad}$ .

### C. Microscope

Most optical traps are built around a conventional light microscope, requiring only minor modifications. This approach reduces the construction of an optical trap to that of coupling the light from a suitable trapping laser into the optical path before the objective without compromising the original imaging capabilities of the microscope. In practice, this is most often achieved by inserting a dichroic mirror, which reflects the trapping laser light into the optical path of the microscope but transmits the light used for microscope illumination. Inverted, rather than upright, microscopes are often preferred for optical trapping because their stage is fixed and the objective moves, making it easier to couple the trapping light stably. The use of a conventional microscope also makes it easier to use a variety of available imaging modalities, such as differential interference contrast and epifluorescence.

With more extensive modifications, a position detector can be incorporated into the trapping system. This involves adding a second dichroic mirror on the condenser side of the microscope, which reflects the laser light while transmitting the illuminating light. In order to achieve the mechanical stability and rigidity required for nanometer scale position measurements, more extensive modifications of the microscope are generally required.<sup>50,59</sup> In the current generation of optical traps, the rotating, multiobjective turret is conventionally replaced with a custom-built single objective holder, along with a mount for the dichroic mirror. The original stage is removed and the microscope is modified to accommodate a more substantial stage platform, holding a crossed-roller bearing stage (for coarse movement) mounted to a piezoelectric stage with feedback (for fine movement). Finally, the condenser assembly is attached to a fine focus transport (similar to that used for the objective) that is then mounted to the illumination column by a rigid aluminum beam.<sup>59</sup>

An alternative to the redesign and retrofitting of a commercial microscope is to build the entire optical trap from individual optical components.<sup>57,103,104</sup> This approach is slightly more involved, as the entirety of the imaging and trapping optical paths have to be designed and built. The increase in complexity, however, can be offset by increased flexibility in the design and a wider choice of components, greater access to the optical paths, and reduced cost.

### D. Objective

The single most important element of an optical trap is the objective used to focus the trapping laser. The choice of objective determines the overall efficiency of the optical trapping system (stiffness versus input power), which is a function of both the NA and the transmittance of the objective. Additionally, the working distance and the immersion medium of the objective (oil, water, or glycerol) will set practical limits on the depth to which objects can be trapped. Spherical aberrations, which degrade trap performance, are proportional to the refractive index mismatch between the immersion medium and the aqueous trapping medium. The deleterious effect of these aberrations increases with focal depth. The working distance of most high NA oil immersion

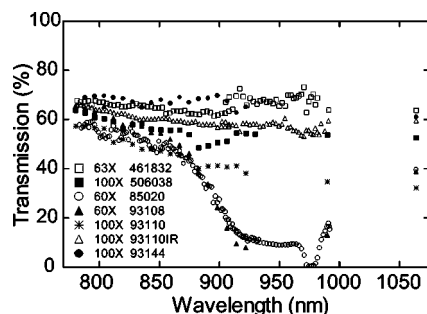


FIG. 4. Microscope objective transmission curves. Transmission measurements were made by means of the dual-objective method. Part numbers are cross-referenced in Table I. The uncertainty associated with a measurement at any wavelength is  $\sim 5\%$  (reprinted from Ref. 95).

objectives is quite short ( $\sim 0.1$  mm), and the large refractive index mismatch between the immersion oil ( $n=1.512$ ) and the aqueous trapping medium ( $n\sim 1.32$ ) leads to significant spherical aberrations. In practice, this limits the maximum axial range of the optical trap to somewhere between 5 and 20  $\mu\text{m}$  from the coverglass surface of the trapping chamber.<sup>104</sup> Trapping deeper into solution can be achieved with water immersion objectives that minimize spherical aberration<sup>105</sup> and which are available with longer working distances. A high NA objective (typically, 1.2–1.4 NA) is required to produce an intensity gradient sufficient to overcome the scattering force and produce a stable optical trap for microscopic objects, such as polystyrene beads. The vast majority of high NA objectives are complex, multielement optical assemblies specifically designed for imaging visible light, not for focusing an infrared laser beam. For this reason, the optical properties of different objectives can vary widely over the near infrared region (Fig. 4).<sup>9,95</sup> Generally speaking, objectives designed for general fluorescence microscopy display superior transmission over the near infrared compared to most general-purpose objectives, as do infrared-rated objectives specifically produced for use with visible and near infrared light (Table I). Given the wide variation in transmission characteristics for different objectives, an objective being considered for optical trapping should be characterized at the wavelength of the trapping light. Manufacturers rarely supply the transmission characteristics of objectives outside the visible portion of the spectrum. When transmission characteristics in the near infrared are provided, the figures may represent an overestimate, since the throughput of the objective is often measured using an integrating sphere, which

also registers scattered light that is not well focused, and hence does not contribute to trapping. To measure the effective transmission of a high NA objective accurately, the dual objective method is preferred,<sup>9,95,106</sup> in which two identical, matched objectives are used to focus and then recollimate the laser beam (the transmission of a single objective is the square root of the transmission for the objective pair). Furthermore, because the transmission may depend on the degree to which light is bent, the laser beam should be expanded to fill the objective rear aperture. It should be noted that the extremely steep focusing produced by high NA objectives can lead to specular reflection from surfaces at the specimen plane, so simply measuring the throughput of an objective by placing the probe of a power meter directly in front of the objective lens results in an underestimation of its transmission. This approach is not recommended.

## E. Position detection

Sensitive position detection lies at the heart of quantitative optical trapping, since nanoscale measurements of both force and displacement rely on a well-calibrated system for determining position. Position tracking of irregularly shaped objects is feasible, but precise position *and force calibration* are currently only practical with spherical objects. For this purpose, microscopic beads are either used alone, or attached to objects of interest as “handles,” to apply calibrated forces. The position detection schemes presented here were primarily developed to track microscopic silica or polystyrene beads. However, the same techniques may be applied to track other objects, such as bacterial cells.<sup>107–109</sup>

### 1. Video based position detection

For simple imaging of a trapped particle, a video camera mounted to the camera port of the microscope (or elsewhere) often suffices. By digitally processing the signal acquired from the camera, and knowing the size subtended by a single pixel (e.g., by calibrating the video picture against a distance standard, such as a ruled objective micrometer), the position of a trapped object can be determined with subpixel accuracy (typically, to within  $\sim 5$  nm or better), using any of several centroid-finding algorithms.<sup>110–112</sup> Video tracking of trapped objects using such algorithms has been implemented in real time,<sup>113,114</sup> but this approach is restricted to video acquisition rates (typically  $\sim 25$ –120 Hz), and the precision is ultimately limited by video timing jitter (associated with frame

TABLE I. Transmission of microscope objectives, cross-referenced with Fig. 2.

Part No.	Manufacturer	Magnification/ Tube length (mm)/ Numerical aperture	Type designation	Transmission ( $\pm 5\%$ )			
				830 (nm)	850 (nm)	990 (nm)	1064 (nm)
461832	Zeiss	63/160/1.2 Water	Plan NeoFluar	66	65	64	64
506038	Leica	100/ $\infty$ /1.4-0.7 Oil	Plan Apo	58	56	54	53
85020	Nikon	60/160/1.4 Oil	Plan Apo	54	51	17	40
93108	Nikon	60/ $\infty$ /1.4 Oil	Plan Apo CFI	59	54	13	39
93110	Nikon	100/ $\infty$ /1.4 Oil	Plan Apo CFI	50	47	35	32
93110IR	Nikon	100/ $\infty$ /1.4 Oil	Plan Apo IR CFI	61	60	59	59
93144	Nikon	100/ $\infty$ /1.3 Oil	Plan Fluor CFI	67	68	—	61

acquisition) or variations in illumination. In principle, temporal resolution could be improved through the use of high speed video cameras. Burst frame rates in excess of 40 kHz can be achieved with specialized complementary metal oxide semiconductor (CMOS) cameras, for example. However, the usefulness of high speed cameras can be limited by computer speed or memory capacity. Current CPU speed limits real-time position tracking to  $\sim 500$  Hz,<sup>115</sup> while practical storage considerations limit the number of high-resolution frames that can be stored to  $\sim 10^5$ , which corresponds to less than 2 min of high-speed video at 1 kHz. Even if these technological hurdles are overcome, high-speed video tracking is ultimately limited by the number of recorded photons (since shorter exposures require more illumination), so spatial resolution decreases as the frame rate increases. Generally speaking, the signal-to-noise ratio is expected to decrease as the square root of the frame rate. The discrepancy between the low video bandwidth ( $\sim 100$  Hz) and the much higher intrinsic bandwidth of even a relatively weak optical trap ( $\sim$ kHz) results in aliasing artifacts, and these preclude the implementation of many of the most effective calibration methods. Furthermore, video-based methods are not well suited to the measurement of the *relative* position of an object with respect to the trap center, further complicating force determination.

## 2. Imaging position detector

Several alternative (nonvideo) methods have been developed that offer precise, high-bandwidth position detection of trapped objects. The simplest of these is to image directly the trapped object onto a quadrant photodiode (QPD),<sup>56,116,117</sup> The diode quadrants are then summed pairwise, and differential signals are derived from the pairs for both  $x$  and  $y$  dimensions. If desired, the differential signals can be normalized by the sum signal from the four quadrants to reduce the dependence of the output on the total light intensity. Direct imaging of a trapped particle is typically restricted to a small zone within the specimen plane, and requires careful coalignment of the trap with the region viewed by the detector. Moreover, the high magnification required to achieve good spatial resolution results in comparatively low light levels at the QPD, ultimately limiting bandwidth and noise performance.<sup>49,50</sup> The latter limitation has been addressed by the use of a diode laser operating just below its lasing threshold, acting as a superbright, incoherent illumination source.<sup>56</sup> Imaging using laser illumination is considered impractical because of the speckle and interference that arise from coherent illumination over an extended region. Various laser phase-randomization approaches may relieve this restriction, but these typically carry additional disadvantages, most often reduced temporal bandwidth.

## 3. Laser-based position detection

Laser-based position detection is appealing, because it is possible to use a single laser for both trapping and position detection. Unlike the imaging detector scheme described above, laser-based detection requires the incorporation of a dichroic mirror on the condenser side of the microscope to couple out the laser light scattered by the specimen. Further-

more, the detector and its associated optics (lens, filters) must be stably mounted on (or next to) the condenser to collect the output light. Two different laser-based position detection schemes have been developed. The first relies on polarization interferometry.<sup>9,49,50,118,119</sup> This method is quite analogous to differential interference contrast (DIC) microscopy, and it relies on a subset of the DIC imaging components within the microscope. Incoming plane polarized laser light is split by a Wollaston prism into two orthogonal polarizations that are physically displaced from one another. After passing through the specimen plane, the beams are recombined in a second Wollaston prism and the polarization state of the recombined light is measured. A simple polarimeter consists of a quarter wave plate (adjusted so that plane-polarized light is transformed into circularly polarized light) followed by a polarizing beam splitter. The intensity in each branch of the beam splitter is recorded by a photodiode, and the normalized differential diode signal supplies the polarization state of the light. A bead centered in the trap introduces an equal phase delay in both beams, and the recombined light is therefore plane polarized. When the bead is displaced from its equilibrium position, it introduces a relative phase delay between the two beams, leading to a slight elliptical polarization after the beams are recombined. The ellipticity of the recombined light can be calibrated against physical displacement by moving a bead a known distance through the optical trap. This technique is extraordinarily sensitive<sup>118</sup> and is, in theory, independent of the position of the trapped object within the specimen plane, because the trapping and detection laser beams are one and the same, and therefore intrinsically aligned. In practice, however, there is a limited range over which the position signal is truly independent of the trap position. A further limitation of this technique is that it is one dimensional: it is sensitive to displacement along the Wollaston shear axis, providing position detection in a single lateral direction.

A second type of laser-based position detection scheme—back focal plane detection—relies on the interference between forward-scattered light from the bead and unscattered light.<sup>59,64,120–122</sup> The interference signal is monitored with a QPD positioned along the optical axis at a plane conjugate to the back focal plane of the condenser (rather than at an imaging plane conjugate to the specimen). The light pattern impinging on the QPD is then converted to a normalized differential output in both lateral dimensions as described above. By imaging the back focal plane of the condenser, the position signal becomes insensitive to absolute bead position in the specimen plane, and sensitive instead to the relative displacement of the bead from the laser beam axis.<sup>120</sup> As with the polarization interferometer, the detection beam and the optical trap are intrinsically aligned, however the QPD detection scheme can supply position information in both lateral dimensions.

Laser-based position detection schemes have also been implemented with a second, low-power detection laser.<sup>49,50,59,81</sup> The experimental complication of having to combine, spatially overlap, and then separate the trapping and detection beams is frequently outweighed by the advantages conferred by having an independent detection laser.

Uncoupling trapping and detection may become necessary, for example, when there are multiple traps produced in the specimen plane, or if the absolute position of a bead is the relevant measure, rather than the relative position of a bead from the optical trap. When dynamic position control of the optical trap is implemented (see below), a separate detection laser permits rapid position calibration of each trapped particle, and greatly simplifies position measurements in situations in which the trap is being moved.<sup>50</sup> The choice of a laser for position sensing is less constrained than that of a trapping laser, and only a few mW of output power suffice for most detection schemes. The total power should be kept as low as feasible to prevent the detection light from generating significant optical forces itself, thereby perturbing the trap. A detection laser wavelength chosen to match the peak sensitivity of the photodetector will minimize the amount of power required in the specimen plane. Separating the detection and trapping wavelengths facilitates combining and separating the two beams, but increases the constraints on the dichroic mirror that couples the laser beams into the microscope. We have found that combining two beams of similar wavelength is most easily accomplished with a polarizing beamsplitter, i.e., the beams are orthogonally plane polarized and combined in the polarizer before entering the microscope. Since the trapping and detection wavelengths are closely spaced, a single reflection band on the coupling dichroic mirror suffices to couple both beams into and out of the microscope. A holographic notch filter in front of the position detector provides  $\sim 6$  orders of magnitude of rejection at the trapping wavelength, permitting isolation and measurement of the much less intense detection beam.

#### 4. Axial position detection

The detection schemes described above were developed to measure lateral displacement of objects within the specimen plane, a major focus of most optical trapping work. Detecting axial motion within the optical trap has rarely been implemented and has not been as well characterized until recently. Axial motion has been determined by: measuring the intensity of scattered laser light on an overfilled photodiode,<sup>123–126</sup> through two-photon fluorescence generated by the trapping laser,<sup>127–130</sup> and by evanescent-wave fluorescence at the surface of a coverglass.<sup>131,132</sup> Although these various approaches all supply a signal related to axial position, they require the integration of additional detectors and, in some cases, fluorescence capability, into the optical trapping instrument. This can be somewhat cumbersome, consequently the techniques have not been widely adopted. The axial position of a trapped particle can also be determined from the total laser intensity in the back focal plane of the condenser.<sup>62,64</sup> The axial position signal derives from the interference between light scattered by the trapped particle and the unscattered beam. On passing through a focus, the laser light accumulates a phase shift of  $\pi$ , known as the Gouy phase.<sup>133</sup> The axial phase shift is given by  $\psi(z) = \tan^{-1}(z/z_0)$ , where  $z_0$  is the Rayleigh range ( $z_0 = \pi w_0^2/\lambda$ , where  $w_0$  is the beam waist and  $\lambda$  is the wavelength of light), and  $z$  is the axial displacement from the focus.<sup>133</sup> Light scattered by a particle located near the focus will preserve the

phase that it acquired prior to being scattered, whereas unscattered light will accumulate the full Gouy phase shift of  $\pi$ . The far-field interference between the scattered and unscattered light gives rise to an axial position-dependent intensity, which can be measured, for example, at the back focal plane of the condenser (see below and Fig. 8). This is the axial counterpart, in fact, of the lateral interference signal described above. Axial position detection can be achieved through a simple variant of quadrant photodiode-based lateral position detection. Recording the total incident intensity on the position detector supplies the axial position of trapped particle relative to the laser focus.<sup>63,64</sup> In contrast to lateral position detection, axial position detection is inversely proportional to the NA of the detector.<sup>62,63</sup> When a single detector is used to measure both lateral and axial position simultaneously, an intermediate detector NA should be used to obtain reasonable sensitivity in all three dimensions.

#### 5. Detector bandwidth limitations

Position detection based on lasers facilitates high bandwidth recording because of the high intensity of light incident on the photodetector. However, the optical absorption of silicon decreases significantly beyond  $\sim 850$  nm, therefore position sensing by silicon-based photodetectors is intrinsically bandwidth limited in the near infrared.<sup>61,134</sup> Berg-Sørensen and co-workers<sup>134</sup> demonstrated that the electrical response of a typical silicon photodiode to infrared light consists of both a fast and a slow component. The fast component results from optical absorption in the depletion region of the diode, where the optically generated electron hole pairs are rapidly swept to the electrodes. This represents the intended behavior of the diode, and is valid at wavelengths that are readily absorbed by the active material, i.e.,  $\lambda < \sim 1 \mu\text{m}$ . At longer wavelengths, however, a slow component also appears in the diode response, due to absorption of light beyond the depletion region. Electron-hole pairs generated in this zone must diffuse into the depletion region before flowing on to the electrodes, a much slower process. Infrared light is poorly absorbed by silicon, resulting in a greater proportion of the incident light being absorbed beyond the depletion region, increasing the relative contribution of the slow component. Thus, the output of the diode effectively becomes lowpass filtered ( $f_{3\text{dB}} \sim 8\text{--}9$  kHz at 1064 nm) in an intensity-, wavelength-, and reverse bias-dependent manner.<sup>134</sup> In principle, the effect of this lowpass filtering could be calculated and compensated, but in practice, this approach is complicated by the intensity dependence of the parasitic filtering. One workaround would be to employ a detection laser at a wavelength closer to the absorption maximum of silicon, i.e., shorter than  $\sim 850$  nm. Two other solutions include using nonsilicon-based detectors employing different photoactive materials, or using silicon-based photodetectors with architectures that minimize the parasitic filtering. Peterman and co-workers measured the wavelength dependence of parasitic filtering in a standard silicon-based detector. They also reported an increased bandwidth at wavelengths up to 1064 nm for an InGaAs diode as well as for a specialized, fully depleted silicon detector.<sup>61</sup> We have found that one commercial position sensitive detector (PSD) (Pa-

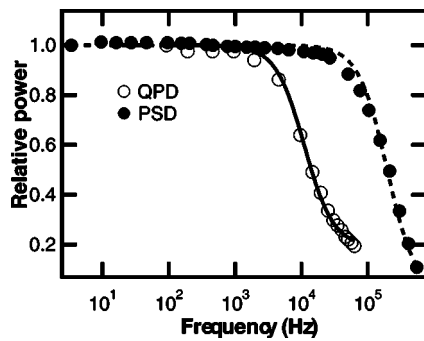


FIG. 5. Comparison of position detector frequency response at 1064 nm. Normalized frequency dependent response for a silicon quadrant photodiode (QPD) (QP50-6SD, Pacific Silicon Sensor) (open circles), and a position sensitive detector (PSD), (DL100-7PCBA, Pacific Silicon Sensor) (solid circles). 1064 nm laser light was modulated with an acousto-optic modulator and the detector output was recorded with a digital sampling scope. The response of the QPD was fit with the function:  $\gamma^2 + (1 - \gamma^2)[1 + (f/f_0)^2]^{-1}$ , which describes the effects of diffusion of electron-hole pairs created outside the depletion layer (Ref. 134), where  $\gamma$  is the fraction of light absorbed in the diode depletion layer and  $f_0$  is the characteristic frequency associated with light absorbed beyond the depletion layer. The fit returned an  $f_0$  value of 11.1 kHz and a  $\gamma$  parameter of 0.44, which give an effective  $f_{3dB}$  of 14.1 kHz, similar to values found in Ref. 134 for silicon detectors. The QPD response was not well fit by a single pole filter response curve. The PSD response, in contrast, was fit by a single pole filter function, returning a rolloff frequency of 196 kHz. Extended frequency response at 1064 nm has also been reported for InGaAs and fully depleted silicon photodiodes (Ref. 61).

cific Silicon Detectors, which supplies output signals similar to those from a QPD, although operating on a different principle), does not suffer from parasitic filtering below  $\sim 150$  kHz with 1064 nm illumination (Fig. 5).

## F. Dynamic position control

Precise, calibrated lateral motion of the optical trap in the specimen plane allows objects to be manipulated and moved relative to the surface of the trapping chamber. More significantly, dynamic computer control over the position and stiffness of the optical trap allows the force on a trapped object to be varied in real time, which has been exploited to generate both force and position clamp measurement conditions.<sup>50,81</sup> Additionally, if the position of the optical trap is scanned at a rate faster than the Brownian relaxation time of a trapped object, multiple traps can be created by time sharing a single laser beam.<sup>49</sup> We consider below the different beam-steering strategies.

### 1. Scanning mirrors

Traditional galvanometer scanning mirrors benefited from the incorporation of feedback to improve stability and precision. Current commercial systems operate at 1–2 kHz with step response times as short as 100  $\mu$ s, and with 8  $\mu$ rad repeatability. The comparatively slow temporal response limits their usefulness for fast-scanning applications, but their low insertion loss and large deflection angles make them a low-cost option for slow-scanning and feedback applications. Recent advances in feedback-stabilized piezoelectric (PZ) systems have resulted in the introduction of PZ scanning mirrors. For the time being, PZ mirrors represent only a slight improvement over galvanometers, with effective op-

eration up to 1 kHz, but just 50 mrad deflection range, and only slightly better resolution and linearity than galvanometers.

### 2. Acousto-optic deflectors

An acousto-optic deflector (AOD) consists of a transparent crystal inside which an optical diffraction grating is generated by the density changes associated with an acoustic traveling wave of ultrasound. The grating period is given by the wavelength of the acoustic wave in the crystal, and the first-order diffracted light is deflected through an angle that depends on the acoustic frequency through  $\Delta\theta = \lambda/fv$ , where  $\lambda$  is the optical wavelength, and  $v$  and  $f$  are the velocity and frequency of the acoustic wave, respectively ( $v/f$  is the ultrasound wavelength). The diffraction efficiency is proportional to depth of the grating, and therefore to the amplitude of the acoustic wave that produced it. AODs are thereby able to control both the trap position (through deflection) and stiffness (through light level). The maximum deflection of an AOD is linearly related to its operating frequency range, and maximum deflections of somewhat over  $1^\circ$  are possible at 1064 nm. AODs are fast: their response times are limited, in principle, by the ratio of the laser spot diameter to the speed of sound within the crystal ( $\sim 1.5 \mu$ s/mm laser diameter for  $\text{TeO}_2$  crystals, slightly less for  $\text{Li}_6\text{NbO}_3$  crystals). In practice, however, the response time of an optical trapping instrument is often limited by other components in the system. A pair of AODs can be combined in an orthogonal configuration to provide both  $x$  and  $y$  deflections of the optical trap. Due to optical losses in the AODs (an  $\sim 80\%$  diffraction efficiency is typical), however, this scheme results in an almost 40% power loss. In addition to mediocre transmission, the diffraction efficiency of an AOD will often vary slightly as a function of its deflection. The resulting position-dependent stiffness variation of the optical trap can either be tolerated (if within acceptable margins for error), calibrated out,<sup>53</sup> or minimized by the selection of a particular range of operating deflections over which the diffraction efficiency is more nearly constant. In practice, however, every AOD needs to be characterized carefully before use for deflection-dependent changes in throughput.

### 3. Electro-optic deflectors

An electro-optic deflector (EOD) consists of a crystal in which the refractive index can be changed through the application of an external electric field. A gradient in refractive index is established in one plane along the crystal, which deflects the input light through an angle  $\theta \propto lV/w^2$ , where  $V$  is the applied voltage,  $l$  is the crystal length, and  $w$  is the aperture diameter. Deflections on the order of 20 mrad can be achieved with a switching time as short as 100 ns, sufficient for some optical trapping applications. Despite low insertion loss ( $\sim 1\%$ ) and straightforward alignment, EODs have not been widely employed in optical trapping systems. High cost and a limited deflection range may contribute to this.

## G. Piezoelectric stage

Piezoelectric stage technology has been improved dramatically through the introduction of high-precision controllers and sensitive capacitive position sensing. Stable, linear, reproducible, ultrafine positioning in three dimensions is now readily achievable with the latest generation of PZ stages. The traditional problems of hysteresis and drift in PZ devices have been largely eliminated through the use of capacitive position sensors in a feedback loop. With the feedback enabled, an absolute positional uncertainty of 1 nm has been achieved commercially. PZ stages have had an impact on practically every aspect of optical trapping. They can provide an absolute, NIST-traceable displacement measurement, from which all other position calibrations can be derived. Furthermore, these stages permit three-dimensional control of the position of the trap relative to the trapping chamber, which has previously proved difficult or inaccurate.<sup>39</sup> The ability to move precisely in the axial dimension, in particular, permits characterization of the longitudinal properties of the optical trap and can be used to eliminate the creep and backlash typically associated with the mechanical (gear based) focusing mechanism of the microscope. Position and force calibration routines employing the PZ stage are faster, more reproducible, and more precise than previously attainable. Finally, a piezoelectric stage can be incorporated into a force feedback loop<sup>86,135–137</sup> permitting constant-force records of essentially arbitrary displacement, ultimately limited by the stage travel ( $\sim 100\ \mu\text{m}$ ) rather than the working range of the position detector ( $\sim 0.3\ \mu\text{m}$ ), the latter being the limiting factor in feedback based on moving the optical trap.<sup>50,59</sup> Stage-based force-feedback permits clamping not only the transverse force, but also the axial force, and hence the polar angle through which the force is applied. Despite these advantages, PZ stages are not without their attendant drawbacks. They are comparatively expensive: a 3D stage with capacitive feedback position sensing plus a digital controller costs roughly \$25,000. Furthermore, communication with the stage controller can be slower than for other methods of dynamically controlling trap position (e.g., AODs or EODs), with a maximum rate of  $\sim 50\ \text{Hz}$ .<sup>59</sup>

## H. Environmental isolation

To achieve the greatest possible sensitivity, stability, and signal-to-noise ratio in optical trapping experiments, the environment in which the optical trapping is performed must be carefully controlled. Four environmental factors affect optical trapping measurements: temperature changes, acoustic noise, mechanical vibrations, and air convection. Thermal fluctuations can lead to slow, large-scale drifts in the optical trapping instrument. For typical optical trapping configurations, a 1 K temperature gradient easily leads to micrometers of drift over a time span of minutes. In addition, acoustic noise can shake the optics that couple the laser into the objective, the objective itself, or the detection optics that lie downstream of the objective. Mechanical vibrations typically arise from heavy building equipment, e.g., compressors or pumps operating nearby, or from passing trucks on a roadway. Air currents can induce low-frequency mechanical vi-

brations and also various optical perturbations (e.g., beam deflections from gradients in refractive index produced by density fluctuations in the convected air, or light scattering by airborne dust particles), particularly near optical planes where the laser is focused.

The amount of effort and resources dedicated to reducing ambient sources of noise should be commensurate with the desired precision in the length and time scale of the measurements. Slow thermal drift may not affect a rapid or transient measurement, but could render meaningless the measurement of a slower process. Several methods of reducing noise and drift have been employed in the current generation of optical traps.

The vast majority of optical trapping instruments have been built on top of passive air tables that offer mechanical isolation (typically,  $-20\ \text{dB}$ ) at frequencies above  $\sim 2\text{--}10\ \text{Hz}$ . For rejection of lower frequencies, actively servoed air tables are now commercially available, although we are not yet aware of their use in this field. Acoustic noise isolation can be achieved by ensuring that all optical mounts are mechanically rigid, and placing these as close to the optical table as feasible, thereby reducing resonance and vibration. Enclosing all the free-space optics will further improve both mechanical and optical stability by reducing ambient air currents. Thermal effects and both acoustical and mechanical vibration can be reduced by isolating the optical trapping instrument from noisy power supplies and heat sources. Diode pumped solid state lasers are well suited to this approach: since the laser head is fiber coupled to the pump diodes, the power supply can be situated outside of the experimental room. A similar isolation approach can be pursued with noisy computers or power supplies, and even illumination sources, whose outputs can be brought to the instrument via an optical fiber. Further improvements in noise performance and stability may require more substantial modifications, such as acoustically isolated and temperature controlled experimental rooms situated in low-vibration areas. The current generation of optical trapping instruments in our lab<sup>59,138</sup> are housed in acoustically quiet cleanrooms with background noise less than the NC30 (OSHA) rating, a noise level roughly equivalent to a quiet bedroom. In addition, these rooms are temperature stabilized to better than  $\pm 0.5\ \text{K}$ . The stability and noise suppression afforded by this arrangement has paved the way for high-resolution recording of molecular motor movement, down to the subnanometer level.<sup>85–87</sup>

## IV. CALIBRATION

### A. Position calibration

Accurate position calibration lies at the heart of quantitative optical trapping. Precise determination of the displacement of a trapped object from its equilibrium position is required to compute the applied force ( $F = -ax$ , where  $F$  is the force,  $a$  is the optical trap stiffness, and  $x$  is the displacement from the equilibrium trapping position), and permits direct measurement of nanometer-scale motion. Several methods of calibrating the response of a position detector have been developed. The choice of method will depend on

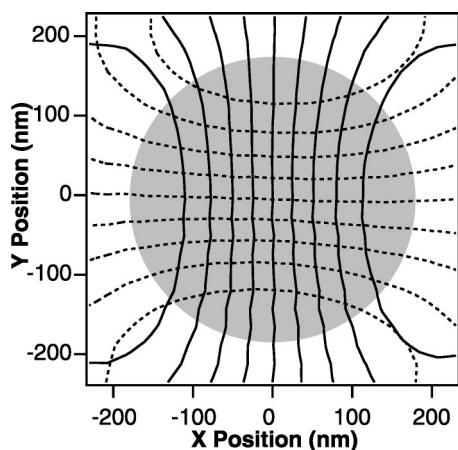


FIG. 6. Lateral two-dimensional detector calibration (adapted from Ref. 59). Contour plot of the  $x$  (solid lines) and  $y$  (dashed lines) detector response as a function of position for a  $0.6\ \mu\text{m}$  polystyrene bead raster scanned through the detector laser focus by deflecting the trapping laser with acousto-optic deflectors. The bead is moved in  $20\ \text{nm}$  steps with a dwell time of  $50\ \text{ms}$  per point while the position signals are recorded at  $50\ \text{kHz}$  and averaged over the dwell time at each point. The  $x$  contour lines are spaced at  $2\ \text{V}$  intervals, from  $8\ \text{V}$  (leftmost contour) to  $-8\ \text{V}$  (rightmost contour). The  $y$  contour lines are spaced at  $2\ \text{V}$  intervals, from  $8\ \text{V}$  (bottom contour) to  $-8\ \text{V}$  (top contour). The detector response surfaces in both the  $x$  and  $y$  dimensions are fit to fifth order two-dimensional polynomials over the shaded region, with less than  $2\ \text{nm}$  residual root mean square (rms) error. Measurements are confined to the shaded region, where the detector response is single valued.

the position detection scheme, the ability to move the trap and/or the stage, the desired accuracy, and the expected direction and magnitude of motion in the optical trap during an experiment. The most straightforward position calibration method relies on moving a bead through a known displacement across the detector region while simultaneously recording the output signal. This operation can be performed either with a stuck bead moved by a calibrated displacement of the stage, or with a trapped bead moved with a calibrated displacement of a steerable trap.

Position determination using a movable trap relies on initial calibration of the motion of the trap itself in the specimen plane against beam deflection, using AODs or deflecting mirrors. This is readily achieved by video tracking a trapped bead as the beam is moved.<sup>49</sup> Video tracking records can be converted to absolute distance by calibrating the charge coupled device (CCD) camera pixels with a ruled stage micrometer ( $10\ \mu\text{m}$  divisions or finer),<sup>49,50</sup> or by video tracking the motion of a stuck bead with a fully calibrated piezoelectric stage.<sup>59</sup> Once the relationship between beam deflection and trap position is established, the detector can then be calibrated in one or both lateral dimensions by simply moving a trapped object through the detector active area and recording the position signal.<sup>50,59,81</sup> Adequate two-dimensional calibration may often be obtained by moving the bead along two orthogonal axes in an “X” pattern. However, a more complete calibration requires raster scanning the trapped bead to cover the entire active region of the sensor.<sup>59</sup> Figure 6 displays the two-dimensional detector calibration for a  $0.6\ \mu\text{m}$  bead, raster scanned over the detector region using an AOD-driven optical trap. A movable optical trap is typically used with either an imaging position detector, or a second low-power laser for laser-based detection (described above). Cali-

brating by moving the trap, however, offers several advantages. Position calibration can be performed individually for each object trapped, which eliminates errors arising from differences among nominally identical particles, such as uniform polystyrene beads, which may exhibit up to a 5% coefficient of variation in diameter. Furthermore, nonspherical or nonidentical objects, such as bacteria or irregularly shaped particles, can be calibrated on an individual basis prior to (or after) an experimental measurement. Because the object is trapped when it is calibrated, the calibration and detection necessarily take place in the same axial plane, which precludes calibration errors arising from the slight axial dependence of the lateral position signals.

Laser-based detection used in conjunction with a movable trap affords additional advantages. Because the trapping and detection lasers are separate, the focal position of the two can be moved relative to one another in the axial dimension. The maximum lateral sensitivity and minimum variation of lateral sensitivity with axial position occur at the focus of the detection laser. The axial equilibrium position of a trapped object, however, lies above the focus due to the scattering force. Since the detection and trapping lasers are uncoupled, the focus of the detection laser can be made coincident with the axial position of the trapped object, thereby maximizing the detector sensitivity while minimizing the axial dependence of the lateral sensitivity.<sup>59</sup> An additional benefit to using an independent detection laser is that it can be more weakly focused to a larger spot size, since it does not need to trap, thereby increasing the usable detection range. Beyond the added complication and cost of building a movable trap, calibrating with a movable trap has some important limitations. The calibration is limited to the two lateral dimensions, which may be inadequate for experiments where the trapped bead is displaced significantly in the axial dimension.<sup>39,82</sup> Due to the  $\sim 4$ – $6$ -fold lower trap stiffness in the axial dimension, a primarily lateral force pulling an object out of the trapping zone may result in a significant axial displacement. In practice, this situation arises when the trapped object is tethered to the surface of the trapping chamber, e.g., when a bead is attached by a strand of DNA bound at its distal end to the coverglass.<sup>39,82,88,135–137</sup> Accurate determinations of displacement and trapping force in such experiments require axial, as well as lateral, position calibration.

Position calibration is most commonly accomplished by moving a bead fixed to the surface through the detection region and recording the detector output as a function of position. Traditionally, such calibrations were performed in one or two lateral dimensions. The advent of servostabilized, 3D piezoelectric (pz) stages has made such calibrations more accurate, easier to perform and—in conjunction with an improved theoretical understanding of the axial position signal—has permitted a full 3D position calibration of an optical trap.<sup>62–64</sup> Whereas full 3D calibration is useful for tracking the complete motion of an object, it is cumbersome and unnecessary when applying forces within a plane defined by one lateral direction and the optical axis. When the trapped object is tethered to the surface of the trapping chamber, for example, it is sufficient to calibrate the axial

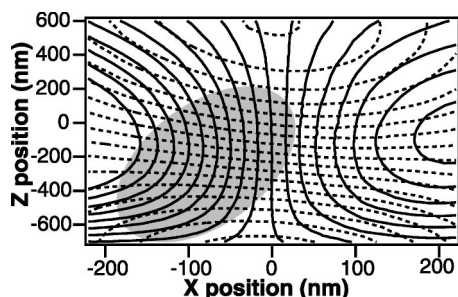


FIG. 7. Axial two-dimensional detector calibration. Contour plot of the lateral (solid lines) and axial (dashed lines) detector response as a function of  $x$  (lateral displacement) and  $z$  (axial displacement) of a stuck  $0.5 \mu\text{m}$  polystyrene bead moving through the laser focus. A stuck bead was raster scanned in  $20 \text{ nm}$  steps in  $x$  and  $z$ . The detector signals were recorded at  $4 \text{ kHz}$  and averaged over  $100 \text{ ms}$  at each point. The lateral contour lines are spaced at  $1 \text{ V}$  intervals, from  $-9 \text{ V}$  (leftmost contour) to  $7 \text{ V}$  (rightmost contour). The axial contour lines are spaced at  $0.02$  intervals (normalized units). Measurements are confined to the region of the calibration shaded in gray, over which the surfaces of  $x$  and  $z$  positions as a function of lateral and axial detector signals were fit to seventh order two-dimensional polynomial functions with less than  $5 \text{ nm}$  residual rms error.

and the single lateral dimension in which the force is applied. Figure 7 displays the results of such a two-dimensional (“ $x-z$ ”) position calibration for a  $0.5 \mu\text{m}$  bead stuck to the surface of the trapping chamber. The bead was stepped through a raster scan pattern in  $x$  (lateral dimension) and  $z$  (axial dimension) while the position signals were recorded. Using a stuck bead to calibrate the position detector has some limitations and potential pitfalls. Because it is difficult, in general, to completely immobilize an initially trapped particle on the surface, it is not feasible to calibrate every particle. Instead, an average calibration derived from an ensemble of stuck beads must be measured. Furthermore, the stuck-bead calibration technique precludes calibrating non-spherical or heterogeneous objects, unless these can be attached to the surface (and stereospecifically so) prior to, or after, the experimental measurements. Due to the axial dependence of the lateral position signals (“ $x-z$  crosstalk”), using a stuck bead to calibrate only the lateral dimension is prone to systematic error. Without axial position information, it is difficult to precisely match the axial position of a stuck bead with the axial position of a trapped bead. Optically focusing on a bead cannot be accomplished with an accuracy better than  $\sim 100 \text{ nm}$ , which introduces uncertainty and error in lateral position calibrations for which the axial position is set by focusing. Therefore, even when only the lateral dimensions are being calibrated, it is useful to measure the axial position signal to ensure that the calibration is carried out in the appropriate axial plane.

### 1. Absolute axial position and measurement of the focal shift

The absolute axial position of a trapped object above the surface of the trapping chamber is an important experimental parameter, because the hydrodynamic drag on an object varies nonlinearly with its height above the surface, due to proximal wall effects (see below and Ref. 9). Absolute axial position measurements may be especially important in situations where the system under investigation is attached to the

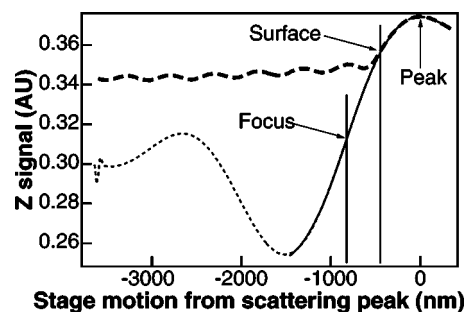


FIG. 8. Axial position signals for a free (heavy dashed line) and stuck (light dashed line) bead as the stage was scanned in the axial direction. All stage motion is relative to the scattering peak, which is indicated on the right of the figure. The positions of the surface (measured) and the focus [calculated from Eq. (5)] are indicated by vertical lines. The axial detection fit [Eq. (5)] to the stuck bead trace is shown in the region around the focus as a heavy solid line.

surface and to a trapped object, as is often the case in biological applications. Force–extension relationships, for example, depend on the end-to-end extension of the molecule, which can only be determined accurately when the axial position of the trapped object with respect to the surface is known. Axial positioning of a trapped object depends on finding the location of the surface of the chamber and moving the object relative to this surface by a known amount. The problem is complicated by the focal shift that arises when focusing through a planar interface between two mismatched indices of refraction e.g., between the coverglass ( $n_{\text{glass}} \sim 1.5$ ) and the aqueous medium ( $n_{\text{water}} \sim 1.3$ ).<sup>139–144</sup> This shift introduces a fixed scaling factor between a vertical motion of the chamber surface and the axial position of the optical trap within the trapping chamber. The focal shift is easily computed from Snell’s law for the case of paraxial rays, but it is neither straightforward to compute nor to measure experimentally when high NA objectives are involved.<sup>144</sup> Absolute axial position determination has previously been assessed using fluorescence induced by an evanescent wave,<sup>131</sup> by the analysis of interference or diffraction patterns captured with video,<sup>113,145</sup> or through the change in hydrodynamic drag on a trapped particle as it approaches the surface.<sup>39</sup> These techniques suffer from the limited range of detectable motion for fluorescence-based methods, and by the slow temporal response of video and drag-force-based measurements.

The position detector sum signal (QPD or PSD output), which is proportional to the total incident intensity at the back focal plane of the condenser, provides a convenient means of both accurately locating the surface of the trapping chamber and measuring the focal shift. In conjunction, these measurements permit absolute positioning of a trapped object with respect to the trapping chamber surface. The detector sum signal as a function of axial stage position for both a stuck bead and a trapped bead are shown in Fig. 8. The stuck bead trace represents the axial position signal of a bead moving relative to the trap. As the bead moves through the focus of the laser (marked on the figure), the phase of light scattered from the bead changes by  $180^\circ$  relative to the unscattered light, modulating the intensity distribution at the back focal plane of the condenser. The region between the extrema

of the stuck-bead curve is well described by the expression for axial sensitivity derived by Pralle and co-workers:<sup>62</sup>

$$\frac{I_z}{I} \propto \left(1 + \left(\frac{z}{z_0}\right)^2\right)^{1/2} \sin[\tan^{-1}(z/z_0)], \quad (5)$$

where an overall scaling factor has been ignored,  $z$  is the axial displacement from the beam waist, and  $z_0 = \pi w_0^2/\lambda$  is the Rayleigh length of the focus, with beam waist  $w_0$  at wavelength  $\lambda$ . The phase difference in the scattered light is described by the arctangent term, while the prefactor describes the axial position dependent intensity of the scattered light. The fit returns a value for the beam waist,  $w_0 = 0.436 \mu\text{m}$ . The equilibrium axial position of a trapped bead corresponds to a displacement of  $0.379 \mu\text{m}$  from the laser focus. A stuck bead scan can also be useful for determining when a free bead is forced onto the surface of the cover slip.

As a trapped bead is forced into contact with the surface of the chamber by the upward stage motion, the free and stuck bead signals merge and eventually become indistinguishable (Fig. 8). The approximate location of the surface with respect to the position of a trapped bead can be determined by finding the point at which both curves coincide. Brownian motion of the trapped bead, however, will shift this point slightly, in a stiffness-dependent manner that will introduce a small uncertainty in the measured position of the surface. The scattering peak in Fig. 8, however, serves as an easily identifiable fiducial reference from which the trapped bead can be moved an absolute distance by subsequent stage motion. In this manner, trapped particles can be reproducibly positioned at a fixed (but uncertain) distance relative to the surface. In order to obtain a precise location of the trapped particle above the surface, both the position of the scattering peak with respect to the surface and the focal shift must be determined. This may be accomplished, for example, by a one-time measurement of the drag on a trapped bead at a series of positions above the scattering peak. The interaction of a sphere with the boundary layer of water near a surface leads to an increase in the hydrodynamic drag  $\beta$ , which can be estimated by Faxen's law for the approximate drag on a sphere near a surface:<sup>9</sup>

$$\beta = \frac{6\pi\eta a}{1 - \frac{9}{16}\left(\frac{a}{h}\right) + \frac{1}{8}\left(\frac{a}{h}\right)^3 - \frac{45}{256}\left(\frac{a}{h}\right)^4 - \frac{1}{16}\left(\frac{a}{h}\right)^5}, \quad (6)$$

which depends only on the bead radius  $a$ , the distance above the surface  $h$ , and the viscosity of the liquid  $\eta$ . By measuring the rolloff frequency or the displacement of the trapped bead as the stage is oscillated (see below), the drag force can be determined at different axial stage positions relative to the scattering peak and normalized to the calculated asymptotic value, the Stokes drag coefficient,  $6\pi\eta a$ . The resulting curve (Fig. 9) is described by a two parameter fit to Eq. (6): a scaling parameter that represents the fractional focal shift and an offset parameter related to the distance between the scattering peak and the coverglass surface. The fit parameters from the curve in Fig. 9 allow absolute positioning of a trapped particle with respect to the surface. The uncertainty in the axial position amounts to roughly 3% of the bead-surface separation, with the residual uncertainty largely due

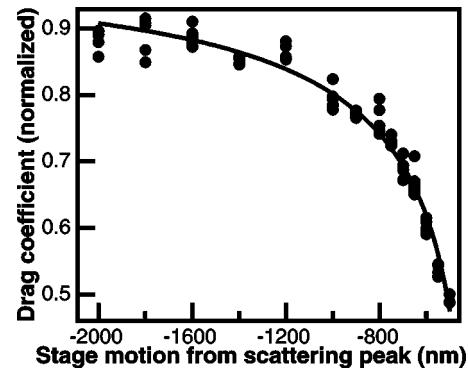


FIG. 9. Normalized drag coefficient ( $\beta_0/\beta$ , where  $\beta_0$  is the Stokes drag on the sphere:  $6\pi\eta a$ ) as a function of distance from the scattering peak. The normalized inverse drag coefficient (solid circles) was determined through rolloff measurements and from the displacement of a trapped bead as the stage was oscillated. The normalized inverse drag coefficient was fit to Faxen's law [Eq. (6)] with a height offset  $\varepsilon$  and scaling parameter  $\delta$ , which is the fractional focal shift, as the only free parameters:  $\beta_0/\beta = 1 - (9/16) \times [a\delta^{-1}(z-\varepsilon)^{-1}] + \frac{1}{8}[a\delta^{-1}(z-\varepsilon)^{-1}]^3 - (45/256)[a\delta^{-1}(z-\varepsilon)^{-1}]^4 - (1/16)[a\delta^{-1}(z-\varepsilon)^{-1}]^5$ , where  $a$  is the bead radius,  $z$  is the motion of the stage relative to the scattering peak,  $\beta_0$  is the Stoke's drag on the bead, ( $6\pi\eta a$ ), and  $\beta$  is the measured drag coefficient. The fit returned a fractional focal shift  $\delta$  of  $0.82 \pm 0.02$  and an offset  $\varepsilon$  of 161 nm. The position of the surface relative to the scattering peak is obtained by setting the position of the bead center,  $\delta(z-\varepsilon)$  equal to the bead radius  $a$ , which returns a stage position of 466 nm above the scattering peak, as indicated in Fig. 8.

to the estimate of the focal shift (which leads to a relative rather than an absolute uncertainty). The position of the surface, calculated from the fit parameters of Fig. 9, is indicated in Fig. 8. The focal shift was  $0.82 \pm 0.02$ , i.e., the vertical location of the laser focus changed by 82% of the vertical stage motion.

The periodic modulation of the axial position signal as a trapped bead is displaced from the surface (Fig. 8) can be understood in terms of an étalon picture.<sup>146</sup> Backscattered light from the trapped bead reflects from the surface and interferes with forward-scattered and unscattered light in the back focal plane of the condenser. The phase difference between these two fields includes a constant term that arises because of the Gouy phase and another term that depends on the separation between the bead and the surface. The spatial frequency of the intensity modulation is given by  $d = \lambda/(2n_m)$ , where  $d$  is the separation between the bead and the cover slip,  $\lambda$  is the vacuum wavelength of the laser, and  $n_m$  is the index of refraction of the medium. This interference signal supplies a second and much more sensitive means to determine the focal shift. The motion of the stage ( $d_s$ ) and motion of the focus ( $d_f$ ) are related through a scaling parameter  $f_s$  equal to the focal shift  $d_f = f_s d_s$ . The interference signal is observed experimentally by stage translations. The measured spatial frequency will be given by  $d_s = \lambda/(2n_m f_s)$ , which can be rearranged to solve for the focal shift  $f_s = \lambda/(2n_m d_s)$ . The focal shift determined in this manner was  $0.799 \pm 0.002$ , which is within the uncertainty of the focal shift determined by hydrodynamic drag measurements (Fig. 9). The true focal shift with a high NA lens is more pronounced than the focal shift computed in the simple paraxial limit, given (from Snell's law) by the ratio of the indices of refraction:  $n_m/n_{\text{imm}} = 0.878$  for the experimental conditions,

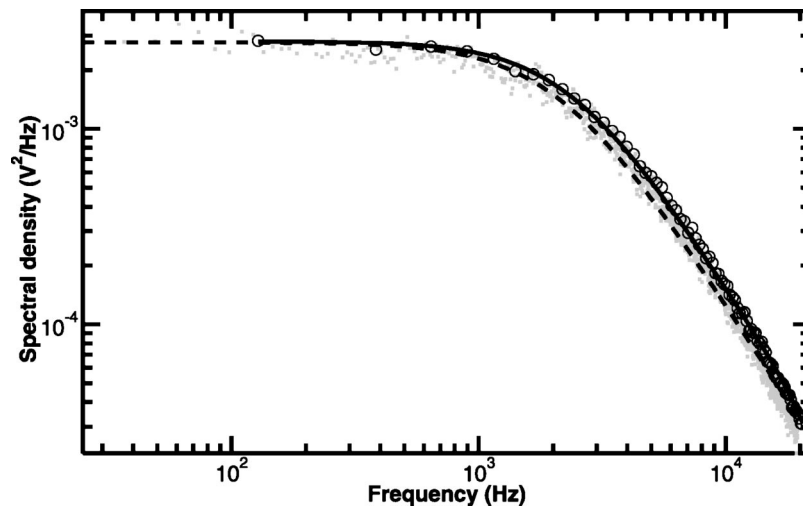


FIG. 10. Power spectrum of a trapped bead. Power spectrum of a  $0.5 \mu\text{m}$  polystyrene bead trapped  $1.2 \mu\text{m}$  above the surface of the trapping chamber recorded with a PSD (gray dots). The raw power spectrum was averaged over 256 Hz windows on the frequency axis (black circles) and fit (black line) to a Lorentzian [Eq. (7)] corrected for the effects of the antialiasing filter, frequency dependent hydrodynamic effects, and finite sampling frequency, as described by Berg-Sørensen and Flyvbjerg (Ref. 148). The rolloff frequency is 2.43 kHz, corresponding to a stiffness of 0.08 pN/nm. For comparison the raw power spectrum was fit to an uncorrected Lorentzian (dashed line), which returns a rolloff frequency of 2.17 kHz. Whereas the discrepancies are on the order 10% for a relatively weak trap, they generally become more important at higher rolloff frequencies.

where  $n_m$  is the index of the aqueous medium (1.33) and  $n_{\text{imm}}$  is the index of the objective immersion oil (1.515). The discrepancy should not be surprising, because the paraxial ray approximation does not hold for the objectives used for optical trapping.<sup>146</sup> The interference method employed to measure the focal shift is both easier and more accurate than the drag-force method presented earlier.

## 2. Position calibration based on thermal motion

A simple method of calibrating the position detector relies on the thermal motion of a bead of known size in the optical trap.<sup>122</sup> The one-sided power spectrum for a trapped bead is<sup>9</sup>

$$S_{xx}(f) = \frac{k_B T}{\pi^2 \beta (f_0^2 + f^2)}, \quad (7)$$

where  $S_{xx}(f)$  is in units of displacement<sup>2</sup>/Hz,  $k_B$  is Boltzmann's constant,  $T$  the absolute temperature,  $\beta$  is the hydrodynamic drag coefficient of the object (e.g.,  $\beta = 6\pi\eta a$  for Stokes drag on a sphere of radius  $a$  in a medium with viscosity  $\eta$ ), and  $f_0$  is the rolloff frequency, related to the trap stiffness through  $f_0 = \alpha(2\pi\beta)^{-1}$  for a stiffness  $\alpha$  (see below). The detector, however, measures the uncalibrated power spectrum  $S_{vv}(f)$ , which is related to the true power spectrum by  $S_{vv}(f) = \rho^2 \cdot S_{xx}(f)$ , where  $\rho$  represents the linear sensitivity of the detector (in volts/unit distance). The sensitivity can be found by considering the product of the power spectrum and the frequency squared  $S_{xx}(f) \cdot f^2$ , which asymptotically approaches the limit  $k_B T (\pi^2 \beta)^{-1}$  for  $f \gg f_0$ . Inserting the relationship between the displacement power spectrum and the uncalibrated detector spectrum in this expression and rearranging gives

$$\rho = [S_{vv}(f) \pi^2 \beta / k_B T]^{1/2}. \quad (8)$$

This calibration method has been shown to agree to within  $\sim 20\%$  of the sensitivity measured by more direct means, such as those discussed above.<sup>122</sup> An advantage to the

method is that it does not require any means of precisely moving a bead to calibrate the optical trap. However, the calibration obtained by this method is valid only for small displacements, for which a linear approximation to the position signal is valid. In addition, the system detection bandwidth must be adequate to record accurately the complete power spectrum without distortion, particularly in the high frequency regime. System bandwidth considerations are treated more fully in conjunction with stiffness determination, discussed below.

## B. Force calibration—stiffness determination

Forces in optical traps are rarely measured directly. Instead, the stiffness of the trap is first determined, then used in conjunction with the measured displacement from the equilibrium trap position to supply the force on an object through Hooke's law:  $F = -\alpha x$ , where  $F$  is the applied force,  $\alpha$  is the stiffness, and  $x$  is the displacement. Force calibration is thus reduced to calibrating the trap stiffness and separately measuring the relative displacement of a trapped object. A number of different methods of measuring trap stiffness, each with its attendant strengths and drawbacks, have been implemented. We discuss several of these.

### 1. Power spectrum

When beads of known radius are trapped, the physics of Brownian motion in a harmonic potential can be exploited to find the stiffness of the optical trap. The one-sided power spectrum for the thermal fluctuations of a trapped object is given by Eq. (7), which describes a Lorentzian. This power spectrum can be fit with an overall scaling factor and a rolloff frequency,  $f_0 = \alpha(2\pi\beta)^{-1}$  from which the trap stiffness ( $\alpha$ ) can be calculated if the drag ( $\beta$ ) on the particle is known (Fig. 10). For a free sphere of radius  $a$  in solution far from any surfaces, the drag is given by the usual Stokes relation  $\beta = 6\pi\eta a$ , where  $\eta$  is the viscosity of the medium. For a bead

trapped nearer the surface of the trapping chamber, additional drag arises from wall effects and must be considered: Faxen's law [Eq. (6)] is appropriate for estimating the drag due to lateral motion. Axial stiffness is also measured via the power spectrum of the axial position signal, but the corrections to the axial drag due to wall effects are larger than those for the lateral drag. The drag on a sphere moving normal to a surface is<sup>147</sup>

$$\beta = \beta_0 \frac{4}{3} \sinh \alpha \sum_{n=1}^{\infty} \frac{n(n+1)}{(2n-1)(2n+3)} \times \left[ \frac{2 \sinh(2n+1)\alpha + (2n+1)\sinh 2\alpha}{4\sinh^2(n+\frac{1}{2})\alpha - (2n+1)^2\sinh^2\alpha} - 1 \right], \quad (9)$$

where

$$\alpha = \cosh^{-1} \left( \frac{h}{a} \right) = \ln \left\{ \frac{h}{a} + \left[ \left( \frac{h}{a} \right)^2 - 1 \right]^{1/2} \right\},$$

$h$  is the height of the center of the sphere above the surface, and  $\beta_0 = 6\pi\eta a$  is the Stokes drag. The sum converges fairly quickly and  $\sim 10$  terms are required to achieve accurate results. Whereas it is tempting to measure trap stiffness well away from surfaces to minimize hydrodynamic effects, spherical aberrations in the focused light will tend to degrade the optical trap deeper in solution, particularly in the axial dimension. Spherical aberrations lead to both a reduction in peak intensity and a smearing-out of the focal light distribution in the axial dimension.

Determining the stiffness of the optical trap by the power spectrum method requires a detector system with sufficient bandwidth to record faithfully the power spectrum well beyond the rolloff frequency (typically, by more than 1 order of magnitude). Lowpass filtering of the detector output signal, even at frequencies beyond the apparent rolloff leads directly to a numerical underestimate of the rolloff frequency and thereby to the stiffness of the optical trap. Errors introduced by low pass filtering become more severe as the rolloff frequency of the trap approaches the rolloff frequency of the electrical filter. Since the trap stiffness is determined solely from the rolloff of the Lorentzian power spectrum, this method is independent of the position calibration, per se. In addition to determining the stiffness, the power spectrum of a trapped bead serves as a powerful diagnostic tool for optical trapping instruments: alignment errors of either the optical trap or the position detection system lead to non-Lorentzian power spectra, which are easily scored, and extraneous sources of instrument noise can generate additional peaks in the power spectrum.

The measurement and accurate fitting of power spectra to characterize trap stiffness was recently investigated by Berg-Sørensen and Flyvbjerg,<sup>148,149</sup> who developed an improved expression for the power spectrum that incorporates several previously ignored corrections, including the frequency dependence of the drag on the sphere, based on an extension of Faxen's law for an oscillating sphere [Faxen's law, Eq. (6), only holds strictly in the limit of *constant* velocity]. These extra terms encapsulate the relevant physics for a sphere moving in a harmonic potential with viscous damping. In addition to this correction, the effects of finite

sampling frequency and signal filtering during data acquisition (due to electronic filters or parasitic filtering by the photosensor) were included in fitting the experimental power spectrum. The resulting fits determine the trap stiffness with an uncertainty of  $\sim 1\%$  and accurately describe the shape of the measured spectra. This work underscores the importance of characterizing and correcting the frequency response of the position detection system to obtain accurate stiffness measurements. Figure 10 illustrates a comparison between the fit obtained with the improved fitting routine and an uncorrected fit.

The power spectrum of a trapped bead can also be used to monitor the sample heating due to partial absorption of the trapping laser light. Heating of the trapping medium explicitly changes the thermal kinetic energy term ( $k_B T$ ) in the power spectrum [Eq. (7)] and implicitly changes the drag term as well,  $\beta = 6\pi\eta(T)a$ , through its dependence on viscosity, which is highly temperature dependent. Peterman and co-workers were able to assess the temperature increase as a function of trapping laser power by determining the dependence of the Lorentzian fit parameters on laser power.<sup>100</sup>

## 2. Equipartition

The thermal fluctuations of a trapped object can also be used to obtain the trap stiffness through the Equipartition theorem. For an object in a harmonic potential with stiffness  $\alpha$ :

$$\frac{1}{2}k_B T = \frac{1}{2}\alpha \langle x^2 \rangle, \quad (10)$$

where  $k_B$  is Boltzmann's constant,  $T$  is absolute temperature, and  $x$  is the displacement of the particle from its trapped equilibrium position. Thus, by measuring the positional variance of a trapped object, the stiffness can be determined. The variance  $\langle x^2 \rangle$  is intimately connected to the power spectrum, of course: it equals the integral of the position power spectrum, i.e., the spectrum recorded by a calibrated detector. Besides its simplicity, a primary advantage of the Equipartition method is that it does not depend explicitly on the viscous drag of the trapped particle. Thus, the shape of the particle, its height above the surface, and the viscosity of the medium need not be known to measure the trap stiffness (although, in fairness, both the particle shape and the optical properties of the medium will influence the position calibration itself). The bandwidth requirements of the position detection system are the same as for the power spectral approach, with the additional requirement that the detector must be calibrated. Unlike the power spectral method however, the variance method does not provide additional information about the optical trap or the detection system. For this reason, care should be taken when measuring the stiffness with the Equipartition method. Because variance is an intrinsically *biased estimator* (it is derived from the square of a quantity, and is therefore always positive), any added noise and drift in position measurements serve only to increase the overall variance, thereby decreasing the apparent stiffness estimate. In contrast, low pass filtering of the position signal results in a lower variance and an apparent increase in stiffness.

### 3. Optical potential analysis

A straightforward extension of the Equipartition method involves determining the complete distribution of particle positions visited due to thermal motions, rather than simply the variance of that distribution. The probability for the displacement of a trapped object in a potential well will be given by a Boltzmann distribution

$$P(x) \propto \exp\left(\frac{-U(x)}{k_B T}\right) = \exp\left(\frac{-\alpha x^2}{2k_B T}\right), \quad (11)$$

where  $U(x)$  is the potential energy and  $k_B T$  is the thermal energy. When the potential is harmonic, this distribution is a simple Gaussian parametrized by the trap stiffness  $\alpha$ . When the potential is anharmonic, the position histogram can be used, in principle, to characterize the shape of the trapping potential by taking the logarithm and solving for  $U(x)$ . In practice, this approach is not especially useful without a considerable body of low-noise/low-drift position data, since the wings of the position histogram—which carry the most revealing information about the potential—hold the fewest counts and therefore have the highest relative uncertainty.

### 4. Drag force method

The most direct method of determining trap stiffness is to measure the displacement of a trapped bead from its equilibrium position in response to viscous forces produced by the medium, generated by moving the stage in a regular triangle wave or sinusoidal pattern. Since forces arise from the hydrodynamics of the trapped object, the drag coefficient, including any surface proximity corrections, must be known. For the case of a sinusoidal driving force of amplitude  $A_0$  and frequency  $f$ , the motion of the bead is

$$x(t) = \frac{A_0 f}{\sqrt{f_0^2 + f^2}} \exp[-i(2\pi f t - \varphi)], \quad (12)$$

$$\varphi = -\tan^{-1}(f_0/f),$$

where  $f_0$  is the characteristic rolloff frequency (above), and  $\varphi$  is the phase delay. Both the amplitude and the phase of the bead motion can be used to provide a measure of trap stiffness.

A triangular driving force of amplitude  $A_0$  and frequency  $f$  results in a square wave of force being applied to the bead. For each period of the motion the bead trajectory is

$$x(t) = \frac{\beta A_0 f}{2\alpha} \left[ 1 - \exp\left(-\frac{\alpha}{\beta} t\right) \right], \quad (13)$$

where  $\alpha$  is the trap stiffness and  $\beta$  is the drag coefficient of the bead, including Faxen's law corrections. Due to the finite response time of the stage, the exponential damping term is convolved with the response time of the stage. Therefore, only the asymptotic value ( $\beta A_0 f / 2\alpha$ ) should be used to obtain a reliable estimate of trap stiffness. Drag-force measurements are slow compared with the thermal motion of the particle, so the bandwidth requirements of the detection system are significantly relaxed. Increasing the amplitude or the frequency of the stage motion generates larger displacements of the trapped bead. By measuring the stiffness as a function of bead displacement, the linear region of the trap over

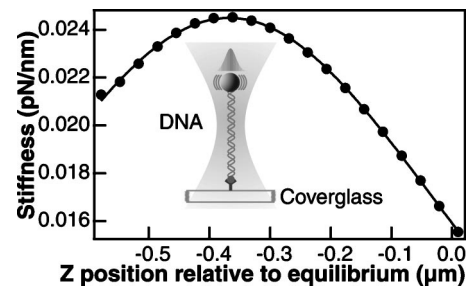


FIG. 11. Axial dependence of lateral stiffness. The experimental geometry for these measurements is depicted in the inset. A polystyrene bead is tethered to the surface of the cover glass through a long DNA tether. The stage was moved in the negative  $z$  direction (axial), which pulls the bead towards the laser focus, and the lateral stiffness was determined by measuring the lateral variance of the bead. The data (solid circles) are fit with the expression for a simple dipole [Eq. (14)], with the power in the specimen plane, the beam waist, and an axial offset as free parameters.

which the stiffness is constant can be easily determined.

A variation on the drag force method of stiffness calibration, sometimes called step response calibration, involves rapidly displacing the trap by a small, fixed offset and recording the subsequent trajectory of the bead. The bead will return to its equilibrium position in an exponentially damped manner, with a time constant of  $\alpha/\beta$  as in Eq. (13).

### 5. Direct measurement of optical force

The lateral trapping force arises from the momentum transfer from the incident laser light to the trapped object, which leads to a change in the direction of the scattered light (Fig. 1). Measuring the deflection of the scattered laser beam with a QPD or other position sensitive detector therefore permits direct measurement of the momentum transfer, and hence the force, applied to the trapped object—assuming that all the scattered light can be collected.<sup>38,57,104</sup> An expression relating the applied force to the beam deflection was presented by Smith *et al.*:<sup>38</sup>  $F = I/c \cdot (\text{NA}) \cdot X/R_{\text{ba}}$  where  $F$  is the force,  $I$  is the intensity of the laser beam,  $c$  is the speed of light,  $\text{NA}$  is the numerical aperture,  $X$  is the deflection of the light, and  $R_{\text{ba}}$  is the radius of the back aperture of the microscope objective. In principle, this approach is applicable to any optical trapping configuration. However, because it necessitates measuring the total intensity of scattered light, it has only been implemented for relatively low NA, counter-propagating optical traps, where the microscope objective entrance pupils are underfilled. In single-beam optical traps, it is impractical to collect the entirety of the scattered light, owing to the higher objective NA combined with an optical design that overfills the objective entrance pupil.

### 6. Axial dependence of lateral stiffness

Three-dimensional position detection facilitates measurement of the axial stiffness and mapping of the lateral stiffness as a function of axial position in the trap. Due to the high refractive index of polystyrene beads typically used in optical trapping studies, there is a correspondingly large scattering force in the axial direction. Consequently, the axial equilibrium position of a trapped polystyrene bead tends to lie well beyond the focus, where the lateral intensity gradient—and hence the lateral stiffness—are significantly

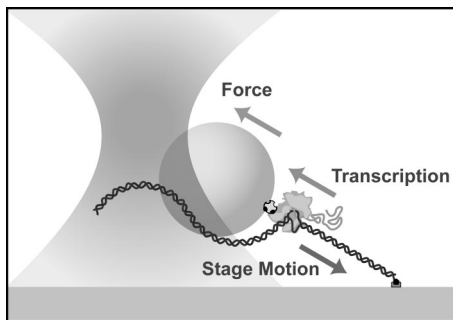


FIG. 12. Cartoon of the experimental geometry (not to scale) for single-molecule transcription experiment. Transcribing RNA polymerase with nascent RNA (gray strand) is attached to a polystyrene bead. The upstream end of the duplex DNA (black strands) is attached to the surface of a flowchamber mounted on a piezoelectric stage. The bead is held in the optical trap at a predetermined position from the trap center, which results in a restoring force exerted on the bead. During transcription, the position of the bead in the optical trap and hence the applied force is maintained by moving the stage both horizontally and vertically to compensate for motion of the polymerase molecule along the DNA (adapted from Ref. 87).

reduced from their values at the focus. In experiments in which beads are displaced from the axial equilibrium position, the change in lateral trapping strength can be significant. The variation of lateral stiffness as a function of axial position was explored using beads tethered by DNA (1.6 μm) to the surface of the flow chamber (Fig. 11, inset). Tethered beads were trapped and the attachment point of the tether was determined and centered on the optical axis.<sup>39</sup> The bead was then pulled vertically through the trap, i.e., along the axial dimension, by lowering the stage in 20 nm increments. At each position, the lateral stiffness of the trap was ascertained by recording its variance, using the Equipartition method. The axial force applied to the bead tether can increase the apparent lateral stiffness, and this effect can be computed by treating the tethered bead as a simple inverted pendulum.<sup>150,151</sup> In practice, the measured increase in lateral stiffness (given by  $\alpha_x = F_a/l$ , where  $\alpha_x$  is the lateral stiffness,  $F_a$  is the axial force on the bead, and  $l$  is the length of the tether) resulted in less than a 3% correction to the stiffness and was thereafter ignored in the analysis. An average of 12 measurements is shown in Fig. 11, along with a fit to the lateral stiffness based on a simple dipole and zero-order Gaussian beam model.<sup>152</sup>

$$\alpha_x(z) = \frac{8n_m p}{c w_0} \left(\frac{a}{w_0}\right)^3 \left(\frac{m^2 - 1}{m^2 + 2}\right) \left(1 + \left(\frac{z}{z_0}\right)^2\right)^{-2}, \quad (14)$$

where  $n_m$  is the index of refraction of the medium,  $p$  is the laser power in the specimen plane,  $c$  is the speed of light,  $m$  is the ratio of the indices of refraction of the bead and the medium, and  $w_0$ ,  $z$  and  $z_0$  are the beam diameter at the waist, the axial displacement of the particle relative to the focus, and the Raleigh range, respectively (as previously defined). The data are well fit by this model with the exception of the laser power, which was sixfold lower than the actual power estimated in the specimen plane. A significant discrepancy was anticipated since it had been previously shown that for particle sizes on the order of the beam waist, the dipole approximation greatly overestimates the trap stiffness.<sup>152</sup> The other two parameters of interest are the beam waist and the

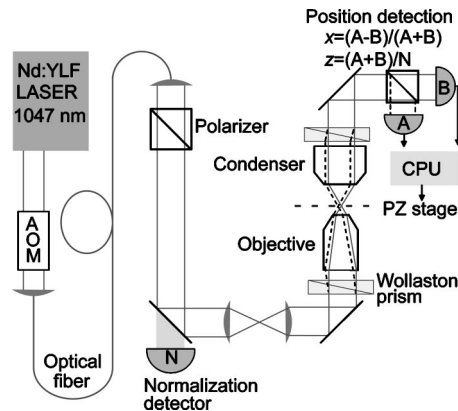


FIG. 13. The optical trapping interferometer. Light from a Nd:YLF laser passes through an acoustic optical modulator (AOM), used to adjust the intensity, and is then coupled into a single-mode polarization-maintaining optical fiber. Output from the fiber passes through a polarizer to ensure a single polarization, through a 1:1 telescope and into the microscope where it passes through the Wollaston prism and is focused in the specimen plane. The scattered and unscattered light is collected by the condenser, is recombined in the second Wollaston prism, then the two polarizations are split in a polarizing beamsplitter and detected by photodiodes A and B. The bleedthrough on a turning mirror is measured by a photodiode (N) to record the instantaneous intensity of the laser. The signals from the detector photodiodes and the normalization diode are digitized and saved to disk. The normalized difference between the two detectors (A and B) gives the lateral,  $x$  displacement, while the sum signal (A+B) normalized by the total intensity (N) gives the axial,  $z$  displacement.

equilibrium axial position of the bead in the trap. The fit returned distances of 0.433 μm for the beam waist and 0.368 μm for the offset of the bead center from the focal point. These values compare well with the values determined from the fit to the axial position signal, which were 0.436 and 0.379 μm, respectively (see above). The variation in lateral stiffness between the optical equilibrium position and the laser focus was substantial: a factor of 1.5 for the configuration studied.

### V. TRANSCRIPTION STUDIED WITH A TWO-DIMENSIONAL STAGE-BASED FORCE CLAMP

Our interest in extending position detection techniques to include the measurement of force and displacement in the axial dimension arose from the study of processive nucleic acid enzymes moving along DNA (Fig. 12). The experimental geometry, in which the enzyme moving along the DNA pulls on a trapped bead, results in motion of the bead in a plane defined by the direction of the lateral force and the axial dimension. In previous experiments, the effects of axial motion had been calculated and estimated, but not directly measured or otherwise calibrated.<sup>39,82</sup> Improvements afforded by three-dimensional piezoelectric stages permitted the direct measurement of, and control over, the separate axial and lateral motions of the trapped bead. We briefly describe this instrument and the implementation of a two-dimensional force clamp to measure transcription by a single molecule of RNA polymerase.<sup>87</sup>

The optical layout and detection scheme are illustrated in Fig. 13. An existing optical trap<sup>39,153</sup> was modified by adding a normalizing photodetector to monitor the bleedthrough of the trapping laser after a 45° dielectric mirror and a

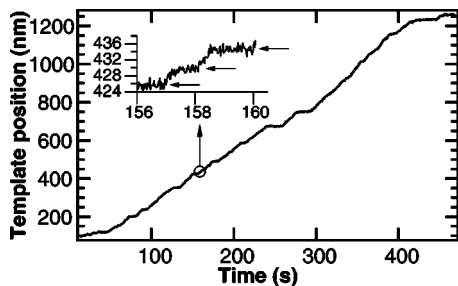


FIG. 14. Two-dimensional, stage based force clamp. Position record of a single RNA polymerase molecule transcribing a 3.5 kbp (1183 nm) DNA template under 18 pN of load. The  $x$  and  $z$  position signals were low pass filtered at 1 kHz, digitized at 2 kHz, and boxcar averaged over 40 points to generate the 50 Hz feedback signals that controlled the motion of the piezoelectric stage. Motion of the stage was corrected for the elastic compliance of the DNA (Ref. 39) to recover the time-dependent contour length, which reflects the position of the RNA polymerase on the template. Periods of roughly constant velocity are interrupted by pauses on multiple timescales. Distinct pauses can be seen in the trace, while shorter pauses ( $\sim 1$  s) can be discerned in the expanded region of the trace (inset: arrows).

feedback-stabilized three-axis piezoelectric stage (Physik Instrumente P-517.3CD and E710.3CD digital controller) to which the trapping chamber was affixed. The optical trap was built around an inverted microscope (Axiovert 35, Carl Zeiss) equipped with a polarized Nd:YLF laser (TFR, Spectra Physics,  $\lambda = 1047$  nm, TEM<sub>00</sub>, 2.5 W) that is focused to a diffraction-limited spot through an objective (Plan Neofluar 100 $\times$ , 1.3 NA oil immersion). Lateral position detection based on polarization interferometry was implemented. The trapping laser passes through a Wollaston prism below the objective producing two orthogonally polarized and slightly spatially separated spots in the specimen plane; these act as a single trap. The light is recombined by a second Wollaston prism in the condenser, after which it passes through a quarter-wave plate and a polarizing beamsplitter. Two photodetectors measure the power in each polarization, and the difference between them, normalized by their sum, supplies the lateral position signal. The sum of the detector signals normalized by the incident laser power (from the normalizing detector) provides the axial position signal.<sup>62,64</sup> The axial position signal is a small fraction of the total intensity and is roughly comparable to the intensity noise of the laser. Normalizing the axial position signal with reference to the instantaneous incident laser power, therefore, provides a significant improvement in the signal-to-noise ratio. The two-dimensional position calibration of the instrument, obtained by raster scanning a stuck bead, is shown in Fig. 7. Stiffness in the lateral dimension was measured by a combination of rolloff, triangle-wave drag force, and variance measurements. Stiffness in the axial dimension was measured using the rolloff method and was found to be  $\sim$ eightfold less than the lateral stiffness.

Single-molecule transcription experiments were carried out with an RNA polymerase specifically attached to the beads and tethered to the surface of the trapping chamber via one end of the template DNA (Fig. 12). Tethered beads were trapped, the surface position was determined as described above, and the bead was centered over the attachment point of the DNA tether, at a predetermined height. Once these initial conditions were established, the two-dimensional

force-clamp routine was begun. The stage was moved in both the axial and lateral directions until the trapped bead was displaced by a predetermined distance from its equilibrium position. Position signals were recorded at 2 kHz and boxcar averaged over 40 points to generate a 50 Hz signal that was used to control the motion of the stage. In this fashion, the displacement of the bead in the trap, and hence the optical force, was held constant as the tether length changed by micron-scale distances during RNA polymerase movement over the DNA template. The motion of RNA polymerase on the DNA can be calculated from the motion of the stage (Fig. 14). Periods of constant motion interrupted by pauses of variable duration are readily observed in the single-molecule transcription trace shown in Fig. 14. Pauses as short as 1 s are readily detected (Fig. 14, inset). Positional noise is on the order of 2 nm, while drift is less than 0.2 nm/s.

Two-dimensional stage based force clamping affords a unique advantage. Since the stiffness in both dimensions is known, the force vector on the bead is defined and constant during an experiment. Tension in the DNA tether opposes the force on the bead, therefore the angle of the DNA with respect to the surface of the trapping chamber is similarly defined and constant. More importantly, the change in the DNA tether length can be calculated from the motion of the stage in one dimension and the angle calculated from the force in both dimensions. As a result, such measurements are insensitive to drift in the axial dimension, which is otherwise a significant source of instrumental error.

## VI. PROGRESS AND OVERVIEW OF OPTICAL TRAPPING THEORY

Optical trapping of dielectric particles is sufficiently complex and influenced by subtle, difficult-to-quantify optical properties that theoretical calculations may never replace direct calibration. That said, recent theoretical work has made significant progress towards a more complete description of optical trapping and three-dimensional position detection based on scattered light. Refined theories permit a more realistic assessment of both the capabilities and the limitations of an optical trapping instrument, and may help to guide future designs and optimizations.

Theoretical expressions for optical forces in the extreme cases of Mie particles ( $a \gg \lambda$ ,  $a$  is the sphere radius) and Raleigh particle ( $a \ll \lambda$ ) have been available for some time. Ashkin calculated the forces on a dielectric sphere in the ray-optic regime for both the TEM<sub>00</sub> and the TEM<sub>01</sub><sup>\*</sup> ("donut mode") intensity profiles.<sup>69</sup> Ray-optics calculations are valid for sphere diameters greater than  $\sim 10\lambda$ , where optical forces become independent of the size of the sphere. At the other extreme, Chaumet and Nieto-Vesperinas obtained an expression for the total time averaged force on a sphere in the Rayleigh regime<sup>154</sup>

$$\langle F^i \rangle = \left( \frac{1}{2} \right) \text{Re}[\alpha E_{0j} \partial^j (E_0^i)^*], \quad (15)$$

where  $\alpha = \alpha_0 (1 - \frac{2}{3} i k^3 \alpha_0)^{-1}$  is a generalized polarizability that includes a damping term,  $E_0$  is the complex magnitude of the electric field,  $\alpha_0$  is the polarizability of a sphere given by Eq.

(4), and  $k$  is the wave number of the trapping laser. This expression encapsulates the separate expressions for the scattering and gradient components of the optical force [Eqs. (1) and (3)] and can be applied to the description of optical forces on larger particles through the use of the coupled dipole method.<sup>155</sup> In earlier work, Harada and Asakura calculated the forces on a dielectric sphere illuminated by a moderately focused Gaussian laser beam in the Rayleigh regime by treating the sphere as a simple dipole.<sup>152</sup> The Rayleigh theory predicts forces comparable to those calculated with the more complete generalized Lorenz–Mie theory (GLMT) for spheres of diameter up to  $\sim w_0$  (the laser beam waist) in the lateral dimension, but only up to  $\sim 0.4\lambda$  in the axial dimension.<sup>152</sup> More general electrodynamic theories have been applied to solve for the case of spheres of diameter  $\sim \lambda$  trapped with tightly focused beams. One approach has been to generalize the Lorenz–Mie theory describing the scattering of a plane wave by a sphere to the case of Gaussian beams. Barton and co-workers applied fifth-order corrections to the fundamental Gaussian beam to derive the incident and scattered fields from a sphere, which enabled the force to be calculated by means of the Maxwell stress tensor.<sup>76,77</sup> An equivalent approach, implemented by Gouesbet and co-workers, expands the incident beam in an infinite series of beam shape parameters from which radiation pressure cross sections can be computed.<sup>80,156</sup> Trapping forces and efficiencies predicted by these theories are found to be in reasonable agreement with experimental values.<sup>157–159</sup> More recently, Rohrbach and co-workers extended the Rayleigh theory to larger particles through the inclusion of second-order scattering terms, valid for spheres that introduce a phase shift,  $k_0(\Delta n)D$ , less than  $\pi/3$ , where  $k_0 = 2\pi/\lambda_0$  is the vacuum wave number,  $\Delta n = (n_p - n_m)$  is the difference in refractive index between the particle and the medium, and  $D$  is the diameter of the sphere.<sup>65,66</sup> For polystyrene beads ( $n_p = 1.57$ ) in water ( $n_m = 1.33$ ), this amounts to a maximum particle size of  $\sim 0.7\lambda$ . In this approach, the incident field is expanded in plane waves, which permits the inclusion of apodization and aberration transformations, and the forces are calculated directly from the scattering of the field by the dipole without resorting to the stress tensor approach. Computed forces and trapping efficiencies compare well with those predicted by GLMT,<sup>66</sup> and the effects of spherical aberration have been explored.<sup>65</sup> Since the second-order Rayleigh theory calculates the scattered and unscattered waves, the far field interference pattern, which is the basis of the three-dimensional position detection described above, is readily calculated.<sup>63,64</sup>

## VII. NOVEL OPTICAL TRAPPING APPROACHES

Optical trapping (OT) has now developed into an active and diverse field of study. Space constraints preclude a complete survey of the field, so we have chosen to focus on a small number of recent developments that seem particularly promising for future applications of the technology.

### A. Combined optical trapping and single-molecule fluorescence

Combining the complementary techniques of OT and single-molecule fluorescence (SMF) presents significant technological challenges. Difficulties arise from the roughly 15 orders of magnitude difference between the enormous flux of infrared light associated with a typical trapping laser (sufficient to bleach many varieties of fluorescent dye through multiphoton excitation) compared to the miniscule flux of visible light emitted by a single excited fluorophore. These challenges have been met in a number of different ways. Funatsu and co-workers built an apparatus in which the two techniques were employed sequentially, but not simultaneously.<sup>160</sup> In a separate development, Ishijima and co-workers were able to trap beads attached to the ends of a long (5–10  $\mu\text{m}$ ) actin filament while simultaneously monitoring the binding of fluorescent Adenosine triphosphate (ATP) molecules to a myosin motor interacting with the actin filament.<sup>161</sup> In this way, the coordination between the binding of ATP to myosin and the mechanical motion of the actin filament (detected via the optical trap) was determined. This experiment demonstrated the possibility of simultaneous—but not spatially coincident—OT and SMF in the same microscope field of view. In a more recent development, both simultaneous and spatially coincident OT and SMF have been achieved, and used to measure the mechanical forces required to unzip short duplex regions [15 base pair (bp)] of double-stranded DNA.<sup>138</sup> Dye-labeled hybrids were attached via a long ( $\sim 1000$  bp) DNA “handle” to a polystyrene bead at one end (using the 3' end of one strand) and to the coverglass surface at the other (using the 5' end of the complementary strand). In one experiment, the adjacent terminal ends of the two strands of the DNA hybrid were each labeled with tetramethylrhodamine (TAMRA) molecules. Due to their physical proximity, these dyes self-quenched (the quenching range for TAMRA is  $\sim 1$  nm). The DNA hybrid was then mechanically disrupted (“unzipped”) by applying a force ramp to the bead while the fluorescence signal was monitored. The point of mechanical rupture detected with the optical trap was coincident with a stepwise increase in the fluorescence signal, as the two dyes separated, leaving behind a dye attached by one DNA strand to the coverglass surface, as the partner dye was removed with the DNA strand attached to the bead. Control experiments with fluorescent dyes attached to either, but not both, DNA strands verified that the abrupt mechanical transition was specific for the rupture of the DNA hybrid and not, for example, due to breakage of the linkages holding the DNA to the bead or the coverglass surface.

### B. Optical rotation and torque

Trapping transparent microspheres with a focused Gaussian laser beam in TEM<sub>00</sub> mode produces a rotationally symmetric trap that does not exert torque. However, several methods have been developed to induce the rotation of trapped objects.<sup>20,52,162</sup> Just as the change of linear momentum due to refraction of light leads to the production of force, a change in angular momentum leads to torque. Cir-

cularly polarized light carries spin angular momentum, of course, and propagating optical beams can also be produced that carry significant amounts of orbital angular momentum, e.g., Laguerre–Gaussian modes.<sup>163</sup> Each photon in such a mode carries  $(\sigma+l)\hbar$  of angular momentum, where  $\sigma$  represents the spin angular momentum arising from the polarization state of the light and  $l$  is the orbital angular momentum carried by the light pattern. The angular momentum conveyed by the circular polarization alone, estimated at  $\sim 10$  pN nm/s per mW of 1064 nm light, can be significantly augmented through the use of modes that carry even larger amounts of orbital angular momentum.<sup>164</sup> Transfer of both orbital and spin angular momentum to trapped objects has been demonstrated for absorbing particles.<sup>102,165</sup> Transfer of spin angular momentum has been observed for birefringent particles of crushed calcite,<sup>166</sup> and for more uniform microfabricated birefringent objects.<sup>167,168</sup> Friese and co-workers derived the following expression for the torque on a birefringent particle:<sup>166</sup>

$$\tau = \frac{\varepsilon}{2\omega} E_0^2 \{ [1 - \cos(kd(n_0 - n_e))] \sin 2\varphi - \sin(kd(n_0 - n_e)) \cos 2\varphi \sin 2\theta \}, \quad (16)$$

where  $\varepsilon$  is the permittivity,  $E_0$  is the amplitude of the electric field,  $\omega$  is the angular frequency of the light,  $\varphi$  describes the ellipticity of the light (plane polarized,  $\varphi=0$ ; circularly polarized,  $\varphi=\pi/4$ ),  $\theta$  represents the angle between the fast axis of the quarter-wave plate producing the elliptically polarized light and the optic axis of the birefringent particle,  $k$  is the vacuum wave number ( $2\pi/\lambda$ ), and  $n_0$  and  $n_e$  are the ordinary and extraordinary indices of refraction of the birefringent material, respectively. Theoretically, all the spin angular momentum carried in a circularly polarized laser beam can be transferred to a trapped object when it acts as a perfect half-wave plate, i.e.,  $\varphi=\pi/4$  and  $kd(n_0-n_e)=\pi$ . For the case of plane polarized light, there is a restoring torque on the birefringent particle that aligns the fast axis of the particle with the plane of polarization.<sup>166</sup> Rotation of the plane of polarization will induce rotation in a trapped birefringent particle.

Whereas the transfer of optical angular momentum is a conceptually attractive means of applying torque to optically trapped objects, several other techniques have been employed towards the same end. In one scheme, a high order asymmetric mode, created by placing an aperture in the far field of a laser beam, was used to trap red blood cells: these could be made to spin by rotating the aperture.<sup>169</sup> A more sophisticated version of this same technique involves interfering a Laguerre–Gaussian beam with a plane wave beam to produce a spiral beam pattern.<sup>170</sup> By changing the relative phase of the two beams, the pattern can be made to rotate, leading to rotation in an asymmetric trapped object.<sup>48</sup> Alternatively, the interference of two Laguerre–Gaussian beams of opposite helicity ( $l$  and  $-l$ ) creates  $2l$  beams surrounding the optical axis, which can be rotated by adjusting the polarization of one of the interfering beams.<sup>46</sup> Additionally, a variety of small chiral objects, such as microfabricated “optical propellers,” can be trapped and made to rotate in a symmet-

ric Gaussian beam due to the optical forces generated on asymmetrically oriented surfaces.<sup>171–174</sup>

Rotation of trapped particles is most commonly monitored by video tracking, which is effectively limited by frame rates to rotation speeds below  $\sim 15$  Hz, and to visibly asymmetric particles (i.e., microscopic objects of sufficient size and contrast to appear asymmetric in the imaging modality used). Rotation rates up to 1 kHz have been measured by back focal plane detection of trapped  $0.83 \mu\text{m}$  beads sparsely labeled with  $0.22 \mu\text{m}$  beads to make these optically anisotropic.<sup>175</sup> Backscattered light from trapped, asymmetric particles has also been used to measure rotation rates in excess of 300 Hz.<sup>102,166</sup>

### C. Holographic optical traps

Holograms and other types of diffractive optics have been used extensively for generating complex, high-order optical trapping beams,<sup>20,52,162,165,176</sup> such as the Laguerre–Gaussian modes discussed above. Diffractive optical devices may also be used to synthesize multiple optical traps with arbitrary intensity profiles.<sup>20,91,177–179</sup> A diffractive element placed in a plane optically conjugate to the back aperture of the microscope objective produces an intensity distribution in the specimen plane that is the Fourier transform of the pattern imposed by the element,<sup>177</sup> and several computational methods have been developed to derive the holographic pattern required for any given intensity distribution in the specimen plane.<sup>91,92,180</sup> Generally speaking, diffractive elements modulate both the amplitude and the phase of the incident light. Optical throughput can be maximized by employing diffractive optics that primarily modify the phase but not the amplitude of the incident light, termed kinoforms.<sup>91</sup> Computer-generated phase masks can also be etched onto a glass substrate using standard photolithographic techniques, producing arbitrary, but fixed, optical traps.

Reicherter and co-workers extended the usefulness of holographic optical trapping techniques by generating three independently movable donut-mode trapping beams with an addressable liquid crystal spatial light modulator (SLM).<sup>181</sup> Improvements in SLM technology and real-time hologram calculation algorithms have been implemented, allowing the creation of an array of up to 400 optical traps, in addition to the creation and three-dimensional manipulation of multiple, high order, trapping beams.<sup>92,182,183</sup> Multiple optical traps can also be generated by time sharing, using rapid-scanning techniques based on AODs or galvo mirrors,<sup>49,50</sup> but these are typically formed in just one or two axial planes,<sup>184</sup> and they are limited in number. Dynamic holographic optical tweezers can produce still more varied patterns, limited only by the optical characteristics of the SLM and the computational time required to generate the hologram. Currently, the practical update rate of a typical SLM is around 5 Hz, which limits how quickly objects can be translated.<sup>92</sup> Furthermore, the number and size of the pixels in the SLM restrict the complexity and the range of motion of generated optical traps,<sup>92</sup> while the pixelation and discrete phase steps of the SLM result in diffractive losses. Faster refresh rates ( $>30$  Hz) in a holographic optical trap have recently been reported with a SLM based on ferroelectric, as opposed to

nematic, materials.<sup>185</sup> Further improvements in SLM technology should expand the possible applications of dynamic, holographic optical traps.

## VIII. PROSPECTS

The nearly 2 decades that have passed since Ashkin and co-workers invented the single beam, gradient force optical trap have borne witness to a proliferation of innovations and applications. The full potential of most of the more recent optical developments has yet to be realized. On the biological front, the marriage of optical trapping with single-molecule fluorescence methods<sup>138</sup> represents an exciting frontier with enormous potential. Thanks to steady improvements in optical trap stability and photodetector sensitivity, the practical limit for position measurements is now comparable to the distance subtended by a single base pair along DNA, 3.4 Å. Improved spatiotemporal resolution is now permitting direct observations of molecular-scale motions in individual nucleic acid enzymes, such as polymerases, helicases, and nucleases.<sup>86,87,186</sup> The application of optical torque offers the ability to study rotary motors, such as  $F_1F_0$  ATPase,<sup>187</sup> using rotational analogs of many of the same techniques already applied to the study of linear motors, i.e., torque clamps and rotation clamps.<sup>50</sup> Moving up in scale, the ability to generate and manipulate a myriad of optical traps dynamically using holographic tweezers<sup>20,92</sup> opens up many potential applications, including cell sorting and other types of high-throughput manipulation. More generally, as the field matures, optical trapping instruments should no longer be confined to labs that build their own custom apparatus, a change that should be driven by the increasing availability of sophisticated, versatile commercial systems. The physics of optical trapping will continue to be explored in its own right, and optical traps will be increasingly employed to study physical, as well as biological, phenomena. In one groundbreaking example from the field of nonequilibrium statistical mechanics, Jarzynski's equality<sup>188</sup>—which relates the value of the equilibrium free energy for a transition in a system to a *nonequilibrium* measure of the work performed—was put to experimental test by mechanically unfolding RNA structures using optical forces.<sup>189</sup> Optical trapping techniques are increasingly being used in condensed matter physics to study the behavior (including anomalous diffusive properties and excluded volume effects) of colloids and suspensions,<sup>21</sup> and dynamic optical tweezers are particularly well suited for the creation and evolution of large arrays of colloids in well-defined potentials.<sup>20</sup> As optical trapping techniques continue to improve and become better established, these should pave the way for some great new science in the 21st century, and we will be further indebted to the genius of Ashkin.<sup>3</sup>

## ACKNOWLEDGMENTS

The authors thank members of the Block Lab for advice, suggestions, and helpful discussions. In particular, Elio Abbondanzieri helped with instrument construction and all aspects of data collection, Joshua Shaevitz supplied Fig. 6, and Megan Valentine and Michael Woodside supplied valuable comments on the manuscript. We also thank Henrik Flyv-

bjerg, Kirstine Berg-Sørensen, and the members of their labs for sharing results in advance of publication, for critical reading of the manuscript, and for help in preparing Fig. 10. Finally, we thank Megan Valentine, Grace Liou, and Richard Neuman for critical reading of the manuscript.

- <sup>1</sup>A. Ashkin, *Phys. Rev. Lett.* **24**, 156 (1970).
- <sup>2</sup>A. Ashkin and J. M. Dziedzic, *Appl. Phys. Lett.* **19**, 283 (1971).
- <sup>3</sup>A. Ashkin *et al.*, *Opt. Lett.* **11**, 288 (1986).
- <sup>4</sup>A. Ashkin, *IEEE J. Sel. Top. Quantum Electron.* **6**, 841 (2000).
- <sup>5</sup>S. Chu *et al.*, *Phys. Rev. Lett.* **57**, 314 (1986).
- <sup>6</sup>A. Ashkin, J. M. Dziedzic, and T. Yamane, *Nature (London)* **330**, 769 (1987).
- <sup>7</sup>A. Ashkin and J. M. Dziedzic, *Science* **235**, 1517 (1987).
- <sup>8</sup>M. J. Lang and S. M. Block, *Am. J. Phys.* **71**, 201 (2003).
- <sup>9</sup>K. Svoboda and S. M. Block, *Annu. Rev. Biophys. Biomol. Struct.* **23**, 247 (1994).
- <sup>10</sup>A. D. Mehta, J. T. Finer, and J. A. Spudich, *Methods Enzymol.* **298**, 436 (1998).
- <sup>11</sup>A. D. Mehta *et al.*, *Science* **283**, 1689 (1999).
- <sup>12</sup>S. C. Kuo, *Traffic* **2**, 757 (2001).
- <sup>13</sup>A. Ishijima and T. Yanagida, *Trends Biochem. Sci.* **26**, 438 (2001).
- <sup>14</sup>Y. Ishii, A. Ishijima, and T. Yanagida, *Trends Biotechnol.* **19**, 211 (2001).
- <sup>15</sup>S. Jeney, E. L. Florin, and J. K. Horber, *Methods Mol. Biol.* **164**, 91 (2001).
- <sup>16</sup>S. Khan and M. P. Sheetz, *Annu. Rev. Biochem.* **66**, 785 (1997).
- <sup>17</sup>R. Simmons, *Curr. Biol.* **6**, 392 (1996).
- <sup>18</sup>C. Bustamante, J. C. Macosko, and G. J. Wuite, *Nat. Rev. Mol. Cell Biol.* **1**, 130 (2000).
- <sup>19</sup>M. D. Wang, *Curr. Opin. Biotechnol.* **10**, 81 (1999).
- <sup>20</sup>D. G. Grier, *Nature (London)* **424**, 810 (2003).
- <sup>21</sup>D. G. Grier, *Curr. Opin. Colloid Interface Sci.* **2**, 264 (1997).
- <sup>22</sup>J. K. H. Horber, *Atomic Force Microscopy in Cell Biology* (Academic, San Diego, 2002), pp. 1–31.
- <sup>23</sup>H. Lowen, *J. Phys.: Condens. Matter* **13**, R415 (2001).
- <sup>24</sup>R. Bar-Ziv, E. Moses, and P. Nelson, *Biophys. J.* **75**, 294 (1998).
- <sup>25</sup>P. T. Korda, M. B. Taylor, and D. G. Grier, *Phys. Rev. Lett.* **89**, 128301 (2002).
- <sup>26</sup>L. A. Hough and H. D. Ou-Yang, *Phys. Rev. E* **65**, 021906 (2002).
- <sup>27</sup>B. H. Lin, J. Yu, and S. A. Rice, *Phys. Rev. E* **62**, 3909 (2000).
- <sup>28</sup>J. C. Crocker and D. G. Grier, *Phys. Rev. Lett.* **77**, 1897 (1996).
- <sup>29</sup>J. C. Crocker and D. G. Grier, *Phys. Rev. Lett.* **73**, 352 (1994).
- <sup>30</sup>C. Bustamante, Z. Bryant, and S. B. Smith, *Nature (London)* **421**, 423 (2003).
- <sup>31</sup>C. Bustamante *et al.*, *Curr. Opin. Struct. Biol.* **10**, 279 (2000).
- <sup>32</sup>L. H. Pope, M. L. Bennink, and J. Greve, *J. Muscle Res. Cell Motil.* **23**, 397 (2002).
- <sup>33</sup>J. F. Allemand, D. Bensimon, and V. Croquette, *Curr. Opin. Struct. Biol.* **13**, 266 (2003).
- <sup>34</sup>A. Janshoff *et al.*, *Angew. Chem., Int. Ed.* **39**, 3213 (2000).
- <sup>35</sup>B. Onoa *et al.*, *Science* **299**, 1892 (2003).
- <sup>36</sup>J. Liphardt *et al.*, *Science* **292**, 733 (2001).
- <sup>37</sup>Z. Bryant *et al.*, *Nature (London)* **424**, 338 (2003).
- <sup>38</sup>S. B. Smith, Y. J. Cui, and C. Bustamante, *Science* **271**, 795 (1996).
- <sup>39</sup>M. D. Wang *et al.*, *Biophys. J.* **72**, 1335 (1997).
- <sup>40</sup>T. T. Perkins *et al.*, *Science* **264**, 822 (1994).
- <sup>41</sup>T. T. Perkins, D. E. Smith, and S. Chu, *Science* **264**, 819 (1994).
- <sup>42</sup>T. T. Perkins *et al.*, *Science* **268**, 83 (1995).
- <sup>43</sup>K. Wang, J. G. Forbes, and A. J. Jin, *Prog. Biophys. Mol. Biol.* **77**, 1 (2001).
- <sup>44</sup>A. Ashkin, *Proc. Natl. Acad. Sci. U.S.A.* **94**, 4853 (1997).
- <sup>45</sup>D. McGloin, V. Garces-Chavez, and K. Dholakia, *Opt. Lett.* **28**, 657 (2003).
- <sup>46</sup>M. P. MacDonald *et al.*, *Science* **296**, 1101 (2002).
- <sup>47</sup>V. Garces-Chavez *et al.*, *Nature (London)* **419**, 145 (2002).
- <sup>48</sup>L. Paterson *et al.*, *Science* **292**, 912 (2001).
- <sup>49</sup>K. Visscher, S. P. Gross, and S. M. Block, *IEEE J. Sel. Top. Quantum Electron.* **2**, 1066 (1996).
- <sup>50</sup>K. Visscher and S. M. Block, *Methods Enzymol.* **298**, 460 (1998).
- <sup>51</sup>J. E. Molloy, *Methods Cell Biol.* **55**, 205 (1998).
- <sup>52</sup>J. E. Molloy and M. J. Padgett, *Contemp. Phys.* **43**, 241 (2002).
- <sup>53</sup>G. J. Brouhard, H. T. Schek III, and A. J. Hunt, *IEEE Trans. Biomed. Eng.* **50**, 121 (2003).

- <sup>54</sup>M. P. Sheetz, in *Laser Tweezers in Cell Biology. Methods in Cell Biology*, edited by L. Wilson and P. Matsudaira (Academic, San Diego, 1998), Vol. 55.
- <sup>55</sup>S. M. Block, in *Noninvasive Techniques in Cell Biology*, edited by J. K. Foskett and S. Grinstein (Wiley-Liss, New York, 1990), pp. 375–402.
- <sup>56</sup>S. E. Rice, T. J. Purcell, and J. A. Spudich, *Methods Enzymol.* **361**, 112 (2003).
- <sup>57</sup>S. B. Smith, Y. Cui, and C. Bustamante, *Methods Enzymol.* **361**, 134 (2003).
- <sup>58</sup>S. M. Block, in *Constructing Optical Tweezers, Cell Biology: A Laboratory Manual*, edited by D. Spector, R. Goldman, and L. Leinward (Cold Spring Harbor Press, Cold Spring Harbor, NY, 1998).
- <sup>59</sup>M. J. Lang *et al.*, *Biophys. J.* **83**, 491 (2002).
- <sup>60</sup>E. Fallman and O. Axner, *Appl. Opt.* **36**, 2107 (1997).
- <sup>61</sup>E. J. G. Peterman *et al.*, *Rev. Sci. Instrum.* **74**, 3246 (2003).
- <sup>62</sup>A. Pralle *et al.*, *Microsc. Res. Tech.* **44**, 378 (1999).
- <sup>63</sup>A. Rohrbach, H. Kress, and E. H. Stelzer, *Opt. Lett.* **28**, 411 (2003).
- <sup>64</sup>A. Rohrbach and E. H. K. Stelzer, *J. Appl. Phys.* **91**, 5474 (2002).
- <sup>65</sup>A. Rohrbach and E. H. Stelzer, *Appl. Opt.* **41**, 2494 (2002).
- <sup>66</sup>A. Rohrbach and E. H. Stelzer, *J. Opt. Soc. Am. A Opt. Image Sci. Vis* **18**, 839, (2001).
- <sup>67</sup>J. D. Jackson, *Classical Electrodynamics*, 2nd ed. (Wiley, New York, 1975).
- <sup>68</sup>A. Ashkin, *Methods in Cell Biology* (Academic, San Diego, 1998), Vol. 55, pp. 1–27.
- <sup>69</sup>A. Ashkin, *Biophys. J.* **61**, 569 (1992).
- <sup>70</sup>E. Fallman and O. Axner, *Appl. Opt.* **42**, 3915 (2003).
- <sup>71</sup>A. T. O'Neill and M. J. Padgett, *Opt. Commun.* **193**, 45 (2001).
- <sup>72</sup>N. B. Simpson *et al.*, *J. Mod. Opt.* **45**, 1943 (1998).
- <sup>73</sup>M. E. J. Friese *et al.*, *Appl. Opt.* **35**, 7112 (1996).
- <sup>74</sup>E. Almaas and I. Brevik, *J. Opt. Soc. Am. B* **12**, 2429 (1995).
- <sup>75</sup>J. P. Barton, *J. Appl. Phys.* **64**, 1632 (1988).
- <sup>76</sup>J. P. Barton and D. R. Alexander, *J. Appl. Phys.* **66**, 2800 (1989).
- <sup>77</sup>J. P. Barton, D. R. Alexander, and S. A. Schaub, *J. Appl. Phys.* **66**, 4594 (1989).
- <sup>78</sup>P. Zemanek, A. Jonas, and M. Liska, *J. Opt. Soc. Am. A Opt. Image Sci. Vis* **19**, 1025 (2002).
- <sup>79</sup>G. Gouesbet and G. Grehan, *Atomization Sprays* **10**, 277 (2000).
- <sup>80</sup>K. F. Ren, G. Greha, and G. Gouesbet, *Opt. Commun.* **108**, 343 (1994).
- <sup>81</sup>K. Visscher, M. J. Schnitzer, and S. M. Block, *Nature (London)* **400**, 184 (1999).
- <sup>82</sup>M. D. Wang *et al.*, *Science* **282**, 902 (1998).
- <sup>83</sup>G. J. Wuite *et al.*, *Nature (London)* **404**, 103 (2000).
- <sup>84</sup>R. S. Rock *et al.*, *Proc. Natl. Acad. Sci. U.S.A.* **98**, 13655 (2001).
- <sup>85</sup>S. M. Block *et al.*, *Proc. Natl. Acad. Sci. U.S.A.* **100**, 2351 (2003).
- <sup>86</sup>T. T. Perkins *et al.*, *Science* **301**, 1914 (2003).
- <sup>87</sup>K. C. Neuman *et al.*, *Cell* **115**, 437 (2003).
- <sup>88</sup>K. Adelman *et al.*, *Proc. Natl. Acad. Sci. U.S.A.* **99**, 13538 (2002).
- <sup>89</sup><<http://www.cellrobotics.com>>
- <sup>90</sup><<http://www.arryx.com/home1.html>>
- <sup>91</sup>E. R. Dufresne *et al.*, *Rev. Sci. Instrum.* **72**, 1810 (2001).
- <sup>92</sup>J. E. Curtis, B. A. Koss, and D. G. Grier, *Opt. Commun.* **207**, 169 (2002).
- <sup>93</sup><<http://www.palm-mikrolaser.com>>
- <sup>94</sup>S. P. Gross, *Methods Enzymol.* **361**, 162 (2003).
- <sup>95</sup>K. C. Neuman *et al.*, *Biophys. J.* **77**, 2856 (1999).
- <sup>96</sup>H. Liang *et al.*, *Biophys. J.* **70**, 1529 (1996).
- <sup>97</sup>I. A. Vorobjev *et al.*, *Biophys. J.* **64**, 533 (1993).
- <sup>98</sup>A. Ashkin and J. M. Dziedzic, *Ber. Bunsenges. Phys. Chem. Chem. Phys.* **93**, 254 (1989).
- <sup>99</sup>Y. Liu *et al.*, *Biophys. J.* **68**, 2137 (1995).
- <sup>100</sup>E. J. G. Peterman, F. Gittes, and C. F. Schmidt, *Biophys. J.* **84**, 1308 (2003).
- <sup>101</sup>A. Schonle and S. W. Hell, *Opt. Lett.* **23**, 325 (1998).
- <sup>102</sup>M. E. J. Friese *et al.*, *Phys. Rev. A* **54**, 1593 (1996).
- <sup>103</sup>G. J. Wuite *et al.*, *Biophys. J.* **79**, 1155 (2000).
- <sup>104</sup>W. Grange *et al.*, *Rev. Sci. Instrum.* **73**, 2308 (2002).
- <sup>105</sup>S. Inoue and K. R. Spring, *Video Microscopy: The Fundamentals*, 2nd ed. (Plenum, New York, 1997).
- <sup>106</sup>H. Misawa *et al.*, *J. Appl. Phys.* **70**, 3829 (1991).
- <sup>107</sup>S. C. Kuo and J. L. McGrath, *Nature (London)* **407**, 1026 (2000).
- <sup>108</sup>Y. L. Kuo *et al.*, *Arch. Androl* **44**, 29 (2000).
- <sup>109</sup>S. Yamada, D. Wirtz, and S. C. Kuo, *Biophys. J.* **78**, 1736 (2000).
- <sup>110</sup>M. K. Cheezum, W. F. Walker, and W. H. Guilford, *Biophys. J.* **81**, 2378 (2001).
- <sup>111</sup>R. E. Thompson, D. R. Larson, and W. W. Webb, *Biophys. J.* **82**, 2775 (2002).
- <sup>112</sup>J. C. Crocker and D. G. Grier, *J. Colloid Interface Sci.* **179**, 298 (1996).
- <sup>113</sup>C. Gosse and V. Croquette, *Biophys. J.* **82**, 3314 (2002).
- <sup>114</sup>M. Keller, J. Schilling, and E. Sackmann, *Rev. Sci. Instrum.* **72**, 3626 (2001).
- <sup>115</sup>V. Croquette (personal communication).
- <sup>116</sup>J. T. Finer, R. M. Simmons, and J. A. Spudich, *Nature (London)* **368**, 113 (1994).
- <sup>117</sup>J. E. Molloy *et al.*, *Biophys. J.* **68**, S298 (1995).
- <sup>118</sup>W. Denk and W. W. Webb, *Appl. Opt.* **29**, 2382 (1990).
- <sup>119</sup>K. Svoboda *et al.*, *Nature (London)* **365**, 721 (1993).
- <sup>120</sup>F. Gittes and C. F. Schmidt, *Opt. Lett.* **23**, 7 (1998).
- <sup>121</sup>F. Gittes and C. F. Schmidt, *Biophys. J.* **74**, A183 (1998).
- <sup>122</sup>M. W. Allersma *et al.*, *Biophys. J.* **74**, 1074 (1998).
- <sup>123</sup>L. P. Ghislain and W. W. Webb, *Opt. Lett.* **18**, 1678 (1993).
- <sup>124</sup>L. P. Ghislain, N. A. Switz, and W. W. Webb, *Rev. Sci. Instrum.* **65**, 2762 (1994).
- <sup>125</sup>I. M. Peters *et al.*, *Rev. Sci. Instrum.* **69**, 2762 (1998).
- <sup>126</sup>M. E. J. Friese *et al.*, *Appl. Opt.* **38**, 6597 (1999).
- <sup>127</sup>E. L. Florin *et al.*, *J. Struct. Biol.* **119**, 202 (1997).
- <sup>128</sup>E. L. Florin, J. K. H. Horber, and E. H. K. Stelzer, *Appl. Phys. Lett.* **69**, 446 (1996).
- <sup>129</sup>Z. X. Zhang *et al.*, *Appl. Opt.* **37**, 2766 (1998).
- <sup>130</sup>A. Jonas, P. Zemanek, and E. L. Florin, *Opt. Lett.* **26**, 1466 (2001).
- <sup>131</sup>K. Sasaki, M. Tsukima, and H. Masuhara, *Appl. Phys. Lett.* **71**, 37 (1997).
- <sup>132</sup>A. R. Clapp, A. G. Ruta, and R. B. Dickinson, *Rev. Sci. Instrum.* **70**, 2627 (1999).
- <sup>133</sup>A. E. Siegman, *Lasers University Science Books* (Sausalito, CA, 1986), p. 1283.
- <sup>134</sup>K. Berg-Sorensen *et al.*, *J. Appl. Phys.* **93**, 3167 (2003).
- <sup>135</sup>S. J. Koch and M. D. Wang, *Phys. Rev. Lett.* **91**, 028103 (2003).
- <sup>136</sup>B. D. Brower-Toland *et al.*, *Proc. Natl. Acad. Sci. U.S.A.* **99**, 1960 (2002).
- <sup>137</sup>S. J. Koch *et al.*, *Biophys. J.* **83**, 1098 (2002).
- <sup>138</sup>M. J. Lang, P. M. Fordyce, and S. M. Block, *J. Biol.* **2**, 6 (2003).
- <sup>139</sup>T. D. Visser and S. H. Wiersma, *J. Opt. Soc. Am. A Opt. Image Sci. Vis* **9**, 2034 (1992).
- <sup>140</sup>S. H. Wiersma *et al.*, *J. Opt. Soc. Am. A Opt. Image Sci. Vis* **14**, 1482 (1997).
- <sup>141</sup>S. H. Wiersma and T. D. Visser, *J. Opt. Soc. Am. A Opt. Image Sci. Vis* **13**, 320 (1996).
- <sup>142</sup>K. Carlsson, *J. Microsc.* **163**, 167 (1991).
- <sup>143</sup>P. Bartlett, S. I. Henderson, and S. J. Mitchell, *Philos. Trans. R. Soc. London, Ser. A* **359**, 883 (2001).
- <sup>144</sup>S. Hell *et al.*, *J. Microsc.* **169**, 391 (1993).
- <sup>145</sup>J. Radler and E. Sackmann, *Langmuir* **8**, 848 (1992).
- <sup>146</sup>K. C. Neuman, E. A. Abbondanzieri, and S. M. Block (unpublished).
- <sup>147</sup>H. Brenner, *Chem. Eng. Sci.* **16**, 242 (1961).
- <sup>148</sup>K. Berg-Sørensen and H. Flyvbjerg, *Rev. Sci. Instrum.* **75**, 594 (2004).
- <sup>149</sup>I. M. Toliæ-Nørrelykke, K. Berg-Sørensen, and H. Flyvbjerg, *Comput. Phys. Commun.* **159**, 225 (2004).
- <sup>150</sup>T. R. Strick *et al.*, *Biophys. J.* **74**, 2016 (1998).
- <sup>151</sup>T. R. Strick *et al.*, *Science* **271**, 1835 (1996).
- <sup>152</sup>Y. Harada and T. Asakura, *Opt. Commun.* **124**, 529 (1996).
- <sup>153</sup>K. Svoboda and S. M. Block, *Cell* **77**, 773 (1994).
- <sup>154</sup>P. C. Chaumet and M. Nieto-Vesperinas, *Opt. Lett.* **25**, 1065 (2000).
- <sup>155</sup>P. C. Chaumet and M. Nieto-Vesperinas, *Phys. Rev. B* **61**, 4119 (2000).
- <sup>156</sup>G. Gouesbet, B. Maheu, and G. Grehan, *J. Opt. Soc. Am. A Opt. Image Sci. Vis* **5**, 1427 (1988).
- <sup>157</sup>Y. K. Nahmias and D. J. Odde, *Int. J. Quantum Chem.* **38**, 131 (2002).
- <sup>158</sup>W. H. Wright, G. J. Sonek, and M. W. Berns, *Appl. Opt.* **33**, 1735 (1994).
- <sup>159</sup>W. H. Wright, G. J. Sonek, and M. W. Berns, *Appl. Phys. Lett.* **63**, 715 (1993).
- <sup>160</sup>T. Funatsu *et al.*, *Biophys. Chem.* **68**, 63 (1997).
- <sup>161</sup>A. Ishijima *et al.*, *Cell* **92**, 161 (1998).
- <sup>162</sup>K. Dholakia, G. Spalding, and M. MacDonald, *Phys. World* **15**, 31 (2002).
- <sup>163</sup>S. M. Barnett and L. Allen, *Opt. Commun.* **110**, 670 (1994).
- <sup>164</sup>L. Allen *et al.*, *Phys. Rev. A* **45**, 8185 (1992).
- <sup>165</sup>H. He *et al.*, *Phys. Rev. Lett.* **75**, 826 (1995).
- <sup>166</sup>M. E. J. Friese *et al.*, *Nature (London)* **394**, 348 (1998).

- <sup>167</sup>E. Higurashi, R. Sawada, and T. Ito, *J. Micromech. Microeng.* **11**, 140 (2001).
- <sup>168</sup>E. Higurashi, R. Sawada, and T. Ito, *Phys. Rev. E* **59**, 3676 (1999).
- <sup>169</sup>S. Sato, M. Ishigure, and H. Inaba, *Electron. Lett.* **27**, 1831 (1991).
- <sup>170</sup>M. Padgett *et al.*, *Am. J. Phys.* **64**, 77 (1996).
- <sup>171</sup>E. Higurashi *et al.*, *Appl. Phys. Lett.* **64**, 2209 (1994).
- <sup>172</sup>E. Higurashi *et al.*, *J. Appl. Phys.* **82**, 2773 (1997).
- <sup>173</sup>R. C. Gauthier, *Appl. Phys. Lett.* **67**, 2269 (1995).
- <sup>174</sup>R. C. Gauthier, *Appl. Opt.* **40**, 1961 (2001).
- <sup>175</sup>A. D. Rowe *et al.*, *J. Mod. Opt.* **50**, 1539 (2003).
- <sup>176</sup>H. He, N. R. Heckenberg, and H. Rubinsztein-Dunlop, *J. Mod. Opt.* **42**, 217 (1995).
- <sup>177</sup>E. R. Dufresne and D. G. Grier, *Rev. Sci. Instrum.* **69**, 1974 (1998).
- <sup>178</sup>P. Korda *et al.*, *Rev. Sci. Instrum.* **73**, 1956 (2002).
- <sup>179</sup>D. M. Mueth *et al.*, *Phys. Rev. Lett.* **77**, 578 (1996).
- <sup>180</sup>J. Liesener *et al.*, *Opt. Commun.* **185**, 77 (2000).
- <sup>181</sup>M. Reicherter *et al.*, *Opt. Lett.* **24**, 608 (1999).
- <sup>182</sup>J. E. Curtis and D. G. Grier, *Opt. Lett.* **28**, 872 (2003).
- <sup>183</sup>Y. Igasaki *et al.*, *Opt. Rev.* **6**, 339 (1999).
- <sup>184</sup>A. van Blaaderen *et al.*, *Faraday Discuss.* **123**, 107 (2003).
- <sup>185</sup>W. J. Hossack *et al.*, *Opt. Express* **11**, 2053 (2003).
- <sup>186</sup>J. W. Shaevitz *et al.*, *Nature (London)* **426**, 684 (2003).
- <sup>187</sup>H. Noji *et al.*, *Nature (London)* **386**, 299 (1997).
- <sup>188</sup>C. Jarzynski, *Phys. Rev. Lett.* **78**, 2690 (1997).
- <sup>189</sup>J. Liphardt *et al.*, *Science* **296**, 1832 (2002).

# Lab 6: Optical tweezers: membrane and cell

**Location:** NE47-215b

**PI:** Matt Lang

**Lab Instructor:** John Mills

## Summary

Optical tweezers that exert forces up to hundreds of picoNewtons can probe the mechanical properties of membranes and cells. Standard tweezers experiments involve optically trapping small microspheres attached to specific cell membrane locations which serve as grips to deform the cell membrane locally (tether experiments) or entire cell (cell stretch experiments). Calibration of optical trap forces on the microspheres allows quantitative measurement of static and dynamic cell mechanical properties. In this laboratory module, two experiments will be performed: membrane tether pulling of B-cells and cell stretch tests of erythrocytes.

## Recommended Reading

D. Raucher and M. P. Sheetz, "Characteristics of a Membrane Reservoir Buffering Membrane Tension," *Biophys. J.* **77**.

J. P. Mills *et al.*, "Nonlinear Elastic and Viscoelastic Deformation of the Human Red Blood Cell with Optical Tweezers," *Mol. Cell Biol.* **1**.



# Characteristics of a Membrane Reservoir Buffering Membrane Tension

Drazen Raucher and Michael P. Sheetz

Department of Cell Biology, Duke University Medical Center, Durham, North Carolina 27710 USA

**ABSTRACT** When membrane-attached beads are pulled vertically by a laser tweezers, a membrane tube of constant diameter (tether) is formed. We found that the force on the bead (tether force) did not depend on tether length over a wide range of tether lengths, which indicates that a previously unidentified reservoir of membrane and not stretch of the plasma membrane provides the tether membrane. Plots of tether force vs. tether length have an initial phase, an elongation phase, and an exponential phase. During the major elongation phase, tether force is constant, buffered by the “membrane reservoir.” Finally, there is an abrupt exponential rise in force that brings the tether out of the trap, indicating depletion of the membrane reservoir. In chick embryo fibroblasts and 3T3 fibroblasts, the maximum tether lengths that can be pulled at a velocity of 4  $\mu\text{m/s}$  are  $5.1 \pm 0.3$  and  $5.0 \pm 0.2$   $\mu\text{m}$ , respectively. To examine the importance of the actin cytoskeleton, we treated cells with cytochalasin B or D and found that the tether lengths increased dramatically to  $13.8 \pm 0.8$  and  $12.0 \pm 0.7$   $\mu\text{m}$ , respectively. Similarly, treatment of the cells with colchicine and nocodazole results in more than a twofold increase in tether length. We found that elevation of membrane tension (through osmotic pressure, a long-term elevation of tether force, or a number of transitory increases) increased reservoir size over the whole cell. Using a tracking system to hold tether force on the bead constant near its maximal length in the exponential phase, the rate of elongation of the tethers was measured as a function of tether force (membrane tension). The rate of elongation of tethers was linearly dependent on the tether force and reflected an increase in size of the reservoir. Increases in the reservoir caused by tension increases on one side of the cell caused increases in reservoir size on the other side of the cell. Thus, we suggest that cells maintain a plasma membrane reservoir to buffer against changes in membrane tension and that the reservoir is increased with membrane tension or disruption of the cytoskeleton.

## INTRODUCTION

One of the most important properties of the plasma membrane is to serve as a flexible continuous barrier between the cell constituents and the external environment. Active cells undergo rapid morphological changes and can withstand changes in medium osmolarity. It is clear that the plasma membrane is very active, since dramatic changes in cell morphology often require large changes in membrane area. The plasma membrane cannot stretch to accommodate the changes, since the maximum elastic stretching of a membrane is about 4% (Evans and Skalak, 1979; Waugh, 1983) at lytic tensions, which are 100- to 1000-fold greater than normal (Dai and Sheetz, 1995, 1997). Therefore, additional membrane must be drawn from internal compartments of the cell. In a similar manner, the cell must accommodate changes in medium osmolarity that would cause cell swelling. In our previous studies, we have found that the cell plasma membrane tension is constant under normal conditions and even major osmotic perturbations cause relatively minor changes in tension (Dai et al., 1998). Thus, the cell must have mechanisms to regulate membrane tension. A working hypothesis maintains that tension is tied to membrane traffic and membrane-cytoskeleton adhesion and serves to regulate several important cell functions, including

endocytosis rate and motility. Control of membrane traffic through membrane tension could help to maintain the correct plasma membrane area.

The traffic of membrane to and from the plasma membrane is rapid in most cells and membrane could be added in response to morphological or osmotic changes. However, membrane tensions have a variation of 10%, whereas to increase the plasma membrane area by only 1  $\mu\text{m}^2$  in a typical cell (1000  $\mu\text{m}^2$  of plasma membrane) would cause a 500% increase in membrane tension. A membrane reservoir could buffer variations in membrane tension. The concept of a membrane reservoir has been considered for platelets and phagocytic cells. In platelets, there are many invaginations of the plasma membrane that contain the membrane needed for the extension of long filopodia following platelet activation. Excess membrane must be available in macrophages to provide the plasma membrane that is endocytosed during phagocytosis. Several previous studies of the membrane reservoir have focused on measuring variations in the plasma membrane surface area of macrophages (Burwen and Satir, 1977; Petty et al., 1981). Using scanning electron microscopy, Petty et al. (1981) have shown that the macrophage surface folds decrease dramatically after phagocytosis, suggesting that the membrane reservoir in macrophages is contained in surface folds. A reservoir of membrane in either invaginations or surface folds could buffer changes in membrane tension. Therefore, in order to elucidate the nature and to characterize the dynamics of the membrane reservoir, it is necessary to find a method for probing the relative size of the membrane reservoir during chemical or mechanical perturbations.

Received for publication 28 July 1998 and in final form 16 July 1999.

Address reprint requests to Michael P. Sheetz, Department of Cell Biology, Duke University Medical Center, 388 Nanaline Duke Bldg., Research Drive, Durham, NC 27710. Tel.: 919-684-8085; Fax: 919-684-8592; E-mail: mike.sheetz@cellbio.duke.edu.

© 1999 by the Biophysical Society

0006-3495/99/10/1992/11 \$2.00

There is evidence of a membrane reservoir that does serve as a buffer of membrane tension from studies of tethers in a variety of cells. When a latex bead attached to the cell plasma membrane is moved away from the cell, a thin cylindrical strand (tether) of membrane material is extended that links the bead and cell. During this process, membrane flows from the cell plasma membrane into the growing tether (Dai and Sheetz, 1995). The force on the tether does not increase with increasing tether length over many micrometers. In neurons, tethers hundreds of micrometers in length can be formed with no measurable change in tether force. A logical explanation for the constant force with length is that the membrane is being drawn from a reservoir that buffers membrane tension. Therefore, the tether phenomenon presents an excellent opportunity to probe the size of the membrane reservoir that buffers changes in membrane tension.

Membrane tension has been measured with membrane tethers in a variety of cellular and model membrane situations. Although in pure lipid vesicles the force on the tether is directly related to the in-plane tension and the bending stiffness of the lipid bilayer (Waugh et al., 1992; Evans and Yeung, 1994), in biological membranes there is an additional term that arises from membrane-cytoskeleton adhesion. Because the membrane and the cytoskeleton adhere to one another and the cytoskeleton does not move into the tethers, there is a separation of membrane components from their cytoskeleton binding sites in the tether. Membrane components in the tether will have a higher free energy because of the absence of cytoskeleton and will tend to leave the tether for the membrane in contact with the cytoskeleton. This results in a membrane osmotic pressure in the bilayer between the tether and the rest of the plasma membrane that increases the tether force (Dai and Sheetz, 1995; Waugh, 1983). In cases where blebs have formed on cells, we have found that the force on tethers formed on blebs is less than half the tether force of tethers formed on cytoskeleton-containing regions (Dai and Sheetz, unpublished results). Thus, the membrane-cytoskeleton adhesion contributes the major portion of the tether force.

Using tether length as a method for characterization of the membrane reservoir, we examined the effect of cytoskeleton disruption, osmotic pressure, and increased membrane tension on the reservoir size. Fibroblasts were used as the experimental cells because they have a relatively smooth surface, and we found experimentally that the apparent reservoir was small. An interesting observation of these studies is that the reservoir is accessible throughout the whole cell. The behavior of the cells has important implications for the organization of the plasma membrane and the cell cytoskeleton.

## MATERIALS AND METHODS

### Cell culture

Chick embryo fibroblasts and 3T3 mouse fibroblasts were grown in monolayers at 37°C in 5% CO<sub>2</sub>. The cells were maintained in Dulbecco's

modified Eagle's medium (DMEM, Gibco BRL, Grand Island, New York) containing 10% fetal bovine serum, 1 mM L-glutamine, and 50 IU/ml penicillin/streptomycin (Gibco). One day before the experiments, the cells were removed from culture with trypsin/EDTA and seeded into Petri dishes that contained several 24 × 50 mm glass coverslips.

### Bead preparation

To prepare IgG-coated beads 40 μl of 2.5% carboxylated polystyrene microparticles (1 μm diameter, Polysciences, Warrington, PA) were placed into an Eppendorf centrifuge tube (1.5 ml capacity). The Eppendorf tube was then filled with 0.1 M carbonate buffer prepared by adding 0.1 M Na<sub>2</sub>CO<sub>3</sub> to 0.1 M NaHCO<sub>3</sub> until the pH was 9.6. The beads were then pelleted by centrifugation at 2000 × g at 4°C for 10 min. The supernatant was removed using a Pasteur pipette and the pellet was resuspended in carbonate buffer and centrifuged one more time. Using the same procedure, the beads were then washed twice in 0.02 M sodium phosphate buffer, prepared by adding 0.02 M Na<sub>2</sub>HPO<sub>4</sub> to 0.02 M NaH<sub>2</sub>PO<sub>4</sub> until the pH was adjusted to 4.5. The pellet was then resuspended in 0.625 ml of sodium phosphate buffer and 0.625 ml of 2% carbodiimide solution (1-(3-dimethylaminopropyl)-3-ethyl carbodiimide hydrochloride dissolved in phosphate buffer) was added dropwise. The beads were then mixed for 3–4 h at room temperature using a rotary shaker, washed twice with phosphate solution, and washed two more times with Dulbecco's phosphate buffered saline (DPBS, Gibco BRL, Grand Island, NY). Then the beads were resuspended in 100 μl of PBS and incubated overnight at 4°C with 20 μl of 1 mg/ml mouse IgG (Sigma, St. Louis, MO). Unbound IgG was washed out with PBS, and the beads were then resuspended in 1 ml of 1 mg/ml bovine serum albumin-PBS to block unreacted sites, rinsed by pelleting, and resuspended in DMEM three times. For the experiments, the bead solution was diluted 30 times.

### Laser tweezers manipulation

Cells were observed with a video-enhanced differential interference contrast (DIC) microscope (IM-35, Zeiss, Oberkochen, Germany). The laser trap consisted of a polarized beam from a near-infrared (1064 nm) Nd:YAG laser (model 116Fn, Quantronix Corp., Smithtown, NY) which was expanded by a 3X beam expander (Newport Corporation, Irvine, CA) and then focused through an 80 mm focal achromatic lens (Melles Griot, Irvine, CA).

For the tether length experiments, beads were held for 4–5 s on the cell surface with the laser tweezers and then the membrane tether was pulled out with a constant velocity of 4 μm/s by a piezoceramic-driven stage (Wye Creek Instruments, Frederick, MD). The force of the tether on the bead was estimated from the measured displacement of the bead in the trap. The position of the bead in the trap was analyzed from video records of the experiments using the nanometer-level tracking program (Gelles et al., 1988). Calibration of force was performed by flowing solution past a trapped bead at a known velocity and calculating the force from Stokes' law (Kuo and Sheetz, 1993).

### Feedback tracking of particle position

To keep the particle at a defined distance from the center of the trap, we have modified the tracking algorithm that was originally applied by Choquet et al. (1996) to the output of a quadrant detector (see under Membrane Dynamics and Fig. 4.).

## RESULTS

### Membrane tether force during tether elongation

To characterize the dependence of the tether force on tether length, IgG-coated beads were held on the cell surface

approximately 4–5 s (Fig. 1 *a*) and then pulled with optical tweezers forming thread-like membrane tethers (Fig. 1 *b*). The membrane tethers were pulled at a constant rate until the beads escaped from the laser tweezers. After the beads escaped from the laser tweezers, the membrane tethers rapidly retracted back (Fig. 1 *c*). As shown in Fig. 1 *d*, the profile of the force vs. tether length during tether elongation consisted of three parts. After the initial tether formation, there was a small increase in force over the first micrometer. Force then reached a plateau and further elongation did not affect tether force, suggesting that membrane was drawn from a reservoir. Finally, there was an abrupt exponential rise in force that brought the tether out of the trap, indicating

depletion of the membrane reservoir. If the tether elongation was dependent upon membrane stretching, then tether force should increase with tether length. However, the presence of a plateau in the force vs. tether length profile implies that additional membrane is available for tether elongation from a buffered reservoir. Under control conditions, the plateau phase in chick embryo fibroblasts and 3T3 cells was 5  $\mu\text{m}$  (range, 3–7  $\mu\text{m}$ ), when pulled at a velocity of 4  $\mu\text{m/s}$ . We have also measured length of the plateau phase at different pull rates (Fig. 1 *e*). From Fig. 1 *e* it is clear that tethers are longer with a slower pull rate. The slower rate may allow more time for vesicles underlying the plasma membrane to incorporate into the membrane and therefore produce longer

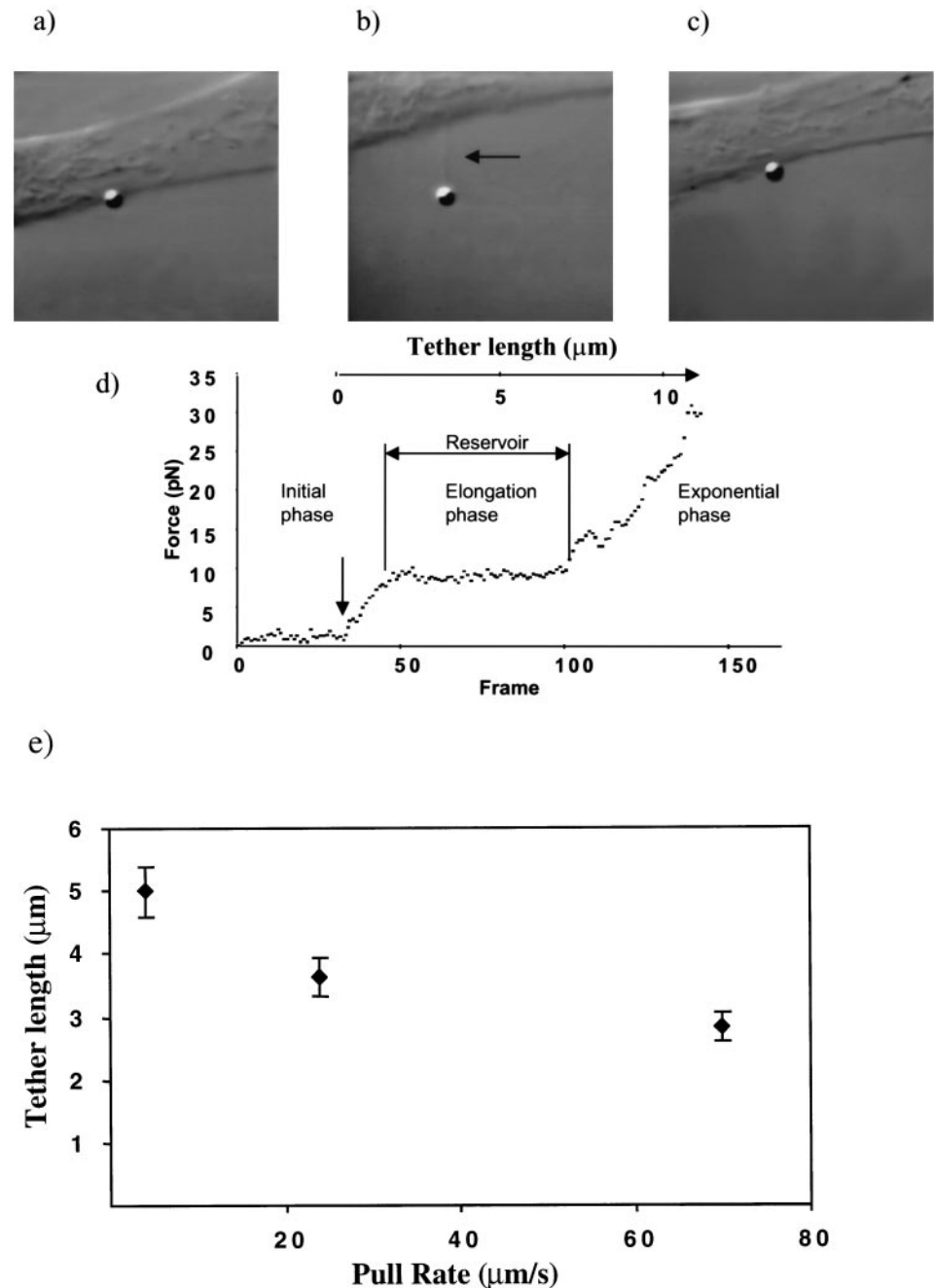


FIGURE 1 A bead trapped with laser optical tweezers was held on the cell surface for 4–5 s (*a*) and a membrane tether (*arrow*) was formed by pulling out the bead with constant velocity of 4  $\mu\text{m/s}$  (*b*). (*c*) After the bead escaped the trap the tether rapidly retracted. (*d*) Tether force with time during the tether formation. (*e*) Tether elongation with response to different pull rates.

tethers. Alternatively, cytoskeleton could be rearranging under the high tension, which should be time-dependent as well. In the following experiments membrane tethers were pulled at a constant rate of  $4 \mu\text{m/s}$  until the bead escaped from the laser tweezers, indicating depletion of the membrane reservoir.

### Role of the cytoskeleton

The cytoskeleton, which is associated with the plasma membrane, determines the shape of the cell and it is intimately involved in mechanical functions of the plasma membrane. In the cytoskeletal network, microtubules and microfilaments are important structural components. To understand the influence of these filamentous proteins on the membrane reservoir, we modified their polymerization state with drugs. When actin polymerization was inhibited with cytochalasin B, the tether length increased almost threefold with respect to the tether length of untreated cells (Fig. 2). Similarly, 2.5-fold longer tethers were formed when cells were treated with cytochalasin D. Disruption of microtubules by nocodazole and colchicine resulted in 1.7- and 2.3-fold longer tethers (Fig. 2), respectively, when compared to untreated cells. In contrast, when microtubules were stabilized with taxol, tethers became 27% shorter than the tethers of untreated cells. Therefore, alteration in the organization in the actin or microtubule cytoskeleton results in a dramatic change in tether length, suggesting that the

cytoskeleton plays an important role in limiting the size of the available membrane reservoir.

### Membrane reservoir during osmotic swelling

When cells are exposed to a hypotonic solution, osmotic imbalance induces water influx through the plasma membrane and consequently causes cell swelling. In order to prevent cell lysis under swelling pressure, it is necessary to increase the membrane area of the cell. To quantify changes in the size of the membrane reservoir associated with osmotic swelling, we measured the tether length of 3T3 fibroblasts before, during, and immediately after incubation in hypotonic solutions. As shown in Fig. 3, when cells were exposed to a solution containing 90% medium, tether length decreased only 7%. Immediately after the solution was exchanged for normal medium, the tether length increased by 15% with respect to control cells. Similarly, for cells exposed to 70% and 50% medium the tether length decreased by 18% and 25%, respectively, during expansion. After exchange of hypotonic solutions for an isotonic medium, tether length increased by 25% for cells exposed to 70% medium and 35% for cells previously exposed to 50% medium. These results indicate that an increase in membrane tension due to osmotic swelling reduces the size of the available membrane reservoir. However, immediately after recovery from osmotic swelling there is an increase in tether lengths, suggesting that additional membrane has been

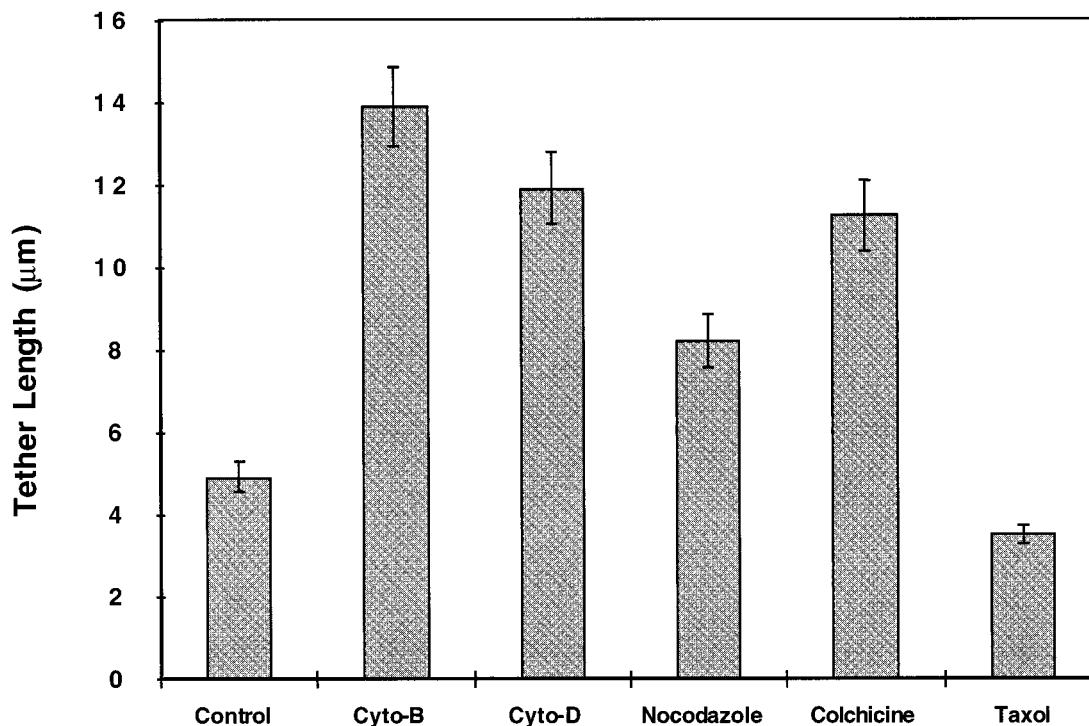
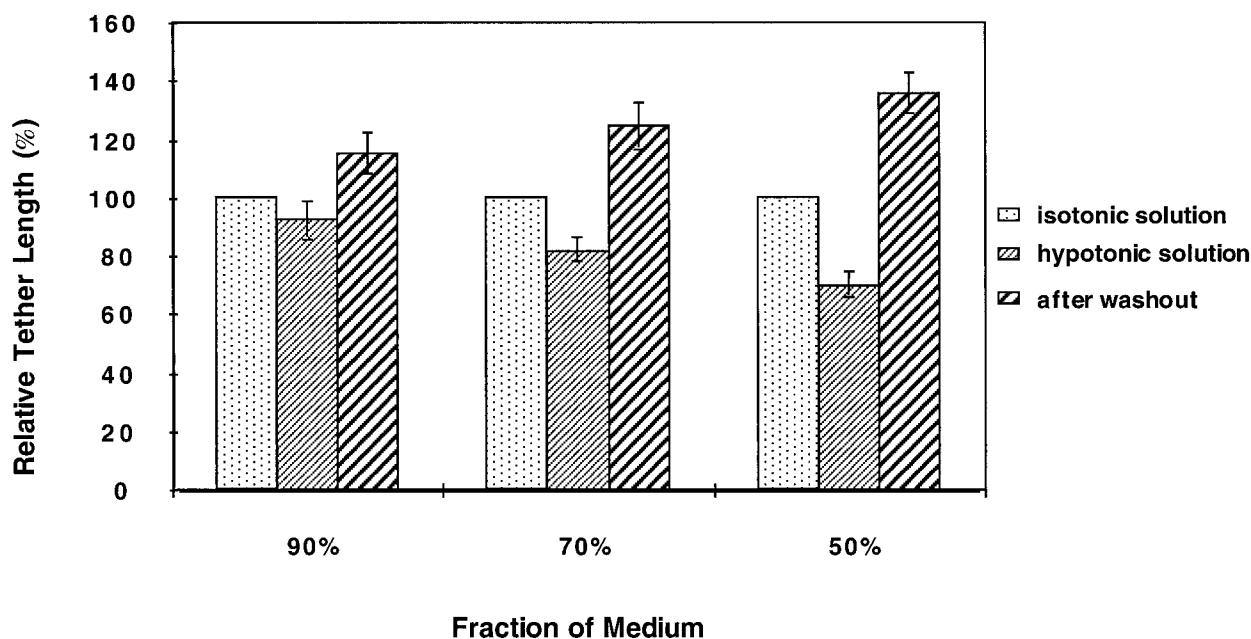


FIGURE 2 Influence of the cytoskeleton on the membrane reservoir. Tether length before and after the treatments with cytochalasin B ( $10 \mu\text{M}$ ), cytochalasin D ( $10 \mu\text{M}$ ), nocodazole ( $10 \mu\text{g/ml}$ ), colchicine ( $1 \mu\text{g/ml}$ ), and taxol ( $0.5 \mu\text{M}$ ). Control solution was exchanged with treatment solutions and cells were incubated 10 min before starting the measurements. Error bars indicate S.E.M. for 3–5 tether length measurements on 15–20 cells.

a)



b)

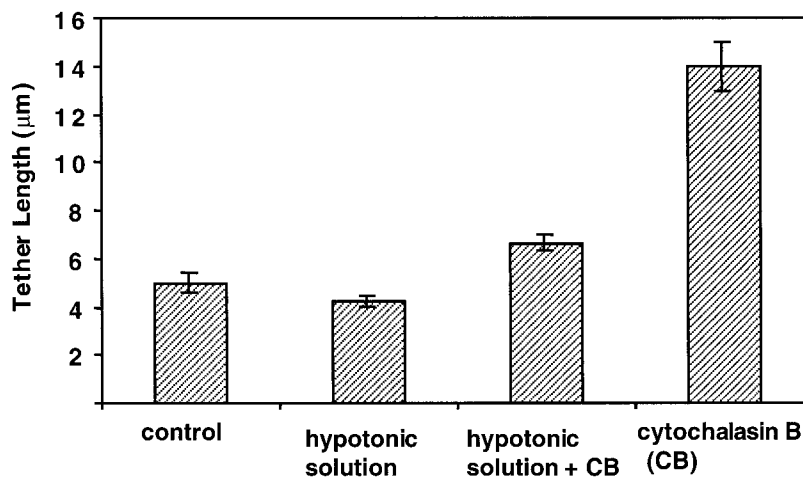


FIGURE 3 (a) Tether lengths during osmotic swelling and recovery. Tether lengths were normalized to tether lengths measured in isotonic solution (coarse dots). Light hatching, cells were incubated 10 min in hypotonic solution containing 90%, 70%, or 50% media. Heavy hatching, tether lengths immediately after cells were returned to isotonic solution. (b) Tether length in presence of 10  $\mu$ M cytochalasin B and hypotonic solution (70% medium). Measurements were done within 3–10 min after addition of hypotonic solution and cytochalasin B or hypotonic solution alone. Error bars indicate S.E.M. for 3–5 tether length measurements on 12–15 cells.

added to the plasma membrane reservoir in response to increased osmotic pressure and perhaps increased membrane tension. We also measured tether length in presence of cytochalasin B and hypotonic solutions. As shown in Fig. 3 *b* there is about 20% increase in tether length in presence of cytochalasin B with respect to cells treated with hypotonic solution alone. These measurements were done within 3–10 min after addition of hypotonic solution and cytochalasin B or hypotonic solution alone. This suggests that

rearrangement of underlying cytoskeleton during osmotic swelling may increase the size of membrane reservoir.

### Membrane dynamics

Since increased membrane tension with osmotic swelling is found to increase membrane area (Dai et al., 1998), a tether under high force in the exponential phase should increase in

length by causing membrane addition. In order to characterize the rate of membrane addition as a function of tension, we have measured the rate of tether elongation while a constant force was applied to the bead holding the tether in the exponential phase (Fig. 1). The force of the tether on the bead was estimated from the measured displacement of the bead in the trap. To keep a particle at a defined position from the center of the trap we have used a modified tracking algorithm, which relies upon output of a quadrant detector Choquet et al. (1997).

A diagram of the tracking system used to hold the bead at a position of known force in the tweezers is shown in Fig. 4 *a*. When the particle was at the desired position in the tweezers, the feedback system was activated to hold the bead's position in the trap constant. As an external force is applied to the trapped bead and the position of the bead in the trap changes, a voltage from the computer is sent directly to the power supply for the piezoelectric element of the x-y stage. The stage then moves to keep the bead at the defined position from the center of the trap, thereby maintaining a constant force on the bead.

Fig. 4 *b* shows the tether force during the tether pulling sequence. A bead was held on the surface of the cell by the laser trap. A tether was pulled with constant velocity and after the reservoir was depleted, the bead was held at a constant force in the tweezers. Application of high constant force to the tether resulted in a linear increase in reservoir length as shown in Fig. 4 *c*. Tether elongation was measured from the change in the position of a reference bead, which was attached to the coverslip surface. Similarly, we have measured rates of reservoir elongation for tethers over the range of 5–32 pN. As shown in Fig. 4 *d*, we have found that tether length increased at a rate directly proportional to the tether force. When the tethers were released, they always retracted rapidly and immediate reformation of tethers showed that the reservoir size had been increased.

### A number of tether pulls expand a continuous membrane reservoir

If the membrane reservoir is accessible from the whole cell surface, then expansion of the reservoir from increased tension on one side of the cell should be detected on the other side of the cell. A simple mechanism to expand the membrane reservoir is to pull a bead out of the trap a number of times. The high force transient at the end of the pull causes a rapid increase in the reservoir size. When a membrane tether was repeatedly formed using the same bead and the tether length was measured (Fig. 5 *a*), the tether length increased with subsequent pulls. Fig. 5 *b* shows the tether length during five successive tether pulls normalized to the tether length measured during the first pull. Tether length increased linearly with the number of pulls; after five pulls, membrane tethers were 37% longer than tethers formed during the first pull.

The increases in tether length with number of tether pulls could represent increases in reservoir size over the whole

cell surface or a local phenomenon. We designed the following experiment to determine the nature of the increase in reservoir size. First, we measured the tether length on one side of the cell on position 1 (Fig. 6, *inset*). Then by using five successive tether pulls, we recruited additional membrane on the other side of the cell at position 2. Finally, we measured the tether length at position 1 again. As shown in Fig. 6, the average tether length at position 1 increased by 34% when we recruited additional membrane at position 2 of the cell. It is important to note that this 34% increase in tether length compares very well to the 37% increase in tether lengths after five successive pulls (Fig. 5), suggesting that the same amount of membrane which is recruited on one side of the cell is also available on the other side of the cell. There was no difference in tether length at position 1, when the tether length was measured without successive pulls at position 2. To check for the reversibility of the membrane recruitment seen with successive tether formation, we formed a membrane tether with the same bead approximately 20 s after completing a succession of pulls. As shown in Fig. 5 *b*, there is no difference in tether length between the first pull and the post-sequential pull, indicating that the membrane recruited into a membrane tether was absorbed after the tether was relaxed. These results indicate that membrane, which is recruited at a localized area of the cell, is available throughout the whole cell.

## DISCUSSION

We have reported here experiments designed to measure the size of the plasma membrane reservoir and its dynamic properties. Membrane tethers were extracted at a constant rate until the bead escaped from the laser tweezers, indicating depletion of the membrane reservoir, and therefore its relative size. The actual area of membrane drawn into the tethers was 3–10  $\mu\text{m}^2$ , which is a relatively small fraction of the total membrane area (approximately 1000  $\mu\text{m}^2/\text{cell}$ ). We have shown that during tether formation the initial rise in tether force is followed by a plateau where tether force does not change with the tether length. At the end of a pull, there is an exponential rise in tether force that brings the bead out of the laser trap, defining the tether length. Decreasing the cell cytoskeleton structural integrity with the cytochalasins, nocodazole, or colchicine caused an increase in tether length whereas increasing microtubule density with taxol decreased the size of the membrane reservoir. Thus, we suggest that cytoskeleton rigidity plays a role in limiting the size of the membrane reservoir. We found that an increase in membrane tension due to osmotic swelling reduces the size of the membrane reservoir while the cell is under the higher tension. However, the increase in tether lengths immediately after recovery from osmotic swelling indicates an increase in the size of the membrane reservoir in response to increased osmotic pressure. We have also measured the rate of tether elongation when a constant force was applied to the bead holding the tether. By measuring the

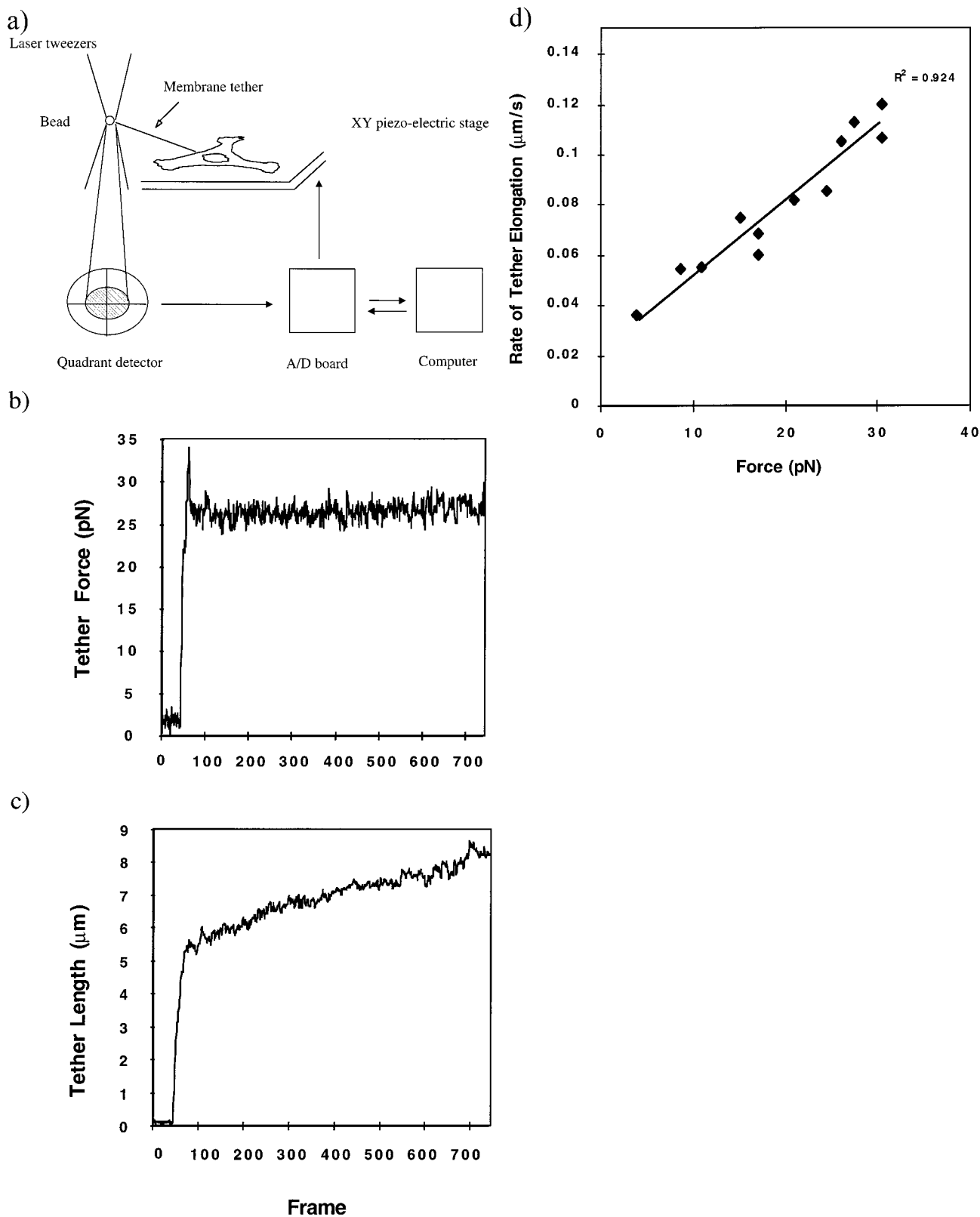
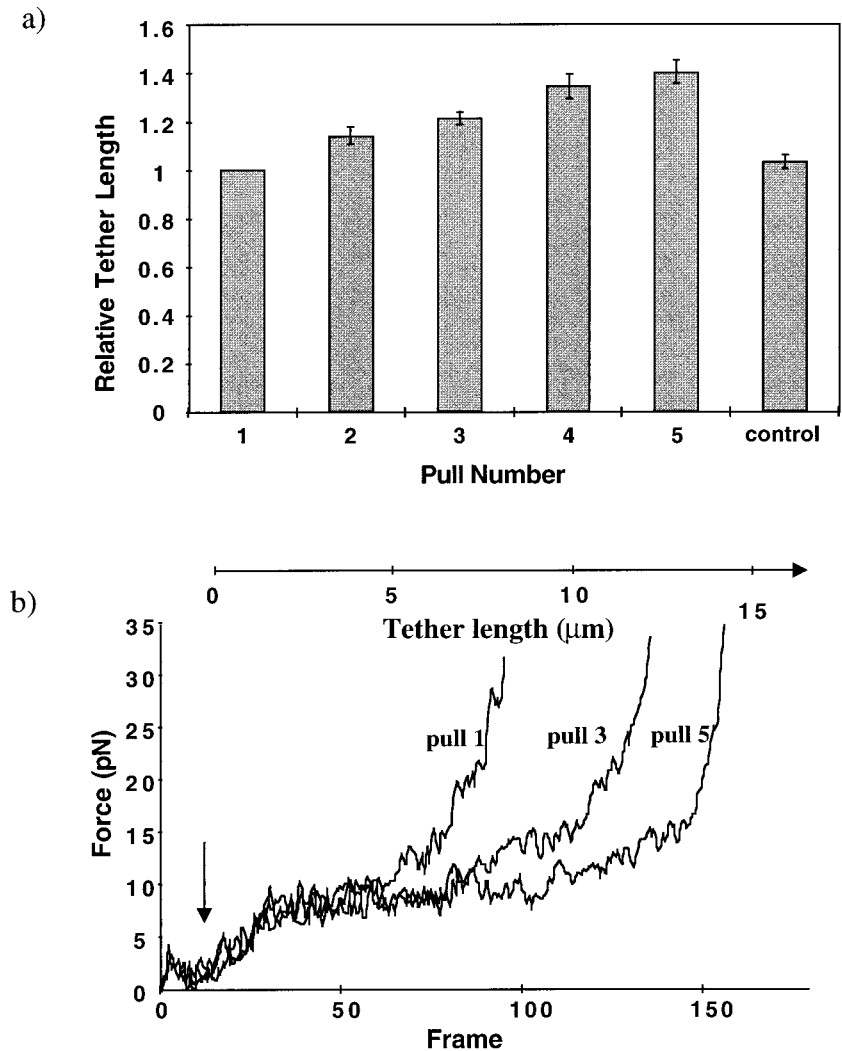


FIGURE 4 (a) Diagram of the tracking system that holds a bead at a constant position in the laser optical trap so that constant force is applied to the bead. (b) Force applied to the bead during a typical constant-force experiment and corresponding tether elongation. (c) Tether elongation was measured by simultaneously monitoring the position of a stationary bead firmly attached to the glass coverslip. (d) Different constant force measurements and corresponding rates of tether elongation.

FIGURE 5 Effect of a number of tether pulls on tether length. Membrane tethers were pulled with constant velocity of  $4 \mu\text{m/s}$  and tether lengths at which the bead escaped from the trap was measured (*a*). After the bead escaped the trap the tether rapidly retracted. A number of membrane tethers were extracted with the same bead. The time between tether pulls was less than 1 s. As a control for reversibility of the tether elongation, a post-sequential pull was performed 20 s after five successive pulls. *b* shows the tether force during the multiple tether formation.



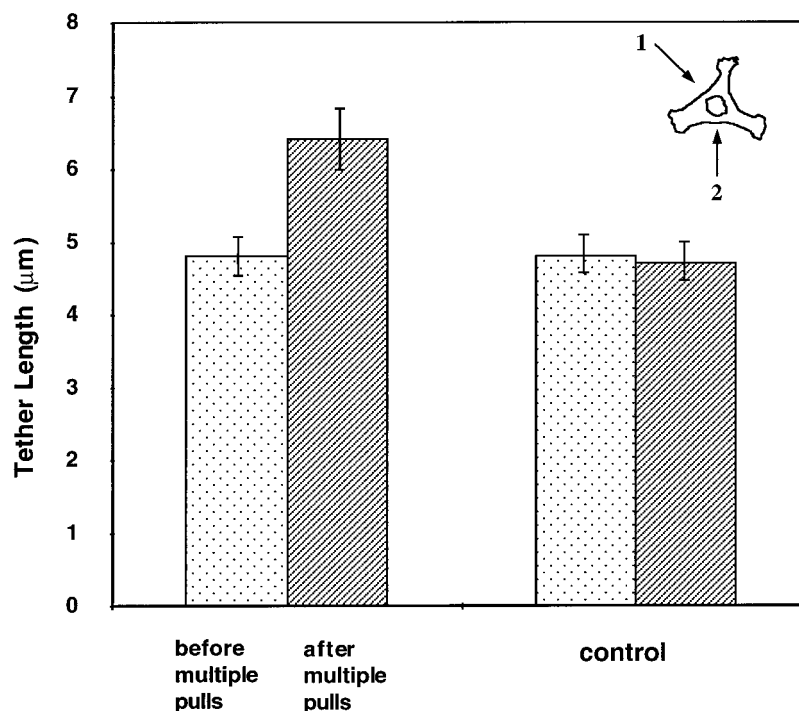
rates of tether elongation for various forces we have found that the rate of tether elongation is directly proportional to the applied tether force. Increased membrane tension caused an increase in reservoir area over time indicating that additional membrane was recruited into the reservoir. The increase in membrane reservoir on one side of the cell resulted in an increase on the other side of the cell, indicating that the membrane reservoir is continuously distributed throughout the cell.

Previous studies of the membrane reservoir did not attempt to quantify its size, but rather they only confirmed its existence. In immunolocalization electron microscopy studies Nielsen et al. (1993) observed that in rat kidney cells the membrane reservoir consists of water channel-laden vesicles from the apical cytosol. Using the same method Escolar et al. (1989) found that peripheral and deep channels of the open canalicular system in platelets represents a membrane reservoir that can be evaginated onto the platelet surface during interaction with other surfaces. However, to characterize the membrane reservoir it is necessary to have a method to measure its relative size.

One of the first quantitative studies of the membrane reservoir was based on monitoring changes in cell surface morphology, implying that the membrane reservoir is contained in surface folds, microvilli or in membrane ruffles. That was accomplished by Burwen and Satir (1977) who followed changes in surface morphology of secreting mast cells by scanning electron microscopy. To assess the possible relationship between secretory activity and surface folding they measured surface fold lengths per unit of smooth sphere surface area. This method was employed by Petty et al. (1981) to measure the variations in size of the membrane reservoir in macrophages during antibody-dependent phagocytosis. However, the size of the membrane reservoir is estimated only from surface folds, and therefore this method may not be appropriate to some other cell types.

Our understanding of the structural interaction between the plasma membrane and the cytoskeleton has changed as a result of many recent studies of membrane mechanical properties including membrane tension measurements (Waugh et al., 1992; Evans and Yeung, 1994; Waugh and Hochmuth, 1987). Of particular relevance here is the con-

FIGURE 6 Tether length on one side of the cell before and after a number of tether pulls on the other side of the cell. Tether length was measured at position 1 of the cell (*inset*) before and after a number of tether pulls at position 2. The time between the tether pulls on position 1 before and after a number of tether pulls at position 2 was less than 5 s. As a control experiment we measured the tether length at position 1, paused approximately 5 s, and then measured the tether length at the same position.



cept that the membrane and the cytoskeleton adhere to each other through many weak interactions, perhaps lipid-protein bonds. This leads to a continuum behavior in the interaction such that in neuronal growth cones, a 10–15% increase in the plasma membrane area does not cause separation of cytoskeleton and membrane. Further, upon restoration of isotonicity to hypotonically swollen cells, the excess membrane conforms to the cytoskeleton in deep invaginations, which rapidly are resorbed into the cell (Dai et al., 1998). In this work we have used laser tweezers to pull on membrane-attached latex beads and form membrane tethers. Since the membrane in a tether is drawn from the plasma membrane, the maximum tether length which can be pulled reflects the relative size of a membrane reservoir. Besides introducing a new method for quantification of the membrane reservoir, we have also demonstrated that this method may be applied during various conditions opening the way for further studies of the membrane reservoir.

### Role of the cytoskeleton

The cortical cytoskeleton determines cellular shape, coordinates cell locomotion, and may present a regulative barrier to endocytosis and exocytosis (Aunis and Bader, 1988). Clearly, other studies have shown that the cytoskeleton plays an important structural and regulatory role in a variety of membrane processes (reviewed in Bretscher, 1991). Both the tubulin containing microtubules and the actin containing microfilaments form distinct structures within the cell which are associated with the plasma membrane itself. In this work we have demonstrated that disruption of the cytoskeleton network increases the size of the membrane

reservoir, while stabilization of microtubules reduces the size of the available membrane reservoir.

Although the alteration of cell shape caused by cytochalasin and nocodazole may cause an initial change in the reservoir, the rapid dynamics of the reservoir suggest these agents cause a stable change in the reservoir. The cytoskeleton determines the shape of cell surface structures like microvilli, microspikes, filopodia, and membrane ruffles. Disruption of the underlying cytoskeletal network may transform a cell with many surface structures into a cell with more planar topology, generating excess membrane; however, recovery of the excess membrane occurred in 20 s in membrane expansion studies. Thus, the tether length after 30 min in the presence of cytochalasin or nocodazole should represent a change to a new steady-state value of the reservoir. The steady-state values of the cell that could affect apparent reservoir size are cytoskeletal rigidity and membrane-cytoskeleton interaction. Because both microtubules and actin filaments contribute significantly to cellular rigidity (Duszyk et al., 1989) but actin filaments are more tightly linked to the membrane-cytoskeleton interaction, we favor the idea that the rigidity change is most important. Since changes in cell shape sometimes may require large changes in membrane area, membrane must be added perhaps initially from the membrane reservoir and then from internal membrane stores. Therefore changes in cell shape and membrane addition must be carefully coordinated to maintain a significant membrane reservoir.

### Osmotic swelling

There are many studies and experiments testing the effect of changes in the osmolarity of solutions upon growth of the

cells and upon individual cell structures. In early studies Hogue (1919) observed morphological changes in fibroblasts from embryonic chick heart in hypotonic solution. She found that a hypotonic solution induces water influx through the plasma membrane and the resulting hydrostatic pressure caused an enlargement of the cell cytoplasm and its separation into granular and clear areas. Rapid enlargement of the cell requires an increase in plasma membrane area. Since enlargement is considerably faster than the rate of synthesis of the membrane proteins and lipids, most of the plasma membrane must be drawn from internal membrane stores. The reservoir area is only several square micrometers, whereas the expansion of the surface area can be tens to hundreds of square micrometers. The reservoir can provide a buffer against fluctuations in tension that would otherwise lead to lysis but clearly does not provide all the membrane needed for cellular shape changes.

In this study, we have shown that during an increase in osmotic pressure there is a rapid proportional decrease in the size of the membrane reservoir indicating that the size of the reservoir is inversely proportional to the plasma membrane tension. The notion that cell surface is unchanged, and that the membrane needed to prevent cell lysis is coming from the unfolding of surface folds is supported by cell capacitance measurements. Immediately after addition of hypotonic solution cell capacitance does not change (K. Strange, personal communication). Instead there is a delayed increase in capacitance, indicating that it takes time before there is addition of membrane to the cell surface. Similarly, Graf et al. (1995) have used the whole-cell patch-clamp technique to study changes in membrane conductance and membrane capacitance after osmotic swelling in rat hepatocytes. The rise in conductance was not correlated with changes in capacitance, neither in time after the initiation of cell swelling nor in magnitude. Therefore, they concluded that an osmotically induced increase in conductance is probably a result of the activation of existing channels in the plasmalemma and not a result of the fusion of vesicle membranes containing ionic channels. In addition, using whole cell patch clamp techniques, membrane capacitance was measured in rat astrocytes in primary tissue culture within 9 min of exposure to 220 mOsm, 190 mOsm, and 145 mOsm PBS (Olson and Li, 1997), with each of these hypoosmotic exposures, no change occurred in membrane capacitance. When we measured the size of the membrane reservoir immediately after the osmotic pressure was reduced to normal by returning the cell to isotonic media, we found that the increase in the size of the membrane reservoir was proportional to the applied osmotic pressure. Because the changes in reservoir size that we observe are very small (<0.5% of the membrane area) they do not correspond to these capacitance changes, but rather could represent much slower membrane addition process or the relaxation of cell shape, e.g., actin depolymerization as after cytochalasin addition.

We have also measured the dynamics of reservoir expansion as a function of membrane tension in the bilayer plane

from the force exerted on a particle attached to a membrane tether. When tensions were applied to the cell, the reservoir expanded linearly with time. We found that the rate of increase of the reservoir area as measured by tether elongation was directly proportional to the tension applied through the tether. From these studies we concluded that when tensions were applied to the cell, either by osmotic pressure or through the membrane tether, membrane material is incorporated into the membrane reservoir either from internal membrane stores or cell rounding. This suggests that the rate of addition to the plasma membrane from internal stores or cell rounding is directly proportional to the tension applied to the plasma membrane.

### Working hypothesis

These results are consistent with the hypothesis that there is a reservoir of plasma membrane that serves to buffer against fluctuations in the plasma membrane tension for the whole cell. This reservoir could be an invagination of the plasma membrane that was under tension derived from a molecular motor pulling on an inward directed tether or a membrane projections. Under high tension the reservoir would decrease in size but when tension dropped from a high level, the reservoir would pick up the excess membrane and increase in size. We find that when the membrane tension is increased, the reservoir is small in size (at the maximum tether length very small increases in tether length cause very large changes in tether force). Under high tension, the cell adds membrane to the plasma membrane in an apparent attempt to restore the reservoir. Upon release of the high membrane tension, the reservoir takes up some of the added membrane and has an increased size until a new steady state is established. Although we suggest that an invagination could be the anatomical basis for the reservoir, an evagination such as a microspike or filopodium could also serve the same purpose. Further studies are needed to define the nature of the reservoir.

It has been postulated that membrane tension provides a physical mechanism to control the area of the plasma membrane (Sheetz and Dai, 1996). This hypothesis was based in part on observations that an increase in membrane tension, caused by osmotic swelling, increased membrane area as a result of increased membrane secretion (Dai et al., 1998). The increase in reservoir size with high membrane tension could result from an increase in plasma membrane area. Therefore there is evidence for the notion that membrane tension controls the net incorporation of membrane material into the plasma membrane.

Alternatively, the increase in membrane tension could cause cell rounding such as in mitosis (Raucher and Sheetz, 1999). During rounding the membrane reservoir would increase dramatically in size as well. In plant protoplasts there are indications that traffic from an intracellular membrane pool to the plasma membrane depends upon the tension of the plasma membrane (reviewed in Kell and Glaser, 1993).

Wolfe et al. (1985) have shown that increased tension in the plane of the plasma membrane of plant protoplasts leads to an increase in plasma membrane area up to threefold in some cases and that a decrease leads to a decrease in plasma membrane area. During osmotically induced volume contraction protoplast plasma membrane remained smooth and volume contraction was accompanied by endocytic vesiculation (Gordon-Kamm and Steponkus, 1984). Kell and Glaser (1993) postulated that membrane expansion by exocytotic incorporation of vesicle membranes is controlled by the mechanical forces, which are imposed on the plasma membrane. Therefore, it is very likely that the plasma membrane tension represents an important physical mechanism to control incorporation of membrane material into the plasma membranes of all cell types. A reservoir to buffer fluctuations in membrane tension would be an important factor in the physiological control of tension.

## REFERENCES

- Aunis, D., and M. F. Bader. 1988. The cytoskeleton as a barrier to exocytosis. *J. Exp. Biol.* 139:253–266.
- Bretscher, A. 1991. Microfilament structure and function in the cortical skeleton. *Annu. Rev. Cell Biol.* 7:337–374.
- Burwen, S. J., and B. H. Satir. 1977. Plasma membrane folds on the mast cell surface and their relationship to secretory activity. *J. Cell Biol.* 74:690–697.
- Choquet, D., D. P. Felsenfeld, and M. P. Sheetz. 1997. Extracellular matrix rigidity causes strengthening of integrin-cytoskeletal linkages. *Cell.* 88:39–48.
- Dai, J., Sheetz M. P., Wan, H., and Morris, C. 1998. Membrane tension in swelling and shrinking molluscan neurons. *J. Neurosci.* 18:6681–6692.
- Dai, J., and M. P. Sheetz. 1995. Mechanical properties of neuronal growth cone membranes studied by tether formation with laser optical tweezers. *Biophys. J.* 68:988–996.
- Duszyk, M., Schwab, B., Zahalak, G. I., Qian H., and E. L. Elson. 1989. Cell poking: quantitative analysis of indentation of thick viscoelastic layers. *Biophys. J.* 55:683–690.
- Escobar, G., E. Leistikow, and J. G. White. 1989. The fate of the open canalicular system in surface and suspension activated platelets. *Blood.* 76:1983–1988.
- Evans, E. A., and R. Skalak. 1979. *Mechanics and Thermodynamics of Biomembranes.* CRC Press, Boca Raton, FL.
- Evans, E. A., and A. Yeung. 1994. Hidden dynamics in rapid changes of bilayer shape. *Chem. Phys. Lipids.* 73:39–56.
- Gelles, J., B. J. Schnapp, and M. P. Sheetz. 1988. Tracking kinesin-driven movements with nanometer scale precision. *Nature.* 331:450–453.
- Gordon-Kamm, W. J., and P. L. Steponkus. 1984. Lamellar-to-hexagonal II phase transitions in the plasma membrane of isolated protoplasts after freeze-induced dehydration. *Proc. Natl. Acad. Sci. USA.* 81:6373–6377.
- Graf, J., M., Rupnik, G., Zupancic, and R., Zorec. 1995. Osmotic swelling of hepatocytes increases membrane conductance but not membrane capacitance. *Biophys. J.* 68:1359–63.
- Hogue, M. J. 1919. The effect of hypotonic and hypertonic solutions on fibroblasts of the embryonic chick heart in vitro. *J. Physiol.* 19:617–631.
- Kell, A., and R. F. Glaser. 1993. On the mechanical and dynamic properties of plant cell membranes: their role in growth, direct gene transfer and protoplast function. *J. Theor. Biol.* 160:41–62.
- Kuo, S. C., and Sheetz, M. P. 1993. Force of single kinesin molecules measured with optical tweezers. *Science.* 260:232–234.
- Nielsen, S., S. R. DiGiovanni, E. I. Christensen, M. A. Knepper, and H. W. Harris. 1993. Cellular and subcellular immunolocalization of vasopressin-regulated water channel in rat kidney. *Proc. Natl. Acad. Sci. USA.* 90:11663–11667.
- Olson, J. E., and G. Z. Li. 1997. Increased potassium, chloride, and taurine conductances in astrocytes during hypoosmotic swelling. *Glia.* 20:254–261.
- Petty, R. P., D. G. Haefman, and H. M. McConnel. 1981. Disappearance of macrophage surface folds after antibody-dependent phagocytosis. *J. Cell Biol.* 89:223–229.
- Raucher, D., and M. P. Sheetz. 1999. Membrane expansion increases endocytosis rate during mitosis. *J. Cell Biol.* 144:497–506.
- Sheetz, M. P., and Dai, J. 1996. Modulation of membrane dynamics and cell motility by membrane tension. *Trends Cell Biol.* 6:85–89.
- Waugh, R. E. 1983. Effects of abnormal cytoskeletal structure on erythrocyte membrane mechanical properties. *Cell. Motil.* 3:609–622.
- Waugh, R. E., J. Song, S. Svetina, and B. Zeks. 1992. Local and nonlocal curvature elasticity in bilayer membrane by tether formation from lecithin vesicles. *Biophys. J.* 52:391–400.
- Waugh, R. E., and R. M. Hochmuth. 1987. Mechanical equilibrium of thick, hollow, liquid membrane cylinders. *Biophys. J.* 52:391–400.
- Wolfe, J. M., Dowgert, M. F., and P. L. Steponkus. 1985. Dynamics of membrane exchange of the plasma membrane and the lysis of isolated protoplasts during rapid expansions in area. *J. Membrane Biol.* 86:127–138.

# Nonlinear Elastic and Viscoelastic Deformation of the Human Red Blood Cell with Optical Tweezers

J. P. Mills<sup>1</sup>, L. Qie<sup>2</sup>, M. Dao<sup>1</sup>, C. T. Lim<sup>2</sup> and S. Suresh<sup>1,3</sup>

**Abstract:** Studies of the deformation characteristics of single biological cells can offer insights into the connections among mechanical state, biochemical response and the onset and progression of diseases. Deformation imposed by optical tweezers provides a useful means for the study of single cell mechanics under a variety of well-controlled stress-states. In this paper, we first critically review recent advances in the study of single cell mechanics employing the optical tweezers method, and assess its significance and limitations in comparison to other experimental tools. We then present new experimental and computational results on shape evolution, force–extension curves, elastic properties and viscoelastic response of human red blood cells subjected to large elastic deformation using optical tweezers. Potential applications of the methods examined here to study diseased cells are also briefly addressed.

## 1 Introduction and overview

Optical tweezers are finding increasing application in the study of single biological cells. Ashkin et al (1987) used infrared laser beams to optically trap and manipulate single cells. An optical trap was used by Svoboda et al (1992) to isolate the membrane skeleton from a red blood cell, which was treated with a non-ionic detergent, so as to study the effect of ionic strength on the contraction of the spectrin network. Bronkhorst et al (1995) employed triple traps to deform and to explore shape recovery of red blood cells.

Direct tensile stretching of the human red blood cell using optical tweezers to extract elastic properties was first reported by Hénon et al (1999) who attached two silica beads non-specifically to diametrically opposite ends of

the cell, trapped both beads with laser beams, and imposed tensile elastic deformation on the cell by moving the trapped beads in opposite directions. Forces were calibrated by subjecting a trapped bead to counter flow following the procedures outlined by Svoboda and Block (1994) and Simmons et al (1996). Stokes' law was used to estimate the force on the trapped bead from known fluid velocity. With a 1.064  $\mu\text{m}$  Nd:YAG laser beam of 605 mW maximum emission power and silica beads 2.1  $\mu\text{m}$  in diameter, they imposed maximum tensile forces that were estimated to be 56 pN on discocytic and osmotically swollen, nearly spherical cells. By employing simple analytical expressions based on two-dimensional linear elastic, small deformation, idealization of the cell, they examined variations in only the transverse diameter of the cell with applied force, and ignored possible contributions to deformation arising from the bending stiffness of the cell membrane and cytoskeleton. Finite contact between the beads and the cell membrane during stretching by optical tweezers was also not considered. The in-plane shear modulus of the cell membrane was estimated from this approach to be  $2.5 \pm 0.4 \mu\text{N/m}$ . This estimate is lower than the range of shear modulus values of 4 to 10  $\mu\text{N/m}$  obtained from a number of independent investigations which employed the more commonly known micropipette aspiration technique (Evans and Skalak, 1980; Hochmuth and Waugh, 1987; Discher et al, 1998; Boal, 2002). Studies by the same group (Lenormand et al, 2001) employing triple bead optical tweezers measurements showed that the area expansion modulus and shear modulus of red blood cells were higher in an isotonic buffer than in a low hypotonic buffer.

Sleep et al (1999) also estimated elastic properties of the human red blood cells by optical tweezers where two polystyrene latex beads of 1  $\mu\text{m}$  diameter were trapped using a 1.047  $\mu\text{m}$  Nd:YLF laser beam. In this experiment, one bead was held fixed and the other moved with a second trap to induce tensile deformation in the cell.

<sup>1</sup> Department of Materials Science and Engineering.

<sup>2</sup> Division of Bioengineering, National University of Singapore, Singapore 117576, Singapore.

<sup>3</sup> Division of Biological Engineering (e-mail: ssuresh@mit.edu), Massachusetts Institute of Technology, Cambridge, MA 02139, USA.

Trap stiffness was estimated from the Brownian motion of the trapped bead. The variation of imposed force, up to a maximum of 20 pN, as a function of the transverse diameter, was reported for permeabilized spherical ghost cells whose deformation at a given force was about one half that of discocytic and osmotically swollen spherical cells. By invoking an axisymmetric cell model of Parker and Winlove (1999), they estimated the in-plane shear modulus from optical tweezers studies to be nearly two orders of magnitude larger than those reported by Hénon et al (1999).

All of the foregoing studies of cell deformation by optical tweezers involve primarily small elastic deformation at low applied forces. The analyses of deformation for extracting elastic properties also invoke rather severe assumptions on cell shape (e.g., idealization of a biconcave cell as a two-dimensional planar disc by Hénon et al (1999), and neglect of the effects of the relatively large contact region between the cell and the beads in this study and in the one by Sleep et al (1999)). Studies of deformation conditions at larger strain levels inevitably require much higher forces, which are conceptually feasible to obtain using the optical tweezers method. In fact, a study of unfolding of titin molecules by Kellermayer et al (1998) reported an estimated stretching force in excess of 400 pN using optical tweezers where a 1046 nm Nd:YAG laser with a maximum power of 1.5 W was used to trap a 3  $\mu\text{m}$  diameter latex bead and where the force calibration was performed using the Stokes' law method.

In principle, the optical tweezers method affords several potential advantages for the study of deformation of single biological cells. (1) It provides a means to impose simple and well-controlled stress states, such as direct tensile stretching in small or large deformation, to biological cells. In this sense, it is complementary to, and conceptually simpler to interpret than, the widely used micropipette aspiration method (Evans and Skalak 1980, Fung 1993). (2) The stress state imposed on the cell can be systematically varied by employing multiple beads which are attached to cell membranes, whereby the constitutive response of the cell membrane and cytoskeleton can be probed for different chemical and biological conditions. (3) Optical tweezers stretching of cells in one or more directions is also amenable to three-dimensional computational simulations which can be used to guide and interpret experimental observations. (4) The relaxation response of the stretched cell upon release of the

tensile stretch in the optical tweezers experiments can also be used to extract the viscoelastic response of the cell. (5) This method further provides a possible means to investigate systematically the effects of the progression of a disease state, such as infestation of the red blood cell with *Plasmodium falciparum* malaria parasite, on the deformation characteristics and elastic and viscoelastic properties of the cell membrane (Mills et al, 2004). Possible complications arising from micropipette aspiration of such infected cells, such as stress concentration at the ends of the micropipette and adhesion of the infected cell to the inner walls of the micropipette, can potentially be circumvented in the optical tweezers method. Despite these advantages, uncertainties exist in the calibration of the force imposed on the cell by the optical tweezers method, which is in the picoNewton to several hundred picoNewton range. Such complications have led to considerable variation and scatter in the experimental data reported previously in the literature. A comparison of the optical tweezers method with other techniques available for the study of mechanics of single cells and populations of cells can be found in recent reviews (Bao and Suresh, 2003; Van Vliet et al, 2003).

The possibility of inducing large elastic deformation in human red blood cells using optical tweezers was also demonstrated recently (see the papers by Dao et al., 2003; Lim et al, 2004 along with the attendant corrigenda). Here, forces as high as about  $193 \pm 20$  pN were estimated to result in strains on the order of 100% in the cell.

In the present paper, we review these developments from earlier work and present refinements and updates to the experimental method and force calibration. Furthermore, a fully nonlinear constitutive model based on a three-stage neo-Hookean elastic response is presented along with new computational simulations of cell deformation to systematically probe the large deformation response of the red blood cell. The predictions are compared with new experimental data obtained in this work. In addition, the values of elastic properties and characteristic time for viscoelastic relaxation extracted from the present optical tweezers experiments on normal human red blood cells are shown to be within the range of values obtained from prior experimental studies that employed the micropipette aspiration technique.

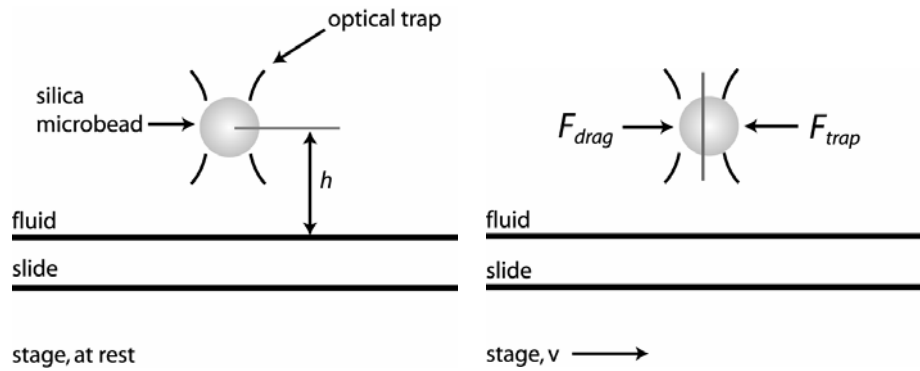


**Figure 1** : Calibration of the optical trap using an escape force method (Svoboda and Block, 1994). A silica microbead,  $4.12 \mu\text{m}$  in diameter, is trapped in fluid (PBS and bovine serum albumin, BSA) at a measured height,  $h = 3 \mu\text{m}$ , above the slide surface. As the microscope stage and fixed slide are translated, the fluid exerts a viscous drag force on the trapped bead. When the viscous drag force is just equal to the escape force, the bead will escape the trap.

## 2 Experimental Method

The optical tweezers system used here comprises a single-bead gradient optical trap. It incorporates an inverted microscope (Leica Microsystems, Wetzlar, Germany) and a laser module (LaserTweezers, Cell Robotics, Inc.). The trapping beam is a 1064 nm Nd:YAG laser with a maximum power of 1.5 W. Focusing the laser through an oil immersion lens ( $100\times$  magnification) forms the optical trap. Silica beads,  $4.12 \mu\text{m}$  in diameter (Bangs Laboratories, USA), are optically trapped by the laser to perform stretch tests. The relatively high laser power and large bead diameter facilitate the exertion of forces on the cell that are about three to six times greater than those reported by the earlier studies (Hénon et al. 1999, Sleep et al. 1999).

### 2.1 Force calibration

The optical tweezers system is calibrated using an escape force method (Svoboda and Block, 1994). In this technique, the force required to dislodge a trapped microbead is calibrated against a known viscous drag force. The calibration procedure involves trapping a silica microbead in fluid (phosphate-buffered saline (PBS) and bovine serum albumin (BSA)) at a measured height,  $h = 3 \mu\text{m}$ , above the glass slide surface. The fluid and height of the trapped bead from the slide surface are kept unchanged throughout calibration and mechanical deformation. As the microscope stage is translated, the fluid exerts a viscous drag force on the trapped bead, as shown

in Fig. 1. The viscous drag force equals the trapping force when the bead just escapes the trap. From the stage velocity,  $v$ , at the point of escape of the trapped bead, the drag force, which is the opposite of the escape force, is estimated as

$$F = \beta v. \quad (1)$$

The viscous drag coefficient,  $\beta$ , for a spherical bead located near a wall is described by Faxen's Law (Svoboda and Block, 1994),

$$\beta = \frac{6\pi\eta r}{1 - \frac{9}{16}(r/h) + \frac{1}{8}(r/h)^3 - \frac{4}{256}(r/h)^4 - \frac{1}{16}(r/h)^5}, \quad (2)$$

where, for the present experiments, the bead radius,  $r = 2.06 \mu\text{m}$ , height of the bead above the wall,  $h = 3 \mu\text{m}$ , and fluid viscosity,  $\eta = 0.0013 \text{ Pa}\cdot\text{s}$ . Notice that Eq. (1) takes the form of Stokes' law,  $F = 6\pi r \eta v$ , for a bead located far from the wall.

The stage-movement technique described here differs somewhat from the fluid-chamber technique used in our earlier work (Dao et al., 2003; Lim et al., 2004). The fluid-chamber technique imposes a viscous drag force by flowing fluid through a narrow channel where a microbead is trapped. Fluid velocity, estimated by tracking the speed of untrapped beads, is used with Eq. (1) to determine the escape force. However, this method is limited by our optical tweezers set-up. First, untrapped beads used to determine fluid velocity should be flowing at the same height above the slide as the trapped bead.

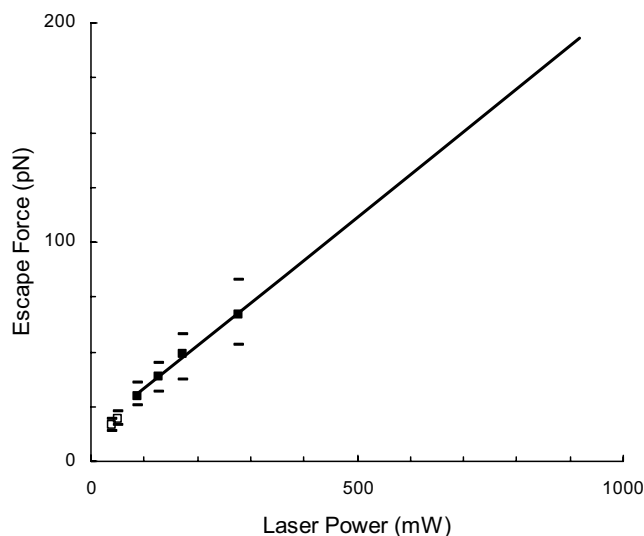


**Figure 2** : Force calibration plot showing the variation of trapping force with laser power for a 1.5 W diode pumped Nd:YAG laser source for a single optical trap system. Non-linear trends below 80mW laser power are not used for extrapolation.

Usually, untrapped beads flow along the surface of the slide, making fluid velocity estimates difficult. Second, steady fluid flow is difficult to achieve for the lowest flow rates. Third, the scatter in calibration results is considerably greater than for the stage-movement technique. The stage-movement technique, used in the current study, provides a more accurate method to determine the velocity of the fluid from known stage velocity, thereby resolving the first two limitations of the fluid-chamber method.

The escape force over a range of laser powers is shown in Fig.2. The reported laser power is measured at the objective lens. At maximum power for the 1.5W laser, only 917 mW of laser power was measured due to losses through the optics. In our system, the stage velocity limits direct calibration to a laser power of only about 300 mW. The escape force for values of higher laser power is linearly extrapolated from the calibration data in Fig. 2. At maximum laser power, corresponding to 917 mW, an escape force of  $193 \pm 20$  pN is predicted. The linear relationship between laser power and escape force is consistent with theoretical predictions (Ashkin, 1992) and empirical findings (Svoboda and Block, 1994).

## 2.2 Sample Preparation

Blood samples from healthy adults are first obtained by a finger prick using a lancet device. The red blood cells are then isolated from the other blood components via a centrifugation process. Subsequently, silica microbeads are added to the isolated red blood cells in PBS with pH 7.4 and stored at  $4^\circ\text{C}$  for 1 hour to allow for spontaneous and nonspecific binding of beads to cells. *In vitro* optical tweezers tests are then performed immediately. All preparations and tests are done at room temperature. The results presented in this paper are based on stretch test data from 16 different red blood cells.

## 2.3 Stretch Tests

Prepared red blood cells with attached silica microbeads are added to a solution of PBS and BSA. As the present experiment involves a single optical trap, one of the two microbeads is adhered to the glass slide while the other is trapped using the laser beam as shown in Fig. 3. This is accomplished by the addition of BSA, which limits microbead adhesion to the slide. Correct bead arrangement can be confirmed by trapping the microbead not attached to the slide. Because the optical trap is located above the slide surface and focal plane, a microbead that is successfully trapped will appear out of focus, indicating that the microbead is not adhered to the slide surface (see right bead in Fig 3 (b)). With this microbead trapped, the stage can be translated to determine if the other microbead is adhered to the slide. Adherence to the slide is confirmed if the adhered microbead moves in a manner consistent with the stage, unaffected by the forces induced by the trapped microbead. In fact, cell stretching is performed by this same method. With one microbead held fixed in the optical trap, moving the microscope stage, which in turn moves the microbead adhered to the glass slide, stretches the cell. A cell is stretched at different laser powers to record cell deformation over a range of forces. All stretch tests are recorded digitally for image analysis of cell deformation. For each stretch test, the axial diameter (in the direction of stretch) and transverse diameter (orthogonal to stretch direction) of the cell are measured from the still-frame image when the trapped bead just escapes the trap. The calibration of laser power to escape force (Fig. 2) determines the force at this instant. The cell diameters are measured from the still-frame image (Fig. 3). Notice that the axial diameter is actually the projected axial diameter because of the height difference

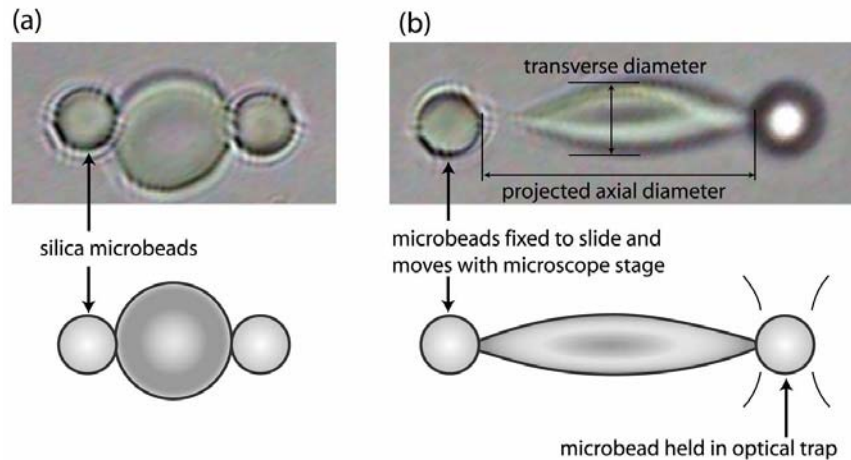


**Figure 3 :** Illustration of an optical trap method for cell stretching. Two silica microbeads, each  $4.12 \mu\text{m}$  in diameter, are non-specifically attached to the red cell at diametrically opposite points. (a) The left bead is anchored to the surface of the glass slide. The optical image corresponds to the unstrained configuration. (b) The right bead is trapped using the optical tweezers. While the trapped bead remains stationary, moving the slide and attached left bead stretches the cell. The optical image shows an example of large deformation of a cell at  $193 \text{ pN}$  of force.

between the beads (Fig. 4). With the trapped bead height known, the actual axial cell diameter is calculated. Also, time dependent properties can be measured from the relaxation of the cell after the trapped bead escapes the trap. By measuring changes in axial and transverse diameters over time as the cell recovers its original shape, viscoelastic properties can be experimentally probed.

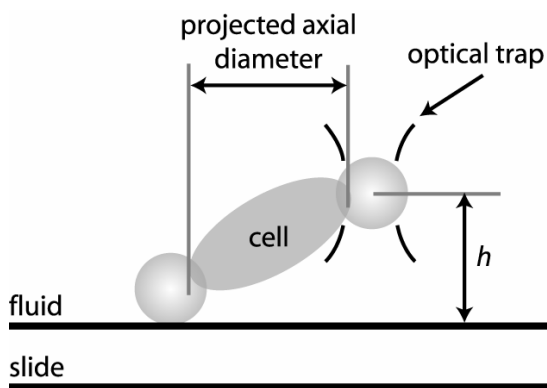


**Figure 4 :** Optical images of stretch tests show the projected axial diameter because of a height difference between trapped and attached beads. With the trapped bead height known, the actual axial cell diameter can be calculated.

### 3 Modeling of Deformation

The spectrin network which underlies the phospholipid bilayer of the human red blood cell is generally considered to impart shear resistance to the cell membrane although the bilayer itself has little resistance to shear deformation. As reviewed by Dao et al. (2003), the effective cell membrane which comprises the phospholipid bilayer and the spectrin network is usually modelled as an incompressible solid (Evans, 1973; Evans and Skalak, 1980) where the membrane shear stress  $T_s$  (expressed in units of force per unit length) is related to the principal stretch ratios,  $\lambda_1$  and  $\lambda_2$ , as

$$T_s = 2\mu\gamma_s = \frac{\mu}{2}(\lambda_1^2 - \lambda_2^2), \quad (3a)$$

$$T_s = \frac{1}{2}(T_1 - T_2) \quad \text{and} \quad \gamma_s \equiv \frac{1}{2}(\epsilon_1 - \epsilon_2) = \frac{1}{4}(\lambda_1^2 - \lambda_2^2) \quad (3b)$$

$$\lambda_1\lambda_2 = 1 \quad (3c)$$

where  $T_1$  and  $T_2$  are the in-plane principal membrane stresses,  $\epsilon_1$  and  $\epsilon_2$  are the in-plane principal Green's strains of the membrane,  $\mu$  is the membrane shear modulus (assumed to be constant and expressed in units of force per unit length) and  $\gamma_s$  is the shear strain. The assumption of a constant area for the cell membrane is usually invoked, as indicated by equation (3c).

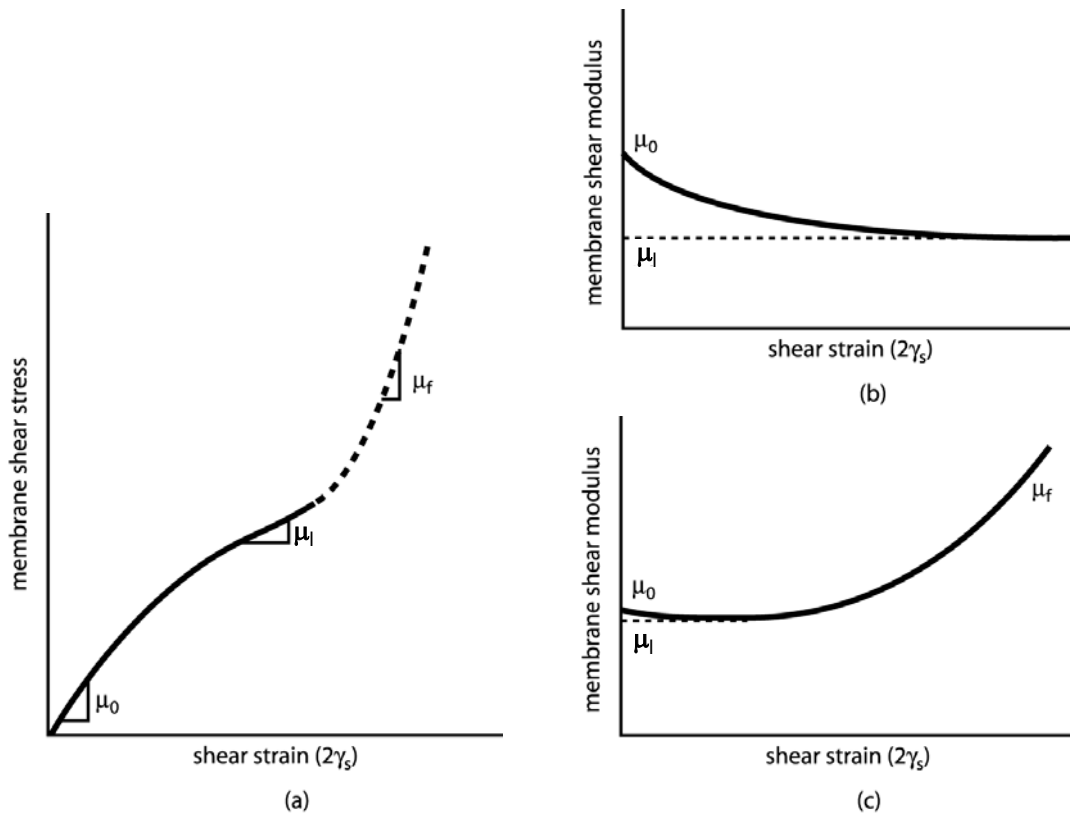


**Figure 5** : Schematic illustration of the hyperelastic constitutive response used in some of the computational simulations. (a) Uniaxial stress-strain response. (b) The variation of the membrane shear modulus with the progression of deformation of the first order hyperelasticity model, where strains are representative of the large deformation response achieved in the present optical tweezer experiments. (c) The variation of the membrane shear modulus with respect to shear strain of a higher order hyperelastic model.

Other possible constitutive models can also be explored in the context of the deformation of red blood cells. One such approach entails use of a hyperelastic effective material model for capturing the large deformation response of the membrane. Dao et al. (2003) used the simplest first order formulation using a one-parameter Neo-Hookean form where the strain energy potential function (Simo and Pister, 1984) is of the form,

$$U = \frac{G_0}{2} (\lambda_1^2 + \lambda_2^2 + \lambda_3^2 - 3), \quad (4a)$$

where the assumption of incompressibility (constant volume) is also invoked. Here  $G_0$  is the initial value of bulk shear modulus, and  $\lambda_i$  ( $i = 1-3$ ) are the principal stretches. The incompressibility condition implies that  $\lambda_1 \lambda_2 \lambda_3 = 1$ . Further refinements to this approach are explored here by invoking a higher order formulation (a two-parameter

Yeoh form (Yeoh, 1990)) whereby

$$U = \frac{G_0}{2} (\lambda_1^2 + \lambda_2^2 + \lambda_3^2 - 3) + C_3 (\lambda_1^2 + \lambda_2^2 + \lambda_3^2 - 3)^3. \quad (4b)$$

In the computations, we take values of the parameter  $C_3$  to be those which best match experimental data ( $C_3 = G_0/30$  in the current study). The potential function  $U$  defines the nonlinear elastic stress-strain behavior. When the initial membrane thickness is  $h_0$ , the constitutive description of eqs. (4) results in the initial in-plane membrane shear modulus  $\mu_0 = G_0 h_0$ . Figure 5(a) schematically shows the uniaxial stress-strain response of such a neo-Hookean hyperelastic material, the membrane elasticity modulus typically decreases from its initially high value,  $\mu_0$ , to a relatively smaller value,  $\mu_1$ , at larger strains, before attaining a higher value,  $\mu_f$ , again

prior to final failure. The slope of the membrane shear stress ( $T_s$ ) versus shear strain ( $2\gamma_s$ ) is therefore initially a decreasing function of shear strain (see Fig. 5(b)) and eventually a rapidly increasing function of shear strain (see Fig. 5(c)). For the simple first order neo-Hookean material described by eq. (4a), only the first stage ( $\mu_0$ ) and the second stage ( $\mu_1$ ) will be considered subsequently. For the higher order response described by eq. (4b), the first stage ( $\mu_0$ ) and the third stage ( $\mu_f$ ) will be the most important characteristic regions described. Specifically,  $\mu_1$  (for the Neo-Hookean description) or  $\mu_f$  (for the Yeoh description) is taken here at a relatively large stretch ratio of  $\lambda_1 = 3$  or 2 respectively under direct uniaxial tension. The neo-Hookean rubber elasticity model for the membrane entails two material parameters: the initial shear modulus  $\mu_0$  and the second stage, large deformation modulus  $\mu_1$ . In the current first order model, choice of one value of the two parameters also determines the other; while introducing higher order term  $C_3$  results in independent variations of  $\mu_0$  and  $\mu_f$ , see Figure 5(c). Choice of values for these parameters, which facilitate the matching of computational predictions with experimental results, has been systematically explored, and reported in this paper and in Dao et al (2003).

When the constant membrane area constraint, i.e.  $\lambda_1\lambda_2=1$  (where  $\lambda_3=1$ ), is added to eq. (4a), the constitutive description of eq. (4a) is equivalent to that of eq. (3). With this additional constraint, the in-plane membrane shear modulus stays at a constant value of  $\mu = G_0h_0$  throughout the entire deformation history (Dao et al, 2003).

While the foregoing analytical descriptions for the thin shell employ a single material property, i.e., the membrane shear modulus, more comprehensive analyses involving computational simulations of cell deformation invoke another material parameter in addition to the in-plane shear modulus  $\mu$ : the bending modulus  $B$ . It is generally known that the contribution to the uniaxial tensile elastic deformation of the red blood cell from the bending modulus is much less than that from the shear modulus. Therefore, a typical (fixed) value of  $B = 2 \times 10^{-19}$  N·m is assumed in all the computations unless specified otherwise. We match the computational simulations with experimentally observed evolution of axial and transverse cell diameter at different forces imposed by the optical tweezers, and then extract shear modulus on the basis of the foregoing constitutive assumptions.

Computational simulations of large deformation stretch-

ing of the cell by optical tweezers were performed using three-dimensional finite element analysis of the biconcave red blood cell containing the cytosol in the interior. Because of symmetry in the optical tweezers loading geometry, it suffices to simulate one half of the cell contacted by a bead. Symmetric boundary conditions with 12,000 three-dimensional shell elements were employed in the simulations using the general purpose finite element program, ABAQUS (ABAQUS, 2002). Full details of the computations can be found in Dao et al. (2003). As noted there, the volume of the fluid inside the cell was kept constant in the simulations.

#### 4 Results

Figure 6 shows that observed shape changes are matched by computation when  $\mu_0$  was assumed to be  $7.3 \mu\text{N/m}$  (with  $\mu_f = 19.2 \mu\text{N/m}$ ) using a higher order hyperelastic model described by eq. (4b). The contact size,  $d_c$ , was taken to be  $2 \mu\text{m}$  in this set of calculations. The left column in the figure is a sequence of optical images revealing large deformation response of the red blood cell at different stretching forces. At 193 pN, the axial diameter of the cell increases by 50% and the transverse diameter is reduced by more than 40%. The middle column shows contours of constant maximum principal strain at corresponding stretching forces; logarithmic strains at sites of contact between the cell and the beads can reach values of approximately 100% at a stretching force of 193 pN. The right column shows one half of the computed full three-dimensional shape of the cell at different imposed forces; the structural folding observed at large strains appears to contribute significantly towards the shrinking in the transverse direction. Evidence of such folding is also seen experimentally, as for example in the lower images in the left column of Fig. 6.

Note that in the original results reported by Dao et al (2003) and Lim et al (2004), the maximum forces imposed on the cell were estimated to be on the order of 400 pN. These original estimates were subsequently revised and corrected in corrigenda to the original publications, on the basis of recalibration and new experimental data which revealed lower maximum forces. Here we include only the revised and corrected experimental data.

Comparisons of predicted and measured changes in axial and transverse diameters of the cell using the neo-Hookean model in eq. (4a) are plotted in Fig. 7 for  $\mu_0 = 5.3, 7.3$  and  $11.3 \mu\text{N/m}$  (with  $\mu_1 = 2.4, 3.3$  and  $5.0 \mu\text{N/m}$ ,

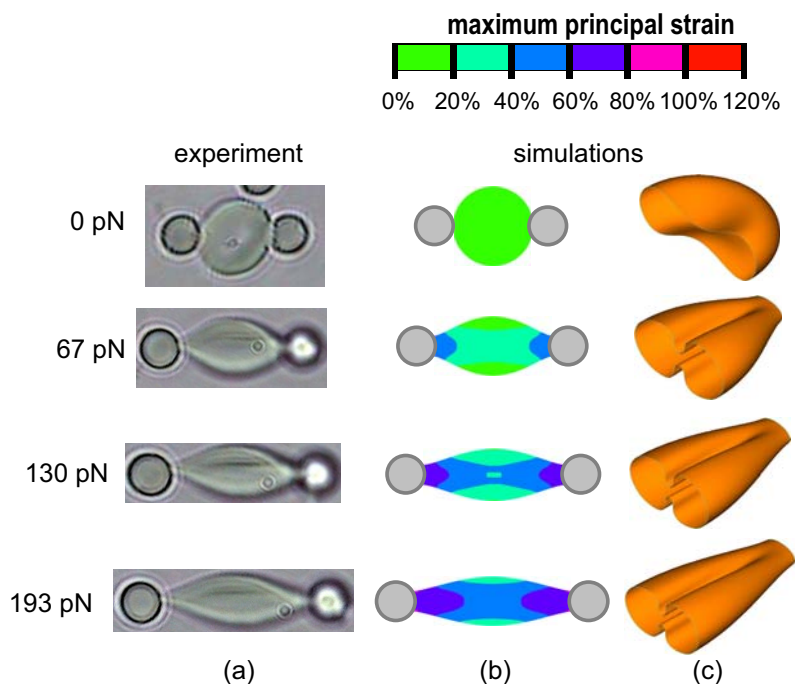


**Figure 6** : Images of the red cell being stretched from 0 pN to 193 pN. The images in the left column are obtained from experimental video photography whereas the images in the center column (top view) and in the right column (half model 3D view) correspond to large deformation computational simulation of the biconcave red cell (with  $\mu_0 = 7.3 \mu\text{N/m}$ ,  $\mu_f = 19.2 \mu\text{N/m}$ ). The middle column shows a plan view of the stretched biconcave cell undergoing large deformation at the forces indicated on the left. The predicted shape changes are in reasonable agreement with observations. The color contours in the middle column represent spatial variation of constant maximum principal strain. The right column shows one half of the full three-dimensional shape of the cell at different imposed forces; here, the membrane was assumed to contain a fluid, which preserved the internal volume.

respectively). Again the contact size  $d_c$  was taken to be  $2 \mu\text{m}$ . Simulations capture experimental trends over the range of 0–88 pN load well, while they deviate towards the softer side gradually after 88 pN load. Alternatively, if we invoke the constitutive response given in eq. (3) with constant area for the cell membrane in our three-dimensional computational simulation, a fixed value of the membrane shear modulus,  $\mu_0 = \mu_l = \mu_f = 5.5 \mu\text{N/m}$  appears to match the average values of our experimental observations of variations in axial and transverse diameter of the cell with the applied force within the 0–88 pN range (see Fig. 7). In the computational images, the existence of the cytosol inside the membrane prevents contact between the upper and lower surfaces. From the experimental evidence and computational results, significant membrane folding was often observed similar to those shown in Fig. 6 (left column and right column).

Comparisons of predicted and measured changes in axial

and transverse diameters of the cell using the higher order Yeoh model in eq. (4b) are plotted in Fig. 8 for  $\mu_0 = 5.3, 7.3$  and  $11.3 \mu\text{N/m}$  (with  $\mu_f = 13.9, 19.2$  and  $29.6 \mu\text{N/m}$ , respectively). Again the contact size  $d_c$  was taken to be  $2 \mu\text{m}$ . Simulations capture experimental trends over the entire range of experimental data well, including the small deformation range and the error bars. Comparing Figs. 7 and 8, it is seen that the higher order model apparently provides a much better match with experiments at high stretching ratios than the first order hyperelastic model.

The in-plane shear modulus  $\mu_0 = 5.3\text{--}11.3 \mu\text{N/m}$ , and  $\mu_l = 2.4\text{--}5.0 \mu\text{N/m}$  estimated from the experimental results and simulations reported in this paper are lower than the earlier values predicated upon higher optical force assumptions. The present corrected values are comparable to the range of  $4.0\text{--}10 \mu\text{N/m}$  reported in the literature where the estimates have been principally based on

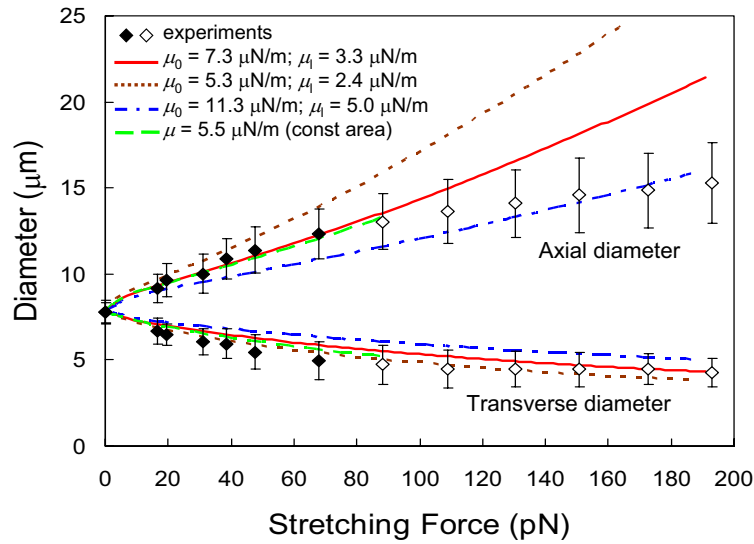


**Figure 7** : Variation of measured axial and transverse diameter (solid line with scatter band) of red cell against stretching force of optical tweezers during large deformation. The dotted, solid and dash-dotted lines represent computational predictions for the axial/transverse diameter with  $\mu_0= 5.3, 7.3$  and  $11.3 \mu\text{N/m}$ , and with  $\mu_t= 2.4, 3.3$  and  $5.0 \mu\text{N/m}$ , respectively, invoking the neo-Hookean first order hyperelastic constitutive response, eq. (4a), which assumes constant volume. The computational model uses the three-dimensional biconcave disk with a contact diameter of  $2 \mu\text{m}$ . Also shown are the predictions of simulations assuming constant membrane area, represented by long dashed lines, using the model given by eq. (3).

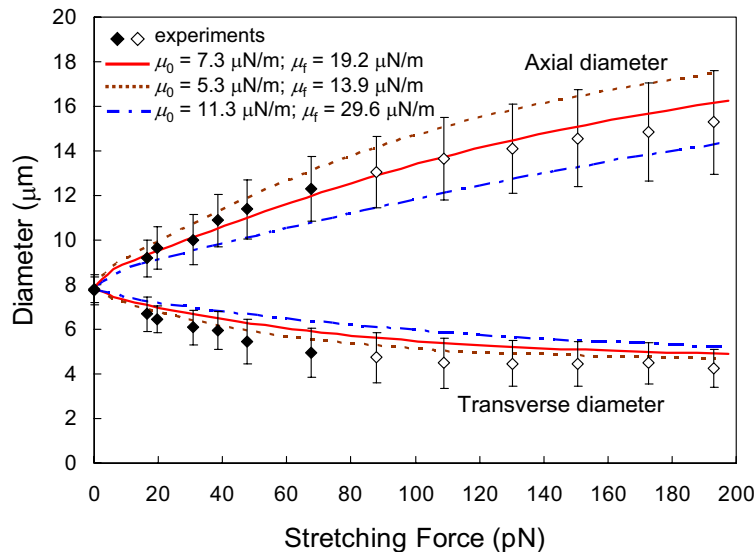


**Figure 8** : Variation of measured axial and transverse diameter (solid line with scatter band) of red cell against stretching force of optical tweezers during large deformation. The dotted, solid and dash-dotted lines represent computational predictions for the axial/transverse diameter with  $\mu_0= 5.3, 7.3$  and  $11.3 \mu\text{N/m}$ , and with  $\mu_f= 13.9, 19.2$  and  $29.6 \mu\text{N/m}$ , respectively, invoking a higher order hyperelastic constitutive response, eq. (4b), which assumes constant volume. The computational model uses the three-dimensional biconcave disk with a contact diameter of  $2 \mu\text{m}$ .

micropipette aspiration experiments. These values are also more in line with expectations than those derived from the earlier optical tweezers studies of Hénon et al (1999) and Sleep et al (1999) for small elastic deformation, indicating that possible effects of calibration as well as analysis of the data may have influenced the inference of elastic properties extracted from these optical tweezers experiments.

Video images of the elastic relaxation response of the stretched cell upon release of the force induced by stretching with optical tweezers can be used to infer the viscoelastic properties of the cell membrane. Hochmuth et al (1979) estimated the recovery characteristic time  $t_c$  of the red blood cell to be

$$\frac{(\lambda_1^2 - 1)(\lambda_{1,\max}^2 + 1)}{(\lambda_1^2 + 1)(\lambda_{1,\max}^2 - 1)} = \exp\left(-\frac{t}{t_c}\right) \quad (5)$$

where  $\lambda_{1,\max}$  is the initial (maximum) value of the stretch ratio of the red cell and the characteristic time for relaxation is given by

$$t_c = \frac{\eta}{\mu} \quad (6)$$

where  $\eta$  is the coefficient of surface viscosity of the cell membrane, and  $\mu$  is the in-plane shear modulus of the membrane. Figure 9 shows the corresponding best fit to the experimental data on relaxation using eq. (5). Using relaxation data from eight different experiments, the characteristic time is estimated to be  $t_c = 0.19 \pm 0.06$  s. It is of interest to note here that micropipette aspiration experiments have led to estimates of characteristic time of relaxation from large deformation of the red blood cell to be in the range 0.10–0.30 s (Chien et al 1978; Hochmuth 1987). With membrane shear modulus  $\mu$  taken to be approximately 2.4–11.3  $\mu\text{N/m}$ , the corresponding membrane viscosity,  $\eta$ , calculated from eq. (6) and Fig. 9 is about 0.3 to 2.8 ( $\mu\text{N/m}$ )·s, which compares well with the literature values of 0.6 to 2.7 ( $\mu\text{N/m}$ )·s found using micropipette experiments (Hochmuth 1987).

Three-dimensional computational simulations of the loading response are performed by incorporating the viscoelastic term to the constitutive behavior of the cell membrane by modifying eq. (3) as (Evans and Hochmuth, 1987; Dao et al, 2003),

$$T_s = \frac{\mu}{2} (\lambda_1^2 - \lambda_1^{-2}) + 2\eta \frac{\partial \ln \lambda_1}{\partial t} \quad (7)$$

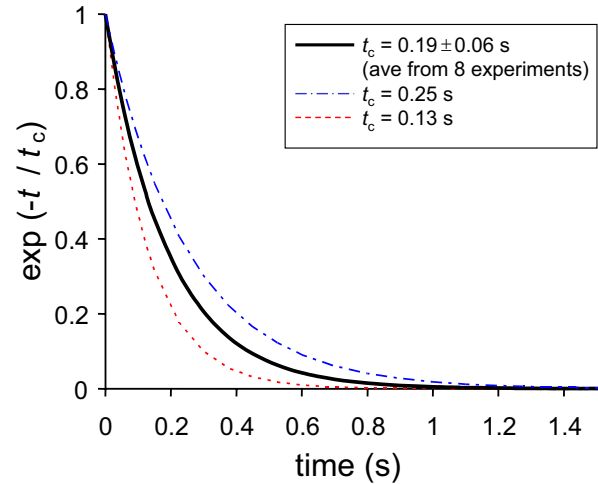


**Figure 9** : Best fit to the experimental relaxation data. Using relaxation data from eight different experiments, the characteristic time was estimated to be  $t_c = 0.19 \pm 0.06$ s using eq. (6).

where  $t$  is time, and  $t_c$  is the characteristic time for relaxation. For  $t_c = 0.19$  s and an estimated stretch rate of  $\dot{\lambda}_1 = 0.3 \text{ s}^{-1}$ , the error caused by ignoring membrane viscosity during the loading stage is found to be negligibly small.

## 5 Concluding Remarks

In this paper, we have presented a critical assessment of recent advances in the use of the optical tweezers method for the study of single living cells. Through new experimental data, calibration methods and three-dimensional computational modelling, it is also shown that direct *in vitro* force-displacement relationships for human red bloods can be obtained reproducibly from such experiments by deforming the cells at large elastic strains. It is further demonstrated that the elastic properties of the human red blood cell, particularly the in-plane shear modulus, estimated from the large deformation optical tweezers experiments falls within the range of values derived from prior studies that made use of the micropipette aspiration experiments. These findings of the present work modify earlier claims that employed optical tweezers for cell deformation where apparent artefacts from calibration methods and/or interpretation of experiments could have contributed to the inferred differences in elastic properties. The characteristic time for viscoelastic relax-

ation inferred from the optical tweezers method is also consistent with those estimated from micropipette aspiration experiments.

The results so established in this paper provide additional opportunities for the application of the optical tweezers technique for further study of single cell mechanics. For example, the feasibility to obtain direct force–extension curves using this method provides new possibilities for the systematic and quantitative investigation of the effects of disease states on mechanical response of living cells. With this information, the connections among elastic or viscoelastic properties of the cell, the chemical/biochemical environment of the cell and the onset and progression of diseases can be studied with a level of precision which may not be attainable with other experimental methods. Recent experimental studies by Mills et al (2004) on the infestation of human red blood cells by *Plasmodium falciparum* malaria parasites have demonstrated that reproducible force–extension curves providing critical quantitative insights into the effects of parasite maturation inside the cell on the elastic and viscoelastic responses could be extracted from the optical tweezers method. This technique could circumvent some of the experimental difficulties in probing the deformation characteristics of malaria-infected cells through micropipette aspiration where cell rigidity and enhanced adhesion of the cell membrane to the glass surface could lead to significant uncertainty and scatter in experimental data (e.g., Glenister et al, 2002). As noted earlier, the optical tweezers method also affords the flexibility to explore deformation characteristics under different well-controlled stress states which can be induced through the use of multiple beads that are strategically attached to the cell membrane for trapping and stretching.

The three-dimensional modelling approach outlined in this paper is predicated upon a continuum formulation. It is of interest to note that quantitative analysis of mechanical deformation by optical tweezers have also been performed by recourse to molecular level modelling of the spectrin network (Li et al, 2004). These simulations provide estimates of elastic properties which are consistent with experimental observations.

**Acknowledgement:** This work was supported by the Nano Biomechanics Lab, Division of Bioengineering at the National University of Singapore and the Laboratory for Experimental and Computational Micromechanics at

the Massachusetts Institute of Technology (MIT). Partial funding of this work was provided by the Singapore-MIT Alliance, and a Faculty of Engineering Research Grant from NUS.

### Supplementary Material

Video images of computational simulations of deformation of the human red blood cell during optical tweezers stretching are posted on the website which can be accessed through the electronic archive of this paper.

### References

- ABAQUS, Inc.** (2002): ABAQUS User's Manual, Version 6.3, ABAQUS, Inc., Pawtucket, RI, USA.
- Ashkin, A.; Dziedzic, J. M.; Yamane, T.** (1987): Optical Trapping and Manipulation of Single Cells Using Infrared-Laser Beams. *Nature* 330, 769-771.
- Ashkin, A.; Schutze, K.; Dziedzic, J. M.; Euteneuer, U.; Schliwa, M.** (1990): Force generation of organelle transport measured in vivo by an infrared laser trap. *Nature* 348, 346-348.
- Bao, G.; Suresh, S.** (2003): Cell and molecular mechanics of biological materials. *Nature Materials* 2, 715-725.
- Boal, D.** (2002): *Mechanics of the Cell*, Cambridge University Press, Cambridge, U.K.
- Bronkhorst, P. J. H.; Streekstra, G. J.; Grimbergen, J.; Nijhof, E. J.; Sixma, J. J.; Brakenhoff, G. J.** (1995): A new method to study shape recovery of red blood cells using multiple optical trapping. *Biophys. J.* 69, 1666-1673.
- Chien, S.; Sung, K. L. P.; Skalak, R.; Usami, S.** (1978): Theoretical and Experimental Studies on Viscoelastic Properties Erythrocyte-Membrane. *Biophys. J.* 24, 463-487.
- Dao, M.; Lim, C. T.; Suresh, S.** (2003): Mechanics of the human red blood cell deformed by optical tweezers. *J. Mech. Phys. Solids* 51, 2259-2280.
- Discher, D. E.; Boal, D. H.; Boey, S. K.** (1998): Simulations of the erythrocyte cytoskeleton at large deformation. II. Micropipette aspiration. *Biophys. J.* 75, 1584-1597.
- Evans, E. A.** (1973): New Membrane Concept Applied to Analysis of Fluid Shear- Deformed and Micropipette-Deformed Red Blood-Cells. *Biophys. J.* 13, 941-954.

- Evans, E. A.; Skalak, R.** (1980): Mechanics and Thermal Dynamics of Biomembranes, CRC Press, Inc., Boca Raton, Florida, USA.
- Fung, Y. C.** (1993): Biomechanics : mechanical properties of living tissues, Springer-Verlag, New York, USA.
- Glenister, F. K.; Coppel, R. L.; Cowman, A. F.; Mohandas, N.; Cooke, B. M.** (2002): Contribution of parasite proteins to altered mechanical properties of malaria-infected red blood cells. *Blood* 99, 1060-3.
- Henon, S.; Lenormand, G.; Richert, A.; Gallet, F.** (1999): A new determination of the shear modulus of the human erythrocyte membrane using optical tweezers. *Biophys. J.* 76, 1145-1151.
- Hochmuth, R. M.** (1987): Properties of Red Blood Cells. In *Handbook of Bioengineering*, (eds. R. Skalak and S. Chien), McGraw-Hill, Inc., New York, USA.
- Hochmuth, R. M.; Worthy, P. R.; Evans, E. A.** (1979): Red-Cell Extensional Recovery and the Determination of Membrane Viscosity. *Biophys. J.* 26, 101-114.
- Kellermayer, M. S. Z.; Smith, S. B.; Bustamante, C.; Granzier, H. L.** (1998): Complete Unfolding of the Titin Molecule under External Force. *Journal of Structural Biology* 122, 197-205.
- Li, J.; Dao, M.; Lim, C. T.; Suresh, S.** (2004): Spectrin-Level Analysis of Shape Evolution and Large Deformation Elasticity of the Erythrocyte. *Manuscript in preparation*.
- Lim, C. T.; Dao, M.; Suresh, S.; Sow, C. H.; Chew, K. T.** (2004): Large deformation of living cells using laser traps. *Acta Materialia* 52, 1837-1845. See also corrigendum (2004): *Acta Materialia* 52, 4065-4066.
- Mills, J. P.; Qie, L.; Dao, M.; Tan, K.; Lim, C. T.; Suresh, S.** (2004): Direct force-displacement responses of red blood cells altered by different stages of *Plasmodium falciparum* malaria infection. *Manuscript in preparation*.
- Parker, K. H.; Winlove, C. P.** (1999): The deformation of spherical vesicles with permeable, constant- area membranes: Application to the red blood cell. *Biophys. J.* 77, 3096-3107.
- Simmons, R. M.; Finer, J. T.; Chu, S.; Spudich, J. A.** (1996): Quantitative measurements of force and displacement using an optical trap. *Biophysical Journal* 70, 1813-1822.
- Simo, J. C.; Pister, K. S.** (1984): Remarks on Rate Constitutive-Equations for Finite Deformation Problems - Computational Implications. *Computer Methods in Applied Mechanics and Engineering* 46, 201-215.
- Sleep, J.; Wilson, D.; Simmons, R.; Gratzer, W.** (1999): Elasticity of the red cell membrane and its relation to hemolytic disorders: An optical tweezers study. *Biophys. J.* 77, 3085-3095.
- Svoboda, K.; Block, S. M.** (1994): Biological Applications of Optical Forces. *Annual Review of Biophysics and Biomolecular Structure* 23, 247-285.
- Svoboda, K.; Schmidt, C. F.; Branton, D.; Block, S. M.** (1992): Elastic Properties of Extracted Red-Blood-Cell Membrane Skeletons. *Faseb Journal* 6, A523-A523.
- Van Vliet, K. J.; Bao, G.; Suresh, S.** (2003): The biomechanics toolbox: experimental approaches for living cells and biomolecules. *Acta Materialia* 51, 5881-5905.
- Yeoh, O. H.** (1990): Characterization of Elastic Properties of Carbon-Black-Filled Rubber Vulcanizates. *Rubber Chem. Technol.* 63, 792-805.

## Lab 7: Advanced instrumentation in the teaching lab

**Location:** 16-352

**PI:** Scott Manalis and Matt Lang

**Lab Instructors:** Maxim Shusteff, Marcio von Muhlen and David Appleyard

### Summary

This session makes use of the atomic force microscopy (AFM) and optical trapping experiments used to teach an undergraduate instrumentation laboratory. Using a home-built and easily-manipulated AFM, you will learn basic imaging techniques, take some simple force curves for elastic modulus, and make a measurement of thermal energy. Using similarly scaled-down optical traps, you will learn calibration methods for the optical traps and perform experiments on the molecular motors of *E. coli* bacteria. The documents under "Recommended Reading" on the GEM4 wiki provide the essential background for both instruments and an overview of the experiments.  
(<http://www.openwetware.org/wiki/GEM4labs>)



# The teaching AFM: Part 1

## Alignment, Calibration, and Noise

### 1 Objectives

1. Learn the function of our class AFM system's components and the relationship between them.
2. Practice aligning the AFM optics.
3. Learn how to calibrate the AFM to relate its output signal to physical cantilever deflection.
4. Measure the mechanical vibration noise in the AFM system with the cantilever free and in contact.

### 2 The Atomic Force Microscopy (AFM) System

This section describes the various components of the AFM you will use in the lab, and particularly how they differ in operation from a commercial AFM. During the lab, we will talk about the operational principles of a standard AFM. It may also be helpful to review some of the References in Section 4 at the end of this module. A photo of our AFM setup is provided in Figure 4 at the end of this section for you to refer to as you learn about the instrument.

#### 2.1 Power-on

For our AFMs to run, you must turn on three things: (1) the detection laser, (2) the photodetector, and (3) piezo-driver power supply. The photodetector has a battery that provides reverse bias, and the others have dedicated power supplies (refer to Figure 4 at the end of this section for where these switches are located). *When you finish using the AFM, don't forget to turn off the three switches you turned on at the beginning: laser power supply, photodetector, and piezo power supply.*

#### 2.2 Scanner system

To be useful for imaging, an AFM needs to scan its probe over the sample surface. Our microscopes are designed with a fixed probe and a movable sample, so whenever we talk about moving the tip relative to the sample, we will always only move the sample. The sample is actuated for scanning and force spectroscopy measurements by a simple piezo disk, shown in Figure 1, which is divided

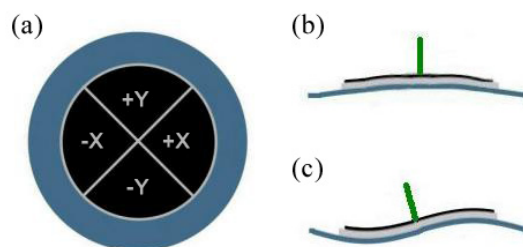


Figure 1: This is a schematic of the piezo disk used to actuate the AFM's sample stage. The circular electrode is divided into quadrants as shown in (a) to enable 3-axis actuation. When the same voltage is applied to all quadrants, the disk flexes as shown in (b), giving z-axis motion. Differential voltages applied to opposite quadrants, produce the deflection shown in (c), which moves the stage along the x- and y-axes, with the help of the offset post, represented here by the vertical green line.

into quadrants and flexes to move the post on which the sample stage rests. The piezo disk is controlled from the MATLAB scanning software, and you will learn more about this in the next module.

For motions along the z-axis (vertically), there are three regimes of motion:

**Manual (coarse):** turning the knob on the red picomotor with your hand (clockwise moves the stage up).

**Picomotor (medium):** using the joystick to drive the picomotor (pushing the joystick forward moves the stage upward).

**Piezo-disk (fine):** actuating the piezo disk over a few hundred nanometers using the MATLAB software.

For coarse positioning along the x- and y-axis, the micrometers on the positioning stage are used.

**WARNING: The AFM probes can be broken by running them into the sample — avoid “crashing” the tip into the surface, or worse bumping the stage into the die or fluid cell. Use caution when moving the sample up and down.**

### 2.3 Optical system

Our microscopes use a somewhat different optical readout from a standard AFM to sense cantilever deflection. Rather than detecting the *position* of a laser beam that reflects off the back surface of the cantilever, we measure the *intensity* of a diffracted beam. To do this, a diode laser with wavelength  $\lambda = 635nm$  is focused onto the interdigitated (ID) “finger” structure, and we observe the brightness of one of the reflected spots (referred to as “modes”) using a photodiode. This gives us information about the *relative displacement* of one set of fingers relative to the other — this is useful if one set is attached to the cantilever, and the other to some reference surface.

As the cantilever deflects, and the out-of-plane spacing between the ID fingers changes, the reflected diffractive modes change their brightness, as shown in Figure 2. However, a complication of using this system is the non-linear output characteristic of the mode intensities. As the out-of-plane deflection of the fingers increases, each mode grows alternately brighter and dimmer. The

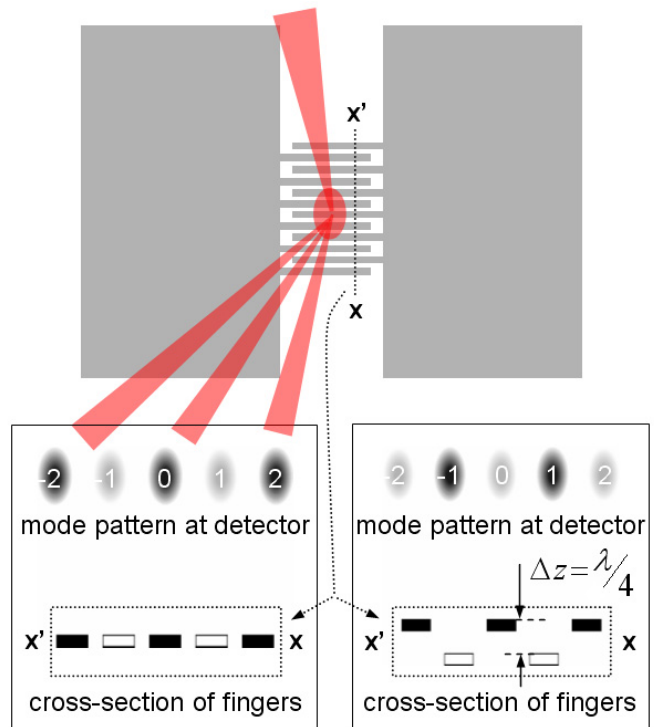


Figure 2: A drawing of the interdigitated (ID) interferometric fingers, with the detection laser shown incident from the top of the figure. When the finger sets are aligned, as in the left box above, the even-numbered modes are brightest, and odd modes are darkest. When they displace relative to each other by a distance of a quarter of the laser wavelength  $\lambda$ , the situation reverses, shown on the right. This repeats every  $\lambda/4$  in either direction.

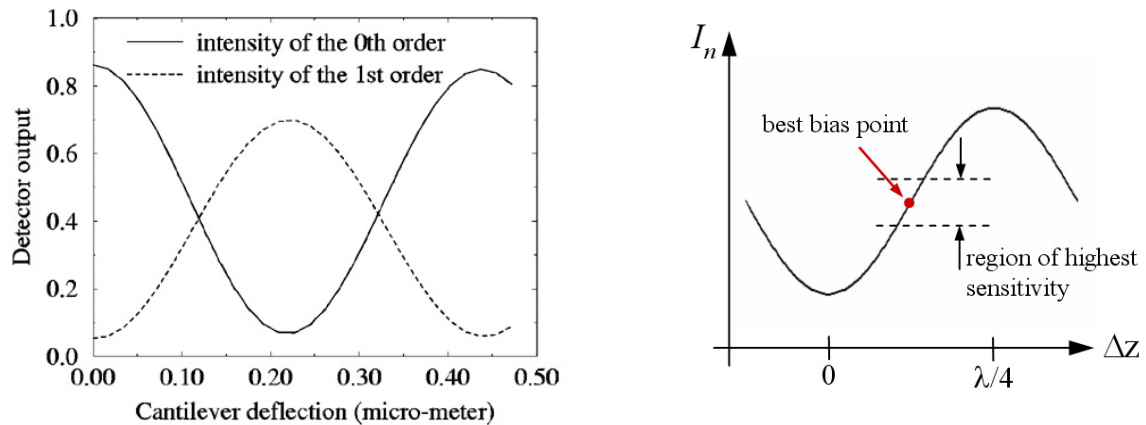
intensity  $I$  of odd order modes vs. finger deflection  $\Delta z$  has the form

$$I \propto \sin^2 \left( \frac{2\pi}{\lambda} \Delta z \right),$$

and for odd modes, the sine is replaced by a cosine. The plot in Figure 3(a) shows graphically the intensity of two adjacent modes as a function of displacement.

This nonlinearity causes the sensor's sensitivity to depend critically on the operating point along this curve at which a measurement is done. To make useful measurements, the ID interferometer therefore needs to be *biased* to a spot on the  $\sin^2$  curve where the function's slope is greatest - midway between the maximum and minimum, as sketched in Figure 3(b). This can be done with our devices by simply adjusting the position of the laser spot side to side on the finger grating - the grating is not perfectly flat due to residual stress, and thus provides a simple biasing method.

At this point, it's worth remembering the distinction between *calibration*, *sensitivity* and *resolution* - terms which will be used frequently in the context of the AFM, but whose precise meaning isn't always made explicit. Be sure you're clear on the differences between them.



(a) The non-linear intensities of the 0<sup>th</sup> and 1<sup>st</sup> order modes plotted as a function of cantilever displacement.

(b) The desired operating point for maximum deflection sensitivity is shown here on the  $\sin^2$  output characteristic of the ID fingers.

Figure 3: The characteristic output of the ID interferometric sensor.

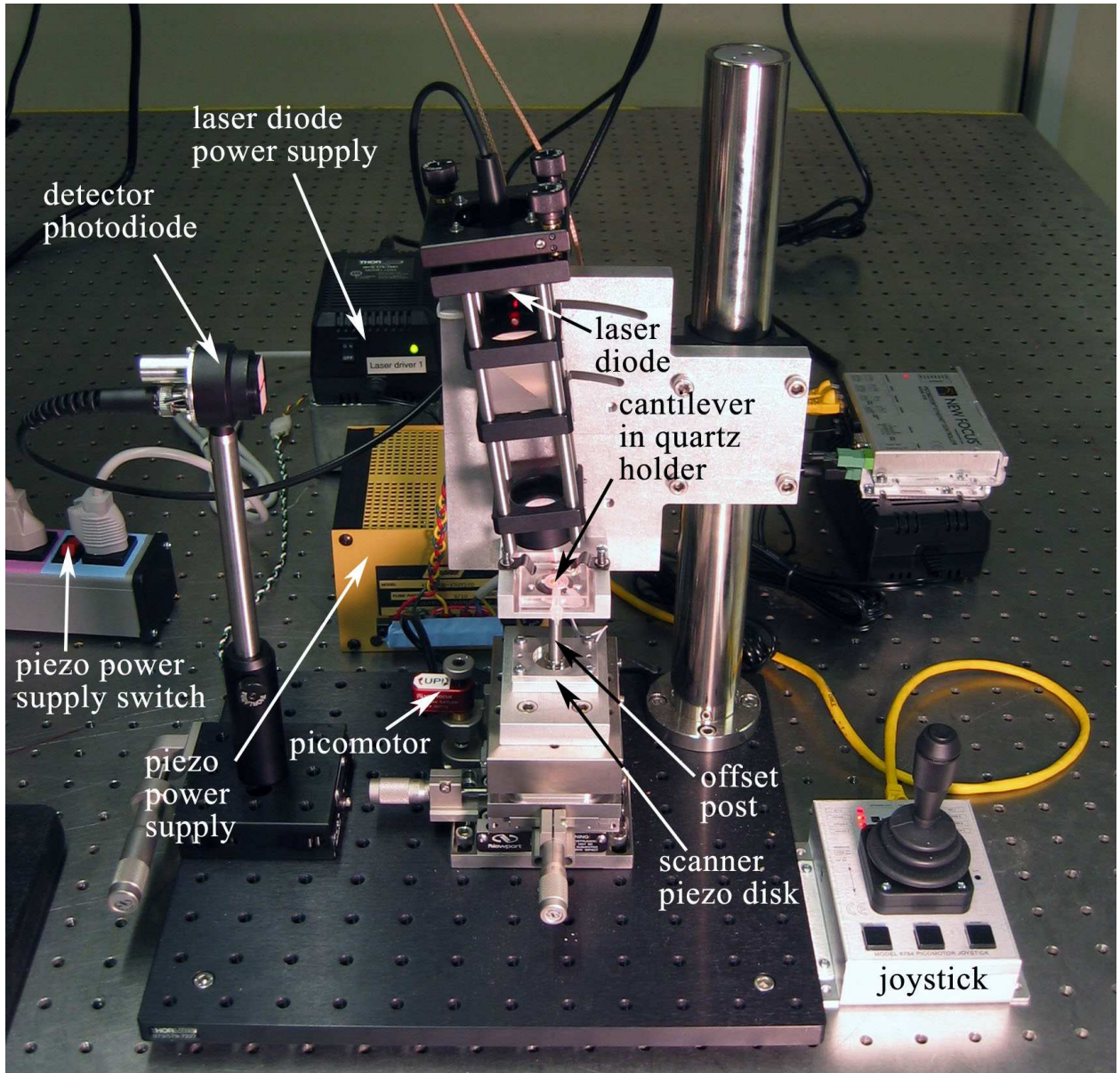


Figure 4: The AFM setup, with major components indicated.

### 3 Lab Procedures

#### 3.1 Laser alignment and diffractive modes

To get a cantilever position readout, the laser needs to be well focused on the interdigitated fingers of the cantilever. Use the white light source and stereo-microscope to look at the cantilever in its holder. The laser spot should be visible as a red dot (there may be other reflections or scattered laser light, but the spot itself is a small bright dot). Adjust its position using the knobs on the laser mount, until it hits the interdigitated fingers (use the cantilever schematic in Figure 5 as a reference).

When the laser is focused in approximately the right position, the paper “screen” around the slit on the photodetector will allow you to see the diffraction pattern coming out of the beam splitter. Observe the reflections on this screen while adjusting the laser position until you see several evenly spaced modes. Make sure you aren’t misled by reflections from other parts of the apparatus — some may look similar to the diffraction pattern, but aren’t what you’re looking for.

Before engaging the AFM, start the piezo z-modulation scan in the MATLAB software using the default frequency and amplitude of 2Hz and 8V. (Note: Be sure the mode switch on the rear of the AFM head is flipped down to “force spec. mode,” and make sure to turn on the piezo power supply using the color-coded switch on the table.) Carefully bring the tip near the surface, first by hand, then very slowly with the joystick. When you make contact, you will see the modes on the photodetector fluctuate in brightness. Because of the device geometry, only the central long cantilever with the tip will make contact with the sample surface.

#### 3.2 Calibration and biasing

If you observe the intensity signal on the oscilloscope in x-y mode, you should see something like the plots shown in Figure 6: a flat line that breaks into a  $\sin^2$  function at a certain x-value (whether it starts upward or downward depends on the mode you choose). The flat line is the cantilever out of contact, and the oscillating section is the cantilever bending, after making contact with the sample.

For the types of noise measurement that we will do, the signal needs to be at the maximum-slope position along the output curve when it’s not in contact with the surface. If necessary, use the offset on your voltage amplifier to position the  $\sin^2$  so that it is centered around zero. Then, set the out-of-contact bias point by moving the position of the laser focus on the fingers until the flat section of your force spec. curve is approximately at zero volts, halfway between the maximum and minimum, as in Figure 6(c).

To relate the mode intensity output to a physical deflection, we can take advantage of the fact that a mode’s brightness goes from fully bright to fully dim as the fingers deflect through a distance of  $\lambda/4$ . This way, by relating this displacement to the amplitude of the  $\sin^2$  curve, you can determine the cantilever sensitivity in nm/V.

You will also need to multiply the calibration by a correction factor to account for the location of the diffraction fingers with respect to the tip of the cantilever (you can assume that the deflected shape of the cantilever fits a second-order polynomial).

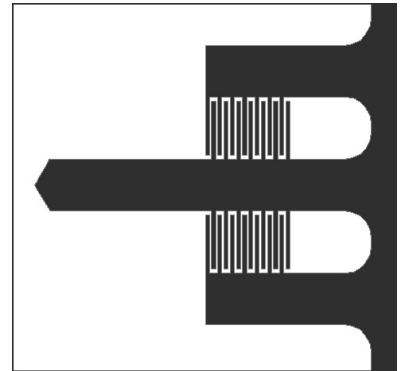


Figure 5: Plan view of the imaging cantilever geometry. The central (imaging) beam dimensions are length  $L = 400\mu m$ , and width  $b = 60\mu m$ . The finger gratings begin  $117\mu m$  from the base and end  $200\mu m$  from it.

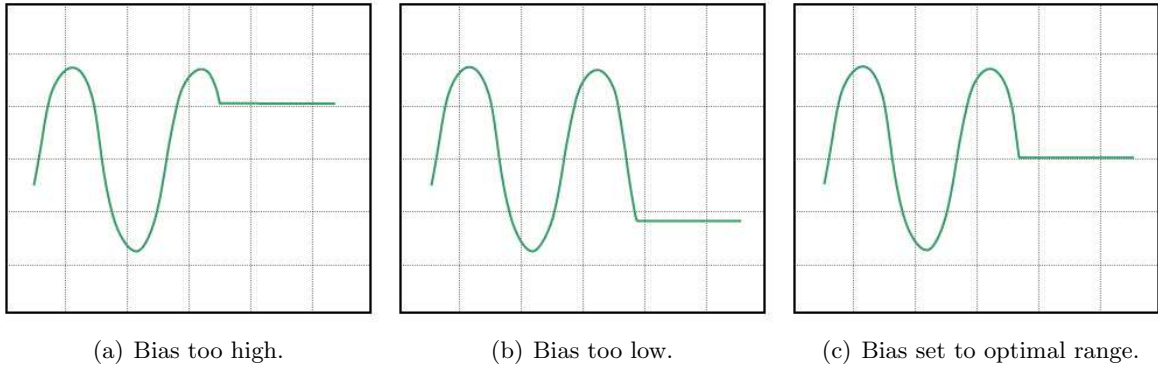


Figure 6: Proper setting of the bias point for the measurements we'll make in this lab.

## 4 Helpful References

1. Basic Operating Principles of AFM.
  - a. A website with a basic description:  
[http://www.weizmann.ac.il/Chemical\\_Research\\_Support/surflab/peter/afmworks](http://www.weizmann.ac.il/Chemical_Research_Support/surflab/peter/afmworks)
  - b. One with some more detail:  
<http://saf.chem.ox.ac.uk/Instruments/AFM/SPMoptprin.html>
  - c. If these really stimulate your interest, this is a more comprehensive site on Scanning Probe Microscopy (SPM), of which AFM is a subset:  
<http://www.mobot.org/jwcross/spm/>
2. The paper that started it all.  
 G. Binnig, C. F. Quate, Ch. Gerber, "Atomic Force Microscope" *Physical Review Letters* **56**(3):930-933, 1986.
3. Using interferometric ID fingers for position detection.
  - a. The original paper:  
 S. R. Manalis, S. C. Minne, A. Atalar, C. F. Quate, "Interdigitated cantilevers for atomic force microscopy," *Applied Physics Letters* **69**(25):3944-3946, 1996.
  - b. A more thorough treatment:  
 G. G. Yaralioglu, S. R. Manalis, A. Atalar, C. F. Quate, "Analysis and design of an interdigital cantilever as a displacement sensor," *Journal of Applied Physics*, **83**(12):7405-7415, 1998.
4. A nice review of using the AFM in biology.  
 D. Fotiadis, S. Scheuring, S. A. Müller, A. Engel, D. J. Müller, "Imaging and manipulation of biological structures with the AFM," *Micron*, **33**(4):385-397, 2002.

# The teaching AFM: Part 2

## Imaging with the AFM

### 1 Objectives

1. Learn to set up and prepare the AFM for imaging.
2. Image several different samples with the AFM.
3. Use the AFM to measure physical dimensions of imaged features.
4. Use the AFM to measure the elastic modulus and surface adhesion force of a sample.

### 2 The AFM Scan Control Software

The software that interfaces with the AFM is an application that runs in MATLAB. It is launched by typing ‘`scannergui`’ in the MATLAB command window. Its main function is to systematically scan the probe tip back-and-forth across the sample, recording the cantilever deflection information at each point, line by line, and assembling that data into an image. Figure 1 shows a screen capture of the scanner control window, and an overview of its operation is provided below.

#### 2.1 Overview of Controls

Many of these are self-explanatory, such as the START IMAGING and STOP buttons, as well as the image area in the lower right, which displays the image currently being scanned. Some notes are given below on features that are not immediately obvious.

To begin with, it’s easiest to simply use the default settings on all these controls, and to experiment with changing them as you become more familiar with the tool.

**Scan Parameters** - The *Scan size* sets the length and width of the image in nanometers (always a square shape), but its accuracy depends on having the correct value for *Scan sensitivity* (which should already be set for you, but may require calibration). The *Scan frequency* (lines per second) sets the speed of the tip across the surface, and together with the *Number of lines* affects the amount of detail you will see in the image. Setting the *Y-scan direction* tells the scanner whether to start at the top or the bottom of an image, and the *trace/retrace* selector determines whether each line is recorded as the tip scans to the left or to the right.

**Scope View** - As the tip scans back and forth, this plots the tip deflection data for each line. Useful for quantitative feature height measurements.

**Scanner Waveforms** - Shows the voltage waveforms driving the piezo scanner, for each scan line that is taken. Helpful for knowing where in the image the current scan line is located, and the output level of the waveforms driving the scanner.

**Z-mod Controls** - These are only active during a z-mod scan, and have no effect when taking an image. For more on this mode, see Section 2.4 below.

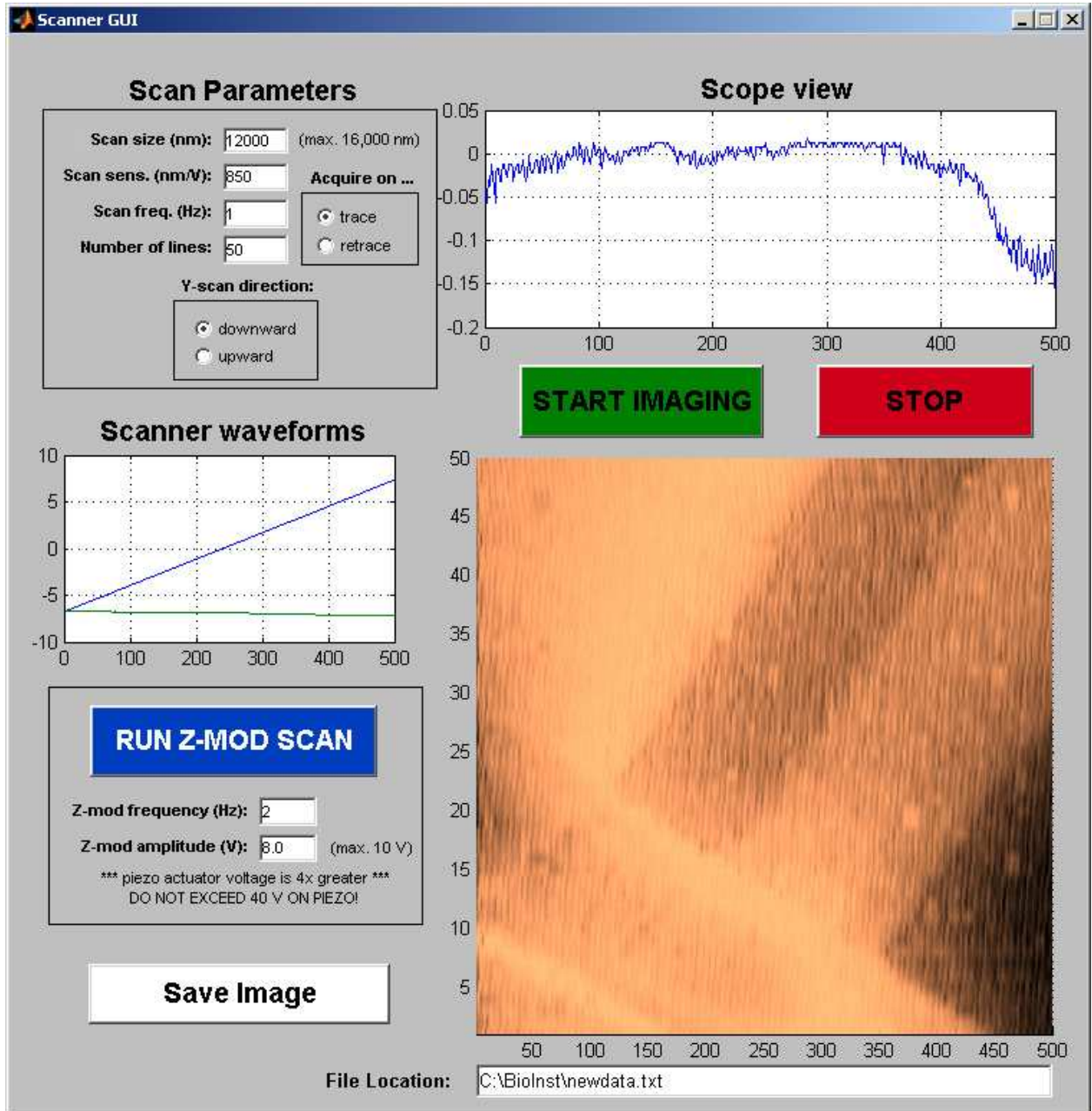


Figure 1: The Scanner GUI window. The AFM is scanning a  $12 \times 12 \mu\text{m}$  area, at a rate of one line per second, and is currently near the bottom of the image.

## 2.2 Cantilever probes for imaging

The probes we will use for imaging are shown in Figure 2 with relevant dimensions. The central beam has a tip at its end, which scans the surface. The shorter side beams to either side have no tips and remain out of contact. The side beams provide a reference against which the deflection of the central beam is measured; the ID grating on either side may be used. When calibrating the detector output to relate voltage to tip deflection, remember to include a correction factor to account for the ID finger position far away from the tip.

## 2.3 Image Mode Operation

This is the primary operating regime of the AFM, and provides a continuous display of the surface being scanned, as the probe is gradually rastered up and down the image area. To use this mode, the switch on the back of the AFM must be flipped upward. It is important to remember that the maximum scan area is only about  $15\mu m$  square, and adjusting the position of the sample under the tip requires only the smallest movements of the stage micro-positioners. Also keep in mind that there is a delay after START IMAGING is pressed and before the scan begins, as the actuator drive signals are buffered to the I/O hardware.

## 2.4 Z-mod (force spectroscopy) Operation

In this mode, the piezo moves the sample only along the  $z$ -axis – i.e. straight up and down (hence z-mod, short for z-modulation). To use this mode, the switch on the back of the AFM must be flipped downward. Besides being helpful during calibration and biasing of the readout laser, this mode is used to perform force spectroscopy experiments, in which tip-sample forces can be measured as the tip comes into and out of contact with the sample.

(Note that the red STOP button is also used to stop a z-mod scan).

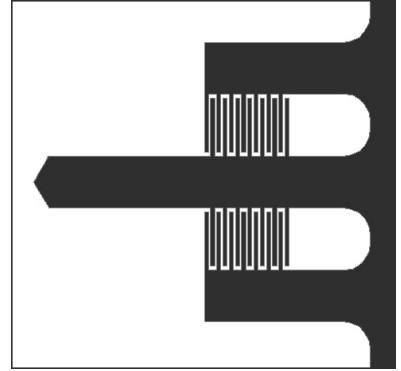
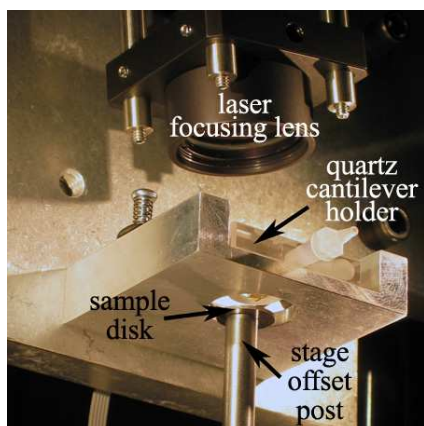


Figure 2: Plan view of the imaging cantilever geometry. The central (imaging) beam dimensions are length  $L = 400\mu m$ , and width  $b = 60\mu m$ . The finger gratings begin  $117\mu m$  from the base and end  $200\mu m$  from it.

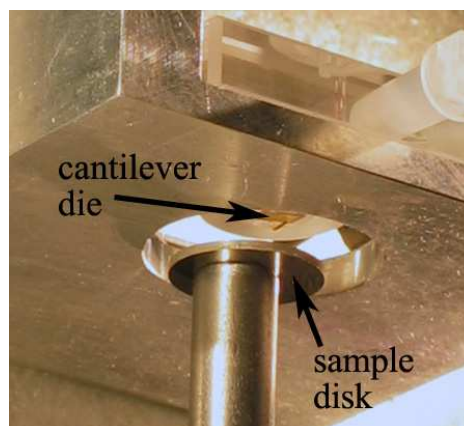
### 3 Lab Procedures

#### 3.1 Sample Loading and Positioning

Correctly mounting a sample in the AFM is a key part of obtaining quality images. Our samples are always mounted on disks, which are magnetically held to the piezo actuator offset post. The AFM can image only a small area near the center of the opening in the metal cantilever holder, so be sure that the area of interest for imaging ends up there.



(a) A photo of the underside of the cantilever mount, with the sample disk lowered for changing samples.



(b) A close-up view of the opening into which the sample rises, showing the cantilever die and sample disk.

When changing or inserting a sample disk, the 3-axis stage must be lowered far enough for the disk to clear the bottom opening of the cantilever mount, as shown in the figures above. This requires a large travel distance, so exercise caution when bringing the sample back up to the cantilever, and take care not to damage the probe.

In addition, as you change samples, it is critical to reposition the offset post as nearly centered as possible on the actuator disk, to ensure true horizontal motion in the x-y plane (Centering the sample disk at the top of the offset post is not critical; rather, it's the position of the **bottom end of the post on the piezo scanner disk**. For instance, in figure 3(b) above the sample disk is visibly off-center).

Once the sample is in proximity to the cantilever, follow the procedures that you learned in the previous lab module to align the laser, engage the tip with the surface, and view a force curve.

#### 3.2 Imaging

The general approach to imaging is to (1) set the overall output signal range and offset while in the z-mod regime, (2) stop the z-mod scan and bring the probe into contact with the surface, and (3) carefully adjust the cantilever deflection to give the desired bias point, and (4) start the image scan.

Correct biasing is key to obtaining good images. If you are not yet comfortable with choosing and setting an appropriate bias point for the cantilever's optical readout, it is worth reviewing that material from the previous module.

For imaging, the bias does not necessarily need to be set at maximum sensitivity when out of contact. Rather, the signal should be at *maximum slope (in the middle of its travel range) when the probe is engaged, and exerting a small amount of force on the surface*. Remember that the more force the probe applies to the surface, the more wear and damage to the probe and surface can result.

The samples available for imaging are calibration gratings and *E. coli* bacteria on a silicon dioxide surface. Unlike commercial instruments, our AFMs do not have an integrated optical viewing system, so when positioning the sample it is difficult to determine exactly what spot on the sample the probe tip will scan. Use the stereo-microscope (at moderate magnification) and a fiber-light to observe the tip and position it as well as you can. Temporarily turning off the sensing laser will make it easier to see. You can also move the sample “on the fly”, as you’re imaging, but it takes some practice to make small enough stage movements. You will also likely have to readjust the bias point (also fine to do on the fly).

## Measuring Image Dimensions

When it’s necessary to determine the size of imaged features, the *Scan size* control is your most handy reference. This gives the size of the image square, which can be quickly related to features in the image. If needed, the scan size can be changed to make imaged features fit in the image window as desired.

NOTE: the *Scan sensitivity* is pre-set to an approximate value, but if you would like more precise lateral feature measurements, it’s worth verifying the calibration of the *Scan sensitivity*. This can be done by scanning a reference with precisely known feature sizes (such as a calibration grating), and adjusting the *Scan sensitivity* until the actual image size matches the *Scan size* setting.

Finally, for feature height (*z*-axis) measurements, they can be made by observing the SCOPE VIEW of the AFM software. The waveform displayed as the AFM scans over a feature shows the feature height dimensions as voltages — the calibration that you’ve done to these voltages to nanometers of tip displacement will give you feature sizes.

## 3.3 Elastic Modulus Measurements

[For these measurements, we’ll use the shortest and stiffest cantilevers available to us, which will give the best signal. These have very similar geometry to the long cantilevers in Figure 2, but have a length of  $250\mu\text{m}$ , and a width of  $50\mu\text{m}$ . The fingers begin  $43\mu\text{m}$  from the base and end  $125\mu\text{m}$  from it. Ask your lab instructor to provide you with a short cantilever when you are ready.]

As you know, some of the most useful applications of AFMs in biology take advantage of their ability to measure very small forces. We’ll use this capability to measure the elastic moduli of some soft samples, to simulate mapping cell wall elastic properties, similarly to the 2003 paper by Touhami *et al.* in *Langmuir*.

As seen in this paper, samples with different elastic moduli change the slope of the in-contact portion of the force curve, when using the optical lever sensor. For our non-linear ID sensor, the equivalent of the changing slope is a changing *period* for the  $\sin^2$  function. Just as softer samples cause lower slope with the optical lever, softer samples give the output function of the ID sensor a longer period, with greater spacing between the peaks (see figure 4(a) below).

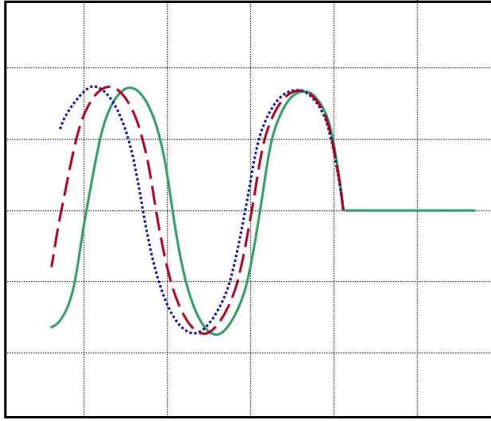
The approach for measuring modulus is to first take a force curve on a hard reference sample, considered to have infinite hardness. We will use a bare silicon nitride surface. This allows us to determine how the x-axis signal corresponds to stage movements.

You’ll want to bias this measurement similarly to measuring noise — the output should be at the middle of the output range when out of contact (See Fig. 4(b)).

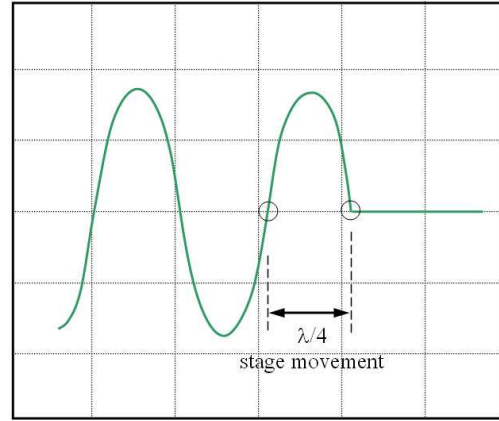
After your measurement of the hard sample, switch to the more compliant PDMS elastomer samples, and run force curves on them.

Make sure to capture the plots of the force curves for later analysis, described in Section ??.

To get good force curves:



(a) Force curves for samples of varying hardness. The green (solid) curve is for a hard sample, the red (dashes) curve is softer, and blue (dots) curve is softest.



(b) Preferred biasing and calibration on a hard surface for measuring elastic modulus, and corresponding physical stage movement

1. Don't change the biasing or laser position between samples – if you do, the force curves you get can't be compared one to another.
2. Careful initial biasing at the middle of output range is worth it — this will make a big difference in ease of data analysis.
3. After you've brought each sample into contact and are satisfied with the Z-modulation range, run the scan at slow speed (e.g. 0.5Hz) for the cleanest force curves.

### Data Analysis

According to Touhami *et al.*, the depth  $\delta$  of an indentation made by a conical tip (approximately true for ours) is related to the applied force  $F$  by

$$F = \frac{2}{\pi} \tan \alpha \left( \frac{E}{1 - \nu^2} \right) \delta^2 ,$$

where  $\alpha$  is the half-angle of the conical tip, and  $E$  and  $\nu$  are the elastic (Young's) modulus and the Poisson's ratio of the substrate material, respectively.

Substituting in appropriate values for  $\alpha$  ( $35.3^\circ$ ) and  $\nu$  (0.25), we are left with

$$F = 0.60E\delta^2 ,$$

in which we need only the force and indentation  $\delta$  values to calculate modulus.

The force  $F$  is calculated by treating the cantilever as a Hookian spring, which obeys the law  $F = kz$ , where  $k$  is the spring constant and  $z$  the tip deflection. For the  $250\mu\text{m}$  long cantilever, assume a spring constant of 0.118 N/m.

Finally, all that remains is to calculate indentation depths for the soft materials from the difference in the period of the  $\sin^2$  output between their force curves and the one for the hard sample. Corresponding forces are derived from the cantilever deflection. Don't forget at all points to include the factor that relates cantilever tip deflection to finger deflection.

## The teaching AFM: Part 3

### Thermomechanical noise and Boltzmann's constant

#### 1 Objectives

1. Use your knowledge of the AFM system and associated instrumentation to record the vibrational noise spectrum of a cantilever probe.
2. Estimate the value of Boltzmann's Constant  $k_B$  from the cantilever vibrational spectrum.

#### 2 Background

##### 2.1 Theory: Thermomechanical Noise in Microcantilevers

For simplicity of analysis, we model the cantilever as a harmonic oscillator with one degree of freedom, similar to a mass on a spring, as discussed in lecture. According to the Equipartition Theorem, the thermal energy present in the system is simply related to the cantilever fluctuations as follows:

$$\frac{1}{2}k_B T = \frac{1}{2}k \langle \Delta z^2 \rangle,$$

where  $\langle \Delta z^2 \rangle$  is the mean-square deflection of the cantilever,  $T$  is the absolute temperature,  $k$  is the cantilever spring constant, and  $k_B$  is Boltzmann's Constant (yes, this notation can be confusing — take care to keep these  $k$ s straight).

The characteristic transfer function of the second-order resonant system has the form

$$|G(\omega)| = \sqrt{\frac{4k_B T}{Qk\omega_0}} \sqrt{\frac{1}{\left(1 - \frac{\omega^2}{\omega_0^2}\right)^2 + \frac{1}{Q^2} \frac{\omega^2}{\omega_0^2}}},$$

in which  $\omega_0$  and  $Q$  are the (angular) resonant frequency and quality factor, respectively. At low frequencies, ( $\omega \ll \omega_0$ ) this expression yields what's called the "thermomechanical noise limit" (see Figure 1 for an illustration):

$$\delta = \sqrt{\frac{4k_B T}{Qk\omega_0}}.$$

These relations suggest several possible approaches that can be taken for determining  $k_B$ , for which you will need the values of several parameters. These include (1) the quality factor  $Q$  and resonant frequency  $\omega_0$  of the resonator (2) the cantilever's mean-square deflection  $\langle \Delta z^2 \rangle$ , and (3) its spring constant  $k$ .

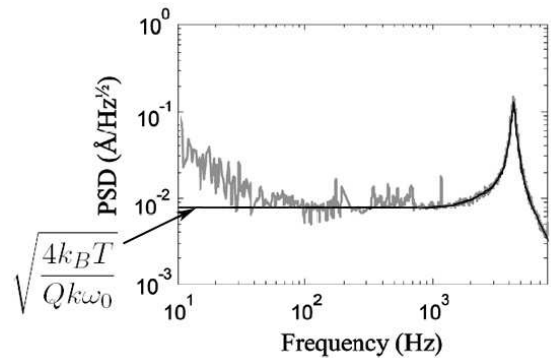


Figure 1: A data plot of a cantilever's noise spectrum, with an ideal transfer function  $G(\omega)$  fit on top (dark line). Note that  $G(\omega)$  is flat at low frequencies, at the thermomechanical limit, as indicated. In contrast, real data has more  $1/f$ -type noise present at lower frequencies (see Section 3.2).

1. The **quality factor** and **resonant frequency** can be obtained from taking the noise PSD of the vibrating cantilever. If your intuitive sense for them is good, you can estimate these quantities directly from the plot, or determine them more precisely by fitting an ideal transfer function to the noise data, and extracting the fitting parameters (more on this in Section ??).
2. The **mean-square deflection** is readily available from either time-domain or PSD data of the cantilever thermal noise. Recall that these are related through Parseval's theorem as follows:

$$\langle \Delta z^2 \rangle = \int_0^\infty S(\omega) d\omega ,$$

where  $S(\omega)$  is the PSD function of  $\Delta z$ . By now, you know enough MATLAB spectral analysis techniques to make these measurements.

3. The **spring constant** (stiffness) can be analytically calculated from geometrical parameters in two ways (see Section 2.2 for cantilever dimensions). From basic mechanical beam-bending analysis of a rectangular cantilever the stiffness  $k$  can be expressed as

$$k = \frac{Ebh^3}{4L^3} ,$$

in which  $E$  is the elastic (Young's) modulus of the beam material, and  $L$ ,  $b$  and  $h$  are the length, width, and thickness of the beam, respectively ( $b$  is used for the width to avoid confusion with angular frequency  $\omega$ ).

This method, however, does not always yield accurate results — can you suggest why? Another analytical model for the spring constant was devised by Sader and coworkers<sup>1</sup>, and it relies on measuring the cantilever's resonant frequency:

$$k = 0.2427\rho_c hbL\omega_{vac}^2,$$

where  $\rho_c$  is the mass density of the material,  $L$ ,  $b$ , and  $h$  are the same geometrical parameters as above, and  $\omega_{vac}$  is the cantilever's resonant frequency in vacuum. For the purposes of these calculations, you can assume that the resonant frequency that you will measure in air  $\omega_{air}$  is 2% lower than  $\omega_{vac}$ . (*remember the factor of  $2\pi$  when interconverting between  $\omega$  and  $f$  in your equations*).

Suitable material parameters to use for the low-stress silicon nitride ( $\text{Si}_x\text{N}$ ), out of which these cantilevers are made are  $\rho_c = 3400\text{kg/m}^3$ , and  $E = 250\text{GPa}$ . As mentioned before, for complete cantilever dimensions, see Figure 2 in Section 2.2.

---

<sup>1</sup>J. E. Sader, *et al*, "Calibration of rectangular atomic force microscope cantilevers," *Review of Scientific Instruments*, **70**(10):3967-3969, 1999.

## 2.2 Cantilevers for Thermal Noise Measurements

The probes you will use for this lab are different than what you've used for imaging and force measurements. Their plan view is shown in Figure 2.

For noise measurement purposes, we'd like a clean vibrational noise spectrum, which is best achieved using a matched pair of identical cantilevers. The configuration with a central long beam and reference side-beams has extra resonance peaks in the spectrum that make it harder to interpret. With the geometry in Figure 2 the beams have identical spectra which overlap and reinforce each other. Using a pair of identical beams also helps to minimize any common drift effects from air movements or thermal gradients.

*There are two sizes of cantilever pairs available.* Choose either size to make your measurement. For the long devices,  $L = 350\mu\text{m}$  and the finger grating starts  $140\mu\text{m}$  and ends  $250\mu\text{m}$  from the cantilever base. For the short devices,  $L = 275\mu\text{m}$ , and the fingers are between  $93\mu\text{m}$  and  $175\mu\text{m}$  from the base. The width and thickness of all of the cantilevers is  $b = 50\mu\text{m}$  and  $h = 0.8\mu\text{m}$ , respectively.

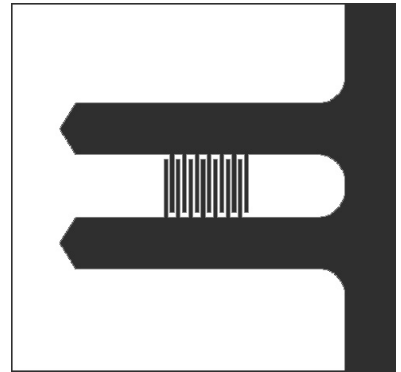


Figure 2: Plan view showing the geometry of a differential cantilever pair. We assume that because the beams are fabricated so close together, their material properties and dimensions are identical.

## 3 Lab Procedures

### 3.1 Alignment, Calibration, Biasing

By now you're familiar with aligning, calibrating, and biasing. The major difference in this case is performing the z-modulation scan for calibration.

Because this device is a pair of identical cantilevers, simply bringing it down to a surface will deflect both beams equally. A z-mod scan will show approximately zero deflection of one beam relative to the other. Instead, we want to bend only one of the beams, while keeping the other unbent. To do this, you'll have a sample with a sharp step edge. The goal is to position the cantilever pair above this edge such that one of the beams will be on the surface, and the other will hang in free space. A z-mod scan should then deflect only one of the beams, giving us the calibration curve we want.

A few additional remarks to guide you:

- Remember to flip the “imaging/z-mod” mode switch on the back of the AFM to the proper position.
- Reflections of the laser from the edge of the substrate can interfere with the diffractive modes. If this is the case, try repositioning the sample edge, perhaps using only the corner to bend one of the cantilevers, until the  $\sin^2$  shape improves.
- As you've done several times, bias the force curve for maximum sensitivity when out of contact — the flat portion of the curve should be placed midway between the maximum and minimum.

## 3.2 Recording Thermomechanical Noise Spectra

Once you're happy with your calibration and biasing, withdraw the lever's tip from the surface, making sure that the bias point stays where you set it. Use the LabVIEW "Spectrum Analyzer" to record the thermal noise signal coming from the freely vibrating cantilever. Once you are happy with how the spectrum looks, save it to a .txt file of your choice.

You only need to measure the noise spectrum down to about 50-100Hz. Below this frequency,  $1/f$ -type or "pink" noise dominates. You are welcome to measure this if you are interested, but it is of limited use for determining  $k_B$ . For very low-frequency measurements, anti-aliasing and proper input coupling becomes very important. If you are interested in this, your lab instructor can provide guidance.

Some guidelines for getting a good noise spectrum:

- Choose a sampling frequency at least  $2\times$  higher than the highest frequency of interest, or about  $10\times$  higher than the first resonance peak of the cantilever.
- Use AC coupling on your voltage amplifier, and use a gain of 100-1000.
- If necessary, add a low-pass anti-aliasing filter (recall Module 1) at an appropriate frequency to eliminate high-frequency components being "folded" over into the frequency region of interest.
- Recall from the previous lab that, if you prefer, you can also measure the time-domain signal directly, and later calculate its PSD in MATLAB. You can decide which technique you prefer.

## 3.3 Data Analysis with MATLAB

Once you bring your saved PSD data into MATLAB (`[Fvec,PSDvec]=load('filename')` is the syntax you want), you can manipulate it as you wish. To fit the second-order transfer function  $G(\omega)$  to the noise data, we'll use the `lsqcurvefit` routine from MATLAB's optimization toolbox, which does a least-squares curve fit, as you may have guessed. We're aiming to do something similar to what you see in Figure 1, where an ideal function is overlaid on real noise data.

To make the fit converge easily, we'll separate the nonlinear  $f_0$  and  $Q$  parameters from the linear scaling factor. When doing the fitting, it is helpful not to use the whole frequency range of your data. Instead, crop your PSD data to a suitable range around the resonant peak — the vectors `xdata` and `ydata` used below are *cropped* PSD frequency and magnitude data, respectively, extracted from `Fvec` and `PSDvec`.

First, you'll need a MATLAB function `transfunc` to generate the *unscaled* transfer function (i.e. the thermomechanical noise scaling factor is 1 here – refer to the equations on page 1):

$$|G(\omega)| = \frac{1}{\sqrt{\left(1 - \frac{\omega^2}{\omega_0^2}\right)^2 + \frac{1}{Q^2} \frac{\omega^2}{\omega_0^2}}}.$$

The function takes the  $f_0$  (note that this is *real* frequency in Hz, and not angular frequency in rad/sec) and  $Q$  parameters as input, with a vector of frequencies, and outputs corresponding PSD magnitude data:

```
function [output]= transfunc(params,xdata)
% params [f_0 Q]
x=xdata/params(1); % x-matrix to contain freq. points normalized to f/f_0
output=sqrt(1./((1-x.^2).^2 + (x/params(2)).^2));
```

Then, create a function `scaling` to do the linear scaling, and calculate the thermomechanical noise level (the left-divide operation actually does a least-squares fit):

```
function [y]=scaling(params,xdata,ydata)
unscaled=transfunc(params,xdata);
A=unscaled\ydata; % note the left-divide here!
y=unscaled*A;
```

Finally, use the `lsqcurvefit` routine, supplying an appropriate initial guess for  $f_0$  and  $Q$ :

```
options=optimset('TolFun',1e-50,'tolX',1e-30);
p=lsqcurvefit('scaling',[f_guess Q_guess], xdata, ydata, [], [], options, ydata);
```

This will return the best  $f_0$  (again in Hz, not in rad/sec) and  $Q$  parameters after the fit as a two-element vector `p`. Now you just need the scaling pre-factor, which you can get by left-dividing the full-range fit function by the PSD magnitude data (the left-divide again gives you a least-squares fit “for free”):

```
A=(transfunc(p,full_xdata))\full_ydata;
```

Here `full_xdata` and `full_ydata` are the full-range frequency and magnitude PSD vectors, rather than just the cropped sections used for the fit algorithm. You can now see how well the fit worked, by plotting it on top of the original PSD data:

```
Gfit = A*transfunc(p,full_xdata); loglog (full_xdata, Gfit);
```

# Optical Trapping in the Teaching Lab

## 1 Lab Objective

1. Become familiar with the fundamentals of optical trapping.
2. Learn to calibrate the optical traps for position detection and force measurement.
3. Use calibration information to observe the rotation of *E. coli* bacteria, and determine the forces required to stop this rotation.

## 2 The Optical Trapping System

### 2.1 Background

Arthur Ashkin developed the first optical traps in the 1970's working at Bell Laboratories. Since the discovery of this technology, optical traps have been applied to pure physics and biological applications from atomic cooling to DNA unzipping. State of the art instruments used for biological applications can apply pico-Newton forces and provide sub nanometer position resolution.

Optical forces are generated by a laser beam that is focused using a high numerical aperture (NA) objective. These forces come from the conservation of momentum of photons refracting through the trapped object, and will work for any object whose index of refraction is greater than the surrounding medium. A gradient force component draws an object into the center of the trap and a scattering force component pushes the object along the direction of light propagation. Unless there is a steep gradient of light intensity, the scattering force will push the object out of the trap; however, when using a high numerical aperture objective, the gradient of light near the focal point is large enough to balance the scattering force and trap the object. The trap location ends up slightly beyond the focal point.

If you'd like to learn more about optical trapping fundamentals, Google yields excellent results, and you can also skim any of the papers referenced in the footnotes of this document.

Theoretical calculations of the forces exerted by an optical trap on the trapped object generally fall into two regimes: (1) when the trapping wavelength is greater than the diameter of the trapped object  $\lambda > d$  — called the Rayleigh scattering treatment, and (2) when the wavelength is much less than the diameter of the trapped object  $\lambda < d$  — the Mie scattering treatment. Since we are using a  $\lambda = 975nm$  laser, and the beads and bacteria we'll be trapping are approximately  $1 - 2\mu m$  in diameter, our situation is actually at the boundary of these regimes, and we will not concern ourselves with precisely calculating optical forces.

### 2.2 System Overview

Make sure you are able to identify the major system components (*in italics*). The light source used for trapping in our instruments is a *975nm diode laser*. Its beam is steered through optics that expand the beam and direct it into the high-NA *objective lens* positioned under the sample. The objective focuses the laser to form the trap, and the transmitted and scattered light is captured by the *condenser lens*, and reflected onto the *QPD position detector* (more about this in Section 4.1).

Along nearly the same optical path, but in the reverse direction, a *white light source* is used for optical observation. Its light passes down through the condenser, trap, and objective, and is

reflected into a *CCD camera*. This is a simple white-light microscope, very similar to what you built.

The *3-axis positioning stage* that holds the sample slide is controlled along two axes by joystick-driven picomotors. These will be used during position calibration, as well as “driving” the trap around.

### Optical path

A schematic of the optical layout is given in Figure 1. The red line gives the path of the trapping laser (from source to QPD), and the blue line a second short-wavelength excitation laser (used for fluorescence experiments), which we will not use in this lab. The white light for sample observation follows the broad white line, from Illumination light source to the Camera.

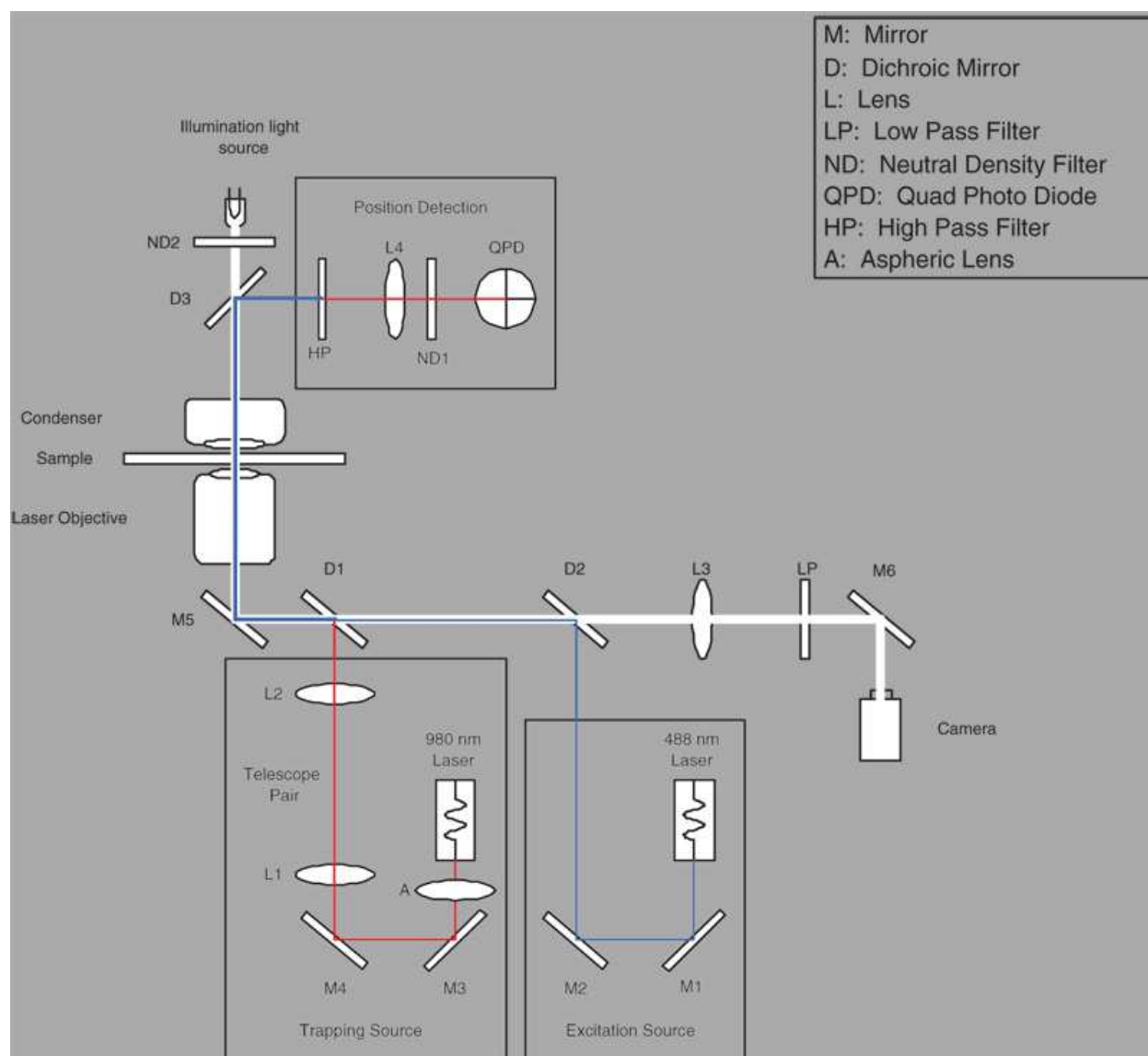


Figure 1: The optical layout of the trapping system (including the optional 488nm fluorescence branch, which is not used in this lab, indicated by the blue line).

## 2.3 Safety

### Laser Radiation

The trapping diode laser has a maximum operating power of 175mW, placing it in the Class IIIB category. It is important that you familiarize yourself with the beam path and avoid interrupting the path with your hands, any other body parts, or reflective items like rings, watches or other jewelry. It is imperative that you ***do not look directly at the beam or any reflection of the beam***. Appropriate safety goggles will be made available to you. There should be no need for you to put your hand in the beam at any time.

### Biological Materials

Most of the trapping experiments will be run using small diameter glass and polystyrene beads. ***Please use the available nitrile gloves*** both for cleanliness, personal safety and to reduce sample contamination of samples. A genetically altered version of *E. coli* will be used for the last section of the laboratory. These *E. coli* are live and infectious, so glove use is absolutely mandatory. After the experiment is finished, discard the slide containing the *E. coli* sample as directed by the laboratory instructor. As always, wash hands with soap after completing the laboratory, and do not bring food or drink into the lab.

### Operating Precautions

In order for the optical trap to work well, a very precise laser alignment is required. Any slight bump of mirrors or lenses can significantly shift this and render an instrument unusable. The laser diode is coupled to a fiber optic; this fiber is sensitive to being crimped, kinked, or otherwise stressed and can be broken if not handled carefully. Be gentle with the optics on the microscope and check with a laboratory instructor before adjusting knobs not explicitly specified in the directions. It is much easier to realign the trap if only one optic has been moved, so if there is a problem, please contact the lab instructor before attempting to solve the problem yourself.

## 3 Experiments Overview

1. Using a sample slide for calibrating the position detector, find a bead attached to the glass surface. Run the LabVIEW position calibration VIs to relate the voltage output of the position detector to bead displacement in nanometers.
2. Using the same slide, up to three different methods can be used to calculate the trap stiffness and compare their results.
3. A different sample slide contains a suspension of *E. coli* bacteria. Focus on the sample and find spinning bacteria. Using the position and force calibrations that you have done, measure their rotation rates, and calculate the forces required to stop the *E. coli* from spinning.

## 4 Lab Procedures

### 4.1 Position Detection

For detection, the laser light scattered from the trapped object is captured with a Quadrant Photodiode (QPD) to provide a position signal for the bead location. The QPD outputs a voltage signal for the  $x$ - and  $y$ -axes of bead displacement. These signals must be related to the physical position of a bead, and the goal of this part is to record voltage vs. position data for each axis. More information about this detection method can be found in Gittes and Schmidt<sup>1</sup>.

In order to calibrate the position detection, a relationship between the QPD output voltages and position data must be determined. On our system, joystick-driven picomotors are installed for  $x$ - and  $y$ -axis movement. These motors have been pre-calibrated and travel  $30nm$  per step. The calibration is performed by finding a  $1\mu m$  bead attached to the glass surface (the high-salt buffer of this sample makes the bead stick to the glass by hydrophobic interaction), and then scanning it along the  $x$ - and  $y$ -axis while monitoring the QPD signal. A more precise method of calibration involves moving the bead in a grid pattern using either the stage, or a separate optical trap, but our stage positioning does not have enough repeatability to enable this.

#### Voltage vs. position measurement

1. Run the QPD Alignment VI. Its upper panel displays the raw  $x$  and  $y$  signals independently, while the bottom panel shows them plotted one vs. the other, giving an indication of position on the QPD.

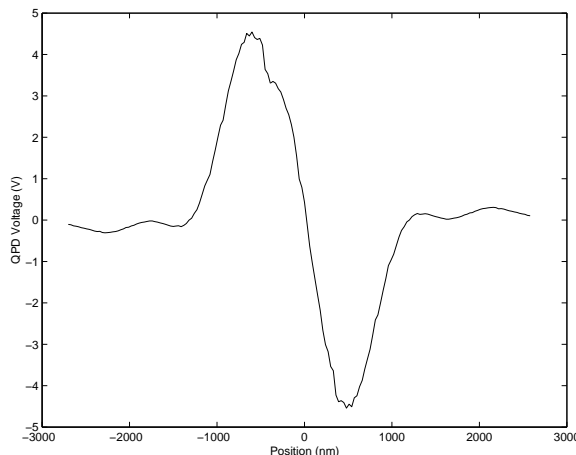


Figure 2: Sample position detection calibration curve for motion along a single axis.

2. Using the Joystick, maneuver the bead to the center of the trap. To find the centering location, scan the stage in one axis while watching the displacement of that axis signal on the QPD Alignment VI. As shown in Figure 2, when the bead is far away on either side of the trap center, the signal should rest at 0 (if not, your lab instructor will help realign the QPD). As the bead moves through the trap the signal will move to some maximum value  $X_{max}$ , then move through zero to a minimum  $-X_{max}$ , before finally returning to 0 as the bead leaves the other side of the trap. The goal is to place the bead at the point of maximal

---

<sup>1</sup>F. Gittes, C. F. Schmidt, "Interference model for back-focal-plane displacement detection in optical tweezers." *Optics Letters*, **23**(1):7-9, 1998.

sensitivity, which should occur at the 0 point between  $X_{max}$  and  $-X_{max}$ . This will place the bead in the center of the linear portion of the voltage response as shown in Figure 2.

3. Repeat the above to center the other axis. It may take several iterations of both axes to be confident that the trap is correctly centered.
4. Stop the QPD Alignment VI.
5. Open the Position Calibration VI.
6. Select an axis, enter the number of steps ( $\approx 100$  for a  $1\mu m$  bead), and the 30 nm/step calibration factor.
7. Run the Position Calibration VI, and SAVE the calibration data that is generated.
8. Repeat these steps to get a calibration curve for the other axis (assume the same nm/step calibration for both motors).

## 4.2 Force Calibration

For calculating the forces exerted by the trap, the key parameter we need to know is its stiffness. We will look at three different ways to measure it.

In general, for small displacements  $x$  from the equilibrium position, the optical trap is considered to be a harmonic potential, which means that trapped particles experience a Hookian restoring force  $F = -\alpha x$ , and the potential energy stored due to displacement is  $\frac{1}{2}\alpha x^2$ . Here  $\alpha$  is called the *stiffness* of the trap, and is analogous to the spring constant  $k$  of a mass-spring system.

### Equipartition

As you no doubt remember, the Equipartition Theorem states that each degree of freedom in a harmonic potential will contain  $\frac{1}{2}k_B T$  of energy. Therefore, one method of finding the trap stiffness is by evaluating the variance in position  $\langle \Delta x^2 \rangle$  due to thermally induced position fluctuations:

$$\frac{1}{2}k_B T = \frac{1}{2}\alpha \langle \Delta x^2 \rangle \quad (1)$$

This should already be familiar to you from similar measurements done with thermomechanical noise in cantilevers. Note, however, that this method requires precise position calibration of the detector, and due to the squared quantity, is sensitive to noise and drift. Further reading on this method can be found in Neuman and Block<sup>2</sup>.

### Noise PSD Roll-off

Another way of deriving the trap stiffness is by analyzing the power spectrum of a trapped bead's thermally-induced motions. This power spectrum, in units of [displacement/Hz<sup>1/2</sup>] has the form:

$$S_{xx}(f) = \sqrt{\frac{k_B T}{\pi^2 \beta (f_0^2 + f^2)}}, \quad (2)$$

where  $\beta$  is the hydrodynamic drag coefficient  $\beta = 3\pi\eta d$ , in which  $d$  is the bead diameter, and  $\eta$  is the viscosity of the medium. Again, similarly to cantilever thermomechanical noise, the roll-off corner frequency can be extracted from a fit of this function to the measured power spectrum. Once known, the corner frequency is related to the trap stiffness as follows:

---

<sup>2</sup>K. C. Neuman, S. M. Block. "Optical trapping." *Review of Scientific Instruments*, **75**(9):2787-2809, 2004.

$$\alpha = f_0 2\pi\beta . \quad (3)$$

For a full derivation and further information about this method, you may want to consult the references in the footnotes<sup>3</sup>.

### Stokes drag

A third method of calculating the trap's stiffness is by calculating the drag force  $F = -\alpha x$  exerted on a bead as the stage is moved. The most basic formulation is

$$\alpha x = \beta v = 3\pi\eta d v , \quad (4)$$

where  $v$  is the flow velocity. Note that this equation only applies for constant velocity.

### Laser Power Dependence

Both the position calibration, as well as the stiffness of the trap depend greatly on the power output of the  $975nm$  trapping laser. If the measurements you make are dependent on accurate position calibration, you'll need to recalibrate when you change the laser power.

### Data Collection

**Equipartition and Roll-off** – Open the Equipartition VI. Trap a bead and, using the objective focus adjustment micrometer, move the bead away from the surface. Using the stage micrometers, move the bead away from any nearby obstructions (tape, dust, other beads).

Using the SpectrumAnalyzer VI that you are familiar with from the AFM labs, take the power spectrum of a bead's thermal motion at the trap center, recording a separate spectrum for the x- and y-axes. This data will yield two ways of calculating trap stiffness, as described above.

**Stokes drag** – Open the Stokes VI. Again, trap a bead and move it away from the surface and any obstructions. The Stokes VI will run the bead back and forth at various stage velocities – thus it's important that the stage micrometers have ample movement left and that there are few beads in the area.

Run the Stokes VI program, watch the movement on the monitor, if additional beads fall into the trap, discard the data. If this is a consistent problem, ask for help from a lab instructor.

Make sure to run the stokes program for both the x- and y-axes.

**Laser power** – You should repeat your force measurements at three or four varying power values to obtain the force-power dependence. Use any of the methods above that you prefer, over a range of 25-125mW laser output. Describe the relationship you see, and explain why you used the force calibration method you chose.

---

<sup>3</sup>M. W. Allersma *et al.* "Two-Dimensional Tracking of ncd Motility by Back Focal Plane Interferometry." *Biophysical Journal*, **74**:1074-1085, 1998.

### 4.3 *E. coli* Rotation

#### Goals

1. Using the position detection ability of the optical trap, determine (a) the typical rotation velocity of spinning bacteria, and (b) the distribution of rotational speeds.
2. Using the force application ability of the optical trap, determine the stall force of the bacteria. Assume that displacement from the trap center is  $100nm$  when enough force is applied to hold the bacteria.

#### Data Analysis

1. Rotation: Take the power spectrum of your trace to determine the rotational frequency. Plot both the PSD and the trace. Does the PSD of your X and Y QPD voltages agree?  
Describe the distribution of rotational speeds. Why do you think this is?
2. Stall Force: For a first approximation, the force exerted on the bacteria can be assumed to be that exerted on a  $1\mu m$  bead.

# Lab 8: Atomic force microscopy imaging of cells

**Location:** 8-111

**PI:** Krystyn Van Vliet

**Lab Instructor:** Sunyoung Lee

## Summary

In this laboratory, you will use the atomic force microscope to image the structure and stiffness of living and chemically fixed human microvascular endothelial cells. The pN- to nN-scale mechanical force used to create these images allows you to observe both the micrometer-scale height of these cells, as well as the nanometer-scale cytoskeletal network beneath the cell surface. Because the cells are living and imaged under near in vitro conditions, it is possible to observe cell processes in real time, including migration, response to drugs added to the imaging media, and of course apoptosis. It is also possible to compare the near-surface structure of living and diseased cells. If time allows, you will also observe the near-field optical / fluorescent image of these cell surfaces.

## Recommended Reading

D. Pesen and J. H. Hoh, "Micromechanical Architecture of the Endothelial Cell Cortex," *Biophys. J.* **88**.

N. Almqvist *et al.*, "Elasticity and Adhesion Force Mapping Reveals Real-Time Clustering of Growth Factor Receptors and Associated Changes in Local Cellular Rheological Properties," *Biophys. J.* **86**.



# Micromechanical Architecture of the Endothelial Cell Cortex

Devrim Pesen and Jan H. Hoh

Department of Physiology, Johns Hopkins University School of Medicine, Baltimore, Maryland

**ABSTRACT** Mechanical properties of living cells are important for cell shape, motility, and cellular responses to biochemical and biophysical signals. Although these properties are predominantly determined by the cytoskeleton, relatively little is known about the mechanical organization of cells at a subcellular level. We have studied the cell cortex of bovine pulmonary artery endothelial cells (BPAECs) using atomic force microscopy (AFM) and confocal fluorescence microscopy (CFM). We show that the contrast in AFM imaging of these cells derives in large part from differences in local mechanical properties, and AFM images of BPAEC reveal the local micromechanical architecture of their apical cortex at  $\sim 125$  nm resolution. Mechanically the cortex in these cells is organized as a polygonal mesh at two length scales: a coarse mesh with mesh element areas  $\sim 0.5\text{--}10 \mu\text{m}^2$ , and a finer mesh with areas  $< 0.5 \mu\text{m}^2$ . These meshes appear to be intertwined, which may have interesting implications for the mechanical properties of the cell. Correlated AFM-CFM experiments and pharmacological treatments reveal that actin and vimentin are components of the coarse mesh, but microtubules are not mechanical components of the BPAEC apical cortex.

## INTRODUCTION

Cell mechanics are fundamental to cell shape, motility, division, tissue organization, and other biologically important properties and processes (Alberts et al., 1994; Howard, 2001; Boal, 2002). The mechanical properties of many cell types have been studied extensively, and living cells are known to be complex and heterogeneous visco-elastic structures (Elson, 1988; Evans, 1989; Pollard et al., 2000). Although the molecular underpinnings for cell mechanics are not fully understood, it is clear that cytoskeleton plays a central role. Actin, microtubules, and intermediate filaments are structural components of the cytoskeleton with unique mechanical properties, and rheological measurements of purified cytoskeletal preparations show that these have visco-elastic properties similar to whole cells (Janmey et al., 1991, 1994; Gittes et al., 1993; Kojima et al., 1994; Kurachi et al., 1995). Pharmacological disruption of actin causes a significant change in cell mechanics (Rotsch and Radmacher, 2000; Yamada et al., 2000; Wakatsuki et al., 2001); likewise, genetic disruption of cytoskeletal proteins has significant mechanical consequences (Janssen et al., 1996; Weber et al., 1999). As a result of this close relationship between cytoskeleton and mechanics, cytoskeletal organization is sometimes taken to reflect mechanical organization (e.g., Heidemann et al., 2000; Ingber et al., 2000). However, there is little direct information about the spatial micromechanical organization of living cells at a subcellular level.

The cytoskeleton is partitioned to carry out specific functions in a cell; one organizational unit is the cortical cytoskeleton (CS), which comprises the cytoskeleton con-

nected to and in close proximity to the plasma membrane and is often treated separately in mechanical models of cells (Evans, 1989; Yeung and Evans, 1989; Dong et al., 1991; Karcher et al., 2003). Freeze fracture deep etch electron microscopy provides highly detailed views of the CS and reveals a complex filamentous network (Satcher et al., 1997; Heuser, 2000). Immunofluorescence microscopy of CS frequently shows a diffuse submembrane label (Tsukita and Yonemura, 1999; Flanagan et al., 2001). Where details of the cytoskeleton organization can be seen, it is difficult to unambiguously identify the cortical component, unless cells are very thin and thus have little non-CS (Lazarides, 1975; Galbraith et al., 1998).

Vascular endothelial cells are an interesting system for studying functionally important aspects of cytoskeleton and mechanics (Dudek and Garcia, 2001; Helmke and Davies, 2002; Lee and Gotlieb, 2002; Ogunrinade et al., 2002). These cells are found in a mechanically active environment and are required to withstand shear stress, blood pressure, and changes in pressure due to breathing cycles. The cortex of these cells faces the blood stream and is important for responding to external forces, and transmitting force, as well as controlling cell shape. In this study, we used atomic force microscopy (AFM), confocal fluorescence microscopy (CFM), and anti-cytoskeletal drugs to characterize the micromechanical architecture of the cortex in bovine pulmonary artery endothelial cells (BPAECs). We show that the cortex in these cells is mechanically organized as a polygonal mesh on two levels: a coarse mesh with dimensions on the order of several micrometers and a fine overlapping mesh with dimensions on the order of hundreds of nanometers. These meshes appear to be intertwined and are in part composed of actin and vimentin.

*Submitted July 16, 2004, and accepted for publication October 4, 2004.*

Address reprint requests to Dr. Jan H. Hoh, Dept. of Physiology, Johns Hopkins School of Medicine, 725 N. Wolfe St., Baltimore, MD 21205. Tel.: 410-614-3795; E-mail: jhoh@jhmi.edu.

© 2005 by the Biophysical Society

0006-3495/05/01/670/10 \$2.00

doi: 10.1529/biophysj.104.049965

## MATERIALS AND METHODS

### Cell culture

BPAECs, Eagle's minimum essential medium, and fetal bovine serum were from American Type Culture Collection (Manassas, VA). BPAECs were maintained on petri dishes or gelatin coated glass coverslips in Eagle's minimum essential medium supplemented with 20% fetal bovine serum at 5% CO<sub>2</sub> and 37°C. The cells were fed every 2–3 days and passaged when confluent. Passages 17–22 were used.

### AFM imaging

AFM imaging was performed with a Multimode or Bioscope AFM equipped with large area scanners (>100 μm × 100 μm), with a Nanoscope IIIa controller (Digital Instruments, Santa Barbara, CA). The Bioscope was mounted on an Olympus inverted optical microscope. For imaging live cells in solution, unsharpened (radius of curvature ~50 nm) silicon nitride cantilevers with nominal force constants of 0.01 or 0.03 Newtons/meter were used (Nanoprobes, Digital Instruments). Ambient tapping of fixed and dried cells was performed with single crystal silicon cantilevers (model TESP; Digital Instruments). Live cell imaging was performed in fluid contact mode at room temperature and atmospheric CO<sub>2</sub>. The imaging buffer was phosphate buffered saline (Invitrogen, Carlsbad, CA) supplemented with 1.2 mM CaCl<sub>2</sub>, 1.2 mM MgCl<sub>2</sub>, 5 mM Hepes, and 1 g/L glucose. For pharmacological treatments of BPAEC cortex, stock solutions of cytochalasin B (1 mg/ml in dimethylsulfoxide (DMSO)) and nocodazole (4 mg/ml in DMSO) were prepared. The final concentrations of drugs were determined after estimating the amount of imaging buffer present in the fluid holder before drug addition. Since DMSO can increase the temperature upon mixing with aqueous buffers, first 50–100 μl imaging buffer was smoothly pipetted out of the fluid holder channels and it was mixed with 1–5 μl of stock drug solution. After reaching room temperature, this solution was added to the fluid holder and mixed gently to ensure rapid drug delivery to cells. Imaging parameters were empirically optimized to produce clear images with minimal distortion or damage to the cells. Typically, scan rates were 60–120 μm/s, resulting in image acquisition times of 4–16 min depending on the scan size. BPAECs could be imaged for up to 4 h, during which time the cells remained adherent and high quality images could be collected. With extended imaging the fenestrae between cells began to expand, exposing the substrate. We interpret this as an indicator of cell deterioration in response to the AFM imaging. Further imaging resulted in loss of cells from the surface.

### Local mechanical measurements

AFM force curves over confluent BPAEC monolayers were collected using the same cantilevers as for imaging at rates of ~10 μm/s. The relative trigger on the microscope was set to 50 nm or less to prevent inadvertent damage to the cell. The force curves were used to determine the elastic modulus as described previously (Radmacher et al., 1996; Costa and Yin, 1999). Force calculations use nominal values for cantilever stiffness, and hence should be considered accurate to within a factor of two.

### Confocal immunofluorescence microscopy

For correlated AFM-CFM experiments, cells cultured on gelatin (Sigma, St. Louis, MO) coated CELLocate glass coverslips (Brinkmann, Westbury, NY) were imaged by AFM and immediately fixed in 3.7% paraformaldehyde for 10 min. The fixative was added to the cells <1 min after completing the AFM imaging. Cells were then permeabilized with 0.2% Triton-X-100 in PBS for 5 min and blocked with 1% BSA in PBS for 30–60 min. The cells were then treated with Alexa Fluor 488 phalloidin (Molecular Probes, Eugene, OR), monoclonal anti-β-tubulin-Cy3 antibody (~1:50–1:100) or monoclonal anti-

vimentin-Cy3 antibody (~1:50–1:100) (Sigma) in 1% BSA in PBS for 1 h. Finally, cells were washed with PBS, and mounted on slides with ProLong media (Molecular Probes). An UltraView Confocal microscope (PerkinElmer, Wellesley, MA) was used to collect immunofluorescent images. Areas to examine were determined by using bright field light micrographs collected during AFM imaging on the Bioscope in conjunction with the locator grid.

### Scanning electron microscopy

Cells grown on coverslips were fixed with 3% glutaraldehyde, 0.1 M Hepes, 2 mM CaCl<sub>2</sub> pH 7.2, for 30 min at room temperature. Cells were then rinsed twice using 0.1 M Hepes with 3 mM CaCl<sub>2</sub> for 10 min, followed by a rinse in 0.1 M sodium cacodylate with 3 mM CaCl<sub>2</sub> for 10 min, and post fixed in reduced osmium (1% OsO<sub>4</sub>, 0.8% K<sub>4</sub>FeCn<sub>6</sub>, 0.1 M sodium cacodylate, 3 mM CaCl<sub>2</sub>) for 1 h on ice. After a brief water rinse, cells were en-bloc stained in 2% uranyl acetate (filtered) for 1 h in the dark. Samples were dehydrated using a series of ethanol incubations and then treated with 100% hexamethyldisilazane (Polysciences, Warrington, PA) for 10 min. Coverslips were then placed on Whatman No. 1 filter paper (cell side up) and allowed to dry. Finally, coverslips were attached to carbon sticky tabs affixed to scanning EM stubs and evaporated with 1 nm of chromium in a Denton DV-502A high vacuum evaporator operating at 50 mA and 2 × 10<sup>-7</sup> torr. Cells were viewed and digitized on a Leo 1530 Field Emission Scanning EM operating at 1 kV.

### Image display and data analysis

AFM data were analyzed with Image SXM and SuperMapper, a custom software suite developed with Interactive Data Language (Research Systems, Boulder, CO). The deflection images were processed to optimize brightness and to enhance contrast. Immunofluorescence data were optimized for brightness and contrast using Adobe Photoshop. Correlated areas were determined visually by overlaying AFM deflection images on CFM images, and manually varying the transparency of the AFM imaged. Mesh element areas were estimated by ((A1 × A2)/2).

## RESULTS

### AFM images reveal the micromechanical organization of the cortex

BPAECs grow in confluent monolayers, and AFM images show a general morphology that is consistent with that seen by light and electron microscopy. Cells are typically tens of micrometers in diameter, and heights range from a few hundred nanometers at the periphery to ~4 μm toward the center (Fig. 1, A–D). In addition, these cells display a complex highly organized filamentous network. The AFM is a sensitive surface probe; however, when soft materials such as living cells are probed with an AFM tip, local mechanical differences result in differential surface deformations and contribute to contrast in the images. Scanning EM and AFM images of fixed endothelial cells show a relatively smooth surface, with none of the filamentous features seen in AFM images of living cells (Fig. 1, C and D) (Chazov et al., 1981; Schaeffer et al., 1993). Hence the contrast in the AFM images of living BPAECs derives in substantial part from local mechanical properties; in particular the filamentous structures are mechanical features from the cortical regions of these cells.

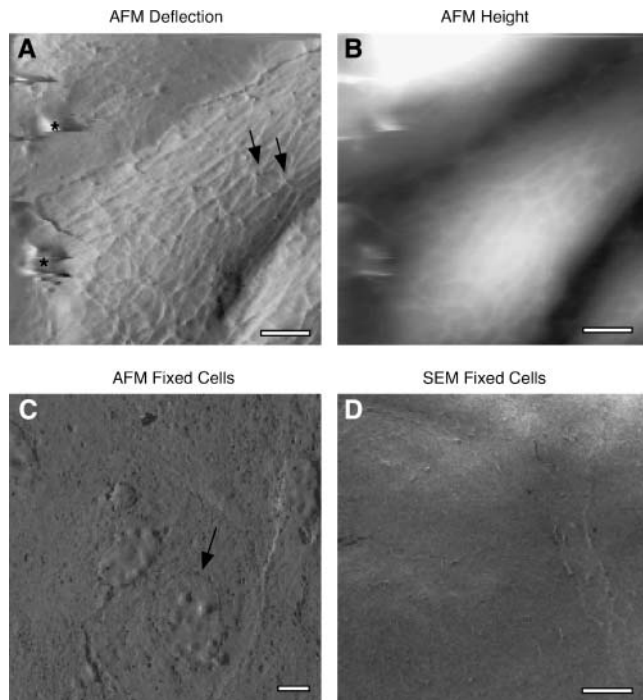


**FIGURE 1** Mechanically based contrast in AFM images of BPAECs. (A) AFM deflection image. (B) Corresponding AFM height image of BPAECs imaged in a physiological saline. Generally the applied force was on the order of 1 nN, the scan rate was 60  $\mu\text{m/s}$ , and the image acquisition time was between 4–16 min. Overall cell morphology is similar to that seen by light microscopy or scanning EM; however, significant additional detail is seen. The deflection images show an intricate mesh of filaments; other features seen in the images include focal points with 5–8 converging filaments (*arrows*). The smeared features (*asterisk*) are imaging artifacts. (C) AFM image of fixed BPAECs shows no filamentous structures; however, the cell boundaries and nuclei (*arrow*) are visible. The latter is likely visible because the membrane collapses over the nucleus during dehydration. (D) Likewise, scanning EM of BPAEC shows cell boundaries but no filamentous mesh. Thus, contrast for the fine features seen in A is attributed to differences in local mechanical properties. Z-range of the gray scale in B is 0–4  $\mu\text{m}$ . Scale bars are 5  $\mu\text{m}$ .

### Architecture of the endothelial cortex

The filamentous network at the cell cortex is organized as a complex polygonal mesh. Visually the mesh appears to be structured on two length scales, one on the order of a few hundred nanometers and the other on the order of a few micrometers (Fig. 2). The larger mesh is composed of prominent and hence relatively stiff features, with a wide range of forms. The fine mesh is composed of thin filaments with weak contrast, and typically visible inside the large mesh elements. The fine mesh elements are more uniform in appearance, and have areas  $\sim 0.05\text{--}0.5 \mu\text{m}^2$ . In places the fine filaments run on top of the thicker filaments, and are thus closer to the plasma membrane. Other thin filaments appear to run underneath the thick filaments, although because of the weak contrast from the thin filaments the possibility that all thin filaments run on top of the thick filaments cannot be strictly excluded. Thus, the cell cortex might be described as

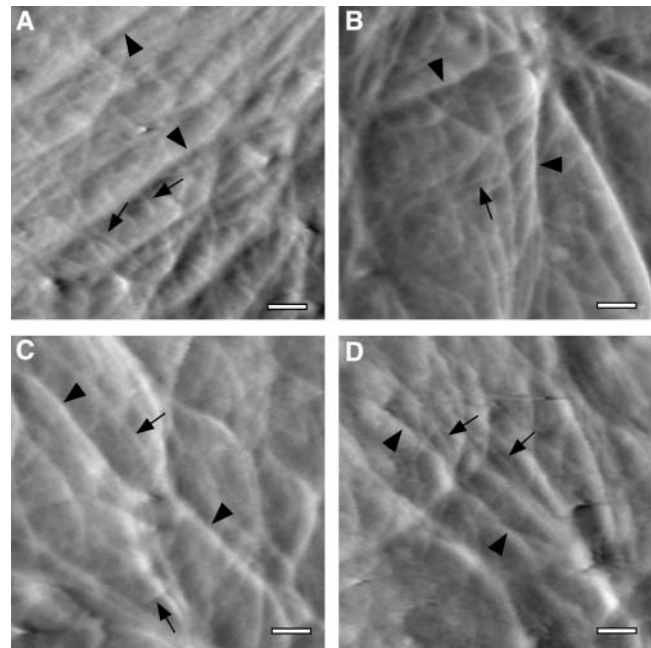


**FIGURE 2** Cortical mesh appears to be organized at two predominant length scales. (A–D) High magnification deflection AFM images of living BPAECs in a physiological saline. The filamentous mesh appears to be organized on two length scales, with coarse mesh (*arrowheads*) and fine mesh filaments (*arrows*). The coarse mesh forms larger elements and is easier to identify, whereas the fine mesh elements have much smaller dimensions. Further, contrast in the fine mesh is weak, making it difficult to completely trace. In places, the fine mesh runs over the coarse mesh and is thus more proximal to the membrane. In other places, the mesh may run under the coarse mesh, or is not visible due to the weak contrast. Thus, the two meshes are likely intertwined, although it is possible that the fine mesh is layered over the coarse mesh. Lateral resolution in these images is  $\sim 125 \text{ nm}$ . Scale bars are 1  $\mu\text{m}$ .

a coarse mesh intertwined with a fine one, or possibly a fine mesh layer over a coarse mesh.

Closer examination of the coarse mesh reveals that the thick filaments course across the monolayer surface, and in places give the appearance of being continuous with neighboring cells. Thick filaments often converge at “star-like” focal points, where, on average, 3–4 filamentous structures radiate from a single point; these are distributed over the entire apical surface. Such star-like focal points have previously been observed by electron microscopy, and it has been suggested that they are vertices of actin geodesics (Lazarides, 1975; Heuser and Kirschner, 1980). Less frequently there were also focal points with 5–8 converging filaments. To characterize the mesh elements we measured the long axis ( $A_1$ ), short axis ( $A_2$ ), and asymmetry ( $M_{A_1/A_2}$ ) in 67 mesh elements from nine different cells (Fig. 3). Individual elements were found to be relatively asymmetric with  $A_1 = 4.4 \pm 2.3 \mu\text{m}$  (mean  $\pm$  SD),  $A_2 = 1.6 \pm 1 \mu\text{m}$ , and  $M_{A_1/A_2} = 2.8 \pm 1.3$ . In elongated cells the major axis of mesh elements tends to align with the major axis of the cells. Examination of the internal branch angles in these mesh

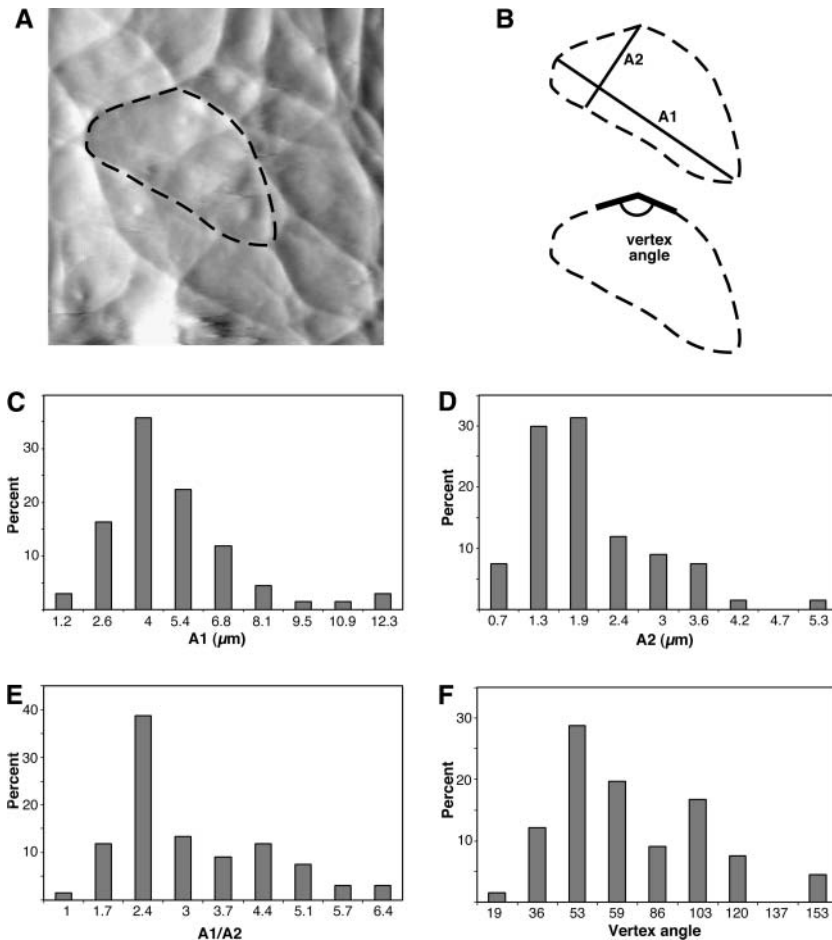


FIGURE 3 Coarse mesh elements are asymmetric and micrometer scale. Shapes of the coarse mesh elements were examined by hand tracing mesh boundaries ( $n = 67$ ). To characterize the mesh, we described individual mesh elements by their longest axis ( $A1$ ), longest axis perpendicular to  $A1$  ( $A2$ ), and the ratio of the two axes ( $M_{A1/A2}$ ). (A) Example of traced coarse mesh element in a BPAEC deflection image and (B) definitions of parameters examined. Histograms of measured dimensions show that (C) the long axis of the cells is on average  $4.4 \mu\text{m}$ , (D) the short axis is on average  $1.6 \mu\text{m}$ , and (E) the average aspect ratio is 2.8. (F) Internal angles of the coarse mesh elements show a bimodal distribution with peaks at  $53^\circ$  and  $103^\circ$  ( $n = 66$ ).

elements reveals a bimodal distribution with peaks at  $53^\circ$  and  $103^\circ$  ( $n = 66$ ). These discrete distributions suggest that the branches do not form from random crossings of filaments. Proteins such as filamin, spectrin, and Arp2/3 can organize actin into networks with characteristic angles (Hartwig and Shevlin, 1986; Hansen et al., 1997; Pollard and Borisy, 2003). We note that scanning did not significantly perturb the lateral organization of the filaments. This is apparent from the shape of features in the image, which show little dependence on scan direction. Further, comparison of trace and retrace images showed little or no scan direction related orientation of the filaments (data not shown).

Analysis of AFM deflection images of BPAECs reveals that the best resolution obtained is  $\sim 125 \text{ nm}$  along the fast scan axis, as determined from the spectral composition of the data (data not shown) (Joy, 2002). Thus, applying the Nyquist criterion, the resolution of 512 pixel/line images larger than  $32 \mu\text{m}$  is limited by sampling frequency, whereas images smaller than  $32 \mu\text{m}$  are limited by other aspects of the image acquisition. This resolution assessment agrees well with visual inspection of images, where the point-to-point resolution is determined from features such as spacing between individual filaments and their widths.

## Cortex mechanics

The AFM imaging presented above provides a detailed picture of the lateral mechanical organization of the cortex, but does not address variations as a function of distance beneath the plasma membrane. AFM force measurements can be used to quantitate local mechanical properties, and are also sensitive to changes in mechanical properties as a function of indentation depth (Radmacher et al., 1995; Costa and Yin, 1999). Micromechanical measurements on BPAECs using the AFM show that the average elastic modulus is in the range of  $0.2\text{--}2 \text{ kPa}$ , in agreement with previous studies on endothelial cells (Satcher and Dewey, 1996; Hochmuth, 2000; Mathur et al., 2000, 2001) (Fig. 4). Force curves collected at different positions on individual cells show that the cell body appears to be two- to threefold softer than the cell periphery, though it is known that the hard surface under a soft sample affects force measurements more as the sample thickness decreases (Costa and Yin, 1999). Thus, mechanical measurements on the cell body, where the cell reaches its maximum height, will have the least impact from the underlying hard surface (Charras et al., 2001; Dimitriadis et al., 2002). For force curves collected near the center of the

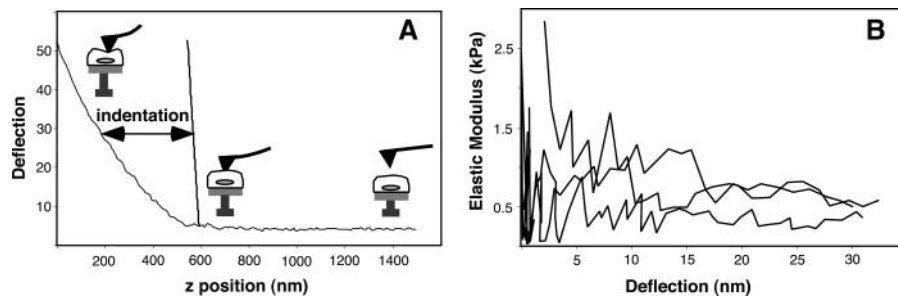


FIGURE 4 Mechanical definition of the BPAEC cortex. (A) AFM force curves on BPAECs show an indentation of  $\sim 600$  nm at the imaging force, which set an upper limit for the thickness of the cortex. However, cell viscosity will contribute significantly, and the effective cortical region is likely to be on the order of a couple hundred nanometers. (B) Plots of elastic modulus as a function of deflection, corresponding to indentations up to  $1 \mu\text{m}$ , show little variation as a function of indentation.

cell, the measured modulus appears to be independent of indentation depth for indentations up to  $\sim 1 \mu\text{m}$  (i.e., up to 25% strain). Furthermore, these force measurements show that at a force of 1 nanoNewton (nN) (typical imaging force), the upper indentation depth is  $\sim 600$  nm (at a scan rate of  $\sim 10 \mu\text{m/s}$ ). It should be noted that at small deflections these measurements are very noisy, and it is possible that some nonuniform behavior is buried in this portion of the data.

### Actin is a major contributor to the cortical micromechanical architecture

To identify the molecular components that underlie the mechanical architecture visualized by AFM we performed correlated AFM-CFM and pharmacological treatments. For correlated AFM-CFM experiments, bright field light micrographs were collected during AFM imaging of living cells grown on locator coverslips. Cells were fixed immediately (within  $\sim 1$  min) after AFM imaging and stained for actin, vimentin, or microtubules. The locator grid then allowed fluorescence imaging of the same area where the AFM image was collected. CFM images show that actin filaments are present throughout the cell, and comparison of AFM images with fluorescence images show a direct correspondence for a number of filamentous and polygonal features (Fig. 5). In particular, comparing the more basal CFM slices with the AFM image, there are features in the thin periphery where the CFM and AFM images show the same features. However, toward the center of the cell, the CFM shows a number of strongly staining stress fibers that are not seen in the AFM image. In the more cortical slices the CFM staining is relatively weak and shows scattered spots of F-actin and few filamentous structures, in agreement with previous observations (Galbraith et al., 1998). Here a direct correlation is more difficult, but again the CFM appears to show several features similar to those seen in the AFM image. A double staining for actin and vimentin again shows a number of features in the AFM image that can be correlated with actin staining (Fig. 6). Vimentin filaments are more prevalent in the central regions of the cell than in the cell periphery. Generally the vimentin-based structures have a curly pattern of staining with filaments crossing each other multiple times, and in a few instances there are features that can be correlated to the AFM images. Staining for microtubules did not produce features that could

be readily identified in the AFM images (data not shown). Thus, of the features that can be accounted for in the AFM images, actin is the most significant component, whereas vimentin is less prevalent and microtubules are not detected.

To gain further insight into the molecular identity of the mechanical features seen in the AFM images we examined the effect of the actin disrupting drug cytochalasin B and microtubule disrupting drug nocodazole on the appearance of BPAECs. High concentration ( $50 \mu\text{M}$ ) of cytochalasin B causes dramatic effects within 5 min: the filamentous network disappears, the cell surface becomes smooth, cells lose their mechanical strength, shape, and finally structural integrity (Fig. 7). During AFM imaging experiments we make sure that the probe applies the minimum force that gives good contrast. However, when cells lose their mechanical strength due to disruption of the cytoskeleton/mechanical elements, they cannot withstand even the small forces, and the probe ends up scraping cells from the surface. When a lower concentration ( $1 \mu\text{M}$ ) of cytochalasin B is used, the cell maintains integrity for a significantly longer time. In this case the filamentous network disappears more gradually and the cells take on a somewhat granular appearance. In stark contrast to cytochalasin, treatment with nocodazole did not produce a loss of any features; instead there was an increase in the density of filaments (Fig. 8). Here it should be noted that nocodazole is known to promote actin polymerization (Ballestrem et al., 2000). These cells appear to reorganize the filamentous features with time, and the morphology of the cells appears to reflect an increase in tension in the plane of the monolayer. In conjunction with this apparent change in tension the cell monolayer also initially becomes smoother with smaller variations in height, although height variations are eventually restored (Fig. 9).

## DISCUSSION

A significant barrier to understanding the micromechanical and cortical architecture of living cells are the methods currently available. Mechanical measurements of living cells have largely been confined to measurements of whole cells or large regions of cells, using methods such as cell poking, micropipette aspiration, and stretching (Zahalak et al., 1990; Hochmuth, 2000; Basso and Heersche, 2002). Small area measurements of mechanics by magnetic twisting or optical

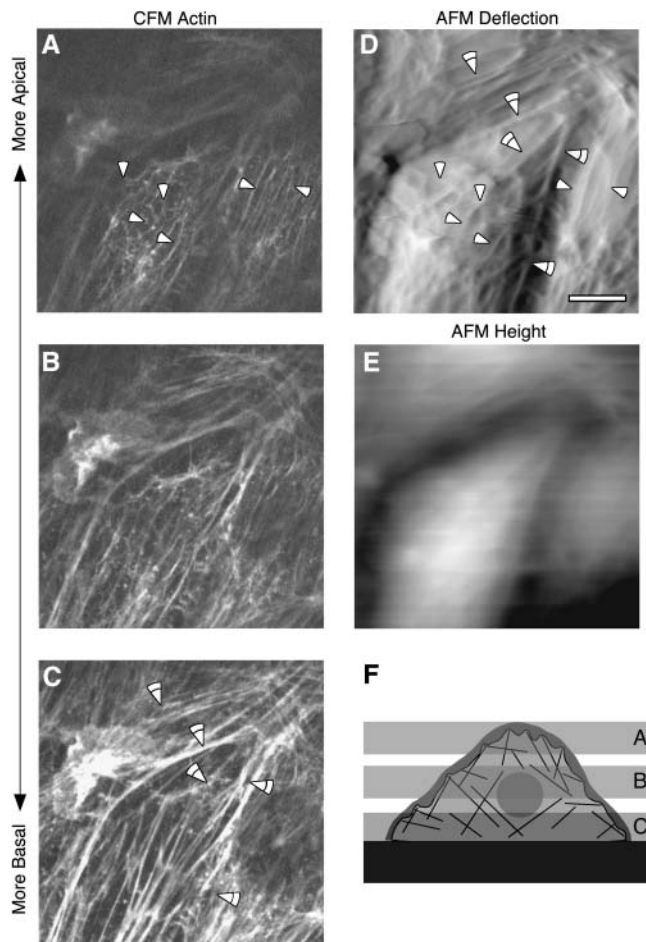


**FIGURE 5** Correlated AFM and CFM of cells stained for actin. An AFM image of living BPAECs was collected and the cells were immediately fixed and processed for immunofluorescence. (A–C) Confocal microscopy planes of fixed cells. (D) AFM deflection image of living BPAEC in solution. (E) Corresponding height image. Cells were stained for actin using Alexa-phalloidin. The CFM images show that actin filaments are present throughout the cell. Note that the basal stress fibers are not seen in the AFM images. However, a careful comparison of AFM images with fluorescence images shows a direct correspondence for a number of filamentous and polygonal features. Correlated features are marked with arrowheads. (F) Schematic illustrating the spatial relationships between the AFM and confocal images. The horizontal gray planes represent optical confocal slices, whereas the dark gray area represents the cell cortex imaged by the AFM probe. Scale bar is 10  $\mu\text{m}$ . Z-range in the height image is 0–4  $\mu\text{m}$ .

tweezers are too sparse to provide a detailed mechanical picture (Wang and Ingber, 1994; MacKintosh and Schmidt, 1999). Spatially resolved AFM force measurements offer a more detailed mechanical map of living cells (Radmacher et al., 1996; Hofmann et al., 1997; A-Hassan et al., 1998; Vinckier and Semenza, 1998). However, thinking about micromechanical organization of cells is often based substantially on images of the cytoskeleton produced by immunofluorescence and EM, and the independent cell mechanics measurements described above. But it is clear that the organization of cytoskeleton per se does not provide

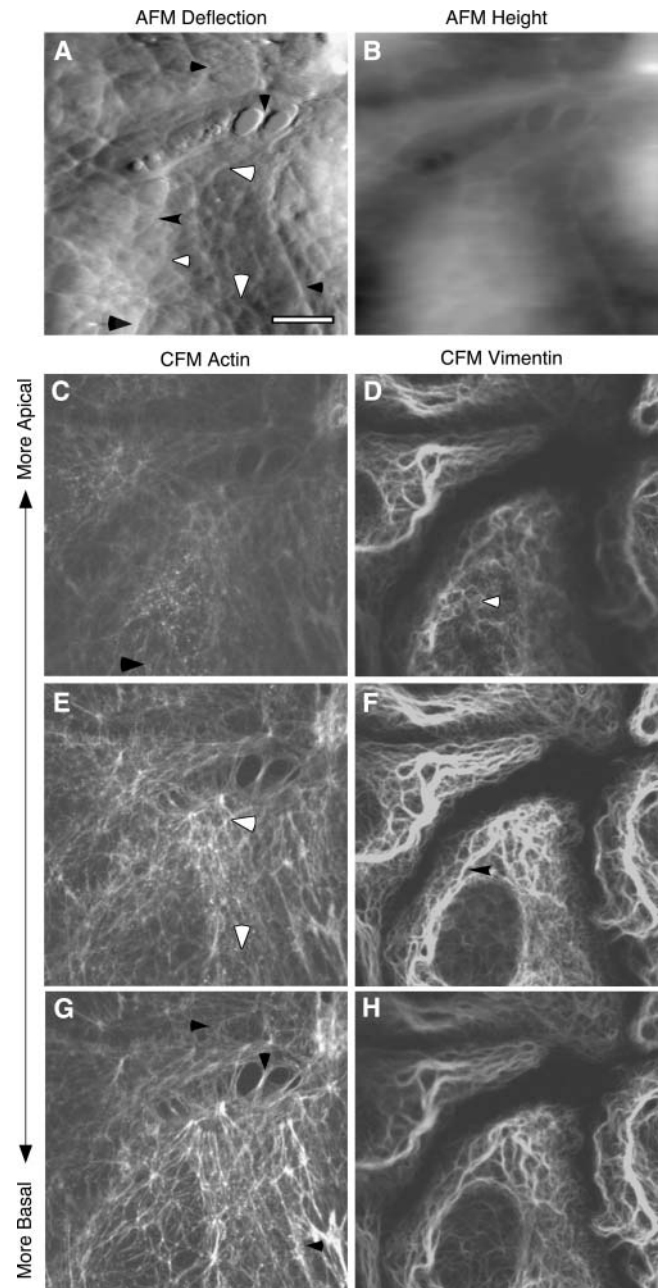


**FIGURE 6** Correlated AFM and CFM of cells double stained for actin and vimentin. AFM image on living BPAECs was collected and the cells were immediately fixed and processed for immunofluorescence. (A) The deflection image shows details of the mesh-like cortical organization, whereas (B) the height image better reflects the overall cell shape. Confocal planes of cells stained for actin using Alexa-phalloidin (C, E, and G) and vimentin using Cy3-anti-vimentin antibody (D, F, and H). Correlated features are marked with arrowheads. Scale bar is 10  $\mu\text{m}$ . Z-range in the height image is 0–4  $\mu\text{m}$ .

a complete mechanical picture; one also needs to know where and how strongly different cytoskeletal components are connected, among other things. Thus, in the absence of a complete biochemical description of the system, there is a need for a high-resolution mechanical picture.

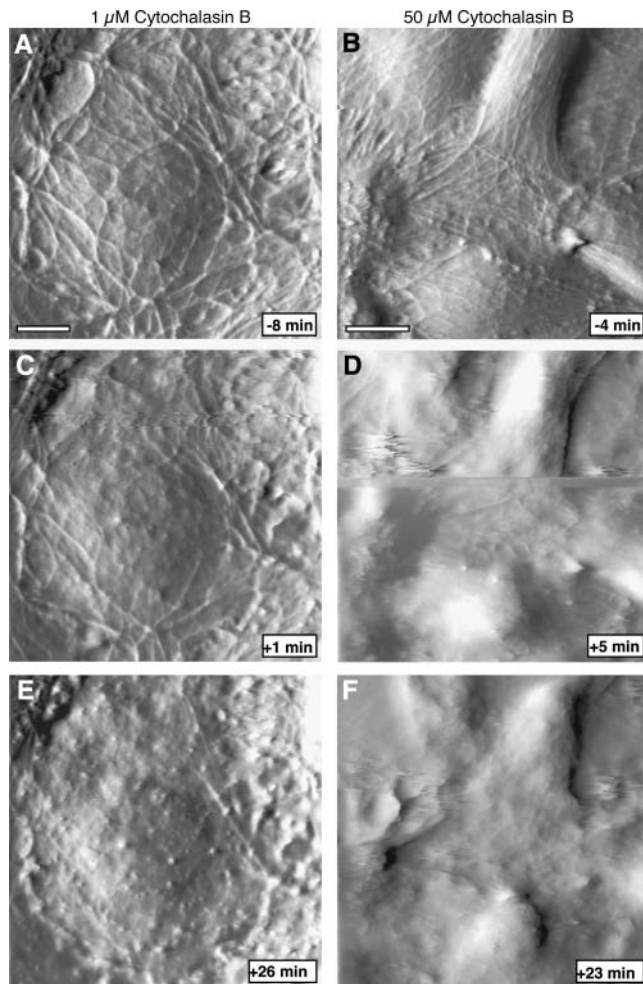


**FIGURE 7** Treatment with cytochalasin B abolishes most filamentous features. Time series of AFM deflection images collected before and after exposure of cells to cytochalasin. (A–C) Cells were treated with 1  $\mu\text{M}$  cytochalasin B at time 0 min. Scale bar is 5  $\mu\text{m}$ . (D–F) Cells were treated with 50  $\mu\text{M}$  cytochalasin B at time 0 min. Scale bar is 10  $\mu\text{m}$ . Low concentration of cytochalasin B results in gradual loss of filamentous structures, whereas high concentration abolishes all features within 5 min.

Here we have found that the AFM imaging offers an approach to directly examine micromechanical organization of the cell cortex at very high resolution. This work follows a number of other AFM studies of living cells (e.g., Henderson et al., 1992; Barbee et al., 1994; Hoh and Schoenenberger, 1994; Putman et al., 1994; Braet et al., 1997; Quist et al., 2000) but differs in that we conclude that for a certain class of features in BPAECs the contrast is almost entirely mechanical in origin (Fig. 10). Although there is no formal way of uncoupling topographic features from mechanical features in AFM images of living cells, evidence here is that virtually all fine structure seen in AFM images derives from differential mechanical properties. This conclusion is based on the mechanical nature of live cell AFM imaging and a comparison of scanning EM or AFM of fixed cells with live cell AFM images. The images of fixed cells

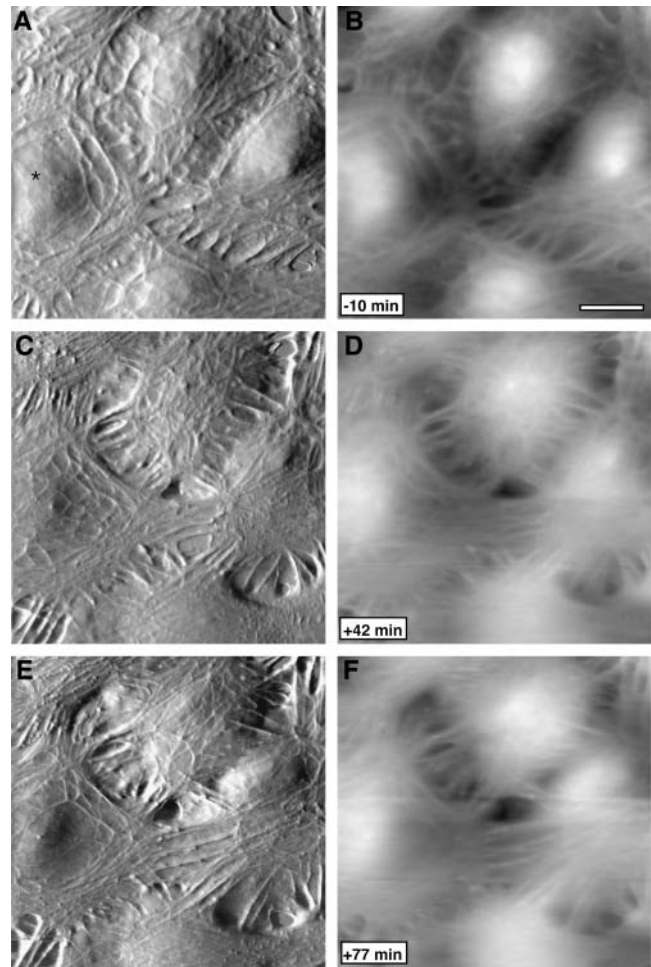


**FIGURE 8** Nocodazole treatment of BPAECs produces an increase in filamentous structures. Time series of AFM (A–C) deflection images and (D–F) corresponding height images collected before and after exposure to nocodazole. Cells were treated with  $\sim 50 \mu\text{M}$  nocodazole at time 0 min. There is an increase in the filamentous structures by 42 min, followed by a lateral reorganization. For example, the cell marked with an asterisk redistributes the filamentous features to the cell periphery by 77 min. Scale bar is 5  $\mu\text{m}$ .

show a smooth surface with no filamentous features, whereas the live cell AFM images show a highly complex mesh of filaments. This is consistent with an extensive body of scanning EM images of cells prepared using a variety of methods; we are not familiar with a single instance of scanning EM where such features are seen at the plasma membrane (from the extracellular side).

The view of the micromechanical architecture of BPAECs that results from the AFM imaging is far more detailed than apparent from confocal microscopy, although consistent with deep etch electron microscopy of similar cells that shows a complex network of cortical cytoskeleton. We conclude that the filamentous features in the AFM images represent the cytoskeleton based on three lines of reasoning. To begin with, the observed structures are highly reminiscent of cytoskeletal morphology. Further, the correlated AFM and

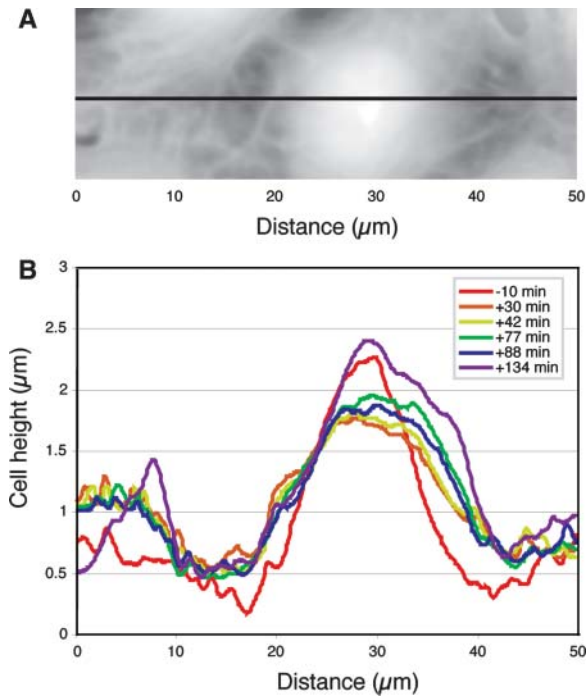


FIGURE 9 Changes in height of BPAEC due to nocodazole treatment. Cells were treated with  $\sim 50 \mu\text{M}$  nocodazole at time 0 min. (A) AFM height image of BPAEC. The black line shows position of the cross section. (B) A cross-section profile is collected at the same position at different time points. Cell height decreases by 30 min and stays low for at least 1 h. Cells regain their height by 134 min.

immunofluorescence data demonstrate that some of the filaments are actin and vimentin. Finally, treatment with anticytoskeletal drugs produces corresponding changes in the AFM images. This interpretation is also consistent with previous AFM imaging of living cells, where similar features have been attributed to the cytoskeleton using immunological or pharmacological approaches (Henderson et al., 1992; Rotsch and Radmacher, 2000). This conclusion is also

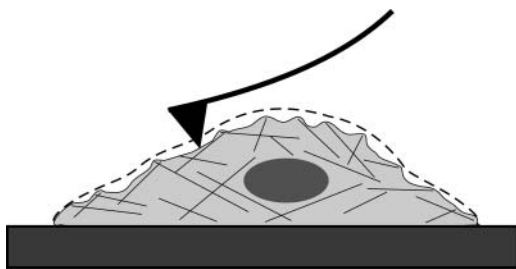


FIGURE 10 Schematic illustrating contrast mechanism for micromechanical AFM imaging of cells. Contour of the cell before imaging is shown as a dashed line. During AFM imaging the tip moves along the apical surface of the cell and interacts with structures in the cortex by differential deformation. Soft structures such as the lipid membrane are easily deformed, whereas stiff structures such as cytoskeleton resist the applied force. As a result, the contrast derives in large part from local mechanical properties of the sample.

consistent with the generally accepted finding that cytoskeleton is a major determinant of cellular mechanics and has physical properties that can give rise to mechanical features seen in the images. Because the AFM is a surface imaging tool, only structures on the apical side of cells interact with the probe, and the imaging is limited to the cell cortex. Here we define the cortex as what is accessible to the AFM in a typical imaging experiment. The maximum indentation depth of  $\sim 600 \text{ nm}$  (at an imaging force of  $\sim 1 \text{ nN}$ ) sets an upper limit for the amount of deformation. A lower limit for the layer thickness is estimated assuming that only the membrane, not the underlying cytoskeleton, deforms during imaging. In typical images this value is in the range 10–50 nm. For a variety of reasons the deformation is unlikely to be near either of these limits, and we estimate the thickness of this region to be a few hundred nanometers. Thus, our working hypothesis is that the contrast in our AFM images results from the variations in the micromechanical organization of the cell surface, which in turn reflects the organization of the CS of these vascular endothelial cells.

The correlated AFM-CFM and pharmacology experiments demonstrate that actin contributes to the micromechanical architecture in the BPAEC cortex. This is consistent with previous studies that have shown actin to be a significant contributor to the CS (Lazarides, 1975; Heuser and Kirschner, 1980; Condeelis, 1981; Bretscher, 1991). We were also able to identify features in the AFM images that correlate with vimentin staining but not tubulin. However, many features seen in the AFM images could not be assigned to any of the proteins for which we stained. Nonetheless, polygonal shape and branch angles suggest that many of the unidentified features are actin. Further, it is exceptionally difficult to visualize CS by CFM; on the other hand, the AFM provides very high contrast and suboptical resolution images of the cell cortex. Thus, it is likely that very thin cortical filaments of actin, vimentin, or microtubules are seen in the AFM but cannot be visualized by CFM. There are also other candidate molecules for which we have not yet stained, and there may also be unexpected molecules that contribute to cortical mechanics. Finally, the data collection may complicate the image correlation; in particular the time for fixation after AFM imaging allows for minor changes to cytoskeleton. Identification of all the features seen in the AFM images will require further work and possibly novel labeling approaches. The results from pharmacological treatments of BPAEC CS further support the finding that actin is a central mechanical component of the cortex in these cells. Cytochalasin B led to disruption of the filamentous network, whereas nocodazole resulted in an increase of filamentous structures. The latter result is attributed to the fact that nocodazole has been shown to increase the number of actin filaments (Ballestrin et al., 2000).

The organization of the cortical mesh reported here has interesting implications for the mechanical properties of cells. Both the intertwined mesh and layered mesh models present a unique mechanical picture of the cell. A cortex composed

solely of a fine mesh would produce a cell that is very soft, whereas a coarse mesh would result in a more rigid cell, but leave large soft spots on the surface. Combining the two by intertwining a fine mesh with a coarse mesh, produces a mechanically stable structure on both long and short length scales. An intertwined mesh would allow for mechanically coupled responses to external forces acting on the cell, whereas layered meshes could in principle respond more independently. In terms of remodeling and the level of coordination in the CS, an intertwined mesh would suggest that cortical remodeling of the fine mesh and the coarse mesh is highly coordinated. Although the data do not exclude the layered mesh model, in our view it is unlikely that the two meshes are fully separated and we favor the intertwined mesh model.

A general concern with AFM imaging of living cells is that the imaging process in some way perturbs the cells. In our experiments, it is clear that extended imaging does cause the cells to respond; imaging for more than 1.5–2 h results in a significant enlargement of fenestrae and eventually causes the cells to detach. On shorter time scales we do not see any obvious effects that are tip induced. When we vary the time interval between images the rate of movement remains constant, suggesting that the cell is not responding to the repeated imaging. However, we can not exclude the possibility that the initial contact between tip and cell initiates some of the events described here, in particular since endothelial cells sense and respond to mechanical forces (Helmke and Davies, 2002; Ingber, 2002).

Mechanical properties of isolated cytoskeletal components have been studied in significant detail. Mechanics of whole living cells have also been studied, although generally with modest spatial resolution relative to dimensions of the cell. However, the connection between molecular mechanics and cellular mechanics, which depends on the micromechanical organization of the cell remains poorly understood. The results presented here reveal the micromechanical architecture for length scales on the order of 100 nm to 100  $\mu$ m, which bridges the length scales of macromolecular assemblies with whole cells and small cell assemblies. Thus, the capability to visualize micromechanical architecture of the endothelial cortex at high resolution presents the opportunity to further connect molecular mechanics with cellular mechanics.

We thank Dr. Michael Edidin, Dr. Joseph Garcia, Dr. Susan Craig, and Dr. Douglas Robinson for helpful discussions. We also acknowledge Michael Delannoy and the Johns Hopkins School of Medicine Microscopy Facility for assistance with the scanning electron microscopy. We are also very grateful to Marlene Carlyle and Digital Instruments/Veeco for loan of the BioScope AFM used in the work described here.

This work was supported in part by a grant from the National Institutes of Health (HL076241).

## REFERENCES

- A-Hassan, E., W. F. Heinz, M. D. Antonik, N. P. D'Costa, S. Nageswaran, C. A. Schoenenberger, and J. H. Hoh. 1998. Relative microelastic mapping of living cells by atomic force microscopy. *Biophys. J.* 74:1564–1578.
- Alberts, B., D. Bray, J. Lewis, M. Raff, K. Roberts, and J. D. Watson. 1994. *Molecular Biology of the Cell*. Garland, New York.
- Ballestrem, C., B. Wehrle-Harler, B. Hinz, and B. A. Imhof. 2000. Actin-dependent lamellipodia formation and microtubule-dependent tail retraction control-directed cell migration. *Mol. Biol. Cell.* 11:2999–3012.
- Barbee, K. A., P. F. Davies, and R. Lal. 1994. Shear stress-induced reorganization of the surface topography of living endothelial cells imaged by atomic force microscopy. *Circ. Res.* 74:163–171.
- Basso, N., and J. N. Heersche. 2002. Characteristics of in vitro osteoblastic cell loading models. *Bone.* 30:347–351.
- Boal, D. 2002. *Mechanics of the Cell*. Cambridge University Press, Cambridge, UK.
- Braet, F., R. De Zanger, and E. Wisse. 1997. Drying cells for SEM, AFM and TEM by hexamethyldisilazane: a study on hepatic endothelial cells. *J. Microsc.* 186:84–87.
- Bretscher, A. 1991. Microfilament structure and function in the cortical cytoskeleton. *Annu. Rev. Cell Biol.* 7:337–374.
- Charras, G. T., P. P. Lehenkari, and M. A. Horton. 2001. Atomic force microscopy can be used to mechanically stimulate osteoblasts and evaluate cellular strain distributions. *Ultramicroscopy.* 86:85–95.
- Chazov, E. I., A. V. Alexeev, A. S. Antonov, V. E. Koteliansky, V. L. Leytin, E. V. Lyubimova, V. S. Repin, D. D. Sviridov, V. P. Torchilin, and V. N. Smirnov. 1981. Endothelial cell culture on fibrillar collagen: model to study platelet adhesion and liposome targeting to intercellular collagen matrix. *Proc. Natl. Acad. Sci. USA.* 78:5603–5607.
- Condeelis, J. S. 1981. Reciprocal interactions between the actin lattice and cell membrane. *Neurosci. Res. Program Bull.* 19:83–99.
- Costa, K. D., and F. C. P. Yin. 1999. Analysis of indentation: implications for measuring mechanical properties with atomic force microscopy. *J. Biomech. Eng.* 121:462–471.
- Dimitriadis, E. K., F. Horkay, J. Maresca, B. Kachar, and R. S. Chadwick. 2002. Determination of elastic moduli of thin layers of soft material using the atomic force microscope. *Biophys. J.* 82:2798–2810.
- Dong, C., R. Skalak, and K. L. Sung. 1991. Cytoplasmic rheology of passive neutrophils. *Biorheology.* 28:557–567.
- Dudek, S. M., and J. G. Garcia. 2001. Cytoskeletal regulation of pulmonary vascular permeability. *J. Appl. Physiol.* 91:1487–1500.
- Elson, E. L. 1988. Cellular mechanics as an indicator of cytoskeletal structure and function. *Annu. Rev. Biophys. Chem.* 17:397–430.
- Evans, E. A. 1989. Structure and deformation properties of red blood cells: concepts and quantitative methods. *Methods Enzymol.* 173:3–35.
- Flanagan, L. A., J. Chou, H. Falet, R. Neujahr, J. H. Hartwig, and T. P. Stossel. 2001. Filamin A, the Arp2/3 complex, and the morphology and function of cortical actin filaments in human melanoma cells. *J. Cell Biol.* 155:511–517.
- Galbraith, C. G., R. Skalak, and S. Chien. 1998. Shear stress induces spatial reorganization of the endothelial cell cytoskeleton. *Cell Motil. Cytoskeleton.* 40:317–330.
- Gittes, F., B. Mickey, J. Nettleton, and J. Howard. 1993. Flexural rigidity of microtubules and actin filaments measured from thermal fluctuations in shape. *J. Cell Biol.* 120:923–934.
- Hansen, J., R. Skalak, S. Chien, and A. Hoger. 1997. Spectrin properties and the elasticity of the red blood cell membrane skeleton. *Biorheology.* 34:327–348.
- Hartwig, J. H., and P. Shevlin. 1986. The architecture of actin filaments and the ultrastructural location of actin-binding protein in the periphery of lung macrophages. *J. Cell Biol.* 103:1007–1020.
- Heidemann, S. R., P. Lamoureaux, and R. E. Buxbaum. 2000. Opposing views on tensegrity as a structural framework for understanding cell mechanics. *J. Appl. Physiol.* 89:1670–1678.
- Helmke, B. P., and P. F. Davies. 2002. The cytoskeleton under external fluid mechanical forces: hemodynamic forces acting on the endothelium. *Ann. Biomed. Eng.* 30:284–296.

- Henderson, E., P. G. Haydon, and D. S. Sakaguchi. 1992. Actin filament dynamics in living glial cells imaged by atomic force microscopy. *Science*. 257:1944–1946.
- Heuser, J. 2000. The production of ‘cell cortices’ for light and electron microscopy. *Traffic*. 1:545–552.
- Heuser, J. E., and M. W. Kirschner. 1980. Filament organization revealed in platinum replicas of freeze-dried cytoskeletons. *J. Cell Biol.* 86:212–234.
- Hochmuth, R. M. 2000. Micropipette aspiration of living cells. *J. Biomech.* 33:15–22.
- Hofmann, U. G., C. Rotsch, W. J. Parak, and M. Radmacher. 1997. Investigating the cytoskeleton of chicken cardiocytes with the atomic force microscope. *J. Struct. Biol.* 119:84–91.
- Hoh, J. H., and C. A. Schoenberger. 1994. Surface morphology and mechanical properties of MDCK monolayers by atomic force microscopy. *J. Cell Sci.* 107:1105–1114.
- Howard, J. 2001. *Mechanics of Motor Proteins and the Cytoskeleton*. Sinauer Press, Sunderland, MA.
- Ingber, D. E. 2002. Mechanical signaling and the cellular response to extracellular matrix in angiogenesis and cardiovascular physiology. *Circ. Res.* 91:877–887.
- Ingber, D. E., S. R. Heidemann, P. Lamoureux, and R. E. Buxbaum. 2000. Opposing views on tensegrity as a structural framework for understanding cell mechanics. *J. Appl. Physiol.* 89:1663–1670.
- Janmey, P. A., U. Euteneuer, P. Traub, and M. Schliwa. 1991. Viscoelastic properties of vimentin compared with other filamentous biopolymer networks. *J. Cell Biol.* 113:155–160.
- Janmey, P. A., S. Hvidt, J. Kas, D. Lerche, A. Maggs, E. Sackmann, M. Schliwa, and T. P. Stossel. 1994. The mechanical-properties of actin gels - elastic-modulus and filament motions. *J. Biol. Chem.* 269:32503–32513.
- Janssen, K. P., L. Eichinger, P. A. Janmey, A. A. Noegel, M. Schliwa, W. Witke, and M. Schleicher. 1996. Viscoelastic properties of F-actin solutions in the presence of normal and mutated actin-binding proteins. *Arch. Biochem. Biophys.* 325:183–189.
- Joy, D. C. 2002. SMART—a program to measure SEM resolution and imaging performance. *J. Microsc.* 208:24–34.
- Karcher, H., J. Lammerding, H. Huang, R. T. Lee, R. D. Kamm, and M. R. Kaazempur-Mofrad. 2003. A three-dimensional viscoelastic model for cell deformation with experimental verification. *Biophys. J.* 85:3336–3349.
- Kojima, H., A. Ishijima, and T. Yanagida. 1994. Direct measurement of stiffness of single actin filaments with and without tropomyosin by in vitro nanomanipulation. *Proc. Natl. Acad. Sci. USA.* 91:12962–12966.
- Kurachi, M., M. Hoshi, and H. Tashiro. 1995. Buckling of a single microtubule by optical trapping forces: direct measurement of microtubule rigidity. *Cell Motil. Cytoskeleton.* 30:221–228.
- Lazarides, E. 1975. Immunofluorescence studies on the structure of actin filaments in tissue culture cells. *J. Histochem. Cytochem.* 23:507–528.
- Lee, J. S., and A. I. Gotlieb. 2002. Microtubule-actin interactions may regulate endothelial integrity and repair. *Cardiovasc. Pathol.* 11:135–140.
- MacKintosh, F. C., and C. F. Schmidt. 1999. Microrheology. *Curr. Opin. Colloid Interface Sci.* 4:300–307.
- Mathur, A. B., A. M. Collinsworth, W. M. Reichert, W. E. Kraus, and G. A. Truskey. 2001. Endothelial, cardiac muscle and skeletal muscle exhibit different viscous and elastic properties as determined by atomic force microscopy. *J. Biomech.* 34:1545–1553.
- Mathur, A. B., G. A. Truskey, and W. M. Reichert. 2000. Atomic force and total internal reflection fluorescence microscopy for the study of force transmission in endothelial cells. *Biophys. J.* 78:1725–1735.
- Ogunrinade, O., G. T. Kameya, and G. A. Truskey. 2002. Effect of fluid shear stress on the permeability of the arterial endothelium. *Ann. Biomed. Eng.* 30:430–446.
- Pollard, T. D., L. Blanchoin, and R. D. Mullins. 2000. Molecular mechanisms controlling actin filament dynamics in nonmuscle cells. *Annu. Rev. Biophys. Biomol. Struct.* 29:545–576.
- Pollard, T. D., and G. G. Borisy. 2003. Cellular motility driven by assembly and disassembly of actin filaments. *Cell.* 112:453–465.
- Putman, C. A. J., K. O. Vanderwerf, B. G. Degrooth, N. F. Vanhulst, and J. Greve. 1994. Viscoelasticity of living cells allows high-resolution imaging by tapping mode atomic-force microscopy. *Biophys. J.* 67:1749–1753.
- Quist, A. P., S. K. Rhee, H. Lin, and R. Lal. 2000. Physiological role of gap-junctional hemichannels. Extracellular calcium-dependent isosmotic volume regulation. *J. Cell Biol.* 148:1063–1074.
- Radmacher, M., M. Fritz, and P. K. Hansma. 1995. Imaging soft samples with the atomic force microscope: gelatin in water and propanol. *Biophys. J.* 69:264–270.
- Radmacher, M., M. Fritz, C. M. Kacher, J. P. Cleveland, and P. K. Hansma. 1996. Measuring the viscoelastic properties of human platelets with the atomic force microscope. *Biophys. J.* 70:556–567.
- Rotsch, C., and M. Radmacher. 2000. Drug-induced changes of cytoskeletal structure and mechanics in fibroblasts: an atomic force microscopy study. *Biophys. J.* 78:520–535.
- Satcher, R., C. F. Dewey, Jr., and J. H. Hartwig. 1997. Mechanical remodeling of the endothelial surface and actin cytoskeleton induced by fluid flow. *Microcirculation.* 4:439–453.
- Satcher, R. L., Jr., and C. F. Dewey, Jr. 1996. Theoretical estimates of mechanical properties of the endothelial cell cytoskeleton. *Biophys. J.* 71:109–118.
- Schaeffer, R. C., Jr., F. Gong, M. S. Bitrick, Jr., and T. L. Smith. 1993. Thrombin and bradykinin initiate discrete endothelial solute permeability mechanisms. *Am. J. Physiol.* 264:H1798–H1809.
- Tsukita, S., and S. Yonemura. 1999. Cortical actin organization: lessons from ERM (ezrin/radixin/moesin) proteins. *J. Biol. Chem.* 274:34507–34510.
- Vinckier, A., and G. Semenza. 1998. Measuring elasticity of biological materials by atomic force microscopy. *FEBS Lett.* 430:12–16.
- Wakatsuki, T., B. Schwab, N. C. Thompson, and E. L. Elson. 2001. Effects of cytochalasin D and latrunculin B on mechanical properties of cells. *J. Cell Sci.* 114:1025–1036.
- Wang, N., and D. E. Ingber. 1994. Control of cytoskeletal mechanics by extracellular matrix, cell shape, and mechanical tension. *Biophys. J.* 66:2181–2189.
- Weber, I., J. Niewohner, and J. Faix. 1999. Cytoskeletal protein mutations and cell motility in Dictyostelium. *Biochem. Soc. Symp.* 65:245–265.
- Yamada, S., D. Wirtz, and S. C. Kuo. 2000. Mechanics of living cells measured by laser tracking microrheology. *Biophys. J.* 78:1736–1747.
- Yeung, A., and E. Evans. 1989. Cortical shell-liquid core model for passive flow of liquid-like spherical cells into micropipets. *Biophys. J.* 56:139–149.
- Zahalak, G. I., W. B. McConnaughey, and E. L. Elson. 1990. Determination of cellular mechanical properties by cell poking, with an application to leukocytes. *J. Biomech. Eng.* 112:283–294.

# Elasticity and Adhesion Force Mapping Reveals Real-Time Clustering of Growth Factor Receptors and Associated Changes in Local Cellular Rheological Properties

N. Almqvist,<sup>\*†</sup> R. Bhatia,<sup>†</sup> G. Primbs,<sup>†</sup> N. Desai,<sup>‡</sup> S. Banerjee,<sup>§</sup> and R. Lal<sup>†</sup>

<sup>\*</sup>Department of Applied Physics & Mechanical Engineering, Luleå University of Technology, Luleå, Sweden; <sup>†</sup>Neuroscience Research Institute, University of California, Santa Barbara, California USA; <sup>‡</sup>NutraSweet Company, Chicago, Illinois USA; and <sup>§</sup>Department of Chemical Engineering, University of California, Santa Barbara, California USA

**ABSTRACT** Cell surface macromolecules such as receptors and ion channels serve as the interface link between the cytoplasm and the extracellular region. Their density, distribution, and clustering are key spatial features influencing effective and proper physical and biochemical cellular responses to many regulatory signals. In this study, the effect of plasma-membrane receptor clustering on local cell mechanics was obtained from maps of interaction forces between antibody-conjugated atomic force microscope tips and a specific receptor, a vascular endothelial growth factor (VEGF) receptor. The technique allows simultaneous measurement of the real-time motion of specific macromolecules and their effect on local rheological properties like elasticity. The clustering was stimulated by online additions of VEGF, or antibody against VEGF receptors. VEGF receptors are found to concentrate toward the cell boundaries and cluster rapidly after the online additions commence. Elasticity of regions under the clusters is found to change remarkably, with order-of-magnitude stiffness reductions and fluidity increases. The local stiffness reductions are nearly proportional to receptor density and, being concentrated near the cell edges, provide a mechanism for cell growth and angiogenesis.

## INTRODUCTION

Receptors and ion channels transmit regulatory information from the outside environment to the cell interior and play a crucial role in maintaining metabolic homeostasis and in the sustenance of organisms (Pawson, 1995; Antonova et al., 2001; Horio et al., 1997; Sugiyama et al., 1997; Jefford and Dubreuil, 2000; Rameh and Cantley, 1999; Crouch et al., 2001). The molecular basis of receptor/channel action is being studied extensively using biochemical strategies, but little is known about the spatial localization, density, distribution, and molecular structure involved, although these spatial features are thought to exert localized control over cell function. For example, the clustering of growth factor receptors, e.g., vascular endothelial growth factor receptor (VEGFR) is implicated in endothelial cell growth and migration (Thomas, 1996). To obtain such direct structural information it is crucial to develop and apply techniques for molecular-resolution imaging of cellular specimens in their native hydrated states.

Several new scanning probe techniques are being developed to map membrane macromolecules. Of these, atomic force microscopy (AFM) allows molecular resolution imaging in aqueous media (Lal and John, 1994) and the study of intermolecular interactions using functionalized AFM probes (Zhang et al., 2002; Baumgartner et al., 2000;

Yuan et al., 2000; Boland and Ratner, 1995; Dammer et al., 1996; Hinterdorfer et al., 1996). Single-molecule force spectroscopy was previously used to examine cell-cell adhesion properties (Benoit et al., 2000). Although such an approach would be useful for mapping overall interactions between small cells, its relevance to mapping regional distribution of macromolecules in the cell plasma membrane is uncertain. Another approach maps the local ion channel currents, from which the channel density and distribution are derived (Korchev et al., 2000). Application of this approach for mapping membrane receptors without any channel-like activity is limited. However, recently modified commercial AFMs, linked to a confocal microscope, have been successfully used to measure and map adhesion forces between ligands and receptors on the surface of living cells (Horton et al., 2002; Aileen and Moy, 2000).

Here we apply a similar method that uses AFM force-volume mapping (Quist et al., 2000; Rhee et al., 1998) to identify and map regional distribution as well as ligand- or antibody-induced real-time clustering of receptors on the cell surface. The approach allows simultaneous imaging of the resultant changes in micromechanical properties and cytoskeletal reorganization with nanoscale resolution (Quist et al., 2000; Shroff et al., 1995; Parbhu et al., 1999).

As an appropriate physiological sample, we have examined spatial distribution of VEGFR, the receptor for vascular endothelial growth factor (VEGF). VEGF is an important angiogenic factor in human and animal tissues. VEGF acts selectively on vascular endothelial cells to increase their permeability to circulating macromolecules and stimulate endothelial cell growth (Thomas, 1996; Wang et al., 2001). VEGF is a homodimeric glycoprotein that interacts with its receptors in the plasma membrane of vascular endothelial

*Submitted July 23, 2003, and accepted for publication December 5, 2003.*

N. Almqvist and R. Bhatia contributed equally to this work.

Address reprint requests to Ratnesh Lal, Neuroscience Research Institute, University of California, Santa Barbara, CA 93106. Tel.: 805-893-2350; Fax: 805-893-2005; E-mail: lal@lifesci.ucsb.edu.

© 2004 by the Biophysical Society

0006-3495/04/03/1753/10 \$2.00

cells. Three cell membrane receptors tyrosine kinases, Flt (also designated as VEGF-R1), Flk-1 (also designated KDR or VEGF-R2), and Flt-4 are involved in endothelial cell growth (Meyer et al., 1999; Neufeld et al., 1999). Two members of this receptor class, Flt and Flk-1, have been shown to represent high affinity receptors for vascular endothelial growth factor. At present, very little is known about the molecular structure, distribution, and clustering of VEGF receptors in endothelial cell plasma membrane. Moreover, the VEGFR clustering-induced short-term and dynamic cellular biophysical changes are not well understood.

We have used AFM tips conjugated with anti-Flk-1 antibody for semiquantitative measurements of binding (or unbinding) forces between anti-Flk-1 antibody and VEGF-R2 (Flk-1). Measurements were made both *in vitro* as well as *in vivo* (in live) endothelial cells. Distribution and density of VEGFRs were mapped in the cell plasma membrane using the receptor-antibody interaction and force-volume mapping technique. Antibody and ligand induced real-time clustering and redistribution of VEGFRs. VEGFR clustering altered cell local elastic properties significantly.

## MATERIALS AND METHODS

### Chemicals and reagents

Silane (3-aminopropylmethyldiethoxysilane) was purchased from Sigma-Aldrich (St. Louis, MO). VEGF was purchased from PeproTech (Rocky Hill, NJ). Flk-1 (a VEGFR2), goat affinity-purified, site-directed, polyclonal anti-Flk-1 antibody, and the blocking peptide (the peptide against which the antibody was raised) were purchased from Santa Cruz Biotechnology (Santa Cruz, CA).

### Cell culture

Bovine aortic endothelial cells (KOM-1 cell line) were cultured on sterile plastic petri dishes as described (Bhatia et al., 2000), in Dulbecco's modified Eagle's medium containing glucose, 10 mM HEPES, 2 mM glutamine, 100 units/ml penicillin, 100 mg/ml streptomycin, and 10% heat-inactivated calf serum (Life Technologies, Rockville, MD) (Yauch et al., 1997). Cells were grown in an incubator maintained at 37°C temperature and 5% CO<sub>2</sub>.

### Immunofluorescence labeling

Donkey anti-rabbit-IgG conjugated with cy-3 was purchased from Jackson Laboratory (Bar Harbor, ME). Cells grown on glass coverslips were fixed with 4% paraformaldehyde for 10 min, and washed with PBS, and PBS containing 3% bovine serum albumin and 1% donkey serum, to minimize any nonspecific binding. Cells were then incubated with antibody against Flk-1 (0.1 μg/ml) in PBS containing 3% BSA and 1% donkey serum for 1 h. After washing, the sample was incubated, for 1 h, with a cy-3 conjugated donkey anti-rabbit antibody (1:400 dilutions) under the same condition as for the primary antibody. Immunofluorescence images were captured with a Bio-Rad MRC 1024 laser confocal microscope (Bio-Rad Laboratories, Hercules, CA) using a 60× Nikon Plan Apo oil-emersion lens with 1.4 NA.

## Atomic force microscopy and preparation of functionalized AFM tips

AFM images and force measurements were recorded with either a commercial multimode AFM (Digital Instruments Nanoscope III, Veeco Instruments, Santa Barbara, CA) or a bioscope AFM with an integrated inverted light microscope (a prototype of Digital Instruments *Bioscope*) using the NanoScope III software (Version 4.23R2; Digital Instruments) as described (Quist et al., 2000).

Standard commercially available, 200-μm long Si<sub>3</sub>N<sub>4</sub> cantilevers, with integrated tips (Digital Instruments) and a nominal spring constant,  $k$ , of 0.06 N/m were used. The approximate nominal spring constant value was verified by measuring the spring constants on five cantilevers from the same batch with the thermal fluctuation method (Hutter and Bechhoefer, 1993) in both air and fluid. Our measurements yielded similar results in air as in a fluid. The measured value was  $k = 0.063 \pm 0.003$  N/m, including a 16% correction due to the calibration of the amplitude in static mode. Due to systematic errors, we estimated the uncertainty to be at least 15–20%. The cantilever tips used in our study were conjugated with antibody. The spring constant of silanated and antibody conjugated tips were  $k = 0.060 \pm 0.005$  ( $n = 5$ ). Such correspondence is consistent with previous studies by Cleveland and the Hansma group (Cleveland and Manne, 1993) which indicated that a small increase in the tip mass (as would occur when the antibody is conjugated to the tip) does not change the spring constant significantly. Moreover, whenever feasible, we used the same conjugated tip for experiments involving internal control—for example, in mapping interactions between antibody and receptor alone, adding online inhibitor of their interactions (e.g., blocking peptide). Also, although semiquantitative estimate of interaction forces are described, the main emphasis is on the relative change as a function of specific perturbations.

The cantilever tips were functionalized by silanization with 3-aminopropylmethyl-diethoxysilane by vapor deposition or by immersion in a solution of 2% silane in toluene. A drop of 2 μg/ml of anti-Flk-1 IgG was then placed on the silanized tip for 10 min, to adsorb to the functionalized tip. The antibody-conjugated tips were then washed thoroughly with PBS and water to remove loosely attached antibodies. These tips were used immediately, without being dried, for obtaining the interaction-force curves and the force-volume maps.

## Sample preparation and force measurements

### *In vitro* force spectroscopy

The mica surface was silanized and imaged to ensure the uniformity of the silane layer. Flk-1 receptor (10 μg/ml; 10–20 μl vol) was adsorbed on the silanized mica for 10 min at room temperature. Unattached or loosely attached receptors were removed by washing the mica surface thoroughly with water. AFM was used to image the presence and the distribution of Flk-1 receptors in fluid. Once a low concentration of individual VEGF receptors were identified in an AFM image, the tip-receptor interaction force curves were recorded after positioning the tip over a receptor. A series of force curves were recorded in MilliQ water or PBS, *in vitro*, between the anti-Flk-1-antibody conjugated to a functionalized tip and the Flk-1 receptor adsorbed on mica to measure the specific unbinding forces.

To determine the specificity of the antibody-VEGFR interaction, the blocking peptide (the peptide against which the antibody was raised) was then added online and successive force-curves were measured again after 10 min of incubation with the blocking peptide. As additional control experiments, the force curves were also recorded: 1), with a nonspecific antibody (Mouse IgG) conjugated to the functionalized tip in identical experimental conditions; 2), between the nonfunctionalized tips and the receptors; and 3), between the nonfunctionalized tips and the fresh silanized mica.

### *In vivo force-volume maps*

The same technique used to measure the unbinding force *in vitro* was used to measure the unbinding forces *in vivo*, i.e., between the anti-Flk-1 antibody (conjugated to AFM tip) and the VEGF receptors present in the plasma membrane of live, cultured endothelial cells. The force curves were recorded in HEPES-buffered OPTI-MEM reduced serum medium (7.3 pH) in petri dishes on cells 2–3 days after seeding (Bhatia et al., 2000). The usage of this medium was necessary to maintain normal cell morphology and viability (Bhatia et al., 2000). The force mapping between isolated VEGFR and its antibody was conducted in a more defined operating environment—water or PBS. No significant difference in the interaction force between single receptor and antibody was observed *in vitro*. As the main focus of the whole study is to examine real-time receptor clustering in the cell plasma membrane and this required relative change in overall force field and not the actual single receptor-antibody/ligand adhesion/de-adhesion force, the imaging medium is presumed to play very little (if any) role in our analysis.

Force-volume data were collected by the force-volume map technique as described previously (Quist et al., 2000; Rhee et al., 1998). It allows force curves to be acquired as a function of the lateral position on the specimen surface. One complete force curve was recorded at each position while the AFM tip was raster scanned across the surface of the sample in  $64 \times 64$  measuring points. The force curves were collected with a  $z$ -deflection rate of  $15\text{--}20 \text{ nm (ms)}^{-1}$  and with a maximum cantilever deflection (relative trigger). The total recording time for a complete image was typically 7–8 min. The relative trigger point was typically set to 20 or 40 nm (1.2 or 2.4 nN). A topographic image ( $64 \times 64$  pixels) was stored simultaneously in the force-volume map.

The specificity of the antibody-VEGFR interaction in the cell plasma membrane was determined as described above for *in vitro* study: the blocking peptide was added online and successive force maps were collected at 10-min intervals. As additional control experiments, the same cell was imaged before the addition of VEGF or antibody, with either a regular  $\text{Si}_3\text{N}_4$  or a tip functionalized with a nonspecific antibody (Mouse IgG). Real-time receptor clustering was imaged by collecting successive force-volume maps with an anti-Flk-1-antibody-functionalized tip, after the addition of VEGF or anti-Flk-1-antibody in the imaging medium, respectively. All AFM imaging was performed at  $25\text{--}27^\circ\text{C}$  room temperature and the data were analyzed, as described below, with the previously described protocols developed in our lab.

### AFM data analysis

A complete AFM force curve (force-displacement curve) is a plot of the measured forces, on the AFM cantilever probe, as function of the  $z$ -piezo-displacement,  $z$ , for a complete cycle of the AFM probe approaching and retracting the sample. The measured force is  $F = k\delta$ , where  $k$  is the cantilever spring constant and  $\delta$  is the cantilever deflection. Force curves were analyzed to investigate: 1), force-induced dissociation of the single molecular bonds; 2), the total de-adhesion between antigen-antibody complexes by evaluating qualitative differences in dissipated energy; and 3), the sample elasticity. The AFM force-volume data was imported and analyzed offline with tools developed within the IGOR Pro 4.00 (Wave-metrics, Lake Oswego, OR) data analysis software.

When the antibody-conjugated tip is brought into contact (the approach phase) with the cell surface receptors, the antibody and its specific receptors bind with attractive forces. Upon tip retraction, the antibody-receptor bonds (adhesion) keep them in contact to a certain retract distance (the hysteresis phase). The antibody-receptor bond breaks then and the measured de-adhesion force is equivalent to the antibody-receptor unbinding force. However, the retrace phase of the force curve may contain multiple quantized staircase steps (multiple bond-breaking points), each representing specific molecular interactions or unbinding events. Several different methods were used to evaluate the unbinding forces. The retract force curves were evaluated to find all individual force de-adhesion steps. The first

and second derivatives of a curve were used to find all local force minima and maxima and calculate the unbinding forces. To minimize effects from noise, a step was only counted when the second derivative and the step height were above the manually specified threshold values. This automatic evaluation of the unbinding forces from these force curves is nontrivial since the measured rupture forces are small and are the result of multiple unbinding, sequential breaking, and possibly nonspecific molecular interactions, molecular stretching, etc. Sequential unbinding events without any specific effect is recognized in the force curves as the unbinding force drops to zero in between the different ruptures. In the case of multiple specific bindings, for example from the different binding sites of the antibody, parallel breakage, as multiples of the single specific bonds, would be detected. The analysis is complicated if the detected broken interactions arise from a number of different interacting molecules or variable strength of bonds. Then the weakest bonds will break first and the measured forces will not necessarily reflect the unbinding strength. However, at the last unbinding (de-adhesion) step, the measured unbinding force is still accurate and hence eventual single unbinding events can be detected. Therefore, the last step representing the final break point during hysteresis phase of the tip retraction was used to estimate the single-molecule unbinding force (Gad et al., 1997; Benoit et al., 2000).

The last de-adhesion (unbinding) force steps of the antibody-receptor interaction force curves were compiled into histograms or used to plot spatially resolved unbinding force images. Still, it was shown that histograms of all the force steps yielded similar qualitative result as when measuring only the last step. The grouping interval in the histograms was set identical to the sampling interval in the digitally stored AFM force curve data, typically a few picoNewtons. The sampling bin was smaller than the nominal AFM force resolution of  $10\text{--}15 \text{ pN}$  (Cappella and Dietler, 1999). Altogether, since unbinding is a stochastic process in nature, a specific unbinding event should show up as a peak of several bins in the histogram. Since the absolute value of the measured unbinding force depends on the  $z$ -position scan rate, we used similar scan rates in all experiments.

The force-volume measurements were also used to visualize spatially resolved maps of the total de-adhesion between antigen-antibody complexes. Generally, such maps, for each data point, show the maximum adhesion force or an area in the force curve plot. Dissipative forces give hysteresis between the trace and retrace force curves; the hysteresis corresponds to the amount of dissipated energy. The relative dissipated energy can be calculated as the area between the trace and retrace force curves (Stark et al., 2001; Marti et al., 1995; Bery et al., 2001). Maps of relative dissipated energy discussed in this article are evaluated by a trapezoidal integration of the area enclosed by the force curves in force-displacement coordinates. As the force curves could contain hydrodynamic drag component, the force values were first subjected to a minor correction before the integration.

### Modeling sample elasticity

Sneddon mechanics (Sneddon, 1965) was used to evaluate sample elasticity from the force-volume measurements. Calculations were made for both a spherical indenter and a conical indenter. We used the latter in this study since the so-called Sneddon exponent (VanLandingham et al., 1997) generally indicated a more conical than spherical indentation geometry. In the case of a conical indenter, the piezo position,  $z$ , versus cantilever deflection can be expressed as

$$z - z_0 = d - d_0 + \sqrt{\frac{k\pi(1 - \nu^2)}{2E \cot \alpha}} \sqrt{d - d_0}. \quad (1)$$

Here  $\nu$  is the Poisson's ratio,  $\alpha$  is the semivertical angle of the indenter, i.e.,  $\pi/2$  minus half the opening angle ( $70^\circ$ ) of the cone, and  $z_0$ ,  $d_0$  are the contact point and the free deflection value, respectively. We assume  $\nu = 0.5$  and use  $k = 0.06 \text{ N/m}$  for the calculations in this article. A nonlinear, two-parameter, numerical curve fit was used to fit the model to the force distance data in

a previously used iterative procedure (Almqvist et al., 2001). The contact point was estimated as the intersection between the extrapolated line-fit of the zero-force part of the curve and the curve-fit of the contact part of the curve. Therefore, precautions were taken for any linear change of the force curve in the noncontact region and the  $d_0$ -value was corrected accordingly. We also reduced the influence of substrate effects due to thinning of the cell. At a certain indentation of the sample, the AFM tip senses the underlying substrate and the force curve is significantly influenced with a steeper slope. For this reason, our automatic task of extracting the Young's (elastic) modulus  $E$  makes a curve fit to the model between  $d_0$  and the point where the slope of the force curve is 90% of the "hard surface slope" measured on the substrate. In addition, we also used manual inspection of the force curves and of the surface heights.

## RESULTS AND DISCUSSION

### Unbinding forces

We first examined the specific molecular interaction force between the isolated receptor Flk-1 (VEGF-R2) adsorbed on a silanized mica surface and the antibody (anti-Flk-1 IgG) conjugated to the AFM tip. The functionalized AFM tip was positioned above an individual receptor and a number of force curves (10–50) were measured over a series of experiments to qualitatively measure the unbinding force between receptor-antibody pairs. The upper force curve in Fig. 1 A reveals large unbinding steps (arrows) between the antibody-conjugated tip and the VEGFR adsorbed on to a mica substrate. The lower curve is a more typical curve for the interaction between receptor and antibody. Fig. 1 B shows a histogram of the correspondent manually measured unbinding forces.

The specificity of the antibody-receptor interaction was determined by complementary sets of control experiments. The unbinding force (Fig. 1 A) was abolished, i.e., the hysteresis in the force curve was eliminated when the blocking peptide (the peptide against which the antibody was raised) was added online (Fig. 1 C). Preliminary data suggest that, by sequential competitive binding, the blocking peptide could reveal multiple receptor-antibody bindings and, as such, could be used to find single binding events even when there are complex interactions. Also, no appreciable unbinding force was observed between the Flk-1 receptors and the regular, non-antibody-conjugated silicon nitride tips (data not shown). Similarly, no hysteresis in the force curve was observed when imaging a freshly cleaved mica surface with non-antibody-conjugated silicon nitride tips under identical fluid conditions.

Generally the unbinding forces varied between 60 and 240 picoNewtons (pN). However, manual inspection yielded frequent occurrence of unbinding forces 60–100 pN, and possibly multiples thereof. For example, unbinding forces of 240 pN could correspond to simultaneous breaking of four 60-pN interactions. The absolute value of the unbinding force is semiquantitative, at best. However, it is apparent that the technique and our approach are sufficient to determine specific receptor-antibody interactions. As described in

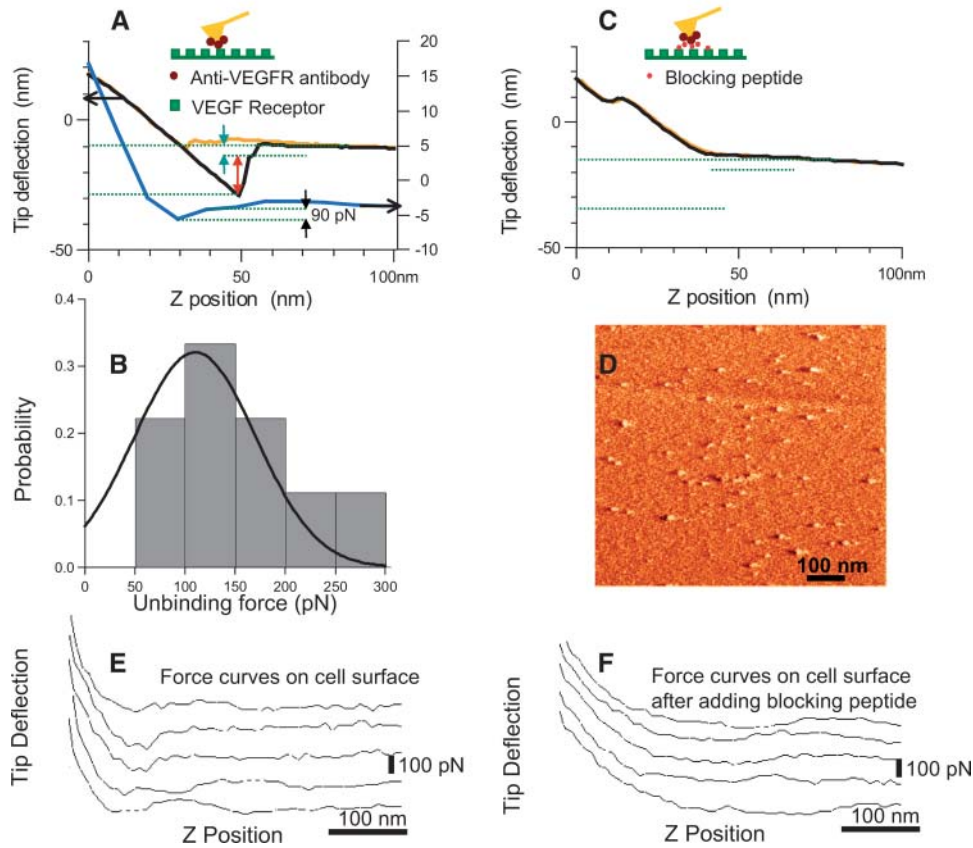
Materials and Methods, force measurement errors are attributed to the following: 1), a lack of precise determination of the spring constant of the antibody-conjugated AFM tip; 2), a rather large  $z$ -position scan rate (overestimated force); 3), neglecting eventual geometric effects of the finite-sized tip radius; and 4), surface forces due to the eventual presence of an electrical double layer.

Previous studies have reported unbinding forces, from in vitro study, of  $60 \pm 10$  pN for biotin/antibiotin (Dammer et al., 1996),  $49 \pm 10$  pN for ferritin/antiferritin, and  $40 \pm 4$  pN for fluorescein/antifluorescein (Ros et al., 1998) single antigen-antibody interaction, and higher multiples for multiple interactions. Our semiquantitative result of a VEGFR-antibody unbinding force of  $60 \pm 10$  pN is consistent with these studies.

The binding/unbinding forces measured in our study are specific to antibody-receptor interactions and not due to unspecific binding processes. An important control for this is the absence of binding events, presumably due to the blocking of the binding sites when the blocking peptide was added in the imaging medium and/or due to a decrease in the total number of binding events when an excess amount of antibody was added in the medium. Moreover, no measurable binding force was observed between the VEGF receptor (Flk-1) adsorbed on mica and a nonspecific antibody mouse IgG onto the tip (unpublished data).

The same technique, as used to measure the unbinding force in vitro (between the isolated VEGF receptor adsorbed on the mica surface and the anti-Flk-1 antibody conjugated to the AFM tip), was used to measure the unbinding forces in vivo, i.e., between the anti-Flk-1-antibody (conjugated to AFM tip) and the VEGF receptors present in the plasma membrane of live cultured endothelial cells. In the in vivo condition, multiple unbinding forces were observed in most of the force curves at each receptor surface (Fig. 1 E), in contrast to predominantly single unbinding steps observed between isolated receptors adsorbed onto mica and the antibody-conjugated tip. In the presence of the blocking peptide (which was added online after the force-curves between the antibody and VEGFRs had been acquired), the interaction between the antibody and VEGF receptor was inhibited, and basically no hysteresis was observed in the force curves (Fig. 1 F), i.e., the unbinding force was eliminated. The force curves in Fig. 1 E indicates a larger adhesion force versus no adhesion force in the presence of the blocking peptide (see also Fig. 1 F).

The binding force measured between the receptors in the cell plasma membrane and the antibody (anti-flk1) anchored to the AFM tip show correspondence to the in vitro experiment. However, on addition of excess anti-Flk-1-antibody in the imaging medium, there was a significant decrease in the total number of binding events but not a complete inhibition. This could be due to the complexity of physicochemical factors and cellular processes involved in the case of receptors present in the cell surface.



uted on a silanized mica surface. (E) Adhesion force between VEGF receptor (flk-1) on endothelial cell and AFM tip conjugated with an antibody (anti-flk-1). (F) Force curves on the cell after adding the blocking peptide. The force curves in E indicates larger adhesion force versus no adhesion force in the presence of the blocking peptide (F).

FIGURE 1 Adhesion (unbinding/binding) forces between VEGF receptor and its antibody. (A) Adhesion force between isolated VEGF receptor (flk-1) adsorbed on the mica substrate and AFM tip conjugated with an antibody (anti-flk-1). The top AFM force curves with deflection scale to the left show the approach (yellow) and retract (black) curve, respectively. The retract curve reveals large multiple de-adhesion steps (arrows) and specific interaction between the antibody (anti-Flk-1) on the tip and the receptors on mica surface. The last unbinding step (green arrow) is attributed to unbinding of a single receptor-antibody pair. The lower blue curve (with deflection scale to the right) shows a more typical interaction. The expected single pair unbinding is  $\sim 100$  pN and might correspond to single/double binding. (B) Probability histogram of manually measured unbinding forces from force curves measured as in A. (C) Control; competitive inhibition. The force curve in A between the antibody on the tip and the receptors on mica surface is abolished by online addition of the blocking peptide against which the antibody was made. (D) AFM tapping mode amplitude image of the VEGF receptors sparsely distributed

The interaction-force histograms obtained using the tip without any antibody and the tip with a nonspecific antibody were similar, suggesting that these tips interact nonspecifically with the cell surface. Various glycoproteins, sugar molecules, adhesion molecules, and other macromolecules present in the cell plasma membrane could contribute to such nonspecific adhesions.

The multiple unbinding steps present in the force measurement curve, when using anti-Flk-1-antibody-conjugated tips, could be due to the presence of two Fab fragments of the antibody. Two Fab fragments could bind to a single receptor producing two separate unbinding (de-adhesion) steps on retraction, or two Fab fragments could bind independently depending on a number of factors like the distribution of receptors on the cell surface and the orientation of the antibody. Moreover, since the cell surface is soft, the contact area between the AFM tip and the cell surface will be large, which further favors the occurrence of multiple molecular bonds and large adhesion. The likelihood of single molecular interactions should be significantly higher in the *in vitro* experiments, since the density and the distribution of the interacting molecules (VEGFRs, in this case) can be optimized.

## Redistribution and clustering of plasma membrane receptors

With standard contact mode AFM imaging, the endothelial cells could be imaged without any imaging-induced structural artifacts for an extended period of time as described previously (Bhatia et al., 2000). Fig. 2, A and B, shows examples of real-time AFM imaging of endothelial cells. Online addition of 25 nM VEGF, an important angiogenic factor in human and animal tissues, induced cytoskeletal reorganization and cellular growth. However, as expected, within a short period (2 h) of imaging, the cell growth/reorganization was very small, and was normally not observable under light microscopy. AFM images show a clear difference in the image contrast reflective of differing viscoelasticity; cells after VEGF incubation show fewer cytoskeletal details (Fig. 2 B, top cell) and a changing cell boundary. Previous studies have reported considerably pronounced cell growth after a longer duration (8–10 h or longer) of VEGF incubation. In the present study, the cell elastic property changed considerably (see below) and the endothelial cells became softer after the addition of VEGF or anti-VEGFR-antibody in the imaging medium. A qualitative

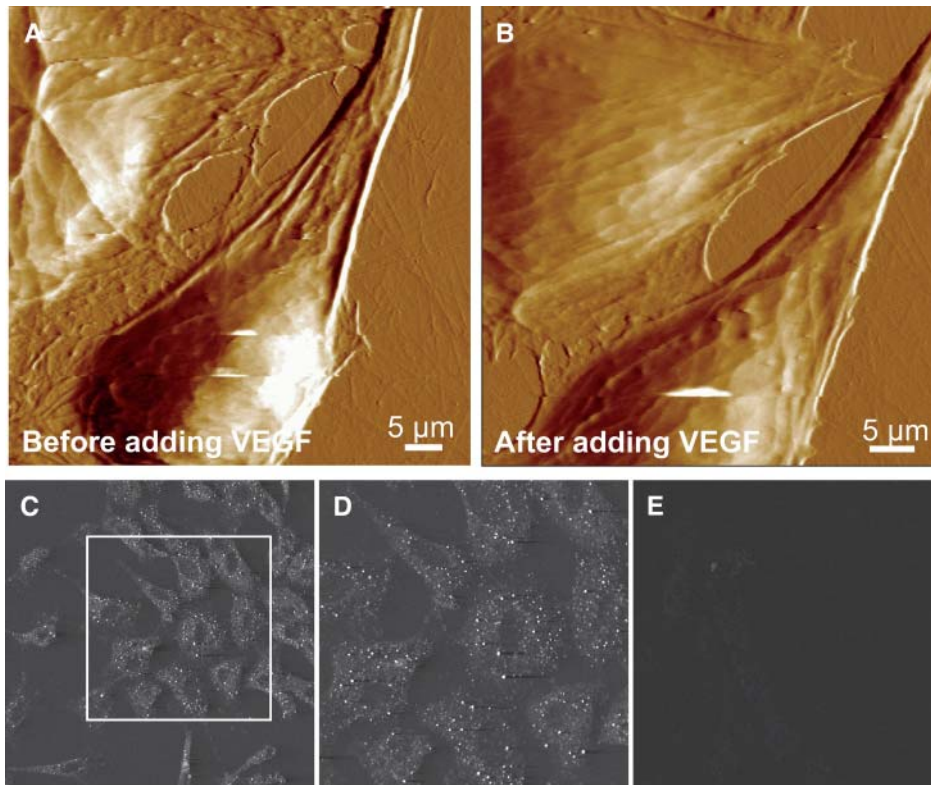


**FIGURE 2** AFM images of endothelial cells showing VEGF induced cytoskeletal reorganization, (A) before adding VEGF and (B) 2 h after adding VEGF (25 nM). Cytoskeletal reorganization as well as a change in the elasticity is observed. Cell softness is reflected in a loss of fine ultrastructural details. (C–D) Immunofluorescence labeling of Flk-1 receptors in the plasma membrane. Endothelial cells show immunolabeling with a polyclonal anti-Flk-1 antibody followed by cy-3 conjugated secondary antibody. D shows a zoomed image of a portion of C. Receptors are distributed throughout the cell surface with a higher density along the cell periphery. (E) Endothelial cells show no immunolabeling with a nonspecific antibody followed by cy-3 conjugated secondary antibody.

change in the cell softness is reflected as a loss of ultrastructural details (Fig. 2, A–B).

The presence of VEGF receptors in the endothelial cell plasma membrane is evident from immunofluorescence labeling of these receptors with anti-Flk-1-antibody and fluorescently labeled with cy3 conjugated secondary antibody (Fig. 2, C and D). Fig. 2, C and D, show single slices in confocal images of immunofluorescence labeling and show a lack of label above the cell nucleus. However, the integrated confocal image of whole-cell immunolabeling indicates that VEGF receptors are distributed throughout the cell surface but at a slightly higher density along the cell periphery (data not shown). The punctuated immunolabeling pattern with a higher density along the cellular periphery (Fig. 2, C and D) is consistent with the presence of punctuate regions of different elasticity measured in our study, as discussed later.

Receptor clustering and distribution were examined using force-volume mapping as described earlier and not by the method used for the force measurements shown in Fig. 1. The force maps were first recorded with a regular  $\text{Si}_3\text{N}_4$  tip (which serves as a control), then with a tip conjugated with anti-Flk-1 antibody, and then again after the excess antibody was added in the solution. Fig. 3, A–C, shows the result with the conjugated tip before addition of the antibodies. The unbinding forces in the *in vivo* whole-cell experiments varied between 30 and 400 pN. There was a more complex set of unbinding forces than in the *in vitro* experiments. Significantly, there were multiple interactions between in-

dividual receptors with the antibody present on the tip and the receptors on the cell surface (Fig. 3 B). The final force step, after which the receptor and antibody completely separated, was analyzed to estimate the single antibody-receptor unbinding forces. Fig. 3 C shows one example of the data compiled in such histogram. Typically, >3000 steps were used for the plot. The histogram of the last unbinding forces, shown in Fig. 3 C, has the predominant unbinding force  $\sim 60\text{--}70$  pN. This is similar to the unbinding force observed *in vitro*. Maps of the spatial distribution of the last unbinding force between the antibody functionalized AFM tip and the cell membrane did not reveal any characteristic features in distribution of plasma membrane receptors. This is consistent with the uniformly distributed receptors found with immunofluorescence labeling (Fig. 2). The distribution of unbinding forces (data not shown), when the tip conjugated with the nonspecific antibody (another control) was used on the same cell, did not reveal this unbinding force. Hence, the result from the *in vivo* experiments semi-quantitatively agrees with the characteristic unbinding force measured between the antibody-functionalized AFM tip and the isolated VEGF receptors *in vitro*. The correspondence between unbinding forces measured *in vitro* and *in vivo*, suggests that the force-volume map can be used to map the heterogeneous distribution of cell surface macromolecules (channels and receptors) using functionalized AFM tips.

The interaction force was further measured in the presence of excess antibody in the imaging media. The evaluation of

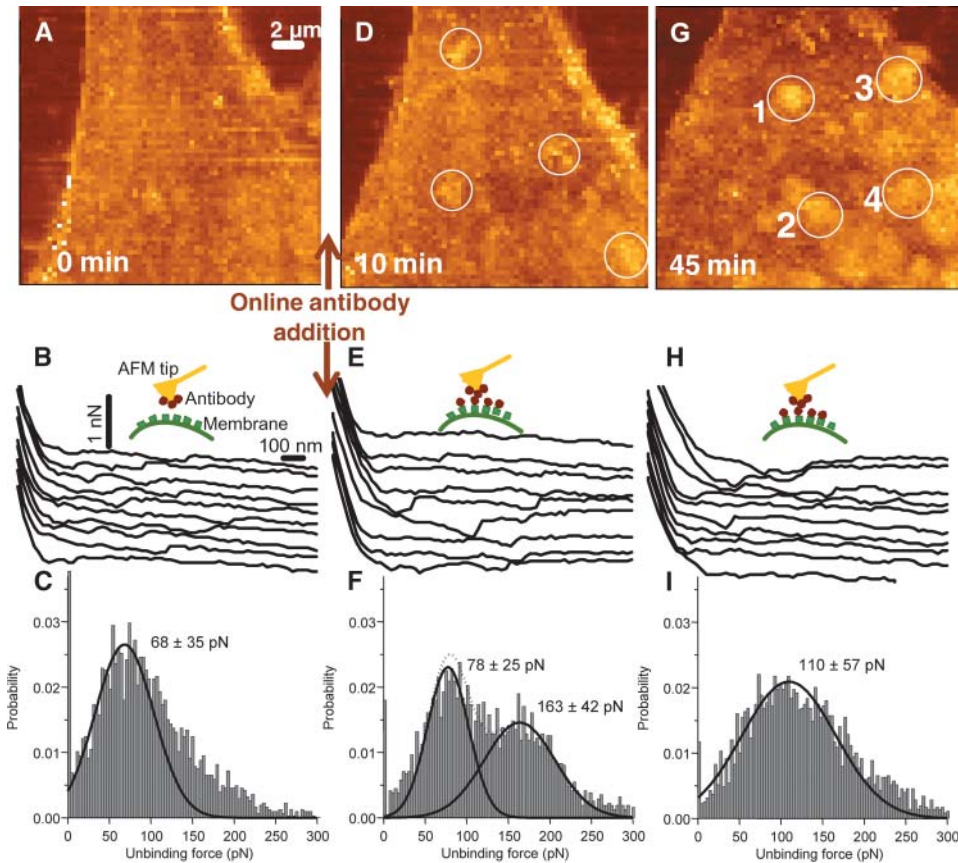


**FIGURE 3** Force maps on endothelial cells in real-time. (A–C) Specific interaction probed with a  $\text{Si}_3\text{N}_4$  tip functionalized with anti-Flk-1. (A) Force map. (B) Force curves taken at various points on the cell from the map shown in A. The curves are offset with respect to zero force. (C) Probability histogram of the unbinding forces of the force curves from the force map in A. The histogram is fitted with a Gaussian and the corresponding maxima and  $\sigma$  is indicated in the figure. The dominant unbinding force  $\sim 60$ – $70$  pN suggests breakage of single receptor-antibody bonds. (D–F) Competitive inhibition probed with the anti-Flk-1 functionalized  $\text{Si}_3\text{N}_4$  tip, 10 min after adding antibody in the recording medium. The panels correspond to A–C. The characteristic unbinding force is suppressed and the measured forces are shifted toward higher values. (G–I) Corresponds to A–C, but at 45 min after adding antibody in the recording medium. The micrometer-sized brighter spots in G are identified as receptor clusters. A few of the clusters are marked by numbers 1–4.

these data revealed the appearance of micrometer-sized spots (clusters) on the cell surface in the excess antibody media. Representative force-volume images from the Nanoscope software are shown in Fig. 3, A, D, and G. These images, in each point, show the tip-sample force at a specified  $z$ -piezo position. There was continuous reorganization of these clusters and the cluster size increased with time as evident in the force maps (Fig. 3, A, D, and G), the maps of dissipated energy (not shown), and in the elasticity maps (Fig. 4 in the next subsection). Maximum clustering was observed 45 min after online addition of antibody, and a few of these clusters are marked with circles and numbered 1–4 in Fig. 3 G. The clusters appeared to be concentrating more toward the cellular boundaries, consistent with the mitogenic activity of VEGFR and the cell growth pattern. Similar clustering of VEGFRs was also observed after adding VEGF online, although the VEGF-induced clustering was less pronounced (data not shown).

As before, the individual unbinding forces between the antibody and VEGFRs were analyzed from the single force curves within a force map (Fig. 3, B, E, and H). The unbinding mostly occurred in several steps for both the sequential-type unbindings and the more complex multiple unbindings. For example, in the force curves of the force map shown in Fig. 3 A, 43% of the force curves have two or

more unbinding points and 66% of these curves had increasing unbinding steps outwards from the surface.

In the presence of excess antibody, the number of measured characteristic antibody-receptor unbinding events (at 60–70 pN) were reduced (compare Fig. 3 C with F and I), possibly due to competing inhibition of interactions of the AFM tip-attached antibody and the plasma membrane receptors. Hence, we could not identify the spatial distribution of clusters simply from maps of the final unbinding step. However, the unbinding forces did not disappear (Fig. 3, E and H). Instead, as seen in Fig. 3 F, additional unbinding forces appear at a higher magnitude (170–190 pN) and the force distribution widens out in time (Fig. 3 I). This could be due to the complexity of other factors and cellular processes not expected in the *in vitro* study. Even in the histogram for the force curves obtained when a regular  $\text{Si}_3\text{N}_4$  tip (without any antibody and serving as a control) was used on the same cell, some adhesion between the tip and the cell surface was observed (data not shown). However, the magnitude of the unbinding forces was then more uniformly distributed in the range of 30–95 pN. The images of calculated total de-adhesion (maps not shown), i.e., the dissipated energy calculated as the area between the trace and retrace force curves, reveal the same qualitative features as the force-volume images. Large total interactions (unbind-

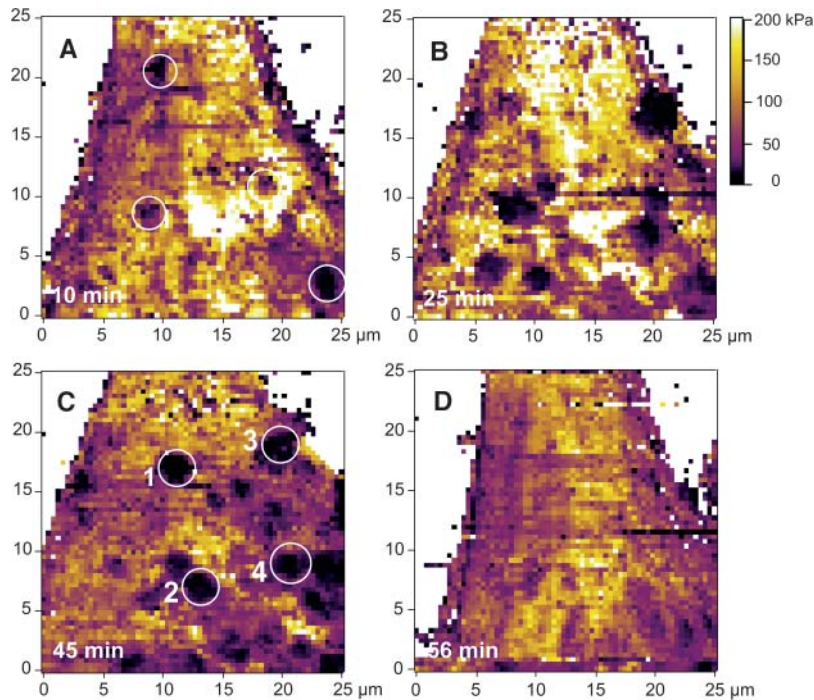


FIGURE 4 Elasticity maps of the evaluated Young's modulus on endothelial cells in real-time, showing clustering of VEGF receptors on the cell surface. The images are color-coded according to the color bar, from 0 kPa (dark) to 200 kPa (bright yellow). The images show the elasticity at different time points after adding anti-flk-1 antibody in the imaging solution: (A) 10 min after addition; (B) 25 min after addition; (C) 45 min after addition; and (D) 56 min after addition. A few regions with lower elasticity are marked with numbers 1–4 in C. These are the same regions showing receptor clusters in Fig. 3 G (marked as 1–4). The regions underlying the receptor clusters appeared as less stiff.

ing) were detected on cluster-like regions, whereas these large de-adhesions were not detected at noncluster regions.

The nature of the experimental paradigm suggests that the excess of the antibody in the imaging medium should compete with the antibody conjugated to the AFM tip for the same binding sites on the VEGFRs. Such condition should give rise to reduced adhesion forces, although individual antibody-receptor binding would still be present. Consistent with such possibility, the clusters diminished significantly 60 min after the addition of IgG as was seen in the maps of dissipated energy (and is further demonstrated in the next subsection).

The clustering and activation of growth factor receptors in general has been reported to precede the formation of receptor dimmers and the subsequent receptor autotyrosin phosphorylation (Jefford and Dubreuil, 2000). Such receptor clusterings could be mediated by appropriate ligands (the ligand-induced clustering) (Kirsch and Betz, 1998) as well as by antibodies (Yauch et al., 1997; Gao et al., 2000). In our study, ligand-induced clustering (after online addition of VEGF) was less pronounced. This is consistent with the results from several other studies and suggests that VEGF binding to endothelial cell receptors induces receptor dimerization, i.e., for each VEGF, two receptors will be clustered. On the other hand, each antibody could bind to several receptors and hence the receptor size would be considerably larger and the clustering would be faster as well. This results in subsequent binding and phosphorylation of the downstream mediators, and also leads to increased cellular calcium (Meyer et al., 1999) and the reorganization of the actin and microtubule cytoskeleton necessary for the

cell growth and migration. During such reorganization, the cellular elastic properties would change as well. We examined such changes in real-time and simultaneously, as discussed in the next subsection.

### Elasticity maps and underlying cytoskeletal elements

The elasticity maps obtained at different times after online addition of anti-Flk-1-antibody are shown in Fig. 4. Initially, the number and total area of low elasticity spots, i.e., clusters, increased and after 45 min almost 20% of the total cell surface was composed of clusters. The difference in elasticity between the individual clusters and the surrounding cytoskeleton significantly increased during the first 25 min after the addition of anti-VEGFR-antibody in the imaging medium (Fig. 4 B). The elasticity maps derived from the force-maps showed significant changes in the local elasticity. Interestingly, the regions underlying the receptor clusters appeared less stiff (compare Fig. 3 G with Fig. 4 C, positions 1–4). The Young's modulus changes were unexpectedly large. The modulus was between 50 and 120 kPa on the outer cell regions and at the leading edge, and ~3–6 kPa around the nucleus and under the receptor clusters.

The decreased elasticity on the clusters causes the AFM tip to indent the surface and form a large set of bonds, increasing the total adhesion upon removal. However, it is difficult to directly correlate the binding force and the change in the elasticity. The elasticity distribution depends on the interaction between the receptors and the cytoskeletal filaments beneath the cellular surface. The localized re-

duction in cell stiffness is consistent with a signal transduction mechanism wherein a localized clustering of VEGF receptors would induce reorganization of the underlying cytoskeletal network (as required for the cellular growth and migration). In addition, the VEGF-induced elevation of cellular calcium (Meyer et al., 1999) will also alter cell elasticity (Quist et al., 2000). Significantly, the change in stiffness was observed within minutes of real-time receptor clustering and was reciprocal to the cluster size, i.e., reciprocal to the receptor density. Thus increased clustering resulted in decreased stiffness. Such real-time mapping of the receptor clustering and of the resultant rapid changes in the cellular biophysical properties is unique to the technique described in this study.

Previous studies have used a longer duration, usually 8–10 h, of ligand- or antibody-induced receptor clustering, to examine changes in the resulting cellular biophysical properties. Such a paradigm suggests that the receptor-clustering induced signal transduction process underlying cellular growth and migration is relatively slow. Alternately, this could reflect a lack of high temporal and spatial resolution techniques for simultaneously mapping receptor clustering as well as the resultant change in the cellular biophysical properties. Moreover, the change in the elastic properties was transient in our study, suggesting a wavelike change in the local cytoskeletal network as the cell undergoes progressive growth and development.

### Implications of results

The VEGF receptor clustering, illustrated in this work, is an example of the dynamic receptor clustering process that mediates various physiological cellular activities. For example, clustering of neurotransmitter receptors at presynaptic regions provides the anatomical basis for receiving an array of synaptic inputs necessary for information processing in the vertebrate brain (Antonova et al., 2001; Horio et al., 1997; Sugiyama et al., 1997; Kirsch and Betz, 1998). Receptor clustering is required for polarized assembly of ankyrins (Jefford and Dubreuil, 2000). Receptor clustering and cytoskeletal association is required for receptor-mediated adhesion to extracellular matrix and for the differential clustering of CD4, and T-cell receptors are required for ligand recognition (Krummel et al., 2000), etc. Measurements of such real-time receptor clustering and of the resultant rapid and order-of-magnitude changes in cellular elastic properties have not been reported previously. The technique described in this study is uniquely suited for such investigations, i.e., to map the distribution and clustering of various biological macromolecules on the cell surface as well as their resulting effects on cellular physical properties.

The remarkably large decreases in local cell stiffness induced by the clustering of VEGF receptors provide a mechanism for cell growth. The rapidity with which these effects can be induced by the appropriate stimuli could have

interesting implications, such as enhancing the prospects for rapid angiogenesis and accelerated vascularization, which in turn could help in the recovery of injured vascular tissue (Gill et al., 2001).

We acknowledge technical help in the AFM studies from Drs. Arjan Quist, Hai Lin, and Ashok Parbhu. We also acknowledge helpful suggestions of the reviewers.

This work was supported by grants from the National Science Foundation (to R.L., S.B.), the National Institutes of Health (to R.L.), the Philip Morris External Grant Program (to R.L.), the Santa Barbara Cottage Hospital Research Grant Program (to R.L., G.P.), and the Swedish Research Council's contract 2001-2585 (to N.A.).

### REFERENCES

- Aileen, C., and T. M. Moy. 2000. Cross-linking of cell surface receptors enhances cooperativity of molecular adhesion. *Biophys. J.* 78:2814–2820.
- Almqvist, N., Y. del Amo, B. L. Smith, N. H. Thomson, Å. Bartholdson, M. Brzenski, R. Lal, and P. K. Hansma. 2001. Micromechanical and structural properties of a pennate diatom investigated by atomic force microscopy. *J. Microsc.* 202:518–532.
- Antonova, I., O. Arancio, A. C. Trillat, H.-G. Wang, L. Zablow, H. Udo, E. R. Kandel, and R. D. Hawkins. 2001. Rapid increase in clusters of presynaptic proteins at onset of long-lasting potentiation. *Science*. 294:1547–1550.
- Baumgartner, W., P. Hinterdorfer, W. Ness, A. Raab, D. Vestweber, H. Schindler, and D. Drenckhahn. 2000. Cadherin interaction probed by atomic force microscopy. *Proc. Natl. Acad. Sci. USA*. 97:4005–4010.
- Benoit, M., D. Gabriel, G. Gerish, and H. E. Gaub. 2000. Discrete interactions in cell adhesion measured by single-molecule force spectroscopy. *Nat. Cell Biol.* 2:313–317.
- Berry, M., T. J. McMaster, A. P. Corfield, and M. J. Miles. 2001. Exploring the molecular adhesion of ocular mucins. *Biomacromolecules*. 2: 498–503.
- Bhatia, R., H. Lin, and R. Lal. 2000. Fresh and globular amyloid- $\beta$  protein (1–42) induces rapid cellular degeneration: evidence for A $\beta$  channel-mediated cellular toxicity. *FASEB J.* 14:1233–1243.
- Boland, T., and B. D. Ratner. 1995. Direct measurement of hydrogen bonding in DNA nucleotide bases by atomic force microscopy. *Proc. Natl. Acad. Sci. USA*. 92:5297–5301.
- Cappella, B., and G. Dietler. 1999. Force-distance curves by atomic force microscopy. *Surf. Sci. Rep.* 34:1–104.
- Cleveland, J., and S. Manne. 1993. A nondestructive method for determining the spring constant of cantilevers for scanning force microscopy. *Rev. Sci. Instrum.* 64:403–405.
- Crouch, M. F., D. A. Davy, F. S. Willard, and L. A. Berven. 2001. Activation of endogenous thrombin receptors causes clustering and sensitization of epidermal growth factor receptors of Swiss 3T3 cells without transactivation. *J. Cell Biol.* 152:263–273.
- Dammer, U., M. Hegner, D. Anselmetti, P. Wagner, M. Dreier, W. Huber, and H. J. Guntherodt. 1996. Specific antigen/antibody interactions measured by force microscopy. *Biophys. J.* 70:2437–2441.
- Gad, M., A. Itoh, and A. Ikai. 1997. Mapping cell wall polysaccharides of living microbial cells using atomic force microscopy. *Cell Biol. Int.* 21:697–706.
- Gao, B., C. Blumenstock, F. A. Minnear, and T. M. Saba. 2000. Increased recycling of integrins by lung endothelial cells in response to tumor necrosis factor. *J. Cell Sci.* 113:247–257.
- Gill, M., S. Diaz, K. Hattori, M. L. Rivera, D. Hicklin, L. Witte, L. Girardi, R. Yurt, H. Himel, and S. Rafii. 2001. Vascular trauma induces rapid but transient mobilization of VEGFR2<sup>+</sup>AC133<sup>+</sup> endothelial precursor cells. *Circ. Res.* 88:167–174.

- Hinterdorfer, P., W. Baumgartner, H. J. Gruber, K. Schilcher, and H. Schindler. 1996. Detection and localization of individual antibody-antigen recognition events by atomic force microscopy. *Proc. Natl. Acad. Sci. USA.* 93:3477–3481.
- Horio, Y., H. Hibino, A. Inanobe, M. Yamada, M. Ishii, Y. Tada, E. Satoh, Y. Hata, Y. Takai, and Y. Kurachi. 1997. Clustering and enhanced activity of an inwardly rectifying potassium channel, Kir4.1, by an anchoring protein. *J. Biol. Chem.* 272:12885–12888.
- Horton, M., G. Charras, and P. Lehenkari. 2002. Analysis of ligand-receptor interactions in cells by atomic force microscopy. *J. Recept. Signal Transd.* 22:169–190.
- Hutter, J. L., and J. Bechhoefer. 1993. Calibration of atomic force microscope tips. *Rev. Sci. Instr.* 64:1868–1873.
- Jefford, G., and R. Dubreuil. 2000. Receptor clustering drives polarized assembly of ankyrin. *J. Biol. Chem.* 275:27726–27732.
- Kirsch, J., and H. Betz. 1998. Glycine-receptor activation for receptor clustering in spinal neurons. *Nature.* 392:717–720.
- Korchev, Y. E., Y. A. Negulyaev, C. R. W. Edwards, I. Vodyanoy, and M. J. Lab. 2000. Functional localization of single active ion channels on the surface of a living cell. *Nat. Cell Biol.* 2:616–619.
- Krummel, M. F., M. D. Sjaastad, C. Wülfing, and M. M. Davis. 2000. Differential clustering of CD4 and CD3 zeta during T-cell recognition. *Science.* 289:1349–1352.
- Lal, R., and S. A. John. 1994. Biological applications of atomic force microscopy. *Am. J. Physiol.* 266:C1–C21.
- Marti, A., G. Hähner, and N. D. Spencer. 1995. Sensitivity of frictional forces to pH on a nanometer scale: a lateral force microscopy study. *Langmuir.* 11:4632–4635.
- Meyer, M., M. Clauss, A. L. Wienhues, J. Waltenberger, H. G. Augustin, M. Ziche, C. Lanz, M. Buttner, H.-J. Rziha, and C. Dahio. 1999. A novel vascular endothelial growth factor encoded by Orf virus, VEGF-E, mediates angiogenesis via signaling through VEGFR-2 (KDR) but not VEGFR-1 (Flt-1) receptor tyrosine kinases. *EMBO J.* 18:363–374.
- Neufeld, G., T. Cohen, S. Gengrinovitch, and Z. Poltorak. 1999. Vascular endothelial growth factor (VEGF) and its receptors. *FASEB J.* 13:9–22.
- Parbhu, A., W. Bryson, and R. Lal. 1999. Disulfide bonds in the outer layer of keratin fibers confer higher mechanical rigidity: correlative nano-indentation and elasticity measurement with an AFM. *Biochemistry.* 38:11755–11761.
- Pawson, T. 1995. Protein modules and signaling networks. *Nature.* 373:573–580.
- Quist, A. P., S. K. Rhee, H. Lin, and R. Lal. 2000. Physiological role of gap-junctional hemichannels: extracellular calcium-dependent isoosmotic volume regulation. *J. Cell Biol.* 148:1063–1074.
- Rameh, L. E., and L. C. Cantley. 1999. The role of phosphoinositide 3-kinase lipid products in cell function. *J. Biol. Chem.* 274:8347–8350.
- Rhee, S. K., A. P. Quist, and R. Lal. 1998. Amyloid- $\beta$  protein-(1–42) forms calcium-permeable  $Zn^{2+}$ -sensitive channel. *J. Biol. Chem.* 273:13379–13382.
- Ros, R., F. Schwesinger, D. Anselmetti, M. Kubon, R. Schäfer, A. Plückthun, and L. Tiefenauer. 1998. Antigen binding forces of individually addressed single-chain Fv antibody molecules. *Proc. Natl. Acad. Sci. USA.* 95:7402–7405.
- Shroff, S. G., D. R. Saner, and R. Lal. 1995. Dynamic micromechanical properties of cultured rat atrial myocytes measured by atomic force microscopy. *Am. J. Physiol.* 38:C286–C292.
- Sneddon, I. N. 1965. The relation between load and penetration in the axisymmetric Boussinesq problem for a punch of arbitrary profile. *Int. J. Eng. Sci.* 3:47–57.
- Stark, M., C. Möller, D. J. Müller, and R. Guckenberger. 2001. From images to interactions: high-resolution phase imaging in tapping-mode atomic force microscopy. *Biophys. J.* 80:3009–3018.
- Sugiyama, J. E., D. J. Glass, G. D. Yancopoulos, and Z. W. Hall. 1997. Laminin-induced acetylcholine receptor clustering: an alternative pathway. *J. Cell Biol.* 139:181–191.
- Thomas, K. A. 1996. Vascular endothelial growth factor, a potent and selective angiogenic agent. *J. Biol. Chem.* 271:603–606.
- VanLandingham, M. R., S. H. McKnight, G. R. Palmese, X. Huang, T. A. Bogetti, R. F. Eduljee, and J. W. Gillespie, Jr. 1997. Nanoscale indentation of polymer systems using the atomic force microscope. *J. Adhes.* 64:31–59.
- Wang, W., W. L. Dentler, and R. T. Borchardt. 2001. VEGF increases BMEC monolayer permeability by affecting occluding expression and tight junction permeability. *Am. J. Physiol. Heart Circ. Physiol.* 280:H434–H440.
- Yauch, R. L., D. P. Felsenfeld, S. K. Kraeft, L. B. Chen, M. P. Sheetz, and M. E. Hemler. 1997. Mutational evidence for control of cell adhesion through integrin diffusion/clustering, independent of ligand binding. *J. Exp. Med.* 186:1347–1355.
- Yuan, C. B., A. Chen, P. Kolb, and V. T. Moy. 2000. Energy landscape of streptavidin-biotin complexes measured by atomic force microscopy. *Biochemistry.* 39:10219–10223.
- Zhang, X. H., E. Wojcikiewicz, and V. T. Moy. 2002. Force spectroscopy of the leukocyte function-associated antigen-1 intercellular adhesion molecule-1 interaction. *Biophys. J.* 83:2270–2279.

# Lab 9: Molecular force spectroscopy on living cells

**Location:** 8-214

**PI:** Krystyn Van Vliet

**Lab Instructors:** Dessy Nikova

## Summary

In this laboratory, you will use the atomic force microscope to acquire the mechanical interaction forces between the AFM probe and the surface of living human microvascular endothelial cells. By pushing into the cell surface, the stiffness of various points on the cell can be determined qualitatively. By pulling away from the cell surface, the adhesion force between the probe and specific points on the cell membrane can be measured, including the imaging of single cell surface molecules. Both of these loading approaches are used to infer changes in the cell surface / interior as a function of mechanical or chemical environments, and as a function of disease state.

## Recommended Reading

K. J. Van Vliet and P. Hinterdorfer, "Probing drug-cell interactions," *Nano Today* **1**.

C. Stroh, *et al.* "Single-molecule recognition imaging microscopy," *PNAS* **101**.





# Probing drug-cell interactions

Over the past two decades, the subset of scanning probe microscopy termed atomic force microscopy (AFM) has become a ubiquitous tool to image nanoscale structure and to estimate certain mechanical characteristics of biological entities ranging from DNA to tissues. Various modes of imaging and force spectroscopies have been developed to correlate structure, properties, and chemomechanical interactions of molecules and cells in aqueous environments. These advances in AFM have led rapidly to *in situ* investigations of drug-induced changes in cell structure, membrane stability, and receptor interaction forces.

Krystyn J. Van Vliet<sup>1</sup> and Peter Hinterdorfer<sup>2</sup>

<sup>1</sup>Department of Materials Science and Engineering, Massachusetts Institute of Technology, 77 Massachusetts Avenue, Room 8-237, Cambridge, MA 02139 USA

E-mail: [krystyn@mit.edu](mailto:krystyn@mit.edu)

<sup>2</sup>Institute for Biophysics, Johannes Kepler Universität Linz, Altenbergerstr. 69, A-4040, Linz, Austria

E-mail: [peter.hinterdorfer@jk.uni-linz.ac.at](mailto:peter.hinterdorfer@jk.uni-linz.ac.at)

The AFM was originally developed as an adaptation of another scanning probe microscopy technology, the scanning tunneling microscope, to image nonconductive materials through direct physical contact between a cantilevered probe and a sample surface<sup>1</sup>. Although not originally conceived to image biological structures, the researchers who developed this tool quickly recognized that the piconewton-scale force and nanometer-scale displacement resolutions of the AFM enable the topographical scanning of mechanically compliant materials, including biological structures in aqueous environments. Haberle *et al.* introduced this approach as 'underwater AFM' and demonstrated the capacity to image changes in the structure and topography of capillary-bound red blood cells as a function of hypotonicity and after binding of antibodies. They modestly suggest that this approach enables

*in situ* study of a range of dynamics at the surface of living cells<sup>2</sup>. Current research underscores the significance of this invention, as an increasing array of imaging and force spectroscopy modes have been developed to exploit this simple concept: intermolecular forces can be measured directly and can also be harnessed to image a macromolecular structure with subnanometer spatial resolution.

The operating principles of all AFMs include three key features, as shown in Fig. 1a: a reflective, cantilevered probe; a laser-photodiode-piezocrystal feedback loop that maintains either constant deflection or oscillation amplitude of the cantilever through displacement of the cantilever base in the vertical plane; and a piezo-actuated scanner that translates either the cantilever or the sample in the horizontal plane. Several modifications to the basic imaging modalities (constant contact

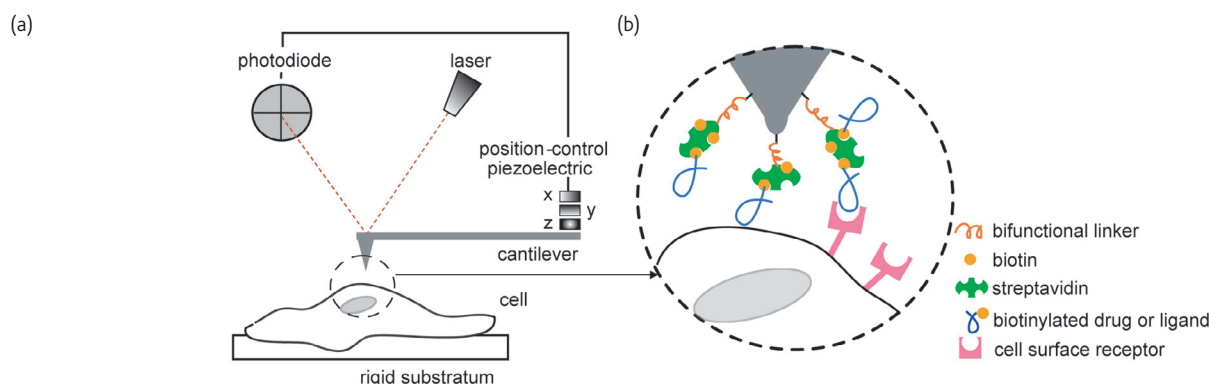


Fig. 1 Schematic of AFM principal components (a) and probe functionalization approaches to quantify intermolecular forces between surfaces such as individual drugs or molecular ligands and cell surface receptors (b). (Adapted from<sup>73</sup>. Reprinted with permission. © 2003 Elsevier.)

mode, or iso-force imaging; and dynamic contact mode, or iso-amplitude imaging) enhance the resolution of hydrated biological structures in fluid and enable direct measurement of intermolecular binding (e.g. electromagnetic oscillation of the free-end of magnetically coated cantilevers, termed MAC mode<sup>3</sup>). As in all scanning probe microscopies, images comprise rastered lines of pixels, and acquired signals are represented as image contrast. Topography or height images indicate micron-scale displacement of the cantilever base. Deflection images indicate the nanoscale error signal in the contact mode iso-force feedback loop, and typically provide impressive image contrast for mechanically heterogeneous structures such as living cells. Amplitude images indicate the error signal in the iso-amplitude feedback loop and are indicative of energy absorption. Phase images indicate the phase lag between the cantilever base and free-end and are also indicative of energy absorption. The interpretation of these images in terms of mechanical properties is an area of active research<sup>4-6</sup>. The independent control of cantilever displacement normal to the sample surface also enables force spectroscopy, the measurement of the force-displacement response resulting from contact at discrete points on the sample surface and/or extension of a biomacromolecule that is chemically adhered to the cantilever and the sample surface. These chemomechanical interactions can be obtained during scanning in various modes to acquire mechanical and binding force concurrently with topography<sup>7</sup>, and relate directly to local mechanical properties<sup>8,9</sup> and intermolecular binding kinetics<sup>10</sup>.

Time-lapsed imaging and force spectroscopy afforded by environmentally controlled AFM has led to significant progress in probing the mechanisms by which biological and synthetic chemicals, including therapeutic drugs, interface with and modify the structure and function of individual living cells in real time. The drug-cell interactions studied cover a wide range of fields and objectives, but the majority of these applications seek to clarify the dynamics of structural adaptations within the cell that correlate with mechanical functions such as motility, reorganization of the cell membrane that serves as the interface between the cell and the extracellular environment, and characterization

of the binding between drugs – here, considered naturally occurring and synthetic therapeutic reagents – to cell surface receptors that induce new metabolic responses. Here, we present an overview of this emerging field, as enabled by direct measurement and analysis of the nanomechanical interactions between molecules.

## Structural dynamics

The earliest reported and most common consideration of drug-cell interactions is in terms of structural adaptations of the whole cell and the intracellular structures of mammalian cells that are adherent, meaning that these cells attach readily to solid surfaces. This mechanical imaging of cell response to drugs that induce morphological differentiation, such as retinoic acid induction of neuroblastoma cells<sup>11</sup>, or that cause disruption of cytoskeletal networks, such as cytochalasin-D disintegration of cytoskeletal actin<sup>12</sup>, was initially considered as a complement to optical microscopy approaches that could provide the same structural information at lower spatial resolution (~400 nm). However, the additional understanding of drug mechanisms afforded by mechanical probing of cells was soon recognized, and discrete indentation force-displacement ( $F-d$ ) responses were analyzed to estimate the mechanical compliance of cells in response to drugs targeting different components of the cytoskeleton<sup>13-16</sup>. In such studies, cells (or at least the probed volumes of the cells) are assumed to act as a linear elastic material that is thick compared to the contact depth  $d$ , and an effective elastic modulus is inferred from the Hertzian elastic solution for a sphere ( $F \propto Ed^{3/2}$ ) or a cone ( $F \propto Ed^2$ ) depending on the cantilevered probe geometry. Fig. 2 illustrates the mechanical consequence of drug-induced disruption of the cytoskeletal network over time, where  $E$  is estimated for each pixel of the image. This approach is not appropriate for rapid structural or mechanical adaptations because of the timescale of such experiments. Imaging speed of a single cell of image size and resolution comparable to Fig. 1a is limited not by the instrument, but by the fragility of the cells, and requires <5 min/image. However, the individual  $F-d$  acquisitions required to construct Figs. 1b and c require on the order of 1 s/pixel and

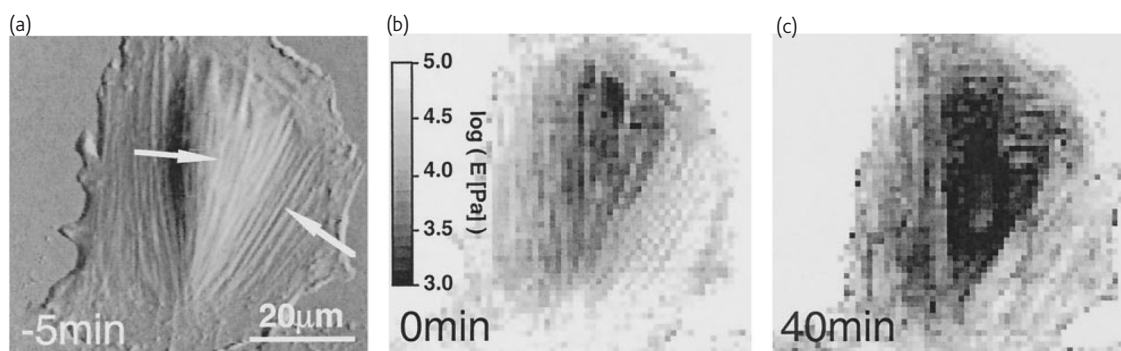


Fig. 2 Increased compliance of NRK fibroblast cells induced by cytoskeletal protein agonists. (a) Deflection or contact-mode error signal image before introduction of 10 mM cytochalasin D; arrows indicate filamentous-actin stress fibers. Effective indentation elastic modulus  $E$  for discrete points along the cell at the time at which this drug is introduced (b) and 40 min post-exposure (c) indicate that disintegration of actin networks correlates directly with increased compliance of the cell. (Reprinted with permission from<sup>15</sup>. © 2000 The Biophysical Society.)

thus >10 min/image, a throughput which decreases directly with increasing image resolution.

The structural adaptations induced by naturally occurring soluble biomolecules is equally valuable, especially when such lipo- and glycoproteins are possible catalysts for pathologies such as Alzheimer’s disease<sup>17</sup>, HIV<sup>18</sup>, and cancers<sup>19</sup>, and therefore candidate targets for new drugs. As demonstrated by Rotsch *et al.*<sup>19</sup> in Fig. 3, so-called growth factors can alter not just the morphology of cancer cell lamellipodia, but also the mechanical compliance of these structures. Such correlations enable testable hypotheses of how cells move, generate, and respond to force (mechanobiology<sup>20</sup>), and can also clarify how drugs affect cell behavior at the functional level<sup>21</sup>. For example, Fig. 4 illustrates direct measurement of increased cell volume for adhered vascular endothelial cells in response to the hormone aldosterone, and reversal of this affect upon the addition of spironolactone, a potential drug to inhibit vasculopathy or abnormal swelling of capillaries<sup>22-24</sup>. Imaging of drug-induced structural dynamics within and between cells in this way is particularly well suited to the study of antibiotic effects on bacteria<sup>25-28</sup>, as these cells are significantly smaller than adherent mammalian cells

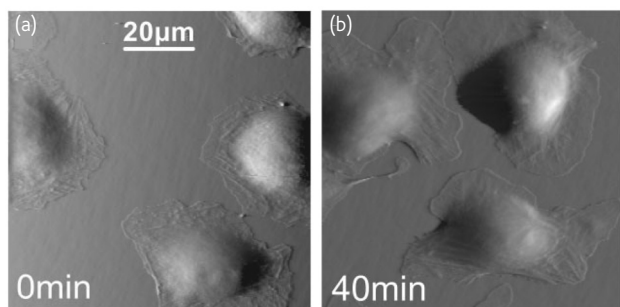


Fig. 3 Deflection or contact-mode error signal images and corresponding force-displacement responses of cancer cells (adenocarcinoma) demonstrate that 5 nM of epithelial growth factor, a naturally occurring protein secreted by tumor cells, induces extension and increased elastic compliance of lamellipodia. This structural/mechanical observation supports the hypothesis that the force generated by the lamellipodia of metastatic tumor cells is due in part to gel-swelling when actin networks are biochemically severed. (Reprinted with permission from<sup>19</sup>. © 2001 Elsevier.)

for which function is increasingly appreciated to depend on both chemical and mechanical cues<sup>29,30</sup>.

### Membrane dynamics

As the cell membrane is the physical and functional interface between the extracellular cues and intracellular genetic machinery that modifies cell function, the dynamics of the cell surface and physical models of this surface in response to soluble drugs or drug delivery vehicles are of keen interest. Pelling *et al.*<sup>31</sup> measured the mechanical oscillations of the yeast cell wall as a function of temperature to estimate the required activation energy of such oscillations (Fig. 5). From the absence of these periodic fluctuations in the presence of sodium azide, a potent inhibitor of adenosine triphosphate (ATP) synthesis within the cell, the authors

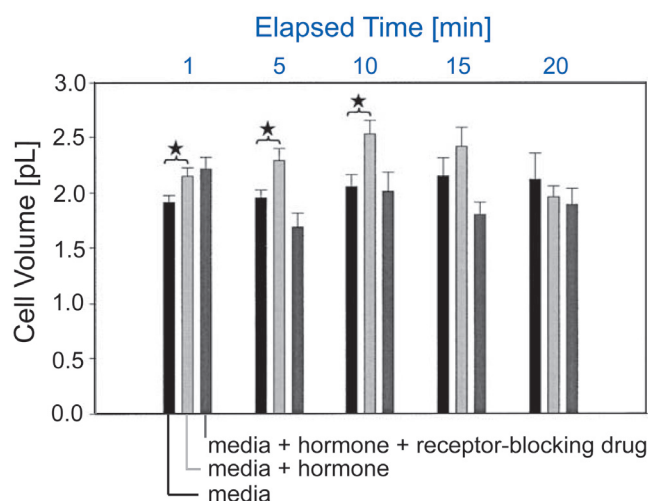


Fig. 4 Three-dimensional topology enables testing of hypotheses regarding drug mechanisms, without idealization of cell shape. Human umbilical vein endothelial cells swell within 1 min post-exposure to soluble aldosterone, a hormone. Stars indicate significant difference in mean values. This swelling is inhibited by the addition of the drug spironolactone, which blocks intracellular receptors, indicating that spironolactone is a possible therapy to prevent capillary swelling that restricts blood flow during inflammation. (Reprinted with permission from<sup>22</sup>. © 2003 Springer.)

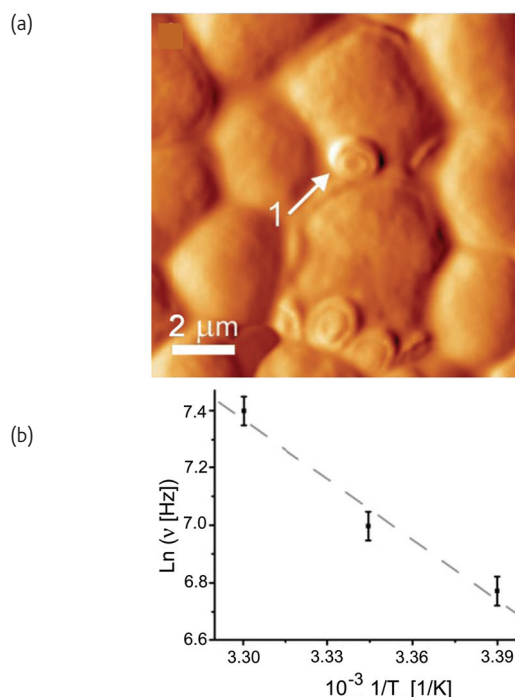


Fig. 5 Direct measurement of cell membrane mechanical oscillations allows consideration of how intracellular mechanosensory proteins are affected by drugs. (a) Deflection or contact-mode error signal image of dead yeast cells adsorbed to mica. Arrow indicates rigid bud scar. (b) Sustained acquisition of the force-displacement response at individual points on living yeast cell walls indicates a temperature-dependent oscillation frequency with activation energy of  $\sim 58$  kJ/mol, consistent with that of molecular motor proteins such as myosin. These oscillations are absent in the presence of sodium azide, which inhibits production of the ATP required by molecular motor proteins. (Reprinted with permission from<sup>31</sup>. © 2004 American Association for the Advancement of Science.)

inferred that these membrane dynamics were the result of ATP-dependent molecular motor proteins such as myosin<sup>31</sup>.

Nonadherent cells such as erythrocytes and lymphocytes must be adhered to rigid substrata in order to analyze them using AFM, and therefore results should be interpreted with caution<sup>32,33</sup>. However,

Girasole *et al.*<sup>34</sup> demonstrate that certain membrane characteristics of erythrocytes are not compromised by this gross change in cell shape, and that membrane undulations characteristic of certain pathologies can be induced by drugs to study the root causes, time course, and possible treatments of such diseases (Fig. 6).

The development of materials for drug<sup>35-40</sup> and gene<sup>41</sup> delivery into cells and cell nuclei requires understanding of how such vehicles interact with the cell membrane, for which time-lapse analysis of membrane dynamics is key<sup>37,42</sup>. Through a combination of AFM and confocal optical microscopy, Almofti *et al.*<sup>36</sup> identified the charge ratio of lipids required to produce lipid-DNA complexes (lipoplexes) that were efficiently incorporated within the cell through direct fusion with the cell membrane (Figs. 7a-c). Shahin *et al.*<sup>43</sup> subsequently demonstrated that the dilation of pore complexes on the nuclear membrane – as may be required of efficient drug or gene delivery – is rapidly induced by the steroid dexamethasone (Fig. 7d). Others have demonstrated nuclear pore dynamics in response to different drugs<sup>44,45</sup>. Considering model and isolated cell membranes, Hong *et al.*<sup>46</sup> demonstrated how dendrimers considered as candidate gene delivery vehicles can induce pore formation of certain phospholipid regions, which may be further developed as a mechanism for gene uptake or mitigated if such porosity compromises cell survival (Fig. 7e). Indeed, the spatial and temporal resolution afforded by AFM imaging provides access to the kinetics of such membrane reorganization in response to drugs, at least in lipid bilayer models adhered to rigid substrata (Fig. 8)<sup>47,48</sup>.

## Cell surface receptor interactions

Certainly, the most basic level of drug-cell interaction is at the intermolecular level, and nanomechanical measurement and *in situ* analysis of such ligand-receptor and antigen-antibody binding provides an unparalleled opportunity to study this initiation of the drug response in living cells. Here, force spectroscopy between molecular pairs can be measured at the single molecule level. For simplification, we will refer to the ligand as the probe-bound molecule, and the receptor as the molecule presented at the sample surface; strictly, a ligand is a molecule

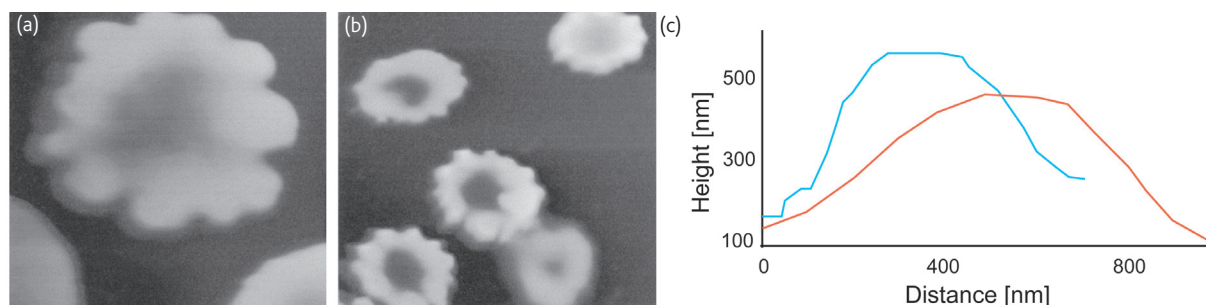
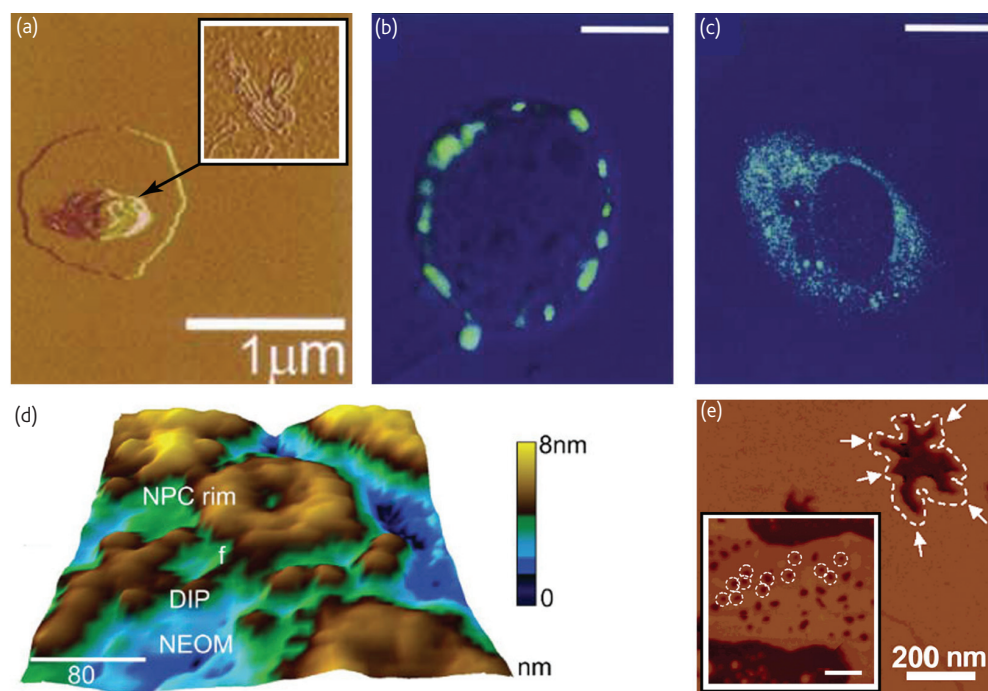
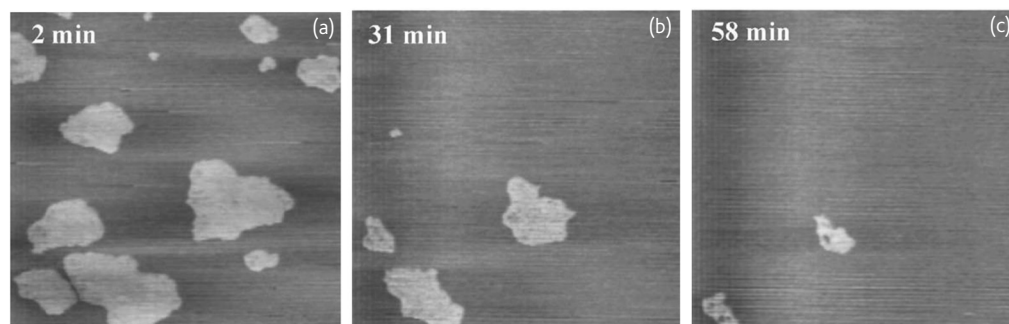


Fig. 6 Drug-induced correlations with membrane morphology of diseased cells can be investigated with limited success in cells that are not adherent *in vivo*, such as erythrocytes (red blood cells). Height images of erythrocytes from human patients with (a) the pathology, anisopoichilocytosis; and (b) no pathology, but incubated with 2 mg/mL lecithin show similar spicule formation. Cell diameter  $\sim 7$   $\mu$ m. (c) Three-dimensional topology of individual membrane protrusions indicates statistical difference in morphology when induced via  $>2$  mg/mL lecithin (blue) or via 200  $\mu$ L chlorprozamine in hypotonic media (red). (Reprinted with permission from<sup>34</sup>. © 2001 Blackwell.)



**Fig. 7** Characterization of drug and gene delivery vehicles and mechanisms enhances vehicle development. (a) Deflection or contact-mode error signal image of lipoplex, a liposome containing DNA (DNA image, inset). Confocal optical microscopy of cells transfected with these lipoplexes for 1 h show the lipoplexes are constrained near the cell membrane in the presence of endocytosis inhibitors (b), whereas cells transfected in the presence of membrane fusion inhibitors do not show such localization (c). Scalebars in (b) and (c) = 10  $\mu\text{m}$ . This study identified the charge ratio required for internalization of lipoplexes for gene delivery. (d) Pores in nuclear membranes (NPCs) are dilated upon exposure to the steroid dexamethosone via induction of protein synthesis (DIP). NEOM is the nuclear envelope outer membrane. Scalebar = 80 nm. (e) Height image of lipid bilayers, representative of cell membranes, show that drug delivery via poly(amidoamine) dendrimers induces ~30 nm-diameter holes that grow via removal of lipids from the initial defect area (arrows). Inset scalebar = 200 nm. (Parts (a), (b), and (c) reprinted with permission from<sup>36</sup>. © 2003 Elsevier. Part (d) reprinted with permission from<sup>43</sup>, © 2005 Wiley.)



**Fig. 8** As model cell membranes, lipid bilayers indicate kinetics of membrane reorganization in response to drugs. Time-lapse height images in constant-deflection mode of a choline phospholipid bilayer comprising DPPC (dipalmitoylphosphatidylcholine, gel phase) and DOPC (dioleoylphosphatidylcholine, fluid phase) on mica show rapid dissolution of the gel phase upon exposure to azithromycin, indicating reduced membrane stability in response to this drug. 7.5  $\mu\text{m}$   $\times$  7.5  $\mu\text{m}$  image size, with grayscale white corresponding to a height of 10 nm. (Reprinted with permission from<sup>48</sup>. © 2004 Elsevier.)

that induces a biochemical response by binding specifically to another molecule, its receptor, via various mechanisms such as change in receptor conformation. A pharmaceutical drug can comprise a portion of a naturally occurring ligand, or an entire antibody that inhibits ligand binding to the intended receptor.

There are several potential advantages of such direct visualization and quantification of drug binding to intact cell surfaces. Firstly, receptor distribution can be mapped with spatial resolution superior to that afforded by immunocytochemical staining (fluorophore-labeled

antibodies), and can be directly correlated with structural and mechanical subcellular features such as cytoskeletal filament association. Secondly, the receptor locations are determined without permanent occlusion of the receptor, enabling time-lapse analysis of receptor binding under modified chemical environments. Thirdly, the unbinding or rupture force  $F_R$  of the molecular pair is measured directly and can be related to binding affinities that characterize ligand binding kinetics. For the disciplines of biophysics and biological engineering as well as the pharmaceutical industry, this nanoscale functional mapping

of molecular interactions enables access to drug mechanisms, comparison of binding affinities among several candidate ligands, and even identification of previously unknown receptors. This approach is particularly well suited to consideration of ligands that are not amenable to conventional (fluorophore or radioactive isotope) labeling and of receptors with relatively low spatial density and mobility. Certainly, the rates of lateral diffusion and internalization of receptors within the cell membrane must be considered with respect to experimentally attainable scanning rates and resolutions. Nanomechanical imaging cannot easily distinguish a single feature that moves with timescales commensurate with the scanning rate from multiple features that do not move, and therefore interpretation of images demonstrating ligand-receptor interactions on living cell surfaces requires particular caution. We do not discuss all of the ligand-cell surface receptor pairs reported to date, but highlight different nanomechanical approaches that demonstrate the specificity of drug-cell interactions.

Key considerations in such experiments include validation of probe functionalization to ensure that the tethered ligand is present and oriented such that it can actively bind its receptor<sup>49,50</sup>; accurate characterization of the cantilever spring constant  $k_c$  to convert deflection  $\delta$  to force  $F = k_c\delta$ <sup>51,52,53</sup>; and demonstration of binding specificity through, for example, competitive binding that eliminates measurable  $F_R$  with the soluble ligand<sup>54</sup> or ion-dependent disruption of receptor binding<sup>55</sup>. Quantification of the ligand-receptor unbinding or rupture force  $F_R$  has been impressively demonstrated for a large number of proteins, with one tethered to the cantilevered probe and the other adhered to rigid substrata such as mica and Au<sup>7,50,56-70</sup>. Of greater relevance to drug-cell interactions,  $F_R$  has also been reported between probe-bound ligands and receptors presented by cells that are typically<sup>16,64,71-74</sup> but not always<sup>54,75,76</sup> chemically fixed. Such ligand-receptor interactions on rigid surfaces or cell membranes were initially acquired 'blindly.' That is, ligand-receptor interrogation consisted of either acquisition of many  $F - d$  responses at individual, randomly selected or topographically interesting sites, with no corresponding image of receptor distribution; or acquisition of single  $F - d$  responses at each of many pixels comprising an image as in Fig. 1b providing a pixelated image of strong binding regions that were considerably larger than individual receptors. This approach is amenable to all custom-built and commercial AFMs, but does not afford mapping of the ligand-receptor interactions with molecular-scale spatial resolution (pixel size larger than hundreds of nanometers) and suffers from low throughput that is insufficient for rapid cell responses. Alternatively, for the  $\sim 10$  nm-scale amplitude typical of magnetically driven oscillation<sup>3</sup>, deconvolution of the amplitude maxima and minima provides image contrast arising from strong probe-sample binding (recognition image) and sample topography (height image), respectively. The molecular resolution of this direct-binding approach, termed recognition imaging, has been demonstrated for several molecular pairs on rigid

surfaces<sup>7,56,77-82</sup>. As shown in Fig. 9 for vascular endothelial cells, the approach provides the potential to image both the receptor distribution and to gather robust ligand-receptor  $F_R$  distributions on cell surfaces.

The extent to which the magnitude of  $F_R$  depends on the ligand-receptor pair, the experimental parameters employed, and the mechanical compliance of the receptor-presenting surface remain open and important questions that are currently being investigated through computational simulations such as steered molecular dynamics<sup>59-61</sup>. For molecules adhered to rigid substrates including chemically fixed cells,  $F_R$  is on the order of 50 pN to 1000 pN (a distribution depending in large part on loading rate, as established through Bell's theorem<sup>10</sup>). This dependence of  $F_R$  distribution on experimental parameters can be used

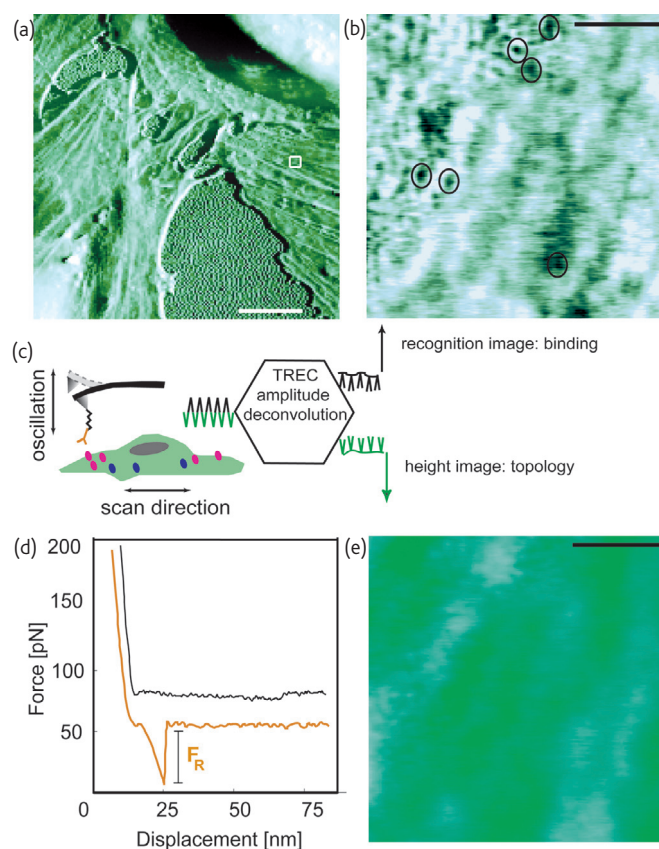


**Fig. 9** Imaging of receptor distribution and ligand/antibody binding on intact cells. (a) Height or topography image of human umbilical vein endothelial cell region in magnetically actuated oscillation mode (MAC). Scalebar = 20  $\mu\text{m}$ . (b) Cantilever deflection during oscillation of a ligand or antibody-functionalized probe can be deconvolved into a recognition image, where image contrast is a function of probe-surface binding (c), and a topography image (d). Scalebars = 500 nm. This deconvolution scheme is termed TREC<sup>®</sup>. Specificity of this binding is demonstrated through competitive inhibition of soluble ligands/antibodies, and changes in binding to or in response to drugs are imaged directly. The rupture force  $F_R$  between the functionalized probe and cell surface can also be measured pointwise to construct spatially coarse maps of receptor presence (orange) or absence (black), or to compare binding avidity in response to drugs. (Parts (a), (b), (d), and (e) are courtesy of S. Lee and K. J. Van Vliet, Massachusetts Institute of Technology. Part (c) adapted from<sup>56</sup>. Reprinted with permission. © 2006 Nature Publishing Group.)

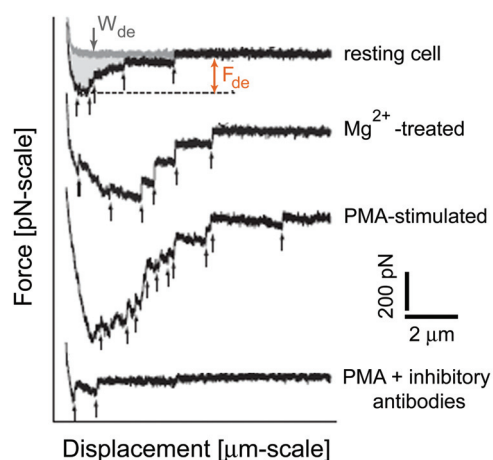


Fig. 10 Adhesion between whole cells and ligand-functionalized rigid surfaces can be explored in the presence of drugs to interpret mechanisms of action. Here, the drug phorbol myristate acetate (PMA) is demonstrated to increase the number of interactions between a cell bound to a cantilevered probe and an intercellular adhesion molecule (ICAM)-functionalized surface and to increase the corresponding work of de-adhesion  $W_{de}$ , but not to affect the quantum of force between the cell surface and this ligand. Disruption of the ICAM receptor via addition of  $Mg^{2+}$  and disruption of ICAM signaling via addition of inhibitory antibodies mitigate this enhanced adhesion in different ways. Cell mechanical compliance also increased with increased cell-ligand adhesion. (Reprinted with permission from<sup>86</sup>. © 2003 The Company of Biologists.)

advantageously to estimate the energy landscape and kinetic quantities governing this interaction. For example, the rate of dissociation between the molecules  $k_{off}$  is inversely proportional to the time required to achieve  $F_R$  at a given applied force, as demonstrated for the  $Ca^{2+}$ -dependency of cadherin-cadherin binding<sup>55</sup>. Such kinetic constants define the speed, specificity, and strength of drug-receptor interactions, while other complementary experimental approaches such as surface plasmon resonance do not provide access to single molecule analysis<sup>58</sup>.

By adhering whole cells to AFM cantilevers, the ligand-receptor interactions governing adhesion between probe-bound and rigid surface-

bound ligands or whole cells can be considered at the single-cell level<sup>83-87</sup>. Although such experiments do not quantify receptor distribution or binding kinetics between individual ligand-receptor pairs, the drug-susceptibility of such intracellular adhesive interactions are key to pathological processes such as adhesion of cancer cells to endothelial cell-lined capillaries during metastasis. By quantifying the work of de-adhesion  $W_{de}$  directly from the  $F-d$  response, it has been demonstrated that phorbol myristate acetate enhances the adhesion of leukocytes to monolayers of vascular endothelial intercellular adhesion molecules (ICAMs) by increasing the number of cancer cell receptors, but not the  $F_R$  between those receptors and ICAMs (Fig. 10)<sup>86</sup>. In contrast, adhesion of leukocytes to adherent endothelial cell monolayers is increased significantly by the stimulation of endothelial cells by tumor necrosis factor- $\alpha$  (Fig. 11), and these mechanisms can be considered together by comparing  $W_{de}$  at endothelial cell-cell junctions with that at cell bodies<sup>83</sup>. Liu *et al.*<sup>85</sup> have applied this whole cell approach to molecular-level adhesion in the search for novel antibiotics that prevent bacterial adhesion to surfaces. They found that the anecdotal prevention of bacterial infections via cranberry juice is not supported by a reduction in adhesion forces between *E. coli* bacteria and inorganic materials in the presence of this acidic media.

## Summary

Applications and modifications of AFM provide the capacity to simultaneously map the structure and chemomechanical interactions of whole cells, membranes, and individual molecular receptors at or below the nanoscale. This enables systematic, *in situ* characterization of the mechanisms governing drug-cell interactions at the *in vitro* level. Although the near-molecular image resolution and single-molecule interaction force resolution of these approaches are impressive, it is important to note several current limitations of this contact-based approach for efficient discovery of new pharmaceutical solutions and understanding of existing mechanisms of drug action. These include restriction to two-dimensional, *in vitro* cell culture environments; low

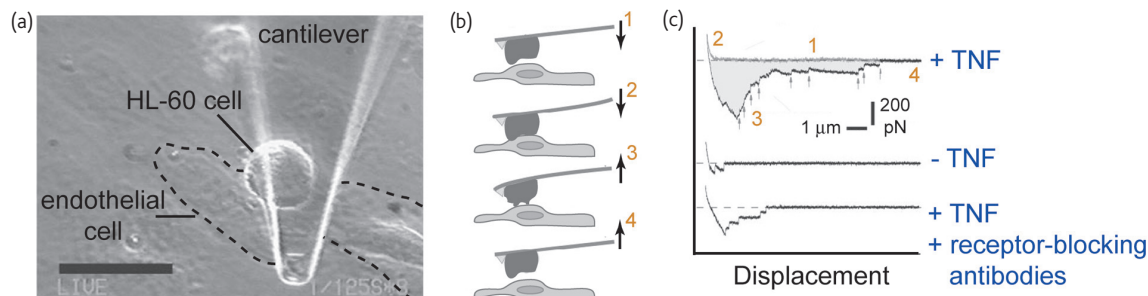


Fig. 11 Cell-cell adhesion can be modulated by drugs and measured through direct force-displacement responses. (a) A human promyelocytic leukemia (HL-60) cell adsorbed to a silicon nitride cantilever is positioned over a human umbilical vein endothelial cell monolayer, e.g. at cell-cell junctions. (b) The force-displacement response during adhesion and de-adhesion is acquired. (c) The work of de-adhesion (shaded) is increased when endothelial cells are stimulated by tumor necrosis factor- $\alpha$  (TNF), and reduced when cell-cell adhesion receptors are blocked by antibody binding. Adhesion between cancer and endothelial cells is required in metastasis, and such studies enable testing of drugs to mitigate this interaction. (Adapted from<sup>83</sup>. Reprinted with permission. © 2004 American Physiological Society.)

throughput relative to the timescale of many cell responses (e.g. translational diffusion of receptors along membranes) and to the variability among cells within a population; and the potential to induce confounding cell responses by mechanical perturbing of the cell surface and its receptors. As these important current constraints are recognized and addressed through experimental and computational innovations, it is expected that this dynamic nanomechanical mapping of ligand-receptor interactions at the single-cell level will be key to scientific

advances in understanding, identifying, and developing therapies that promote human health. 

## Acknowledgments

*KJV gratefully acknowledges the support of the US National Science Foundation Nanoscale Exploratory Research program and the Arnold and Mabel Beckman Foundation Young Investigator Program. PH acknowledges the support of the Austrian National Science Fund and the Austrian Nano and GENAU initiative from the Austrian Ministry of Education, Science and Culture.*

## REFERENCES

- Binnig, G., et al., *Phys. Rev. Lett.* (1986) **56**, 930
- Haberle, W., et al., *J. Vac. Sci. Technol. B* (1991) **9**, 1210
- Leuba, S. H., and Lindsay, S. M., *Biophys. J.* (1998) **74**, A71
- Couturier, G., et al., *J. Phys. D: Appl. Phys* (2001) **34**, 1266
- Erts, D., et al., *J. Phys. Chem. B* (2003) **107**, 3591
- Benmouna, F., et al., *Langmuir* (2003) **19**, 10247
- Kienberger, F., et al., *Acc. Chem. Res.* (2006) **39**, 29
- Sato, M., et al., *J. Biomech.* (2000) **33**, 127
- Sugawara, M., et al., *Hear. Res.* (2002) **174**, 222
- Bell, G. I., *Science* (1978) **200**, 618
- Bonfiglio, A., et al., *Exp. Cell Res.* (1995) **216**, 73
- Bushell, G. R. et al., *Cytometry* (1999) **36**, 254
- Wu, H. W., et al., *Scanning* (1998) **20**, 389
- Braet, F., et al., *J. Electron Microsc.* (2001) **50**, 283
- Rotsch, C. and Radmacher, M., *Biophys. J.* (2000) **78**, 520
- Charras, G. T. and Horton, M. A., *Biophys. J.* (2002) **82**, 2970
- Zhu, Y. J., et al., *FASEB J.* (2000) **14**, 1244
- Barboza, J. M. et al., *Arch. Androl.* (2004) **50**, 121
- Rotsch, C., et al., *Ultramicroscopy* (2001) **86**, 97
- Thompson, M. T., et al., *Biomaterials* (2005) **26**, 6836
- Schneider, S. W., et al., *Pflugers Arch.* (2000) **439**, 297
- Oberleithner, H., et al., *J. Membr. Biol.* (2003) **196**, 163
- Oberleithner, H., *Kidney Int.* (2005) **67**, 1680
- Schneider, S. W., et al., *Cell Biol. Int.* (1997) **21**, 759
- Anderson, R. C., et al., *FEMS Microbiol. Lett.* (2004) **240**, 105
- Braga, P. C., et al., *J. Chemother.* (2002) **14**, 336
- da Silva, Jr., A., and Teschke, O., *Biochim. Biophys. Acta.* (2003) **1643**, 95
- Meincken, M., et al., *Antimicrob. Agents Chemother.* (2005) **49**, 4085
- Thomas, W. E., et al., *Mol. Microbiol.* (2004) **53**, 1545
- Thomas, W., et al., *Biophys. J.* (2006) **90**, 753
- Pelling, A. E., et al., *Science* (2004) **305**, 1147
- Ji, X. L., et al., *World J. Gastroenterol.* (2005) **11**, 1709
- Cheng, Y., et al., *Biochim. Biophys. Acta.* (1999) **1421**, 249
- Girasole, M., et al., *J. Microsc.* (2001) **204**, 46
- Ruozi, B., et al., *J. Drug Target* (2003) **11**, 407
- Almofiti, M. R., et al., *Arch. Biochem. Biophys.* (2003) **410**, 246
- Vu, T. Q., et al., *Nano Lett.* (2005) **5**, 603
- Ruozi, B., et al., *J. Drug Target* (2005) **13**, 295
- Kawaura, C., et al., *FEBS Lett.* (1998) **421**, 69
- Zhao, L., and Feng, S. S., *J. Colloid Interface Sci.* (2006), in press
- Oishi, J., et al., *J. Control Release* (2006) **110**, 431
- Anabousi, S., et al., *Eur. J. Pharm. Biopharm.* (2005) **60**, 295
- Shahin, V., et al., *J. Cell Physiol.* (2005) **202**, 591
- Oberleithner, H., et al., *Pflugers Arch.* (2000) **439**, 251
- Oberleithner, H., et al., *Proc. Natl. Acad. Sci. USA* (1994) **91**, 9784
- Hong, S., et al., *Bioconjug. Chem.* (2004) **15**, 774
- Berquand, A., et al., *Pharm. Res.* (2005) **22**, 465
- Berquand, A., et al., *Biochim. Biophys. Acta.* (2004) **1664**, 198
- Klein, D. C. G., et al., *Chemphyschem.* (2003) **4**, 1367
- Riener, C. K., et al., *Anal. Chim. Acta.* (2003) **497**, 101
- Cleveland, J. P., et al., *Rev. Sci. Instrum.* (1993) **64**, 403
- Baumgartner, W., et al., *Ultramicroscopy* (2000) **82**, 85
- Hinterdorfer, P., et al., *Proc. Natl. Acad. Sci. USA* (1996) **93**, 3477
- Chen, A., and Moy, V. T., *Biophys. J.* (2000) **78**, 2814
- Baumgartner, W., et al., *Proc. Natl. Acad. Sci. USA* (2000) **97**, 4005
- Hinterdorfer, P., and Dufrene, Y. F., *Nat. Methods* (2006) **3**, 347
- Kienberger, F., et al., *Single Molecules* (2001) **2**, 99
- Gamsjaeger, R., et al., *Langmuir* (2004) **20**, 5885
- Raible, M., et al., *J. Biotechnol.* (2004) **112**, 13
- Evstigneev, M. and Reimann, P., *Phys. Rev. E.* (2003) **68**, 045103
- Pierres, A., et al., *Proc. Natl. Acad. Sci. Unit. States Am.* (1998) **95**, 9256
- Zhang, X. H., et al., *Chemphyschem.* (2004) **5**, 175
- Zhang, X. H., and Moy, V. T., *Biophys. Chem.* (2003) **104**, 271
- Zhang, X. H., et al., *Biophys. J.* (2002) **83**, 2270
- Yuan, C. B., et al., *Biochemistry* (2000) **39**, 10219
- Wong, J., et al., *Biomol. Eng.* (1999) **16**, 45
- Micic, M., et al., *Scanning* (1999) **21**, 394
- Eibl, R. H., and Moy, V. T., *Methods Mol. Biol.* (2005) **305**, 439
- Zhang, X., and Moy, V. T., *Biophys. Chem.* (2003) **104**, 271
- Yuan, C., et al., *Biochemistry* (2000) **39**, 10219
- Pfister, G., et al., *J. Cell Sci.* (2005) **118**, 1587
- Lee, S., and Van Vliet, K. J., (2006), unpublished results
- Van Vliet, K. J., et al., *Acta. Mater.* (2003) **51**, 5881
- Trache, A., et al., *Biophys. J.* (2005) **89**, 2888
- Horton, M., et al., *J. Recept. Signal Transduct. Res.* (2002) **22**, 169
- Lundberg, P., et al., *Endocrinology* (2001) **142**, 339
- Riener, C. K., et al., *Anal. Chim. Acta.* (2003) **479**, 59
- Kada, G., et al., *Ultramicroscopy* (2001) **86**, 129
- Stroh, C. M., et al., *Biophys. J.* (2004) **87**, 1981
- Stroh, C. M., et al., *Proc. Natl. Acad. Sci. USA* (2004) **101**, 12503
- Ebner, A., et al., *ChemPhysChem.* (2005), **6**, 897
- Hinterdorfer, P., *Methods Cell Biol.* (2002) **68**, 115
- Zhang, X., et al., *Am. J. Physiol. Heart Circ. Physiol.* (2004) **286**, H359
- Pouliot, J. M., et al., *Biomacromolecules* (2005) **6**, 1122
- Liu, Y., et al., *Biotechnol. Bioeng.* (2006) **93**, 297
- Wojcikiewicz, E. P., et al., *J. Cell Sci.* (2003) **116**, 2531
- Edmondson, K. E., et al., *Biophys. J.* (2005) **89**, 3603

# Single-molecule recognition imaging microscopy

C. Stroh\*<sup>†</sup>, H. Wang\*<sup>‡</sup>, R. Bash\*<sup>§</sup>, B. Ashcroft\*<sup>‡</sup>, J. Nelson<sup>¶</sup>, H. Gruber\*<sup>‡</sup>, D. Lohr<sup>§</sup>, S. M. Lindsay\*<sup>§||\*\*</sup>, and P. Hinterdorfer\*

Departments of <sup>†</sup>Physics and Astronomy, and of <sup>§</sup>Chemistry and Biochemistry, and <sup>¶</sup>Biodesign Institute, Arizona State University, Tempe, AZ 85287; \*Institute for Biophysics, University of Linz, 4040 Linz, Austria; and <sup>||</sup>Molecular Imaging Corporation, 4666 South Ash Avenue, Tempe, AZ 85282

Edited by Calvin F. Quate, Stanford University, Stanford, CA, and approved July 16, 2004 (received for review May 19, 2004)

**Atomic force microscopy is a powerful and widely used imaging technique that can visualize single molecules and follow processes at the single-molecule level both in air and in solution. For maximum usefulness in biological applications, atomic force microscopy needs to be able to identify specific types of molecules in an image, much as fluorescent tags do for optical microscopy. The results presented here demonstrate that the highly specific antibody-antigen interaction can be used to generate single-molecule maps of specific types of molecules in a compositionally complex sample while simultaneously carrying out high-resolution topographic imaging. Because it can identify specific components, the technique can be used to map composition over an image and to detect compositional changes occurring during a process.**

Atomic force microscopy (AFM) is unique in its ability to image single biomolecules and follow biomolecular processes in fluid with nanometer resolution (1); however, images of complex samples can be remarkably hard to interpret, because AFM yields only the shape and volume of the molecule, with no discrimination for the precise types of molecules being imaged. For example, in a sample of chromatin (nucleosomes) plus other proteins, DNA can be identified by its thread-like appearance, but the various protein components look similar, with an image size that depends only marginally on molecular weight. Techniques such as chemical force microscopy (2), force-volume mapping (3), and force curves (4) give information about the specific nature of the molecules being imaged, but they lack the important visual component provided by simultaneous imaging. Here we describe a technique that allows recognition of a specific type of molecule (histone H3) in a complex sample (chromatin) while simultaneously yielding high-resolution topographic images of the same sample. Recognition is efficient, reproducible, and specific. This technique extends the capability of AFM in much the same way as fluorescent tags have extended optical microscopy.

The technique uses an antibody tethered to the AFM tip and depends on the highly specific antibody-antigen recognition reaction between the tip-tethered antibody and its antigen in the sample to identify a specific type of molecule. Antibodies tethered to an AFM tip have been shown previously to bind to specific target molecules during scanning (5), but that work offered no way to separate composition-sensitive signals from topography signals. This difficulty arises because it is difficult to extract a signature of binding while the imaging servo acts to keep the amplitude of oscillation of the probe constant during a scan. The method described here detects antibody-antigen binding through small changes in the absolute (dc) level of the cantilever-deflection signal.

## Materials and Methods

**Preparation of Chromatin Samples.** Nucleosomal arrays containing the mouse mammary tumor virus (MMTV) promoter region were salt-reconstituted to various subsaturated (for clarity in image analysis) levels of nucleosome occupation with HeLa histones exactly as described (6). The arrays were deposited on glutaraldehyde aminopropyltriethoxysilane (GD-APTES)-treated mica, derivatized at 1  $\mu$ M levels with GD (7), and allowed to adsorb for  $\approx$ 40 min.

Human (h)Swi-Snf was prepared as described (8). The prep-

aration contains BSA in a 4:1 molar ratio with hSwi-Snf (further reduction in BSA concentration diminishes remodeling activity). For remodeling studies, nucleosomal arrays were preincubated with hSwi-Snf at stoichiometries of 15 nucleosomal array molecules per hSwi-Snf molecule (8). After deposition, fields are scanned twice. The second scan assesses the effect of the AFM-scanning process on chromatin structure and thus provides the background (tip-induced) level of change. Thus, this important control is carried out on the same samples that will be analyzed for remodeling. After activation of hSwi-Snf by ATP addition, the same fields (and the same set of tethered molecules) are scanned again to determine the changes induced by hSwi-Snf remodeling (8).

**Tethering of Antibodies to AFM Tips.** Polyclonal anti-histone H3 antibodies (Upstate Company, Charlottesville, VA) were thiolated and attached to a polyethylene glycol (PEG) tether on the end of an AFM probe as described (4). Amination of the probe was carried out by exposing a UV-cleaned silicon-nitride probe (Microlever, Veeco, Santa Barbara, CA, coated for MacMode AFM by Molecular Imaging, Tempe, AZ) to aminopropyltriethoxysilane vapor for 1 h.

The H3 antibody was produced against the whole histone, but the N-terminal tails of H3, which project out from the compact nucleosome core, are likely to provide the major antigenic determinant in the chromatin sample. Tips were selected for a strong recognition signal when imaging chromatin, and these signals were invariably blocked by the peptide corresponding to the histone tethered to the tip. For more details, see *Protocol for Modifying AFM Tips with Antibodies*, which is published as supporting information on the PNAS web site.

**AFM Imaging and Separation of the Recognition Signal.** Magnetized cantilevers are driven by a small solenoid using a MacMode dynamic-force microscope from Molecular Imaging. Images were taken in 10 mM NaCl/5 mM phosphate buffer, pH 7.5, with 3-nm peak-to-peak amplitude oscillation at 8 kHz, imaging at 70% set point, and scanning at 1 Hz. Recognition contrast decreased with increasing salt, disappearing at  $\approx$ 0.8 M for this antibody.

The recognition signal was obtained by passing the raw deflection signal from the AFM-scanning head to a PicoTREC signal-processing system (Molecular Imaging). The instrument extracts rapid changes in the value of the positive-going peak signal, filtering the output with a bandpass of  $\approx$ 150 Hz, while compensating for slow changes in dc level in the input caused by instrumental drift. The signal is passed to an auxiliary input to the microscope controller for simultaneous display alongside the topographical image. The microscope servo operates from the

This paper was submitted directly (Track II) to the PNAS office.

Freely available online through the PNAS open access option.

Abbreviations: AFM, atomic force microscopy; MMTV, mouse mammary tumor virus; GD-APTES, glutaraldehyde aminopropyltriethoxysilane; h, human; PEG, polyethylene glycol.

<sup>†</sup>C.S. and H.W. contributed equally to this work.

\*\*To whom correspondence should be addressed. E-mail: stuart.lindsay@asu.edu.

© 2004 by The National Academy of Sciences of the USA

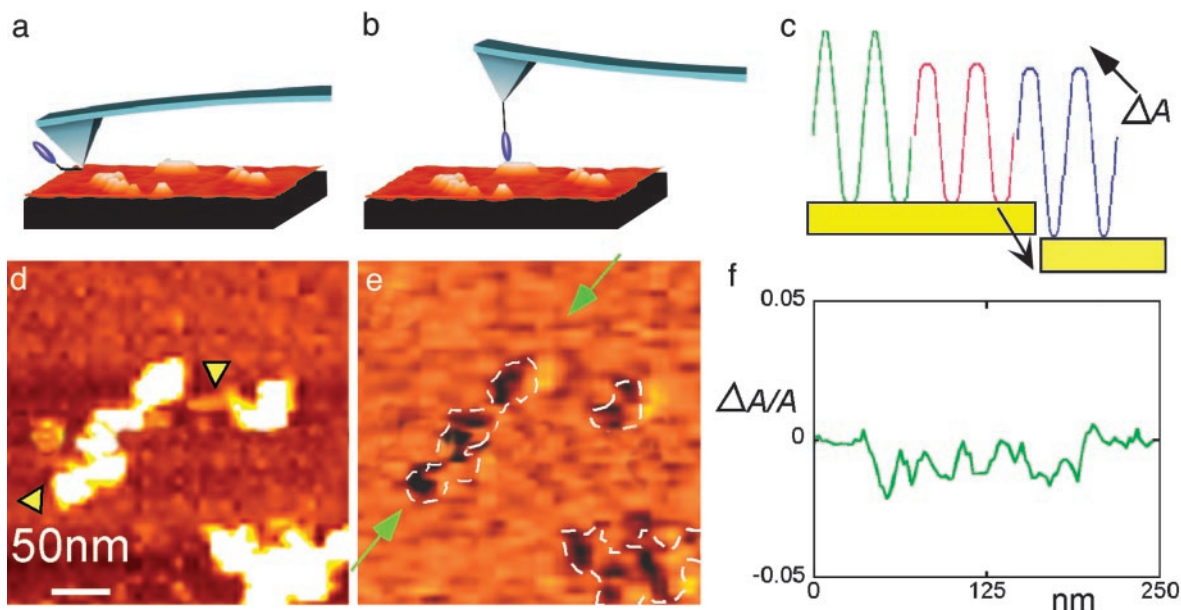


**Fig. 1.** Recognition imaging. When an AFM tip-tethered antibody (blue blob in *a*) binds to its antigen in the sample being scanned (*b*), there is a transient reduction in the oscillation amplitude of the tip (green curve to red curve in *c*). The imaging servo restores the signal amplitude but with the peak signal shifted downward by an amount  $\Delta A$  (blue curve in *c*). This peak shift provides the recognition signal for a specific antigen-antibody recognition event. A topographic image of MMTV arrays and the corresponding recognition image (a “map” of the change in peak signal,  $\Delta A$ ) are shown in *d* and *e*, respectively. These images were obtained simultaneously from one scan of the sample by using an H3-specific antibody tethered to the AFM tip. A plot of the peak signal,  $\Delta A$ , for the portion of the recognition image between the green arrows (*e*) is shown in *f*. The dips in signal correspond well with the location of nucleosomes, and the changes in peak signal (traced in *f*) are in quantitative agreement with theory (see text). The  $x$ - $y$  scale is shown in *d*. The highest features in *d* are  $\approx 5$  nm.

deflection signal in the normal way, which introduces a negligible error (on the order of  $\Delta A$  or 0.06 nm in the present case) into the height display when an antibody binds.

**Filtering and Signal to Noise.** In the limit of heavy damping, where the mechanical  $Q$  factor of the cantilever approaches unity, the rms fluctuation amplitude  $\langle x \rangle$  of a cantilever of resonant frequency  $\nu_0$  measured in a bandwidth  $B$  Hz is given by (9)

$$\langle x \rangle = \sqrt{\frac{k_B T}{K} \frac{2B}{\pi \nu_0}}$$

Thus, a signal-to-noise ratio of 3:1 [with a 0.06-nm signal (see *Results and Discussion*)] requires  $B \approx 0.016 \nu_0$ , which is 130 Hz for the cantilevers used in this work.

**Testing Recognition Specificity and Efficiency.** To check recognition specificity, the solution in the sample cell was completely replaced with a solution of the imaging buffer plus 30  $\mu\text{g}/\text{ml}$  of BSA (kept at the same temperature as the microscope to avoid drift), and the sample was reimaged. This buffer was then replaced with a solution of 30  $\mu\text{g}/\text{ml}$  of an antigen (to the antibody on the tip), and the sample was imaged again. Recognition efficiency is defined conservatively as the ratio of total recognition events to total features in the topographic image that may be nucleosomes. False hits (see Fig. 4, red dot and circle) occur in  $\approx 2\%$  of all recognition features. The efficiency depends on the antibody used and imaging conditions such as salt concentration, and thus each new antibody must be calibrated in the imaging environment. The effective antibody concentration at the surface is high (5), and thus the technique is sensitive to even small amounts of crossreactivity.

## Results and Discussion

**The Technique of Recognition Imaging.** The method described in this report is based on the detection of small shifts in the absolute

dc level of the cantilever-deflection signal that occur when an antibody tethered to the AFM tip (Fig. 1*a*) binds to its antigen in the sample being imaged (Fig. 1*b*), thus interfering with the normal oscillation of the AFM tip (Fig. 1*c*). All of the imaging in this work is carried out in solution, i.e., *in situ*. The antibody is attached near the apex of the tip by means of a 6-nm-long flexible PEG linker (10). This linker leaves the antibody free enough to find and bind properly to its target antigen, but it is short enough to permit accurate localization of the antigen site in the sample (5).

The origin of a recognition signal can be understood by considering the sequence of events that occurs when the oscillating AFM cantilever containing the tip-tethered antibody binds to its antigen in the sample. The green trace in Fig. 1*c* shows the displacement pattern of the cantilever as it taps on a surface submerged in solution (no antigen-antibody interaction). The cantilever motion is heavily damped and is sustained with a sinusoidal magnetic driving force (11). The bottom of the waveform is cut off where the tip hits the hard surface, but the top part of the waveform remains sinusoidal (12). When the tethered antibody binds to an antigen on the surface, the upward extent of the cantilever swing is restricted by the PEG tether, as shown in the red trace. This reduction of the oscillation amplitude on binding is compensated for by the microscope servo, which is engaged (and required) for normal topographic imaging. The servo pulls the probe away from the surface to restore the amplitude to its previous value (blue trace), but now the peak signal is displaced downward by the amount of the original amplitude reduction,  $\Delta A$  (Fig. 1*c*). Thus, a map of the absolute value (i.e., dc-coupled) of this peak voltage, produced simultaneously with the topographic image, shows the location of the antibody-binding events as dark patches.

In principle, the downward-motion displacement of the sample by the microscope servo could cause further reduction of the upper peak amplitude, but the effect is very small because the PEG tether is so much less stiff than the surface.

The amplitude of tip oscillation is adjusted such that the antibody remains bound for most of the time that the tip is in the vicinity of the antigen. Binding and unbinding events occur on each scan line, giving rise to some fluctuation in image width from line to line.

The samples analyzed in this application of the technique are nucleosomal arrays made by reconstituting human histones on a specific DNA fragment containing the MMTV long terminal repeat promoter (6). Samples are deposited onto GD-functionalized mica (GD-APTES) in a flow cell linked to the AFM. The GD-APTES surface tethers the arrays to the surface, allowing repetitive scanning of the same sets of molecules as various reagents are flowed into the cell. The ability to reimagine the same molecules allows the clearest possible comparisons of the effects of changing conditions on the sample molecules. Fig. 1*d* shows a topographic image (two nucleosomal arrays) taken with an AFM tip tethered to an antibody raised against histone H3, one of the proteins that constitute the core of each nucleosome. The corresponding recognition image is shown in Fig. 1*e*. The dark recognition patches and the pattern in which they occur clearly coincide with the positions of the nucleosomes in the topographic image (Fig. 1*d*). Fig. 1*f* is a plot of the recognition signal ( $\Delta A/A$ ) versus distance between the two green arrows in Fig. 1*e*. The dips coincide with recognition spots. They are a few percent of the oscillation amplitude, in agreement with calculations (see below).

**The Basis of Recognition Imaging.** The imaging mechanism can be understood quantitatively as follows. In the absence of structural relaxation, the reduction of the “free” oscillation amplitude,  $A_0$ , to a new value,  $A_z$ , after binding of the antibody is given by (13)

$$\frac{A_0}{A_z} = \frac{S(z/L_0)}{K} + 1, \quad [1]$$

where  $S(z/L_0)$  is the stiffness of the PEG tether at a fractional extension,  $z/L_0$ , of its maximum extended length,  $L_0$ , and  $K$  is the spring constant of the AFM cantilever. An approximate result for the force generated by stretching a worm-like chain is (14)

$$F = \frac{k_B T}{L_p} \left[ \frac{1}{4[1 - (z/L_0)]^2} - \frac{1}{4} + \frac{z}{L_0} \right], \quad [2]$$

where  $L_p$  is the persistence length, and  $k_B T$  can be conveniently taken as 4.1 pN·nm at room temperature. This formula may be differentiated with respect to  $z$  to obtain the stiffness,  $S(z/L_0)$ . For the PEG linker used here,  $L_p = 0.38$  nm and  $L_0 \approx 6$  nm (15). A plot of the force generated by stretching a molecule, and its consequent stiffness as a function of  $z/L_0$ , is given in Fig. 6, which is published as supporting information on the PNAS web site. The force rises rapidly above 20 pN for  $z/L_0 > 0.5$ , leading to potentially increased frequency of breaking of a typical antibody–antigen bond (16). Near this optimum value of  $z/L_0$ ,  $S(z/L_0)$  is  $\approx 2$  pN/nm. Thus, with a cantilever of stiffness  $K = 100$  pN/nm, Eq. 1 predicts that the recognition events will cause a dip in peak amplitude of a few percent of the total amplitude, which is confirmed experimentally by the line trace across the recognition image shown in Fig. 1*f*. In this case, the oscillation amplitude is  $\approx 3$  nm (corresponding to  $z/L_0 \approx 0.5$ ), and so the absolute value of the recognition signal is on the order of 0.06 nm. This value is smaller than broad-band thermal fluctuations of the cantilever, and thus the recognition signal requires filtering (see *Materials and Methods*).

**The Specificity and Efficiency of Recognition Imaging.** The specificity of the recognition process was tested by flowing exogenous proteins into the liquid flow cell in which the sample was being imaged. If the recognition signal is specific, only (added) pro-

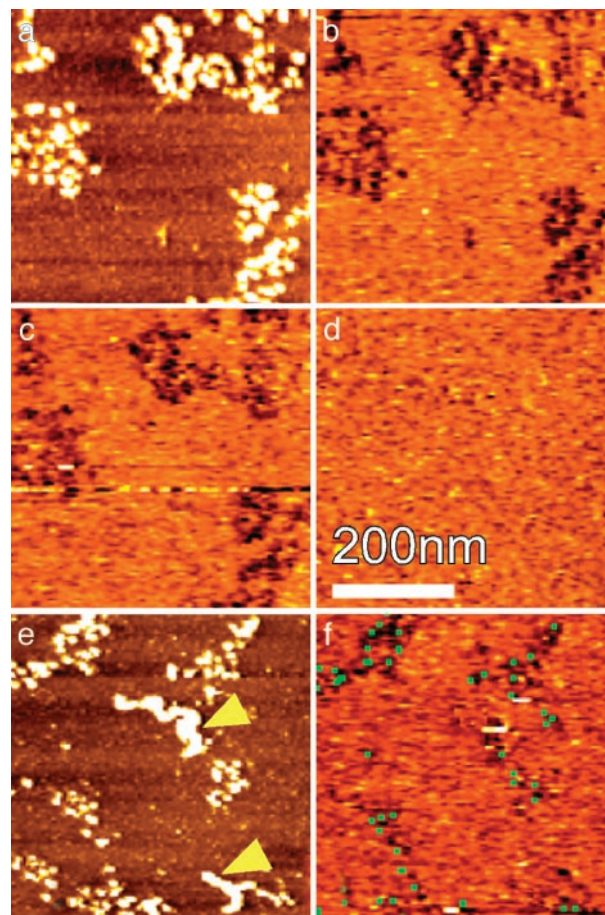


**Fig. 2.** The specificity of recognition imaging. Topographic (a) and recognition (b) images of MMTV nucleosomal arrays similar to those shown in Fig. 1 are shown. Recognition images from the same region of the sample taken after addition of BSA into the sample in the flow cell (c) and then after the addition of ARTKQTARKSTGGKAPRKQLC (which corresponds to the N-terminal tail of histone H3) (d) are also shown. (e) Topographic image of a field with BSA aggregates pointed to by yellow arrowheads. (f) Recognition images of this same field after BSA was added. The recognition image obtained before BSA addition is superimposed on the recognition signal after BSA addition as green dots. The coincidence of the green dots and dark spots demonstrates that the added BSA did not interfere with the H3 recognition.

teins that are antigenic to the antibody on the AFM tip used for imaging will be able to bind to the tip, block the recognition events, and thus disrupt the signal. Such a test is shown in Fig. 2. A typical topographic image of MMTV chromatin and the accompanying recognition image (taken with an anti-histone H3 functionalized tip) are shown in Fig. 2*a* and *b*. Again, recognition spots closely mirror the locations of nucleosomes in the topographic image. When a BSA solution (30  $\mu\text{g}/\text{ml}$ ) is flowed into the sample flow cell, the recognition image is unaffected (Fig. 2*c*). However, if a similar concentration of a peptide corresponding to amino acids 1–20 of the N-terminal tail of histone H3 (sequence shown in the Fig. 2 legend) is then flowed into this sample, the recognition signal is completely abolished (Fig. 2*d*). Thus, the ability of the tip-tethered antibody to produce a recognition signal (Fig. 2*b*) is blocked by an excess of its specific antigen in solution, demonstrating that the recognition signals come from specific interactions between the antibody on the tip and its antigen on the surface. The inability of BSA to alter the recognition signal (Fig. 2*c*) shows that nonspecific protein-binding effects do not affect specific recognition. Note that the images in Fig. 2*a–d* are obtained by sequential rescanning of the

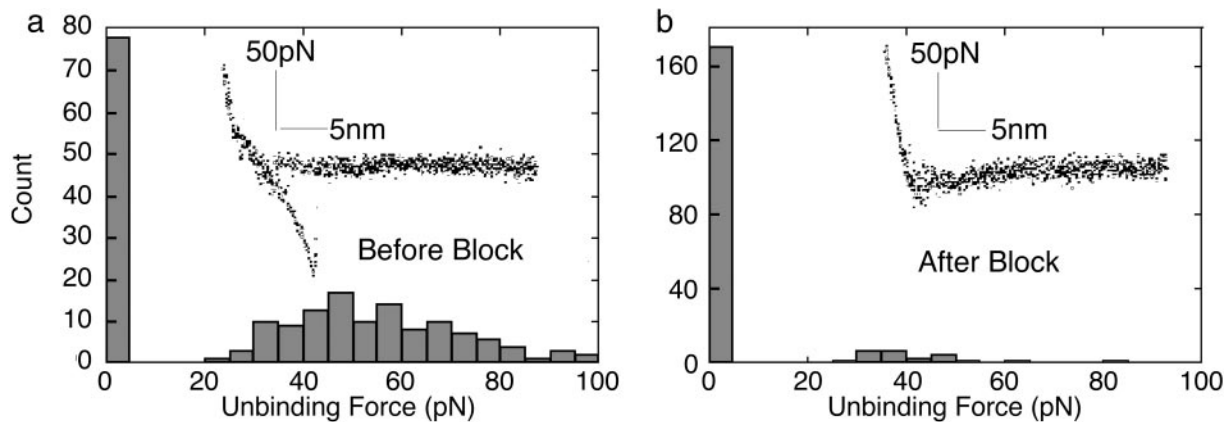


**Fig. 3.** Force curves for antibody-tethered tips. Histograms of the measured adhesion forces for an antibody-tethered tip probing a field of MMTV nucleosomal array molecules (a) and the same tip scanning in the presence of  $30 \mu\text{g/ml}$  of a peptide from the N-terminal tail of histone H3, showing how the blocked antibody does not adhere to the sample surface (b). Two hundred force curves were analyzed for each histogram (bars at the origins are the numbers of force curves in which no adhesion force was measured). (Insets) Typical examples of force-versus-distance curves obtained. The curve in a shows the characteristic single-molecule binding curve characteristic of PEG stretching, whereas the curve in b shows negligible adhesion. The average adhesion forces are  $57 \pm 20$  pN (absence of H3 tail peptide),  $6$  pN (presence of tail peptide),  $116 \pm 63$  pN (PEG tether alone), and  $118 \pm 134$  pN for the bare (clean) tip. Thus, the tethered antibody plays an important role in reducing nonspecific adhesion.

same individual molecules in the same sample, which ensures that trivial, sample-dependent variations cannot affect the analysis. Fig. 2 e and f show another aspect of imaging specificity. When BSA is added (through the flow cell) to these samples, aggregates can accrue on the surface (Fig. 2e, yellow arrowheads on the topographic image). In Fig. 2f, the recognition image obtained from this field before BSA addition is shown as green dots, which are superimposed on the recognition signal obtained

after BSA was adsorbed onto the surface. Clearly, the H3 antibody-tethered tip does not recognize the BSA aggregates, nor do the BSA aggregates interfere with recognition imaging. Thus, the level of nonspecific recognition appears to be minimal.

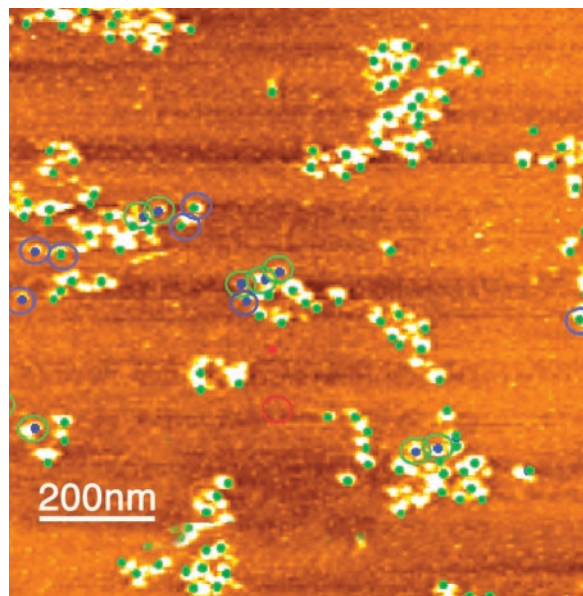


**Fig. 4.** The efficiency and repeatability of recognition imaging. Spots from a recognition image are superimposed (as green dots) on its corresponding topographic image. Features present in the topographic image but not in the recognition image are marked by blue dots. A recognition feature with no corresponding topographic feature (near middle of the image) is marked by a red spot. Changes in recognition events after rescanning are indicated by the circles color-coded with the same scheme (no circle equals no change after rescanning). For example, a feature recognized in the first scan but not in the second is shown by a green dot (recognition in the first scan) surrounded by a blue circle (not recognized on the second scan). The recognition efficiency generally remains  $>90\%$ .

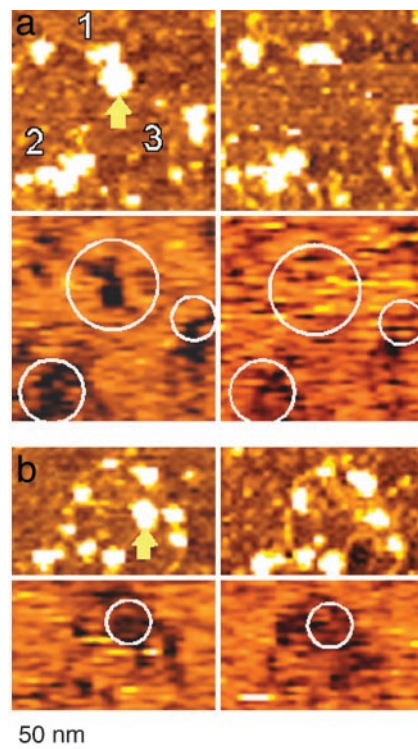


**Fig. 5.** Using recognition imaging to study a complex, biologically relevant process. Some examples of the changes seen after hSwi-Snf activation (by ATP) in deposited MMTV nucleosomal arrays are shown. a and b Upper shows topographic images taken before (Left) and after (Right) ATP addition. a and b Lower shows corresponding recognition images obtained with an anti-H3 tip. Protein loss on ATP addition (yellow arrows in the  $-$ ATP images) is accompanied by loss of the recognition signal showing that the lost features were likely not hSwi-Snf. Molecules labeled 2 and 3 in a appear unchanged in the topographic image but show loss of recognition signal after ATP addition. (The scale shown at the bottom applies to all the images.)

To observe the types of specific binding effects discussed above, it must be the case that nonspecific adhesion forces are smaller than the specific antibody–antigen binding force. To test this theory directly, we have measured the adhesion by using force–distance curves (Fig. 3). We find that an antibody-tethered tip in the presence of blocking antigen shows almost no adhesion to the molecules or surfaces used in these experiments. The average adhesion force is  $57 \pm 20$  pN in the absence of the tail peptide but  $\approx 6$  pN in its presence. This lower average force reflects both a decrease in the value of adhesion and an increased number of curves in which no adhesion was measured at all. Adhesion forces without the antibody (PEG tether alone) are  $116 \pm 63$  or  $118 \pm 134$  pN for a clean (bare) tip. Thus, the blocked antibody is more of a “nonstick” surface than the tip or PEG alone. Perhaps this is a special property of blocked antibodies, because proteins are generally rather sticky.

The efficiency and repeatability of recognition imaging are illustrated in Fig. 4. Here, features in the recognition image are superimposed (as green dots) on the topography image. Most features that look like nucleosomes in the topographic image are associated with a recognition signal. A few exceptions are described in the Fig. 4 legend (see also *Materials and Methods*). Some changes occur when the same sample is rescanned (highlighted by circles), but the recognition efficiency is generally high and remains so on subsequent rescans (data not shown). An average over several images yields  $96 \pm 2\%$  recognition efficiency on the first scan and  $92 \pm 2\%$  after scanning over the same area again.

We also used tips tethered with antibodies to histone H4 or histone H2A to image these nucleosomal array samples (data not shown). Whereas the H3 antibody was raised against the whole protein, the H4 antibody was raised against the N-terminal tail, and the H2A antibody was raised against part of the “acidic patch” on the 11-nm nucleosomal face (17). All antibodies gave similar results with respect to specificity, efficiency of recognition, and reproducibility, indicating a general applicability of the technique.

**Following Compositional Changes During a Biologically Relevant Process.** The major impact of this technique will derive from its ability to monitor specific components in heterogeneous samples while they are undergoing biological processes and at the same time as topographic images are being acquired. An example of this application is presented in Fig. 5 and is taken from AFM studies of the action of the human Swi-Snf (hSwi-Snf) ATP-dependent nucleosome remodeling complex (18) on MMTV promoter nucleosomal arrays (8). These studies can help us

understand how nucleosome remodeling by these types of complexes might take place *in vivo* on this and other promoters.

In these experiments, hSwi-Snf and chromatin are incubated together and then deposited onto GD-APTES in the flow cell linked to the AFM. As described previously, the GD-APTES surface tethers the array molecules, allowing *in situ* images of the same nucleosomal arrays to be taken before ATP is added (hSwi-Snf is inactive) and after ATP addition (hSwi-Snf is activated). The progress of remodeling, therefore, can be followed on individual molecules. Topographic imaging studies using this approach have shown that array molecules can undergo a variety of substantial ATP/hSwi-Snf-dependent conformational changes and have suggested that hSwi-Snf might also trigger compositional changes such as histone loss (8).

Comparison of recognition images before and after ATP addition shows a variety of remodeling changes and confirms the occurrence of compositional changes. A few examples are shown to illustrate the technique. In Fig. 5*a*, the three molecules in the field all show remodeling, as evidenced by release of DNA after ATP addition (8). Recognition images (using H3 antibody-tethered tips) indicate a substantial loss of histone (H3) for all three molecules, including a complete loss of histone recognition for molecule one, and new arrangements of the remaining recognition signal pattern in molecules two and three. Fig. 5*b* shows an example of complete loss of a protein (pointed to by the yellow arrow in the  $-ATP$  image) accompanied by a significant change in the H3 recognition images, suggesting that the protein was a nucleosome and not hSwi-Snf. hSwi-Snf (data not shown) and BSA (see above) are not recognized by the anti-histone antibodies. These various types of changes have been quantified and systematically analyzed (8), but these examples demonstrate the significant enhancement of information obtained when recognition is coupled to topographic imaging.

In conclusion, the addition of recognition imaging gives the atomic force microscope a capability for the identification of specific types of molecules at the single-molecule level without compromising its topographic imaging performance. The technique can be used to analyze the distribution of a specific component in heterogeneous samples or to follow compositional changes that occur during complex processes, thus revealing features that are not evident from topographic images alone. This capability will significantly enhance the usefulness of AFM as a tool for studying biologically relevant samples and processes.

We thank Gordon Hager for supplying hSwi-Snf and the plasmid containing the MMTV long terminal repeat and Jaya Yodh for supplying HeLa histones. This work was supported by the National Cancer Institute.

- Drake, B., Prater, C. B., Weisenhorn, A. L., Gould, S. A. C., Albrecht, T. R., Quate, C. F., Cannell, D. S., Hansma, H. G. & Hansma, P. K. (1989) *Science* **243**, 1586–1589.
- Noy, A., Vezenov, D. V. & Lieber, C. M. (1997) *Annu. Rev. Mater. Sci.* **27**, 381–421.
- A-Hassan, E., Heinz, W. F., Antonik, M. D., D’Costa, N. P., Nageswaran, S., Schoenenberger, C. & Hoh, J. H. (1998) *Biophys. J.* **74**, 1564–1578.
- Hinterdorfer, P., Baumgartner, W., Gruber, H. J., Schilcher, K. & Schindler, H. (1996) *Proc. Natl. Acad. Sci. USA* **93**, 3477–3481.
- Raab, A., Han, W., Badt, D., Smith-Gill, S. J., Lindsay, S. M., Schindler, H. & Hinterdorfer, P. (1999) *Nat. Biotechnol.* **17**, 901–905.
- Bash, R., Wang, H., Yodh, J., Hager, G., Lindsay, S. M. & Lohr, D. (2003) *Biochemistry* **42**, 4681–4690.
- Wang, H., Bash, R., Yodh, J. G., Hager, G. H., Lohr, D. & Lindsay, S. M. (2002) *Biophys. J.* **83**, 3619–3625.
- Wang, H., Bash, R., Yodh, J. G., Hager, G., Lohr, D. & Lindsay, S. M. (2004) *Biophys. J.*, in press.
- Sarid, D. (1992) *Atomic Force Microscopy* (Oxford Univ. Press, New York).
- Haselgrübler, T., Amerstorfer, A., Schindler, H. & Gruber, H. J. (1995) *Bioconjugate Chem.* **6**, 242–248.
- Han, W., Lindsay, S. M. & Jing, T. (1996) *Appl. Phys. Lett.* **69**, 4111–4114.
- Lantz, M., Liu, Y. Z., Cui, X. D., Tokumoto, H. & Lindsay, S. M. (1999) *Surf. Interface Anal.* **27**, 354–360.
- Liu, Y. Z., Leuba, S. & Lindsay, S. M. (1999) *Langmuir* **14**, 8547–8548.
- Bustamante, C., Marko, J. F., Siggia, E. D. & Smith, S. (1994) *Science* **265**, 1599–1600.
- Kienberger, F., Pastushenko, V., Kada, G., Gruber, H., Riener, C., Schindler, H. & Hinterdorfer, P. (2000) *Single Mol.* **1**, 123–128.
- Wilert-Badt, S., Hinterdorfer, P., Gruber, H., Lin, G.-T., Badt, D., Wimmer, B., Schindler, H. & Kinne, R. K.-H. (2002) *Biophys. J.* **82**, 2767–2774.
- Luger, K., Mader, A. W., Richmond, R. K., Sargent, D. F. & Richmond, T. J. (1997) *Nature* **389**, 251–260.
- Schnitzler, G. R., Cheung, C. L., Hafner, J. H., Saurin, A. J., Kingston, R. E. & Lieber, C. M. (2001) *Mol. Cell. Biol.* **21**, 8504–8511.

# Lab 10: BioMEMS force sensor

**Location:** NE47-215c

**PI:** Taher Saif

**Lab Instructors:** Shengyuan Yang

## Summary

We will be showing a bioMEMS force sensor and its application in measuring stretch and compression force response of healthy and malaria-infected human red blood cells. The bioMEMS force sensor is made from pure single crystal silicon, and consist of a probe and flexible beams. The probe is used to contact, indent and stretch the cells, and the flexible beams to measure the cell force response. The probe is about 5  $\mu\text{m}$  wide and 5  $\mu\text{m}$  deep. Each of the flexible beams is about 2 mm long, 1  $\mu\text{m}$  wide and 5  $\mu\text{m}$  deep. We will show how to manipulate the sensor and bring it in contact with the cells, and how the cell force response is measured. Every student will have the chance to try out this manipulation process. Two particular cell force response measurements will also be shown: a poly-L-lysine coated sensor probe will be used to measure (1) the stretch force response of a healthy red blood cell and (2) the compression force response of a malaria-infected red blood cell. For more information about this bioMEMS technique, please refer to the following two papers:

## Recommended Reading

S. Yang and T. Saif, "Micromachined force sensors for the study of cell mechanics," *Rev. Sci. Instrum.* **76**.

S. Yang and T. Saif, "Reversible and repeatable linear local cell force response under large stretches," *Exp. Cell Res.* **205**.



## Micromachined force sensors for the study of cell mechanics

Shengyuan Yang and Taher Saif<sup>a)</sup>

*Department of Mechanical and Industrial Engineering, University of Illinois at Urbana-Champaign, Urbana, Illinois 61801*

(Received 19 August 2004; accepted 21 December 2004; published online 16 March 2005)

A technique using micromachined mechanical force sensors to measure the force response of living cells is introduced. The force sensors consist of a probe and flexible beams. The probe is used to indent and stretch the cells, and the flexible beams are used to measure the cell force response. The stiffness of the sensors is designed at several nanonewtons per micrometer, but can be varied over a wide range. The sensors are fabricated by the SCREAM process. The deformation of the cells and the deflection of flexible beams are measured by an optical microscope coupled with a charge-coupled device camera. Experimental demonstrations show the feasibility, simplicity, and versatility of this technique. It addresses several disadvantages of existing related techniques, and is complementary to many of them. We expect that this new technique will attract significant attention and be employed much more in the study of cell mechanics. © 2005 American Institute of Physics. [DOI: 10.1063/1.1863792]

### I. INTRODUCTION

Increasing experimental evidence shows that a living cell senses mechanical stimuli and responds with biological changes, which in turn may alter cell internal structure and hence its mechanical behavior.<sup>1–11</sup> Uncovering the mechanical response of living cells is, therefore, important from views of traditional materials science and biological science. The techniques developed for measuring the mechanical response<sup>12,13</sup> of living cells include: centrifugation,<sup>14</sup> shear flow,<sup>15</sup> substrate deformation,<sup>16</sup> substrate composition,<sup>17</sup> flexible substrata,<sup>18</sup> embedded particle tracking,<sup>19</sup> multiple-particle-tracking microrheology,<sup>20</sup> magnetic twisting cytometry,<sup>1</sup> magnetic bead microrheometry,<sup>21</sup> micropatterned substrates,<sup>22</sup> micropipette aspiration,<sup>23</sup> optical traps,<sup>24</sup> optical stretcher,<sup>25</sup> magnetic traps,<sup>26</sup> biomembrane force probe,<sup>27</sup> cell poker,<sup>28</sup> atomic force microscopy (AFM),<sup>29</sup> surface force apparatus,<sup>30</sup> glass needles,<sup>31</sup> shear on single cells,<sup>32</sup> microplates,<sup>33</sup> and tensile tester,<sup>34</sup> with the first four dedicated to cell population studies and the rest focused on single cell and/or single biomolecule studies.

The description of the above techniques and a comparison between them are beyond the scope of this article. Interested readers are referred to the reviews in Refs. 9, 12, and 13. Although these techniques have revealed significant insight on mechanical response of single cells and cell populations, they have limitations. First, they only measure certain types or small ranges of cell deformation and force response, or mechanical response of cells at certain states. For example, the substrate-related techniques only account for the traction force between the cells and substrate; magnetic bead-related techniques, optical traps, and AFM only induce small cell deformation and measure small cell force response; micropipette deforms cells by suction and hence

cannot measure the cell indentation mechanical response; microplates and tensile tester only measure suspended cells. Second, the techniques, such as micropipette aspiration, cell poker, AFM, glass needles, microplates, and tensile tester, which measure cell stretch or compression force response, can only measure one component of the force response vector (which normally has three) except AFM, which can measure two (although the measurement of two-component cell force response by AFM has not been reported), and it is difficult to build a system that can measure three force components based on these techniques. Note that a recent article introduces a 3D magnetic twisting device that allows application of a torque to magnetic beads about any chosen axis, and the cell mechanical response can be quantified about this axis.<sup>35</sup> Third, it is difficult to make changes on the measurement systems based on these techniques to adapt to certain measurement applications or working environments. For example, it is difficult to use commercial AFMs with scanning electron microscopes (SEMs) to visualize the structural change of a cell when the cell is stretched or indented by the AFM tip. Fourth, the sensing and control systems for some of the existing techniques are complicated. For example, in magnetic twisting cytometry, complicated hardware is needed to generate and control the required magnet fields. The complexity of commercial AFMs is obvious because of their high-performance optical sensing and feedback electric systems.

In this article, we present a new technique that addresses or improves upon the above disadvantages. In this technique, micromachined mechanical force sensors are used to manipulate cells and measure their force response. The force sensors consist of a probe and some flexible beams. The probe is used to indent or stretch the cells, and the flexible beams to sense the cell force response. Standard optical microscope system is used to record the deformations of the cells and the deflections of the flexible beams. The cell force

<sup>a)</sup>Electronic mail: saif@uiuc.edu

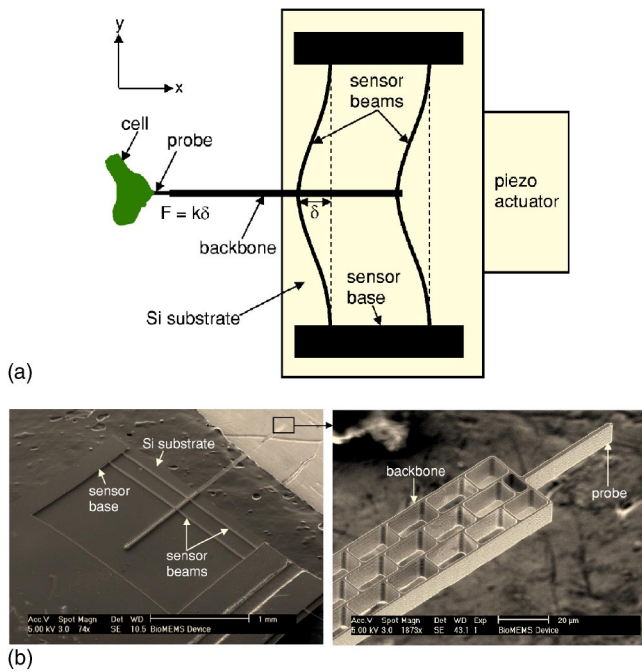


FIG. 1. (Color online) Schematic (a) and SEM image (b) of a mechanical force sensor.

response is simply obtained by multiplying the stiffness of the sensors by the sensor deflections. Compared to the existing techniques, it is simpler and more versatile and offers more flexibility for a wide range of cellular exploration. Preliminary experimental results show the feasibility and the advantages of this technique.

## II. MATERIALS AND METHODS

### A. Force sensor

The schematic and SEM image of a force sensor are shown in Figs. 1(a) and 1(b), respectively. In this sensor, two parallel flexible beams with fixed-fixed boundary conditions serve as the sensor beams. The probe is connected to the sensor beams through a backbone attached to the midpoint of the sensor beams. The chip, on which the sensor is fabricated, is driven by a piezo actuator held by an  $x$ - $y$ - $z$ - $\theta_x$ - $\theta_y$ - $\theta_z$  stage. The actuator moves the chip and hence the probe in the  $x$  direction to indent or stretch a cell. The stiffness of the sensor in the  $x$  direction is much smaller than those in the  $y$  and  $z$  directions due to high aspect ratio (depth-to-thickness ratio) of the beams and their geometry. Thus, only the deflection of the sensor beams and hence the cell force response in the  $x$  direction is measured. The sensor is made of single-crystal silicon (Si) with a Young's modulus  $E=170$  GPa (the beams are aligned in the  $[110]$  direction of single-crystal Si). The length of each sensor beam is  $L = 1.96$  mm. The cross section of the beam is rectangular, with depth (the dimension perpendicular to the paper)  $b = 10.5$   $\mu\text{m}$  and thickness (the dimension parallel to the paper)  $h = 0.77$   $\mu\text{m}$ . The stiffness of the sensor (in the  $x$  direction) is estimated as  $k = 3.4$  nN/ $\mu\text{m}$ , by

$$k = \frac{384EI}{L^3}, \quad (1)$$

where

$$I = \frac{1}{12}bh^3 \quad (2)$$

is the moment of inertia of the beam. The cell force response is then obtained from

$$F = k\delta, \quad (3)$$

with  $\delta$  being the deflection of the sensor beams. The exact value of this sensor stiffness may not be so critical in many cell experiments if one is interested in the qualitative characteristics of cell force response when the sensor stiffness behaves as a scale factor, as in the case of most AFM measurements. The sensor stiffness can also be calibrated independently against another spring with known spring constant. The method of calibration is described in the Appendix, where the stiffness of a sensor is calibrated and compared with that estimated from Eq. (1), and they match closely.

The SCREAM process<sup>36</sup> was used to fabricate the sensor. The process starts with a single-crystal Si wafer (Silicon Quest International). The fabrication steps are as follows (Fig. 2): (a) Grow an oxide ( $\text{SiO}_2$ ) layer ( $\sim 1$   $\mu\text{m}$  thick) on the surface of the Si wafer by thermal oxidation; (b) Pattern the sensor to the oxide surface by photolithography; (c) Anisotropically etch the oxide layer by reactive ion etching (RIE); (d) Anisotropically etch the Si substrate to the desired depth ( $\sim 20$   $\mu\text{m}$ ) by inductively coupled plasma (ICP); (e) Remove the photoresist (PR) layer by oxygen plasma etching; (f) Thermally oxidize the wafer again to put a protecting oxide layer ( $\sim 0.15$   $\mu\text{m}$  thick) on the Si surface; (g) Anisotropically remove the oxide layer on the floor of the patterned trench by RIE (this step reduces the thickness of the top oxide layer as well); (h) Anisotropically etch down the exposed Si again for an additional depth ( $\sim 10$   $\mu\text{m}$ ) by ICP; (i) Isotropically etch the exposed Si to release the beams by ICP; (j) Remove all the oxide by wet hydrofluoric acid etching. Thus, the entire sensor is made of pure single-crystal Si. During the thermal oxidation, Si is consumed to form  $\text{SiO}_2$ . Hence, the longer the oxidation time, the thinner is the remaining Si, and then the softer is the sensor. Thus, the duration of oxidation allows one to achieve various stiffness of the sensor from the same initial design. Note that the last step in the SCREAM process is metallization, which is avoided here.

### B. Experimental system

The experimental system using the sensor to measure the cell force response is shown in Fig. 3. Here, the sensor is fixed to a holder which is mounted on an  $x$ - $y$ - $z$  piezo stage with 1 nm resolution, and the piezo stage is in turn mounted on an  $x$ - $y$ - $z$  mechanical stage with 1  $\mu\text{m}$  resolution. The mechanical stage is mounted on a tilt and rotation platform. An inverted optical microscope (Olympus CK40) with an objective of 10 $\times$  is used to monitor the deformation of the cell and the displacement of the sensor probe. Through an adaptor of 2.5 $\times$ , images are recorded using a cooled CCD

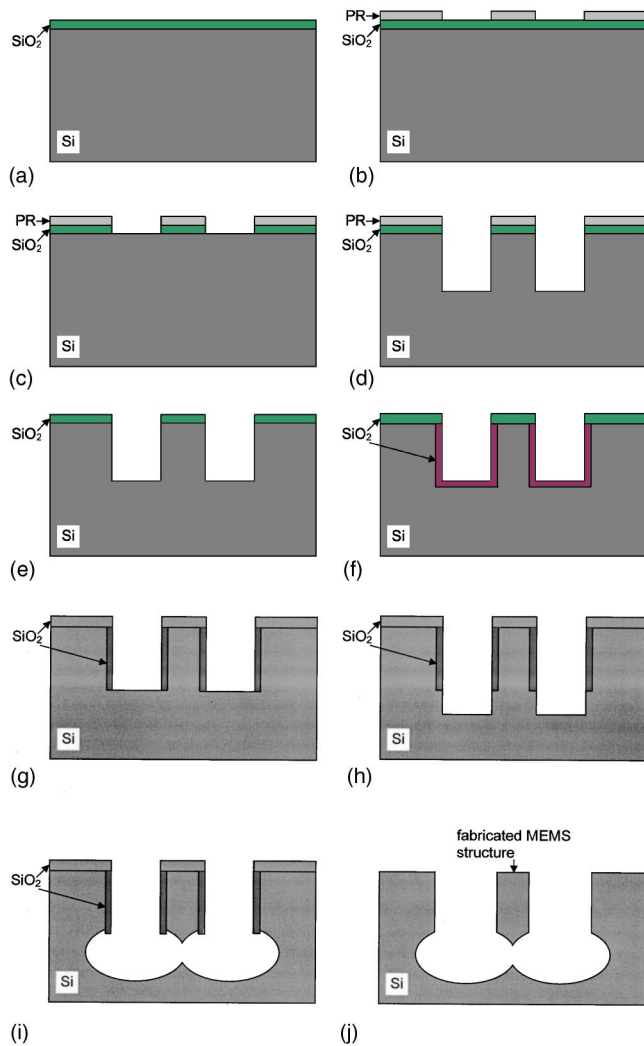


FIG. 2. (Color online) SCREAM process used to fabricate the sensor.

camera (Olympus MagnaFire S99806) with an imaging pixel size of  $1280 \times 1024$  and its image acquisition software. By measuring structures with known sizes, the resolution of the images was determined as  $0.27 \mu\text{m}$  per pixel. Thus, the dimensional measurement accuracy (error) is  $\Delta = 0.27 \mu\text{m} / 2 \approx 0.14 \mu\text{m}$ . The force resolution of the system is estimated as  $k\Delta \approx 0.5 \text{ nN}$  [Eq. (3)]. The cells are cultured in a 35 mm dish, and the sensor is immersed in the culture medium for cell force response measurement. The sensor plane is inclined by 5 deg with respect to the bottom of the culture dish to ensure that the contacting tip of the sensor probe has the lowest elevation.

The deformation of a cell in the  $x$  direction is positive when the cell is elongated, and negative when shortened (indented); the deformation in the  $y$  direction is defined positive upward in the images. The cell force response is positive when the probe–cell interaction is in tensile state. The cell deformation is given by the displacement of the contact point between the cell and the probe, and the sensor deflection is measured from the relative displacements between the probe and the sensor base. In the experimental results shown below, the cell deformations and force response are measured with respect to the initial state where the probe contacts the

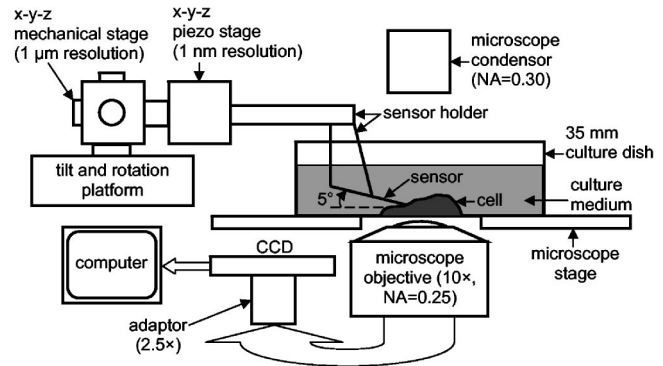


FIG. 3. Experimental system and the sensor to measure the cell force response.

cell. For the experimental results shown in this article, each deformation increment (decrement) was accomplished in 1 s by manually increasing (decreasing) the voltage for the piezo stage. The cell deformation and force response were recorded (by capturing the corresponding phase contrast image) 15 s after each deformation increment (decrement), and the exposure time for capturing the image was less than 1 s. The time delay between two consecutive deformation increments (decrements) was kept at 50 s unless otherwise stated.

To study cell stretch force response, the sensor probe was also functionalized by coating with fibronectin by incubating the sensor in  $50 \mu\text{g} \cdot \text{ml}^{-1}$  fibronectin (BD Biosciences) solution at room temperature for 6 h. It was then taken out for drying at room temperature for 6 h before it was immersed into the culture medium and brought in contact with a cell for 20 min. The cell forms adhesion sites with the probe most likely by integrin activation.<sup>37</sup> The sites are connected to the cytoskeletal structure and thus offer the probe a localized handle to the cytoskeleton.

The cells tested in this article were cultured from CV-1 (ATCC), a monkey kidney fibroblast (MKF) cell line. They were cultured in a medium with 90% DMEM (ATCC) and 10% FBS (ATCC) in an environment with  $37^\circ\text{C}$  temperature, 5%  $\text{CO}_2$ , and were plated for 24–48 h before the experiments. The cell force response measurement was conducted in air at room temperature.

### III. RESULTS

#### A. Cell morphology change due to small mechanical disturbance

The technique introduced above was used to study the morphological change of living cells (attached to the bottom of a dish) due to a mechanical disturbance. In this case, the sensor probe was brought in contact with the cells to laterally indent them by a small amount ( $\sim 2 \mu\text{m}$ ). The change of shape of the cells was recorded for a period of time with the sensor base fixed. Figure 4(a) shows the cell right after the indentation, while Fig. 4(b) shows the state 72 min after Fig. 4(a). We see the obvious shape change of the cell, and the mechanical indentation was reduced, as if the cell was staying away from the probe. Figures 4(c)–4(e) show the results for a different cell. Here, the cell was dividing and was at its

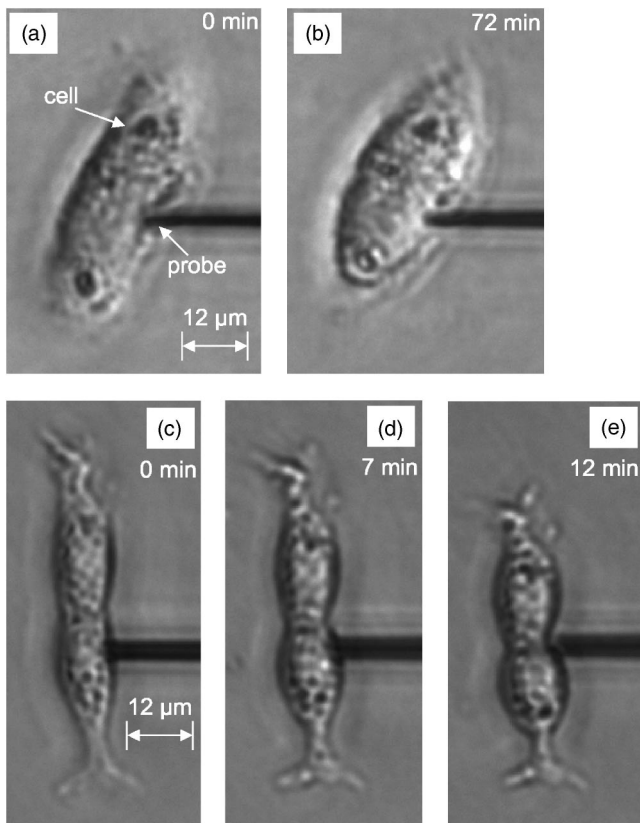


FIG. 4. Morphological changes of two cells due to mechanical disturbance of the sensor probe. (a) Right after the probe indented a monkey kidney fibroblast (MKF); and (b) 72 min after (a). (c) Right after the probe indented an MKF; (d) and (e) seven min and 12 min after (c), respectively.

telophase. Figure 4(c) shows the state right after the probe indented the cell, and Figs. 4(d) and 4(e) are the states 7 min and 12 min after Fig. 4(c), respectively.

### B. One-component force sensing

The technique was used to study the force response of living cells subject to large lateral indentation. In this case, the cells were laterally indented by a small amount (as above) for 20 min. If cell shape change (as observed in Fig. 4) was not observed, further indentation was conducted and the corresponding cell force response was measured. Figure 5 shows the results for a cell under indentation. Figure 5(a) shows the force response. Figures 5(b)–5(f) are representative phase contrast images. In Fig. 5(a), the slope within Figs. 5(b) and 5(c) is larger than that within Figs. 5(c) and 5(d), which may be attributed to partial breaking of the attachment of the cell with the substrate. After the linear force response stage, the cell yielded, i.e., from Figs. 5(d)–5(f) the cell indentation increased without corresponding increase in force response.

A functionalized sensor was used to study cell stretch force response. In this case, the probe of the sensor was brought in contact with the cells for 20 min to form the adhesion site. Figure 6 shows the results for an elongated cell. Here, the focal adhesion connection formed between the probe and the cell is relatively small compared to the cell size, and the induced stretch deformation of the cell is local. Figure 6(a) is the stretch force response. Figures 6(b)–6(f)

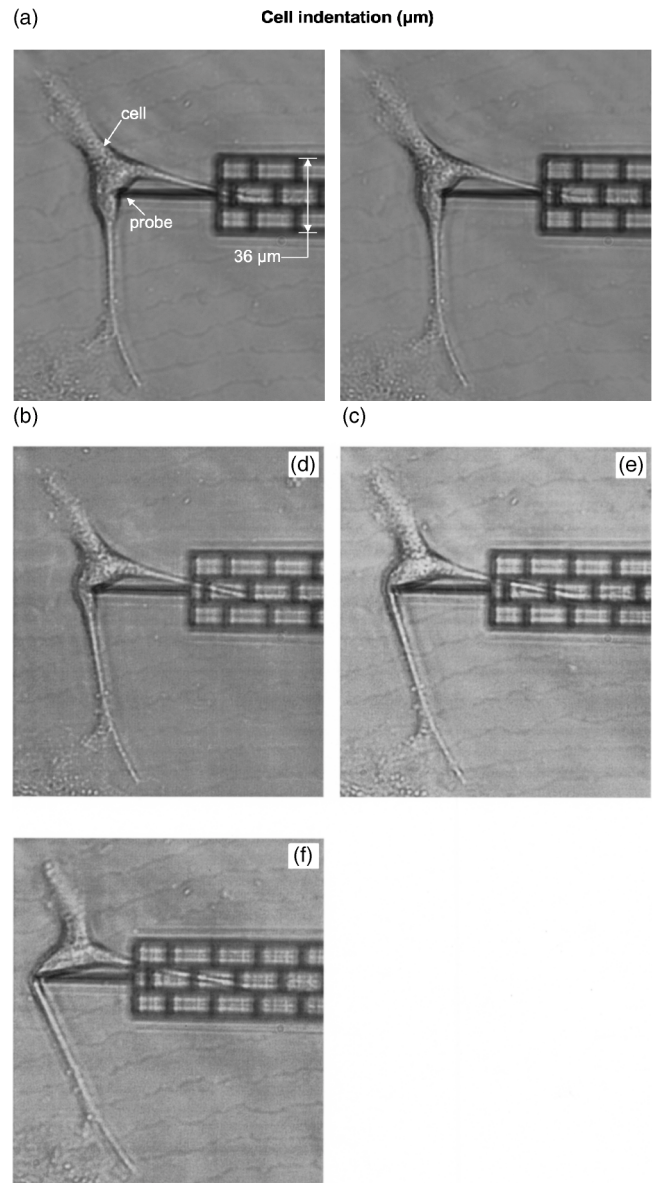
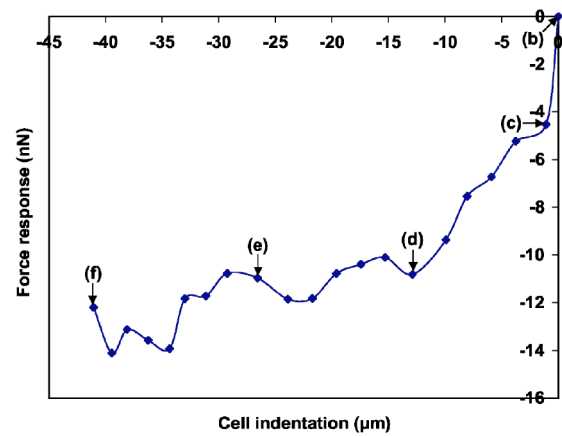


FIG. 5. Force response of an MKF due to large lateral indentation. (a) Force response. (b)–(f) Representative phase contrast images.

are representative phase contrast images. From Figs. 6(b)–6(d) the cell force response is small and does not show a significant trend, possibly because the cytoskeleton has not yet been brought under tension. From Fig. 6(d)–6(f) the cell force response shows a significant linear trend.

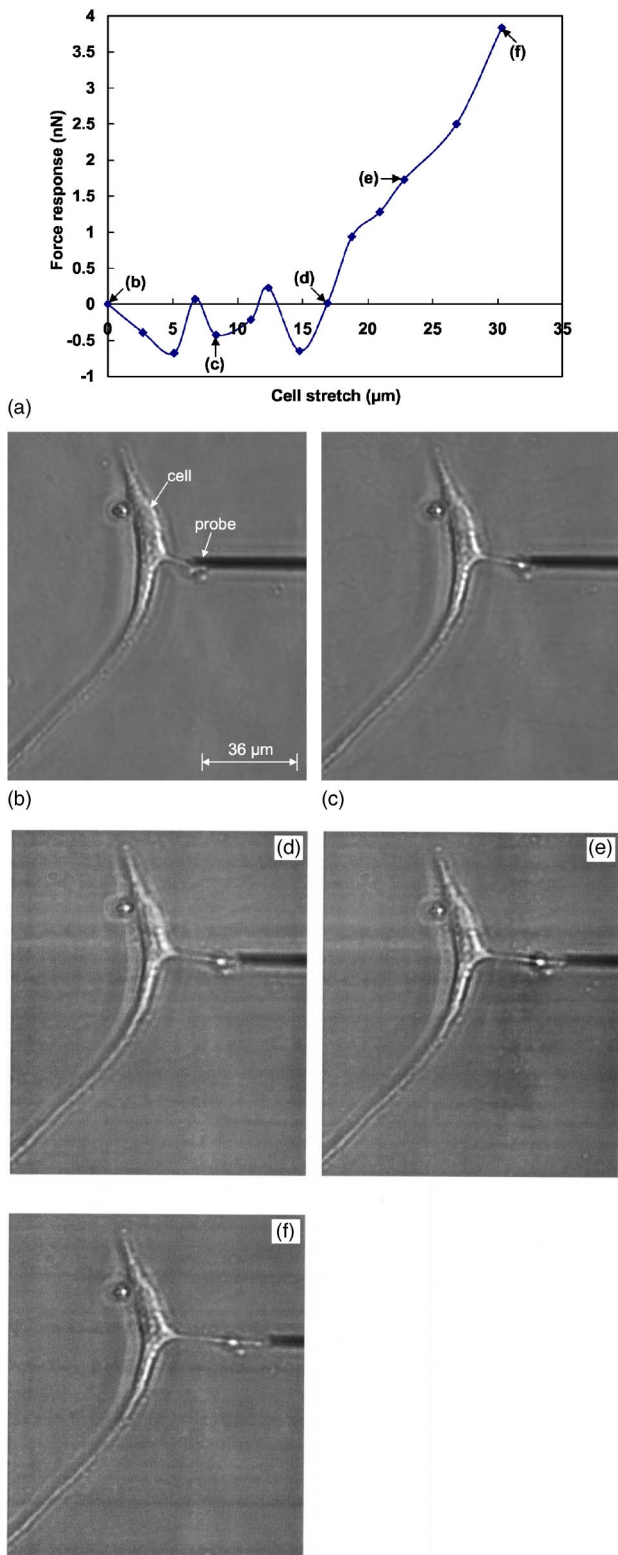


FIG. 6. Stretch force response of an MKF with a small adhesion site with the sensor probe. (a) Force response. (b)–(f) Representative phase contrast images.

In the experiment for Fig. 7, a relatively large adhesion site was formed between the probe and the cell, and the induced stretch deformation of the cell is global, i.e., the entire cell deforms. Figure 7(a) is the stretch force response. Figures 7(b)–7(f) are representative phase contrast images.

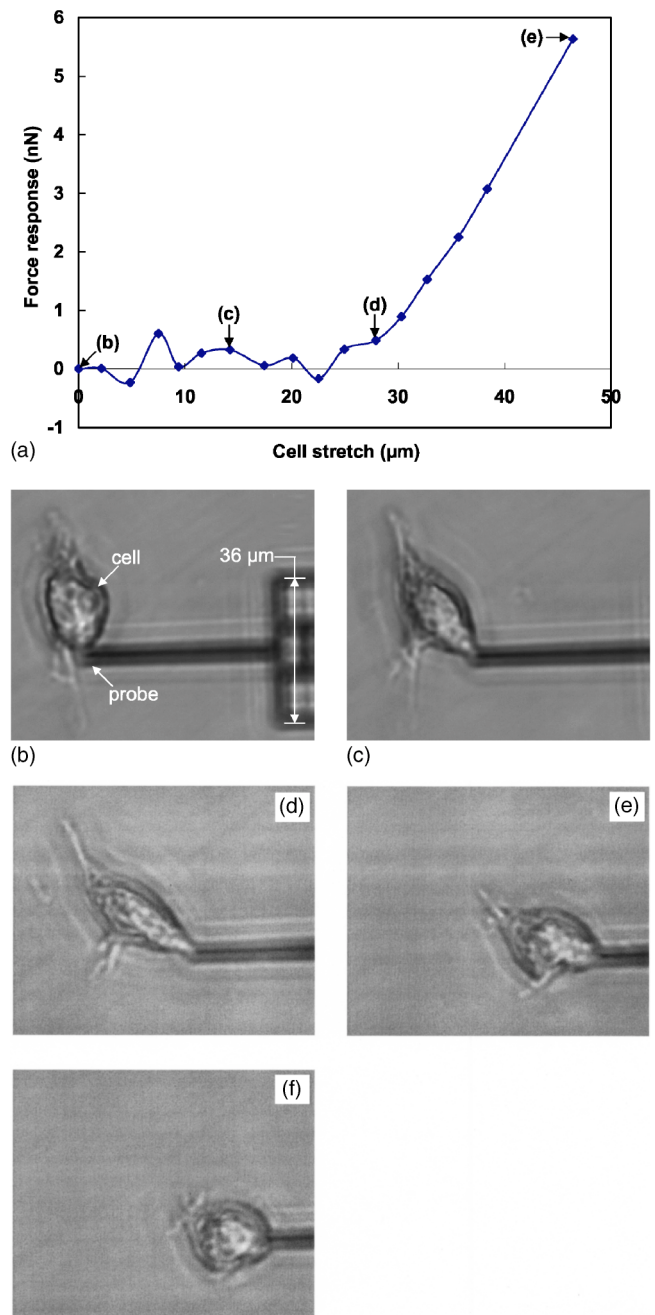


FIG. 7. Stretch force response of an MKF with a large adhesion site with the sensor probe. (a) Force response. (b)–(f) Representative phase contrast images.

The force response is similar to Fig. 6. From Figs. 7(b)–7(d) the cell force response is small and does not show a significant trend, and the cell underwent alignment due to the stretch. From Figs. 7(d) and 7(e), the cell force response is linear, and the cell underwent significant migration. Figure 7(f) is the image taken 85 s after Fig. 7(e).

### C. Two-component force sensing

Although a cell may be deformed in one direction, it may generate force response in orthogonal directions. One needs a sensor that measures the force response in multidirectional

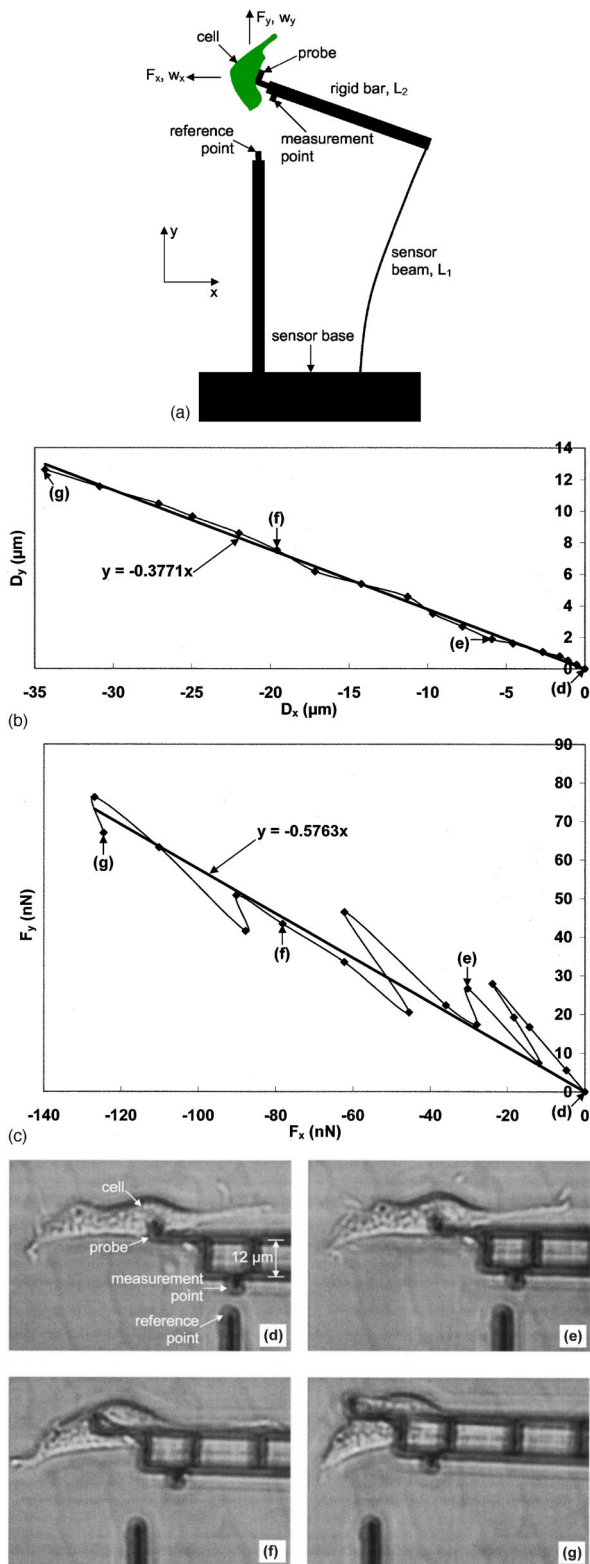


FIG. 8. (Color online) (a) Two-component force sensor. (b) Cell deformation vector. (c) Force response vector. (d)–(g) Representative phase contrast images.

mension as well. Such information may provide insight on the mechanobiological behavior of the cell. In the following we introduce such a force sensor.

Figure 8(a) shows the schematic of the two-component force sensor. Here, the sensor beam deforms due to both

force components  $F_x$  and  $F_y$ , and the probe tip displaces by  $w_x$  and  $w_y$  with respect to the sensor base, in the  $x$  and  $y$  directions, respectively. The force components can be obtained from

$$\begin{bmatrix} F_x \\ F_y \end{bmatrix} = \frac{2EI}{L_1^3} \begin{bmatrix} 6 & 3\frac{L_1}{L_2} \\ 3\frac{L_1}{L_2} & 2\left(\frac{L_1}{L_2}\right)^2 \end{bmatrix} \begin{bmatrix} w_x \\ w_y \end{bmatrix}. \quad (4)$$

The cell deformations  $D_x$  and  $D_y$  are the motion of the probe tip and hence the contact point with the cell with respect to the lab frame of reference. Thus,  $D_x$  and  $D_y$  are different from  $w_x$  and  $w_y$ . If the cell does not have any force response, then  $w_x = w_y = 0$ , but  $D_x$  or  $D_y$  are nonzero. We demonstrate the applicability of the sensor by measuring the force response of a cell. The sensor geometry is  $L_1 = 1$  mm and  $L_2 = 0.429$  mm, with a beam cross section of  $2.0 \times 13.1 \mu\text{m}$ . Thus, by Eq. (4), if  $w_x = 1 \mu\text{m}$ ,  $w_y = 0.5 \mu\text{m}$ , then  $F_x = 28.2$  nN,  $F_y = 36.9$  nN. Figure 8(b) shows the cell deformation vector  $(D_x, D_y)$ , and Fig. 8(c) shows the cell force response vector  $(F_x, F_y)$ , where  $F_y$  is defined positive upward [Fig. 8(a)]. Figures 8(d)–8(g) are representative phase contrast images. The deformation vector is almost linear, and the force response vector is roughly linear. But, the slopes for the corresponding linear fits,  $y = -0.3771x$  and  $y = -0.5763x$ , are different, indicating the anisotropy of the mechanical behavior of the cell.

#### IV. DISCUSSION

The technique presented here, based on micromachined mechanical force sensors, falls into the same category as cell piker, AFM, and glass needles in terms of the basic force sensing principle. But, the above experimental results and the following discussion show the simplicity, versatility, and flexibility of the presented technique, which may not be routinely achieved by the cell piker, AFM, and glass needles, as illustrated by the limitations of the existing techniques given in the Introduction.

The current sensor was designed to measure cell force response due to large stretches and indentations. However, the force resolution ( $\sim 0.5$  nN) of the sensors demonstrated is too large to be useful in the study of single ligand–receptor force interactions, which can be studied by AFM or optical tweezers. By changing the geometry of the microbeams, the combined spring constant of a sensor can be varied from  $10$  pN/ $\mu\text{m}$  to  $1$   $\mu\text{N}/\mu\text{m}$  to reach the necessary force sensitivity requirement. According to Eqs. (1) and (2), the stiffness of a force sensor can be reduced (to reach a higher force resolution) by increasing the length or by decreasing the thickness of the sensor beam, both of which have the same cubic dependence ( $1/L^3$  and  $h^3$ ). For a Si beam with dimension  $L \times b \times h = 3$  mm  $\times$   $10 \mu\text{m}$   $\times$   $0.5 \mu\text{m}$ , we get  $k = 0.25$  nN/ $\mu\text{m}$ . Doubling the length will decrease the stiffness by about an order of magnitude. But, both increasing the length and reducing the thickness will increase the difficulty of fabrication. The stiffness can also be reduced by serial connection of sensor beams. For example, in the design shown in Fig. 9, two more sets of the sensor beams are

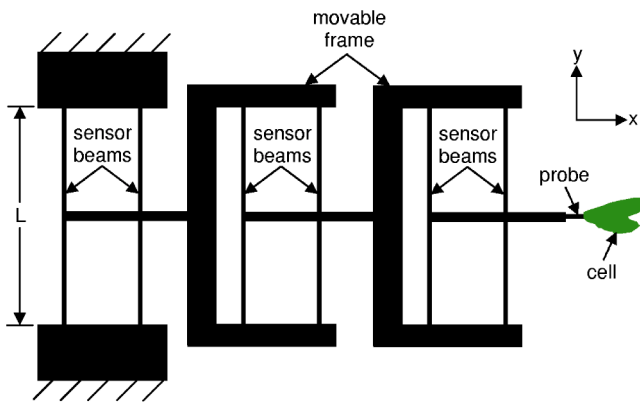


FIG. 9. (Color online) Reducing the stiffness of the force sensor by serially adding the sensor beams.

serially added to the design of Fig. 1, and the total stiffness of the sensor becomes one-third of that in Fig. 1. Sensors with two sets of serially connected sensor beams (pictures not shown) have been successfully fabricated without significantly increasing the difficulty of fabrication. Therefore, in principle we may reduce the stiffness of the sensor to desired lower values by the combined utilization of the above strategies, i.e., increasing the length, reducing the thickness, and using serial connection of sensor beams. Based on the available versatile microelectromechanical systems (MEMS) fabrication technique, various shapes of the sensor probe can be designed to reach desired contact with cells. The probe can then induce small or large deformation, and the sensor can also measure small or large force response. For example, if a sharp tip is used, the sensor works like an AFM, but probing can be done normal or lateral to the surface of the substrate. In the above experiments, because the increase (decrease) of the voltage for the piezo stage was achieved manually, the rate of the induced cell deformation is slow compared with those of AFM and magnetic twisting cytometry. But, by using a computer-controlled power supply for the piezo stage, together with a high-speed camera, higher rates of deformation comparable to those of AFM can be achieved.

Due to the vertical indentation nature of AFM<sup>29,38–40</sup> and small cell thickness, the allowable cell deformation range is limited and the measured cell mechanical behavior needs careful interpretation due to the influence of the substrate. Using the lateral indentation technique, as shown here, this limitation can be avoided.

In this technique, the cell force response is obtained by multiplying the deflection of the sensor beams by their combined spring constant. Thus, no further calculation or interpretation is needed to measure cell force response. The sensors can be incorporated with laser tweezers and environmental SEMs, and in principle there is no need to change these analytical instruments. The sensors can also be redesigned to orient and adapt to specific new applications. The experimental system is much simpler and more flexible compared to the existing techniques, and no specialized detection and control systems are needed.

There is, however, one limitation about this technique. The microforce sensors have to survive the capillary forces as they are immersed from air to liquid, or emerge from

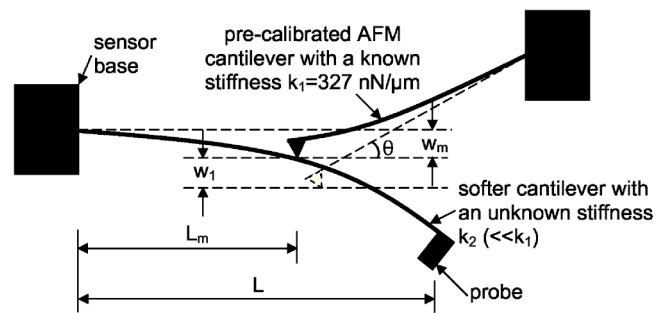


FIG. 10. Calibrating the stiffness of a softer cantilever by a precalibrated AFM cantilever.

liquid to air. For example, the final step in the fabrication process is the wet etching of SiO<sub>2</sub> on the released sensor beams (Fig. 2). The sensors need to be wet-cleaned by chemical solutions, such as water, acetone, and isopropanol, before they are used to measure the force response of living cells. In functionalizing the sensors, they need to be immersed into the relevant liquid coating medium, such as the fibronectin solution used here. When the sensors are used to measure the force response of living cells, they need to be inundated in the liquid cell culture medium. The capillary forces acting on the sensors during these processes may be large enough to damage the structures of the sensor beams. However, our experimental experience suggests that the design of the sensor shown in Fig. 1 normally survives the above liquid processes because the fixed–fixed boundary conditions prevent excessive deflections. Moreover, normally it is the taking-out-of-liquid process that breaks the cantilevered sensor beam in Fig. 8(a), and not the putting-into-liquid process, which may be due to the capillary force for putting-into-liquid process being much smaller than that for taking-out-of-liquid.<sup>41</sup> To minimize the possibility of damage due to the capillary forces from the coating medium, one may choose to coat only the probe part of the sensor in the functionalization step.

Additionally, the contact nature between the sensor probe and the cells is complex. The interaction details between the tip of the sensor probe and the cell surface are currently unknown when the sensor probe is brought in contact with a cell. However, since the materials composing the cell are much softer than that of the probe, the contact region will conform with the shape of the probe.

## ACKNOWLEDGMENT

This work was supported by National Science Foundation (NSF) Grant ECS 01-18003.

## APPENDIX: CALIBRATION OF THE FORCE SENSORS

A commercial AFM (Digital Instruments Dimension 3100) with a precalibrated cantilever may be used to calibrate the stiffness of the force sensors, by measuring the force-deflection relationship of the sensors, for the technique presented in this article. The stiffness of the softest precalibrated commercial AFM cantilever that we could obtain is 327 nN/μm (Veeco Instruments CLFC-NOBO). To demon-

strate the feasibility of this method for calibration of sensor stiffness, and to show how accurate the estimation of sensor stiffness [by Eqs. (1) and (2) based on the measured geometry] could be, another sensor with the same design as that shown in Figs. 1(a) and 1(b) but with a shorter length of 0.962 mm was fabricated, so that the stiffness of the precalibrated cantilever and that of the sensor are close to each other. The cross section of the sensing beam for this sensor has the dimensions  $b=10.3\ \mu\text{m}$  and  $h=0.93\ \mu\text{m}$ . The estimated stiffness is  $k=51\ \text{nN}/\mu\text{m}$ . The corresponding value obtained by the calibration is  $70\ \text{nN}/\mu\text{m}$ . Thus, the error of the estimation is 27% which, in general, is acceptable for absolute force measurement for biological applications. The error of the estimation may arise from the deviation of the cross section of the beams with respect to the idealized rectangular assumption, the nonuniformity of the cross section along the length of the beams, and the measurement error for the beam dimensions.

Softer sensors can also be calibrated by using softer precalibrated cantilevers. Since such soft precalibrated cantilevers are not commercially available, we propose the following approach to develop them. Here, a long cantilever is fabricated from thermally grown  $\text{SiO}_2$  on bare Si wafer. It is well known that  $\text{SiO}_2$  films have uniform thickness. The stiffness of a cantilever depends on its length as  $k \propto 1/L^3$ . Alternatively, the stiffness depends on where it is measured. The  $\text{SiO}_2$  cantilever will be calibrated at  $L_m < L$  (Fig. 10) by the precalibrated AFM cantilever, where  $L_m$  is the position on the cantilever at which the force-deflection relationship is measured and  $L$  is the total length of the cantilever. Then, the stiffness at the tip is simply  $k=k_m(L_m/L)^3$ , with  $k_m$  being the stiffness at  $L_m$ .  $L_m$  is chosen such that the estimation of the stiffness of the cantilever at  $L_m$  is similar to  $k_1 \cos \theta$ , i.e.,  $3EI/L_m^3 \approx k_1 \cos \theta$ , with  $k_1$  being the stiffness of the precalibrated AFM cantilever, and  $\theta$  being the angle between the softer cantilever (to be calibrated) and the AFM cantilever. The reason for this is to reduce the calibration error of the cantilever. Here,  $k_m$  is obtained by  $k_m=(k_1 w_1 \cos \theta)/w_m$  according to the measured force-deflection relationship at  $L_m$ , where  $w_1 \cos \theta$  is the deflection of the AFM cantilever and  $w_m$  is the deflection of the soft cantilever at  $L_m$ . Since the stiffness of the cantilever is inversely proportional to the cube of the cantilever length, this method can be used to establish calibrated cantilevers with stiffness down to two orders of magnitude lower than that of the AFM cantilever. It should be noted, however, that the uniformity of the width of the  $\text{SiO}_2$  cantilever depends on the fabrication accuracy. Since the cantilever will be deformed out of plane, the stiffness of the cantilever depends linearly on width. For a wide cantilever, the inaccuracy introduced by the variation of the width along the length is negligible.

- <sup>1</sup>N. Wang, J. P. Butler, and D. E. Ingber, *Science* **260**, 1124 (1993).
- <sup>2</sup>D. C. Van-Essen, *Nature (London)* **385**, 313 (1997).
- <sup>3</sup>K.-D. Chen, Y.-S. Li, M. Kim, S. Li, S. Yuan, S. Chien, and J. Y.-J. Shyy, *J. Biol. Chem.* **274**, 18393 (1999).
- <sup>4</sup>N. Q. Balaban *et al.*, *Nat. Cell Biol.* **3**, 466 (2001).
- <sup>5</sup>G. T. Charras and M. A. Horton, *Biophys. J.* **82**, 2970 (2002).
- <sup>6</sup>D. J. Webb, J. T. Parsons, and A. F. Horwitz, *Nat. Cell Biol.* **4**, E97 (2002).
- <sup>7</sup>J. D. Humphrey, *Proc. R. Soc. London, Ser. A* **459**, 3 (2003).
- <sup>8</sup>D. E. Ingber, *J. Cell. Sci.* **116**, 1157 (2003).
- <sup>9</sup>G. Bao and S. Suresh, *Nat. Mater.* **2**, 715 (2003).
- <sup>10</sup>D. J. Tschumperlin *et al.*, *Nature (London)* **429**, 83 (2004).
- <sup>11</sup>T. M. Suchyna, S. E. Tape, R. E. Koeppel, O. S. Andersen, F. Sachs, and P. A. Gottlieb, *Nature (London)* **430**, 235 (2004).
- <sup>12</sup>Y. F. Missirlis and A. D. Spiliotis, *Biomol. Eng.* **19**, 287 (2002).
- <sup>13</sup>K. J. Van Vliet, G. Bao, and S. Suresh, *Acta Mater.* **51**, 5881 (2003).
- <sup>14</sup>G. C. Easty, D. M. Easty, and E. J. Ambrose, *Exp. Cell Res.* **19**, 539 (1960).
- <sup>15</sup>M. J. Levesque, R. M. Nerem, and E. A. Sprague, *Biomaterials* **11**, 702 (1990).
- <sup>16</sup>A. J. Banes, J. Gilbert, D. Taylor, and O. Monbureau, *J. Cell. Sci.* **75**, 35 (1985).
- <sup>17</sup>C. M. Lo, H. B. Wang, M. Dembo, and Y. L. Wang, *Biophys. J.* **79**, 144 (2000).
- <sup>18</sup>A. K. Harris, P. Wild, and D. Stopak, *Science* **208**, 177 (1980).
- <sup>19</sup>S. Munevar, Y.-L. Wang, and M. Dembo, *Biophys. J.* **80**, 1744 (2001).
- <sup>20</sup>Y. Tseng, T. P. Kole, and D. Wirtz, *Biophys. J.* **83**, 3162 (2002).
- <sup>21</sup>A. R. Bausch, F. Ziemann, A. A. Boulbitch, K. Jacobson, and E. Sackmann, *Biophys. J.* **75**, 2038 (1998).
- <sup>22</sup>J. L. Tan, J. Tien, D. M. Pirone, D. S. Gray, K. Bhadriraju, and C. S. Chen, *Proc. Natl. Acad. Sci. U.S.A.* **100**, 1484 (2003).
- <sup>23</sup>E. Evans, D. Berk, and A. Leung, *Biophys. J.* **59**, 838 (1991).
- <sup>24</sup>J. W. Dai and M. P. Sheetz, *Biophys. J.* **68**, 988 (1995).
- <sup>25</sup>J. Guck, R. Ananthakrishnan, C. C. Cunningham, and J. Kas, *J. Phys.: Condens. Matter* **14**, 4843 (2002).
- <sup>26</sup>C. Haber and D. Wirtz, *Rev. Sci. Instrum.* **71**, 4561 (2000).
- <sup>27</sup>R. Merkel, P. Nassoy, A. Leung, K. Ritchie, and E. Evans, *Nature (London)* **397**, 50 (1999).
- <sup>28</sup>N. O. Petersen, W. B. McConnaughey, and E. L. Elson, *Proc. Natl. Acad. Sci. U.S.A.* **79**, 5327 (1982).
- <sup>29</sup>S. G. Shroff, D. R. Saner, and R. Lal, *Am. J. Physiol.: Cell Physiol.* **269**, C286 (1995).
- <sup>30</sup>C. A. Helm, W. Knoll, and J. N. Israelachvili, *Proc. Natl. Acad. Sci. U.S.A.* **88**, 8169 (1991).
- <sup>31</sup>S. R. Heidemann, S. Kaech, R. E. Buxbaum, and A. Matus, *J. Cell. Sci.* **145**, 109 (1999).
- <sup>32</sup>A. Yamamoto, S. Mishima, N. Maruyama, and M. Sumita, *Biomaterials* **19**, 871 (1998).
- <sup>33</sup>O. Thoumine, A. Ott, O. Cardoso, and J. J. Meister, *J. Biochem. Biophys. Methods* **39**, 47 (1999).
- <sup>34</sup>H. Miyazaki, Y. Hasegawa, and K. Hayashi, *J. Biomech.* **33**, 97 (2000).
- <sup>35</sup>S. Hu, L. Eberhard, J. Chen, J. C. Love, J. P. Butler, J. J. Fredberg, G. M. Whitesides, and N. Wang, *Am. J. Physiol.: Cell Physiol.* **287**, C1184 (2004).
- <sup>36</sup>K. A. Shaw, Z. L. Zhang, and N. C. MacDonald, *Sens. Actuators, A* **40**, 63 (1994).
- <sup>37</sup>B. Alberts, A. Johnson, J. Lewis, M. Raff, K. Roberts, and P. Walter, *Molecular Biology of the Cell* (Garland Science, New York, 2002).
- <sup>38</sup>H. Miyazaki and K. Hayashi, *Med. Biol. Eng. Comput.* **37**, 530 (1999).
- <sup>39</sup>A. Touhami, B. Nysten, and Y. F. Dufrene, *Langmuir* **19**, 4539 (2003).
- <sup>40</sup>R. E. Mahaffy, S. Park, E. Gerde, J. Kas, and C. K. Shih, *Biophys. J.* **86**, 1777 (2004).
- <sup>41</sup>T. A. Saif, *J. Fluid Mech.* **473**, 321 (2002).

## Reversible and repeatable linear local cell force response under large stretches

Shengyuan Yang, Taher Saif\*

Department of Mechanical and Industrial Engineering, University of Illinois at Urbana-Champaign, 1206 West Green Street, Urbana, IL 61801, USA

Received 25 November 2004, revised version received 16 December 2004

### Abstract

Large stretching and un-stretching force response of adherent fibroblasts is measured by micromachined mechanical force sensors. The force sensors are composed of a probe and flexible beams. The probe, functionalized by fibronectin, is used to contact the cells. The flexible beams are the sensing element. The sensors are made of single crystal silicon and fabricated by the SCREAM process. The maximum cell stretch reached is  $\sim 50 \mu\text{m}$ , which is about twice of the cell initial size, and the time delay between two consecutive stretching/un-stretching steps is 75 s unless otherwise stated. We find that the force response of the cells is strongly linear, reversible, and repeatable, with a small stiffening at the initial deformation stage. Force response of single cells measured before and after cytochalasin D treatment suggests that actin filaments take almost all the cell internal forces due to stretch. These findings may shed light on the increasing understanding on the mechanical behavior of cells and provide clues for making new classes of biological materials having uncommon properties.

© 2005 Elsevier Inc. All rights reserved.

**Keywords:** Cell mechanics; Single living cells; Force response; Large deformation; Linear; Reversible and repeatable; Actin filaments; Microelectromechanical systems (MEMS)

### Introduction

During the past decade, cell mechanics has received increasing attention due to the influence of intracellular and extracellular forces on cell adhesion, migration, growth, differentiation, apoptosis, gene expression, and signal transduction [1–12]. Significant effort has been directed to the measurement of the force response of single living cells due to deformation. Experimental techniques that are employed include micropipettes [13], optical tweezers [14], magnetic twisting cytometry [1], magnetic bead microrheometry [15], atomic force microscopy (AFM) [16], and surface force apparatus [17]. Such efforts revealed significant insight on the mechanical behavior of cells under small deformations ( $\sim 1\text{--}2 \mu\text{m}$  or less). There are, however, numerous instances where the cells may be under large deformation. For

example, a skeletal muscle can contract to half its optimal length or expand by 50% under physiological conditions. Muscle fibers (cells) in the skeletal muscle may also experience such large deformations [18]. In diffuse axonal injury, the microscopic shear strains could be higher than 50% [19]. The shape of initially rounded rabbit dermal fibroblasts, growing in a collagen–GAG matrix, could be elongated up to an average aspect ratio of 2.8 during the first 15 h in culture [20]. In tensile experimental testing of mechanical properties of soft biological tissues that consists of many cells, stretches more than 50% are normally reached, and some of the cells in the tissues should be subjected to stretches larger than 50% [21,22].

Studies on cell mechanical behavior due to large deformations are limited. The tension and oscillatory stiffness of isolated cardiac myocytes were measured by a pair of micropipettes, and it was found that the cell force response relaxes at each stretch increment [23]. The force versus elongation of single rabbit fibroblasts was measured by a pair of micropipettes, and the force response from six

\* Corresponding author. Fax: +1 217 244 6534.

E-mail address: [saif@uiuc.edu](mailto:saif@uiuc.edu) (T. Saif).

cells was averaged and was found to be linear with deformation [24]. The nonlinear force response due to compression was observed for single bovine endothelial cells by a pair of microplates [25]. Linear force response was observed under stretch for single rat fibroblasts by a functionalized biomicroelectromechanical system (bioMEMS)-based force sensor [26].

Studies on the cell unloading mechanical response are rare, regardless of small or large deformation. AFM was used to load and unload single yeast cells by small indentation, and force response was found to be linear and reversible [27]. A pair of microplates was used to compress and decompress suspended single bovine endothelial cells, and nonlinear reversible force response was reported, but no data were presented [25].

A fundamental question related to the cell force response due to deformation is the mechanism by which the cell resists deformation. It is generally believed that actin filaments of cell cytoskeleton play a key role in taking the cell internal forces [1,26,28–30]. Experiments show that the treatment of a cell with Cyto D (cytochalasin D, a drug that disrupts the actin filaments in a cell) significantly decreases the mechanical response of the cell. For example, Cyto D suppressed the stiffening of the cytoskeleton of endothelial cells [1]. In Ref. [31], two sets of single chick fibroblasts were stretched by a fixed amount of deformation, with one set treated with Cyto D and the other untreated. The average tension in the Cyto D-treated fibroblasts was found to decrease, but it did not vanish even after 50 min. Cyto D-treated connective tissue models also showed reduced force response under stretch [32]. Stiffness decrease due to Cyto D was observed for airway smooth muscle cells, but complete suppression was not observed (more than 25% of the stiffness left after treatment with 10  $\mu$ M Cyto D compared to that for the untreated cells) [33].

In this paper, we use functionalized bioMEMS-based force sensors to stretch and un-stretch single living cells and measure their force response. The time span of the experiments is slow enough so that the cells can adapt to the applied stretches biologically. Hence, the measured force response is not only mechanical but biological as well. We show that the force response is strongly linear, reversible, and repeatable with no appreciable creep and relaxation. The force response shows small stiffening at the initial deformation stage. The same cells when tested after Cyto D treatment show negligible force response, giving the direct evidence that actin filaments play a key role in taking the cellular internal forces.

## Materials and methods

### Basic idea

A bioMEMS sensor used here consists of a probe and microflexible beams which act as the cell force sensor

(Fig. 1A). The probe and the sensor beams are made of single crystal silicon. The silicon chip (sensor base) is held by a  $x$ - $y$ - $z$  piezoelectric actuator. The probe is functionalized by coating with fibronectin (to simulate the cell–extracellular matrix adhesion). It is then brought in contact with a cell for 20 min. The cell forms adhesion sites with the probe most likely by focal adhesion complex activation [34]. The cell can be stretched by moving the sensor base away from the cell using the piezoelectric actuator. The cell applies a force on the probe which is measured from the deflection of the beams and their combined spring constant. Fig. 1B schematically shows a stretched cell. Here the spring represents the beams with a combined spring constant  $k$ . In the stretched state, the sensor base is moved by  $R$  to the right by the piezoelectric actuator. The deformation,  $D$ , of the cell is given by the movement of the sensor probe. The deflection of the sensing spring is  $w = R - D$ . Thus the cell force response is  $F = kw$ . Force response of the cell is given by the measured  $(F, D)$  relation. Note that although the spring is linear,  $(F, D)$  relation may be nonlinear. For example, if the cell does not provide any restoring force against deformation, then  $R = D$  and  $F = 0$  for all  $D$ .

### BioMEMS sensors

Two types of bioMEMS sensors were designed and fabricated. Figs. 1C–E show the type of sensors which can only measure the cell force response in the  $x$  direction. Here, two parallel fixed–fixed beams act as the force sensor. They are connected by a backbone structure and hence act as a single spring. A probe is attached to the backbone to contact the cells. The dimension of each beam is length  $\times$  width (in plane)  $\times$  depth = 1.96 mm  $\times$  0.77  $\mu$ m  $\times$  10.5  $\mu$ m, the space between the two beams is 300  $\mu$ m, and the length of the backbone between the right beam and the probe is 1 mm (Fig. 1C). The width and depth of the probe tip that contacts the cells are 2.0  $\mu$ m and 10.5  $\mu$ m, respectively (Fig. 1E). Hence, the sensor is compliant in the  $x$  direction but stiff in the  $y$  and  $z$  directions. In cell force response measurements, the sensor moves in the  $x$  direction, driven by the piezoelectric actuator. Thus, if the cell force response is not collinear with the direction of stretch, i.e.,  $x$  direction, the sensor measures only the  $x$  component of cell force response. The stiffness of the sensor in the  $x$  direction is estimated, from the geometry and elastic modulus of silicon, as 3.4 nN  $\mu$ m<sup>-1</sup>. From the displacement measurement resolution of 0.14  $\mu$ m, we have the force resolution of 0.5 nN.

Fig. 1F schematically shows the class of sensors which can measure the cell force response in both the  $x$  and  $y$  directions. Here, a cantilevered beam acts as the force sensor. A rigid bar is attached to the free end of the beam, and the probe is attached to the free end of the bar. Suppose, the piezoelectric actuator moves the sensor base along the  $x$  direction by  $R_x$ , and the corresponding cell deformations are  $D_x$  and  $D_y$  in the  $x$  and  $y$  directions, respectively. Then the

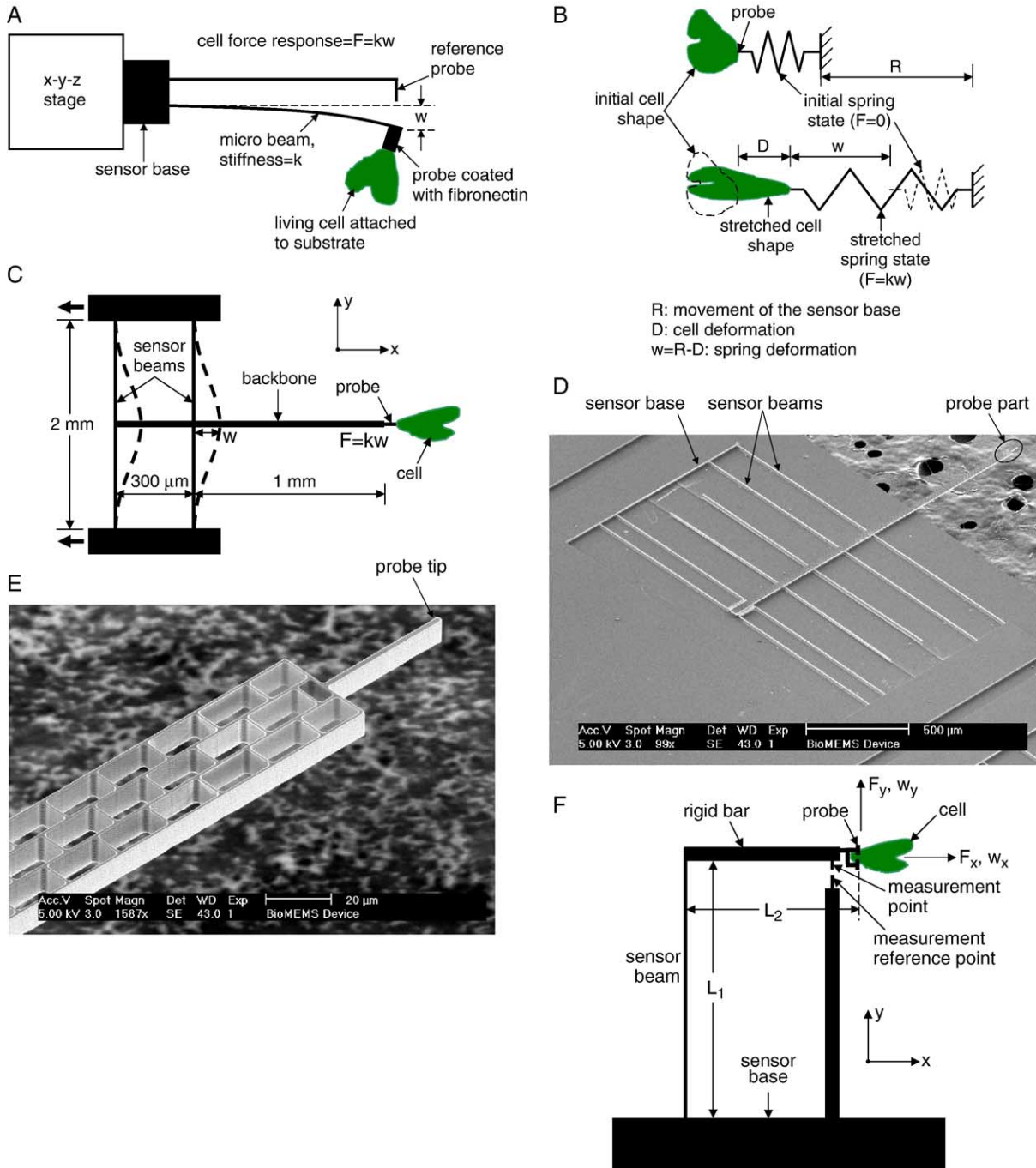


Fig. 1. BioMEMS-based sensors for the study of cell force response. (A) Basic idea of bioMEMS-based method for the study of cell force response. (B) Schematic showing the measurements of cell deformation and deflection of the beams. (C) Schematic of a bioMEMS sensor that can only measure cell force response in the  $x$  direction. (D) Scanning electron microscope image of the sensor sketched in C. (E) Probe part of the sensor that contacts the cells. (F) Schematic of a bioMEMS sensor that can measure cell force response in both the  $x$  and  $y$  directions.

translations (referred to as the sensor deflections in the below) of the probe tip,  $w_x$  and  $w_y$ , with respect to the sensor base in the  $x$  and  $y$  directions, respectively, are given by

$$\begin{aligned} w_x &= R_x - D_x \\ w_y &= D_y. \end{aligned} \quad (1)$$

The cell force components,  $F_x$  and  $F_y$ , in the  $x$  and  $y$  directions, respectively, relate to  $w_x$  and  $w_y$  by

$$\begin{bmatrix} F_x \\ F_y \end{bmatrix} = \frac{2EI}{L_1} \begin{bmatrix} \frac{6}{L_1^2} & \frac{3}{L_1 L_2} \\ \frac{3}{L_1 L_2} & \frac{2}{L_2^2} \end{bmatrix} \begin{bmatrix} w_x \\ w_y \end{bmatrix} \quad (2)$$

where  $E$  is the Young's modulus of the beam and bar  $I$  is the moment of inertia of the cross-section of the beam. The deri-

vation of Eq. (2) is given in Appendix A. Here, the cross-sectional dimensions of the beam are width  $\times$  depth =  $2.0 \mu\text{m} \times 13.1 \mu\text{m}$ , and  $L_1 = 1 \text{ mm}$ ,  $L_2 = 429 \mu\text{m}$ . The force resolution of the measurement system with this type of sensors is estimated as  $0.6 \text{ nN}$ .

### Sensor fabrication

The MEMS devices were fabricated by the SCREAM process [35]: (1) grow  $1 \mu\text{m}$  thick  $\text{SiO}_2$  layer on the surface of the wafer by thermal oxidation; (2) transfer the pattern of the mask for a MEMS sensor to the oxide surface by photolithography; (3) transfer the pattern to silicon by reactive ion etching (RIE); (4) anisotropically etch silicon to the desired depth, about  $20 \mu\text{m}$ , by inductively coupled plasma (ICP); (5) thermally-oxidize the wafer again to put a protecting oxide layer on vertical silicon surface; (6) anisotropically remove the oxide layer on the floor of the patterned trench by RIE; (7) anisotropically etch down the exposed silicon again for an additional depth, about  $10 \mu\text{m}$ , by ICP; (8) isotropically etch the exposed silicon to release the beams, by ICP; (9) remove all the oxide from the device, by wet hydrofluoride acid etching, to get the final sensors made from pure single crystal silicon.

### Cell culture and force response measurement

The MEMS sensors were incubated in  $50 \mu\text{g ml}^{-1}$  fibronectin (BD Biosciences) solution at room temperature for 6 h for coating. The cells were cultured from a monkey kidney fibroblast (MKF) cell line, CV-1 (ATCC). The culture medium contains 90% Dulbecco's Modified Eagle's Medium (ATCC) and 10% fetal bovine serum (ATCC), and the cells were incubated in an incubator with  $37^\circ\text{C}$  temperature, 5%  $\text{CO}_2$  and 98% humidity. The probes of the sensors were brought in contact with the cells for 20 min to form the focal adhesion before the force response measurements started. The force response measurements were conducted at room temperature. An inverted optical microscope (Olympus CK40) with an objective of  $10\times$  was used to monitor the deformation of the cell and the displacement of sensor probes. A cooled CCD camera (Olympus MagnaFire S99806) and its data acquisition software were used for imaging and dimensional measurement.

We define the deformation of a cell in the  $x$  direction as positive when the cell is elongated, and negative when the cell is indented; the deformation in the  $y$  direction is positive upward. The sensor deflection in the  $x$  direction is positive when the probe tip moves towards the right for the configuration in Figs. 1C and F; the sensor deflection in the  $y$  direction is positive upward. Similarly, the cell force response, acting on the probe, in the  $x$  direction is positive when it is towards the right for the configuration in Figs. 1C and F; the cell force response in the  $y$  direction is positive upward. Eqs. (1) and (2) complied with these definitions. The cell deformations, sensor deflections, and force

response were measured relative to the initial configuration of the cell after contact with the probe unless otherwise stated. During all the measurements, the time delay between two consecutive deformations was kept at 75 s unless otherwise stated.

## Results and discussion

### Single component force response

Fig. 2 shows the measured force response of an MKF with one stretching and un-stretching cycle. Clearly, the force response is strongly linear and reversible, with a small stiffening at the initial deformation stage. Fig. 3 shows the measured force response of an MKF with more stretching and un-stretching cycles. The contact between the probe tip and the cell was broken at the end of Stretching-3. Here, although there are significant translations between the loading and unloading curves for the first and second cycles (for example, the unloading curve for the first cycle reaches zero force response at a cell deformation of about  $15 \mu\text{m}$ ), the general trend of the force response is not only strongly linear and reversible, but also strongly repeatable. Note that the force response curve for Un-stretching-2 is significantly higher than that for Stretching-2, which is not possible for a traditional material since the released elastic energy during unloading should be lower than or equal to that gained during loading. But for living cells, this may not be always the case. During the force response measurement, the cells may response to the external stretching by actively producing contraction [32] and rearrange their internal structures, which may result in higher unloading force response than loading force response. The extra energy

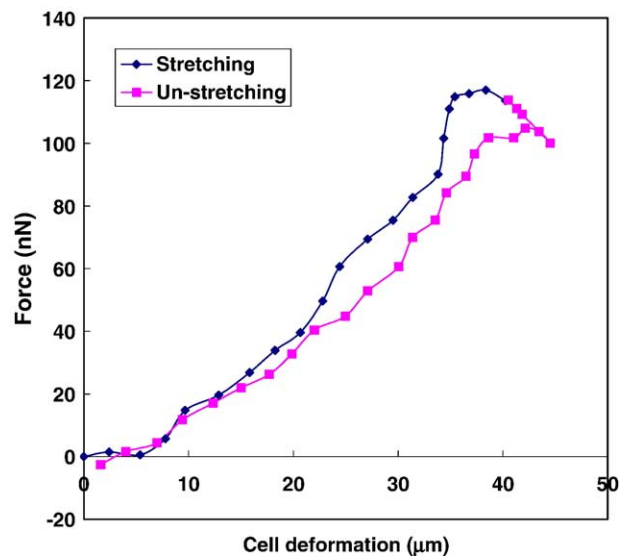


Fig. 2. Measured linear and reversible force response of a monkey kidney fibroblast.

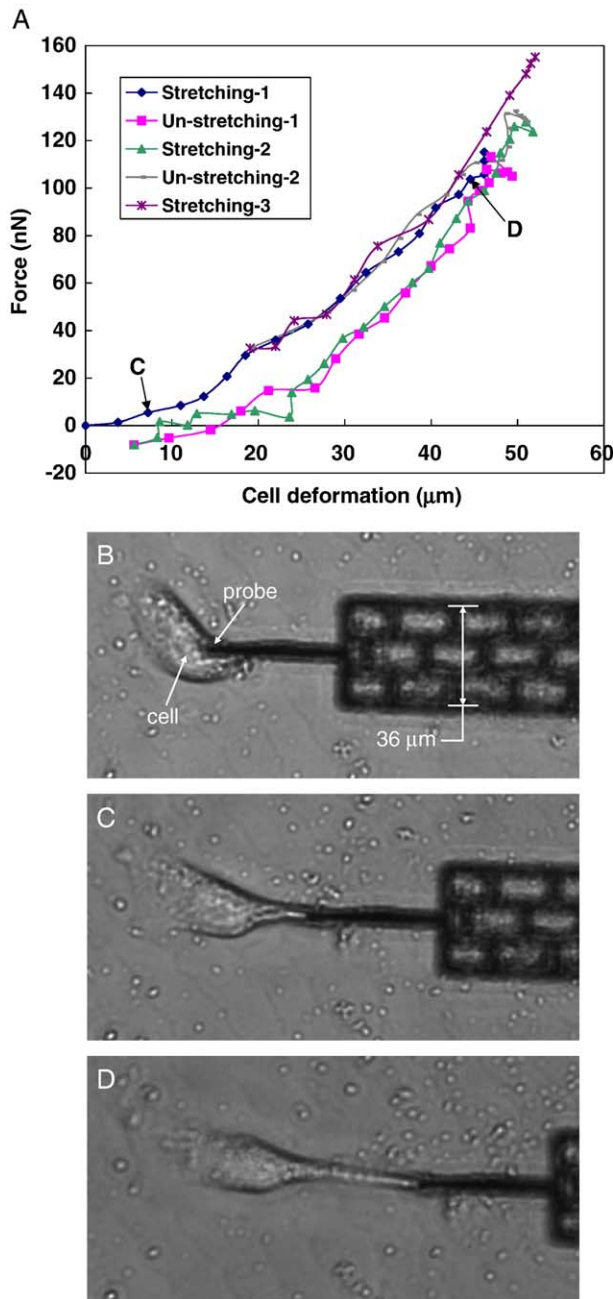


Fig. 3. Measured linear, reversible, and repeatable force response of a monkey kidney fibroblast. (A) Cell force response versus cell deformation. (B–D) Phase images of the MKF right after the probe attachment (no stretch), and at two deformation states corresponding to points C (small stretch) and D (large stretch) in A, respectively.

required for this phenomenon to occur comes from the power plants of the living cells.

The two experiments for Figs. 2 and 3 were done with the sensor shown in Fig. 1C, and the maximum stretching of the cells was about 50 μm, which is approximately twice the cell's initial size (before the stretching experiment). In order to investigate any possible creep/relaxation force response behavior, we varied the time delay between two consecutive force measurements from 1 s to 195 s. We observed a similar

cell force response as shown in Fig. 3A, and no appreciable (within the resolution of the measurement system) cell creep/relaxation was observed. Small permanent deformation was always observed for all the loading rates.

Based on current knowledge on the mechanical behavior of living cells [36–38], for example, cytoskeleton stiffens under deformation [28] and the cell is strongly viscoelastic [16], the force response of a living cell due to a large deformation was expected to be nonlinear and irreversible. Our finding contradicts this expectation. Our finding indicates that the cell response to a large deformation may involve reversible biological and biochemical processes with minimal energy loss, which may provide a possible mechanism that nature has adopted to achieve high energy efficiency in living biological systems [39]. This finding may also provide clues for making new classes of biological materials having uncommon properties. For example, directed growth of biological tissues from cells on designed substrates may have the strong linear, reversible, and repeatable force response under large stretches.

#### Two component force response

The sensor shown in Fig. 1F was used to measure the force response of an MKF. Here, the silicon chip was moved by the piezoelectric actuator in the  $x$  direction. Now, the probe tip moves along both the  $x$  and  $y$  directions, giving cell deformations  $D_x$  and  $D_y$ . Fig. 4A shows the measured sensor deflections  $(w_x, w_y)$ , for the cell as it was stretched and un-stretched. We find that the deflection response is strongly reversible and repeatable for the first three stretching and un-stretching cycles (i.e., Stretching-1 and Un-stretching-1, Stretching-2 and Un-stretching-2, and Stretching-3 and Un-stretching-3). The linear trendline for the Stretching-1 gives  $w_y = -0.61 w_x$ , which is close to the theoretical relationship  $w_y = -0.63 w_x$  for  $F_y = 0$ . However, at the last few data points of Un-stretching-1,  $(w_x, w_y)$  significantly deviates from  $w_y = -0.61 w_x$ , implying  $F_y$ . There is also a significant deviation near the end of Un-stretching-2 and the beginning of Stretching-3 from this linear trendline. But, the overall trend of  $(w_x, w_y)$  for each of the stretching or un-stretching process in these three cycles shows that the force component in the  $y$  direction can be neglected.

Fig. 4B shows the cell deformations,  $(D_x, D_y)$ , for the cyclic cell stretching and un-stretching experiment. Here, the maximum cell deformation for each cycle decreases for the first three cycles. The cell deformation is strongly reversible for each cycle of these three cycles, which implies that the cell recovers its original state by tracing back its original deformation process. Fig. 4C shows the plot of the cell force response versus the corresponding cell deformation in the  $x$  direction. We see strong linear and reversible cell force response for each of the first three cycles of the stretching and un-stretching. We again see that, at some cell deformations, the force response for the unloading processes

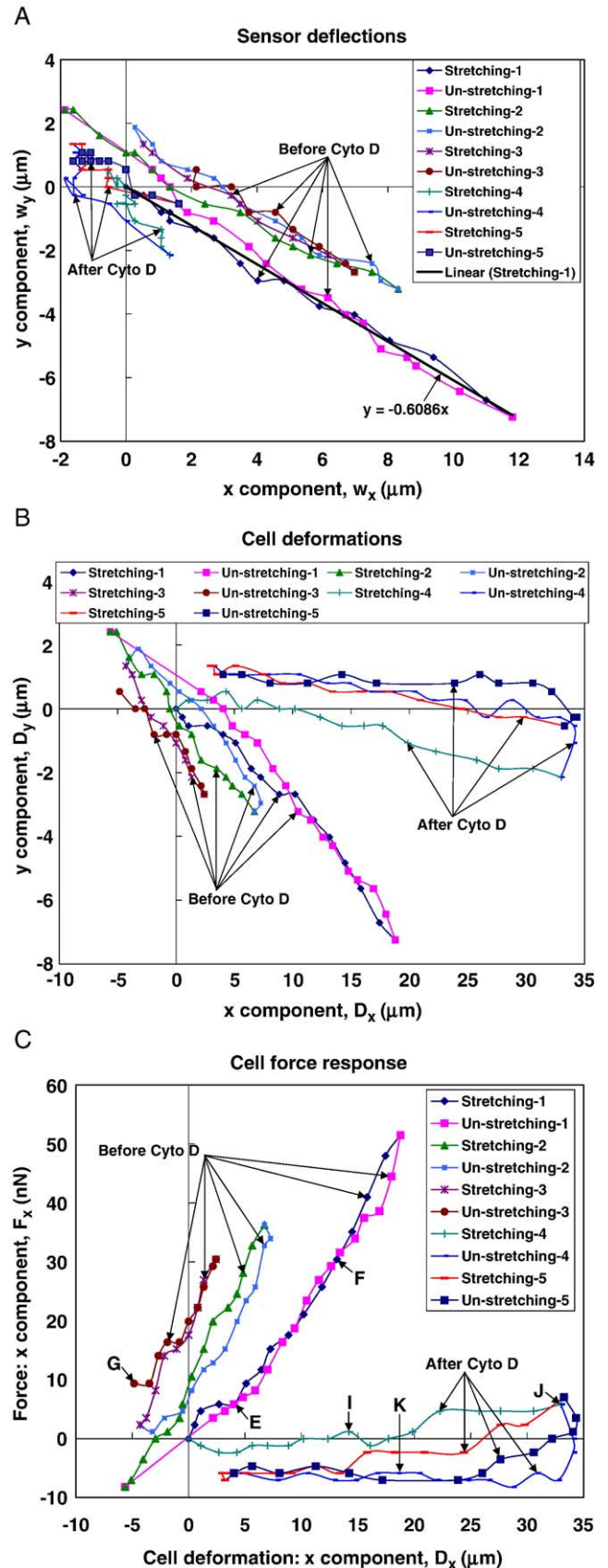
is higher than that for the corresponding loading processes of these three cycles. In Figs. 4B and C, the shifts in the cell deformation and force response plots between the first three stretching and un-stretching cycles are due to the produced permanent deformation in the  $y$  direction. Fig. 4D shows the phase image right before the force response measurement, where the relative displacements between the reference point and the measurement point in the  $x$  direction indicate the force after initial cell deformation. Figs. 4E–G correspond to the points E–G in Fig. 4C, respectively. Figs. 4D–F show that the cell underwent rotation with respect to a fixed point, thus aligning along the stretch direction.

#### Effect of Cyto D treatment

In order to explore the role of actin filaments in taking the cell force response, experiments were carried out on MKFs before and after treating them with Cyto D (Sigma,  $10 \mu\text{g ml}^{-1}$ ). An initial stretch was applied to each cell and its force response was measured. Cyto D was then applied. For the experiment shown in Fig. 4, the cell changed its shape and relaxed (see Figs. 4G and H) within 3 s after the application of Cyto D. Its shape and force response remain unchanged within the following 5 min, after which the cell was stretched and its force response measured. This observation of fast cell relaxation within few seconds and remaining stable afterwards is in contrast to the results reported in Ref. [40], where it took 20–120 min for Cyto D to take effect. There was also no detachment of the cell from the substrate or the probe during the measurements “After Cyto D”. Note the three cycles of stretching and un-stretching measurements (already discussed in the above) conducted before the application of Cyto D are marked by “Before Cyto D” in Fig. 4. The cell deformations, sensor deflections, and force response for “After Cyto D” were measured relative to the initial configuration of the cell when Stretching-4 was started.

In Fig. 4, two cyclic stretching and un-stretching (i.e., Stretching-4 and Un-stretching-4, and Stretching-5 and Un-stretching-5) for “After Cyto D” were done. From Fig. 4A, we see very small sensor deflections for “After Cyto D”. From Fig. 4B, we see a significant decrease in the cell deformation in  $y$  direction for “After Cyto D”. The small cell deformation in the  $y$  direction but large deformation in the  $x$  direction implies that the cell force acting on the sensor is negligible, i.e., the sensor is moving almost as a rigid body in the  $x$  direction. From Fig. 4C, by comparing the trends of the cell force response for “Before Cyto D” and “After Cyto D”, respectively, we see the cell force response is almost 100% suppressed due to treatment of Cyto D, which shows that the actin filaments are the primary contributors in providing cell force response. The hysteresis in cell force response for the first stretching and un-stretching cycle of “After Cyto D” is much larger than “Before Cyto D”.

We also observed significant viscous force response for “After Cyto D”. For example, in the first stretching process



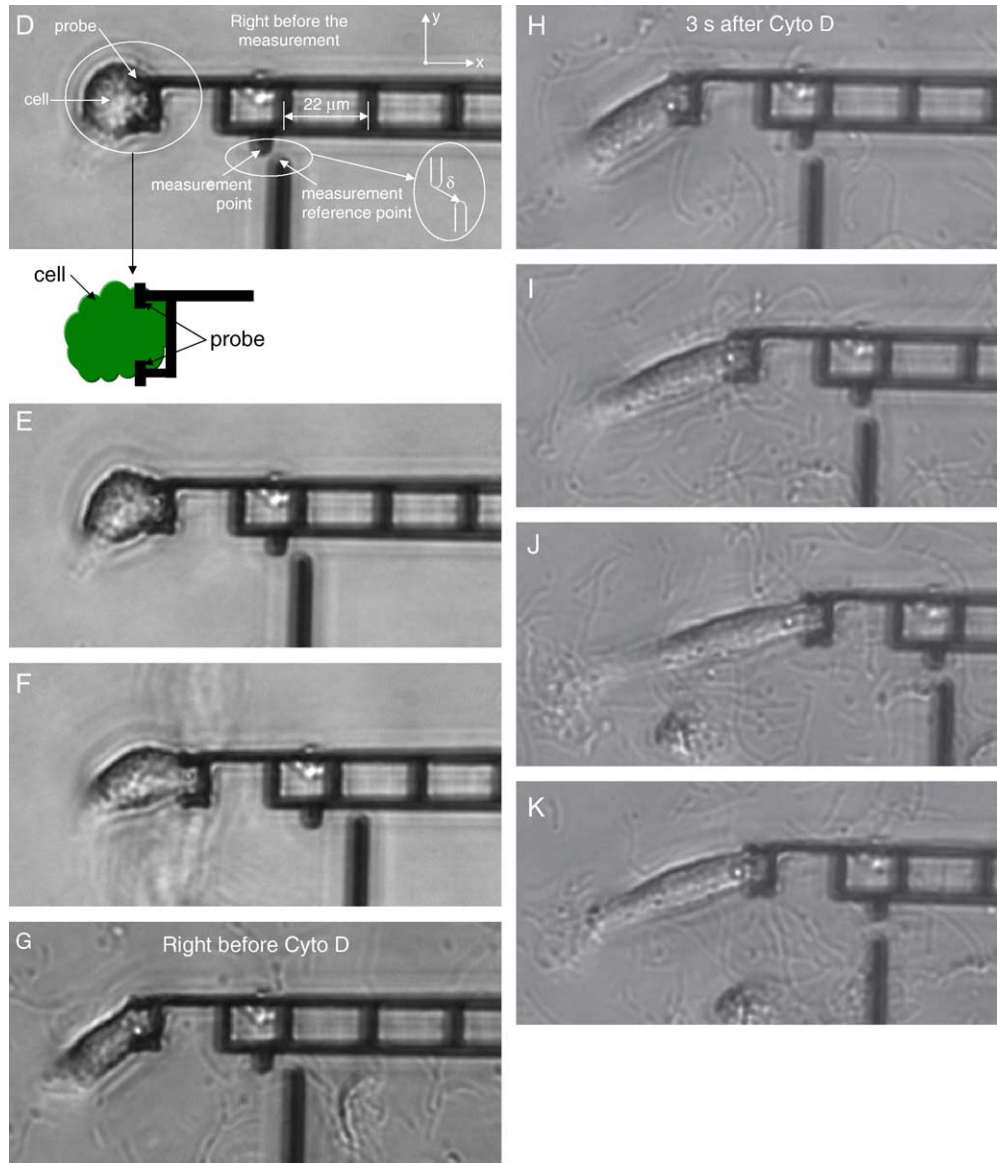


Fig. 4. Cyclic cell stretching and un-stretching force response measurement of a monkey kidney fibroblast by the force sensor shown in Fig. 1F and the effect due to Cyto D treatment. (A) Sensor deflections in the  $x$  and  $y$  directions. (B) Cell deformations in the  $x$  and  $y$  directions. (C) Cell force response versus the cell deformation in the  $x$  direction. (D) Phase image right before the force response measurement. (E–G) Correspond to the phase images for the points E–G for “Before Cyto D” in C, respectively, and G is also the phase image right before the addition of Cyto D. (H) Phase image 3 s after the addition of Cyto D. (I–K) Correspond to the phase images for the points I to K for “After Cyto D” in C, respectively.

for “After Cyto D”, we fixed the sensor base at cell deformations of  $33.0\ \mu\text{m}$  and  $2.1\ \mu\text{m}$  (in the  $x$  and  $y$  directions, respectively). We found, after 1 min, the cell deformations changed to  $34.1\ \mu\text{m}$  and  $1.1\ \mu\text{m}$ , while the  $x$  component cell force relaxed from  $5.8\ \text{nN}$  to 0 (note that the  $x$  component of the absolute cell force response is still not 0 since the cell force response data are measured relative to the initial configuration of the cell after contact with the probe, where the probe is subjected to a small force). In the second stretching process for “After Cyto D”, similarly, we fixed the sensor base at cell deformations of  $33.3\ \mu\text{m}$  and  $0.5\ \mu\text{m}$  in the  $x$  and  $y$  directions, respectively. After 1 min, the corresponding cell deformations changed

to  $34.3\ \mu\text{m}$  and  $0.3\ \mu\text{m}$ , while the  $x$  component cell force relaxed from  $7.0\ \text{nN}$  to  $3.5\ \text{nN}$ . Note that we did not observe any appreciable relaxation for “Before Cyto D”, which suggests that the viscosity of the cell for “After Cyto D” might be much larger than that for “Before Cyto D”. The enhanced viscosity for “After Cyto D” is possibly due to depolymerization of actin filaments (which may increase the viscosity of the cytoplasm). However, in Fig. 4B, for “After Cyto D”, the cell recovers its original state by following the deformation history of the stretching process except the small plastic deformation, which indicates the role of the elastic cell membrane in the recovery process.

Figs. 4G and H show the cell right before the application of Cyto D (i.e., the end point of Un-stretching-3) and 3 s after. The latter shows the decrease of cell force response (compare the sensor deflection). Figs. 4I–K correspond to images for the points I–K for “After Cyto D” in Fig. 4C, respectively. The cell shape and deformation recovery for the un-stretching process is reflected in these figures. Figs. 4H and I show that the cell continued to relax during the initial stretching stage for “After Cyto D”.

## Conclusions

We have demonstrated that functionalized bioMEMS can be applied as a simple basic tool for manipulating living cells and measuring their force response. The cell force response has been shown to be strongly linear, reversible, and repeatable subject to large stretches. Cells aligned with the stretch direction, which makes the transverse force response negligible. Actin filaments have been shown to play a dominant role in taking the cell internal force. Without actin filaments, cell force response is relatively negligible.

## Acknowledgments

We thank Prof. N. Wang of Harvard School of Public Health and Prof. V. I. Gelfand of the Department of Cell and Structural Biology at the University of Illinois at Urbana-Champaign for helpful discussion on this work. This work was supported by NSF (ECS 01-18003).

## Appendix A

For the sensor shown in Fig. 1F, the displacements of the probe tip in the  $x$  and  $y$  directions are induced by either  $F_x$  or  $F_y$  or both. For example,  $F_x$  deforms the sensor beam in the  $x$  direction and rotates its free end. This rotation tilts the rigid bar, which moves the probe tip in the  $y$  direction. Similarly,  $F_y$  also induces sensor deflections in both  $x$  and  $y$  directions. In Fig. 4A, the absolute maximum sensor deflection in the  $x$  direction is 11.8  $\mu\text{m}$ , which is only 1.18% of the length of the sensor beam ( $L_1 = 1$  mm). The absolute maximum sensor deflection in the  $y$  direction is 7.2  $\mu\text{m}$ , which is only 1.68% of the length of the rigid bar ( $L_2 = 429$   $\mu\text{m}$ ). Thus, we assume that the beam is subjected to small deformation and rotation in finding the analytical expressions for the sensor deflections.

The deflection in the  $x$  direction and rotation (positive counterclockwise) at the free end of the beam induced by  $F_x$  alone are given by  $F_x L_1^3/3EI$  and  $-F_x L_1^2/2EI$ , respectively, and such a rotation induces a sensor deflection of  $(-F_x L_1^2/2EI)L_2$  in the  $y$  direction.  $F_y$  creates a bending moment  $F_y L_2$  at the free end of the beam, which in turn alone

induces a deflection in the  $x$  direction and rotation at the free end of the beam of  $-F_y L_2 L_1^2/2EI$  and  $F_y L_2 L_1/EI$ , respectively, and such a rotation induces a sensor deflection of  $(F_y L_2 L_1/EI)L_2$  in the  $y$  direction.

According to the linear superimposition, the total sensor deflections induced by  $F_x$  and  $F_y$  combined are given by

$$w_x = \frac{F_x L_1^3}{3EI} - \frac{F_y L_1^2 L_2}{2EI} \quad \text{and} \quad w_y = -\frac{F_x L_1^2 L_2}{2EI} + \frac{F_y L_1 L_2^2}{EI} \quad (\text{A1})$$

for the  $x$  and  $y$  directions, respectively. By inverting Eq. (A1), Eq. (2) is obtained, which is

$$\begin{bmatrix} F_x \\ F_y \end{bmatrix} = \frac{2EI}{L_1} \begin{bmatrix} \frac{6}{L_1^2} & \frac{3}{L_1 L_2} \\ \frac{3}{L_1 L_2} & \frac{2}{L_2^2} \end{bmatrix} \begin{bmatrix} w_x \\ w_y \end{bmatrix}, \quad (\text{A2})$$

## References

- [1] N. Wang, J.P. Butler, D.E. Ingber, Mechanotransduction across the cell surface and through the cytoskeleton, *Science* 260 (1993) 1124–1127.
- [2] I.S. Sukharev, B. Martinac, V.Y. Arshavsky, C. Kung, Two types of mechanosensitive channels in the *Escherichia coli* cell envelope: solubilization and functional reconstitution, *Biophys. J.* 65 (1993) 177–183.
- [3] D.C. Van-Essen, A tension-based theory of morphogenesis and compact wiring in the central nervous system, *Nature* 385 (1997) 313–318.
- [4] C.S. Chen, M. Mrksich, S. Huang, G.M. Whitesides, D.E. Ingber, Geometric control of cell life and death, *Science* 276 (1997) 1425–1428.
- [5] M.E. Chicurel, C.S. Chen, D.E. Ingber, Cellular control lies in the balance of forces, *Curr. Opin. Cell Biol.* 10 (1998) 232–239.
- [6] K.-D. Chen, et al., Mechanotransduction in response to shear stress, *J. Biol. Chem.* 274 (1999) 18393–18400.
- [7] E.C. Breen, Mechanical strain increase type I collagen expression in pulmonary fibroblasts in vitro, *J. Appl. Physiol.* 88 (2000) 203–209.
- [8] M. Salvador-Silva, C.S. Ricard, O.A. Agapova, P. Yang, M.R. Hernandez, Expression of small heat shock proteins and intermediate filaments in the human optic nerve head astrocytes exposed to elevated hydrostatic pressure in vitro, *J. Neurosci. Res.* 66 (2001) 59–73.
- [9] Y. Sawada, M.P. Sheetz, Force transduction by triton cytoskeletons, *J. Cell Biol.* 156 (2002) 609–615.
- [10] D.J. Webb, J.T. Parsons, A.F. Horwitz, Adhesion assembly, disassembly and turnover in migrating cells-over and over and over again, *Nat. Cell Biol.* 4 (2002) E97–E100.
- [11] C.H. Thomas, J.H. Collier, C.S. Sfeir, K.E. Healy, Engineering gene expression and protein synthesis by modulation of nuclear shape, *Proc. Natl. Acad. Sci. U. S. A.* 99 (2002) 1972–1977.
- [12] P.F. Davies, J. Zilberberg, B.P. Helmke, Spatial microstimuli in endothelial mechanosignaling, *Circ. Res.* 92 (2003) 359–370.
- [13] E. Evans, D. Berk, A. Leung, Detachment of agglutinin-bonded red-blood-cells: 1. Forces to rupture molecular-point attachments, *Biophys. J.* 59 (1991) 838–848.
- [14] J. Sleep, D. Wilson, R. Simmons, W. Gratzer, Elasticity of the red cell membrane and its relation to hemolytic disorders: an optical tweezers study, *Biophys. J.* 77 (1999) 3085–3095.
- [15] A.R. Bausch, F. Ziemann, A.A. Boulbitch, K. Jacobson, E. Sackmann, Local measurements of viscoelastic parameters of adherent cell surfaces by magnetic bead microrheometry, *Biophys. J.* 75 (1998) 2038–2049.

- [16] J. Alcaraz, et al., Microrheology of human lung epithelial cells measured by atomic force microscopy, *Biophys. J.* 84 (2003) 2071–2079.
- [17] C.A. Helm, W. Knoll, J.N. Israelachvili, Measurement of ligand–receptor interactions, *Proc. Natl. Acad. Sci. U. S. A.* 88 (1991) 8169–8173.
- [18] W. Maurel, Y. Wu, N. Magnenat Thalmann, D. Thalmann, *Biomechanical Models for Soft Tissue Simulation*, Springer-Verlag, Berlin, 1998.
- [19] B.J. Pfister, T.P. Weihs, M. Betenbaugh, G. Bao, An in vitro uniaxial stretch model for axonal injury, *Ann. Biomed. Eng.* 31 (2003) 589–598.
- [20] T.M. Freyman, I.V. Yannas, Y.-S. Pek, R. Yokoo, L.J. Gibson, Micromechanics of fibroblast contraction of a collagen–GAG matrix, *Exp. Cell Res.* 269 (2001) 140–153.
- [21] M. Nordin, T. Lorenz, M. Campello, *Biomechanics of tendons and ligaments*, in: M. Nordin, V.K. Frankel (Eds.), *Basic Biomechanics of the Musculoskeletal System*, Lippincott Williams and Wilkins, Philadelphia, 2001, pp. 102–125.
- [22] K. Hayashi, *Mechanical properties of soft tissues and arterial walls*, in: G.A. Holzapfel, R.W. Ogden (Eds.), *Biomechanics of Soft Tissue in Cardiovascular Systems*, Springer Wien, New York, 2003, pp. 15–64.
- [23] R.E. Palmer, A.J. Brady, K.P. Roos, Mechanical measurements from isolated cardiac myocytes using a pipette attachment system, *Am. J. Physiol.* 270 (1996) C697–C704.
- [24] H. Miyazaki, Y. Hasegawa, K. Hayashi, A newly designed tensile tester for cells and its application to fibroblasts, *J. Biomech.* 33 (2000) 97–104.
- [25] N. Caille, O. Thoumine, Y. Tardy, J.-J. Meister, Contribution of the nucleus to the mechanical properties of endothelial cells, *J. Biomech.* 35 (2002) 177–187.
- [26] M.T.A. Saif, C.R. Sager, S. Coyer, Functionalized biomicroelectromechanical systems sensors for force response study at local adhesion sites of single living cells on substrates, *Ann. Biomed. Eng.* 31 (2003) 950–961.
- [27] A. Touhami, B. Nysten, Y.F. Dufrene, Nanoscale mapping of the elasticity of microbial cells by atomic force microscopy, *Langmuir* 19 (2003) 4539–4543.
- [28] D. Stamenovic, N. Wang, Cellular responses to mechanical stress, invited review: engineering approaches to cytoskeletal mechanics, *J. Appl. Physiol.* 89 (2000) 2085–2090.
- [29] D.E. Ingber, Tensegrity I. Cell structure and hierarchical systems biology, *J. Cell Sci.* 116 (2003) 1157–1173.
- [30] K. Yu. Volokh, Cytoskeletal architecture and mechanical behavior of living cells, *Biorheology* 40 (2003) 213–220.
- [31] O. Thoumine, A. Ott, Time scale dependent viscoelastic and contractile regimes in fibroblasts probed by microplate manipulation, *J. Cell Sci.* 110 (1997) 2109–2116.
- [32] T. Wakatsuki, M.S. Kolodney, G.I. Zahalak, E.L. Elson, Cell mechanics studied by a reconstituted model tissue, *Biophys. J.* 79 (2000) 2353–2368.
- [33] S.S. An, R.E. Laudadio, J. Lai, R.A. Rogers, J.J. Fredberg, Stiffness changes in cultured airway smooth muscle cells, *Am. J. Physiol.* 283 (2002) C792–C801.
- [34] B. Alberts, A. Johnson, J. Lewis, M. Raff, K. Roberts, P. Walter, *Molecular Biology of the Cell*, Garland Science, New York, 2002.
- [35] K.A. Shaw, Z.L. Zhang, N.C. MacDonald, SCREAM-I: a single mask, single crystal silicon, reactive etching process for microelectromechanical structures, *Sens. Actuators, A* 40 (1994) 63–70.
- [36] C. Zhu, G. Bao, N. Wang, Cell mechanics: mechanical response, cell adhesion, and molecular deformation, *Annu. Rev. Biomed. Eng.* 2 (2000) 189–226.
- [37] G. Bao, S. Suresh, Cell and molecular mechanics of biological materials, *Nat. Mater.* 2 (2003) 715–725.
- [38] J.D. Humphrey, *Continuum Biomechanics of soft biological tissues*, *Proc. R. Soc. Lond., A* 459 (2003) 3–46.
- [39] H.J. Morowitz, *Foundations of Bioenergetics*, Academic Press, New York, 1978.
- [40] C. Rotsch, M. Radmacher, Drug-induced changes of cytoskeletal structure and mechanics in fibroblasts: an atomic force microscopy study, *Biophys. J.* 78 (2000) 520–535.

# Lab 11: Microfluidics

**Location:** NE47-305ba

**PI:** Chwee Teck Lim

**Lab Instructors:** David Quinn

## Summary

This laboratory will demonstrate the use of microfabricated structures to investigate the mechanical response of cells as they are deformed through narrow microfluidic channels. Specifically, the biorheological behavior of red blood cells at different stages of malaria infection will be studied. Under a known constant pressure differential, it can be seen that the entrance time and velocity through narrow channels (varying from 2 - 8 microns square cross-section) differ between the early and late stage infected and much stiffer red blood cells. It can also be shown that the sufficiently stiff cells cannot pass through the narrowest channels. Analogies can be made between this behavior and that experienced in the body as the cell passes through capillaries of comparable size.

## Recommended Reading

J. P. Shelby *et al.*, "A microfluidic model for single-cell capillary obstruction by Plasmodium falciparum infected erythrocytes," *PNAS*, **100**.

B. Yap and R. D. Kamm, "Mechanical deformation of neutrophils into narrow channels induces pseudopod projection and changes in biomechanical properties," *J. Appl. Physiology*, **98**.



# A microfluidic model for single-cell capillary obstruction by *Plasmodium falciparum*-infected erythrocytes

J. Patrick Shelby\*, John White<sup>†</sup>, Karthikeyan Ganesan\*, Pradipsinh K. Rathod\*<sup>†‡§</sup>, and Daniel T. Chiu\*<sup>‡</sup>

Departments of \*Chemistry and <sup>†</sup>Pathobiology, Box 351700, University of Washington, Seattle, WA 98195-1700; and <sup>§</sup>Seattle Biomedical Research Institute, Seattle, WA 98109

Edited by George M. Whitesides, Harvard University, Cambridge, MA, and approved October 14, 2003 (received for review June 26, 2003)

Severe malaria by *Plasmodium falciparum* is a potentially fatal disease, frequently unresponsive to even the most aggressive treatments. Host organ failure is associated with acquired rigidity of infected red blood cells and capillary blockage. *In vitro* techniques have played an important role in modeling cell deformability. Although, historically they have either been applied to bulk cell populations or to measure single physical parameters of individual cells. In this article, we demonstrate the unique abilities and benefits of elastomeric microchannels to characterize complex behaviors of single cells, under flow, in multicellular capillary blockages. Channels of 8-, 6-, 4-, and 2- $\mu\text{m}$  widths were readily traversed by the 8  $\mu\text{m}$ -wide, highly elastic, uninfected red blood cells, as well as by infected cells in the early ring stages. Trophozoite stages failed to freely traverse 2- to 4- $\mu\text{m}$  channels; some that passed through the 4- $\mu\text{m}$  channels emerged from constricted space with deformations whose shape-recovery could be observed in real time. In 2- $\mu\text{m}$  channels, trophozoites mimicked "pitting," a normal process in the body where spleen beds remove parasites without destroying the red cell. Schizont forms failed to traverse even 6- $\mu\text{m}$  channels and rapidly formed a capillary blockage. Interestingly, individual uninfected red blood cells readily squeezed through the blockages formed by immobile schizonts in a 6- $\mu\text{m}$  capillary. The last observation can explain the high parasitemia in a growing capillary blockage and the well known benefits of early blood transfusion in severe malaria.

**P**lasmodium falciparum is responsible for  $\approx 1$ –2 million deaths every year; severe malaria is typically characterized by brain, spleen, liver, or kidney pathology (1–3; see also [www.who.int/inf-fs/en/fact094.html](http://www.who.int/inf-fs/en/fact094.html)). The severity of *P. falciparum* infection is a function of capillary blockage by infected cells in these organs. Normal erythrocytes are highly deformable liquid-filled compartments (4). They owe their high degree of deformability to low internal viscosity, high surface-area-to-volume ratio, and the highly elastic nature of the erythrocyte membrane and underlying cytoskeleton (2). Particularly during the late stages of parasite development, infected erythrocytes become spherocytic, develop knob-like structures, and lose their native deformability. This loss of deformability is often cited as an important contributing factor in capillary blockage (5).

Given the complications of *in vivo* testing and the lack of a relevant animal model (1), a number of physical approaches have been applied to the study of deformability of infected red blood cells (RBCs), usually on bulk cell populations (6). In pioneering studies, the higher pressures required to pass malaria-infected blood in comparison with normal blood through a polycarbonate filter suggested that infected erythrocytes lacked structural deformability, which in turn contributed to capillary blockage (7, 8). In addition, viscometers, after correction for hematocrit, provided information about the viscosity of erythrocytes (7, 9). Ektacytometry, using diffraction patterns from erythrocytes illuminated with a He-Ne laser in a highly viscous medium such as dextran, provided measurements of erythrocyte deformability in bulk medium (5, 10). Expanding on the concept of filtration,

the single erythrocyte rigidometer (SER) (11, 12) characterizes the time of passage of a single erythrocyte through a micrometer-sized pore (e.g., 5.8  $\mu\text{m}$ ); thus, cell area, volume, and cytoplasmic viscosity were determined. The SER technique has been applied to the study of the physical properties of normal erythrocytes. The rheoscope, which uses fluid shear stress to visualize erythrocyte physical characteristics, allowed study of erythrocyte deformability and the tank tread-like motion of the erythrocyte membrane (13). The rheoscope has been used to characterize the deformability of *P. falciparum*-infected erythrocytes and the recovery of RBCs in the ring stage of infection (14). Micropipette aspiration improved studies on the deformability of a single cell and measurement of membrane viscoelasticity and rigidity (15, 16). The time required for entry, time constant for extensional recovery, and the critical pressure required to aspirate an erythrocyte into a 3- to 3.5- $\mu\text{m}$  diameter pipette have been determined for malaria-infected erythrocytes. Now microfluidics offers opportunities to study properties of single infected-erythrocytes, in real time, in a capillary-like microenvironment.

Microfluidic devices have found numerous applications in biology, biochemistry, and medicine because of their ability to efficiently control and replicate microenvironments (17, 18). They also offer practical benefits such as limiting human exposure to large amounts of biohazardous samples. Microfluidic systems are easy to fabricate, owing to recent advancements in rapid prototyping, and provide an ideal environment for testing either bulk samples or single entities, such as individual cells. Recognizing the need for devices that mimic the capillary microenvironment, many researchers have designed capillary-like channel systems in silicon<sup>†</sup> (19–22) and glass (23) substrates. The ability to fabricate micrometer-sized features in glass and silicon makes these materials attractive options for making capillary-sized structures. Through these studies, it has been possible to record normal erythrocyte area, volume, and deformability. Many of these devices are integrated into comprehensive test platforms with controlled flow rate, temperature, and pressure. This advance enabled researchers to develop systems that closely mimic the *in vivo* environment. Although providing a geometrically similar environment to capillaries, silicon and glass channels do not have structural properties, such as elastic modulus, of capillary tissue. Recently, structural information of normal erythrocytes was determined by using a human erythrocyte microchannel analyzer made in a silicone elastomer (24). In the present study, we apply similar microfluidic techniques to the study of malaria-infected erythrocytes.

This paper was submitted directly (Track II) to the PNAS office.

Abbreviations: RBC, red blood cell; PDMS, poly(dimethylsiloxane).

<sup>†</sup>To whom correspondence should be addressed. E-mail: [rathod@chem.washington.edu](mailto:rathod@chem.washington.edu) and [chiu@chem.washington.edu](mailto:chiu@chem.washington.edu).

<sup>†</sup>Kikuchi, Y., Ohki, H., Kaneko, T. & Sato, K. (1989) *Biorheology* 26, 1055 (abstr.).

© 2003 by The National Academy of Sciences of the USA

## Materials and Methods

**Fabrication of Microchannels.** Fabrication of test channels in poly-(dimethylsiloxane) (PDMS) used rapid prototyping (25). Briefly, a high-resolution chrome mask (Photosciences, Inc., Torrance, CA) was generated from a computer-aided drawing file and etched by an electron beam. The mask was a negative of the channel design and was used in contact photolithography with SU-8 photoresist (MicroChem, Newton, MA) to create a negative “master,” which consisted of bas-relief features of SU-8 on a silicon wafer. From the master, PDMS channels were molded and then sealed irreversibly to a borosilicate glass coverslip by oxidizing the PDMS surface in oxygen plasma, which also caused the channels to become hydrophilic. Access holes to the channels were formed by using a punch made from a 21-gauge needle. Polyethylene tubing (PE20) was then inserted into the access holes, which were slightly smaller than the outer diameter of the tubing, to form a pressure seal between the tubing and the hole. The tubing was attached to a 3-ml syringe through which fluid was introduced into the channel. The length of the constricted portion of the channel was designed to be  $\approx 3$  to 5 times its width. The depth of all channels was restricted to  $2\ \mu\text{m}$  to prevent the disk-shaped erythrocytes from turning on their sides and traversing the constriction.

***P. falciparum*-Infected Erythrocytes.** *P. falciparum* parasites were maintained under standard conditions (26) in a 2% suspension of human A+ erythrocytes in complete medium (RPMI medium 1640 supplemented with 20% human A+ serum; GIBCO/Invitrogen). Mixed-stage parasite cultures were synchronized by two consecutive sorbitol treatments (27) and harvested for analysis at the ring stage (0–6 h postsync), early trophozoite stage (16–21 h postsync), late trophozoite stage (21–24 h postsync), and schizont stage (36–42 h postsync). Giemsa staining of thin smears showed  $>95\%$  purity of the synchronized cultures. Each cell culture sample contained  $\approx 1\%$  of infected erythrocytes.

**Cell Visualization.** The test samples were mounted onto a Nikon TE300 microscope with a Nikon  $\times 100$  Superfluar objective (numerical aperture = 1.3) for bright-field, differential interference contrast, and fluorescence imaging. A high-sensitivity black and white charge-coupled device camera (Cohu, San Diego, CA) was used to capture images. While differential interference contrast imaging readily identified infected erythrocytes, some infected cultures were stained with 2',7'-bis-(2-carboxyethyl)-(5 and 6)-carboxyfluorescein acetoxymethyl ester (BCECF-AM) (Molecular Probes) by using published methods (28). Fluorescent images were obtained by exciting the stained cells with the 488-nm line of a continuous wave Ar<sup>+</sup> ion laser (Spectra-Physics). To prepare the suspension of infected RBCs for flowing through the microchannels,  $\approx 0.5$ -ml culture solution (2% hematocrit and 1% parasitemia) was diluted in  $\approx 0.5$ -ml of complete RPMI medium 1640. The temperature of the sample above the objective was  $25^\circ\text{C}$ . The velocity in the  $20\text{-}\mu\text{m}$  main channel for each experiment was  $\approx 50\ \mu\text{m}\cdot\text{s}^{-1}$ , and the velocities in the constriction varied from  $\approx 125\ \mu\text{m}\cdot\text{s}^{-1}$  in the  $8\text{-}\mu\text{m}$  channel to  $\approx 500\ \mu\text{m}\cdot\text{s}^{-1}$  in the  $2\text{-}\mu\text{m}$  channel, which resulted in a pressure drop across the restriction of  $\approx 0.4\ \text{mmHg}$  ( $1\ \text{mmHg} = 133\ \text{Pa}$ ). The duration of each experiment was  $\approx 15$ – $20$  min. Testing of all infected erythrocytes was completed within  $\approx 1.5$  h after their removal from the controlled incubation environment.

## Results and Discussion

**Fabrication of Microchannels.** The test channels were made of PDMS, which is a two-component silicone-based elastomer. The elastic modulus of PDMS, which can be tuned by adjusting the ratio of catalyst to elastomer, provides a good approximation of

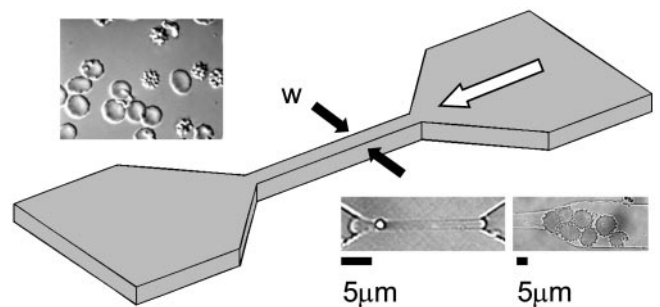


**Fig. 1.** Schematic illustrating the geometry of the microchannel. The constricted segment of the channel (width denoted by  $w$ ) was sized at 8, 6, 4, and  $2\ \mu\text{m}$ . The white arrow represents the direction of fluid flow. (Upper Inset) A differential interference contrast image of normal (smooth) and infected RBCs. (Lower Left Inset) A normal RBC passing through a  $2\text{-}\mu\text{m}$  constriction. (Lower Right Inset) Infected RBCs blocking a  $6\text{-}\mu\text{m}$  constriction.

the geometric and structural properties of capillaries (29). We fabricated the microchannels to mimic capillaries between  $2$ - and  $8\text{-}\mu\text{m}$  in diameter. The average flow velocity in the central channel constriction was chosen to model the natural flow rates in capillaries ( $\approx 100$ – $500\ \mu\text{m}\cdot\text{s}^{-1}$ ) (30). A schematic of the test channels is shown in Fig. 1.

**Behavior of Normal Erythrocytes.** In all tests with normal erythrocytes, little or no adherence to the channel walls was observed. Furthermore, these highly flexible cells passed easily through all channel geometries, including the  $2\text{-}\mu\text{m}$  constriction (see Fig. 1 Lower Left Inset).

**Behavior of Infected Erythrocytes.** To dissect out the factors that influence capillary blockage by infected erythrocytes, RBCs in different stages of infection (ring stage, early trophozoite, late trophozoite, and schizont) were passed through microchannels having different sizes of constriction ( $8$ ,  $6$ ,  $4$ , and  $2\ \mu\text{m}$ ). Fig. 2 A–D shows the behavior of erythrocytes in ring-stage infection. Like normal erythrocytes, these early-stage infected cells passed through channel constrictions of all sizes with no difficulty. In contrast, early trophozoites had difficulties in passing through  $4$ - and  $2\text{-}\mu\text{m}$  channels (Fig. 2 G and H), but they could traverse  $8$ - and  $6\text{-}\mu\text{m}$  channels (Fig. 2 E and F). The first signs indicating a lack of deformability were observed in these early trophozoites. The few erythrocytes with trophozoite-stage parasites that did squeeze through the  $4\text{-}\mu\text{m}$  channels did not recover their shape quickly after their passage through the constriction (Fig. 2G). Fig. 2 I–L shows the behavior of late-stage trophozoites. Similar to the early trophozoites, the late trophozoites blocked the smaller  $4$ - and  $2\text{-}\mu\text{m}$  channels (Fig. 2 K and L) but passed through larger channels with relative ease (Fig. 2 I and J). Erythrocytes in the schizont stage of infection (Fig. 2 M–P) exhibited a markedly increased rigidity. These cells had difficulties passing through the  $6$ -,  $4$ -, and  $2\text{-}\mu\text{m}$  constricted channels (Fig. 2 N–P).

The present studies quantitatively illustrate the channel geometry in which late-stage cells cause blockage. Due to the lack of confounding factors such as ligands on endothelial cells found *in vivo*, the results obtained in our PDMS structures allow us to dissect the contributions of decreased cell deformability and membrane rigidity on movement through capillaries of precise dimensions. The stage-specific effects validate the use of microcapillaries under flow conditions to study capillary blockage.

**Erythrocyte Shape Recovery.** Cranston *et al.* (14) showed that, after flowing through constrictions, recovery time for ring-stage erythrocytes was significantly longer than recovery time for uninfected cells. It is believed that membrane rigidity and

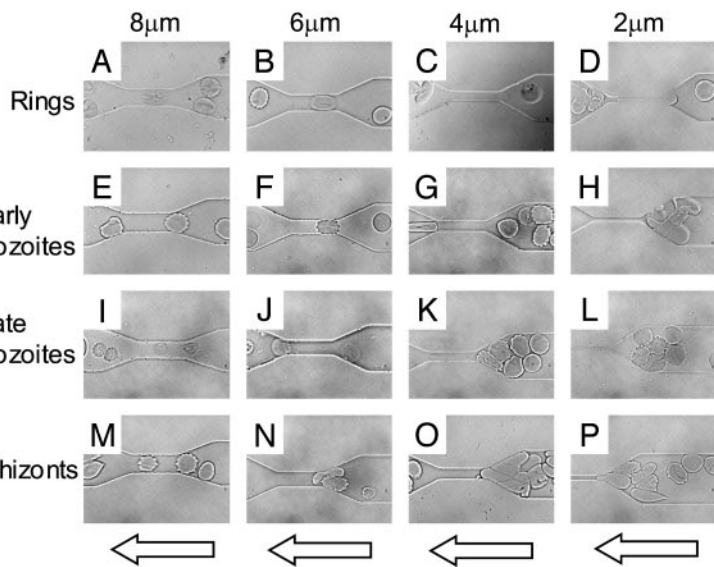


**Fig. 2.** Four sequences of video images of four stages of malaria-infected RBCs (early ring stage, early trophozoite, late trophozoite, and schizont) passing through channel constrictions. (A–D) Ring-stage infected erythrocytes retained much of the structural characteristics of normal erythrocytes and were able to pass through all constricted channels. Early trophozoite (E–H) and late trophozoite (I–L) infected cells passed through the larger 8- and 6- $\mu\text{m}$  channels (E and F; I and J) but eventually blocked the smaller 4- and 2- $\mu\text{m}$  channels (G and H; K and L). (M–P) Schizont stage infected erythrocytes blocked all but the 8- $\mu\text{m}$  channel (M). The arrows indicate direction of flow.

internal viscosity increase as the parasite matures (2); therefore, one would expect erythrocytes in the later stages of infection to have even longer recovery times than cells in the early stages of infection. Fig. 3 shows individual erythrocytes in the early trophozoite stages of infection (Fig. 3A) and in the late schizont stages of infection (Fig. 3B) after being hydrodynamically forced through a 4- $\mu\text{m}$  channel. The trophozoites generally recovered their spherical appearance within  $\approx 30$  sec. The rare schizonts that were forced through the 4- $\mu\text{m}$  channel, however, did not fully recover their spherical shape even after 1–2 min of monitoring.

**Pitting.** Sequestering of trophozoites and schizonts under capillary flow is an important mechanism by which the parasite avoids the spleen, where efficient mechanisms exist to destroy the parasite (5, 31). Schnitzer *et al.* (31) presented *in vivo* electron micrograph evidence for the pitting of parasites from erythrocytes in the cord and sinus areas of the spleen. During pitting,

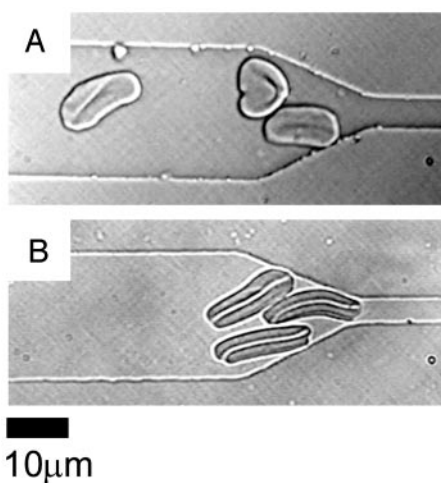


**Fig. 3.** Differences in recovery of compressed infected cells. (A) Early trophozoite stages of infected RBCs were partially distorted after passage through a 4- $\mu\text{m}$  constriction and remained compressed for  $\approx 30$  sec after emerging from the channels. (B) Schizont forms of RBC infections were more severely deformed and did not relax back to their original shape after passage through a 4- $\mu\text{m}$  constriction even 1–2 min after compression.

the intracellular parasite is physically pushed back and eventually dissociated from the normal portion of the erythrocyte as the infected erythrocyte passes through the tiny blood vessels (cord and sinus) in the spleen. Although pitting may have complex mechanisms involving phagocytosis of the parasitic portion of the erythrocyte by a macrophage, initial separation of the parasite from the uninfected portion of the erythrocyte in the tight physical confines in the spleen are important. The product of pitting is a “ghost cell” that is free of the parasite. The parasite-free cell may be returned to circulation. Fig. 4 shows a microfluidic *in vitro* example of pitting with a 2- $\mu\text{m}$  channel. Fig. 4A *Top* shows an infected cell in bright field, before passage through the restriction. Fig. 4B *Top* shows an infected cell, before the restriction, stained with 2',7'-bis-(2-carboxyethyl)-(5 and 6)-carboxyfluorescein acetoxymethyl ester (BCECF-AM) cell stain (32). In Fig. 4A *Middle*, the normal portion of the cell is shown passing through the restriction; however, the parasitized portion of the cell remains in the upstream portion of the channel (i.e., the equivalent of the cord *in vivo*). The cell membrane continues to stretch until its ultimate load limit is exceeded and the membrane ruptures, removing the parasite from the cell. Fig. 4B *Middle* shows rupture of the membrane, an accompanying burst of fluorescence near the restriction, and separation of the parasite from the host RBC (arrow). Fig. 4A *Bottom* shows deformed cells downstream of the restriction. Fig. 4B *Bottom* shows a similar image with a fluorescent parasite (arrow) separated from the erythrocyte, which shows no further fluorescent compartments. It was common to observe ghost cells and cell debris downstream of the smaller-sized channels (e.g., 4 and 2  $\mu\text{m}$ ).

**Normal Erythrocyte Passing Through Blockages.** Fig. 5A shows a normal erythrocyte approaching a blockage formed by seven infected cells in the schizont stage at the entrance to the 6- $\mu\text{m}$  constricted channel. The infected cells fill the entire depth of the channel near the restriction, which makes the passage above and below the blockage impossible. Rather than becoming a static part of the blockage, the normal red cell under flow conditions winds its way through the center of this group of infected cells (Fig. 5B). Fig. 5C shows the cell exiting the blockage as it enters the 6- $\mu\text{m}$  channel, which it easily traverses, as was seen in Figs. 1 and 2.

The above observations have two important implications. (i) It is well known *in vivo*, and now also in our *in vitro* model, that

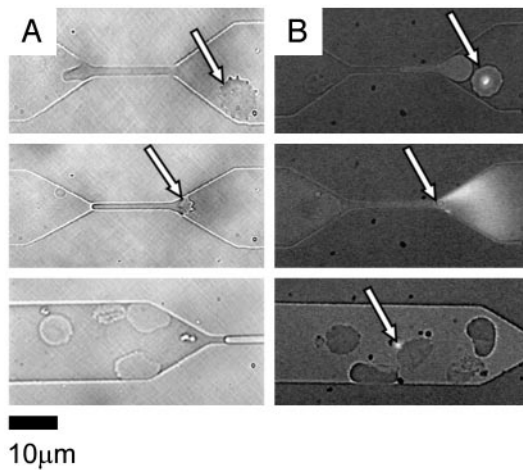


**Fig. 4.** Two video sequences showing pitting of infected RBCs. (A Top) A bright-field image shows an infected RBC before passage through a 2- $\mu\text{m}$  channel (arrow). (Middle) The infected portion of the red cell is left outside the channel (arrow) as the rest of the red cell is squeezed through. (Bottom) Downstream of the constriction, note the deformed red cells and free parasites from other pitting events. (B Top) A fluorescent image shows a stained parasite in an infected cell before entering a channel (arrow). (Middle) The distal end of an infected RBC ruptures (fluorescent burst) during passage through the constriction. (Bottom) Downstream of the constriction, note the deformed red cells and a free fluorescent parasite from another pitting event.

mature forms of infected erythrocytes concentrate to very high parasitemia at the mouth of a blocked capillary. Enrichment of parasitized cells in a growing blockage may increase local concentrations of potential malaria toxins or overstimulate host immunomodulatory responses, which contribute to pathology (33). Although the highly parasitized blockages may in part be due to cytoadherence (1, 33, 34), our model suggests that the ability of uninfected red cells to squeeze through blockages must also be important in expansion of a pathogenic blockage. (ii) Although exchange transfusion is known to alleviate, albeit temporarily, some of the effects of severe malaria (5), the mechanism underlying relief is not obvious. Infected cells causing pathology are unavailable for exchange because they are sequestered in capillaries, often through adherence, rosetting, and agglutination (2, 5, 33). Our experimental model shows that fresh, pliable erythrocytes can squeeze through a blockage. In a transfused patient, this action may temporarily allow delivery of nutrients and removal of toxins from distressed tissue.

## Conclusions

Elastomeric microfluidic channels provide a simple, inexpensive, efficient, and accurate method to study the behavior of *P. falciparum*-infected erythrocytes under capillary-like conditions. In future research, the flexibility and cytoadherence properties of normal and infected cells can be studied by modifying the elastic modulus and the surface chemistry of PDMS microchannels. The latter will allow, under flow, controlled testing of interactions between infected erythrocytes and other RBCs, purified host cell-surface receptors, or even whole endothelial

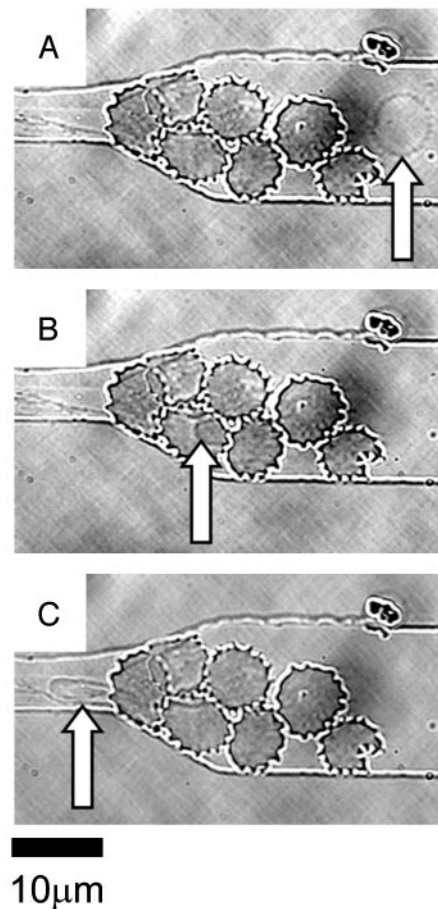


**Fig. 5.** A video sequence showing the passage of a normal erythrocyte through a blockage formed by infected cells. (A) A normal erythrocyte flows smoothly through the main channel (arrow). (B) The normal cell weaves its way through the blockage at the entrance to the 6- $\mu\text{m}$  constriction (arrow) caused by infected RBCs in the schizont stage. (C) The normal cell exits the labyrinth of infected cells and passes easily through the channel constriction (arrow).

cells, owing to the high permeability of gas through PDMS. The system also provides a convenient test platform to screen potential antimalarial drugs that specifically interfere with the mechanics of infected RBCs.

J.P.S. acknowledges support from the University of Washington Center for Nanotechnology for an Integrative Graduate Education and Research Traineeship graduate fellowship. This work was partially supported by National Institutes of Health Grants R01 AI26912 (to P.K.R.) and DA 16249 (to D.T.C.). P.K.R. is a Senior Scholar in Global Infectious Diseases from the Ellison Medical Foundation. This work also received indirect support from the Keck Foundation (University of Washington), the Bill and Melinda Gates Foundation (Seattle Biomedical Research Institute), the Dreyfus Foundation, and the Petroleum Research Fund administered by the American Chemical Society.

1. Miller, L. H., Good, M. F. & Milon, G. (1994) *Science* **264**, 1878–1883.
2. Cooke, B. M., Mohandas, N. & Coppel, R. L. (2001) *Adv. Parasitol.* **50**, 1–86.
3. World Health Organization (March 2002) *Malaria* (W.H.O., Geneva), Fact Sheet No. 94.
4. Evans, E. (1989) *Methods Enzymol.* **173**, 3–35.
5. Dondorp, A. M., Kager, P. A., Vreeken, J. & White, N. J. (2000) *Parasitol. Today* **16**, 228–232.
6. Stuart, J. (1985) *J. Clin. Pathol.* **38**, 965–977.
7. Miller, L. H., Usami, S. & Chien, S. (1971) *J. Clin. Invest.* **50**, 1451–1455.

8. Miller, L. H., Chien, S. & Usami, S. (1972) *Am. J. Trop. Med. Hyg.* **21**, 133–136.
9. Areekul, S. & Yamarat, P. (1988) *J. Med. Assoc. Thailand* **71**, 196–202.
10. Bessis, M. & Mohandas, N. A. (1975) *Blood Cells* **1**, 307–313.
11. Kiesenwetter, H., Dauer, U., Teitel, P., Schmid-Schonbein, H. & Trapp, R. (1982) *Biorheology* **19**, 737–753.
12. Roggenkamp, H. G., Jung, F., Schneider, R. & Kiesenwetter, H. (1984) *Biorheology Suppl.* **1**, 241–243.
13. Fischer, T. M., Stöhr-Liesen, M. & Schmid-Schönbein, H. (1978) *Science* **202**, 894–896.

14. Cranston, H. A., Boylan, C. W., Carroll, G. L., Suter, S. P., Williamson, J. R., Gluzman, I. Y. & Krogstad, D. J. (1984) *Science* **223**, 400–403.
15. Nash, G. B., O'Brien, E., Gordon, S. E. & Dormandy, J. A. (1989) *Blood* **74**, 855–861.
16. Paulitschke, M. & Nash, G. B. (1993). *J. Lab. Clin. Med.* **122**, 581–589.
17. Whitesides, G. M., Ostuni, E., Shuichi, T., Jiang, X. & Ingber, D. E. (2001) *Annu. Rev. Biomed. Eng.* **3**, 335–373.
18. Voldman, J., Gray, M. L. & Schmidt, M. A. (1999) *Annu. Rev. Biomed. Eng.* **1**, 401–425.
19. Wilding, P., Pfahler, J., Bau, H. H., Zemel, J. N. & Kricka, L. J. (1994) *Clin. Chem.* **40**, 43–47.
20. Tracey, M. C., Greenaway, R. S., Das, A., Kaye, P. H. & Barnes, A. J. (1995) *IEEE Trans. Biomed. Eng.* **42**, 751–761.
21. Brody, J. P., Han, Y., Austin, R. H. & Bitensky, M. (1995) *Biophys. J.* **68**, 2224–2232.
22. Sutton, N., Tracey, M. C., Johnston, I. D., Greenaway, R. S. & Rampling, M. W. (1997) *Microvasc. Res.* **53**, 272–281.
23. Cokelet, G. R., Soave, R., Pugh, G. & Rathbun, L. (1993) *Microvasc. Res.* **46**, 394–400.
24. Gifford, C. S., Frank, M. G., Derganc, J., Gabel, C., Austin, R. H., Yoshida, T. & Bitensky, M. W. (2003) *Biophys. J.* **84**, 623–633.
25. McDonald, J. C., Duffy, D. C., Anderson, J. R., Chiu, D. T., Wu, H., Schueller, O. J. A. & Whitesides, G. M. (2000). *Electrophoresis* **21**, 27–40.
26. Trager, W. & Jensen, J. B. (1976) *Science* **193**, 673–675.
27. Schuster, F. L. (2002) *Clin. Microbiol. Rev.* **15**, 355–364.
28. Wissing, F., Sanchez, C., Rohrbach, P., Ricken, S. & Lanzer, M. (2002) *J. Biol. Chem.* **277**, 37747–37755.
29. McDonald, J. C. & Whitesides, G. M. (2002) *Acc. Chem. Res.* **35**, 491–499.
30. Shelby, J. P. & Chiu, D. T. (2003) *Anal. Chem.* **75**, 1387–1392.
31. Schnitzer, B., Sodeman, T. & Mead, M. L. (1972) *Science* **177**, 175–177.
32. Hayashi, M., Yamada, H., Mitamura, T., Horii, T., Yamamoto, A. & Moriyama, Y. (2000) *J. Biol. Chem.* **275**, 34353–34358.
33. Miller, L. H., Baruch, D. I., Marsh, K. & Doumbo, O. K. (2002) *Nature* **415**, 673–679.
34. Crabb, B. S., Cooke, B. M., Reeder, J. C., Waller, R. F., Caruana, S. R., Davern, K. M., Wickham, M. E., Brown, G. V., Coppel, R. L. & Cowman, A. F. (1997) *Cell* **89**, 287–296.

HIGHLIGHTED TOPIC | *Biomechanics and Mechanotransduction in Cells and Tissues*

## Mechanical deformation of neutrophils into narrow channels induces pseudopod projection and changes in biomechanical properties

Belinda Yap<sup>1,2</sup> and Roger D. Kamm<sup>2</sup>

<sup>1</sup>Harvard-MIT Division of Health Sciences and Technology, and <sup>2</sup>Department of Mechanical Engineering and Biological Engineering Division, Massachusetts Institute of Technology, Cambridge, Massachusetts

Submitted 1 November 2004; accepted in final form 4 January 2005

**Yap, Belinda, and Roger D. Kamm.** Mechanical deformation of neutrophils into narrow channels induces pseudopod projection and changes in biomechanical properties. *J Appl Physiol* 98: 1930–1939, 2005. First published January 7, 2005; doi:10.1152/jappphysiol.01226.2004.—Neutrophils traversing the pulmonary microcirculation are subjected to mechanical stimulation during their deformation into narrow capillaries. To better understand the time-dependant changes caused by this mechanical stimulus, neutrophils were caused to flow into a microchannel, which allowed simultaneous visualization of cell morphology and passive rheological measurement by tracking the Brownian motion of endogenous granules. Above a threshold stimulus, mechanical deformation resulted in neutrophil activation with pseudopod projection. The activation time was inversely correlated to the rate of mechanical deformation experienced by the neutrophils. A reduction in shear moduli was observed within seconds after the onset of the mechanical stimulus, suggesting a sudden disruption of the neutrophil cytoskeleton when subjected to mechanical deformation. However, the magnitude of the reduction in moduli was independent of the degree of deformation. Recovery to nearly the initial values of viscoelastic moduli occurred within 1 min. These observations confirm that mechanical deformation of neutrophils, similar to conditions encountered in the pulmonary capillaries, is not a passive event; rather, it is capable of activating the neutrophils and enhancing their migratory tendencies.

viscoelasticity; cell activation; multiple-particle tracking; microfluidics

NEUTROPHILS OFTEN ENCOUNTER narrow capillary segments during their transit through the pulmonary and systemic microcirculations. Because neutrophil diameters (6–8  $\mu\text{m}$ ) often exceed the diameter of a pulmonary capillary (2–15  $\mu\text{m}$ ) (5), neutrophils would almost certainly have to deform in passing from arteriole to venule, particularly in the pulmonary capillary bed, where it has been estimated that a typical flow pathway encompasses 50–100 such capillary segments (13, 14). Measurements of neutrophil shape showed that neutrophils in capillaries are elongated, whereas those in arterioles are nearly spherical, thus confirming the view that neutrophils deform when they encounter narrow capillary segments (5, 12).

Mechanical forces have been recognized to play an important role in modulating the behavior and function of cardiovascular cells in health and disease (15, 17). Although the effects of mechanical stimuli on cells have been a topic of extensive research, much of the focus has been on endothelial cells in the context of atherosclerotic disease. Neutrophil, and

leukocyte activity in general, is assumed to be mediated in large part by biochemical factors, with effects from mechanical stimulation often ignored. However, recent studies have shown that leukocytes are sensitive to fluid shear stress, which can influence their degree of substrate adhesion and the formation of pseudopods and reduce their cytoskeletal stiffness (2, 22, 28). Similarly, the mechanical deformation of neutrophils into narrow pulmonary capillaries, initially considered to be a passive process, is now recognized to enhance adhesiveness to ICAM-1 through upregulation of CD11b/CD18, reorganizing and stabilizing the cytoskeleton, and increasing free intracellular  $\text{Ca}^{2+}$  concentration (21). Consequently, neutrophils likely have the capability of sensing mechanical force or deformation and altering their rheological properties in response. Despite the importance of these effects in the microcirculation, no rheological studies have yet been conducted subjecting neutrophils to the deformations they experience while traversing the pulmonary circulation. Interestingly, one of the established techniques for measuring the viscoelastic properties of neutrophils, the micropipette aspiration method, involves deformation of the cell under a fixed suction pressure into a narrow micropipette (9, 29, 32, 33). This technique mimics the flow condition that the cell experiences while deforming into a pulmonary capillary. The rheological properties deduced from this technique, however, assume that the neutrophil remains passive during deformation and, hence, that its rheology is unchanged when drawn into the pipette. Indeed, some of these micropipette experiments showed some indications of neutrophil activation attributed to mechanical deformation of the cell (8).

In such cases for which mechanical deformation by external forces give rise to a change in rheological properties, it is advantageous to seek methods of measurement that avoid cell manipulation. Multiple-particle-tracking microrheology (23, 24, 34) offers a solution because this method is able to noninvasively measure the local viscoelasticity by monitoring the Brownian motion of endogenous granules present in the cytoplasm of the cell. A similar technique has been applied to locomoting neutrophils, with active manipulation of a granule using an optical trap (37, 38). To examine the effects of mechanical deformation on the behavior and rheological properties of the neutrophils in the pulmonary capillaries, we used microfabrication techniques (27, 35) to construct an in vitro

Address for reprint requests and other correspondence: R. D. Kamm, Dept. of Mechanical Engineering and Biological Engineering Division, Massachusetts Institute of Technology, 77 Massachusetts Ave. NE47-321, Cambridge, MA 02139 (E-mail: rdkamm@mit.edu).

The costs of publication of this article were defrayed in part by the payment of page charges. The article must therefore be hereby marked “advertisement” in accordance with 18 U.S.C. Section 1734 solely to indicate this fact.

polydimethylsiloxane (PDMS) system with dimensions comparable to the pulmonary capillaries. PDMS being optically transparent enabled direct observation of the neutrophil morphology and simultaneously allowed us to employ the technique of multiple-particle-tracking microrheology to directly measure the viscoelastic properties of the cell.

## MATERIALS AND METHODS

**Design and fabrication of microfluidic device.** The design of the microchannel used to mimic a pulmonary capillary and the connecting reservoirs is shown in Fig. 1. A master for this design was fabricated on silicon wafer using the technique of two-level photolithography (20) and subsequently used for replica molding in PDMS (18). Figure 2 shows the finished microfluidic system. The details of the fabrication process can be found in the APPENDIX.

**Macrofluidic system setup.** Pressure differential was imposed across the microchannel by varying the difference in height of water between the upstream and downstream macroreservoirs (Fig. 3). Two upstream macroreservoirs were used: a high-pressure (~60 cmH<sub>2</sub>O) reservoir for purging and cleaning and a low-pressure reservoir for neutrophil perfusions. The upstream low-pressure macroreservoir was attached to a linear translation stage (Edmund Optics, Barrington, NJ) and mounted on a linear slide (Rapid Advance Unislides, Velmex, Bloomfield, NY) enabling both fine-scale (0.01-mm steps) and coarse-scale (1-mm steps) adjustment. A syringe attached to the second port of the upstream microfluidic reservoir allowed the introduction of fluid or cells into the device.

**Neutrophil isolation.** Human venous blood was drawn from healthy volunteers by venipuncture into syringes containing 0.1 M sodium citrate as an anticoagulant. The isolation was in accordance with a protocol approved by the Massachusetts Institute of Technology Committee on Use of Humans as Experimental Subjects. Neutrophils were isolated from mononuclear cells by density gradient centrifugation on Histopaque 1077 (Sigma-Aldrich, St. Louis, MO) at 175 g for 30 min at room temperature. The supernatant plasma layer was

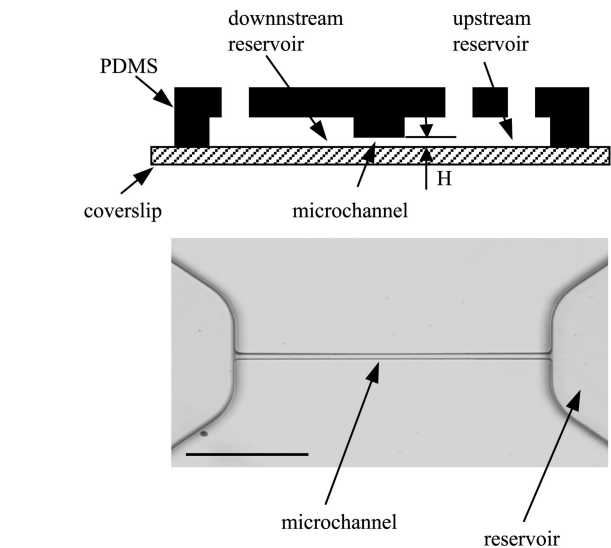


Fig. 2. *Top*: schematic diagram of the finished polydimethylsiloxane (PDMS) microfluidic device with 2 inlet and 1 outlet reservoir ports. The device is sealed on a glass coverslip. *H* represents the microchannel height, which is either 1.5 or 2.5  $\mu\text{m}$ . Diagram is not drawn to scale. *Bottom*: image of microchannel molded from PDMS as seen under a light microscope. Scale bar, 100  $\mu\text{m}$ .

collected for later use in the experiment. The mononuclear layer was carefully removed, and the remaining neutrophil and red blood cell layers were resuspended first in an equal volume of HBSS without Ca<sup>2+</sup> or Mg<sup>2+</sup> (Invitrogen, Carlsbad, CA) and then in a 1:1 dilution of dextran (average molecular weight 500,000, 2% final concentration, Pharmacia, Peapack, NJ). Red blood cells were allowed to sediment for 30 min at room temperature, after which, the neutrophil-rich supernatant was collected, rinsed with HBSS, and centrifuged at 175 g for 5 min at room temperature. Residual red blood cells were removed by hypotonic lysis. Isotonicity was restored by the addition of 45 ml of HBSS without Ca<sup>2+</sup> or Mg<sup>2+</sup>, and the sample was then centrifuged at 175 g for 5 min at room temperature. The isolated neutrophils were resuspended in either HBSS without Ca<sup>2+</sup> or Mg<sup>2+</sup> only, or in medium (HBSS without Ca<sup>2+</sup> or Mg<sup>2+</sup> + 2% autologous plasma). After counting, the neutrophil concentration was adjusted to  $1.0 \times 10^6$  cells/ml, and depending on experimental requirements the

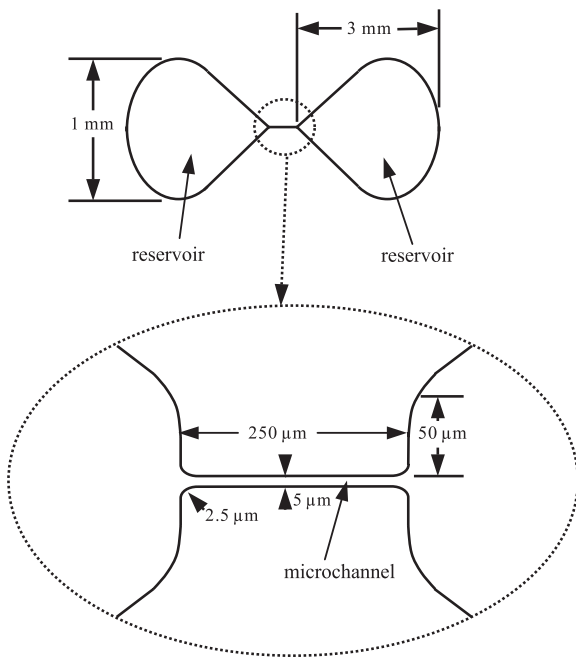


Fig. 1. Schematic showing design of the microchannel and its connecting reservoirs. The microchannel section is enlarged to highlight the channel geometry. The important channel dimensions are: length of 250  $\mu\text{m}$ , width of 5  $\mu\text{m}$ , and inlet radius of curvature of 2.5  $\mu\text{m}$ . Diagrams are not drawn to scale.

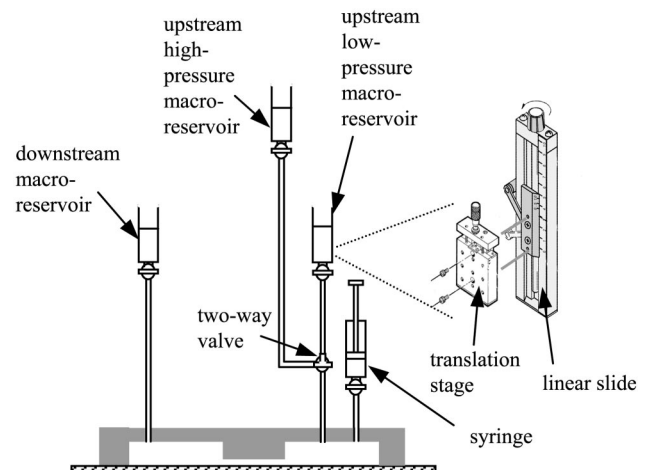


Fig. 3. Schematic showing the macrofluidic system setup and its connections to the microfluidic device. Refer to MATERIALS AND METHODS for explanation on the function of each of the system components.

cells were kept either at room temperature or incubated in a 37°C water bath.

**Optical microscopy.** Neutrophils were observed using a differential interference contrast microscope (Eclipse TE2000, Nikon, Melville, NY) equipped with an oil immersion condenser lens [numerical aperture (NA) 1.4] and a  $\times 100/1.4$  NA Plan Apochromat objective lens. Images were acquired with a video camera (CCD-100, Dage-MTI, Michigan City, IN) and recorded onto a super-VHS tape at 30 frames/s with a cassette recorder (SVO-9500MD, Sony). The movies were then converted into digital form with a computer equipped with a frame-grabber card (Scion LG-3, Frederick, MD).

**Deformation and trapping of neutrophils inside microchannel.** The microfluidic device was first incubated with 1% pluronic F108 solution (PEO/PPO/PEO triblock copolymers, BASF, Mount Olive, NJ) in water for 2 h, which served to passivate the PDMS surface and deter cell adhesion (19). The device was then flushed with medium (HBSS without  $\text{Ca}^{2+}$  or  $\text{Mg}^{2+}$  + 2% autologous plasma) for 15 min. An objective heater (Biotech, Butler, PA) set to 37°C was used for experiments at body temperature.

Neutrophils suspended in medium were then introduced into the upstream microfluidic reservoir. By setting the upstream two-way valve to open to the upstream high-pressure macroreservoir, the cells flowed quickly toward the microchannel entrance zone. In addition, yellow-green fluorescent 0.1- $\mu\text{m}$  microspheres (carboxylate-modified polystyrene fluospheres, Molecular Probes), diluted in HBSS (without  $\text{Ca}^{2+}$  or  $\text{Mg}^{2+}$ ) at a concentration of  $5 \times 10^8$  beads/ml, were introduced into the upstream microfluidic reservoir and used to establish the zero-pressure difference, zero-flow condition.

Finally, the low-pressure macroreservoir was raised to impose the desired pressure differential across the channel, initiating a flow of neutrophils into the microchannel. Once a neutrophil had entered the microchannel, the low-pressure macroreservoir was returned to its initial height, which immediately stopped its flow through the channel.

**Entrance time and time to pseudopod projection.** Neutrophil behavior was recorded from the start of its deformation into the channel up to the formation of the first pseudopod projection either at the leading or trailing edge of the cell. The playback of the video recording allowed precise determination of neutrophil entrance time and the first observation of pseudopod projection. The entrance time was taken to be the interval between when the neutrophil leading edge touched the channel entrance (first contact) and when the trailing edge cleared the channel mouth after deformation. The time to pseudopod formation was defined as the time from first contact to the first appearance of the pseudopod projection.

**Viscoelastic properties of the neutrophil evaluated using multiple-particle-tracking microrheology.** Brownian motion of endogeneous granules inside the neutrophils was monitored using particle-tracking algorithms (3) written in the IDL software (Research Systems, Boulder, CO) from the instant the neutrophil was trapped in the microchannel until the observation of pseudopod projection. The focal plane for particle tracking was selected near the center of the microchannel to minimize wall effects. From the video images, the cytoplasm of the neutrophil was divided into two zones (Fig. 4): *zone 1* was just proximal to the nucleus, and *zone 2* was the remainder of the cytoplasm up to the cell tip. Granules in *zone 1*, as well as granules exhibiting obvious directed active movements in both zones, were excluded from particle tracking. In addition, only granules that appeared circular were selected for tracking, achieved by setting the computer algorithms to track particles with eccentricity of  $\leq 0.3$  (major and minor axis difference of  $< 5\%$ ). Only particles that remained in focus for at least 30 frames were analyzed. Because of the high density of granules present in the neutrophil cytoplasm, all tracks performed by the computer algorithms were visually checked with the original video images to ensure that the same particle was followed throughout a particular track. From these particle trajectories, mean-square displacements, the frequency-dependent elastic modulus ( $G'$ ),

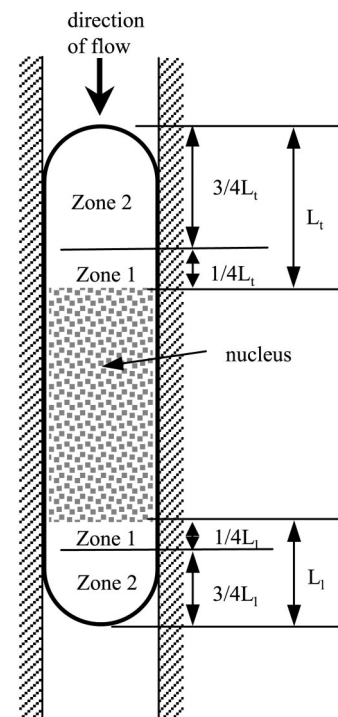


Fig. 4. Schematic diagram illustrating the division of the neutrophil cytoplasm into 2 regions; *zone 1*, proximal to the nucleus; and *zone 2*, distal from nucleus up to the cell leading or trailing edge. Only granules dispersed in *zone 2* were selected for particle tracking.  $L_t$ , length from nuclear boundary to the leading edge;  $L_t$ , length from nuclear boundary to the trailing edge.

and loss modulus ( $G''$ ) were computed according to the methods of Mason et al. (26). The shortest time lag of 1/30 s was chosen for these viscoelastic calculations because it gave the best statistical accuracy. The radius of a typical neutrophil granule was taken to be 300 nm (37) in these computations. Temporal changes in  $G'$  and  $G''$  were examined by performing independent analysis on 5-s time intervals.

As control, the multiple-particle-tracking technique was also performed on round passive neutrophils (Fig. 5A). Neutrophils suspended in medium were introduced into a small chamber formed between a glass slide and coverslip. Again, granules close to the nucleus were excluded from the particle track.

Studies were also performed on adherent and spread neutrophils (Fig. 5B) on a glass coverslip. Neutrophils suspended in HBSS without  $\text{Ca}^{2+}$  or  $\text{Mg}^{2+}$  were introduced into a glass slide and coverslip chamber as before. The absence of plasma in the suspension resulted in adhesion and spreading. Only granules in the cytoplasm that were located at least 2  $\mu\text{m}$  away from the nucleus of the cell were tracked. Values obtained for  $G'$  and viscosity ( $\eta$ ) at 1 Hz were compared with published results of noninvasive intracellular measurement of neutrophils (37). Because the measurements were performed at a higher frequency to allow comparison with the published data, particles chosen for tracking were in focus for at least 100 frames.

**Statistical analysis.** All results are expressed as means  $\pm$  SE. Comparisons of data were carried out using the paired, two-tailed Student's *t*-test, and findings that showed either  $P < 0.05$  or  $P < 0.01$  were considered significant.

**RESULTS**

Neutrophils were introduced into microchannels comprising two different cross-sectional dimensions; a larger cross-sectional area with dimensions of 5  $\mu\text{m}$  in width and 2.5  $\mu\text{m}$  in height, and a second smaller area with channel width of 5  $\mu\text{m}$

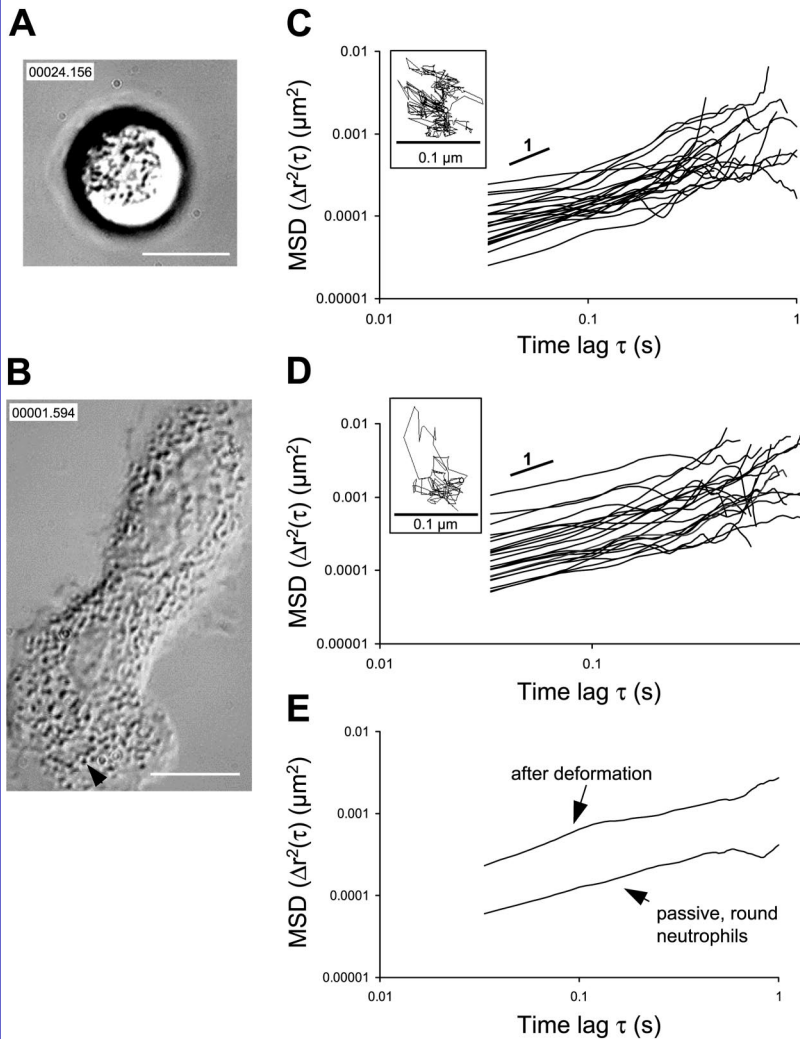


Fig. 5. *A*: image of a round, passive neutrophil. Clearly seen are the endogenous granules in the cytoplasm of the cell. Scale bar, 5  $\mu\text{m}$ . *B*: image of a neutrophil that had spread out on a coverslip showing many endogenous granules dispersed throughout the cytoplasm. As described in MATERIALS AND METHODS, only granules located at least 2  $\mu\text{m}$  away from the nucleus (an example is shown with an arrow) were tracked, whereas granules situated proximal to the nucleus were ignored in the tracking. Scale bar, 5  $\mu\text{m}$ . *C*: individual mean-squared-displacement (MSD) traces of randomly selected endogenous granules for passive, round neutrophils. *Inset*: typical trajectory of the centroid of a granule used to calculate the MSD. *D*: individual MSD traces of randomly selected endogenous granules for neutrophils that have undergone deformation into a microchannel. *Inset*: typical trajectory of the centroid of a granule used to calculate the MSD. *E*: typical plot of average MSD curves for neutrophils before and after exposure to mechanical stimulation.

and height of 1.5  $\mu\text{m}$ . The effective diameter of the microchannels was calculated using the relationship effective diameter =  $\sqrt{4WH/\pi}$ , where  $W$  is width and  $H$  is height, hence, giving us effective diameters of 4.0 and 3.1  $\mu\text{m}$ , denoted by  $D_L$  and  $D_S$ , respectively. Most experiments were carried out at 37°C, but some were also conducted at 23°C to examine the temperature-dependent behavior of the cell. We found experimentally that the threshold pressure for the cell to successfully deform into the microchannels was  $\sim 0.4$  mmH<sub>2</sub>O for  $D_L$ , and  $\sim 2$  mmH<sub>2</sub>O for  $D_S$ . Therefore, different pressure ranges ( $\Delta P$ ) were used for the two channels:  $\Delta P = 1, 10, \text{ and } 50$  mmH<sub>2</sub>O for  $D_L$ ;  $\Delta P = 10 \text{ and } 50$  mmH<sub>2</sub>O for  $D_S$ . The values of  $\Delta P$  chosen were above the threshold pressure for the respective channel diameters but within physiological limits experienced by neutrophils in pulmonary capillaries (16).

Typical trajectories of the granules, individual mean-square displacements, and average mean-square displacement plots for neutrophils before and after mechanical deformation are shown in Fig. 5, *C–E*. A representative sequence of events during neutrophil deformation, followed by trapping and, ultimately, pseudopod formation is depicted in Fig. 6. The location of pseudopod projection occurred randomly (either at the leading or trailing edge of the cell but never at both sites). After

pseudopod formation, the cell would begin to crawl along the microchannel in the direction of the pseudopod protrusion.

An increase in  $\Delta P$  resulted in a decrease in entrance time (Fig. 7) as evidenced, for example, by comparing the data for  $D_L$ , 1 mmH<sub>2</sub>O, 37°C, and  $D_L$ , 10 mmH<sub>2</sub>O, 37°C. Increasing the cross-sectional area of the microchannel produced a similar effect ( $D_S$ , 10 mmH<sub>2</sub>O, 37°C, vs.  $D_L$ , 10 mmH<sub>2</sub>O, 37°C), as was the case when the temperature was raised from 23 to 37°C (e.g.,  $D_L$ , 1 mmH<sub>2</sub>O, 23°C vs.  $D_L$ , 1 mmH<sub>2</sub>O, 37°C).

The time to pseudopod formation is shown in Fig. 8 for different experimental conditions. Pseudopods were observed for  $D_L$ , 1 mmH<sub>2</sub>O and  $D_L$ , 10 mmH<sub>2</sub>O at 37°C, but not for similar conditions at 23°C. Only when  $\Delta P$  was raised to 50 mmH<sub>2</sub>O for the case of  $D_L$ , 23°C, was pseudopod projection observed, and then only after  $\sim 100$  s from the time of cell entry into the channel. For  $D_L$ , 1 mmH<sub>2</sub>O, 23°C and  $D_L$ , 10 mmH<sub>2</sub>O, 23°C, no pseudopod projection was observed even though the cells were monitored for  $> 10$  min.

Because the time to pseudopod activation varied with temperature, we focused on the conditions at 37°C to examine the effect of entrance time. Comparison of experiments carried out at 37°C (Fig. 9) showed a clear inverse correlation between deformation rate (computed as the inverse of entrance time)

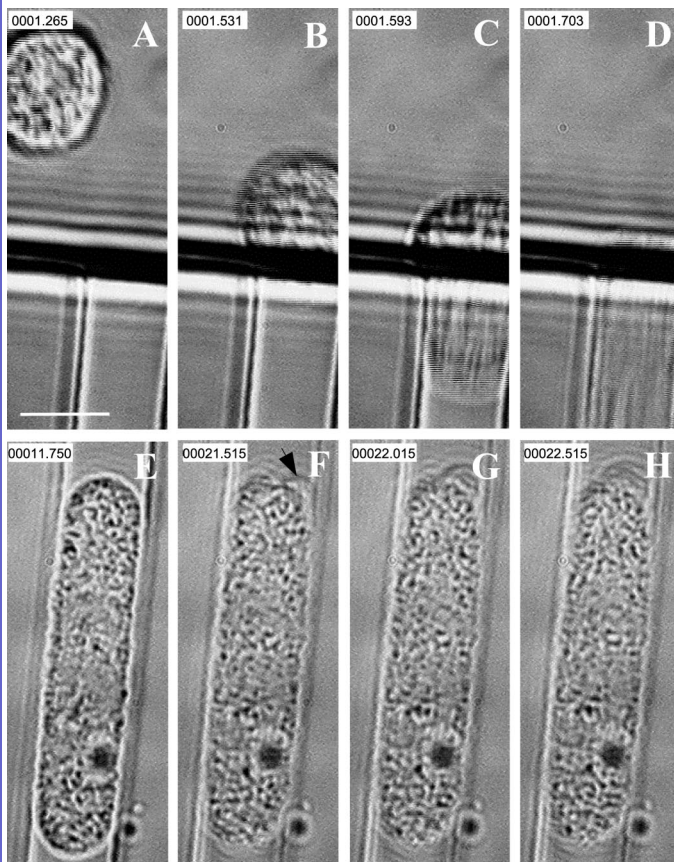


Fig. 6. Image sequence showing a neutrophil flowing toward the microchannel entrance (A), the leading edge of the cell just crossing the channel inlet (B), the cell undergoing deformation (C), the trailing edge of fully deformed cell just clearing the channel mouth (D), and subsequently, the neutrophil was trapped in the channel (E). After some time, the cell can be seen to form a pseudopod projection (F-H). Arrow F points to the location at the trailing edge of the cell where pseudopod protrusion was first seen. Here, the neutrophil was flowing into an effective diameter of 4.0  $\mu\text{m}$  ( $D_L$ ) under a pressure difference of 50  $\text{mmH}_2\text{O}$  at 37°C. Scale bar, 5  $\mu\text{m}$ .

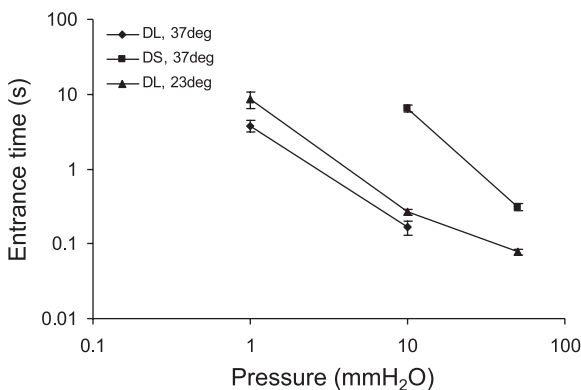


Fig. 7. Entrance time for different experimental conditions. Data are expressed as means  $\pm$  SE. Number of observations for the corresponding experimental conditions are as follows:  $D_L$ , 1  $\text{mmH}_2\text{O}$ , 37°C ( $n = 8$ );  $D_L$ , 10  $\text{mmH}_2\text{O}$ , 37°C ( $n = 8$ );  $D_S$ , 10  $\text{mmH}_2\text{O}$ , 37°C ( $n = 4$ );  $D_S$ , 50  $\text{mmH}_2\text{O}$ , 37°C ( $n = 4$ );  $D_L$ , 1  $\text{mmH}_2\text{O}$ , 23°C ( $n = 5$ );  $D_L$ , 10  $\text{mmH}_2\text{O}$ , 23°C ( $n = 8$ );  $D_L$ , 50  $\text{mmH}_2\text{O}$ , 23°C ( $n = 6$ ).

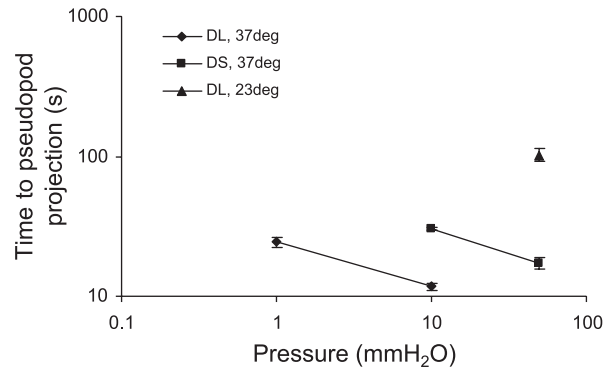


Fig. 8. Time to pseudopod projection for different experimental conditions. Data are means  $\pm$  SE.  $n$  Values for the corresponding experimental conditions are as follows:  $D_L$ , 1  $\text{mmH}_2\text{O}$ , 37°C ( $n = 5$ );  $D_L$ , 10  $\text{mmH}_2\text{O}$ , 37°C ( $n = 8$ );  $D_S$ , 10  $\text{mmH}_2\text{O}$ , 37°C ( $n = 4$ );  $D_S$ , 50  $\text{mmH}_2\text{O}$ , 37°C ( $n = 4$ );  $D_L$ , 50  $\text{mmH}_2\text{O}$ , 23°C ( $n = 5$ ) and  $D_L$ , 10  $\text{mmH}_2\text{O}$ , 23°C ( $n = 6$ ), in which no pseudopod projection was observed even though the cells were monitored for at least 10 min.

and the time of pseudopod formation. These results suggest that neutrophil activation, as reflected by pseudopod formation, will occur more rapidly when neutrophils are subjected to a higher rate of deformation.

To investigate the effects of mechanical deformation on the viscoelastic properties of neutrophils, we used the multiple-particle-tracking method. The technique was first applied to adherent and spread neutrophils (Fig. 5B). Measurements at 1 Hz (see Table 1) revealed a  $G'$  of  $43.8 \pm 5.0 \text{ dyn/cm}^2$  and  $\eta$  of  $2.2 \pm 0.3 \text{ dyn}\cdot\text{s}\cdot\text{cm}^{-2}$ . Round, passive neutrophils introduced into the glass-slide coverslip chamber and allowed to settle on the coverslip were also studied. Due to the presence of plasma in their surrounding medium, the majority of the neutrophils (~98%) remained round (Fig. 5A) and free of pseudopod projection. Some of these adhered nonspecifically to the coverslip, whereas the rest floated loosely at the bottom of the chamber. Because the round, adherent cells remained stationary, they were chosen for particle tracking. The viscoelastic values of neutrophils were  $G' = 242 \pm 21 \text{ dyn/cm}^2$  and  $G'' = 470 \pm 40 \text{ dyn}\cdot\text{cm}^{-2}$  at 37°C, as summarized in Table 1. These values were significantly lower ( $P < 0.05$ ) than the viscoelastic moduli at 23°C ( $G' = 303 \pm 19 \text{ dyn/cm}^2$  and  $G'' = 649 \pm 55 \text{ dyn}\cdot\text{cm}^{-2}$ ), highlighting the effect of temperature on the mechanical properties of the cell.

To study the effect of mechanical deformation on the viscoelastic properties of neutrophils, particle tracking was performed once the cells had entered the microchannel. The experiments were carried out at 37°C. The motion of neutro-

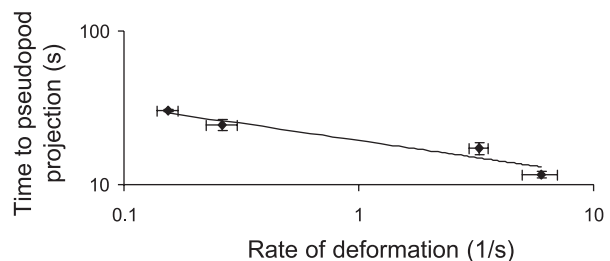


Fig. 9. Effect of rate of deformation on time to pseudopod projection for neutrophils at 37°C.

Table 1. Measurements of  $G'$ ,  $G''$ , and  $G''/G'$ 

	$G'$ , dyn/cm <sup>2</sup>	$G''$ , dyn/cm <sup>2</sup>	$G''/G'$
Adherent, spreading neutrophil, 37°C ( $n = 4$ ; $N = 70$ )	44	14	0.32
Passive, round neutrophil, 37°C ( $n = 4$ ; $N = 51$ )	242	470	1.9
Passive, round neutrophil, 23°C ( $n = 4$ ; $N = 71$ )	303	649	2.1

Elastic modulus ( $G'$ ), loss modulus ( $G''$ ), and their ratio ( $G''/G'$ ), at 1 Hz, of adherent spread neutrophils at 37°C and passive, round neutrophils at 37°C and 23°C.  $n$ , Number of cells;  $N$ , number of granules.

phil granules was monitored as soon as the cell was immobilized and the image focused. Tracking continued until the first observation of pseudopod projection, beyond which the cell began to crawl and granular motion became erratic, complicating the analysis. The temporal changes in  $G'$  and  $G''$  for the different flow conditions are shown in Figs. 10 and 11, respectively. With the use of values obtained for passive, round neutrophils (Table 1) as controls, the data show that mechanical deformation causes a significant drop ( $P < 0.05$ ) in  $G'$  and  $G''$ . For all flow conditions, the mean value of  $G'$  was reduced by ~50–60% from its predeformation value of 242 dyn/cm<sup>2</sup>. Similarly, the mean value of  $G''$  was reduced by ~35–50% after deformation. Interestingly, although mechanical deformation resulted in a softer and less viscous cytoplasm, the drop in magnitude of  $G'$  and  $G''$  was quantitatively similar and independent of the degree of deformation. For the flow conditions of  $D_L$  at 1 (37°C) and 10 mmH<sub>2</sub>O (37°C) and  $D_S$  at 50 mmH<sub>2</sub>O (37°C), the cell maintained the softer, lower  $G''$  until pseudopod projections appeared. However, for the flow condition of  $D_S$  at 10 mmH<sub>2</sub>O (37°C) after the initial drop,  $G'$  and  $G''$  were

seen to recover to roughly their predeformation values before pseudopod projection. This flow condition corresponded to the case of lowest rate of deformation in Fig. 9.

Although quantitative particle tracking was not possible once the neutrophils begin to crawl, observation of random granule motion of the neutrophils showed periodic cycling of enhanced and reduced motion paralleling the cyclic projection of pseudopods during cell locomotion. The granules at the pseudopod leading edge were seen to have increased activity when a new wave of granules first flowed into the pseudopod; however, the granule activity soon diminished and remained low even during the next cycle of pseudopod projection. Only after the new pseudopod had fully extended would granular motion increase again when the next wave of granules entered the newly formed pseudopod. These observations are consistent with those seen in neutrophils locomoting on a flat substrate (37).

## DISCUSSION

This study provides direct evidence that mechanical force of a magnitude comparable to that encountered by a neutrophil during transit through the microcirculation exerts a strong and fundamental effect on cell structure and function. The consequences of mechanical stimulation are immediate, occurring within seconds of stimulation, and substantial. A drop in shear modulus by >60% is observed within seconds of entering a constriction, independent of magnitude of the stimulus. In contrast, pathways leading to migratory behavior are excited in a strain rate-dependent manner, suggesting that these two phenomena may be independently controlled. Taken together, these results suggest an important role for mechanical stimu-

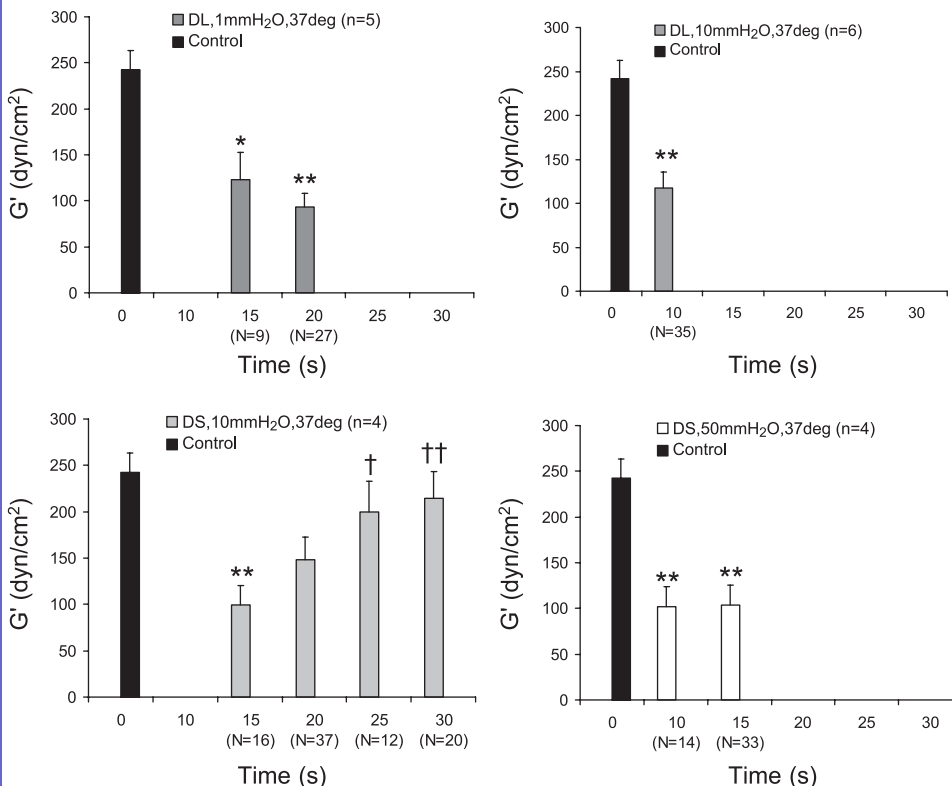


Fig. 10. Temporal change in elastic modulus ( $G'$ ) of neutrophil after mechanical deformation into a microchannel at a lag time of 0.03 s. Graphs show changes in  $G'$  under different flow conditions at 37°C. Time = 0 s represents the instance when the leading edge of the cell had just crossed the channel inlet. The time at which  $G'$  could first be recorded varied due to dissimilar entrance time for the different flow conditions. Value of  $G'$  for passive, round neutrophils at 37°C (Table 1) serves as control. Data are means  $\pm$  SE.  $n$ , Number of cells;  $N$ , no. of granules. \* $P < 0.05$  and \*\* $P < 0.01$  compared with control; † $P < 0.05$  and †† $P < 0.01$  compared with data at time = 15 s.

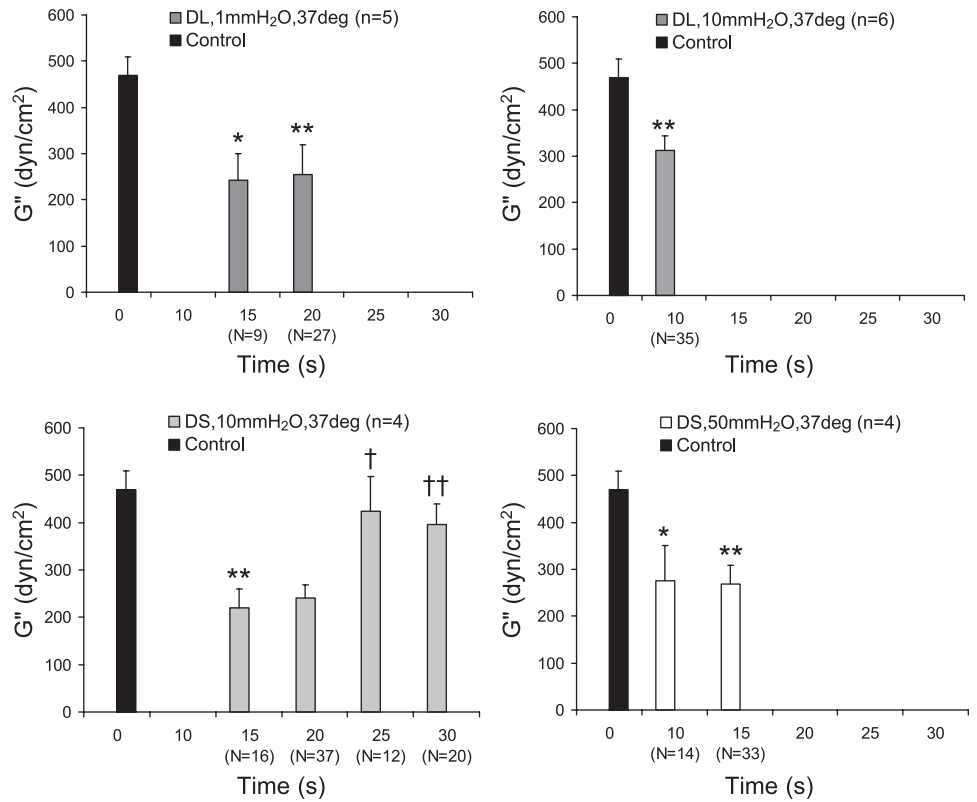


Fig. 11. Temporal change in loss modulus ( $G''$ ) of neutrophil after mechanical deformation into a microchannel at a lag time of 0.03 s. Graphs show changes in  $G''$  under different flow conditions at 37°C. Time = 0 s represents the instance when the leading edge of the cell had just crossed the channel inlet. The time at which  $G''$  could be first recorded varied due to dissimilar entrance time for the different flow conditions. Value of  $G''$  for passive, round neutrophils at 37°C (Table 1) serves as control. Data are means  $\pm$  SE. \* $P < 0.05$  and \*\* $P < 0.01$  compared with control; † $P < 0.05$  and †† $P < 0.01$  compared with data at time = 15 s.

lation of neutrophils, influencing both their rheology and their migratory tendencies.

The combination of microfabrication and particle tracking microrheology allowed us to simultaneously visualize and quantify the response of neutrophils. Previous studies of neutrophil deformation have been conducted using in vitro filtration (7, 21, 31) or micropipette aspiration (6, 30). In the former, large cell numbers enabled studies of changes in deformabilities and biochemical analysis of the changes in F-actin content and free intracellular  $Ca^{2+}$  concentration, for example, but direct rheological measurements were not possible. Micropipette experiments provide data on cell rheology, determined from entrance times, but provide limited data on time-dependent changes in viscoelastic properties or changes in specific cell constituents. Analysis of the thermal motions of endogenous granules would be difficult in this situation due to the requirement of high-resolution optics. In particular, methods used previously to infer rheological properties from micropipette aspiration times assume that the rheological parameters are constant in time and unaffected by the mechanical forces imposed during manipulation of the cell. Our results suggest that this may not be a valid assumption.

The microfluidic device was coupled to a macrofluidic system consisting of a set of reservoirs. Pressure difference was imposed across the microchannel by varying the height of water in the reservoirs. The threshold pressure ( $\Delta P_{thr}$ ) for  $D_L$  and  $D_S$  in the experiment was compared with the theoretical expression  $\Delta P_{thr} = 4\gamma[(1/D_{pipette}) - (1/D_{cell})]$ , where  $D_{pipette}$  is the diameter of the pipette,  $D_{cell}$  is the cell diameter, and the cell cortical tension ( $\gamma = 35$  pN/ $\mu$ m) has been measured previously (39). Due to the rectangular cross section used in the present experiments, we can make only an approximate

comparison by substituting effective diameter for  $D_{pipette}$ . Doing so, we find that the experimentally measured values of  $\Delta P_{thr}$  (0.4 and 2.0 mmH<sub>2</sub>O for the large and small channels, respectively) are somewhat lower than the theoretically predicted values of 1.9 and 2.7 mmH<sub>2</sub>O, but this difference could be attributable to the different cross-sectional shape or entrance geometry. In contrast, entrance times observed in the present experiments were  $\sim 40$  times smaller than those reported in the literature for micropipette aspiration under similar driving pressures and diameters. Cross-sectional shape might also influence entrance times, but the entrance geometry also likely contributes. Previous numerical simulations have shown that entrance times depend strongly on the axial radius of curvature of the entrance (1). This would be consistent with the observation that the entrance to our microchannels tends to be somewhat more rounded than that of a micropipette. However, aside from a slight lowering of the threshold pressure and shorter entrance times, the effects of driving pressure, channel cross-sectional area, and temperature (Fig. 7) are generally consistent with previously published results (8).

Mechanical deformation of neutrophils into the pulmonary capillaries induced pseudopod formation for all experimental conditions at 37°C but only at the higher values of  $\Delta P$  for experiments at 23°C (Fig. 8). Comparing similar experimental conditions, it took considerably longer for pseudopod projection at the lower temperature (10–30 s at 37°C and  $\sim 100$  s at 23°C). Furthermore, the results indicate that, for a given temperature, the time to pseudopod projection is inversely correlated to the rate of deformation of the neutrophil (Fig. 9), which we use here as a measure of the stimulus magnitude. These results are consistent with observations of activation reported in a previous micropipette aspiration study (8) that

reported a transition from passive to active motile state, with activation time varying between 0 and 120 s at 37°C and between 60 and 120 s at 23°C. Hence, our results confirm that mechanical deformation is not a passive event; rather, it leads to neutrophil activation with pseudopod formation if the stimulus is sufficiently large. Above the threshold stimulus, it appears that the time required for activation is dependent on the rate of deformation experienced by the cell, implying the existence of a mechanosensing or signal transduction mechanism in the cell that is able to modulate the response according to the magnitude of the mechanical stimulus. In contrast, we found that neutrophil entrance time behaved in a manner more consistent with a passive cell in that it was determined primarily by the initial value of the shear modulus, which was only slightly dependent on temperature. (Fig. 7).

Our measurements of viscoelastic moduli of adherent, spread neutrophils obtained using the particle tracking system (Table 1) can be compared with published results of Yanai et al. (37), who reported mean values of  $G' = \sim 10 \text{ dyn/cm}^2$  and viscosity  $\eta = \sim 4.0 \text{ dyn}\cdot\text{s/cm}^2$  for the body and trailing region of the neutrophil using an optical trap to excite the granules at frequencies between 0.3 and 3 Hz. Our measurements for  $\eta$  matched closely with the previously published results, whereas the value for  $G'$  was about four times higher. One potential explanation for this difference is that the optical trap technique was capable of measuring only those granules that were freely moving, whereas other particles were too stiff to be oscillated at maximum laser power.

Table 1 also shows the ratio of  $G''$  to  $G'$  for the measurements carried out on adherent, spread neutrophils and those for passive, round cells at 37 and 23°C. Our value of  $G''$ -to- $G'$  ratio of 0.32 for adherent, spread neutrophils matches the value of  $\sim 0.3$  obtained at 0.75 Hz using magnetic twisting cytometry (10). However, there are no similar figures reported in the literature for passive, round cells. Nevertheless, the values of  $G''$ -to- $G'$  ratio of  $\sim 2.0$  for passive, round cells is within the limits of the values (0.25–20) reported for other cell types using various experimental techniques (10, 34, 36).

To gain further insight into the effects of mechanical deformation on the cytoskeletal structure of the neutrophil, the granules of the neutrophils were tracked to monitor the change in rheology of the cell before and after deformation. Mechanical deformation results in a reduction in elastic moduli by 50–60%, within 10–15 s after the initial stimulus, from its value as a passive, round cell before deformation (Figs. 10 and 11). Similarly, the loss moduli drop by 35–50% from the unactivated values of the cells. These data demonstrate that mechanical deformation causes either disruption or remodeling of the neutrophil cytoskeleton. In view of the decrease in viscoelastic properties of the cell, this might be due either to a sudden depolymerization of filamentous actin or rupture of cross-links bridging between actin filaments. The lack of a significant temperature effect on entrance time, in combination with the short time scale of the modulus changes ( $\sim 10$  s), leads us to favor the theory that the rapid deformation ruptures actin cross-links. In contrast, Kitagawa and coworkers (21) observed an immediate but short-lived increase in F-actin, leading them to conclude that mechanical deformation resulted in an increase in actin cross-linking events rather than actin polymerization. Further experiments are required to reconcile these seemingly contradictory results.

Another interesting observation is that the magnitude of drop in the values of  $G'$  and  $G''$  after deformation was found to be independent of the degree of deformation. This is in contrast with the time to pseudopod formation, which correlates with the rate of deformation. Also, neutrophils subjected to low deformation rates were observed to recover much of their modulus reduction within  $\sim 30$  s and return nearly to their initial mechanical state. These data suggest that the extent of depolymerization or loss of actin cross-linking is similar regardless of the magnitude or rate of deformation, at least within the range of these experiments, but the initiation of actin polymerization to form pseudopods is dependent on the magnitude of force transduced. One scenario consistent with these observations is that the large strain deformations effectively shear and rupture many of the actin cross-links, leaving them attached to one filament but displaced relative to their initial cross-linking site. Once the deformation stops, these cross-links can reform but do so in the new, deformed state, returning the cell to its initial mechanical state but in a new, deformed geometry. Thus it appears that the molecular mechanism controlling the depolymerization/actin cross-link breakdown is separate from the mechanism governing pseudopod formation and viscoelastic recovery; however, further experiments would be needed to confirm this.

This evidence of viscoelastic recovery could help explain results from neutrophil recovery experiments after deformation into micropipettes (32). In that study, neutrophils were aspirated fully into a micropipette and held for various periods of time before being expelled. Cells held in the micropipette for a short time ( $< 5$  s) exhibited a rapid elastic rebound immediately after being expelled from the pipette. In contrast, neutrophils held for longer times ( $> 5$  s) displayed a smoother recovery and took much longer to recover to their spherical shape ( $\sim 75$  s to reach 90% of its full recovery compared with  $\sim 55$  s for the short holding time). These observations can be explained on the basis of the rapid fall and slower recovery of modulus after deformation observed in the present experiments. Cells ejected immediately after being aspirated would have a low internal modulus and few cross-links; thus their surface tension could rapidly return the cell to a spherical shape. Cells held for a longer period would remodel due to reformation of actin cross-links; on ejection, the cell would need to remodel once again but this time under the action of a much smaller restoring force that was due to surface tension alone.

We recognize that the multiple particle tracking technique used in this investigation has limitations, especially compared with the recently developed method of two-particle microrheology (4, 11). In multiple particle tracking, granule size must be estimated, introducing error (a factor of  $\sim 2$ ) into the viscoelastic modulus obtained. In two-particle microrheology, the cross-correlated motion of pairs of particles is independent of particle size and shape and is unaffected by the coupling between the particles and the medium. Unfortunately, measurement by the two-particle technique requires data collection over a much longer period of time than the multiple particle tracking method, hence preventing us from monitoring temporal changes in the cell. The two-particle microrheology technique is more suitable for measurements where the behavior of the cells is relatively unchanged over the period of data collection (25). Thus we resort to the multiple particle tracking method in the present study, and in the application of this technique, we



maximized the accuracy of the results by eliminating granules that are not circular and also by selecting granules of almost equal size. Because active motion can only cause an apparent reduction in modulus (greater granular motion), however, these results represent a lower bound on modulus.

In summary, this study shows that mechanical deformation of neutrophils into pulmonary capillaries results in activation of the cell by inducing cytoskeletal remodeling, leading to changes in viscoelastic properties and pseudopod projection. Hence, mechanical deformations are capable of activating a neutrophil, providing a migratory stimulus and thereby enhancing their tendency to transmigrate across the endothelium.

#### APPENDIX

The design of the microchannel was drawn in AutoCAD (Autodesk, San Rafael, CA) for fabrication on chromium masks (Photronics, Brookfield, CT) (Fig. 1). The fabrication of the master utilized the technique of two-level photolithography. Silicon wafers [100 mm, 425–525  $\mu\text{m}$ , 1–10  $\Omega$  (1-0-0); Transition Technology International, Sunnyvale, CA] were spin-coated with the first layer of SU-8 2002 photoresist (Microchem, Newton, MA) to a thickness of either 1.5 or 2.5  $\mu\text{m}$ , and prebaked at 95°C for 2 min. The resist was then exposed to ultraviolet light with an intensity of 10 mW/cm<sup>2</sup> for 11.5 s through the first chromium mask with features of the microchannel and the reservoirs. The resist was postbaked at 95°C for 2 min, which cross-linked the regions exposed to ultraviolet light. Next, a second layer of SU-8 2010 photoresist was spin-coated to a thickness of 15  $\mu\text{m}$  on top of the first layer, followed by prebaking at 95°C for 4 min. The second chromium mask with features of the reservoirs only was aligned, and the photoresist was exposed for 20 s. After postbaking again at 95°C for 3 min, SU-8 developer (Microchem) was used for 5 min to develop the features in both resist layers. Finally, the height of the microchannel was checked with a profilometer (Dektak 2, Veeco Instruments, Woodbury, NY).

When the master was successfully fabricated, the device was formed in PDMS by replica molding. The master of photoresist was first treated with trimethylchlorosilane (Sigma-Aldrich, St. Louis, MO) to prevent adhesion of PDMS to the master after curing. A curing agent and PDMS prepolymer (SYLGARD 184 Silicone Elastomer Kit, Dow Corning, Midland, MI) were mixed together and degassed for 5 min to remove air bubbles. The mixture was then poured onto the master and cured in an oven at 80°C for 3 h. When cured, the PDMS was removed by peeling off the master. Inlet and outlet reservoir ports were formed by punching the PDMS with a 16-gauge adapter needle. Through these bored tunnels, inlet and outlet tubes would later be inserted, which allowed connection of the microfluidic device to the external macrofluidic system.

The final step involved sealing the PDMS to a glass coverslip. The coverslip was also spin-coated with a thin layer of the same PDMS elastomer and cured in the oven. Both the microdevice and the coverslip were subjected to plasma oxidation for 30 s (Plasma Cleaner, Harrick Scientific, Ossining, NY), after which the surfaces were brought together to form an irreversible seal and produce the finished device (Fig. 2).

#### ACKNOWLEDGMENTS

The authors thank Thierry Savin and Patrick S. Doyle for assistance with particle tracking, Jorge M. Ferrer and Matthew J. Lang for microscopy assistance, and Hayden Huang for cell preparation.

#### GRANTS

Support from the National Heart, Lung, and Blood Institute (P01 HL-64858), a Whitaker Foundation Graduate Student Fellowship, and National University of Singapore Overseas Graduate Scholarship (to B. Yap) is gratefully acknowledged.

#### REFERENCES

1. **Bathe M, Shirai A, Doerschuk CM, and Kamm RD.** Neutrophil transit times through pulmonary capillaries: the effects of capillary geometry and fMLP-stimulation. *Biophys J* 83: 1917–1933, 2002.
2. **Coughlin MF and Schmid-Schonbein GW.** Pseudopod projection and cell spreading of passive leukocytes in response to fluid shear stress. *Biophys J* 87: 2035–2042, 2004.
3. **Crocker JC and Grier DG.** Methods of digital video microscopy for colloidal studies. *J Colloid Interface Sci* 179: 298–310, 1996.
4. **Crocker JC, Valentine MT, Weeks ER, Gisler T, Kaplan PD, Yodh AG, and Weitz DA.** Two-point microrheology of inhomogeneous soft materials. *Phys Rev Lett* 85: 888–891, 2000.
5. **Doerschuk CM, Beyers N, Coxson HO, Wiggs B, and Hogg JC.** Comparison of neutrophil and capillary diameters and their relation to neutrophil sequestration in the lung. *J Appl Physiol* 74: 3040–3045, 1993.
6. **Dong C, Skalak R, and Sung KLP.** Cytoplasmic rheology of passive neutrophils. *Biorheology* 28: 557–567, 1991.
7. **Downey GP, Doherty DE, Schwab B, Elson EL, Henson PM, and Worthen GS.** Retention of leukocytes in capillaries—role of cell-size and deformability. *J Appl Physiol* 69: 1767–1778, 1990.
8. **Evans E and Kukan B.** Passive material behavior of granulocytes based on large deformation and recovery after deformation tests. *Blood* 64: 1028–1035, 1984.
9. **Evans E and Yeung A.** Apparent viscosity and cortical tension of blood granulocytes determined by micropipet aspiration. *Biophys J* 56: 151–160, 1989.
10. **Fabry B, Maksym GN, Butler JP, Glogauer M, Navajas D, and Fredberg JJ.** Scaling the microrheology of living cells. *Phys Rev Lett* 87: 148102-1–148102-4, 2001.
11. **Gardel ML, Valentine MT, Crocker JC, Bausch AR, and Weitz DA.** Microrheology of entangled F-actin solutions. *Phys Rev Lett* 91: 158302, 2003.
12. **Gebb SA, Graham JA, Hanger CC, Godbey PS, Capen RL, Doerschuk CM, and Wagner WW.** Sites of leukocyte sequestration in the pulmonary microcirculation. *J Appl Physiol* 79: 493–497, 1995.
13. **Hogg JC.** Neutrophil kinetics and lung injury. *Physiol Rev* 67: 1249–1295, 1987.
14. **Hogg JC, Coxson HO, Brumwell ML, Beyers N, Doerschuk CM, Macnee W, and Wiggs BR.** Erythrocyte and polymorphonuclear cell transit-time and concentration in human pulmonary capillaries. *J Appl Physiol* 77: 1795–1800, 1994.
15. **Huang HD, Kamm RD, and Lee RT.** Cell mechanics and mechanotransduction: pathways, probes, and physiology. *Am J Physiol Cell Physiol* 287: C1–C11, 2004.
16. **Huang YQ, Doerschuk CM, and Kamm RD.** Computational modeling of RBC and neutrophil transit through the pulmonary capillaries. *J Appl Physiol* 90: 545–564, 2001.
17. **Ingber DE.** Mechanobiology and diseases of mechanotransduction. *Ann Med* 35: 564–577, 2003.
18. **Jo BH, Van Lerberghe LM, Motsegood KM, and Beebe DJ.** Three-dimensional micro-channel fabrication in polydimethylsiloxane (PDMS) elastomer. *J Microelectromech Sys* 9: 76–81, 2000.
19. **Jo S and Park K.** Surface modification using silanated poly(ethylene glycol)s. *Biomaterials* 21: 605–616, 2000.
20. **Juncker D, Schmid H, Bernard A, Caelen I, Michel B, de Rooij N, and Delamarque E.** Soft and rigid two-level microfluidic networks for patterning surfaces. *J Micromech Microengin* 11: 532–541, 2001.
21. **Kitagawa Y, VanEeden SF, Redenbach DM, Daya M, Walker BAM, Klut ME, Wiggs BR, and Hogg JC.** Effect of mechanical deformation on structure and function of polymorphonuclear leukocytes. *J Appl Physiol* 82: 1397–1405, 1997.
22. **Kitayama J, Hidemura A, Saito H, and Nagawa H.** Shear stress affects migration behavior of polymorphonuclear cells arrested on endothelium. *Cell Immunol* 203: 39–46, 2000.
23. **Kole TP, Tseng Y, Huang L, Katz JL, and Wirtz D.** Rho kinase regulates the intracellular micromechanical response of adherent cells to rho activation. *Mol Biol Cell* 15: 3475–3484, 2004.
24. **Kole TP, Tseng Y, Jiang I, Katz JL, and Wirtz D.** Intracellular mechanics of migrating fibroblasts. *Mol Biol Cell* 16: 328–338, 2005.
25. **Lau AWC, Hoffman BD, Davies A, Crocker JC, and Lubensky TC.** Microrheology, stress fluctuations, and active behavior of living cells. *Phys Rev Lett* 91: 2003.

26. **Mason TG, Ganesan K, van Zanten JH, Wirtz D, and Kuo SC.** Particle tracking microrheology of complex fluids. *Phys Rev Lett* 79: 3282–3285, 1997.
27. **McDonald JC, Duffy DC, Anderson JR, Chiu DT, Wu HK, Schueller OJA, and Whitesides GM.** Fabrication of microfluidic systems in poly-(dimethylsiloxane). *Electrophoresis* 21: 27–40, 2000.
28. **Moazzam F, Delano FA, Zweifach BW, and Schmidsonbein GW.** The leukocyte response to fluid stress. *Proc Natl Acad Sci USA* 94: 5338–5343, 1997.
29. **Needham D and Hochmuth RM.** Rapid flow of passive neutrophils into a 4  $\mu$ -M pipette and measurement of cytoplasmic viscosity. *J Biomech Eng* 112: 269–276, 1990.
30. **Schmid-Schonbein GW, Sung KLP, Tozeren H, Skalak R, and Chien S.** Passive mechanical-properties of human-leukocytes. *Biophys J* 36: 243–256, 1981.
31. **Selby C, Drost E, Wraith PK, and Macnee W.** In vivo neutrophil sequestration within lungs of humans is determined by in vitro filterability. *J Appl Physiol* 71: 1996–2003, 1991.
32. **Transontay R, Needham D, Yeung A, and Hochmuth RM.** Time-dependent recovery of passive neutrophils after large deformation. *Biophys J* 60: 856–866, 1991.
33. **Tsai MA, Frank RS, and Waugh RE.** Passive mechanical-behavior of human neutrophils—power-law fluid. *Biophys J* 65: 2078–2088, 1993.
34. **Tseng Y and Wirtz D.** Mechanics and multiple-particle tracking microheterogeneity of alpha-actinin-cross-linked actin filament networks. *Biophys J* 81: 1643–1656, 2001.
35. **Whitesides GM, Ostuni E, Takayama S, Jiang XY, and Ingber DE.** Soft lithography in biology and biochemistry. *Annu Rev Biomed Eng* 3: 335–373, 2001.
36. **Yamada S, Wirtz D, and Kuo SC.** Mechanics of living cells measured by laser tracking microrheology. *Biophys J* 78: 1736–1747, 2000.
37. **Yanai M, Butler JP, Suzuki T, Kanda A, Kurachi M, Tashiro H, and Sasaki H.** Intracellular elasticity and viscosity in the body, leading, and trailing regions of locomoting neutrophils. *Am J Physiol Cell Physiol* 277: C432–C440, 1999.
38. **Yanai M, Butler JP, Suzuki T, Sasaki H, and Higuchi H.** Regional rheological differences in locomoting neutrophils. *Am J Physiol Cell Physiol* 287: C603–C611, 2004.
39. **Yeung A and Evans E.** Cortical shell-liquid core model for passive flow of liquid-like spherical cells into micropipets. *Biophys J* 56: 139–149, 1989.

